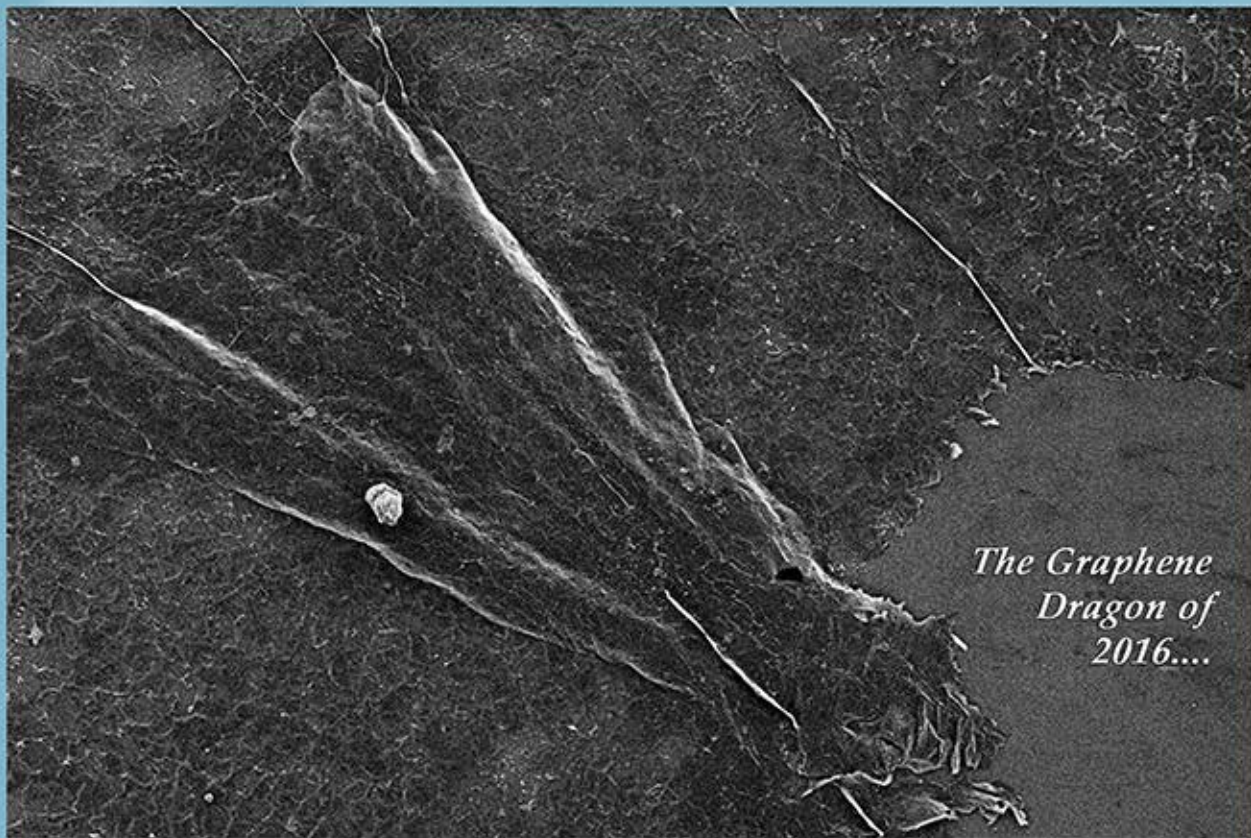


2015-2016 CORNELL NANOSCALE FACILITY RESEARCH ACCOMPLISHMENTS



*The Graphene
Dragon of
2016....*

2 μ m


WD = 1.8 mm

Aperture Size = 30.00 μ m

Width = 56.25 μ m

Signal A = InLens

Mag = 4.52 K X

EHT = 0.800 kV

Pixel Size = 54.94 nm

Signal B = InLens

CNF



250 Duffield Hall
343 Campus Road
Ithaca NY 14853-2700

Phone: 607.255.2329 • Fax: 607.255.8601
Email: information@cnf.cornell.edu • Web Site: www.cnf.cornell.edu

**CNF LESTER B. KNIGHT DIRECTOR:
CHRISTOPHER OBER**

**DIRECTOR OF OPERATIONS:
DONALD TENNANT**

**CNF IS A MEMBER OF THE
NATIONAL NANOTECHNOLOGY
COORDINATED INFRASTRUCTURE**
(www.nnci.net)

and is supported by:
The National Science Foundation,
the New York State Office of Science, Technology and Academic Research,
Cornell University, Industry, and our Users.

*The 2015-2016 CNF Research Accomplishments
are also available on the web as secure PDF documents:
http://www.cnf.cornell.edu/cnf_2016cnfra.html*

© 2016

**CORNELL NANOSCALE SCIENCE & TECHNOLOGY FACILITY
:: 2015-2016 RESEARCH ACCOMPLISHMENTS ::**

TABLE OF CONTENTS

TECHNICAL REPORTS BY SECTIONII-IV
DIRECTORS' INTRODUCTION V-VIII
2015 PATENTS, PRESENTATIONS & PUBLICATIONS IX-XX
PHOTOGRAPH CREDITS XX
ABBREVIATIONS & MEANINGS ... XXI-XXVI
TECHNICAL REPORTS 2-203
INDEXES 204-208

BIOLOGICAL APPLICATIONS, 2-55

Retinal Implant Project... .. 2	Design and Application of Microfluidic Devices to Study Cell Migration in Confined Environments. 30
Body-on-a-Chip Models for Drug Screening.. ... 4	Micro-Fabricated Sample Holder for Cryogenic Small Angle X-Ray Scattering Experiments ..32
Microfluidic Device for Aptamer-Based Cancer Cell Capture and Genetic Mutation Detection 6	Near-Field Optical Trapping for High-Throughput Nanoparticle Analysis... ..34
Microfluidic Device for Single Cell Genetic and Epigenetic Analysis.. ... 8	Fabrication of DNA Stabilizing Nanofluidic Channels for High-Resolution Optical Imaging of Transcription <i>in vitro</i> .. 36
Scalable Sensor Array Platform for Analysis of Quantal Transmitter Release Events10	Microfabricated Devices for Cell Organization 38
A MEMS Microtensiometer for Sensing Water Potential in Plants and Soils 12	Temporal Correlation Between SNARE Conformational Change and Vesicle Fusion 40
Silicon Nitride Cantilevers for Muscle Myofibril Force Measurements14	Deoxyribonucleic Acid (DNA)-Based Organic Light-Emitting Diode Device Fabrication... ..42
Biomimetic Models of the Tumor Microenvironment and Angiogenesis16	Microfluidic Chip for Drop-seq Platform44
Patterned Surfaces for Studying IgE Receptor Mediated Signaling and Plasma Membrane Trafficking..18	Etching Micropatterns on Si Wafers towards PDMS Protein Casting on Hydrogels..46
Progress Towards Achieving Nanophotonic Trapping for Precise Manipulation of Biomolecular Arrays on Si ₃ N ₄ Waveguides. ..20	Manufacture of SU-8 Microfluidic Channel Molds for the Study of Biofilms in Bioelectrochemical Systems... .. 48
Generalized Microfluidic Immunosensor for Antibody Detection... .. 22	New Approaches to Elucidate the Structure of the Tomato Fruit Cuticle 50
KS-Detect: A Solar Thermal Microfluidic PCR Platform for Health Diagnostics in Resource Limited Settings. 24	Handheld Chem/Biosensor Combining Metasurfaces and Engineered Sensor Proteins to Enhance SPR... .. 52
Fabrication of Elastomeric Microposts with Step-Changes in Rigidity..26	Creating an On-Chip and High Throughput Alternative to Optical Tweezers 54
Ultra-Thin Glass Windows for Biological Small Angle X-Ray Scattering28	

CHEMISTRY, 56-63

Modified Co-Planar Waveguides for Investigating Organic Semiconductors using MRFM.	56
Chemical Bonding Across the Periodic Table at High and Ambient Pressures ...	58
Mid-Infrared Transparent Substrate for Alkylsiloxane Monolayers... ..	60
Micrometer-Scale Coplanar Waveguides for Nanoscale Magnetic Resonance Imaging ...	62
Charge Injection in Boron Nitride Nanosheets.. ...	64

ELECTRONICS, 64-85

Electro Static Quadrupole Fabrication Using Silicon... ..	66
Silicon Dioxide and Polymer-Based Transient Electronics with Rubidium Fuel for Electrical to Thermal Energy Amplification.	68
Novel Electronic and Optoelectronic Devices Using Layered Materials.	70
GaN-on-GaN p-n Power Diodes with $BV > 3.48$ kV and $R_{on} = 0.95$ m Ω ·cm ² : A Record High Figure-of-Merit of 12.8 GW/cm ²	72
Vertical Ga ₂ O ₃ Schottky Barrier Diodes on Single-Crystal β -Ga ₂ O ₃ <-201> Substrates ...	74
Fabrication of High Voltage Vertical GaN Schottky Barrier Diodes	76
Two-Dimensional Heterojunction Interlayer Tunneling FET Process Development.. ...	78
Extreme Electron Density Devices	80
Processing and Characterization of Wide-Bandgap Oxide Semiconductor Materials and Devices.	82
Surface Acoustic Wave Devices with Piezoresistive Graphene Pickup... ..	84

MATERIALS, 86-111

Millisecond Crystallization Kinetics of InGaO ₃ (ZnO) _m	86
Recent Progress in Nanoparticle Photoresist Development for EUV Lithography.	88
Oxide Nanoparticle EUV Photoresist Studies ..	90
Electrical Annealing of Thin Films Using Nanocalorimetry	92
Confinement & Template Assisted Assembly of Functional Colloids.	94

Mimicry of Biological Adhesion Through Fabrication of Fibrillar Surfaces	96
Block Copolymer-Directed Gyroidal Mesoporous Superconductors	98
Investigation on Hydrogen Diffusivity in Palladium-Based Alloys.	100
Charge Transport and Localization in Atomically Coherent Quantum Dot Solids	102
Nanostructured Polymer Brush.	104
Genetically Designed Photonic Crystal Nanocavities	106
Immobilization of Cubic Boron Nitride Particles on Silicon and Quartz Substrates	108
Silicon-Based Anti-Reflection Coating for Terahertz Optics.	110

MECHANICAL DEVICES, 112-129

Thermal Effects in One- and Two- Dimensional Micro-Electro-Mechanical Resonators.	112
Self-Folding with Graphene Bimorphs	114
Near Zero Power Electrostatic Switches	116
Micro Components for Self-Calibrating Inertial Sensors.. ...	118
Particle Fabrication for Rheology Measurement of Structured Suspensions... ..	120
HBAR as a High Frequency High Stress Generator.	122
The Nanoaquarium; A Device for <i>in situ</i> Electron Microscopy of Processes in Liquids	124
Fabrication of Holey SiN Membranes	126
High Temperature Near-Field Thermal Rectifier.	128

OPTICS &

OPTO-ELECTRONICS, 130-147

Nano-Optomechanical Devices and Applications... ..	130
High Visibility Time-Energy Entangled Photon Pairs from a Si Microdisk Resonator	132
Label-Free Characterization of Protein Aggregates and Nanoparticles Using Near-Field Light Scattering Microscopy	134
Fabrication of Silicon SPADs	136
Titanium Dioxide Enables Visible Integrated-Evanescent Raman Sensors	138

OPTICS, CONTINUED

Fabrication of Custom Diffractive
Fourier Optics Devices for Functional
Neuronal Imaging Using
Extended Volume MFM 140

Pixelated Polarizer for IR Focal Plane Array... 142

Making Silicon Grating Test Samples
for Scatterometry System 144

Fabricating Self-Rolling Microtubes
for Tuning Semiconductor Bandgaps 146

PHYSICS &

NANOSTRUCTURE PHYSICS, 148-185

Nanosecond-Timescale Low Error Switching
of In-Plane Magnetic Tunnel Junctions
Through Dynamic Oersted-
Field Assisted Spin-Hall Effect 148

Strong Spin-Hall Effect
in the Antiferromagnet PtMn 150

Generating Controllable Polarization
Spin Currents through the
Anomalous Hall Effect in FeGd 152

Creating Skyrmions
Using Spin Transfer Torque.. . . . 154

Measuring the Spin-Hall Effect
in Rare Earth Thin Films 156

Current-Generated Spin-Orbit Torques
in MoS₂ / Ferromagnet Bilayers. 158

Electronic Transport of Topological
1D Channels in 2D Materials 160

Vortex Dynamics in Nanofabricated
Superconducting Devices... 162

Large Scale van der Waals Electronics
with Atomic Level Controllability 164

Fabrication of Nanofluidic Cavities
for Superfluid ³He Studies 166

Fabrication of Nanoscale Josephson Junctions
for Quantum Coherent
Superconducting Circuits... 168

Development of Superconductor
Circuits for Readout of Quantum
Nanomechanical Resonators 170

Fabrication of Superconducting Devices
for Quantum Information Science 172

Teepee-like Photonic Crystal with High
Absorption and Very Low Reflection... 174

Chiral Atomically Thin Films 176

Phase Sensitive Imaging of Magnetization
Dynamics in Spin Hall Multilayers. 178

Continuous Dynamical Decoupling of a Single
Nitrogen-Vacancy Center in Diamond 180

Fabrication of Aligned Substrates 182

Chromium to Optimize Spin-Orbit
Torques on Magnetic Devices... 184

PROCESS &

CHARACTERIZATION, 186-203

Improving Dopant Activation
in III-V Materials using
Laser Spike Annealing 186

Charge Trapping and Degradation in
Organic and Quantum Dot Transistors
Studied using KPFM... 188

Physically-Based Spatial Varying Anisotropic
BRDF for Metal-Finishing Surface... 190

Nanoscale Periodic Features with
DUV and 5x Stepper Lithography 192

GaN Vertical Power p-n Diodes on
Ammonothermal GaN Substrates;
A Process Development at CNF 194

Growing Silicon Oxide using
Dry Deposition Process to Support
R&D Work at U. of Pennsylvania. 196

Growth and Characterization
of Ultra-Strong Multi-Layer Graphene 198

Experimental Study of the Resolution
Limits – and PDMS and Electroplating
Applications – of ADEX/SUEX
Dry Photolithographic Film... 200

Two-Step Photolithography for Fabrication
of High Aspect Ratio SU-8 Rings.. . . . 202

INDEXES, 204-208

CORNELL NANOSCALE SCIENCE & TECHNOLOGY FACILITY :: 2015-2016 RESEARCH ACCOMPLISHMENTS ::

DIRECTORS' INTRODUCTION

As the new CNF Director, I (cko) would like to use this forum to introduce myself to the community. I am excited about the new job and about the new opportunities afforded by the creation of the National Nanotechnology Coordinated Infrastructure (NNCI), a network focused on nanoscience and nanotechnology. As the users of CNF know, we have first-rate facilities and outstanding staff who are dedicated to helping our users achieve success in all their efforts. As a long time user of CNF, I am always very impressed with the enthusiasm of the staff for teaching new users and working with them to solve interesting and often difficult problems. We especially wish to thank our users for their contributions to this publication, and we hope that you will find this collection of work to be informative and impressive, both for the quality of the research and for the breadth of fields in which the tools of nanotechnology are enabling new breakthroughs.

CNF is now supported by the National Science Foundation through its funding of the NNCI, an integrated network of sixteen university-based user facilities established in September 2015 to serve the needs of researchers in the fields of nanoscale science, engineering and technology. NNCI provides users from across the nation—from academia, small and large industry, and government—with open access to leading edge tools and processes for nanofabrication, synthesis, characterization, design, simulation, and device integration. I especially want to thank Dan Ralph for steering the CNF on its course for the last few years and for leading us to successful membership in NNCI.

As my first activity as CNF director, I attended the kick off meeting for the NNCI in Salt Lake City. We have a combination of schools from the old network and many new schools bringing a new set of skills to the new network. I am impressed by the energy and excitement of the NNCI and

look forward to its future successes. We welcome inquiries from all researchers about CNF's capabilities and the new network, especially those with no previous experience in nanofabrication, since the outstanding staff members of the CNF are highly skilled at teaching new users.

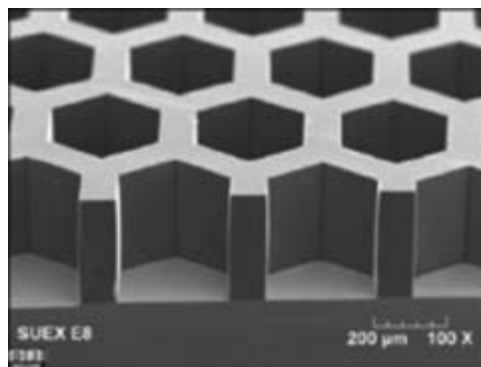
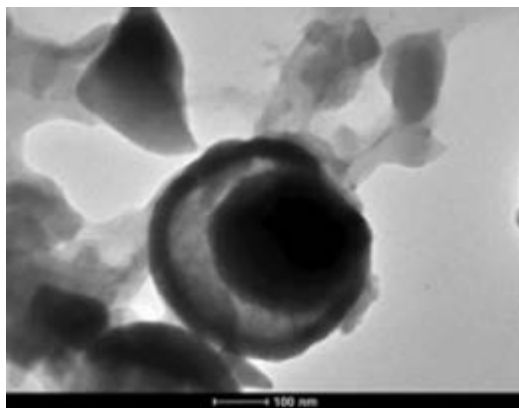
New Equipment & Capabilities

The CNF continues to upgrade its capabilities. New tools have been acquired and new processes developed over the past year and represent a significant investment in renewing and enhancing lab capabilities. Please see the CNF website for the names of the staff members to contact for further information or training.

- Everbeing International Corp has donated a new EB-6 electrical probe station that will be installed soon. The new system will replace our old probe system and will supply better vibration isolation, a dark box, and we purchased a new heated chuck to replace our current set up.
- A Metricon Prism Coupler system with five wavelength sources was added to the lab this year to allow high precision measurement of index of refraction for a wide range of dielectrics. The system also can measure waveguide losses and is already helping groups to develop novel waveguide stacks.
- A new Bruker Quantax 200 Energy Dispersive Spectrometer was added to our Zeiss Supra SEM to provide elemental mapping capability using a silicon drift detector.
- A new KLA- Tencor P7 stylus profilometer has arrived and training is underway to get all our users up to speed quickly on the new system.



- Process for ALD Coated Nanoparticles: CNF staff and student fellows have developed in-house methods for producing large quantities of monodisperse titania nanoparticles then applied atomic layer deposition processes for thin coatings. The transmission electron microscope image above shows a nicely formed alumina coating on a titania particle.
- Working with Oxford Instruments, our staff have developed recipes for etching magnetic materials used in magnetic tunnel junctions, for MRAM applications in our Oxford Cobra etcher.
- We have added pre-cast photosensitive dried sheets of photosensitive epoxy from DJ DevCorp. These allow films from 5 μm to 500 μm to be applied using a custom laminator. We expect these to be a popular alternative for μ fluidic work.
- In the deep etch area, CNF staff have worked with researchers at CHESS to optimize a modified deep silicon etch to achieve deep etching of germanium wafers.



Educational Outreach

The CNF participates in numerous educational outreach activities, operating both a national and an international program via NSF Research Experience for Undergraduates (REU) funding. The CNF REU Program takes undergraduate students from across the United States and exposes them to CNF's state of the art facility and our world class staff. The five 2016 students worked for ten summer weeks focussing on research in micro and nanotechnology. A second group of six interns spent part of the summer in Japan. The current issue of the NanoMeter has more on the CNF REU Program, and you'll also find Lynn Rathbun's article explaining the inter-

national (iREU) program and this year's iREU interns.

We are grateful to the National Science Foundation for its continued funding for our REU activities, but we also seek corporate funds to augment this program. Please contact Dr. Lynn Rathbun, our REU Programs Manager, to discuss corporate sponsorship (rathbun@cnf.cornell.edu).

CNF continues to host many educational tours, workshops and special events at Cornell. These include our short course, "Technology & Characterization at the Nanoscale" (CNF TCN), open to participants from academia, industry, and government. It includes lectures and demonstrations, and also hands-on lab activities in the cleanroom. The next short course will be offered in January 2017.

Over the past year, CNF has hosted visits and tours and staffed events for over 3700 participants; from prospective graduate students and new faculty members, to visiting dignitaries and corporate executives, public events, and special groups. These include over 124 distinct visits and events. We again hosted signature outreach events that included the 4H Career Explorations and the Jr FIRST LEGO League. We also enjoy meeting and working with middle and high school students—introducing them to the nano-world we live in. Contact Ms. Melanie-Claire Mallison with your visit request (mallison@cnf.cornell.edu).

As always, we welcome your comments about CNF and its operations, as well as suggestions for improvement.

Chris Ober

Lester B. Knight Director,
Cornell NanoScale Facility (CNF)
director@cnf.cornell.edu

Donald Tennant

Director of Operations, CNF
tennant@cnf.cornell.edu

**CORNELL NANOSCALE SCIENCE & TECHNOLOGY FACILITY
:: 2015-2016 RESEARCH ACCOMPLISHMENTS ::**

**A SELECTION OF 2015 CNF-RESEARCH RELATED
PATENTS, PRESENTATIONS & PUBLICATIONS**

- "3D culture regulates tumor hypoxia response and angiogenesis via inflammatory pathway"; DelNero, P., Lane, M., Verbridge, S.S., Kwee, B., Rabbany, P., Hempstead, B. Stroock, A.D., Fischbach, C., *Biomaterials*, 55, 110-118 (2015).
- "3D functional imaging of *C. elegans* sensory neurons by multifocus microscopy"; Abrahamsson, S., Seeing is Believing-Imaging the Processes of Life, EMBL Heidelberg, Germany (2015).
- "3D-Nano-Integrated Battery"; Abruna, H., G. Rodriguez-Calero, J. Werner, U. Wiesner, Patent App Filed, 7175-01-US, United States, 8/28/15, 62/211,159 (2015).
- "A critical analysis of the feasibility of pure strain actuated giant magnetostrictive nanoscale memories"; Gowtham, P. G., Rowlands, G. E. and Buhman, R. A., *Journal of Applied Physics* 118, doi:10.1063/1.4935521 (2015).
- "A microfabricated fixed path length silicon sample holder improves background subtraction for cryoSAXS"; Hopkins, J., A. Katz, S.P. Meisburger, M. Warkentin, R. Thorne and L. Pollack, *Journal of Applied Crystallography*, Volume: 48 Pages: 227-237 (2015).
- "A Microscope for Imaging Individual Macromolecules"; Marohn, J. A., 5th International Nano-MRI Conference; Institute for Quantum Computing; University of Waterloo, Canada (July 26-31, 2015).
- "Accelerating *ab initio* path integral molecular dynamics with multilevel sampling of potential surface"; Geng, H. Y., *Journal of Comput. Physics*, 283, 299-311 (2015).
- "Amplifier and Array for Measuring Small Current"; Minch, B.A., S. Bandla Ayers, US Patent 9,086,400, Application. No. 12/744,891 (issued July 21, 2015).
- "An array microhabitat system for high throughput studies of microalgal growth under controlled nutrient gradients"; Kim, B.J., L.V. Richter, N. Hatter, C.-K. Tung, B.A. Ahner, and M. Wu, *Lab Chip*, 15: 3687-3694 (2015).
- "Angle Sensitive Photogates; Pixel, System, Algorithms, Methods, and Applications"; Jayasuriya, S., A. Molnar, S. Sivaramakrishnan, Patent Converted, 6955-01-US, United States, 3/17/15, 62/134,122 (2015).
- "Angle Sensitive Photogates: Pixel, System and Algorithms"; Alyosha Molnar, Disclosure Filed - by Cornell, 6955, Disclosure Date 1/20/15 (2015).
- "Apparatus and Method for Point-of-Collection Measurement of a Biomolecular Reaction"; D. Erickson, S. Lee, M. Mancuso, Patent App Filed, 6044-03-US, United States, 3/10/15, 14/427,049 (2015).
- "Apparatus for Imparting Phase Shift to Input Waveform"; Foster, M, A Gaea, D Geraghty, M Lipson, R Salem, A Foster, US Patent 9182776 B2 (Nov 10, 2015).
- "Approaches to *In situ* Calibration of Inertial Sensors and 6DOF mm-scale Piezoelectric Stages"; A. Lal, Patent App Filed, 7250-01-US, USA, 62/248,017 (10/29/2015).
- "Body-on-a-Chip devices for drug testing: opportunities and limitations"; Shuler, M.L., World Pre-clinical Congress, Boston, MA. (June 10-12, 2015).
- "Body-on-a-Chip' Technology and Supporting Microfluidics"; Smith, A.S.T, C.J., Long, C. McAleer, X. Guo, M. Esch, J.M. Prot, M. Shuler, and J.J. Hickman, *Human-based Systems for Translational Research*, Chapt. 7. R. Coleman. RSC Drug Discovery Series No. 41. (2015).
- "Broadband mid-infrared frequency comb generation in a Si₃N₄ microresonator"; Luke, K., Y. Okawachi, M. Lamont, A. Gaeta, and M. Lipson, *Optics Letters*, Vol. 40, No. 21, 4823-4826 (19 Oct. 2015).
- "Building "Body-on-a-Chip" systems for drug development"; Shuler, M.L., AICHE Annual Meeting, Salt Lake City, UT. (November 8-14, 2015); MRS Annual Mtg, Boston, MA. (Nov. 2015).
- "Can multi-organ chips be used for drug development studies?"; Shuler, M.L., SELECTBIO Organ-on-a-Chip. Boston, MA. (July 8-9, 2015).
- "Cancer cell migration through 3-D environments causes nuclear rupture and DNA damage. Platform presentation selected from submitted abstract"; Lammerding, J, Biomedical Engineering Society Annual Meeting. Tampa, FL (Oct. 10, 2015).
- "Cavity-Enhanced On-Chip Absorption Spectroscopy"; M. Lipson, A. Nitkowski, Issued Patent, 4419-02-US, USA, 11/16/09, 12/619,326, 3/31/15, 8,992,836 (2015).
- "Cell migration through confining 3-D environments causes transient nuclear rupture in vitro and in vivo, promoting DNA damage and requiring ESCRT-components to restore nuclear envelope integrity"; Poster presentation selected from submitted abstract, Denais, CM, et al., American Society for Cell Biology Annual Meeting. San Diego, CA (Dec. 13, 2015).
- "Challenges and opportunities in 2D crystals: graphene and beyond"; Xing, G.H., Science and Technology of 2D Materials Workshop, Invited, Orlando (August 2015).

- "Characterizing protein aggregation by observing confined Brownian fluctuations in a near-field optical trap"; O'Dell, D., Schein, P., Kang, P., Erickson, D., Photonics West, San Francisco (Feb-15).
- "Chemical etch rate and x-ray structure of reactive sputtered c-axis aligned crystalline $\text{In}_x\text{Ga}_y\text{Zn}_z\text{O}_4$ films"; Zhu, B., Lynch, D.M., Chung, C.-Y., Ast, D.G., Greene, R.G., Thompson, M.O., ECS J. of Solid State Science and Technology, Vol.4, No.5, pp.Q43-Q45 (2015).
- "Circuits and Devices Based on Enhanced Spin Hall Effect for Efficient Spin Transfer Torque"; R. Buhrman, M.-H. Nguyen, C.-F. Pai, D. Ralph, Patent App Filed, 6764-04-PC, PCT/US15/41039 (7/17/2015).
- "Coherent Control of a Nitrogen-Vacancy Center Spin Ensemble with a Diamond Mechanical Resonator"; MacQuarrie, E., T. Gosavi, A. Moehle, N. Jungwirth, S. Bhavé, and G. Fuchs, *Optica* 2, 233 (2015).
- "Coherent Control of a Nitrogen-Vacancy Center Spin Ensemble with a Diamond Mechanical Resonator"; Guo, F., E. R. MacQuarrie, T. A. Gosavi, A. M. Moehle, N. R. Jungwirth, S. A. Bhavé, and G. D. Fuchs, March Meeting of the APS, San Antonio, TX; Cornell NanoScale Science and Technology Annual Meeting, Ithaca, NY; Spintech VIII, Basel, Switzerland; MRS Spring Meeting, San Francisco, CA (2015).
- "Coherent control over diamond nitrogen-vacancy center spins with a mechanical resonator"; Fuchs, G. D., Invited Talk, March Mtg of the APS, San Antonio TX; Invited Talk, META 2015, New York, NY (2015).
- "Coherent Supercontinuum from a SiN Waveguide"; Johnson, A., A. Klenner, K. Luke, E. Stranford, M. Lamont, Y. Okawachi, F. Wise, M. Lipson, U. Keller, and A. Gaeta, CLEO, OSA Technical Digest (online) OSA paper SF2D.1. (2015).
- "Collapse of DNA under alternating electric fields"; Zhou, C., Riehn R., *Phys Rev E*. Jul 20;92(1):012714. <http://link.aps.org/doi/10.1103/PhysRevE.92.012714> (2015).
- "Coloring, Stitching, and Twisting for Atomically Thin Circuitry"; Park, J., 2D Materials and Devices meeting, Army Research Laboratory, Adelphi, MD (Oct-15); MRS Fall Mtg, Boston, MA (Dec-15).
- "Colossal magnetoelectric effect induced by parametric amplification"; Wang, Y., T.-D. Onuta, C.J. Long, Y. Geng, I. Takeuchi, *App.Phys.Letters* 107, 192902 (2015).
- "Comparative mechanisms of cancer cell migration through 3D matrix and physiological microtracks"; Carey, S., A. Rahman, C. Kraning-Rush, B. Romero, S. Somasegar, O. Torre, R. Williams, and C. Reinhart-King, *Am J Physiol Cell Physiol.*, 308(6):C436-47 (2015).
- "Comprehensive models of human primary and metastatic colorectal tumors in immunodeficient and immunocompetent mice by chemokine targeting"; Chen, H.J., et al., *Nat Biotechnol.* 33(6):656-660. (2015).
- "Conductivity and microstructure of combinatorially sputter-deposited nitride thin films"; O'Dea, J. R., et al., *Chem. of Mater.*, 27, 4515-4524, doi: 10.1021/cm504599s. (2015).
- "Continuous dynamical decoupling of a single diamond nitrogen-vacancy center spin with a mechanical resonator"; MacQuarrie, E. R., T. A. Gosavi, S. A. Bhavé, and G. D. Fuchs, *Phys. Rev. B* 92, 224419, (2015).
- "Control of Electron Beam-Induced Au Nanocrystal Formation Kinetics through Solution Chemistry"; Park, J.H.; Schneider, N.; Grogan, J.; Reuter, M.; Bau, H.; Kodambaka, S.; and Ross, F., *Nano Letters* 15 (8) 5314-20. DOI: 10.1021/acs.nanolett.5b01677 (2015).
- "Control of polystyrene-block-poly(methyl methacrylate) directed self-assembly by laser-induced millisecond thermal annealing"; Jacobs, A. G., B. Jung, J. Jiang, C. K. Ober, M. O. Thompson, *J of Micro/Nanolithography, MEMS and MOEMS*, 14(3), 031205. (2015).
- "Controlled inter-mode cross-talk in optical waveguides"; Lipson, M., L. H. Gabrielli, SG Johnson, D. Liu, US Patent 9031362 B2 (2015).
- "Controlled Inter-Mode Cross-Talk in Optical Waveguides"; L. Gabrielli, S. Johnson, M. Lipson, D. Liu, Issued Patent, 5770-03-US, United States, 6/19/14, 14/309,552, 5/12/15, 9,031,362 (2015).
- "Controlling Carbon Nanotube Mechanics with Optical Microcavities"; Zhang, M., A. Barnard, P. McEuen, and M. Lipson, CLEO, OSA Technical Digest (online), OSA paper FTu4B.8. (2015).
- "Controlling Friction Characteristics of Resilient Members Using Near-surface Microstructures"; Jagota, A., et al., Patent application PCT/US16/18332 (2015).
- "Controlling thermo-optic response in microresonators using bi-material cantilevers"; Guha, B., and Lipson, M., *Opt. Lett.*, 40, 103 (01 Jan. 2015).
- "Cosmic microwave background measurements with the Atacama Cosmology Telescope"; Niemack, M.D., IAU General Assembly, Meeting #29, id.2257831 (Aug-15).
- "Coupled MEMS Structure for Motion Amplification"; S. Desai, A. Netravali, M. Thompson, Issued Patent, 3807-04-KR, South Korea, 4/17/09, 10-2009-7007914, 6/30/15, 10-1534351 (2015).
- "Coupling Superconducting Qubits and Metamaterials"; Flourde, B. L. T., Quantum Metamaterials Conference: Spetses, Greece (June 1, 2015).
- "Cryogenic Graphene Electrooptic Modulator"; Michal Lipson, Disclosure Filed - by Joint Owner, 7245, Disclosure Date 10/23/15 (2015).
- "Decrease of Lamin A/C expression enhances nuclear deformability and 3-D migration in cancer cells. Poster presentation selected from submitted abstract"; Denais, C, Gilbert R, Zhang K, Davidson PM, Krause M, Keat-ten Lindert M, Wolf K, Lammerding J., Biomedical Engr Society (BMES) Annual Meeting. Tampa, FL (9-Oct-15).
- "Dependence of the efficiency of spin Hall torque on the transparency of Pt-ferromagnetic layer interfaces"; Pai, C.-F., Y. Ou, L.H. Vilela-Leão, D. C. Ralph, and R. A. Buhrman, *Physical Review B* 92, doi:10.1103/PhysRevB.92.064426 (2015).

- "Dependence of the Spin Hall Torque Efficiency on the Transparency of Pt-Ferromagnetic Layer Interfaces"; Pai, C.-F., Y. Ou, D. C. Ralph and R. A. Buhrman, March Meeting of APS, San Antonio, Texas (March 2-6, 2015).
- "Dephasing of Superconducting Asymmetric Transmon Qubits"; Hutchings, M., M. Ware, C. Howington, B.L.T. Plourde, March Meeting of the American Physical Society Bulletin, San Antonio, TX. (2015).
- "Deposition conditions and HRTEM characterization of CAAC IGZO"; Lynch, D.M., Zhu, B., Levin, B.D.A., Muller, D.A., Ast, D.G., Greene, R.G., Thompson, M.O., Digest of Technical Papers - SID International Symposium, Vol.46, Book 1, pp.308-311 (2015).
- "Design of a microfluidic device to quantify dynamic intra-nuclear deformation during cell migration through confining environments"; Davidson, PM, Sliz J, Isermann P, Denais C, Lammerding J., Integrative Biology. 7: 1534-1546 (2015).
- "Detecting Charge Carrier Interactions in Organic Semiconductors Using Fluctuation Microscopy, Poster"; Dwyer, R. P., R. F. Loring, and J. A. Marohn, Materials Research Society Fall Meeting; Boston, Massachusetts (Nov 29-Dec 4, 2015).
- "Detection of DNA and poly-L-lysine using CVD graphene-channel FET biosensors"; Kakatkar, Aniket, T S Abhilash, R De Alba, J M Parpia and H G Craighead, Nanotechnology, 26, Number 12 DOI: 10.1088/0957-4484/26/12/125502 (2015).
- "Determination of the thermal noise limit of graphene biotransistors"; Crosser, M. S., M. A. Brown, P. L. McEuen, E. D. Minot, Nano Lett. 15, 5404-5407 (2015).
- "Device for Recovery and Isolation of Biomolecules"; Harold Craighead, Christine Tan, Patent App Filed, 5088-04-US, United States, 6/10/15, 14/735,874 (2015).
- "Devices for Terahertz Signal Generation"; Ehsan Afshari, Ruonan Han, Patent Converted, 6475-01-US, United States, 2/20/15, 62/119,100 (2015).
- "DNA Brushing Shoulders: Targeted Looping and Scanning of Large DNA Strands"; Azad, Z., Roushan M, Riehn R., Nano Lett. Jul 13;150713103730004. <http://pubs.acs.org/doi/abs/10.1021/acs.nanolett.5b02476> (2015).
- "Dopant activation and deactivation in InGaAs during sub-millisecond thermal annealing"; Sorg, V.C., Zhang, S.N., Hill, M., Clancy, P., Thompson, M.O., ECS Transaction, Vol.66, No.4, pages 117-124 (2015).
- "Doubledisk nonlinear optomechanics"; Lu, X., J. Y. Lee, and Q. Lin, Frontiers in Optics/Laser Science, FW6C.7 Proceedings (2015).
- "Dual-pumped degenerate Kerr oscillator in a silicon nitride microresonator"; Okawachi, Y., M. Yu, K. Luke, D. Carvalho, S. Ramelow, A. Farsi, M. Lipson, and A. Gaeta, Opt. Lett. 40, 5267-5270 (2015).
- "Dynamic wavelength converter"; Preble, S., M. Lipson, Issued Patent, 3941-03-US, United States, 2/24/09, 12/438,716, 7/21/15, 9,086,584 (2015).
- "Effect of Laser Annealing on the Structure of Amorphous Porous SiCOH Materials"; Raymunt, A.M., Bell, R.T., Thompson, M.O. and Clancy, P., J. of Physical Chem C, Vol.119, No.22, pages 12616-12624 (2015).
- "Effect of PEDOT:ClO₄ with Tunable Work Functions on Performance of Bulk Heterojunction Solar Cells"; Li, X., R. Dwyer, and J. A. Marohn, Northeast Regional Meeting of the American Chemical Society; Ithaca, New York (June 10-13, 2015).
- "Electrically Gated Three-Terminal Circuits and Devices Based on Spin Hall Torque Effects in Magnetic Nanostructures"; R. t Buhrman, L. Liu, C.-F. Pai, D. Ralph, Patent Allowed, 6029-04-KR, South Korea, 3/6/15, 10-2015-7006023; Issued Patent, 6029-03-US, United States, 2/6/15, 14/420,335; Patent App Filed, 6029-05-CN, Chi4/1/15, 201380051532; Patent App Filed, 6029-06-US, United States, 14/986,331 (2015).
- "Electro-optic effect in silicon nitride"; Miller, S., Y. Lee, J. Cardenas, A. Gaeta, and M. Lipson, CLEO, OSA Technical Digest (online), OSA paper SF1G.4 (2015).
- "Electro-optic modulator structures, related methods and applications"; Lipson, M., S Manipatruni, L Chen, K Preston, Issued Patent, 5112-03-US, United States, 11/14/12, 13/697,866, 12/22/15, 9,217,830 (2015).
- "Electro-Optic Modulator Using Cavity-Coupled Bus Waveguide"; Michal Lipson, Christopher Phare, Patent App Filed, 6902-02-PC, Not Applicable (PCT App), 11/9/15, PCT/US2015/059795 (2015).
- "Electro-Osmotic Apparatus, Method, and Applications"; P. Steen, M. Vogel, Issued Patent, 5010-03-US, United States, 7/23/12, 13/574,702, 4/7/15, 8,998,584 (2015).
- "Electro-Ultrasonic Devices for Nerve Stimulation and Treatment"; A. Lal, Patent Converted, 7004-01-US, United States, 3/16/15, 62/133,982 (2015).
- "Electron Beam Nucleic Acid Sequencing"; L. Bellan, H. Craighead, Patent App Filed, 3856-04-US, United States, 14/810,413 (7/27/2015).
- "Electron Microscopy during Controlled Release of Water from a Liquid Cell into Vacuum"; Schneider, N.M., M.M. Norton, F.M. Ross, and H.H. Bau, MRS Fall Meeting, poster Paper number VV10.04 (2-Dec-15).
- "Electropolymerization onto Flexible Substrates for Electronic Applications"; H. Abruna, S. Conte, K. Hernandez-Burgos, W. Li, D. Ralph, N. Ritzert, G. Rodriguez-Calero, C. Tan, Patent App Filed, 6272-02-PC, 4/3/15, PCT/US15/24276 (2015).
- "Electrostatic MEMS vibration energy harvester for HVAC applications"; Oxaal, J., M. Hella, D.A. Borca-Tasciuc, J. of Physics: Conference Series 660 (1), 012050 (2015).
- "Endothelial cell dynamics during anastomosis in vitro"; Diaz-Santana, A., Shan, M., and Stroock, A.D., Integrative Biology, 7, 454 - 466 (pdf) (2015).
- "Energetics of neutral Si dopants in InGaAs: An ab initio and semiempirical Tersoff model study"; Lee, C.-W., Lukose, B., Thompson, M.O., Clancy, P., Physical Review B - Condensed Matter and Materials Physics, Vol.91, No.9 (2015).

- “Engineering an organotypic colon through recellularization for studying cancer driver genes with transposon-based mutagenesis”; Chen, H.J., Z. Wei, N. Copeland, N. Jenkins and M.L. Shuler, BMES Award Mtg., Tampa, FL. (Oct. 7-10, 2015).
- “Engineering damping in insulating magnet-metal bilayers using ultrathin spacer layers”; Aradhya, S.V., C.L. Jermain, H. Paik, J.T. Heron, D.G. Schlom, D.C. Ralph and R. A. Buhrman, March Meeting of APS, San Antonio, Texas (March 2-6, 2015).
- “Enhanced On-Chip SERS Based Biomolecular Detection Using Electrokinetically Active Microwells”; C. Batt, D. Erickson, Y. S. Huh, A. Lowe, Issued Patent, 4519-04-US, USA, 8/18/11, 13/124,296, 6/16/15, 9,057,099 (2015).
- “Enhancement of Friction against a Rough Surface by a Ridge-Channel Surface Microstructure”; Bai, Y., C.-Y. Hui, B. Levrard, and A. Jagota, *Langmuir*, 31 (27), pp 7581-7589. DOI: 10.1021/la503838e (2015).
- “Enhancement of the Anti-Damping Spin Torque Efficacy of Platinum by Interface Modification”; Nguyen, M.-H., C.-F. Pai, K. Nguyen, D. Muller, D. C. Ralph, and R. A. Buhrman, *Appl. Phys. Lett.* 106, 222402, doi:10.1063/1.4922084 (2015).
- “Enhancing Nuclear Polarization for Nanoscale Magnetic Resonance Imaging”; Isaac, C. E., C. Gleave, P. Nasr, and J. A. Marohn, NE Regional Mtg of the ACS; Ithaca, NY (June 10-13, 2015).
- “Enhancing nuclear polarization for nanoscale magnetic resonance imaging”; Poster, Isaac, C., C. Gleave, P. Nasr, H. L. Nguyen, and J.A. Marohn, 5th International nano-MRI conference; Institute for Quantum Computing; University of Waterloo, Canada (July 26-31, 2015).
- “Enhancing the Efficiency of the Spin Hall Effect for Magnetic Excitation and Switching.”; Buhrman, R. A., Ralph, D. C. Nguyen, M.H. and Pai, C. F., PCT/US15/41039 (Filed 7/17/2015).
- “Esaki Diode van der Waals Vertical Heterojunctions with Broken Energy Band Alignment”; Yan, R., S. Fathipour, Y. Han, B. Song, S. Xiao, M. Li, N. Ma, V. Protasenko, D. A. Muller, D. Jena, and H. G. Xing, 56th Electronic Material Conference (EMC), Columbus, OH (Jun 2015).
- “Esaki diodes in van der Waals heterojunctions with broken-gap energy band alignment”; Yan, R., S. Fathipour, Y. Han, B. Song, S. Xiao, M. Li, N. Ma, V. Protasenko, D. A. Muller, D. Jena, and H. G. Xing, *Nano Lett.* 15 (9), 5791 (2015).
- “ESPPRESSO: Energy in Signal Powered Piezoelectric RF Energy Sensors and Spectrum Organization”; A. Lal, A. Molnar, Patent App Filed, 7221-01-US, United States, 10/13/15, 62/240,602 (2015).
- “Evanescent-Field Optical Readout of Graphene Mechanical Motion at Room Temperature”; Cole, Brawley, Adiga, De Alba, Parpia, Ilic, Craighead, and Bowen, *Phys. Rev. App.*, 3, 024004 doi.org/10.1103/PhysRevApplied.3.024004 DOI: http://dx.doi.org/10.1103/PhysRevApplied.3.024004 (2015).
- “Fiber-waveguide Evanescent Coupler”; B. Guha, M. Lipson, Patent App Filed, 6318-03-US, United States, 10/22/15, 14/786,339 (2015).
- “Field Flow, Radiation Damage, and Biological Sample Preparation on a Chip”; Gillilan, R.E., NSLS II ABBIX Beamlines Meeting, Session A: Brookhaven National Laboratory, Upton NY (April 21-22, 2015).
- “Floating Gate Based Sensor Apparatus and Related Floating Gate Based Sensor Applications”; K. Jayant, E. Kan, Patent App Filed, 6365-03-US, United States, 12/4/15, 14/896,010 (2015).
- “Flow Cells For Electron Microscope Imaging With Multiple Flow Streams”; Grogan, J., and Bau, H., United States Patent 9,196,457. (Awarded 11/24/2015).
- “Fluid Flow Device Containing Nanotubes and Method for Cell Trafficking Using Same”; A. Hughes, M. King, Issued Patent, 4920-04-CN, Chi6/8/12, 201080056108, 9/2/15, ZL20100056107.8 (2015).
- “Folded graphene nanochannels via pulsed patterning of graphene”; Silvestre, I., A. Barnard, S. Roberts, P. McEuen, R. Lacerda, *App.Phys.Let.* 106, 153105 (2015).
- “Frequency comb offset detection using supercontinuum generation in silicon nitride waveguides”; Mayer, S., A. Klenner, A. R. Johnson, K. Luke, M. R. E. Lamont, Y. Okawachi, M. Lipson, A. L. Gaeta, and U. Keller, *Optics Express*, Vol. 23, Issue 12 (15 June 2015).
- “Fusion Pore Opening”; Lindau, M., 17th Int’l Symposium on Chromaffin Cell Bio., Cairns, QLD Australia (2015).
- “Graphene electro-optic modulator with 30 GHz bandwidth”; Phare, C.T., Y.-H. D. Lee, J. Cardenas and M. Lipson, *Nature Photonics* 9, 511-514 doi:10.1038/nphoton.2015.122 (13 July 2015).
- “Graphene Kirigami”; McEuen, P.L., MIT Active Matter Workshop (April 2015).
- “Graphene Kirigami”; Bles, M.K., A.W. Barnard, P.A. Rose, S.P. Roberts, K.L. McGill, P.Y. Huang, A.R. Ruyack, J.W. Kevek, B. Kobrin, D.A. Muller, and P.L. McEuen, *Nature* 524, 204-207 (2015).
- “Graphene nanoribbons formed by a sonochemical graphene unzipping using flavin mononucleotide as a template”; Yoon, W., Y. Lee, H. Jang, M. Jang, J. S. Kim, H. S. Lee, S. Im, D. Boo, J. Park, and S. Y. Ju, *Carbon*, 81, 629-638 (2015).
- “Graphene-based solid state devices capable of emitting electromagnetic radiation and improvements thereof”; Morreale, Jay P, Assignee: p-brane LLC, Appl. No.: 14/235,184 PCT no.: PCT/US12/48453 (2015).
- “HBAR as high frequency high stress generator”; Gosavi, T.A., E.R. MacQuarrie, G.D. Fuchs and S.A. Bhave, IEEE International Ultrasonics Symposium, Taipei, Taiwan, pp. 1-4 (October 21-24, 2015).
- “High mobility, dual layer, c-axis aligned crystalline/amorphous IGZO thin film transistor”; Chung, C.-Y., Zhu, B., Greene, R.G., Thompson, M.O., Ast, D.G., *Applied Physics Letters*, Vol.107, No.18 (2015).

- "High-frequency and high-quality silicon carbide optomechanical microresonators"; Lu, X., J. Y. Lee, and Q. Lin, *Sci. Rep.* 5, 17005 (2015).
- "High-performance three-atom-thick semiconducting films with wafer scale homogeneity"; Kang, K., S. Xie, L. Huang, Y. Han, P. Y. Huang, K. F. Mak, C.-J. Kim, D. A. Muller, and J. Park, *Nature*, 520, 656-660 (2015).
- "High-purity single-mode photon source for integrated quantum photonics"; Lu, X., W. Jiang, J. Zhang, and Q. Lin, *SPIE Sensing Technology and Applications*, 950018-950018-9 (2015).
- "High-Q silicon carbide photonic-crystal cavities"; Lee, J., X. Lu, and Q. Lin, *Appl. Phys. Lett.* 106, 041106 (2015).
- "High-Resolution Bioprinting of Thick-Walled Arteries Using Embedded Vasa Vasorum Structures"; J. Min, B. Mosadegh, R. Shepherd, Patent Converted, 7134-01-US, United States, 7/16/15, 62/193,412 (2015).
- "High-Throughput Microplate-Based Microcolumn Device for the Selection of Aptamers, Characterization of the Selection Process, and Other Chromatographic Processes"; Reinholt, S., K. Szeto, A. Ozer, J. Benitez, F. Duarte, J. Pagano, L. Yao, J. Lis, H. Craighead, PITTCO, New Orleans, LA (12-Mar-15).
- "Highly Efficient Self-Referencing of a 1-GHz Diode-Pumped Solid-State Laser Using a SiN Chip"; Mayer, A. K., A. Johnson, K. Luke, M. Lamont, Y. Okawachi, M. Lipson, A. Gaeta, and U. Keller, *CLEO, OSA Technical Digest* (online), OSA paper SW4G.6. (2015).
- "Hong-Ou-Mandel Interference between Transverse Spatial Waveguide Modes"; Mohanty, M. Z., S. Ramelow, P. Nussenzveig, and M. Lipson, *CLEO, OSA Technical Digest* (online), OSA paper FTu4A.5. (2015).
- "Image reconstruction in nanoscale magnetic resonance imaging, Poster"; Nguyen, H. L. and J. A. Marohn, 5th Int'l nano-MRI conference; Inst for Quantum Computing; University of Waterloo, Canada (July 2015).
- "Imaging Device and Method"; L. Gabrielli, U. Leonhardt, M. Lipson, T. Tyc, Issued Patent, 5210-03-CN, Chi9/3/10, CN201080052819.2, 2/25/15, ZL201080052819.2 (2015).
- "Imaging Magnetic Dynamics with Heat and Light, Poster"; Bartell, J., D.H. Ngai, F. Guo, Z. Leng and G.D. Fuchs, Gordon Research Conference on Spin Dynamics, Hong Kong (2015).
- "Insights from plants: tunable nano-flows induced by drying"; Vincent, A R, A Szenicer, A Stroock, APS Division of Fluid Dynamics Mtg. APS Division of Fluid Dynamics Mtg. Boston, MA (November 22-24, 2015).
- "Integrated Circuits Based Biosensors"; V. Gund, A. Lal, Patent App Filed, 6595-02-PC, Not Applicable (PCT App), 1/27/15, PCT/US15/13154 (2015).
- "Integrated Switch for Mode-Division Multiplexing (MDM) and Wavelength-Division Multiplexing (WDM)"; Stern, B., X. Zhu, C. Chen, L. Tzuang, J. Cardenas, K. Bergman, and M. Lipson, *CLEO, OSA Technical Digest* (online), OSA paper STh1F.2. (2015).
- "Integrated switch for simultaneous mode-division multiplexing (MDM) and wavelength-division multiplexing (WDM)"; Stern, B., Zhu, X., Chen, C. P., Tzuang, L. D., Cardenas, J., Bergman, K., and Lipson, M., arXiv:1502.04692. (17 Feb 2015).
- "Interstitial flows promote an amoeboid over mesenchymal motility of breast cancer cells revealed by a three dimensional microfluidic model"; Huang, Y.L., C.-K. Tung, A. Zheng, B. J. Kim, and M. Wu, *Integr. Biol.*, DOI: 10.1039/C5IB00115C (2015).
- "Investigating Image Reconstruction Methods for Magnetic Resonance Force Microscopy"; Nguyen, H. L. and J. A. Marohn, Northeast Regional Meeting of the ACS; Ithaca, New York (June 10-13, 2015).
- "Investigation of gap-closing interdigitated capacitors for electrostatic vibration energy harvesting"; Oxaal, J, D Foster, M Hella, DA Borca-Tasciuc, *J of Micromechanics and Microengineering* 25 (10), 105010 (2015).
- "Lab-on-a-Bird: biophysical monitoring of flying birds"; Gumus, A., Lee, S., Karlsson, K., Gabrielson, R., Guglielmo, C., Winkler, D., Erickson, D., *PLOS-One*, 10(4): e0123947 (2015).
- "Lamin A/C Deficiency Reduces Circulating Tumor Cell Resistance to Fluid Shear Stress"; Mitchell, MJ, Denais C, Chan M, Wang Z, Lammerding J, King MR., *Am J Phys - Cell Physiology*. 309(11): C736-746 (2015).
- "Laser spike annealing of DSA photoresists"; Jiang, J., Jacobs, A., Thompson, M.O., Ober, C.K., *Journal of Photopolymer Science and Technology*, Vol.28, No.5, pages 631-634 (2015).
- "Layered Materials for Electronics"; Xing, Grace Huili, US-EU workshop on 2D Layered Materials and Devices, Invited, Arlington, VA (April 2015).
- "Light Field Image Sensor, Method and Applications"; P. Gill, A. Molnar, A. Wang, Issued Patent, 4895-04-CN, Chi6/26/13, 201180062807, 9/23/15, ZL 2011 8 0062806.8 (2015).
- "LINC'd in-Nuclear positioning in cell migration (and beyond). Invited lecture/seminar"; Lammerding, J, Labex CellTisPhyBio Workshop on Cell Motility. Institut Curie, Paris, France (25-Mar-15).
- "Linear Optical Phase Modulators"; J. Gonzalez, Y. Lee, M. Lipson, Patent App Filed, 6754-02-US, United States, 7/27/15, 14/810,444 (2015).
- "Linear silicon PN junction phase modulator"; Lee, Y., J. Cardenas, and M. Lipson, *CLEO, OSA Technical Digest* (online) OSA paper SW3N.5. (2015).
- "Low cost cell culture platforms for Body-on-a-Chip applications"; Esch, M.B., D. Applegate and M.L. Shuler, BMES Annual Mtg, Tampa, FL. (Oct.2015).
- "Low cost Multi-organ in vitro systems for efficacy"; Shuler, M.L., 5th AIMBS/NIH Workshop on Validation and Quantification of New In Vitro Tools and Models for the Pre-clinical Drug Discovery Process, Bethesda, MA. (Feb. 12, 2015).

- “Low loss titanium dioxide waveguides and resonators using a dielectric lift-off fabrication process”; Evans, C. C., C. Liu, and J. Suntivich, *Opt. Express*, 23 9, 11160-11169 (2015).
- “Low-Loss Titanium Dioxide Waveguides for Integrated Evanescent Raman Spectroscopy”; Evans, C. C., C. Liu, and J. Suntivich, *CLEO, OSA Technical Digest*, paper SM3O.4.; CLEO, San Jose, CA (May 11 2015).
- “Low-Noise Gigahertz Frequency Comb from Diode-Pumped Solid-State Laser using Silicon Nitride Waveguides”; Mayer, A.K., A. Johnson, K. Luke, M. Lamont, Y. Okawachi, M. Lipson, A. Gaeta, and U. Keller, *Advanced Solid State Lasers, OSA Technical Digest* (online) OSA paper Ath4A.5. (2015).
- “Low-Noise Silicon Mid-Infrared Frequency Comb”; Griffith, Y. O., J. Cardenas, A. Gaeta, and M. Lipson, *CLEO, OSA Technical Digest* (online), OSA paper SF1D.5. (2015).
- “Magnetically Actuated Single-Walled Carbon Nanotubes”; Roberts, S.P., A.W. Barnard, C.M. Martin, M.K. Blees, J.S. Alden, A.R. Ruyack, and P.L. McEuen, *Nano Lett.* 15, 5143-5148 (2015).
- “Master-Slave Locking of Optomechanical Oscillators over a Long Distance”; Shah, S.Y., M. Zhang, R. Rand, M. Lipson, *Phys. Rev. Lett.* 114, 113602, (17 March 2015).
- “Matrix microenvironment in metastatic migration”; Reinhart-King, C., *Workshop on Cell-Matrix Mechanobiology: Current State and Future Directions*, UIUC (October 2015).
- “Mechanical and Structural Cues within the 3D Microenvironment in Metastatic Cell Migration”; Reinhart-King, Cynthia, *American Society of Cell Biology*, San Diego, CA (December 2015).
- “Method and Apparatus Including Nanowire Structure”; A. Lal, Y. Lu, *Issued Patent*, 4926-04-CN, Chi6/12/12, 201080056429, 9/30/15, CN102714137 (2015).
- “Method of Actuating an Internally Transduced PN-Diode-Based Ultra High Frequency Michromechanical Resonator”; S. Bhave, E. Hwang, *Issued Patent*, 4909-03-US, United States, 7/29/11, 13/193,685, 1/27/15, 8,941,191 (2015).
- “Methods and Apparatus for Monitoring Interactions Between Particles and Molecules Using Nanophotonic Trapping”; D. Erickson, P. Kang, *Patent App Filed*, 6719-02-US, United States, 8/12/15, 14/824,423 (2015).
- “Methods and systems for object identification and for authentication”; Craighead, H., *U. S. Patent #9,007,213* (Issued April 14, 2015).
- “Methods for Determining the Relative Abundance of Epigenetic Modifications in Single Cells,”; Craighead, H., *New Invention Disclosure #7263* (5-Nov-15).
- “Microfluidic Chip Having On-Chip Electrically Tunable High-Throughput Nanophotonic Trap”; Wang, M., M. Lipson, M. Soltani, *United States Patent Application* 20150336097; *Patent Allowed*, 6163-03-US, United States, 6/22/15, 14/654,839 (2015).
- “Microfluidic platform for 3D human primary liver cell culture with inflammation capability”; Esch, M.B., J.-M. Prot, Y. Wang, P. Miller, D. Applegate and M.L. Shuler, *BMES Annual Meeting*, Tampa, FL (Oct. 7-10, 2015).
- “Microgrooves and fluid flows provide preferential passageways for sperm over pathogen *Trichomonas foetus*”; Tung, C.-k., L. Hu, A.G. Fiore, F. Ardon, D.G. Hickman, R.O. Gilbert, S.S. Suarez, and M. Wu, *Natl. Acad. Sci. USA Proc.* 112, 5431 (2015).
- “Micropatterns and PDMS microdevices for the investigation of cardiac muscle cell structure and function. Invited poster and platform presentation”; Swei, A, Davidson PM, Fedorchak G, Lammerding J, 2015 National Nanotechnology Infrastructure Network (NNIN) REU Convocation. Ithaca, NY (Aug.2015).
- “Microscopic Studies of the Fate of Charges in Organic Semiconductors: Scanning Kelvin Probe Measurements of Charge Trapping, Transport, and Electric Fields in p- and n-type Devices”; Smieska, L. M., PhD thesis, Cornell University, url: <http://hdl.handle.net/1813/40969>. (2015).
- “Microwave mode structure of superconducting metamaterial resonators”; Wang, H., F. Rouxinol, B. Plourde, M. LaHaye, *March Meeting of the American Physical Society Bulletin*, San Antonio, TX. (2015).
- “Mobile health for global health”; Erickson, D., *China-America Frontiers of Engineering Symposium*, National Academy of Engineering, Irvine, CA (Jun-15).
- “Modeling the Dynamics of Remobilized CO₂ within the Geologic Subsurface”; Huber, E, D Koch, A Stroock, *APS Division of Fluid Dynamics Meeting*. Boston, MA (November 22-24, 2015).
- “Modular cell culture platform with passive fluid controls for GI tract-liver tissue co-culture”; Esch, M.B. and M.L. Shuler, *AICHE Annual Meeting*, Salt Lake City, UT. (November 8-14, 2015).
- “Monolayer films of semiconducting metal dichalcogenides, methods of making same”; Park, J., *US Provisional Patent application* 62/148387 (2015).
- “Monolithic PZT Actuator, Stage, and Method for Making”; S. Ardanuc, A. Lal, S. Nadig, *Patent App Filed*, 6306-03-US, United States, 10/19/15, 14/785,442 (2015).
- “Monolithic Silicon Acousto-Optic Modulator Structure and Method”; S. Bhave, S. Sridaran, *Issued Patent*, 4267-05-CN, Chi9/26/12, 201180016156, 3/4/15, ZL201180016155.9 (2015).
- “Monolithic Source of Tunable Narrowband Photons for Future Quantum Networks”; Ramelow, S., A. Farsi, S. Clemmen, K. Luke, M. Lipson, and A. Gaeta, *CLEO, OSA Tech Digest* (online) OSA paper FM2A.7. (2015).
- “Multi-cellular 3D human primary liver cell culture elevate metabolic activity under fluidic flow”; Esch, M.B., Prot, J, Wang, Y.I., Miller, P., Llamas-Vidales, J.R., Naughton, B.A., Applegate, D.R., and M.L. Shuler, *Lab Chip*, 15: 2269-2277. PMID 25857666 (2015).

- "Multi-organ chips for drug development"; Shuler, M., SELECTBIO Lab-on-a-Chip, Microfluidics and Microarrays World Congress. San Diego, CA. (Sept.2015).
- "Multi-stable Synchronization of Delay-Coupled Optomechanical Oscillators"; Shah, S., M. Zhang, and M. Lipson, CLEO, OSA Technical Digest (online) OSA paper STh3I.8. (2015).
- "Multiferroic dynamic memory and the colossal ME effect based on heterostructured cantilever"; Takeuchi, I., MRS Fall Meeting, Invited presentation (Dec. 3rd, 2015).
- "Multiferroic operation of dynamic memory based on heterostructured cantilevers"; Onuta, T., Y. Wang, S.E. Lofland, and I. Takeuchi, Adv.Mats 27, 202-206 (2015).
- "MultiFocus Polarization Microscope (MF-PolScope) for 3D polarization Imaging of up to 25 Focal Planes Simultaneously"; Abrahamsson, S., S.B. Mehta, A. Verma, M. McQuilken, C.I. Bargmann, A.S. Gladfelter, and R. Oldenbourg, Opt. Express 23: 7734-7754 (2015).
- "Multimodal Sensor, Method of Use, and Method of Fabrication"; A. Lakso, V. Pagay, M. Santiago, D. Sessoms, A. Stroock, Patent App Filed, 6335-03-US, USA, 12/11/15, PCT/US1442435; Patent App Filed, 6335-04-AU, Australia, 12/18/15, 2014277891 (2015).
- "Nano bubble migration in a tapered conduit in the asymptotic limit of zero capillary and Bond numbers"; Norton, M., F. Ross, H. Bau, Bulletin of the APS, 68th Annual Meeting of the APS Division of Fluid Dynamics, Boston, MA, p 358. (Nov.2015).
- "Nanofluidics and the Nano-Bio Interface"; Craighead, H., Annual Conference of the National Academy of Inventors, Pasadena, Ca, Invited talk (19-Mar-15).
- "Nanophotonic detection of freely interacting molecules on a single influenza virus"; Kang, P., P. Schein, X. Serey, D. O'Dell, D. Erickson, Scientific Reports, 5 12087 (2015).
- "Nanophotonic Force Microscopy: Characterizing Particle-Surface Interactions Using Near-field Photonics"; Schein, P., Kang, P., O'Dell, D., Erickson, D., Nano Letters 15(2), 1414-1420 (2015).
- "Nanophotonic force microscopy: measuring particle-surface interactions using near-field photonics"; Schein, P., Kang, P., Erickson, D., Photonics West, San Francisco (Feb-15).
- "Nanopore-Containing Substrates with Aligned Nanoscale Electrodes and Methods of Making and Using Same"; J. Alden, A. Barnard, A. Cortese, P. McEuen, Patent App Filed, 6798-02-PC, 12/1/15, PCT/US15/63224 (2015).
- "Nanoscale Functional Imaging of Organic Materials"; Marohn, J. A., Mechanical Engineering Colloquium; State University of New York at Binghamton, Binghamton, New York (November 19, 2015).
- "Nanoscale optical positioning of single quantum dots for bright and pure single-photon emission"; Sapienza, L., M. Davaco, A. Badolato, and K. Srinivasan, Nat. Commun. 6, 7833. DOI: 10.1038/ncomms8833 (2015).
- "Nanowire Functionalized Fiber and Fabrics"; J. Hinestroza, M. Kuno, M. Zhukovskiy, Patent Converted, 6684-01-US, USA, 62/108,209 (1/27/2015).
- "Nature Inspired Fabric of Unidirectional Liquid Transport"; J. Fan, Disclosure Filed - by Cornell, 7216, Disclosure Date 10/5/15 (2015).
- "Near-field Light Scattering Techniques for Measuring Nanoparticle-Surface Interaction Forces"; Schein, P., Ashcroft, C.K., O'Dell, D., Adam, I.S., DiPaolo, B., Sabharwal, M., Shi, Ce., Hart, R., Earhart, C., Erickson, D., J. of Lightwave Technology, 33(16), 3494-3502 (2015).
- "Near-Field Radiative Heat Transfer between Integrated Nanostructures using Silicon Carbide"; St-Gelais, R., L. Zhu, B. Guha, S. Fan, and M. Lipson, CLEO, OSA Technical Digest (online) OSA paper FTh4E.1. (2015).
- "Near-field radiative heat transfer between nanostructures in the deep sub-wavelength regime"; St-Gelais, R., L. Zhu, S. Fan, M. Lipson, arXiv: 1509.08005 (2015).
- "New developments in ligand-stabilized metal oxide nanoparticle photoresists for EUV lithography"; Ober, C. K., J. Jiang, B. Zhang, L. Li, E. P. Giannelis, J. S. Chun, M. Neiser, R. Sierra-Alvares, SPIE 9422, EUV Lithography VI. 942207 Proceedings (2015).
- "Non-Faradaic Electrochemical Detection of Exocytosis from Mast and Chromaffin Cells Using Floating-Gate MOS Transistors"; Jayant, K., A.Singhai, Y.Cao, J.B.Phelps, M.Lindau, D.A.Holowka, B.A.Baird and E.C.Kan, Sci. Rep. 5: 18477 (2015).
- "Non-muscle myosin IIB is critical for nuclear translocation during 3-D invasion"; Thomas, DG, Yenepalli A, Denais CM, Rape A, Beach JR, Wang Y, Schiemann WP, Baskaran H, Lammerding J, Egelhoff TT., J Cell Biol. 210(4): 583-594 (2015).
- "Nonvolatile Flash Memory Structures Including Fullerene Molecules and Methods for Manufacturing the Same"; E. Kan, H. Richter, R. Sivarajan, V. Vejins, Q. (Sarah) Xu, Issued Patent, 5195-04-US, United States, 12/23/13, 14/138,294, 12/22/15, 9,219,166 (2015).
- "Nuclear envelope rupture and repair during cell migration in confined 3-D environments"; Lammerding, J; Invited platform presentation, ASCB Annual Meeting, Special Interest Subgroup. San Diego, CA (Dec. 12, 2015); Invited presentation, Current Trends in Biomedicine Workshop: The Nuclear Lamina in Health and Disease. Baeza, Spain (16-Nov-15); Invited presentation, Nuclear Dynamics: Design & Principles Symposium, Wenner-Gren Foundation. Sweden (20-Aug-15); Invited presentation, Invadosome Consortium-6th biannual congress: Integrated Mechano-Chemical Signals in Invasion. Saint Paul de Vence, France (20-Oct-15).
- "Octave-spanning coherent supercontinuum generation in a silicon nitride waveguide"; Johnson, A. M., A. Klenner, K. Luke, E. Lamb, M. Lamont, C. Joshi, Y. Okawachi, F. Wise, M. Lipson, U. Keller, and A. Gaeta, Opt. Lett. 40, 5117-5120. (2015).
- "On lattice stability and the high pressure melting mechanism of dense hydrogen up to 1.5 TPa"; Geng, H. Y., R. Hoffmann, and Q. Yu., Phys. Rev. B 92, 104103 (2015).

- "On-Chip Integrated Gas Sensor Based On Photonic Sensing"; Lipson, M., A Gaeta, A Griffith, J Cardenas, R Lau, Y Okawachi, R Fain, United States Patent Application 20150323450 (11/12/2015); Patent App Filed, 6694-02-US, USA, 5/7/15, 14/706,935 (2015).
- "On-chip mode-division multiplexing switch"; Stern, B., X. Zhu, C.P. Chen, L.D. Tzuang, J. Cardenas, K. Bergman, and M. Lipson, *Optica*, Vol. 2, No. 6, (29 May 2015).
- "On-Chip Optical Squeezing"; Dutt, A., K. Luke, S. Manipatruni, A.L. Gaeta, P. Nussenzveig, and M. Lipson, *Phys. Rev. Applied* 3, 044005 (13 April 2015).
- "Optical Force Based Biomolecular Analysis in Slot Waveguides"; D. Erickson, M. Lipson, S. Moore, B. Schmidt, A. Yang, Issued Patent, 4438-04-CN, Chi5/11/11, 200980145053.X, 11/25/15, ZL200980145053.X (2015).
- "Optical Mode-Division Multiplexing Using Selected Mode Coupling Between An Optical Resonator And A Signal Transmission Line"; Lipson, M., L-W Luo, LH Gabrielli., US Patent Application 20150188659 (2015).
- "Optical modulators and beam steering based on electrically tunable plasmonic material"; Shi, K., and Z. Lu, *Journal of Nanophoton.* 9, 093793 (2015).
- "Optical nonlinearities in high-confinement silicon carbide waveguides"; Cardenas, J., M. Yu, Y. Okawachi, C. Poitras, R. Lau, A. Dutt, A. Gaeta, and M. Lipson, *Optics Letters*, V40, N17, 4138-4141 (01 Sept. 2015).
- "Optical Trapping Apparatus, Methods and Applications Using Photonic Crystal Resonators"; Y-F. Chen, D. Erickson, Issued Patent, 5224-03-US, United States, 6/29/12, 13/520,033, 6/16/15, 9,057,825 (2015).
- "Optical Waveguides from a Lithographically-Defined Wetting of a High-Index Liquid"; Evans, C. C., E. Hsu, M. Ji, C. Liu, and J. Suntivich, CLEO, OSA Technical Digest, paper STu1K.5. (2015).
- "Optical Waveguides from a Lithographically-Defined Wetting of a High-Index Liquid"; Evans, Hsu, Ji, Liu and Suntivich, CLEO, San Jose, CA (May 2015).
- "Optofluidic Photobioreactor Apparatus, Method, and Applications"; D. Erickson, D. Sinton, Issued Patent, 5200-05-CN, Chi7/15/13, 201180065338, 3/25/15, ZL201180065337.5 (2015).
- "Optofluidics: Photonic Technologies for Mobile and Global Health"; Erickson, D.; ASME 4th Global Congress on NanoEngineering for Medicine and Biology-Minneapolis, MN (Apr-15); European Optical Society 3rd Conference on Optofluidics, Munich, Germany (Jun-15); Frontiers in Optics-San Jose, CA (Oct-15); Int'l Mechanical Eng. Congress and Exposition, Houston, TX (Nov. 2015).
- "Optomechanical Sensors Based on Coupling Between Two Optical Cavities"; S. Bhave, D. Hutchison, Issued Patent, 5631-03-US, United States, 4/8/14, 14/350,542, 6/30/15, 9,069,004 (2015).
- "Organ-on-a-Chip: technologies and Applications"; Shuler, M.L. and J.J. Hickman, SELECTBIO Lab-on-a-Chip, Microfluidics and Microarrays World Congress. San Diego, CA (Sept 28-30, 2015).
- "Orthogonal Processing of Organic Materials Used in Electronic and Electrical Devices"; M. Chatzichristidi, P. Dodson (f/k/a Taylor), J.-K. Lee, G. Malliaras, C. Ober, A. Zakhidov, Issued Patent, 4385-08-US, United States, 8/28/14, 14/471,095, 12/15/15, 9,213,238 (2015).
- "Oxide nanoparticle EUV (ONE) photoresists: current understanding of the unusual patterning mechanism"; Jiang, J.; Zhang, B.; Yu, M.; Li, L.; Neisser, M.; Chun, J.S.; Giannelis, E.P.; Ober, C.K., *Journal of Photopolymer Science and Technology*, 28(4), 515-518. (2015).
- "Parametric Comb Generation via Nonlinear Wave Mixing in High-Q Optical Resonator Coupled to Built-In Laser Resonator"; A. Gaeta, A. Johnson, M. Lipson, Y. Okawachi, Patent App Filed, 6264-03-US, United States, 10/22/15, 14/786,319 (2015).
- "Parametric Frequency Conversion in Silicon Carbide Waveguides"; Cardenas, Miller, Okawachi, Ramelow, Griffith, Farsi, Gaeta, and Lipson, CLEO, OSA Technical Digest (online), OSA paper SF1D.7. (2015).
- "Pathologically Relevant Tumor Microenvironments for High-Throughput Drug Screening"; C. Fischbach, Issued Patent, 4342-02-US, United States, 7/29/09, 12/510,925, 8/4/15, 9,097,702 (2015).
- "Phase Transition Memories and Transistors"; M. Kim, S.H. Lee, R. Sundararaman, S. Tiwari, Issued Patent, 4440-03-USA, 11/23/11, 13/322,379, 3/24/15, 8,987,701 (2015).
- "Phase-sensitive imaging of ferromagnetic resonance using ultrafast heat pulses"; Guo, F., J. M. Bartell, D. H. Ngai, and G. D. Fuchs, *Phys. Rev. Applied* 4, 044004 (2015).
- "Phenotypic Sorting in Cancer Metastasis"; Reinhart-King, C.a, NSF Workshop on the Physics of Living Systems, (November 2015).
- "Photonic Chips Based on Multimode Fiber-to-Waveguide Coupling"; F. Barbosa, J. Gonzalez, M. Lipson, A. Mohanty, B. Stern, Patent Converted, 7078-01-US, United States, 5/8/15, 62/159,117 (2015).
- "Photopatterning of Indomethacin Thin Films: An Environmentally Friendly Photoresist"; Camera, K.L., J. Gómez-Zayas, M. D. Ediger, C.K. Ober, *ACS Applied Materials and Interfaces*, 7(42), 23398-23401. (2015).
- "Piezoelectric and Logic Integrated Delay Line Memory"; J. Kuo, A. Lal, Patent App Filed, 6542-02-PC, 2/3/15, PCT/US15/14324 (2015).
- "Polarization spectroscopy of defect-based single photon sources in ZnO"; Jungwirth, N. R., H. -S. Chang, M. Jiang, and G. D. Fuchs, The Third Infinity: 2nd Conference on Physics of Biological and Complex Systems, Guttingen, Germany (2015).
- "Polysilicon photodetector, methods and applications"; Lipson, M., K. Preston, US Patent 9153715 B2. (2015).
- "Polysilicon Photodetector, Methods and Applications"; M. Lipson, K. Preston, Issued Patent, 5244-03-US, United States, 10/13/14, 14/512,738, 10/6/15, 9,153,715 (2015).

- "Precise Partition of Micro/Nanoparticles in an Electro-Optofluidic Platform"; Soltani, M., F. Ye, J.L Killian, J. Lin, M. Lipson, MD Wang, *Biophysical Journal* (2015).
- "Predicting Appearance from Measured Microgeometry of Metal Surfaces"; Dong, Z., B. Marschner, and D. Greenberg, *ACM Transactions on Graphics*, library link: <http://dl.acm.org/citation.cfm?id=2815618> (Dec-15).
- "Processing of Multimode Optical Signals"; M. Lipson, B. Stern, Patent App Filed, 6904-02-PC, PCT/US2015/067229 (2015).
- "Processing-structure-property relationships in laser-annealed PbSe nanocrystal thin films"; Trembl, B.E., Robbins, A.B., Whitham, K., Smilgies, D.-M., Thompson, M.O., Hanrath, T., *ACS Nano*, Vol.9, No.4, pages 4096-4102 (2015).
- "Pumpless microfluidic platform for drug testing on human skin equivalents"; Abaci, H.E., Gledhill, K., Guo, Z., Christiano, A.M., and M.L. Shuler, *Lab Chip* 15(3): 882-888. (2015).
- "Pumpless microfluidics blood brain barrier model for drug screenings"; Wang, Y., H. Abaci, J. Hickman and M. Shuler, *BMES Annual Mtg*, Tampa, FL (Oct.2015).
- "Quantifying and Optimizing Spin-Orbit Torques in Magnetic Multilayer Nanostructures"; Buhrman, R. A., Gordon Research Conference on Spin Dynamics in Nanostructures, The Hong Kong University of Science and Technology, Invited talk, China, (July 26-31, 2015).
- "Quantum control and decoherence protection of single nitrogen-vacancy center spins with a mechanical resonator"; Fuchs, G. D., Invited Talk, The Third Infinity: 2nd Conference on Physics of Biological and Complex Systems, Güttingen, Germany (2015).
- "Quasi-Linear Spin Torque Nano-Oscillators"; Buhrman, R. A., Lee, O. and Ralph, D. C., WO2014110603-A1; US2015372687-A1. PCT/US14/11555 (Filed 1/14/2015).
- "Qubit Readout with Josephson Photomultipliers"; Ribeill, G., I. Pechenezhski, T. Thorbeck, C. Howington, M. Hutchings, L. Govia, F. Wilhelm, B.L.T. Plourde, R. McDermott, March Meeting of the American Physical Society Bulletin, San Antonio, TX. (2015).
- "Readout of superconducting qubits with a Josephson photomultiplier"; Howington, C., M. Hutchings, G. Ribeill, R. McDermott, B.L.T. Plourde, March Meeting of the American Physical Society Bulletin, San Antonio, TX. (2015).
- "RFID Device, Methods and Applications"; E. Kan, Y. Ma, Patent App Filed, 5944-03-US, United States, 1/8/15, 14/413,523 (2015).
- "Scalable Integration of Long-Lived Quantum Memories into a Photonic Circuit"; Mouradian, S.L., T. Schröder, C.B. Poitras, L. Li, J. Goldstein, E.H. Chen, M. Walsh, J. Cardenas, M.L. Markham, D.J. Twitchen, M. Lipson, and D. Englund, *Phys. Rev. X* 5, 031009 (21 July 2015).
- "Secret ingredients in Thin-TFET: a 2D material based transistor"; Xing, Grace Huili, AVS annual meeting, Invited, San Jose (Oct. 2015).
- "Self-destructing Chip"; A. Lal, C. Ober, Disclosure Filed - by Joint Owner, 6981, Disclosure Date 2/11/15 (2015).
- "Self-destructing Chip"; S. Ardanuc, K. Camera, S. Eickhoff, V. Gund, J. Kriz, A. Lal, C. Ober, J. Ridley, A. Ruyack, S. Tin, Patent App Filed, 6981-02-US, United States, 3/17/15, 14/660,726 (2015).
- "Self-Folding With Graphene Bimorphs"; Cohen, Itai, Physics Colloquia, Harvard University; Materials Science and Engineering Colloquia, Northwestern University (2015).
- "Signal quality, radiation damage, and microfluidics at high-flux x-ray sources, Poster"; Gillilan, R.E., C. Wang, L. Lin, International Small Angle Scattering Meeting, Berlin, Germany (16-Sep-15).
- "Silicon Acousto-Optic Modulator Structure and Method"; S. Bhawe, S. Sridaran, Issued Patent, 4267-04-US, United States, 7/24/12, 13/556,617, 5/19/15, 9,036,951 (2015).
- "Silicon and silicon carbide nonlinear photonics, (Tutorial Talk)"; Lin, Q., The 7th Int'l Conference on Information Optics and Photonics, Nanjing, China (2015).
- "Silicon carbide microresonators with high optical Q and large Kerr nonlinearity for nonlinear optics"; Lu, X., J. Lee, S. Rogers, and Q. Lin, *CLEO/QELS, FTH1D.3 Proceedings* (2015).
- "Silicon-chip mid-infrared frequency comb generation"; Griffith, A.G., Lau, R.K.W, Cardenas, J., Okawachi, Y., Mohanty, A., Fain, R., Lee, Y.H.D., Yu, M., Phare, C.T., Poitras, C.B., Gaeta, A.L., and Lipson, M., *Nat. Commun* (24 Feb 2015).
- "Silicon-chip source of bright photon pairs"; Jiang, W. C., X. Lu, J. Zhang, O. Painter, and Q. Lin, *Optics Express* Vol. 23, Issue 16, pp. 20884-20904, doi: 10.1364/OE.23.020884. (2015).
- "Silicon-Chip-Based Optical Frequency Combs"; Gaeta, A, AFRL-AFOSR-VA-TR-2015-0365. (2015).
- "Silicon-Nitride Platform for Narrowband Entangled Photon Generation"; Ramelow, S., A. Farsi, S. Clemmen, D. Orquiza, K. Luke, M. Lipson, A.L. Gaeta, arXiv:1508.04358 [quant-ph] (2015).
- "Smartphone Based Molecular Diagnostics for Mobile and Global Health"; Erickson, D., Photonics West, San Francisco, CA (Feb. 2015).
- "Soft Actuator and Methods of Fabrication"; B. MacMurray, R. Shepherd, H. Zhao, Patent App Filed, 6577-02-PC, PCT/US15/25183 (2015).
- "Solid-state 3D-Nano-Integrated Battery"; H. Abruna, U. Wiesner, Disclosure Filed - by Cornell, 7175, Disclosure Date 8/26/15 (2015).
- "Spatiotemporal Imaging of Gigahertz Frequency Magnetization Dynamics Using the Time Resolved Anomalous Nernst Effect"; Bartell, J., D. H. Ngai, Z. Leng, and G. D. Fuchs, March Meeting of the APS, San Antonio, TX (2015).

- “Spectrally Efficient Comb Source with Coupled Microresonators”; Okawachi, Y., S. Miller, S. Ramelow, K. Luke, A. Farsi, M. Lipson, and A. Gaeta, CLEO, OSA Technical Digest (online), OSA paper SM2M.3. (2015).
- “Spin Hall effect (SHE) and spin transfer torque (STT) effect-based device has metal insertion layer which is in contact with and located between, ferromagnetic layer and SHE layer”; Buhrman, R. A., M. Nguyen, C. Pai, and D. C. Ralph, Patent Application PCT/US15/41039 (filed July 17, 2015).
- “Spin Hall Effect Apparatus, Method and Applications”; Buhrman, R., D. Ralph, L. Liu, and C.-F. Pai, US Patent 9,105,832. (Granted Aug. 11, 2015).
- “Spin Hall Effect Magnetic Apparatus, Method and Applications”; Buhrman, R. A., Ralph, D. C. Liu, L. and Pai, C. F, WO2013025994-A2; WO2013025994-A3; KR2014044941-A; US2014169088-A1; CN103890855-A; KR1457511-B1; US9105832-B2; US2015348606-A1. (Issued 8/11/2015).
- “Spin orbit torques in magnetic nanostructures”; Buhrman, R. A., 1st (ImPACT) International Symposium on Spintronic Memory, Circuit and Storage, Tokyo International Exchange Center, Invited talk, Aomi, Tokyo, JAPAN (June 21-22, 2015).
- “Spin Transfer Torques from Spin-Orbit Interactions in Heavy Metals and Topological Insulators”; Ralph, D.C., SPIE Optics + Photonics, San Diego, CA (Aug. 2015).
- “Spin Transfer Torques from Spin-Orbit Interactions in Heavy Metals and Topological Insulators”; Ralph, D.C., French-US Workshop on Nanoelectronics, New York University, New York, NY (Sept. 14-15, 2015).
- “Spin Transfer Torques from the Spin Hall Effect and from Topological Insulators”; Ralph, D.C., March Meeting of the APS, San Antonio, TX (March 2-6, 2015).
- “Spin-phonon interactions in diamond”; Fuchs, G. D., Invited Talk, B2 Institute and the Institute for Theoretical Atomic, Molecular, and Optical Physics Winter Graduate School, Tucson, AZ (2015).
- “Spin-Torque Switching with the Giant Spin Hall Effect”; Ralph, D.C., March Meeting of the American Physical Society, San Antonio, TX (March 2-6, 2015).
- “Spin-transfer torque generated by a topological insulator”; Mellnik, A., March Meeting of the American Physical Society, San Antonio, TX (March 2-6, 2015).
- “Squish and Squeeze-Nuclear Mechanics in 3-D Cell Migration”; Lammerding, J; Invited presentation, NCI Physical Science in Oncology Centers (PS-OC) Symposium. National Cancer Institute. Rockville, MD (23-Jul-15); Invited presentation, Physics of cells: From molecules to systems (PhysCell 2015) EMBO Meeting. Bad Staffelstein, Germany (Sept. 3, 2015); Invited seminar, Labex CelTisPhyBio Workshop on Cell Motility. Institut Curie, Paris, France (25-Mar-15).
- “Stable immobilization of an enzyme on an organic transistor via a polymer brush”; Welch, M. E., T. Doublet, C. Bernard, G. Malliaras, and C.K. Ober, J. Polym. Sci., Part A-Polym. Chem. 53(2), 372-377. (2015).
- “Stacked Waveguide Reactors with Gradient Embedded Scatterers for High-Capacity Water Cleaning”; Ahsan, S., Gumus, A., Erickson, D., Optics Express, 23(24), A1664-A1671 (2015).
- “Stretchable Electroluminescent Devices and Methods of Making and Using Same”; C. Larson, S. Li, B. Peele, S. Robinson, R. Shepherd, Patent App Filed, 6857-01-US, United States, 11/3/15, 62/250,172 (2015).
- “Strongly Modulated Friction of a Film-Terminated Ridge-Channel Structure”; He, Z., C.-Y. Hui, B. Levrard, Y. Bai, A. Jagota, Scientific Reports 6 26867; doi: 10.1038/srep26867. (2015).
- “Structures and Methods for Electronically and Mechanically Linked Monolithically Integrated Transistor and MEMS/NEMS Devices”; K. Amponsah, A. Lal, Issued Patent, 5271-03-US, United States, 5/31/13, 13/990,830, 10/13/15, 9,159,710 (2015).
- “Studying the mechanism of hybrid nanoparticle EUV photoresists”; Zhang, B., L. Li, J. Jiang, M. Neisser, J.S. Chun, C. K. Ober, E. P. Giannelis, SPIE 9425, Advances in Patterning Mechanisms and Process XXXII. 94251E Proceedings (2015).
- “Studying the Mechanism of Hybrid Nanoparticle Photoresists: Effect of Particle Size on Photopatterning”; Li, L.; Chakrabarty, S.; Spyrou, K.; Ober, C.; Giannelis, E., Chem. Mater., 27(14), 5027-5031. (2015).
- “Superconducting Circuitry for Quantum Electromechanical Systems”; LaHaye, M.D., Rouxinol, F., Hao, Y., Shim, S-B. and Irish, E.K., Proc of the SPIE, Quantum Information and Computation XIII, 95001D (2015).
- “Superconducting metamaterials and qubits”; Plourde, B. L. T., H. Wang, F. Rouxinol, M. D. LaHaye, SPIE 9500, Quantum Information and Computation XIII, 95000M. Proceedings of the, (2015); SPIE Quantum Information and Computation XIII: Baltimore, MD (April 23, 2015).
- “Surface Acoustic Waves for Traveling Spin-Wave Resonance Spectroscopy”; Gowthan, P., T. Moriyama, D. C. Ralph and R. A. Buhrman, March Meeting of APS, San Antonio, Texas (March 2-6, 2015).
- “Surface Enhanced Raman Scattering (SERS) Apparatus, Methods, and Application”; A. Chung, D. Erickson, Y.S. Huh, Issued Patent, 5319-02-US, United States, 8/29/12, 13/597,688, 4/7/15, 9,001,322 (2015).
- “Surgically Implanted Micro-platforms and Microsystems in Arthropods and Methods Based Thereon”; A. Bozkurt, J. Ewer, A. Lal, A. Paul, Issued Patent, 3872-03-US, United States, 9/24/09, 12/518,847, 11/3/15, 9,173,384 (2015).
- “Suspended silicon slotted microring resonators with ultra-high optical quality”; Jiang, W. C., and Q. Lin, SPIE 9367, 936708 Proceedings (2015).
- “Synchronization and Phase Noise Reduction in Micromechanical Oscillator Arrays Coupled through Light”; Zhang, M., S. Shah, J. Cardenas, and M. Lipson, Phys.Rev.Let., V.115, No. 16, 163902 (16 October 2015).

- "Synchronization of Delay-coupled Micromechanical Oscillators"; Shah, S.Y., M. Zhang, R. Rand, M. Lipson, 2015arXiv151108536S (2015).
- "System and Method for Cryogenic Optoelectronic Data Link"; K. Bergman, A. Kadin, M. Lipson, O. Mukhanov, C. Phare, I. Vernik, Patent App Filed, 7245-01-US, United States, 11/18/15, 62/256,991 (2015).
- "System and Methods for Moving Objects Individually and in Parallel"; H. Lipson, R. MacCurdy, A. Macner, C. Perich, P. Steen, Issued Patent, 5716-02-US, United States, 2/18/13, 13/769,534, 3/31/15, 8,992,183 (2015).
- "Systematic study of ligand structures of metal oxide EUV nanoparticle photoresists"; Jiang, J., M. YU, B. Zhang, M. Neisser, J.S. Chun, E. P. Giannelis, C. K. Ober, SPIE 9422, EUV Lithography VI. 942222, Proceedings (2015).
- "TEER measurement techniques for in vitro barrier model systems"; Srinivasan, B., Kolli, A.R., Esch, M.B., Abaci, H.E., Shuler, M.L., and J.J. Hickman, Journal of Lab Automation. 20:107-126 (2015).
- "Temperature dependence of current induced effective spin-orbit torques in perpendicular magnetic anisotropy systems"; Ou, Y., C-F Pai, G. Rowlands, J. Park, D. C. Ralph and R. A. Buhrman, March Meeting of APS, San Antonio, Texas (March 2-6, 2015).
- "Testing Time Reversal Symmetry in Artificial Atoms,"; Brito, F., Rouxinol, F., LaHaye, M.D. and Caldeira, A.O., New Journal of Physics 17, 075002 (2015).
- "The Enhancement of spin Hall torque efficiency and reduction of Gilbert damping in spin Hall metal/normal metal/ferromagnetic trilayers"; Nguyen, M.-H., C.-F. Pai, D. C. Ralph and R. A. Buhrman, March Meeting of APS, San Antonio, Texas (March 2-6, 2015).
- "The molecular machine of vesicle fusion"; Lindau, M., Chemistry Colloquium, Binghamton University, Binghamton, NY (2015).
- "The nanomechanical mechanism of exocytotic fusion pore formation"; Lindau, M., Molecular Physiology, School of Medicine, University of Western Sydney, (2015); Queensland Brain Institute, University of Queensland, Brisbane, QLD Australia (2015).
- "The role of lamin A/C on nuclear mechanics, rupture, and DNA damage in breast cancer cell migration"; Poster presentation based on submitted abstract, Denais, CM, Gilbert R, Isermann P, Davidson PM, McGregor A, Krause M, Wolf K, Lammerding J., 9th European Conference on Intermediate Filaments in Health and Disease. Stockholm, Sweden (June 24-26, 2015).
- "The role of lamins A/C on nuclear deformability and rupture during 3-D cell migration"; Presentation based on selected abstract, Lammerding, J, 9th European Conference on Intermediate Filaments in Health and Disease. Stockholm, Sweden (25-Jun-15).
- "The Science, Technology, and Art of Graphene"; McEuen, P.L., Advanced Semiconductor Manufacturing Conference (May 2015).
- "The Spatial Distribution of Dose Rate during Liquid Cell Electron Microscopy"; Schneider, N.M., F.M. Ross, and H.H. Bau, MRS Fall Meeting, selected for oral presentation, Paper number VV5.08 (1-Dec-15).
- "Thermal Diodes Based on Near-Field Radiation"; Lipson, M., AFRL-RY-WP-TR-2015-0163 (October 2015).
- "Thickness Dependent Magnetoelastic Effects and Perpendicular Magnetic Anisotropy in the Ta/CoFeB/MgO System"; Stiehl, G., P. Gowtham, D. C. Ralph and R. A. Buhrman, March Meeting of APS, San Antonio, Texas (March 2-6, 2015).
- "Thin-TFET: a 2D material based transistor"; Xing, G.H., Steep Transistors Wkp, Invited, Notre Dame (Oct. 2015).
- "THz devices based on 2D electron systems"; Xing, G.H., Int'l Conference on Solid State Devices and Materials (SSDM), Invited, Sapporo, Japan (Sept. 2015).
- "Time super-resolution microscopy - A rapid change in SNAP-25 precedes fusion on the millisecond time scale"; Lindau, M., Department of Neurology, Columbia University Medical Center, New York, NY. (2015); Laboratoire de Physiologie Cérébrale, Université Paris Descartes, Paris, France (2015).
- "Time-Resolved Magneto-Thermal Microscopy of Spin Hall Effect Driven Dynamics"; Guo, F., J. M. Bartell, G. D. Fuchs, Spintech VIII, Basel, Switzerland (2015).
- "Tissue Engineered, 3D Collagen Microsphere Scaffold (MSS) Expedites Cellular Invasion and Neovascularization"; Zhang, P., O. Asanbe, W. Landford, A. Jacoby, R. Hooper, A. Stroock, J. Spector., Plastic and Reconstructive Surgery Council Annual Meeting. Seattle, WA. (May 14 - 16, 2015).
- "Titanium Dioxide Integrated Photonics - Evanescent-Wave Raman Scattering for Label-Free Chemical Identification"; Evans, C. C., C. Liu, and J. Suntivich, MRS, San Francisco, CA (Apr 9 2015).
- "Towards a table-top microscope for nanoscale magnetic imaging using picosecond thermal gradients"; Bartell, J., D.Ngai, Z.Leng, G.Fuchs, Nat. Commun. 6, 8460 (2015).
- "Transfer printing of CVD graphene FETs on patterned substrates"; Abhilash, T. S., R. De Alba, N. Zhelev, H. G. Craighead and J. M. Parpia, Nanoscale, 7, 14109-14113 DOI: 10.1039/C5NR03501E (2015).
- "Transient laser heating induced hierarchical porous structures from block copolymer-directed self-assembly"; Tan, K.W., Jung, B., Werner, J.G., Rhoades, E.R., Thompson, M.O., Wiesner, U., Science, Vol.349, No.6243, pp. 54-58 (2015).
- "Traveling surface spin wave resonance spectroscopy using surface acoustic waves"; Gowtham, P. G., Moriyama, T., Ralph, D. C. and Buhrman, R. A., Journal of Applied Physics 118, doi:10.1063/1.4938390 (2015).
- "Tunable frequency combs based on dual microring resonators"; Miller, S., Y. Okawachi, S. Ramelow, K. Luke, A. Dutt, A. Farsi, A. Gaeta, and M. Lipson, Optics Express V23, Issue 16, 21527-21540 (07 Aug. 2015).

- “Tunable Optical Apparatus, Method, and Applications”; M. Lipson, S. Manipatruni, G. Wiederhecker, Issued Patent, 5033-03-US, United States, 11/13/12, 13/697,560, 6/16/15, 9,057,829 (2015).
- “Tunable optical excitations in twisted bilayer graphene form strongly bound excitons”; Patel, H., R. W. Havener, L. Brown, Y. Liang, L. Yang, J. Park, and M. W. Graham, *Nano Letters*, 15, 5932-5937. (2015).
- “Tunable Squeezing Using Coupled Ring Resonators on a Silicon Nitride Chip”; Dutt, A., S. Miller, K. Luke, J. Cardenas, A.L. Gaeta, P. Nussenzeveig, M. Lipson, arXiv:1506.03791 (11 June 2015).
- “Twin photon pairs in a high-Q silicon microresonator”; Rogers, S., X. Lu, W. C. Jiang, and Q. Lin, *Appl. Phys. Lett.* 107, 041102 (2015).
- “Twin photon pairs in a high-Q silicon microresonator”; Rogers, S., X. Lu, W. C. Jiang, and Q. Lin, *CLEO/QELS, FTu1A.6* (2015).
- “Ultimate GaN vertical transistor: PolarMOS”; Xing, G.H., International Conference on Nitride Semiconductors (ICNS), Invited, Beijing, China (Aug. 2015).
- “Ultra-low Power Multi-modal RF and Physical Sensors Using NEMS Switches and Piezoelectric Bimorphs”; A. Lal, A. Molnar, Disclosure Filed - by Cornell, 7221, Disclosure Date 10/12/15 (2015).
- “Ultra-pure single-mode photon generation in high-Q silicon microdisks”; Lu, X., W. Jiang, J. Zhang, and Q. Lin, *CLEO/QELS, FM2A.1 Proceedings* (2015).
- “Ultrasonic Horn Actuated Microprobes based Self-Calibrating Viscosity Sensor”; R. Abhishek, A. Lal, Issued Patent, 4948-04-CN, Chi3/18/13, CN201180044775.3, 8/12/15, ZL201180044775.3 (2015).
- “Ultrasound Wave Generating Apparatus”; G. Lewis Jr., W. Olbricht, Issued Patent, 4392-07-US, United States, 1/7/11, 13/003,201, 5/5/15, 9,024,507 (2015).
- “Understanding of PS-b-PMMA phase segregation under laser-induced millisecond thermal annealing”; Jacobs, A.G., Liedel, C., Ober, C.K., Thompson, M.O., SPIE - The International Society for Optical Engineering, Vol.9423, Proceedings of, (2015).
- “Unexpected Roles of NMMIIA in Glioma Biology. Poster presentation selected from submitted abstract”; Picariello, H, Crish J, Canoll P, Lammerding J, Scarl R, Rai V, Egelhoff T, Rosenfeld S., American Society for Cell Biology (ASCB) Annual Meeting. San Diego, CA (Dec. 13, 2015).
- “Unique opportunity to harness polarization in GaN to override the conventional power electronics figure-of-merits”; Xing, Grace Huili, Device Research Conference (DRC), Invited, Columbus, Ohio (June 2015).
- “Upgrade of MacCHESS facility for X-ray scattering of biological macromolecules in solution”; Acerbo, A. S., Cook, M. J., and Gillilan, R. E., *Journal of Synchrotron Radiation*, 22(1), 180-186. (2015).
- “Using microfluidics and microfabrication to study stem cell dysfunction in muscular dystrophy and cardiomyopathies. Invited presentation”; Lammerding, J, Cornell Stem Cell Symposium. Cornell University. Ithaca, NY (13-Jun-15).
- “Utilizing Scanning Kelvin Probe Microscopy to Visualize Microsecond Charging Transients in Photovoltaic Materials”; Nathan, S. R. and J. A. Marohn, 12th International Symposium on Functional π -Electron Systems (F π -12); University of Washington; Seattle, Washington (July 19-24, 2015).
- “Valley degeneracy breaking by magnetic field in monolayer MoSe₂”; MacNeil, D., C. Hikes, K. F. Mak, Z. Anderson, A. Kornanyos, V. Zolyomi, J. Park, and D. C. Ralph, *Phys. Rev. Letts.*, 114, 037401. (2015).
- “Vertical oriented lamellar formation of fluorine- and silicon-containing block copolymers without neutral layers”; Takano, H.; Wang, L.; Tanaka, Y.; Maeda, R.; Kihara, N.; Seino, Y.; Sato, H.; Kawamonzon, Y.; Miyagi, K.; Minegishi, S.; Ober, C.K.; Hayakawa, T.; J. of Photopolymer Science and Tech, 28(5), 649-652. (2015).
- “Viewing SNAREs at work”; Lindau, M., 10th Cell Biology Days, Institut Curie, Orsay, France (2015).
- “Waveguide-based single-shot temporal cross-correlator”; Fridman, M., Y. Okawachi, S. Clemmen, M. Ménard, M. Lipson and A.L. Gaeta, *Journal of Optics*, Volume 17, Issue Number 3 (02 Feb. 2015).
- “Widely Tunable Morphologies in Block Copolymer Thin Films Through Solvent Vapor Annealing Using Mixtures of Selective Solvents”; Chavis, M.A., D.-M. Smilgies, U.B. Wiesner and C.K. Ober, *Adv. Func. Mater.*, 25(20), 3057-3065. (2015).

COVER CREDIT:

The cover images are from “Growth and Characterization of Ultra-Strong Multi-Layer Graphene”; CNF Project Number 2386-15, Principal Investigator Sol M. Gruner, and User Gabrielle Illava; MacCHESS and Biophysics/Physics; Cornell University. Background: Figure 1, Fold of MLG graphene after transfer to silicon nitride TEM grid that allows for side view of multiple layers. Inset: Figure 4, The graphene dragon, an interesting fold of MLG after transfer to silicon nitride TEM grid. Full report starts on page 198.

REDUCE REUSE RECYCLE

**CORNELL NANOSCALE SCIENCE & TECHNOLOGY FACILITY
:: 2015-2016 RESEARCH ACCOMPLISHMENTS ::**

COMMONLY USED ABBREVIATIONS & THEIR MEANINGS

μl microliter	BDM 2,3-butanedione monoxime
μm micron, micrometer	BES bioelectrochemical system
μN micro-Newtons	BHJ bulk heterojunction
μs microsecond	Bi bismuth
Ω Ohm	BiOCl bismuth oxychloride
< is less than	BioSAXS... .. biological small angle x-ray scattering
> is greater than	BN boron nitride
\sim approximately	BOE... .. buffered oxide etch
1D one-dimensional	BOX buried oxide layer
2D two-dimensional	BPB bisphenol base
2DEG two-dimensional electron gas	BPF bisphenol F
3D three-dimensional	Br... .. bromine
3DOM carbon three-dimensionally ordered macroporous carbon	BRDF bidirectional reflectance distribution function
^3He helium-3	BSA... .. bovine serum albumin
^4He helium-4	BST barium strontium titanate
$\alpha\text{-Al}_2\text{O}_3$ sapphire	BTO... .. barium titanate
$\alpha\text{-Si}$ amorphous silicon	C carbon
A&M. Agricultural & Mechanical	C centigrade
AC alternating current	C-V capacitance-voltage
AFM atomic force microscopy/ microscope	C_3N_4 carbon nitride
AFOSR Air Force Office of Scientific Research	C_4F_8 octafluorocyclobutane, or perfluorocyclobutane
Ag silver	CAAC... .. c-axis-aligned crystalline
agLDL aggregated low-density lipoproteins	CaCO_3 calcium carbonate
AgNO_3 silver nitrate	CAD... .. computer-aided design
AgSR silver-alkanethiolate	CaF_2 calcium fluoride
AIC aluminum-induced crystallization	CCI Centers for Chemical Innovation
Al aluminum	CCMR Cornell Center for Materials Research
Al_2O_3 aluminum oxide	CCS... .. continuous compositional spreads
ALD... .. atomic layer deposition	Cd cadmium
AlGaN... .. aluminum gallium nitride	CdS cadmium sulfide
AM amplitude modulation	CdSe cadmium selenide
APD... .. avalanche photodiode	CDW charge-density-wave
APS... .. advanced photon source	Ce... .. cerium
Ar... .. argon	CF_4 carbon tetrafluoride or tetrafluoromethane
ARC... .. anti-reflective coating	CFD computational fluid dynamics
ArF argon fluoride	CFMA... .. carbon-fiber microelectrode amperometry
As... .. arsenic	CH_4 methane
AST... .. aspartate transaminase	CHES... .. Cornell High Energy Synchrotron Source
atm standard atmosphere (as a unit of pressure)	CHF_3 trifluoromethane
ATRP atom transfer radical polymerization	CIGS copper indium gallium diselenide
Au gold	CION colloidal iron oxide nanoparticles
AuNPs... .. gold nanoparticles	Cl... .. chlorine
B boron	Cl_2 chlorine gas
B_4C boron carbide	Cl_2/SF_6 chlorine sulfur hexafluoride
<i>B. subtilis</i> <i>Bacillus subtilis</i>	cm centimeter
BAM bisphenol aminomethyl	CMOS... .. complementary metal oxide semiconductor
BCL_3 boron trichloride	

CMOSFET	complementary metal oxide field effect transistor
CMP	chemical mechanical polishing
CNF	Cornell NanoScale Science & Technology Facility
CNL	charge neutrality level
CNS	Cornell Center for Nanoscale Systems
CNTFET	carbon nanotube field-effect transistor
Co	cobalt
CO ₂	carbon dioxide
Co ₃ O ₄	cobalt oxide
COF	covalent organic framework
CoFeAl	cobalt iron aluminum
CoFeB	cobalt iron boron
CoP	cobalt porphyrin
CPC	colloidal photonic crystal
CPD	contact potential difference
CpG	cytosine-phosphate-guanine
Cr	chromium
CRDS	cavity ring-down spectrometer
cryoSAXS	cryogenic small angle x-ray scattering
CTC	circulating tumor cell
CTC	composite thermal capacitors
CTE	coefficients of thermal expansion
CTL	confinement tuning layer
Cu	copper
Cu ₂ ZnSnS ₄	copper zinc tin sulfide
CuAlO ₂	copper aluminum oxide
CVD	cardiovascular disease
CVD	chemical vapor deposition
CW	continuous wave
CXRF	confocal x-ray fluorescence microscopy
DARPA	Defense Advanced Research Projects Agency
DC	direct current
DCB	double cantilever beam
DCE	1,2-dichloroethane
DCM	dichloromethane
<i>de novo</i>	Latin expression meaning "from the beginning," "afresh," "anew," "beginning again."
DEP	dielectrophoresis
DFT	density functional theory
DFT	discrete Fourier transform
DH-PSF	double helix point-spread function
DI	de-ionized
DIC	differential interference contrast
DMF	dimethyl formamide
DNA	deoxyribonucleic acid
DNP	dynamic nuclear polarization
DODAB	dimethyl dioctadecyl ammonium bromide
DOE	United States Department of Energy
DPPC	1,2-dipalmitoyl-sn-glycero-3-phosphocholine
DPPG	1,2-dimyristoyl-sn-glycero-[phospho-rac-(1-glycerol)]
DRAM	dynamic random access memory
DRIE	deep reactive ion etch
DSA	directed self assembly
dsDNA	double-stranded DNA
DUV	deep ultraviolet
e-beam	electron beam lithography
<i>E. coli</i>	<i>Escherichia coli</i>
EB	exchange bias
EBID	electron beam induced deposition
EBL	electron beam lithography
ECD	electrochemical detectors
ECM	extracellular matrix
EDS	energy dispersive spectroscopy
EDTA	ethylenediaminetetraacetic acid
EELS	electron energy loss spectroscopy
EG	ethylene glycol
EIS	electrochemical impedance spectroscopy
ELISA	enzyme-linked immunosorbent assays
EMCCD	electron multiplying charge coupled device
EO	electro-optic
EOT	equivalent oxide thickness
EPICs	electronic photonic integrated circuits
EPR	enhanced permeability and retention
Er	erbium
ErAs	erbium arsenide
ESM	effective screening medium
EUV	extreme ultraviolet
<i>ex situ</i>	Latin phrase that translated literally as 'off-site' -- to examine the phenomenon in another setting than where it naturally occurs
<i>ex vivo</i>	Latin for "out of the living" -- that which takes place outside an organism
F	fluorine
FcCOOH	ferrocenecarboxylic acid
FDA	United States Food & Drug Administration
FDMA	fluorinated perfluorodecyl methacrylate
FDMNES	finite-difference method approach to predicting spectroscopic transitions
Fe	iron
Fe ₂ O ₃	iron oxide
FeCl ₃	iron(III) chloride, aka ferric chloride
FeDRAM	ferroelectric dynamic random access memory
FEM	finite element method
FES	functional electrical stimulation
FESEM	field-emission scanning electron microscopy/microscope
FET	field-effect transistor
FFTs	fast Fourier transforms
fg	femto gram
FIB	focused ion beam
FIR	far infrared
fj	femto Joules
FLT	field-like torque
FM	frequency modulation
FMR	ferromagnetic resonance
FOTS	fluorosilane, tridecafluoro-1,1,2,2-tetrahydrooctyltrichlorosilane
FRAP	fluorescence recovery after photobleaching
FRET	fluorescence resonance energy transfer
FTIR	Fourier transform infrared spectroscopy
FWM	four-wave mixing
Ga	gallium
GaAs	gallium arsenide

GaAsN	gallium arsenide nitride	HSQ	hydrogen silsesquioxane
GaInNAs	gallium indium nitride arsenide	HSQ/FOX	negative electron beam resist hydrogen silsesquioxane
GaN	gallium nitride	Hz	Hertz
GaP	gallium phosphide	<i>I-V</i>	current-voltage
GaSb	gallium antimonide	I/O	input/output
GASP	growth advantage in stationary phase	IARPA	Intelligence Advanced Research Projects Activity
GB	glass bead	IC	integrated circuit
GBLMA	α -gamma butyrolactone methacrylate	ICP	inductively coupled plasma
GC	gas chromatograph	ICP-MS	inductively coupled plasma mass spectroscopy
GC-C-IRMS	gas chromatography combustion isotope ratio mass spectrometry	ICP-RIE	inductively coupled plasma reactive ion etcher
Gd	gadolinium	IFVD	impurity free vacancy diffusion
Ge	germanium	IGERT	Integrative Graduate Education and Research Traineeship
GEDI μ devices	geometrically enhanced differential immunocapture microdevices	IGZO	indium gallium zinc oxide
GFET	graphene field effect transistor	IID	impurity induced disordering
GHz	gigahertz	IIEI	ion implant enhanced interdiffusion
GI	gastrointestinal	IJCMSSE	International Journal of Computational Materials Science & Surface Engineering
GMFI	gross mean fluorescence intensity	In	indium
GMR	giant magnetoresistance	<i>in situ</i>	Latin phrase that translates literally as 'in position' -- to examine the phenomenon exactly in place where it occurs
GNR	gold nanorod	<i>in vitro</i>	Latin for "within glass" -- refers to studies in experimental biology that are conducted using components of an organism that have been isolated from their usual biological context in order to permit a more detailed or more convenient analysis than can be done with whole organisms.
GNR	graphene nanoribbons	<i>in vivo</i>	Latin for "within the living" -- experi- mentation using a whole, living organism
GPa	gigapascal	InAlN	indium aluminum nitride
GPC	gel permeation chromatography	InAs	indium arsenide
GPS	global positioning system	InAs NWs	indium arsenide nanowires
GRIN	gradient refractive index	INDEX	Institute for Nanoelectronics Discovery and Exploration
GUI	graphical user interface	InGaAsN	indium gallium arsenide nitride
GVD	group-velocity dispersion	InGaZnO ₄	indium gallium zinc oxide
h	hours	InP	indium phosphide
H	hydrogen	IPA	isopropyl alcohol
H-NMR	hydrogen-1 nuclear magnetic resonance spectroscopy	IPE	Ion & Plasma Equipment, Inc.
H ₂ O ₂	hydrogen peroxide	IPT	in-plane torque
HAMA	hydroxyl adamantyl methacrylate	IR	infrared
HAuCl ₄	chloroauric acid	iREU	International Research Experience for Undergraduates Program
HBAR	high-overtone bulk acoustic resonator	IRMS	isotope ratio mass spectrometry
hBN	hexagonal boron nitride	IrO ₂	iridium oxide
HBr	hydrogen bromide	IrO _x	iridium oxide
hcp	hexagonal close packing	ISFET	ion-sensitive field effect transistor
HCP1	Heme Carrier Protein 1	ITO	indium tin oxide
He	helium	J/m	Joules/meter
HEMTs	high electron mobility transistors	JP-8	Jet Propellant 8
Hf	hafnium	κ	dielectric constant
HF	hydrofluoric acid	K	Kelvin (a unit of measurement for temperature)
HfB ₂	hafnium diboride	K	potassium
HFEs	hydrofluoroethers	kDa	kilodaltons
HfO ₂	hafnium dioxide	KFM	Kelvin force microscopy
Hg	mercury		
high- κ	high dielectric constant		
HMDS	hexamethyldisilazane		
HMGB	high-mobility group box protein		
HOMO-LUMO	highest occupied molecular orbital & lowest unoccupied molecular orbital		
HOPG	highly oriented pyrolytic graphite		
HRS	high resistance state		
HRTEM	high-resolution transmission electron microscopy		
HS-ssDNA	thiol terminated single stranded deoxyribonucleic acid		

kg.. .. .	kilogram	MRFM.. .. .	magnetic resonance force microscopy
kHz.. .. .	kilohertz	MRI.. .. .	magnetic resonance imaging
KOH	potassium hydroxide	ms	millisecond
KPFM... .. .	Kelvin probe force microscopy	MSM.	metal-semiconductor-metal
L/D... .. .	length-to-diameter ratio	MTJ... .. .	magnetic tunneling junction
La.. .. .	lanthanum	mTorr	millitorr
LAO.. .. .	lanthanum aluminum oxide	mV	millivolt
LASSP	Laboratory of Atomic & Solid State Physics	MVD.	molecular vapor deposition
LED... .. .	light-emitting diode	MWNT.	multiwalled carbon nanotube
LER... .. .	line edge roughness	MΩ	megaohms
Li... .. .	lithium	N	nitrogen
LO.	local oscillator	N ₂	nitrous oxide
low-κ	low dielectric constant	nA	nanoAmperes
LPCVD.	low pressure chemical vapor deposition	NaCl	sodium chloride
lpm	liter per minute	NASA... .. .	National Aeronautics & Space Administration
LRS	low resistance state	Nb	niobium
LSPR.	localized surface plasmon resonance	Nb ₃ Sn	triniobium-tin
LTMD... .. .	layered transition metal dichalcogenide	NBTC	Nanobiotechnology Center, Cornell University
Lu.. .. .	lutetium	NCCR... .. .	National Centers for Research Resources
LWGs	liquid-core/liquid-cladding waveguides	NCs... .. .	nanocrystals
LWR.. .. .	line width roughness	Nd.	neodymium
M-OPTG	microring-based optical pulse-train generator	NEMs	nanoelectromechanical systems
MACE	metal-assisted chemical etching	NEXAFS... .. .	near edge x-ray absorption fine structure
MAMA.	methyl adamantyl methacrylate	NH ₄ F.	ammonium fluoride
MBE... .. .	molecular beam epitaxy	Ni.. .. .	nickel
MCBJ	mechanically controllable break junction	NIH... .. .	National Institutes of Health
MD	molecular dynamics	NIR... .. .	near-infrared
ME	magnetolectric	nL.. .. .	nanoliter
MEG	maleimide-ethylene glycol disulfide	nm.	nanometer
MEMs... .. .	microelectromechanical systems	NMP	n-methyl-2-pyrrolidone
MFMR	microfabricated micro-reactors	NMR.	nuclear magnetic resonance microscopy / spectroscopy
MgO	magnesium oxide	NNCI	National Nanotechnology Coordinated Infrastructure
MGs... .. .	molecular glasses	NORIS.. .. .	nanometrology optical ruler imaging system
MHz	megahertz	NPR	nonlinear polarization rotation
micron.. .. .	micrometer, aka μm	NPs... .. .	nanoparticles
MIFIS	metal-insulator-ferroelectric- insulator-semiconductor	NPs... .. .	nanopores
min	minutes	ns... .. .	nanosecond
ml.. .. .	milliliter	NSF... .. .	National Science Foundation
mm	millimeter	NSF-SGER	National Science Foundation Small Grants for Exploratory Research
mM	millimolar	NSOM.. .. .	near-field scanning optical microscopy
MMA-MAA.	methyl-methacrylate-co-methacrylic acid	NSSP.	nanostructured semipolar
mmHg.. .. .	millimeters of mercury; unit of pressure measurement	NV	nitrogen-vacancy
MnO ₂ NPs	manganese oxide nanoparticles	NVM.	non-volatile memory
Mo.	molybdenum	NW FETs.. .. .	nanowire field-effect transistors
MOCVD... .. .	metal oxide chemical vapor deposition	NYSTAR... .. .	New York State Office of Science, Technology & Academic Research
MONOS... .. .	metal/oxide/nitride/oxide/semiconductor	O	oxygen
MOS.. .. .	metal oxide semiconductor	OFET	organic field effect transistor
MoS ₂	molybdenum disulfide	Oh number	Ohnesorge number
MOSFET	metal oxide semiconductor field effect transistor	OLED	organic light-emitting diode
MOVPE	metal organic vapor phase epitaxy	ONO	oxide/nitride/oxide
MPM.	multiphoton microscopy	ONR-MURI	Office of Naval Research Multidisciplinary University Research Initiative
MQCA... .. .	magnetic quantum-dot cellular automata	OPS... .. .	optical particle sizer
MQW	multiple quantum well		
MRA	multifunction reconfigurable antenna		
MRAM	magnetic random access memory		

OPV	organic photovoltaic cells	PSMO	praseodymium strontium manganite
OST-MRAM	orthogonal spin-transfer magnetic random access memory	PS μ M	phase separation micro-molding
OTFT	organic thin-film transistor	Pt.....	platinum
P(VDF-TrFE)	poly[(vinylidene fluoride-co-trifluoroethylene)]	Pt/Ir	platinum/iridium
P/E	program/erase	PTX.....	paclitaxel
Pa	Pascals	PV	photovoltaic
PAB.....	post-apply bake	PVA.....	poly-vinyl alcohol
PaC	Parylene-C	PVC	polyvinyl chloride
PAE.....	power-added efficiency	PVD.....	physical vapor deposition
PAG	photoacid generator	PVDF	polyvinylidene fluoride
PAMAM.....	polyamidoamine	PVP.....	polyvinylpyrrolidone
PANOMs	planarized apertures for near-field optical microscopy	Py	permalloy, Ni ₈₁ Fe ₁₉
Pb.....	lead	PZT.....	lead zirconate titanate (PbZr _{0.52} Ti _{0.48} O ₃)
PBG.....	photonic bandgap	Q	quality factor
PBPK	physiologically-based pharmacokinetic	QD	quantum dots
PbS	lead sulfide	QW	quantum well
PBS	phosphate-buffered saline	QWI.....	quantum well intermixing
PbSe.....	lead selenide	RA	resistance-area
PC	persistent current	Re number.....	Reynolds number
PC	photocurrent	REU	Research Experience for Undergraduates Program
PCB.....	printed circuit board	RF.....	radio frequency
PCBM.....	[6,6]-phenyl-C61-butyric acid methyl ester; a fullerene derivative	RF MEMS.....	radio frequency microelectromechanical systems
PCM.....	phase change material	RFID	radio frequency identification
PCN.....	photonic crystal nanocavity	RIE	reactive ion etch
Pd.....	palladium	RMS or rms	root mean square
PD	photodetector	RNA.....	ribonucleic acid
PDMS.....	polydimethylsiloxane	ROS.....	reactive oxygen species
PE-GNR.....	polyelectrolyte gold nanorod	RPEVCD	remote plasma-enhanced chemical vapor deposition
PEB	post-exposure bake	RRAM	resistive random access memory
PEC.....	photoelectrochemical	RTA.....	rapid thermal anneal
PECVD	plasma enhanced chemical vapor deposition	RTD	resistance temperature device
PEDOT:PSS.....	poly(3,4-ethylenedioxythiophene): poly(styrenesulfonate)	s	seconds
PEG.....	polyethylene glycol	S	sulfur
PEI	polyethyleneimine	SA-MOVPE	selective area metal organic vapor phase epitaxy
PFM.....	piezo-response force microscopy	SABC	surface active block copolymers
PGMA	poly(glycidyl methacrylate)	SAED	selected area electron diffraction
pH	a measure of the activity of hydrogen ions (H ⁺) in a solution and, therefore, its acidity	SAMs	self-assembled monolayers
Ph.D.....	doctorate of philosophy	SAXS.....	small angle x-ray scattering
PhC.....	photonic crystal	Sb	antimony
PID	proportional-integral-derivative	SBH.....	Schottky barrier height
PL.....	photoluminescence	Sc.....	scandium
pL.....	picoliter	SCAN.....	single-chromatin analysis at the nanoscale
PLD.....	pulsed laser deposition	scm.....	standard cubic centimeters per minute
PLGA	poly(lactic-co-glycolic) acid	scCO ₂	supercritical carbon dioxide
PMGI	poly(methyl glutarimide)	SCOFET	single crystal organic field effect transistor
PMMA.....	poly(methyl methacrylate)	SCORE	SNARE Complex Reporter
PmPV	poly(m-phenylenevinylene-co- 2,5-dioctoxy-p-phenylenevinylene)	SDS.....	sodium dodecyl sulfate
poly-Si.....	polycrystalline silicon	Se.....	selenium
POP.....	polyolefin plastomer	sec.....	seconds
PPM.....	photolithographic phase masks	SECM	scanning electrochemical microscopy
PS	polystyrene	SEM	scanning electron microscopy/microscope
PS- <i>b</i> -PMMA.....	polystyrene- <i>block</i> -poly(methyl methacrylate)	SERS	surface enhanced Raman spectroscopy
PSL	polystyrene latex	SF ₆	sulfur hexafluoride
		SFLS.....	supercritical fluid-liquid-solid

SH.	second harmonic	Tg.	glass transition temperature
Si	silicon	TH.	third harmonic
Si ₃ N ₄	silicon nitride	THz.....	terahertz
SiAlON.	silicon aluminum oxynitride	Ti	titanium
SiC	silicon carbide	TiN	titanium nitride
SiH ₄	silane	TiO ₂	titanium dioxide
SiN	silicon nitride	TIR-FRET.	total internal reflection - fluorescence resonance energy transfer
SiNWs	silicon nanowires	TLM.....	transfer length measurement
SiO ₂	silicon dioxide	TM	transverse magnetic
SIROF.....	sputtered iridium oxide film	TMAH.....	tetramethylammonium hydroxide
SLBs.....	supported lipid bilayers	TMOS.....	tetramethylorthosilicate
SLG.....	single-layer graphene	TMR.....	tunneling magnetoresistance
SLM.....	spatial light modulator	TO.	thermo-optic
SLUG	superconducting low-inductance undulatory galvanometer	TO.	torsional oscillator
SML.....	spin memory loss	TO.	transformation optics
SMS.....	single molecule spectroscopy	TPoS.	thin-film piezoelectric-on-substrate
Sn.....	tin	TRT	thermal release tape
SNARE.	soluble n-ethylmaleimide-sensitive factor attachment protein receptor complex	TSVs	through silicon vias
SnO ₂	tin oxide	TTD.....	transverse translational diversity
SNPs	silver nanoparticles	TTV.....	total thickness variation
SNR	signal-to-noise ratio	TXM.....	transmission x-ray microscopy
SOFC	solid oxide fuel cells	UHV	ultra-high vacuum
SOI	silicon-on-insulator	USDA.....	United States Department of Agriculture
SPCM.....	scanning photocurrent microscopy	UV.	ultraviolet
SPD.....	switching phase diagram	UV-Vis.....	ultraviolet-visible
SPR	surface plasmon resonance	V	vanadium
SQUID.....	superconducting quantum interference device	V	voltage
Sr ₂ RuO ₄	strontium ruthenate	VA-CNT.....	vertically aligned carbon nanotube
SRC.....	Semiconductor Research Corporation	vdW.....	van der Waals
SrTiO ₃	strontium titanate	VLS.....	vapor-liquid-solid
ssDNA.....	single-stranded deoxyribonucleic acid	VRMs	voltage regulator modules
ST-FMR	spin torque ferromagnetic resonance	VSM.....	vibrating sample magnetometry
STEM	scanning transmission electron microscopy / microscope	W.....	tungsten
STJ.	superconducting tunnel junction	WDM	wavelength-division multiplexing
STM.....	scanning tunneling microscopy / microscope	We number.....	Weber number
STO.....	strontium titanate	WGM	whispering gallery mode
STT	spin-transfer torques	WSe ₂	tungsten diselenide
STT-MRAM.	spin-transfer torque magnetic random access memory	XeF ₂	xenon difluoride
SVA.....	solvent vapor annealing	XMCD.....	x-ray magnetic circular dichroism
<i>t</i> -BOC	<i>tert</i> -butoxycarbonyl	XPM.....	cross-phase modulation
Ta	tantalum	XPS	x-ray photoelectron spectroscopy
Ta ₂ O ₅	tantalum pentoxide	XRD	x-ray diffraction
TaN.....	tantalum nitride	XRR.....	x-ray reflectivity
TAO _x	tantalum oxide	YB ₂₅	yttrium boride
TCO.....	transparent conducting oxide	YBCO	yttrium-barium-copper-oxide
Te.....	tellurium	YBS	y-branch switch
TE.....	transverse electric	ZMW	zero-mode waveguide
TEC.....	thermionic energy converter	Zn.	zinc
TEER.	transepithelial electrical resistance	ZnCl ₂	zinc chloride
TEM.....	transmission electron microscopy / microscope	ZnO	zinc oxide
TER.....	transepithelial resistance	ZnO:Al	zinc aluminum oxide
TFET.	tunnel field effect transistor	ZnS	zinc sulfide or zinc-blende
TFM.....	traction force microscopy	Zr	zirconium
TFT	thin-film transistor	ZrO ₂	zirconium dioxide
		ZTO	zinc tin oxide

*CORNELL NANOSCALE SCIENCE
& TECHNOLOGY FACILITY*

2015-2016

RESEARCH

ACCOMPLISHMENTS

Retinal Implant Project

CNF Project Number: 657-97

Principal Investigator: Douglas Shire, Ph.D.

Users: Marcus Gingerich, Ph.D., Douglas Shire, Ph.D.

*Affiliations: Department of Electrical Engineering, Cornell University, (Gingerich, Shire);
Department of Neuro-Ophthalmology, Massachusetts Eye and Ear Infirmary (Gingerich);
Department of Electrical Engineering, Massachusetts Institute of Technology (Shire);
VA Cleveland Healthcare System (Shire); Bionic Eye Technologies, Inc., (Shire, Gingerich)*

*Primary Sources of Research Funding: Louis Stokes Cleveland VA Medical Center;
NIH 1U01EB018873-01; Massachusetts Lions Eye Research Fund*

Contact: dbs6@cornell.edu, mdg37@cornell.edu

Website: <http://www.bostonretinalimplant.org>

Abstract:

The purpose of the Retinal Implant Project is to restore useful vision to patients who are blind with degenerative retinal diseases. The primary illnesses we hope to treat are retinitis pigmentosa (a primary cause of inherited blindness) and age-related macular degeneration (the leading cause of blindness in the developed world). Both these diseases cause the eventual destruction of the photoreceptor cells — rods and cones — in the retina, leaving intact the ganglion cells, which transmit electrical impulses (and hence visual information) to the brain. The ganglion cells may be stimulated, however, with biphasic current pulses from a microfabricated electrode array. Blind surgical volunteers have consistently described visual percepts that resulted from such stimuli, and this has led our team to develop a wireless, implantable retinal prosthesis.



Figure 1: A surgical mockup of the implantable system.

Summary of Research:

The implanted portion of our device consists of power and data secondary receiving coils, and in a sealed titanium (Ti) can, a small number of discrete components, and a custom designed integrated circuit (IC), which consists of circuitry for clock and data recovery, current drivers for electrodes in a

stimulating electrode array, and a programmable function generator capable of stimulating with a wide range of pulse widths and amplitudes. The current outputs drive high-charge capacity sputtered iridium oxide film (SIROF) stimulating electrodes, which in turn give rise to the visual percepts mentioned above.

CNF-fabricated components of this system have included various proof-of-concept test structures and tools used in the research effort and an integrated combination flexible circuit and stimulating electrode array. Si wafers serve as carriers for these freestanding films during processing. The electrode leads are fabricated inside of 'sandwiches' of polyimide and amorphous silicon carbide (SiC), while the SIROF electrodes are reactively sputter-deposited.

Assembly of the intraocular components of the prosthesis is accomplished by flip chip stud bumping of the IC and solder attachment of discrete components onto an internal flexible circuit board that is hermetically sealed into an ultraminiature Ti can. The RF coils are soldered and glued to the integrated external flex-array, which is in turn thermosonically bonded to the hermetic feedthrough of the Ti can. Finally, the thermosonic bonds are protected and insulated with an overmold. An external patient

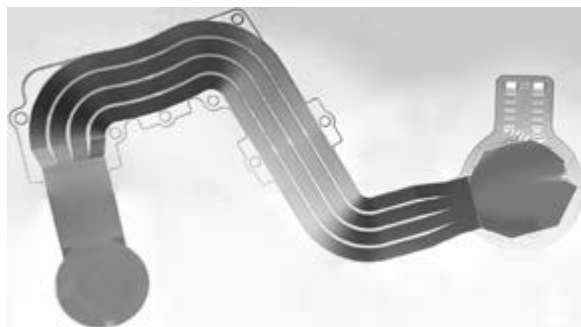


Figure 2: A picture of a single complete electrode array.

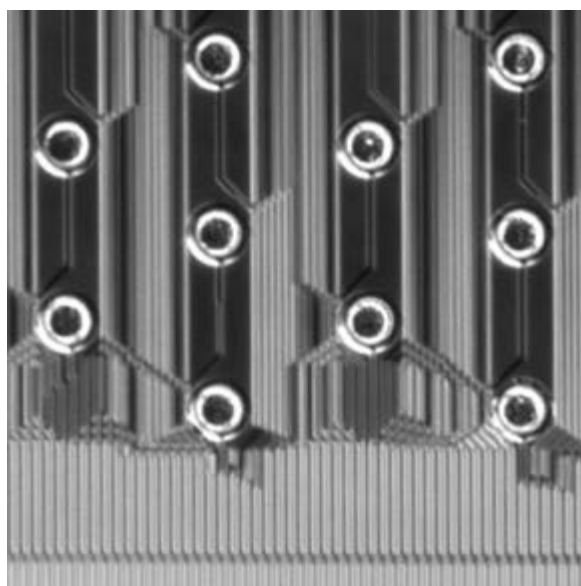


Figure 3: A microscope photograph of the Au bonding bumps and electrical conductors.

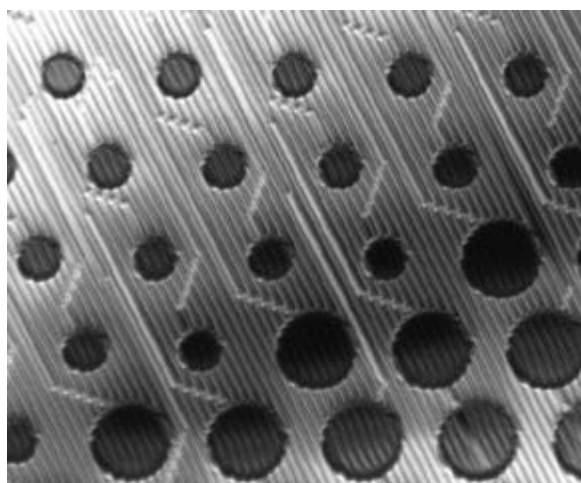


Figure 4: A microscope photograph of the SIROF electrode sites and electrical conductors.

interface unit will consist of a video camera for capturing images, a digital signal processor, and a radio frequency (RF) transmitter and coil to relay power and data to the implanted device.

Scientific challenges still remain in realizing a chronically implantable retinal prosthesis. While our first generation device was primarily encapsulated in polymers for short term proof-of-concept implant studies, our second generation system focused on a system that would last many years *in vivo*. Our latest efforts focused on developing a device with 256+ stimulation channels that is still small enough and of a configuration to be easily implanted in the ocular orbit and continue to function for many years *in vivo*. Thus, a major effort has been the development of a technological platform to build a robust, hermetically packaged, high-density subretinal visual prosthesis with a lifetime of > 10 years in biological saline that is scalable to hundreds of I/O channels.

Recent efforts have focused on optimizing the configuration, fabrication, assembly and surgical techniques in order to build the requisite number of implantable systems needed for pre-clinical trials. Fabrication work at the CNF has focused on building surgical mockup devices as shown in Figure 1. Fabrication of low defect flexible electrode arrays, Figure 2 has also been an area of work. This has presented us with significant challenges due to the large size of the overall devices and the small feature size. The microfabrication process utilizes numerous CNF tools including the Heidelberg 2000 mask writer, MA6 aligner, polyimide YES curing oven, PT72 RIE, SC4500 evaporator, Au electroplating station, as well as metrology tools. In addition to Au plated bonding bumps, Figure 3 shows some of the small conductor features that run the length of the electrode array to connect to the electrode sites shown in Figure 4.

References:

- [1] J. F. Rizzo, J. Wyatt, J. Loewenstein, S. Kelly, and D. Shire, "Methods and Perceptual Thresholds for Short-Term Electrical Stimulation of Human Retina with Microelectrode Arrays," *Investigative Ophthalmology and Visual Science*, vol. 44, no. 12, Dec. 2003, pp. 5355-5361.

Body-on-a-Chip Models for Drug Screening

CNF Project Number: 731-98

Principal Investigator: Michael L. Shuler

Users: Paula Miller, Ying Wang, Jie Lu

Affiliation: Nancy E. and Peter C. Meinig School of Biomedical Engineering, Cornell University

Primary Sources of Research Funding: National Center for Advancing Translational Sciences, National Science Foundation, National Institutes of Health

Contact: MLS50@cornell.edu, pgm6@cornell.edu, ying.wang@cornell.edu, JL3468@cornell.edu

Website: <https://www.bme.cornell.edu/people/profile.cfm?netid=mls50>

Abstract:

We have developed human “Body-on-a-Chip” devices (or microphysiological systems) that could be used to emulate drug distribution, metabolism, and action in the body. The devices were designed based upon a physiologically based pharmacokinetic-pharmacodynamic (PBPK-PD) model, where multiple chambers representing different organs are connected with microfluidic channels to mimic multi-organ interactions within the body.

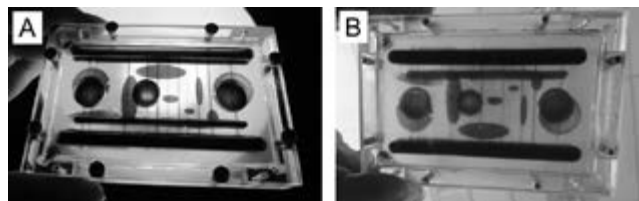


Figure 1: 14-chamber body-on-a-chip device. Trypan Blue was used to visualize the channels and chambers. (A) Top-view. (B) Bottom-view.

Summary of Research:

Design and Demonstration of a Pumpless 14-Compartment Microphysiological System. We describe the design and operation of a pumpless 14 chamber (13 organs) microfluidic cell culture device that supports multi-organ culture of barrier and non-barrier tissues and is suitable for studying the interactive responses among various organs (Figure 1) [1]. Our barrier chamber layer (skin, GI tract, and lung) allows for direct access and/or exposures to chemical or biological reagents forcing these reagents to pass through a barrier of cells established on a microfabricated membrane before exposing the non-barrier tissue chambers (fat, kidney, heart, adrenal glands, liver, spleen, pancreas, bone marrow, brain, muscle) or entering the microfluidic circulation within the device.

Our non-barrier tissue chambers were created as three-dimensional configurations by resuspending cells in hydrogel (PGMatrix). We used cell lines to represent five of these organs (barrier lines; A549 (lung) and Caco2 (GI)) (non-barrier lines; HepG2 C3A (liver), Meg01 (bone marrow), and HK2 (kidney)). The dimensions of our straight duct-like channels to each organ chamber were designed to provide the appropriate perfusion of a culture medium. The organ volumes and organ flow rates that have been reported for an average human male were used to estimate the desired fluid retention times in each organ chamber. The flow through the channels was induced by gravity on a custom programmed rocker platform that enabled pumpless operation and minimized bubble entrapment [2]. The five cell lines survived on chip with high viability (above 85%) for seven days.

This work demonstrates the feasibility of constructing, operating and maintaining a simple, gravity-driven, multi-organ microphysiological system with the capability of measuring cellular functions such as CYP1A1 and CYP3A4 activities, albumin release, urea, maintenance of tight junctions, and presence of surfactant for a sustained period. The silicone cell culture chamber layers and plastic channel layers were patterned using the CO₂ laser VersaLaser at CNF.

Microfluidic Blood-Brain Barrier Model. We developed a microfluidic blood-brain barrier (BBB)

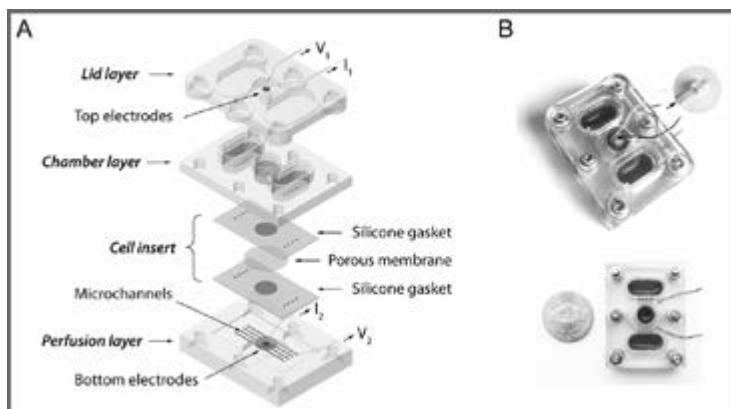


Figure 2: Design of the BBBoC system. (A) Schematic exploded view of the microfluidic platform. The device consists of a cell insert and three 3D printed plastic layers. (B) The assembled device, with or without the lid.

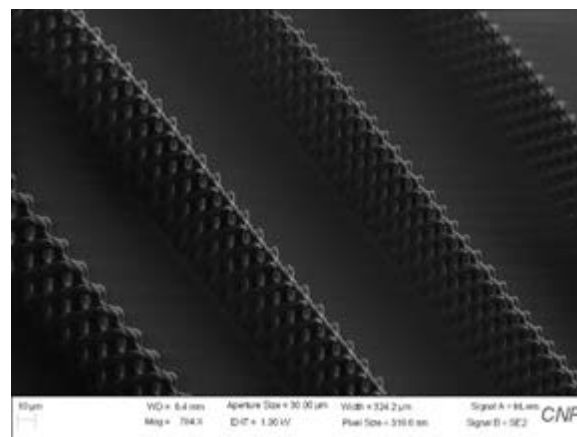


Figure 3: SEM image of micromesh sheets.

model that can be readily adaptable for use in the whole body microphysiological system described above. It consists of a cell insert carrying BBB constructs and a microfluidic culture platform providing luminal perfusion and supporting BBB construct maintenance (Figure 2). The microfluidic system was designed based on the blood residence time in human brain tissues, allowing for medium recirculation at physiologically relevant perfusion rates with no pumps or external tubing. The microfluidic platforms were fabricated with a 3D object printer (Objet 30Pro at CNF) and coated with a conformal layer of parylene-C using a vapor deposition system (PDS-2010 Lab LABCOTER® 2 at CNF) for enhanced chemical resistance and biocompatibility.

We derived brain microvascular endothelial cells from human induced pluripotent stem cells and cocultured them with primary rat astrocytes on the two sides of a porous membrane. The cocultures were then maintained on chip for up to 10 days. This BBBoC model achieved significant barrier integrity as evident by continuous tight junction network formation and *in vivo*-like values of trans-endothelial electrical resistance (TEER). We further evaluated the capacity of our BBBoC model to be used for drug permeability studies using large molecules (FITC-dextran) and small molecule model drugs. Our analyses demonstrated that the permeability coefficients obtained with our model were comparable to *in vivo* values. Our BBBoC model closely mimics physiological BBB barrier functions and will be a valuable tool for screening of drug candidates. The residence time based design of a microfluidic platform will enable integration with other organ modules to simulate multi-organ interactions on drug response.

Biomimetic 3D Microvascular Network. The objective of the project is to develop a porous micro-tubular scaffold for creating biomimetic microvascular networks that can be integrated into our body-on-a-chip system. We are developing a photolithography based approach to create SU-8 micro-mesh sheets as the building block of three dimensional microvascular scaffold (Figure 3). The pore size of the micro-mesh sheets ranges from 3 to 10 μm and the porosity varies from 15% to 40%. The 3D “microvessels” are connected to form microvascular networks, where the vessel diameter covers the range from capillaries, venules to arterioles (10 ~ 40 μm). These micro-vessel scaffolds will be populated with endothelial cells to create perfusable microvascular networks. The porous feature of the micro-mesh scaffolds allows for trans-vascular transport and even for immune cell migration. All the fabrication was done at CNF, using SU-8 photoresist, Oxford Plasma-enhanced chemical vapor deposition (PECVD), SÜSS MA6-BA6 / ABM Contact Aligner and Oxford Etcher. Images were taken with the Zeiss Ultra Scanning Electron Microscope (SEM).

References:

- [1] P. G. Miller and M. L. Shuler, “Design and demonstration of a pumpless 14 compartment microphysiological system,” *Biotechnol. Bioeng.*, vol. 9999, no. xxx, pp. 1-15, 2016.
- [2] J. H. Sung, C. Kam, and M. L. Shuler, “A microfluidic device for a pharmacokinetic-pharmacodynamic (PK-PD) model on a chip,” *Lab Chip*, vol. 10, no. 4, p. 446, 2010.

Microfluidic Device for Aptamer-Based Cancer Cell Capture and Genetic Mutation Detection

CNF Project Number: 762-99

Principal Investigator: Harold G. Craighead

User: Sarah J. Reinholt

Affiliation: School of Applied and Engineering Physics, Cornell University

Primary Source of Research Funding: National Institutes of Health R01 DA030329-03

Contact: hgc1@cornell.edu, sjr236@cornell.edu

Abstract:

Genetic mutations in cancer cells are not only fundamental to the disease, but can also have tremendous impact on the efficacy of treatment. Identification of specific key mutations in a timely and cost-effective manner would allow clinicians to better prescribe the most effective treatment options. We present a novel microfluidic device for specifically capturing cancer cells and isolating their genomic deoxyribonucleic acid (gDNA) for specific amplification and sequence analysis. To filter out rare cancer cells from a complex mixture of cells, nucleic acid aptamers that specifically bind to cancer cells are immobilized within a microchannel containing pillars to improve capture efficiency. The captured cells are lysed and the gDNA is isolated within a secondary micropillar array. This type of isolation enables multiple consecutive rounds of isothermal amplification to amplify different individual genes separately, since the genomic template is retained between subsequent amplifications. The amplified gene samples are sequenced, and the resulting sequence information is compared against the known wildtype gene to identify mutations. This approach offers a way to monitor multiple genetic mutations in the same small population of cells, which is beneficial given the wide diversity in cancer cells, and requires very few cells to be extracted from the patient sample. With this capability for genetic monitoring, precision medicine should be more accessible for the treatment of cancer.

Summary of Research:

Cancer cells contain genetic mutations that allow them to escape the regulatory processes necessary for the healthy function of tissues and organs. Moreover, there are numerous mechanisms for malignancy each with different combinations of genetic mutations, which makes cancer treatment difficult with varying levels of efficacy. Therefore, information about the genetic alterations in specific patient's cells is very valuable when determining the most appropriate treatment.

We have developed a microfluidic device capable of specifically capturing cancer cells and isolating their gDNA for on-chip amplification and subsequent genetic sequencing. Polydimethylsiloxane (PDMS) microchannels are formed using a silicon mold that was fabricated using the photolithography tools in the Cornell NanoScale Facility, and bonded to a

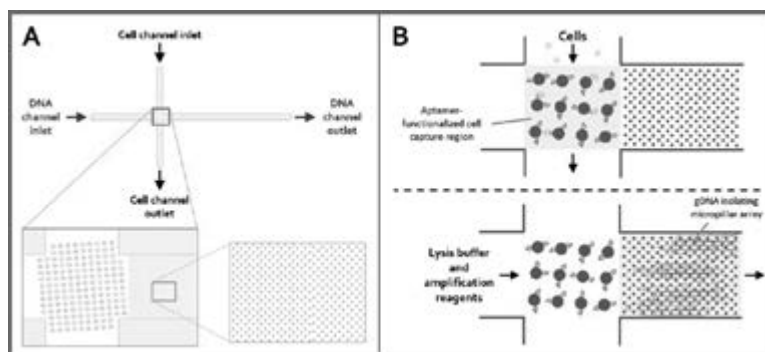


Figure 1: Schematic of the microfluidic device and process. (A) The device consists of two orthogonal microchannels; one for specifically filtering cells from a sample (cell channel), and one for isolating their gDNA (DNA channel). The device contains two micropillar arrays; a cell capture array located at the intersection of the channels, and a DNA isolation array located downstream of the cell capture array in the DNA channel. (B) The cell capture array is functionalized with cancer cell-specific aptamers to selectively filter cancer cells flowing through the cell channel. The captured cells are lysed through the DNA channel, and the gDNA is isolated via physical entanglement on the DNA micropillar array for analysis.

glass substrate. The device contains two orthogonal microchannels (Figure 1A) with a pillar array at the intersection. This array is functionalized with DNA aptamers that bind specifically to cancer cells. The pillar array is rotated 4° to increase the number of collisions cells undergo with the surface, thereby increasing the capture efficiency. A secondary micropillar array isolates the gDNA from the lysed captured cells [1]. This DNA remains entangled in the micropillars during analysis steps, including multiple isothermal amplification reactions (Figure 1B). The amplification product is extracted from the device outlet, and a gene fragment short enough to sequence is acquired via PCR. This gene fragment can then be sequenced to determine any genetic mutations by comparing it to the known wildtype gene.

Aptamers are single-stranded nucleic acids with specific affinity to their target. They are analogous to antibodies, but provide several advantages over antibodies. Aptamers are chemically synthesized with no batch-to-batch variability, much less expensive, more robust, and more easily functionalized. Here, we use a previously-selected aptamer [2] with specific affinity to several types of cancer cells. This aptamer is immobilized on the channel surface via simple streptavidin-biotin interaction with the biotinylated aptamer binding to streptavidin adsorbed on the channel surface. These aptamers capture the cancer cells from the sample. Figure 2A shows HeLa cells being captured in a device containing aptamers, but not in the absence of aptamers. The captured cells are then lysed, and their gDNA is isolated via physical entanglement by the DNA micropillar array. Captured cells were lysed and their gDNA was stained, and Figure 2B indicates that the DNA was in fact isolated by the pillars.

To detect specific genetic mutations, these genes are individually amplified in separate multiple displacement amplification (MDA) reactions using the same gDNA template isolated by the micropillars. Following each amplification, the product is extracted from the device through the outlet, and a smaller gene fragment is isolated via PCR, which is necessary because the MDA product is too large to sequence. These samples will be sequenced using Sanger sequencing, which requires pure samples with a single DNA sequence, and this can be accomplished using our device capable of separate consecutive amplification reactions on the same gDNA. The sequencing results will be compared to the known wildtype genes, and any mutations will be identified. This information can then be passed onto clinicians to make informed recommendations for the most appropriate and effective treatment for each patient.

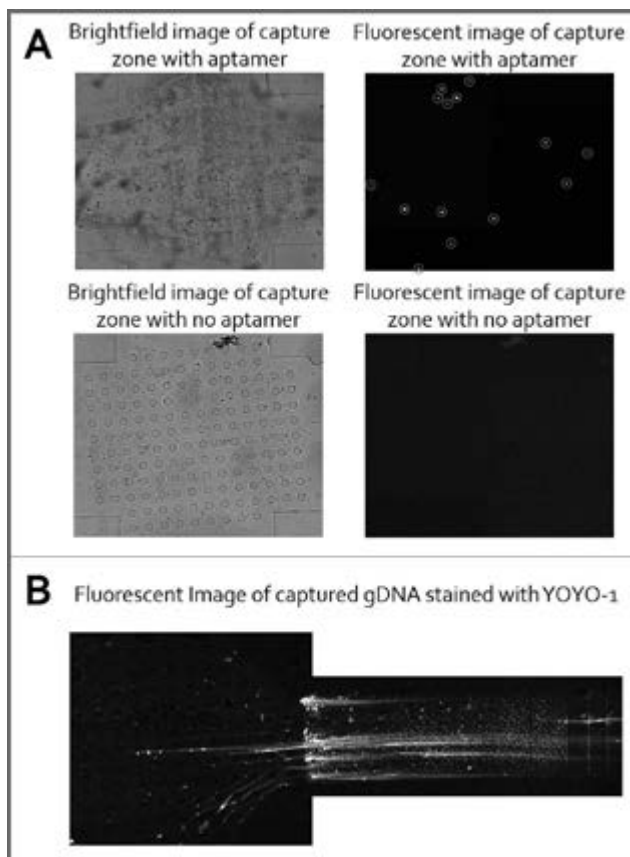


Figure 2: Surface chemistry and aptamer-based capture of HeLa cells. (A) HeLa cells are captured within the cell capture region in the presence of aptamers (upper panels), but no cells are captured in the absence of aptamers (lower panels). (B) gDNA from lysed captured cells was stained with YOYO-1 and imaged to verify its presence on the micropillars.

References:

- [1] Benítez JJ, Topolancik J, Tian HC, Wallin CB, Latulippe DR, Szeto K, Murphy PJ, Cipriany BR, Levy SL, Soloway PD, Craighead HG (2012) Microfluidic extraction, stretching and analysis of human chromosomal DNA from single cells. *Lab Chip* 12:4848. doi: 10.1039/c2lc40955k
- [2] Van Simaey D, López-Colón D, Sefah K, Sutphen R, Jimenez E, Tan W (2010) Study of the molecular recognition of aptamers selected through ovarian cancer cell-SELEX. *PLoS One* 5:e13770. doi: 10.1371/journal.pone.0013770

Microfluidic Device for Single Cell Genetic and Epigenetic Analysis

CNF Project Number: 762-99

Principal Investigator: Harold Craighead

User: Harvey C. Tian

Affiliation: Applied and Engineering Physics, Cornell University

Primary Source of Research Funding: National Cancer Institute

Contact: hgc1@cornell.edu, hct33@cornell.edu

Abstract:

Single cell analysis allows for the study of genetic and epigenetic aberrations and their relation to human disease. Such information is lost when taking the average over a heterogeneous population of cells using bulk analysis methods. However, existing platforms for genetic and epigenetic analysis do not meet the sensitivity threshold to work with the minute quantity of DNA contained within a single cell. Thus prior to analysis, the DNA single cells from must be amplified. Existing amplification techniques are limited in the sense that they are subject to amplification bias, where parts of the genome are more highly represented than the rest of the genome post amplification. In order to overcome this amplification bias on a single cell level, the original template genomic DNA (gDNA) must be either extracted from the amplified product post-amplification or retained through the amplification process. Retaining the gDNA allows for the ability to perform multiple rounds of amplification whereby different parts of the genome are biased each time and finally compiling the amplified product from multiple rounds of amplification to reach a sufficient representation of the entire genome for either downstream analysis for whole genome sequencing (WGA) of a single cell. Here, we describe the use of a polydimethylsiloxane (PDMS) microfluidic device for single cell capture, lysis, DNA extraction, and on-chip chemistries including DNA amplification and sodium bisulfite treatment.

Summary of Research:

A multitude of cells are first introduced into the microfluidic device via hydrodynamic flow. Within the device, separate channels each containing a single capture site physically entraps one cell while excess cells are flowed through the device. Cells are lysed within the capture region and the genomic DNA is subsequently trapped downstream upon an array of micropillars while RNA and cellular debris is washed away.

The entangled DNA can be stained with fluorescent intercalating dye, hybridized with DNA probes, isothermally amplified with molecular displacement amplification (MDA), or collected by releasing the DNA through enzymatic digestion.

During MDA, the original template DNA is neither consumed nor destroyed through the DNA amplification process thereby allowing for multiply rounds of amplification. After collecting the amplified product from the rounds of MDA performed on-chip, off-chip conventional polymerase chain reaction (PCR) or quantitative PCR (qPCR) is used to identify the location of various gene loci of interest.

Scalable Sensor Array Platform for Analysis of Quantal Transmitter Release Events

CNF Project Number: 848-00

Principal Investigator: Manfred Lindau

User: Meng Huang

Affiliation: School of Applied and Engineering Physics, Cornell University

Primary Source of Research Funding: National Institutes of Health

Contact: ML95@cornell.edu, mh2236@cornell.edu

Abstract:

Neurontransmitters are released in a quantal event by fusion with membranes. We develop and fabricate a CMOS sensor array capable of parallel electrochemical detection of vesicle release events from chromaffin cells. To enable amperometry measurement, polarizable platinum electrodes are deposited on the Al/Cu metal contact on the CMOS chip by conformal electron beam evaporation. SU-8 insulation layer is also applied to protect the surface structure of the chip and avoid incomplete coverage of the metal contact by shifting the position of the electrodes as well as form deep wells to trap cells. A silicon wafer with deep etched wells is used as holder for the CMOS chips for better handling and pattern transfer.

Summary of Research:

Neurontransmitters are released into the extracellular space in a process known as exocytosis [1]. The amperometry measurement provides precise details about the released transmitters in a single quantal event. However, amperometric spikes vary from cell to cell even under the same condition [2]. Therefore, a large number of measurements for vesicle release events must be performed to achieve a change in the mean value. Here, we present the CMOS IC sensor array capable of parallel amperometry measurement of vesicle release events and the post-fabrication to enable its functionality.

The CMOS chip has a die dimension of around 3 mm-4 mm. Therefore, direct spin coating of photoresist on the chip will leave a severe side effect and distort the pattern, especially for the viscous SU-8. Here, we fabricate a silicon wafer holder for the chips for better handling and pattern transfer, as shown in Figure 1. First, SPR220-7.0 resist is spin coated on the wafer at 3500 rpm for 30s followed by a 90s soft bake. Then, it is exposed using CNF's ABM contact aligner to transfer the pattern (exact dimension of the die, but with 50 μm margin) on it as a mask layer for etching. After the post exposure bake and development in 726MIF, the wafer is etched using Unaxis 770 deep silicon etcher to make a 250 μm deep well for the chip to fit in.

The CMOS sensor chip is fabricated at MOSIS by On Semiconductor C5F/N. Polarizable electrode materials such as platinum are not offered in this process. Instead, Al/Cu metal contact are deposited to serve as interconnection of the chip. However, amperometry measurement requires polarizable electrodes for low noise current measurement as the oxidation current is usually on the order of pA. Hence, it is necessary to have a post-fabrication process in the CNF clean room to deposit platinum electrodes directly onto the Al/Cu metal contacts for amperometry measurement. AJA

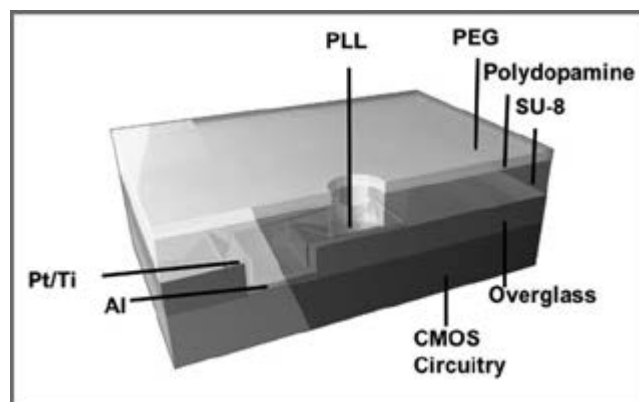


Figure 1: Silicon holder for the IC chip. The size of the etched well is basically exactly the same as the CMOS die, but with a 50 μm margin. The depth of the well is exactly the same with the die in order to have a flat surface that is beneficial for spin coating.

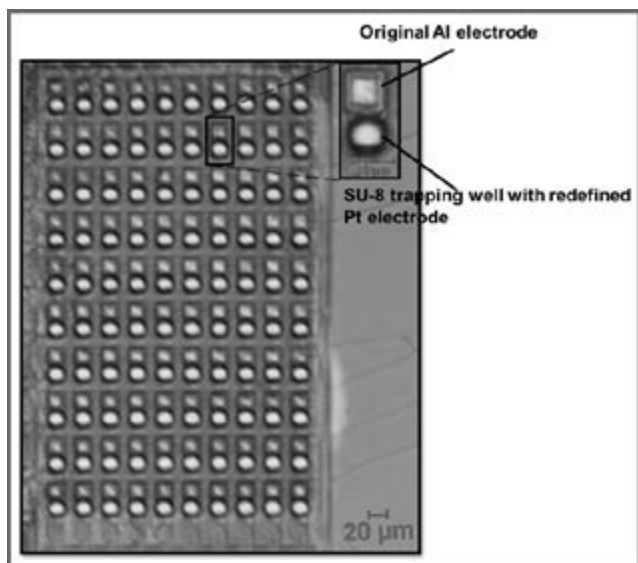


Figure 2: The geometry of shift electrode. The opening of the working area is redefined. In our case, one passivation SU-8 layer is applied with redefined shape (round) of the new opening for better cell trapping.

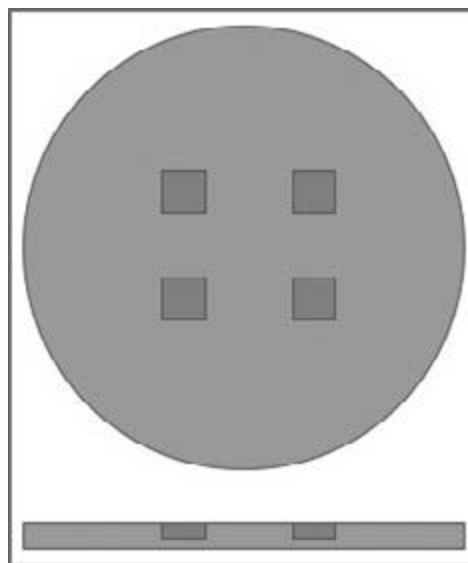


Figure 3: Shift electrode strategy on the CMOS chip. The squares that are out of focus in the image indicate the original electrodes while the rounded openings are SU-8 deep wells redefined on the chip.

sputtering system is used to deposit Ti(60s)/Pt(450s) bilayer with 400w power on the electrode to have a uniform metal film as well as good side wall coverage.

To avoid possible defects such as incomplete coverage of the Pt electrode, a shift electrode strategy is performed to redefine the position and shape of the working electrodes (Figure 2) [4]. The shifted electrodes also enable cell trapping by SU-8 deep wells. The patterned poly(L-lysine) in register with the electrodes will promote cell adhesion, while poly(ethylene glycol) is applied in between wells will resist cell adhesion [5]. Pt electrodes are deposited over the Al/Cu contact, but instead of just covering the contact window, they are extended to cover some part of the overglass. 16 μm SU-8 2025 thick layer is fabricated on the surface of the CMOS chip. Deep wells with 20 μm in diameter are opened by general lithography at the redefined electrode position. The round shape rather than the original square shape of the electrode opening is beneficial for cell trapping (Figure 3). Microcontact printing of poly(L-lysine) and poly(ethylene glycol) will be performed for promotion and resistance of cell adhesion. The product was tested with 50 μM dopamine solution and a large increase in current was observed (Figure 4).

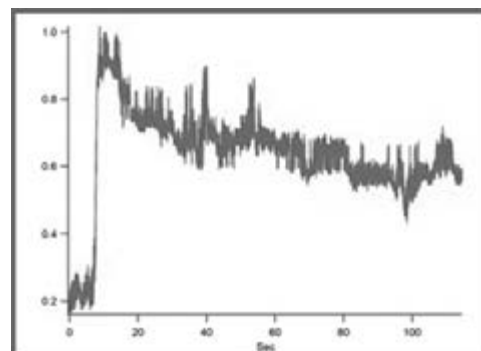


Figure 4: Current measurement with 50 μM dopamine solution. A large increase in current was observed. The vertical axis is voltage in volts and 0.2V indicate 20pA.

References:

- [1] Kisler, K., et al., J. Biomater. Nanobiotech., 2012, 3(2): p.243-53.
- [2] Colliver, TL., et al., J. Neurochem., 2000, 74(3): p. 1086-1097.
- [3] Kim, B., et al., Biosens Bioelectron., 2013, 41: p. 736-744.
- [4] Heer, F., et al. Biosens Bioelectron., 2004, 20(2): p. 358-366.
- [5] Liu, X., et al. Analytical Chem., 2011, 83: p. 2445-2451.

A MEMS Microtensiometer for Sensing Water Potential in Plants and Soils

CNF Project Number: 1119-03

Principal Investigator: Abraham D. Stroock

Users: Michael Santiago-Pinero, Winston L. Black, II, Siyu Zhu, Olivier Vincent

Affiliation: Department of Chemical and Biomolecular Engineering, Cornell University

Primary Source of Research Funding: National Science Foundation (CBET-0747993 and CHE-0924463),

Air Force Office of Scientific Research (FA9550-15-1-0052), the National Institute of Food and Agriculture,

U.S. Department of Agriculture (under Agreement No. 2010-51181-21599)

Contact: abe.stroock@cornell.edu, ms2343@cornell.edu, wlb62@cornell.edu, sz393@cornell.edu

Website: www.stroockgroup.org

Introduction:

We have developed a second generation of a sensor of water status called a microtensiometer. We reported on the first generation in previous years and in a publication [1] and patent [2]. This second generation device is shown in Figure 1 and described in a pending patent [3]. This device measures temperature and water potential (equivalent to the chemical potential of water) in its immediate environment for applications in physical chemical research on the properties of liquid water and in environmental and agricultural contexts. This updated design has the following new characteristics: 1) reduced form factor, 2) patterned membrane to provide localized sensing on one edge, 3) a network of microchannels that provide higher conductance between the internal cavity of liquid and the sensing edge of the device, and 4) platinum wiring to minimize corrosion. Additionally, we have developed environmental packaging strategies on custom PCB boards to allow for use of the device *in situ* within plants and soils.

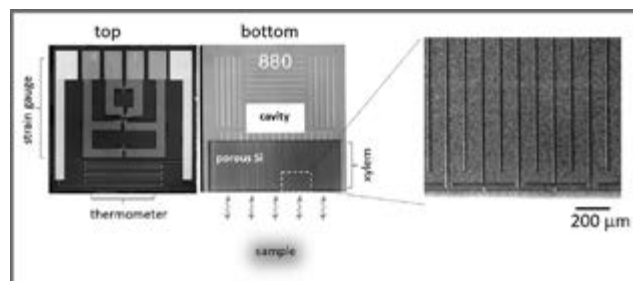


Figure 1: Micrographs of microtensiometer.

Summary of Research:

Motivation. This project seeks to develop a microelectromechanical system (MEMS) tensiometer capable of sensing water potential. Water potential, Ψ (MPa) is a thermodynamic quantity that defines the thermodynamic availability of water for chemical reactions and physical processes such as mass transfer. Of particular interest is the range of Ψ near saturation that occurs in the plants and soil that make up the biosphere. Accurate, *in situ* measurements in this range have not been achievable with current technologies. The ability to perform such measurements has important implication for studying the basic biology of plants and for precision agricultural techniques such as deficit irrigation.

Design. Figure 1 presents images of our microtensiometer. The top view shows the wiring associated with a strain gauge in the form of a

Wheatstone bridge of poly(silicon) piezoresistors and a platinum resistance thermometer. The bottom view shows a cavity that we fill with pure liquid water; the layer of silicon above this cavity acts as a diaphragm, the deflection of which is measured by the strain gauge on the top side. This cavity is connected to the bottom edge via channels and a zone of nano-porous silicon that we form as a thin layer on the bottom side of the wafer; the design of this structure was inspired by the structure of xylem, the conductive tissue in plants. The cavity and microchannels are seal by bonding the bottom side of a glass wafer. As water leaves the cavity through the nanoporous membrane, the pressure of the liquid in the cavity drops until it comes to equilibrium with the external phase of water. We measure the difference in pressure between the inside and outside gives us Ψ and is measured with the calibrated strain gauge.

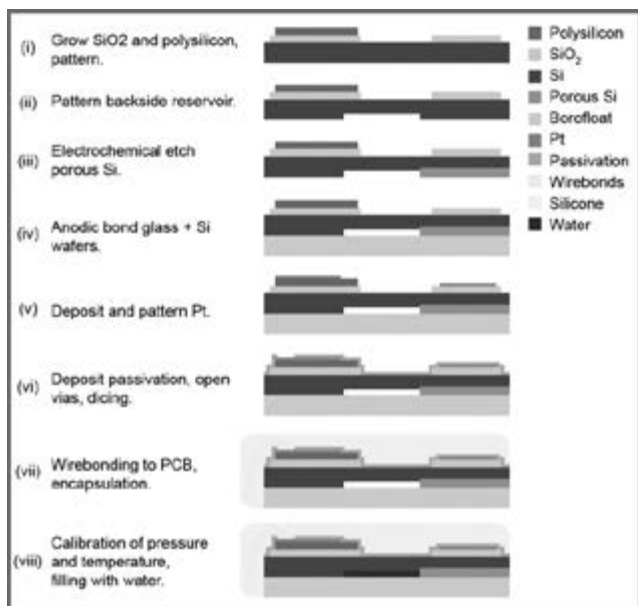


Figure 2: Process flow for fabrication of microtensimeter.

Method. Figure 2 presents an abbreviated representation of our process flow. The important steps in this process are: growth of insulating oxide (B_2 thermal oxide furnace), deposition and patterning of poly(silicon) (LPCVD furnace C4), etching of cavity and microchannels (Oxford 81/82), anodic etching of porous silicon membrane, anodic bonding of silicon to glass (SÜSS SB8e), deposition and patterning of platinum with titanium adhesion layer, deposition of passivation layers (Oxford PECVD), and dicing. After dicing, chips were mounted and wire bonded to custom PCBs and selectively encapsulated in various materials to protect electronic elements from water and while allowing for exchange through the membrane.

Characterization. Packaged devices were calibrated as described previously [1]. Figure 3 presents a multi-

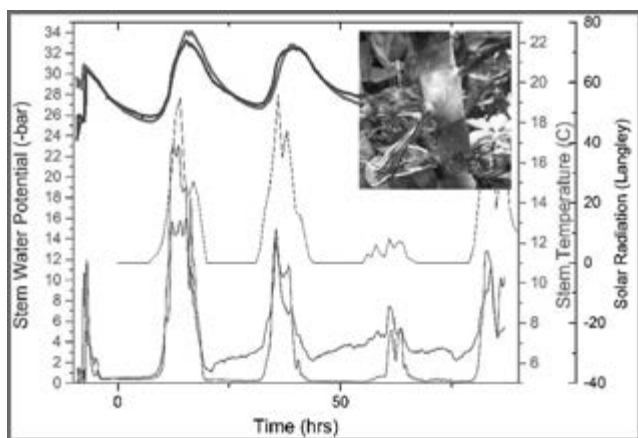


Figure 3: In situ measurements of the stem water potential (Ψ) and temperature in grape (blue) and apple (red) with microtensimeters.

day study of the response of microtensimeters embedded directly within the stems of potted apple (red) and grapevine (blue). As expected, temperature (bold curves) rises and falls each day within the stems. Also as expected, the measured water potential (fine lines) rises to larger tensions (negative pressures) as the plants respond to sun light (black curve) by opening the stomatal valves in their leaves to harvest CO_2 for photosynthesis. When stomates are open, transpiration occurs and places lowers the water potential within the plants to negative values; these values are represent the stress experienced by the plant as it maintains hydration.

Figure 4 presents the measurement of the relationship between local water potential and average water content at two locations within a soil sample; this relationship, called the water retention curve, is an important physical characteristic of a soil. Two microtensimeters were placed within the soil at different depths as indicated in the inset. These measurements in both plants and soils represent unprecedented applications of tensiometry and open new opportunities for the study of transport processes across the biosphere.

Current Efforts. We continue to mature our methods of packaging and embedding the microtensimeters for applications in plant and soil science, agriculture, and engineering contexts. Future iterations of the fabrication may aim to further reduce the form factor of the device to decrease transients and allow for application in small sample volumes.

References:

- [1] Pagay, V., et al. A microtensimeter capable of measuring water potentials below -10 MPa. Lab on a Chip (submitted).
- [2] Stroock, A.D., et al. Microtensimeter sensor, probe and method of use. US Patent No. 8,695,407 (issued 2014).
- [3] Stroock, A.D., et al. Multimodal sensor, method of use, and method of fabrication. App# PCT/US14/42435 (applied 2014).

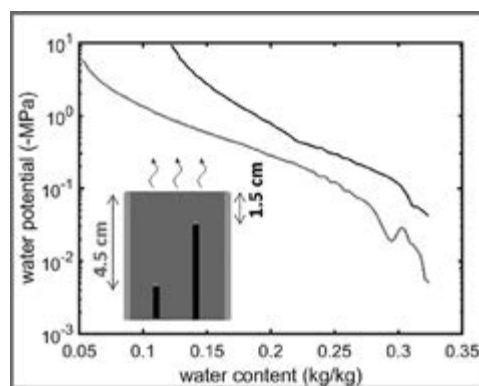


Figure 4: Water retention curves measured in situ with two microtensimeters by the Wind evaporative method.

Silicon Nitride Cantilevers for Muscle Myofibril Force Measurements

CNF Project Number: 1255-04

Principal Investigator: Walter Herzog

Users: Timothy Leonard, Andrew Sawatsky

Affiliation: Faculty of Kinesiology, University of Calgary, Calgary, Canada

Primary Source of Research Funding: Natural Sciences and Engineering Research Council of Canada, Canadian Institutes of Health Research and the Canada Research Chair for Cellular and Molecular Biomechanics

Contact: wherzog@ucalgary.ca, leonard@ucalgary.ca, ajsawats@ucalgary.ca

Website: www.ucalgary.ca/knes

Abstract:

To measure muscle forces in the nano-Newton range, silicon nitride cantilever pairs were manufactured using CNF's 5× stepper photolithography system and tested in our lab in Canada. We investigated titin mechanical properties using a skeletal muscle myofibril model. Our experiments demonstrate that in myofibrils at long sarcomere length and when immunoglobulin (Ig) domain refolding during the shortening cycle is prevented, normalized titin hysteresis in activated muscle behaves differently compared to passive muscle, but only near the last of the 9 stretch shortening cycles.

Summary of Research:

Titin is giant molecular spring present within the sarcomere and is responsible for most of the passive force found in muscle. Titin has elements with different stiffness and visco-elastic properties, which come into play in an orderly fashion with increasing sarcomere length. In skeletal muscle, the I-band region of titin contains two distinct immunoglobulin (Ig) domains, a small N₂A portion, and the PEVK segment [1]. Lengthening a skeletal muscle sarcomere within the physiologically relevant range first causes the Ig domains to straighten out and is then followed by extension of titin's PEVK domain. Both of the Ig regions (proximal and distal) and the PEVK region are thought to be essentially elastic at physiologically relevant sarcomere lengths (SL). However, at SL greater than the physiological range, Ig domains start to unfold during stretch, and this unfolding is thought to be responsible for titin then behaving in a highly visco-elastic manner.

It is believed that stretching of titin at long sarcomere length unfolds Ig domains, while shortening alone does not readily allow for refolding [2]. This implies that in repeat stretch-shortening cycles, the number of already unfolded Ig domains becomes increasingly greater and therefore titin becomes increasingly more elastic and hysteresis would be reduced.

Here, we hypothesized that while titin is a visco-elastic spring at long sarcomere length, hysteresis observed for stretch-shortening cycles will initially be greater for active compared to inactivated muscle because the higher force with activated muscle will result in a more elastic material (less hysteresis) due to greater Ig domain unfolding with the higher force, but will be less than passive muscle by the 9th cycle.

Myofibrils were harvested from psoas muscle obtained from New Zealand White rabbits and were chemically and mechanically isolated as described in our previous work [3]. Single myofibrils were attached to nanofabricated silicon-nitride cantilevers (stiffness 68 pN/nm) [4] for force measurement at one end of the myofibril (resolution < 0.5 nN), and at the other end, a glass pipette needle attached to a piezo-motor for controlling specimen length (Figure 1). Testing was done in a relaxing solution (passive tests) that contained ATP but no calcium, pH = 7, or in activating solution that contained ATP and free calcium with a pCa of 3.5.

Myofibrils were stretched passively (n=6) or activated in a calcium solution and then stretched (n=7) from an average sarcomere length of 2.6 μm by a nominal amount of 3 μm/sarcomere at a speed of 0.1 μm/s/

sarcomere. When the final stretch length was reached, the myofibrils were then immediately subjected to nine small amplitude stretch-shortening cycles of nominal magnitude $0.5 \mu\text{m}$ per sarcomere, and then, following the last of these cycles, released back to the starting length. Mean hysteresis for all the samples was calculated for each of the stretch-shortening cycles.

Figure 2 shows sarcomere length-stress data for two different myofibrils, one active and one passively tested. The peak stress in the active myofibril is much higher ($> 400 \text{ nN}/\mu\text{m}^2$) compared to the un-activated myofibrils ($< 100 \text{ nN}/\mu\text{m}^2$).

Figure 3 shows a summary histogram of hysteresis results for both tests with mean hysteresis for each of the nine stretch-shortening cycles. Figure 4 shows normalized hysteresis for the nine cycles (as a function of input energy for each stretch-shortening cycle). In both figures it can be seen that a steady-state equilibrium in the hysteresis appears by about the 7th cycle, in both active and passive tests. Looking at normalized hysteresis is an interesting comparison in that the normalized hysteresis values are not different early on in the nine cycle tests but by the later cycles (cycle 8 and 9), hysteresis is significantly different in the active tests compared to the passive tests. Hysteresis in these late active tests has not fallen to the levels seen in the passive tests, indicating that hysteresis does not indicate a more elastic behaviour in active muscle. This was not expected and may be due to some unexplained re-folding of titin in the active tests, or may be due in some way to the high calcium concentration that is known to have an effect on titin stiffness.

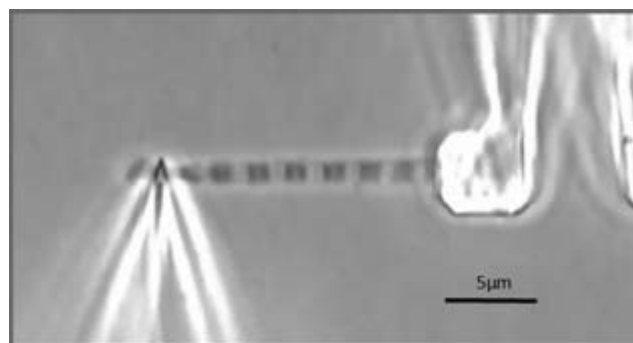


Figure 1: Myofibril attached to a glass needle for stretch-shortening and nano-levers for force measurement. An example of a single myofibril with eight sarcomeres in-series.

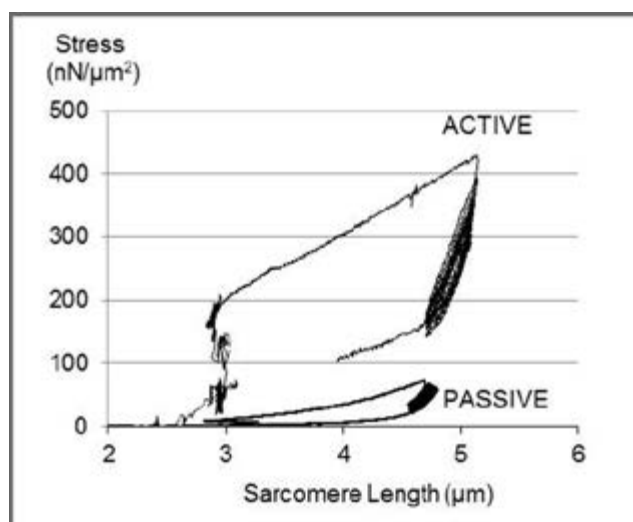


Figure 2: Sarcomere Length versus Stress for two different, single myofibrils. Each test consisted of stretching activated or non-activated myofibrils from ~ 2.8 to $\sim 5.0 \mu\text{m}$ /sarcomere and then superposed nine $0.5 \mu\text{m}$ small amplitude stretch-shortening cycles.

References:

- [1] Granzier and Labeit. Muscle Nerve. 36:740-755, 2007.
- [2] Kellermayer, et al. Science. 276(5315):1112-1116, 1997.
- [3] Joumaa, et al. Eur J Physiol. 455:367-371, 2007.
- [4] M. E. Fauver, et al. IEEE Trans Biomed Eng 45(7), 891, 1998.

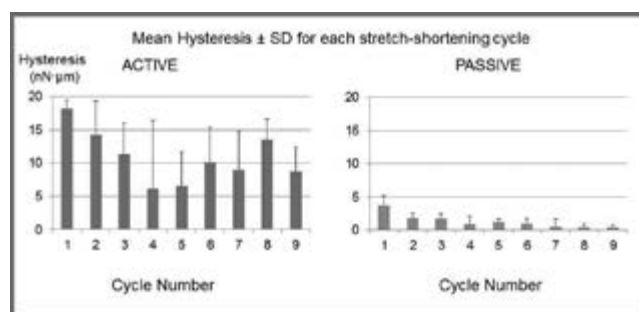


Figure 3: Hysteresis histogram for active and passive myofibrils for each of the nine small amplitude stretch-shortening cycles.

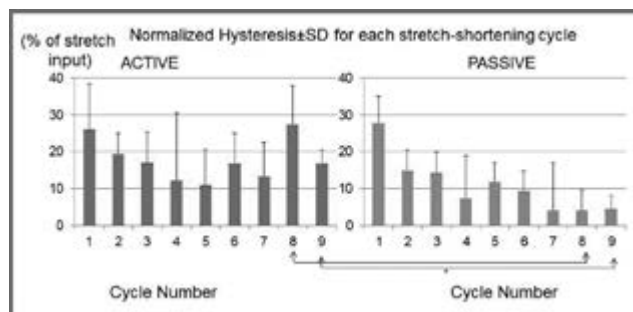


Figure 4: Normalized hysteresis histogram for active and passive myofibrils for each of the nine small amplitude stretch-shortening cycles.

Biomimetic Models of the Tumor Microenvironment and Angiogenesis

CNF Project Number: 1540-07

Principal Investigators: Claudia Fischbach-Teschl, Abraham D. Stroock

Users: Peter DelNero, Lu Ling, John Morgan

Affiliation: Nancy E. and Peter C. Meinig School of Biomedical Engineering, Cornell University

Primary Source of Research Funding: National Institutes of Health

Contact: cf99@cornell.edu, abe.stroock@cornell.edu, pfd28@cornell.edu, LL657@cornell.edu, jpm339@cornell.edu

Websites: www.fischbachlab.org, www.stroockgroup.org

Abstract:

Cancer is a disease of nature and nurture. On the one hand, oncogenic mutations drive the hyperproliferation of malignant cells. On the other hand, tumor growth and metastasis is intimately dependent on the surrounding tissue microenvironment that the cancer cells inhabit. Microvascular perfusion is a critical determinant of this environment. The microcirculatory system mediates the exchange of respiratory gases, metabolites, and drugs. In cancer, abnormal blood flow results in a highly heterogeneous tissue environment, which drives the evolution of increasingly adaptive cancer cell phenotypes. Our project uses tissue engineering and microfluidic approaches to unravel the complex interdependence between cancer cells and the vascular microenvironment, specifically in the context of tissue transport and tumor metabolism.

Summary of Research:

As the primary conduit of oxygen, nutrients, drugs, and other biomolecular signals, the vasculature is a critical determinant of the tumor microenvironment. To explore the interactions between cancer cells and the peripheral blood vessels, we integrated cancer biology and tissue engineering strategies to fabricate artificial tumor mimetics with explicit microvasculature, fully embedded within remodelable hydrogel scaffolds. We are using these *in vitro* models to investigate: 1) the regulation of vascular function and angiogenesis by cancer cells; 2) how microvascular dysfunction disrupts homeostatic tissue perfusion; 3) how populations of tumor cells adapt their metabolic phenotype in response to aberrant transport gradients [1]. By studying tissue-level phenomena, we hope to identify novel insights on disease progression that may inform a more effective use of existing anti-cancer treatments.

To investigate these questions, we typically use the CNF's photolithography tools, the SU-8 processing contact aligner, spin coater, and hot plates, and use

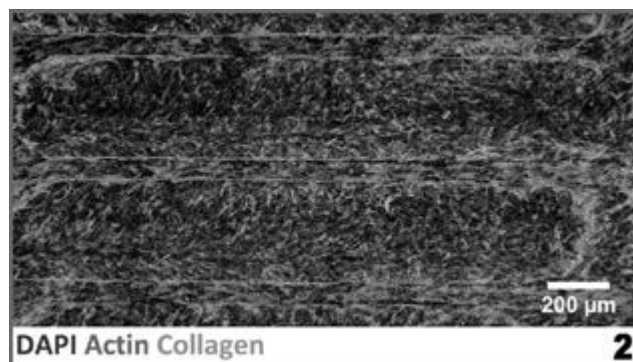
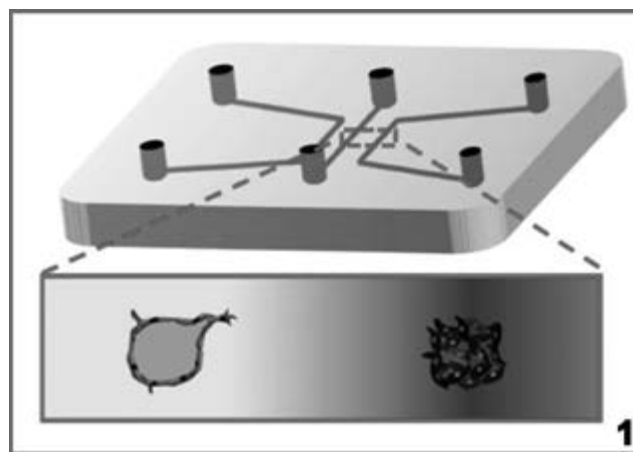
biomaterials-based microfluidic platforms to recapitulate the tumor-vascular microenvironment. In our previous report, we demonstrated the fabrication of endothelialized microvascular structures that displayed membrane barrier function and angiogenic sprouting. This year, we are integrating localized tumor compartments to create a more sophisticated co-culture system. This model allows precise control of microenvironmental conditions and *in situ* analysis of cell status. Moving forward, we aim to use the co-culture model to correlate the emergence of heterogeneous phenotypes within the asymmetric microvascular landscape. If successful, this approach will provide a tool to address previously inaccessible questions about tumor adaptation and evolution during disease initiation, progression, treatment, and recurrence.

In addition, we also performed PDMS soft lithography to generate a collagen-based microwell platform to study the role of extracellular matrix remodeling in tumor angiogenesis [2,3]. Specifically, adipose

stromal cells (ASCs), a major stromal component of mammary microenvironment, simultaneously deposit and contract the tumor matrix. In addition, these cells generate potent pro-angiogenic factors that promote blood vessel growth. We have previously shown that in tumor, ASCs become myofibroblastic cells that exhibit increased matrix remodeling and VEGF secretion. To evaluate the relative contributions of matrix structure and soluble factor secretion, we utilized microfabricated biomaterial-based assays to assess 3D endothelial cell sprouting. Our findings indicate that matrix remodeling by ASCs can be as equally, or even more important than, pro-angiogenic factor secretion in facilitating new vessel growth.

References:

- [1] Peter DelNero, Maureen Lane, Scott S. Verbridge, Brian Kwee, Pouneh Rabbany, Barbara Hempstead, Abraham Stroock, Claudia Fischbach, 3D culture broadly regulates tumor cell hypoxia response and angiogenesis via pro-inflammatory pathways, *Biomaterials*, 2015;55:110-8.
- [2] Young Hye Song, Seung Hee Shon, Mengrou Shan, Abraham Stroock, Claudia Fischbach. Adipose-derived Stem Cells Increase Angiogenesis through Matrix Metalloproteinase-dependent Collagen Remodeling, *Integrative Biology*, 2016;8:205-215.
- [3] R. Seo, P. Bhardwaj, S. Choi, J. Gonzalez, R. C. A. Eguiluz, K. Wang, S. Mohanan, P. G. Morris, B. Du, X. K. Zhou, L. T. Vahdat, A. Verma, O. Elemento, C. A. Hudis, R. M. Williams, D. Gourdon, A. J. Dannenberg, C. Fischbach, Obesity-dependent changes in interstitial ECM mechanics promote breast tumorigenesis. *Sci. Transl. Med.* 7, 301ra130 (2015).



Figures 1-2: Schematic illustration (1) and confocal micrograph (2) of microfluidic biomaterials using lithographically patterned collagen gels.

Patterned Surfaces for Studying IgE Receptor Mediated Signaling and Plasma Membrane Trafficking

CNF Project Numbers: 1726-08, 996-01

Principal Investigator: Barbara A. Baird

Users: Meraj Ramezani, Devin Wakefield

Affiliation: Department of Chemistry and Chemical Biology, Cornell University

Primary Source of Research Funding: NIH R01 GM117552

Contact: bab13@cornell.edu, mr935@cornell.edu, dlw238@cornell.edu

Abstract:

We demonstrate the use of lithographic processes in combination with chemical modification to prepare micron and submicron sized arrays of patterned biomaterial. We have previously explored the application of these patterns to characterizing epidermal growth factor receptor (EGFR) signaling in fibroblast cells [1] and to the uptake mechanisms of aggregated low-density lipoproteins (agLDL) by macrophage cells [2]. Current work aims to investigate IgE-receptor (FcεRI) mediated mast cell responses with a focus on plasma membrane trafficking and the actin cytoskeleton dependence of specific signaling molecules.

Summary of Research:

Bio-patterned surfaces are a powerful tool for exploring a wide range of cellular activities. The surfaces described in this work have enabled further understanding of EGFR-[1] and FcεRI-[3] regulated signaling processes as well as the mechanisms underlying microglia and macrophage mediated β-amyloid degradation [2].

Through standard photolithographic techniques and a polymer lift-off method, cell receptor ligands may be patterned on selected substrates. Glass or silicon wafers, initially coated with a parylene-C polymer film and photoresist, are patterned using the ASML PAS 5500/300C DUV stepper. An oxygen-based etch then transfers the features in photoresist to the parylene layer, creating multiple arrays of individually patterned features (0.25 μm to 2 μm in size) at a range of periodicities (2 μm to 20 μm separation). Subsequent chemical modification on the exposed surface and the final peeling away of the parylene layer establishes spatially defined patterns of ligand as either immobilized protein or fluid supported lipid bilayers. The use of glass substrates (< 200 μm thick) provides an essential surface for real-time imaging by total internal reflection fluorescence microscopy (TIRFM). Further, with the size of a cell at around 15 μm in diameter, these organized features enable direct observation of individual cells making either single or multiple contacts with patterned sites, all within a single microscope field of view.

This technique has become significant for revealing the formation of multi-protein signaling complexes. Following ligand-induced aggregation of FcεRI, localized receptor and downstream signaling responses are readily visualized at the plasma membrane of rat basophilic leukemia (RBL) mast cells.

We have recently characterized the actin cytoskeleton dependence of integrins and important FcεRI-mediated downstream signaling molecules Syk, LAT, and PLCγ1 using this surface-patterned ligand approach (Figure 1). We find β1-containing integrins, including VLA-4, co-cluster with activated FcεRI at patterned ligand sites, and this recruitment accompanies localized fibronectin secretion and ligand-stimulated outward trafficking of integrin-containing recycling endosomes. FcεRI signaling complexes appear to depend on the nature of ligand presentation, and actin cytoskeleton polymerization, together with integrin trafficking, may further serve to effectively organize specific signaling responses for adherent and spread RBL mast cells.

Our ongoing research further investigates stimulated and targeted trafficking of cytoplasmic vesicles in RBL-2H3 mast cells. Two major types of exocytosis occurs through; 1) recycling endosomes, and 2) secretory lysosomes. Micron-size patterns of antigen provide the means for elucidating their distinctive spatial properties. Vesicle-associated membrane proteins (VAMPs) such as VAMP 7 and VAMP8

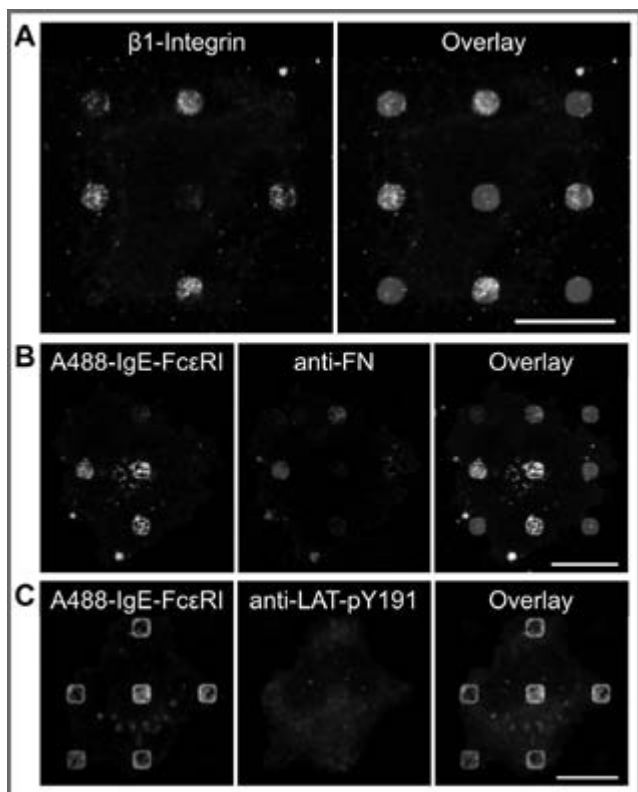


Figure 1: β 1-integrin, fibronectin (FN), and phosphorylated LAT (LAT-pY191) in RBL cells co-cluster with IgE-Fc ϵ RI at patterned DNP-SLB surfaces. (A) Labeling of live RBL cells with an anti- β 1-integrin antibody (green) on patterned DNP-SLB surfaces (red) reveals concentrated fluorescence largely associated with those patterned features in contact with the cell edge. (B) Localized DNP-stimulated secretion of FN (blue) appears to accompany β 1-integrin targeting to the plasma membrane as a potential method to facilitate ligand binding while at activated IgE-Fc ϵ RI sites. (C) Activated LAT (LAT-pY191 (blue)) is weakly visible at patterned DNP-BSA features (not shown). Scale bars 10 μ m.

localize differentially, and pH-sensitive fluorescent tags detected with confocal microscopy and TIRFM enable temporal and spatial monitoring.

Other ongoing research examines the initial steps on Fc ϵ RI signaling cascade to determine stability of protein complexes formed as a result of IgE-Fc ϵ RI clustering [4]. Multivalent antigens such as DNP-BSA can stimulate signaling in Rbl-2H3 cells by aggregation of IgE-Fc ϵ RI but a monovalent antigen such as $\{\epsilon$ -[(2,4 DNP)amino]caproyl-L-tyrosine (DCT) can reverse these complexes to stop the signaling process. By comparing the kinetics of receptor and protein complex dissociation processes we are probing the regulated progression of signaling in mast cells.

References:

- [1] Singhai, Amit; Wakefield, Devin L; Bryant, Kirsten L; Hammes, Stephen R; Holowka, David A; Baird, Barbara. Spatially Defined EGF Receptor Activation Reveals an F-actin-dependent Phospho-Erk Signaling Complex. *Biophysical Journal* 107: 2639-2651 (2014).
- [2] Haka, Abigail A; Grosheva, Inna; Chiang, Ethan N; Buxbaum, Adina R; Baird, Barbara A; Pierini, Lynda M; Maxfield, Frederick R. Macrophages Create an Acidic Extracellular Hydrolytic Compartment to Digest Aggregated Lipoproteins. *Molecular Biology of the Cell* 20: 4932-4940 (2009).
- [3] Wu, Min; Holowka, David A; Craighead, Harold G, Baird, Barbara A. Visualization of Plasma Membrane Compartmentalization with Patterned Lipid Bilayers. *Proceedings of National Academy of Sciences, USA* 101(38): 13798-803 (2004).
- [4] Xu, Keli; Goldstein, Byron; Holowka, David A; Baird, Barbara A. Kinetics of Multivalent Antigen DNP-BSA Binding to IgE-Fc ϵ RI in Relationship to the Stimulated Tyrosine Phosphorylation of Fc ϵ RI. *The Journal of Immunology*, 160(7): 3225-3235(1998).

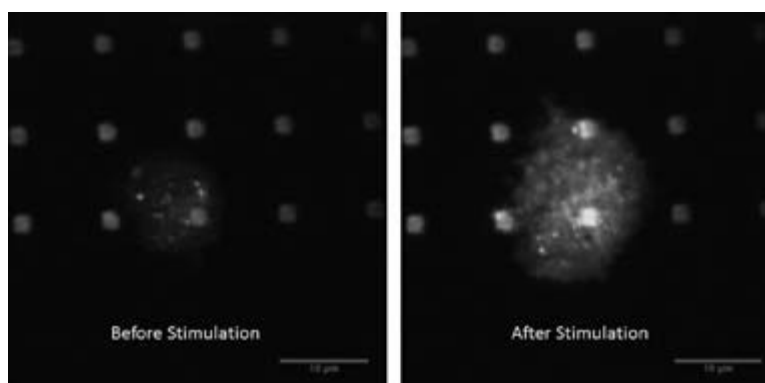


Figure 2: VAMP8-phluorin (green), which label recycling endosomes, co-localizes with clustered IgE-Fc ϵ RI in RBL-2H3 cells. Cells adhere and spread over surfaces with patterned SLB (red), which contain antigen and cause clustering of the IgE-Fc ϵ RI. Scale bars 10 μ m.

Progress Towards Achieving Nanophotonic Trapping for Precise Manipulation of Biomolecular Arrays on Si₃N₄ Waveguides

CNF Project Number: 1738-08

Principal Investigator: Michelle Wang

Users: Fan Ye, Ryan Badman

Affiliations: LASSP, Physics; Cornell University

Primary Source of Research Funding: Howard Hughes Medical Institute

Contact: mdw17@cornell.edu, fy72@cornell.edu, rpb226@cornell.edu

Website: <http://wanglab.lassp.cornell.edu/>

Abstract:

Optical trapping is a powerful manipulation and measurement technique widely employed in the biological and materials sciences. Our lab has developed and implemented an on-chip device based on Si waveguides, coined a nanophotonic standing-wave array trap (nSWAT), that allows for controlled and precise manipulation of trapped nano/micro particle arrays [1]. Here, we report our current successes in achieving Si₃N₄-waveguide based nSWAT devices and ongoing progress in further optimization and biological experimentation. This Si₃N₄ nSWAT works at 1064 nm input laser, has improved biocompatibility, and can achieve 10's of pN trapping force, as well as sub-nm manipulation resolution. These features give the nSWAT comparable manipulation ability as conventional free-space optical traps, while increasing throughput by more than hundred-fold.

Summary of Research:

Optical trapping is a powerful manipulation and measurement technique widely employed in the biological and materials sciences. Miniaturizing bulky and expensive optical trapping instruments onto optofluidic platforms holds promise for high throughput lab-on-chip applications that can be readily integrated with other novel lab-on-chip innovations such as fluorescent detectors or on-chip lasers.

In 2014, using the CNF, Wang Lab researchers (Soltani, et al.) developed and implemented such a device, named the nanophotonic standing-wave array trap (nSWAT), that allows for controlled and precise manipulation of trapped particles with maximum trapping force on the order of 1 pN [1]. Using photonic interference functionalities, an array of stable, three-dimensional on-chip optical traps is formed by the evanescent field at the anti-nodes of a standing-wave along a nanophotonic waveguide. By employing the thermo-optic effect via integrated electric microheaters, the traps can be repositioned at high speed (~ 30 kHz) with nanometer precision. "Dumbbells" were formed with deoxyribonucleic acid (DNA) tethered between two polystyrene (PS) beads, and these could be precisely manipulated and stretched within the nSWAT. Figure 1 (adapted from Ref. [1]) shows an array of DNA dumbbells stably trapped on, and precisely manipulated along, two parallel Si waveguides in an nSWAT device.

The first generation nSWATs are Si waveguide based devices that work at 1550 nm. Although water absorption

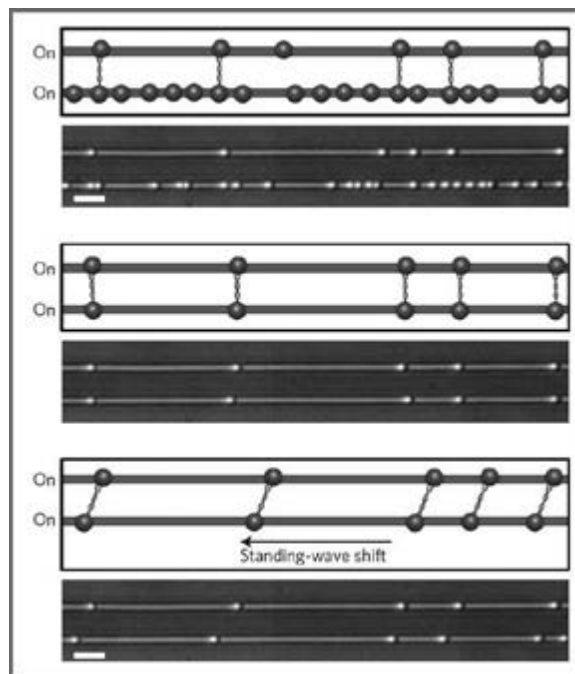


Figure 1: DNA dumbbells, formed with deoxyribonucleic acid (DNA) tethered between two polystyrene (PS) beads, being trapped and manipulated along two parallel waveguides in a nSWAT device. See Ref. [1] for more information. Reproduced with permission from Ref. [1].

at 1550 nm is already quite low, a blue shift of the working wavelength to 1064 nm would reduce the water absorption by 120 fold [2], indicating an ideal compatibility with biological species. To explore this compatibility, using CNF equipment including the low pressure chemical vapor deposition (LPCVD) nitride furnaces, the ASML stepper's deep ultraviolet lithographic processes, and the new high performance C_4F_6 , CH_2F_2 , and SF_6/CH_2F_2 etch chemistries integrated with helium in the Oxford 100 plasma etcher, we have discovered that the Si_3N_4 waveguides at 1064 nm have the aforementioned decreased optical loss, increased biocompatibility, and also have considerable smaller nonlinear effects, as compared to Si, which is vital for high power applications (>1W).

Micro-particle trapping on Si_3N_4 was first demonstrated in 2005 [3], however burnt Si_3N_4 waveguides at powers above 1W have been an unsolved issue in literature [4]. We have overcome all waveguide quality issues using an optimized anneal process in

CNF furnaces together with high performance designs derived from finite element method (FEM) based full wave electromagnetic simulations in COMSOL to solve for the optimal Si_3N_4 waveguide dimensions for maximized trapping force and minimized optical loss (Figure 2).

Using CNF equipment, we have achieved the following goals: (1) fabricate Si_3N_4 waveguides using DUV lithography, instead of e-beam, to achieve low loss waveguides that can potentially tolerate high laser power; (2) create fabrication recipes for protection of microheaters in the presence of biological buffers; (3) optimize Si_3N_4 surfaces for nanoparticle manipulation; and (4) fabricate full Si_3N_4 nSWAT device that successfully traps micro/nano particle arrays. These improvements significantly reduce the nSWAT production time and cost per device without compromising the quality of these devices. We have also performed comprehensive particle trapping calibration of the full Si_3N_4 nSWAT devices, revealing the high trapping force and high manipulation resolution features. Figure 3 displays SEM images of a fabricated Si_3N_4 waveguide with a highly smooth top surface and side walls.

We are in the process of submitting a publication summarizing our work and look forward to demonstrating high impact single molecule experiments on our nSWAT devices in the near future.

References:

- [1] M. Soltani, et al. "Nanophotonic trapping for precise manipulation of biomolecular arrays," *Nature Nanotechnology* 9, 448-452 (2014).
- [2] G. M. Hale and M. R. Querry "Optical constants of water in the 200-nm to 200- μ m wavelength region," *Applied Optics* 12, 555-563 (1973).
- [3] S. Gaugiran, et al. "Optical manipulation of microparticles and cells on SiN waveguides," *Optics Express* 13, 6956-6963 (2005).
- [4] B. S. Ahluwalia, et al. "Fabrication and optimization of Tantalum pentoxide waveguides for optical micro-propulsion," *Proc. SPIE 7604, Integrated Optics: Devices, Materials, and Technologies XIV, 76040W* (2010).

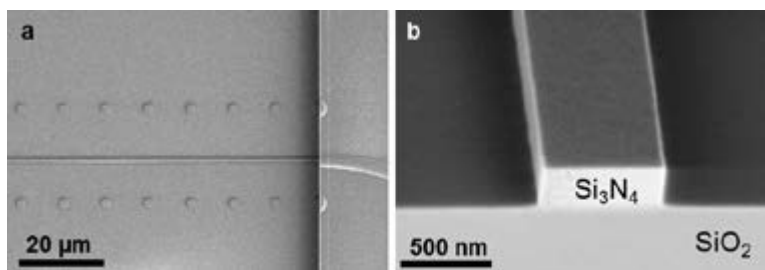
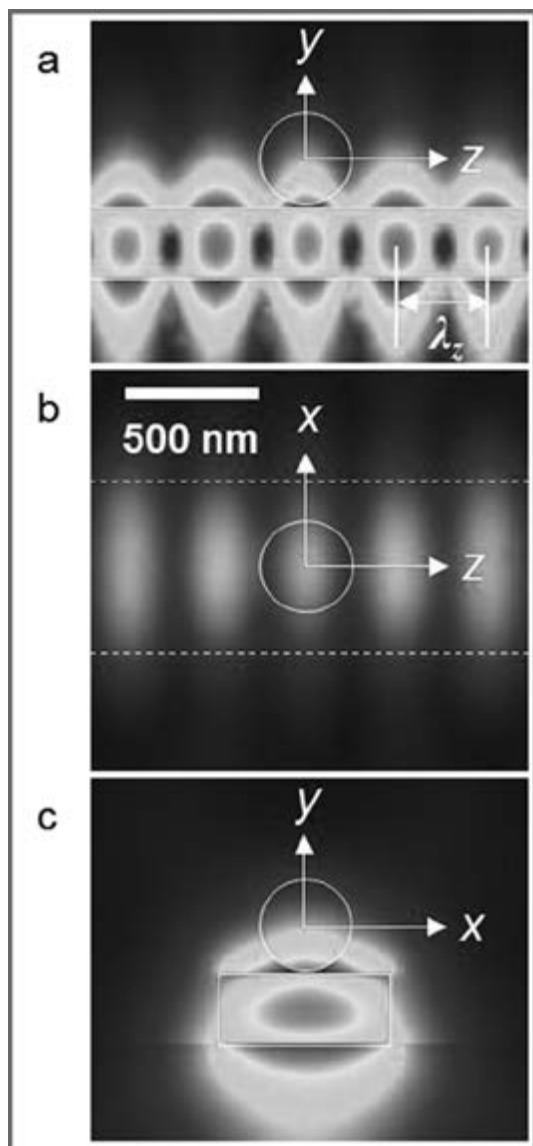


Figure 2, left: Electric field intensity profile for scenario of a PS bead (white circle) trapped in a standing-wave array trap formed by 1064 input laser along a Si_3N_4 waveguide, with cross-sections taken through the center of the PS bead.

Figure 3, above: SEM images of a Si_3N_4 waveguide fabricated by DUV litho. (a) top view of the fluid pool region with exposed Si_3N_4 waveguide on the right (circular dots are fiducial position markers); (b) side view of the cross-section of a Si_3N_4 waveguide.

Generalized Microfluidic Immunosensor for Antibody Detection

CNF Project Number: 1757-09

Principal Investigator: Christopher K. Ober¹

Users: Aibar Nurmukhanov¹, Roselynn Cordero²

Affiliations: 1. Department of Materials Science and Engineering,

2. Department of Chemistry and Chemical Biology; Cornell University

Primary Source of Research Funding: National Science Foundation

Contact: cko3@cornell.edu, an485@cornell.edu, rc634@cornell.edu

Abstract:

Immunosensors are diagnostic devices that convert specific antigen-antibody interactions, by means of a transducer, into an electrical signal. Immunosensors are very efficient, simple, affordable, and cost-effective point-of-care systems for medical diagnosis. Our study focuses on the use of polymer chemistry and photolithography to create a unique microfluidic platform for antibody detection. This immunosensor takes advantage of the antibody catalyzed water oxidation pathway (ACWOP) process, in which all antibodies catalyze the production of hydrogen peroxide that can be electrochemically detected given a certain chemistry. This report focuses on the fabrication of the platform and microfluidic channels that make up our immunosensor device.

Summary of Research:

A pandemic is an infectious disease that affects a large number of people around the globe, sometimes killing millions of people such as the Black Death back in 1350. One of the early ways to detect and treat such diseases is to perform antigen/antibody tests for specific adsorption depending on conjugate molecules. Our immunosensor consists of patterned poly(oligoethylene glycol methacrylate) (POEGMA) polymer brushes on a glass substrate made using atom transfer radical polymerization (ATRP), surrounded by a photosensitizer that was electropolymerized on a gold surface [1]. Photosensitizer is responsible for the production of singlet oxygen that reacts with water to produce hydrogen peroxide that can be detected using electrochemistry and is used to calculate the amount of antibodies adsorbed onto the brush surface given the specific hapten groups (Figure 1) [2].

The fabrication of the platform includes spin-coating a double layer of a lift-off resist (LOR) and a positive-tone photoresist to get an undercut profile for gold deposition and prevent “fencing” issues. An ABM contact aligner was used as a light source for exposure followed by the development of the patterns in a basic solution. Subsequently, chromium (as an adhesion layer) and gold layers were evaporated on the fused

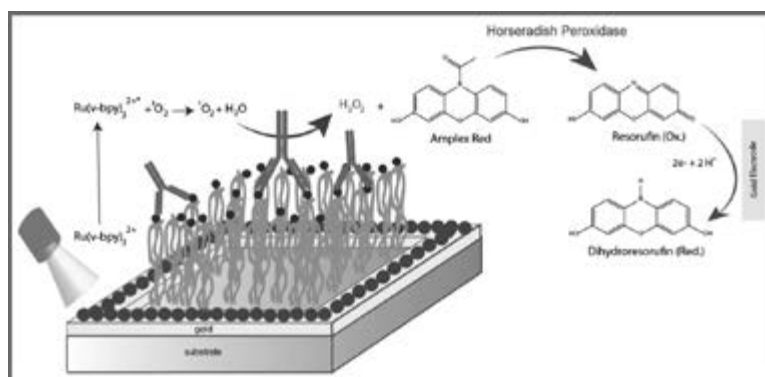


Figure 1: The schematic illustration of the immunosensor based on the ACWOP. Dark blue spheres are hapten groups for specific recognition and binding with Y-shaped antibodies.

silica substrate using an electron gun evaporation system (SC4500 Odd-hour Evaporator). Ultimately, the lift-off process was carried out to remove the resist and obtain patterned gold lines (150 μm) separated by square islands of glass surface (300 μm) as shown in Figure 2. To prevent segregation of gold particles on the substrate surface it's crucial to repeat the lift-off process multiple times placing the platform face down.

The next step was to create microfluidic channels to cap our platform. Initially a master mold was generated using SU-8 negative photoresist by spin coating it

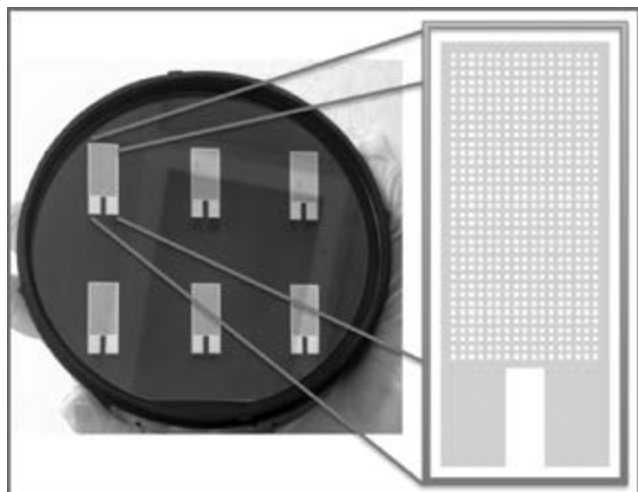


Figure 2: Generalized platform made of fused silica substrate and generated pattern of thin layer of gold lines by lift-off process.

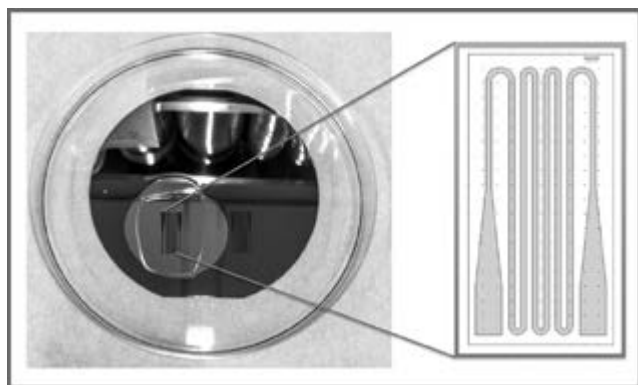


Figure 3: Illustration of one of the master molds using SU-8. Serpentine-like 80 μm -thick features with polydimethylsiloxane (PDMS) on top.

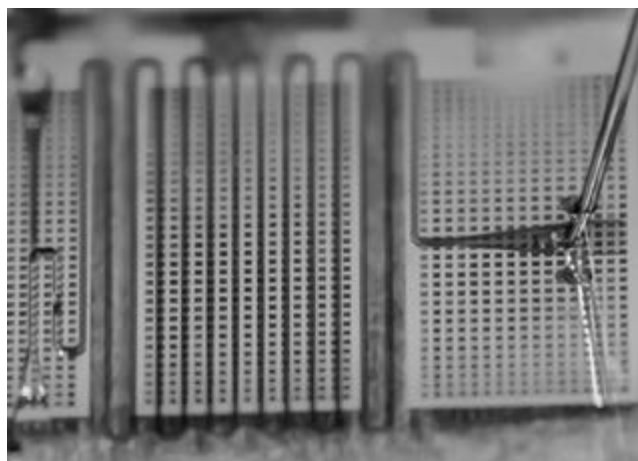


Figure 4: Generation-one microfluidic immunosensor. Food-dye (green) was used to illustrate continuous flow inside the device.

on a silicon wafer. The ABM contact aligner after filtration was used to expose the resist. Development, soft bake, and post exposure bake times are the key parameters to achieve the desired master mold structure (Figure 3). Finally, polydimethylsiloxane (PDMS) was poured over the master mold, cured at 60°C overnight, and peeled away to cap our platform [3]. Conventional plasma bonding of the PDMS to the substrate could not be used because plasma destroys polymer brushes on the surface that are essential features in our device. Hence we came up with the idea of thermal bonding where you partially cure your PDMS, cut it, cover the platform and let it fully cure in the oven for 20-40 minutes. Another non-destructive method that was used is solvent evaporation using ethanol or isopropanol that creates non-covalent bonding between PDMS and the substrate. Multiple microfluidic channel designs were used — one of them is shown in Figure 4.

Our final goal is to test specific adsorption of antibodies to the surface of the polymer brushes by fluorescence using confocal microscopy. In order to achieve fluorescence, specific hapten groups such as (dinitrophenyl) DNP-groups could be used to bind with anti-DNP IgG antibody solution with different concentrations to get different brightness levels. Also, bovine serum albumin (BSA) in phosphate-buffered saline solution could be used to prevent non-specific adsorption of antibodies to the platform or to the PDMS.

References:

- [1] M. Elizabeth Welch, Nicole L. Ritzert, Hongjun Chen, Norah L. Smith, Michele E. Tague, Youyong Xu, Barbara A. Baird, Héctor D. Abruña, and Christopher K. Ober, *Journal of the American Chemical Society*, 2014, 136 (5), 1879-1883.
- [2] Wentworth P., Jones L. H., Wentworth A. D., Zhu X. Y., Larsen N. A., Wilson I. A., Xu X., Goddard, W.A., Janda K. D., Eschenmoser A., Lerner R. A. *Science* 2001, 293, 1806.
- [3] D.B. Weibel, W.R. Diluzio, G.M. Whitesides, *Microfabrication meets microbiology*, *Nat. Rev. Microbiol.*, 5 (2007), pp. 209-218.

KS-Detect: A Solar Thermal Microfluidic PCR Platform for Health Diagnostics in Resource Limited Settings

CNF Project Number: 1858-10

Principal Investigator: David Erickson

User: Ryan Snodgrass

Affiliation: Mechanical Engineering, Cornell University

Primary Source of Research Funding: National Institutes of Health

Contact: de54@cornell.edu, rjs492@cornell.edu

Website: <http://www.ericksonlab.org/>

Abstract:

Polymerase chain reaction (PCR) is a universally used method for deoxyribonucleic acid (DNA) amplification and detection, and has been shown to be an effective means for disease diagnostics. PCR usually requires the use of non-portable, expensive, and energy-intensive equipment such as thermal cyclers, gel electrophoresis systems, and spectrophotometers. These limitations make PCR-based health diagnostics usually unavailable to resource limited settings, where equipment and electricity are unreliable. Here, we present a solar thermal powered unit capable of microfluidic PCR, and we call this device KS-Detect (KS: Kaposi's sarcoma). Kaposi's sarcoma is a skin cancer originating from infection with human herpesvirus 8 (HHV8), most commonly in individuals with HIV. We show that the KS-Detect device is able to amplify and detect KS-positive DNA in samples derived from human cell lines positive for the KS herpesvirus (HHV8 or KSHV).

Summary of Research:

The KS-Detect device delivers polymerase chain reaction (PCR)-based diagnostics to resource limited settings. Such diagnostics are often the most sensitive and specific method for disease diagnostics (compared against serological assay or pathology, for example), but require expensive, energy intensive, and non-portable laboratory equipment such as thermal cycler and gel electrophoresis system. Kaposi's sarcoma (KS) is one such disease common in resource limited settings, which has been shown to be most reliably detected by PCR [1]. However, equipment for PCR is sometimes unavailable or unreliable in communities where KS is most prevalent today (sub Saharan African countries such as Uganda and Kenya), or diagnosis is needed for individuals far from central clinics. Therefore, a portable tool that uses an energy source alternative to electricity will prove useful for the diagnosis of Kaposi's sarcoma and other similar infectious diseases.

The KS-Detect is shown in Figure 1. It is contained in a box that is easily carried in one hand, being the size of a small toolbox. Inside the box fits all tools and reagents needed to conduct solar thermal, microfluidic PCR, as well as tools for result analysis. A lens is used to concentrate sunlight onto a microfluidic

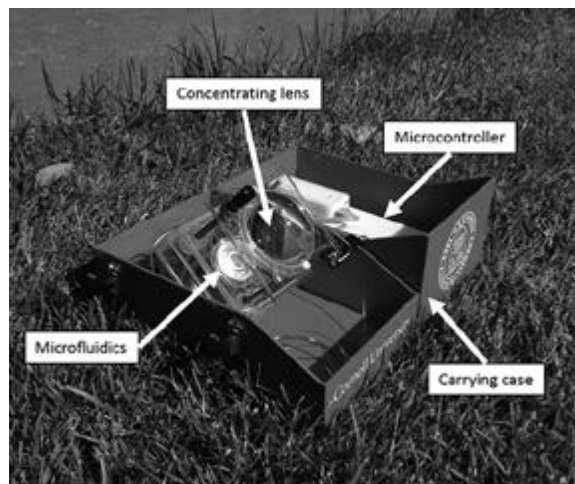


Figure 1: The KS-Detect device, opened and showing internal components. The case can also be closed for easy transportation.

chip made of polydimethylsiloxane (PDMS). Molds for these microfluidic chips were built at the Cornell NanoScale Science and Technology Facility (CNF) using standard photolithography equipment such as the ABM contact aligner. Covering our microfluidic chip is a series of rings that reflect sunlight instead of absorb it on portions that we do not wish to be heated.

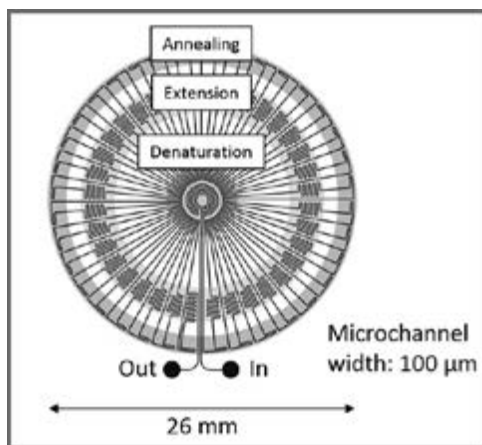


Figure 2: Microfluidic schematic, showing the three different temp regions (shaded areas).

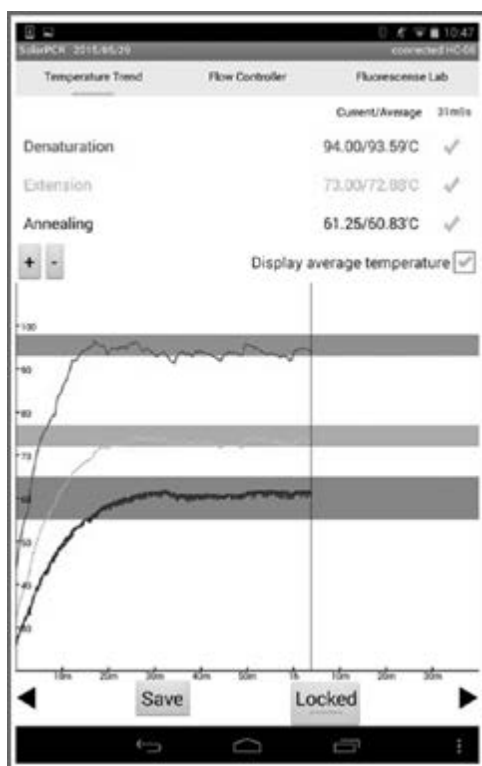
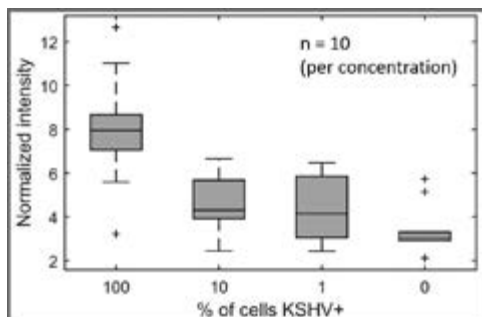


Figure 3: A smartphone application is used to control the device and monitor temperatures of the microfluidic chip.



This selecting heating process creates the three temperature regions necessary to conduct traditional PCR: denaturation ~ 95°C, extension ~ 72°C, and annealing 54-60°C. A schematic of the microfluidic chip is shown in Figure 2. The center of the chip is the hottest, and is thus used for denaturation of the DNA template. The edge of the chip is used to anneal DNA primers to the template, and DNA extension occurs at an intermediate temperature, where we placed a snaking pattern to extend the time the fluid stays in this region (the extension process takes longer than denaturing and annealing). The chip performs 35 cycles of PCR and is about an inch in diameter. Microfluidic PCR was first displayed in the early 1990s and has since been studied in detail, showing much promise for point-of-care diagnostics [2].

The device makes use of simple microcontrollers, thermocouples, and pump to control the microfluidics and monitor device temperatures (Figure 3). The microcontroller easily communicates with a smartphone or tablet using Bluetooth, allowing the device to be used by a wide audience and keeping the overall system cost low. A smartphone or tablet is also used for result analysis. The amplified DNA sample is combined with SYBR green, a non-specific intercalator that fluoresces green in the presence of DNA, and an image is taken with the smartphone or tablet and analyzed via an Android application to give a positive or negative result.

We prepared samples from a combination of two human cell lines, one positive for the KS herpesvirus, and one negative for the KS herpesvirus. We combined the samples into different concentrations of positive and negative cell concentrations (100%, 10%, 1%, 0% positive) and amplified the samples using the KS-Detect using sunlight in Ithaca, NY. Some of our results are shown in Figure 4. Results show that the device is able to detect the KS herpesvirus in samples where a large fraction of cells are KS-positive. Additionally, we found that our solar simulator (array of LEDs) was more efficient in amplifying the samples as compared to using sunlight only, suggesting that a more robust solar tracking system should be developed. Full results and discussion are presented in our most recent publication [3].

References:

- [1] Chang, Cesarman, Pessin, and Lee. Identification of herpesvirus-like DNA sequences in AIDS-associated Kaposi's sarcoma. *Science*. 1994; 266: 1865-1869.
- [2] Zhang and Ozdemir. Microfluidic DNA amplification-a review. *Analytica Chimica Acta*. 2009; 638:115-125.
- [3] Snodgrass, Gardner, Jiang, Fu, Cesarman, and Erickson. KS-Detect - Validation of Solar Thermal PCR for the Diagnosis of Kaposi's Sarcoma Using Pseudo-Biopsy Samples. *PLOS ONE*. 2016. DOI:10.1371/journal.pone.0147636.

Figure 4: Results from the KS-Detect device, when amplifying samples made from human cell lines containing various concentrations of KS herpesvirus (KSHV). Fluorescent levels were captured from a smartphone and intensity levels were calculated using the smartphone application.

Fabrication of Elastomeric Microposts with Step-Changes in Rigidity

CNF Project Number: 1859-10

Principal investigator: Cynthia A. Reinhart-King

User: Jacob VanderBurgh

Affiliation: Meinig School of Biomedical Engineering, Cornell University, Ithaca, New York, USA

Primary Source of Research Funding: National Science Foundation Award 1435755

Contact: cak57@cornell.edu, jav244@cornell.edu

Website: <http://www.cellmechanics.org/>

Abstract:

Rigidity sensing of the vascular endothelium plays an important role in atherosclerosis. To explore the effect of substrate stiffness upon endothelial cell function, we fabricated dense arrays of elastomeric microposts that recapitulate arterial stiffness environments observed *in vivo*. Endothelial cells respond to increasing substrate rigidity by increasing cell spreading. Future work will focus on exploring endothelial response to spatial changes in rigidity.

Summary:

Substrate stiffness profoundly influences cellular functions such as migration, spreading, and differentiation [1-3]. Vascular stiffening occurs during aging and due to poor diet (high-fat, high sugar) due to changes in the extracellular matrix (ECM) microarchitecture while vascular stiffness is an independent predictor of cardiovascular disease, a leading cause of death worldwide [4]. Our lab has shown that vascular stiffening drives increased vascular endothelial permeability, which permits cholesterol uptake and leukocyte extravasation into the vessel wall, hallmarks of atherosclerosis [5]. Currently, we are developing a micropillar model to explore the impact of greater complexity in vascular stiffening upon endothelial cell function.

Negative silicon (Si) masters of micropillars with a step-change in rigidity were fabricated with two-stages of deep reactive-ion etching (DRIE) as described previously (Figure 1) [6]. RCA-cleaned Si wafers with a thin layer of photoresist were first patterned with a 5 \times reduction stepper and a photomask consisting of a hexagonal array of holes. Patterned photoresist was used as a mask for subsequent DRIE on a Unaxis 770 Deep Si Etcher to generate an array of hexagonal holes of uniform depth. Hole depth was controlled by monitoring etch time and utilized to fabricate a library of silicon masters with varying uniform hole depth.

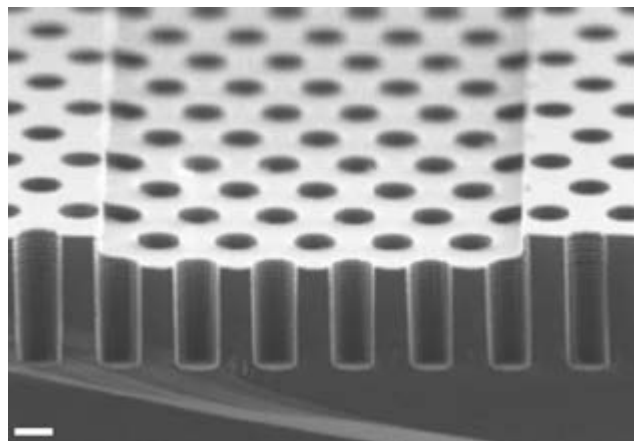


Figure 1: Negative silicon master of micropillars with a step-change in rigidity. Scale bar is 2 μm .

Thick photoresist was subsequently spun onto these arrays to completely fill the cylindrical holes and rectangular strips of photoresist were patterned with an ABM contact aligner. Photoresist was developed such that photoresist dissolved from the surface of the Si wafer, but remained within the cylindrical holes, protecting the bottom of the cylindrical holes during the second DRIE step. Replica molding of the Si negative master with silicone elastomer polydimethylsiloxane

(PDMS) yields coplanar micropillars with regions of shorter (stiff) and taller (compliant) pillars (Figure 2). Pillar height corresponds to perceived substrate stiffness (E_{eff}) as described in Equation 1 in which E is the bulk PDMS modulus of elasticity, r is the pillar radius, and L is the pillar height [7].

Micropillar substrates were coated with fibronectin and seeded with bovine aortic endothelial cells (BAEC). Endothelial cell response to increasing homogeneous substrate rigidity was validated through measurement of projected cell area as a function of effective pillar modulus (data not shown). The projected cell area increased with increasing rigidity, which is consistent with previously reported findings and validates endothelial cells are responding appropriately to the range of micropillar rigidities examined [2]. Future studies will investigate the impact of more complex cues in substrate rigidity upon endothelial cell function.

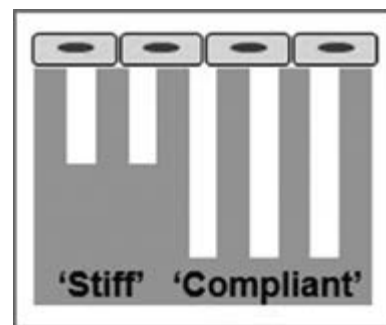


Figure 2: Schematic of micropillars with a step-change in rigidity.

References:

- [1] C. M. Lo, H. B. Wang, M. Dembo, and Y. L. Wang, "Cell movement is guided by the rigidity of the substrate.," *Biophys. J.*, vol. 79, no. 1, pp. 144-152, 2000.
- [2] A. Engler, L. Bacakova, C. Newman, A. Hategan, M. Griffin, and D. Discher, "Substrate Compliance versus Ligand Density in Cell on Gel Responses," *Biophys. J.*, vol. 86, no. 1, pp. 617-628, Jan. 2004.
- [3] A. J. Engler, S. Sen, H. L. Sweeney, and D. E. Discher, "Matrix Elasticity Directs Stem Cell Lineage Specification," *Cell*, vol. 126, no. 4, pp. 677-689, 2006.
- [4] R. M. Weisbrod, T. Shiang, L. Al Sayah, J. L. Fry, S. Bajpai, C. a. Reinhart-King, H. E. Lob, L. Santhanam, G. Mitchell, R. a. Cohen, and F. Seta, "Arterial stiffening precedes systolic hypertension in diet-induced obesity," *Hypertension*, vol. 62, no. 6, pp. 1105-1110, 2013.
- [5] J. Huynh, N. Nishimura, K. Rana, J. M. Peloquin, J. P. Califano, C. R. Montague, M. R. King, C. B. Schaffer, and C. A. Reinhart-King, "Age-Related Intimal Stiffening Enhances Endothelial Permeability and Leukocyte Transmigration," *Sci. Transl. Med.*, vol. 3, no. 112, pp. 112ra122-112ra122, 2011.
- [6] M. T. Breckenridge, R. a. Desai, M. T. Yang, J. Fu, and C. S. Chen, "Substrates with Engineered Step Changes in Rigidity Induce Traction Force Polarity and Durotaxis," *Cell. Mol. Bioeng.*, vol. 7, no. 1, pp. 26-34, 2013.
- [7] M. Ghibaudo, A. Saez, L. Trichet, A. Xayaphoummine, J. Browaeys, P. Silberzan, A. Buguin, and B. Ladoux, "Traction forces and rigidity sensing regulate cell functions," *Soft Matter*, vol. 4, no. 9, p. 1836, 2008.

$$E_{eff} = \frac{27 E r^3}{16 L^3}$$

Equation 1

Ultra-Thin Glass Windows for Biological Small Angle X-Ray Scattering

CNF Project Number: 1940-10

Principal Investigator: Richard E. Gillilan

Users: Jesse Hopkins, Gabrielle Illava, Manjie Huang, Melanie MacMullan

*Affiliations: Macromolecular Diffraction Facility of the Cornell High Energy Synchrotron Source (MacCHESS),
Cornell High Energy Synchrotron Source; Cornell University*

Primary Source of Research Funding: National Institutes of Health GM-103485

Contact: reg8@cornell.edu, jbh246@cornell.edu, GL432@cornell.edu, mh2334@cornell.edu, mm2354@cornell.edu

Website: www.macchess.cornell.edu/MacCHESS/bio_saxs.html

Abstract:

Laser-fabricated microfluidic sample flow chips are a unique component of the biological small-angle x-ray solution scattering (BioSAXS) facility at the Macromolecular Diffraction Facility of the Cornell High Energy Synchrotron Source (MacCHESS). As synchrotron x-ray beams get smaller and more intense, more efficient delivery of smaller samples with less contribution from x-ray window scattering is becoming a priority. New chip design and fabrication methods have now allowed us to integrate novel ultra-thin glass x-ray windows that are capable of holding full vacuum. The high smoothness of amorphous glass film combines with its relative rigidity to give low x-ray scattering background that is relatively stable under the changing mechanical loads of automated sample cell cleaning and drying cycles. In addition to robotically-loaded sample cells, the design has been adapted for use with continuous-flow size-exclusion chromatography coupled to x-ray solution scattering (SEC-SAXS). A wide range of visiting research groups during the 2015 and 2016 synchrotron running periods have used the cells successfully.

Summary of Research:

Biological small-angle x-ray solution scattering (BioSAXS) is a widely used technique at synchrotron light sources that yields structural information from dilute solutions of biological materials [1,2]. Sample cells at such facilities experience a high volume of use over a wide range of sample types, some very prone to surface fouling due to radiation damage.

Disposable plastic sample cells fabricated at CNF using the VersaLaser were introduced previously to help solve this problem (Gillilan R. 2013). The thin polystyrene windows had excellent (low) x-ray scattering properties when new, but degraded with age and use. Though disposable, the sample cells need to last at least 48 hours, a length that exceeds a typical BioSAXS data collection session.

Though more absorbant to x-rays, glass is a good material for SAXS windows due to its high surface smoothness and relative rigidity. Glass capillaries have been used for many years as SAXS sample cells, but surface curvature, thickness, and inconsistency in physical dimensions makes them less than desirable for this purpose. Ultra-thin flat glass film 5 μm thick (Nippon Electric Glass, Japan) was incorporated into

our VersaLaser cut sample chip designs and tested for x-ray scattering properties.

New fabrication protocols were developed that leveraged the chemical resistance of the glass during bonding. Despite being thinner by half than the thinnest x-ray capillary tubes available, the material is able to hold full vacuum across a 0.7 mm \times 5.0 mm window. The background scattering intensity of the glass is lower than previously-used materials and it is resilient against deformation during automated cleaning and drying operations.

Ultra-thin glass windows have been in use for all routine BioSAXS data collection at CHESS since late 2015.

References:

- [1] Skou, S., R. E. Gillilan and N. Ando (2014). "Synchrotron-based small-angle x-ray scattering of proteins in solution." *Nature Protocols* 9(7): 1727-1739.
- [2] Acerbo, A. S., M. J. Cook and R. E. Gillilan (2015). "Upgrade of MacCHESS facility for x-ray scattering of biological macromolecules in solution." *Journal of Synchrotron Radiation* 22(1): 180-186.

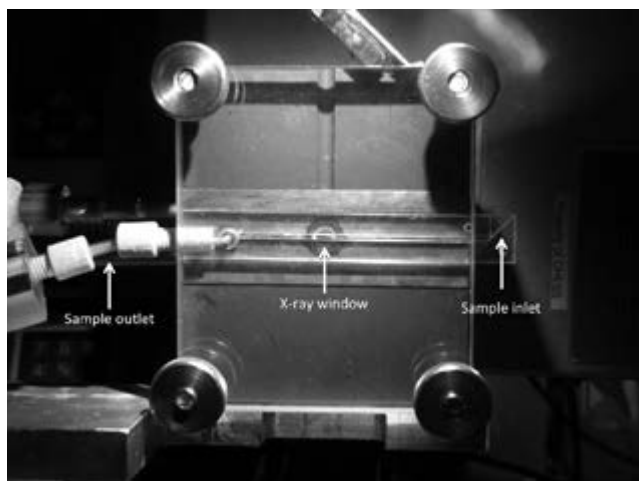


Figure 1: X-ray small angle solution scattering sample chip. Sample is delivered by pipetting robot (not shown) to laser-fabricated chip via microfunnel at right. Pump (left, not shown) delivers sample to x-ray window at center for exposure. Ultra-thin 5 μm glass film window at center holds full vacuum while minimizing background x-ray scatter.

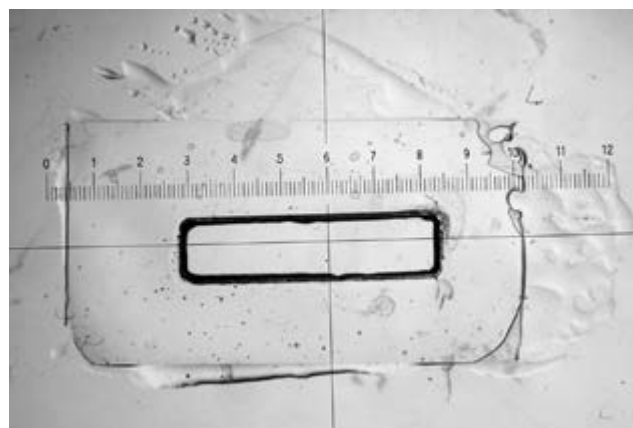


Figure 2: Vacuum-tight ultra-thin glass film bonded to one face piece of PMMA sample cell. Minor beading of edges during laser cutting is evident in this test as are some chips from handling during the fabrication process.

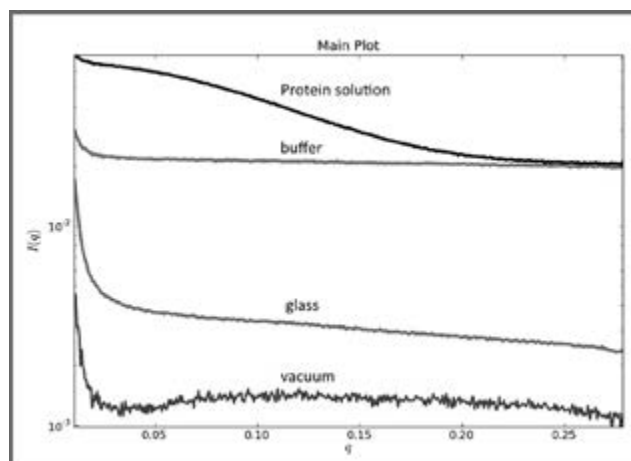


Figure 3: X-ray scattering profile for 5 μm glass film sample cell (two layers). Intensity is in absolute units (cm^{-1}) and momentum transfer is defined as $q = 4\pi \sin(\theta)/\lambda$, where θ is the scattering angle and λ the wavelength of the x-rays. Shown in comparison with vacuum, aqueous buffer, and protein (lysozyme) solution, the gradual slope in the glass profile is unusual for a window material, but low overall.

Design and Application of Microfluidic Devices to Study Cell Migration in Confined Environments

CNF Project Number: 2065-11

Principal Investigator: Jan Lammerding¹

Users: Patricia Davidson¹, Anisa Swei², Gregory Fedorchak¹

*Affiliations: 1. Biomedical Engineering Department and Weill Institute, Cornell University;
2. Biomedical Engineering, Worcester Polytechnic Institute*

Primary Sources of Research Funding: 1. NIH R01 HL082792; DDBCRP Idea Award BC102152; DDBCRP Breakthrough Award BC150580; NSF CAREER award CBET-1254846; Pilot Project Award by the CCM&M through Award Number U54CA143876 from the NCI; 2. NNIN REU Program at Cornell University (NSF Grant # ECCS-0335765)

Contact: jan.lammerding@cornell.edu, patricia.davidson@cornell.edu, aswei@wpi.edu, grf44@cornell.edu

Website: <http://lammerding.wicmb.cornell.edu/>

Abstract:

Metastatic spreading of cancer cells is responsible for the vast majority of cancer deaths. To better understand the biophysical processes and molecular consequences involved in cancer cell migration through tight spaces, we designed a novel microfluidic device that mimics the pore sizes and confining conditions of physiological tissues and that enables high resolution imaging of fluorescently labeled cells. Using these devices, we observed that as cells navigate pores smaller than the size of the nucleus, the nucleus exhibited large deformation and transient loss of nuclear envelope integrity. This led to the uncontrolled exchanged of nucleo-cytoplasmic content, herniation of chromatin across the nuclear envelope, and DNA damage. Cells were able to survive nuclear envelope rupture and restore nuclear envelope integrity using components of the endosomal sorting complexes required for transport (ESCRT) machinery. Our findings indicate that cell migration in confined three-dimensional (3D) environments incurs substantial physical stress on the nuclear envelope and its content, and requires efficient nuclear envelope and DNA damage repair for cell survival.

Summary of Research:

The ability of cells to migrate through tissues and interstitial spaces is an essential factor during development and tissue homeostasis, immune cell mobility, and in various human diseases. Deformation of the nucleus and its associated lamina during 3D migration is gathering increasing interest in the context of cancer metastasis, with one underlying hypothesis being that a softer nucleus, resulting from reduced levels of lamin A/C, may aid tumor spreading. However, attempts to study the migration of cells in confining 3D environments have been hampered by the limited control over pore sizes and confinement when using physiological extracellular matrix protein scaffolds, and by the limited physiological relevance and suitability for high resolution imaging when using synthetic porous membranes.

To address these limitations, we designed and built a polydimethylsiloxane (PDMS) microfluidic device composed of channels with precisely-defined constrictions mimicking physiological environments that enables high resolution imaging of live and fixed cells (Figures 1 and 2). The device promotes easy

cell loading and rapid, yet long-lasting (> 24 hours) chemotactic gradient formation without the need for continuous perfusion. Using this device, we obtained detailed, quantitative measurements of dynamic nuclear deformation as cells migrate through tight spaces (Figure 3), revealing distinct phases of nuclear translocation through the constriction, buckling of the nuclear lamina, and severe intranuclear strain [1]. Furthermore, we found that lamin A/C-deficient cells exhibited increased and more plastic nuclear deformations compared to wild-type cells but only minimal changes in nuclear volume, implying that low lamin A/C levels facilitate migration through constrictions by increasing nuclear deformability rather than compressibility.

In addition, we made the striking observation that breast cancer, fibrosarcoma, and human skin fibroblast cells exhibited transient loss of nuclear envelope integrity during confined 3D migration, which coincided with the nucleus passing through the tight constrictions. Nuclear envelope rupture was visualized using fluorescent reporters consisting of

green fluorescent protein (GFP) fused to a nuclear localization sequence that rapidly escapes into the cytoplasm when nuclear envelope integrity is lost and that is re-imported into the nucleus once nuclear envelope integrity is restored (Figure 4). Nuclear envelope rupture was associated with transient influx of fluorescently labeled cytoplasmic proteins into the nucleus. We confirmed that similar nuclear envelope rupture also occurred during cell migration in collagen matrices and during cancer cell invasion in living mice. Irrespective of the experimental model, the incidence of nuclear envelope rupture increased exponentially with decreasing pore size and reached > 90% when the nuclear height was confined to 3 μm . Nuclear envelope rupture *in vitro* and *in vivo* was often accompanied by protrusion of chromatin through the nuclear lamina. The incidence of such ‘chromatin herniations’ increased significantly with decreasing pore sizes and with depletion of lamins. Cells that had passed through microfluidic constrictions had more nuclear fragments positive for gamma-H2AX, a marker of DNA double-strand breaks, than cells that had not yet entered the constrictions. To assess the functional relevance of nuclear envelope repair, we quantified cell viability after rupture. Under normal conditions, the vast majority (> 90%) of cells survived even repeated nuclear envelope rupture. Inhibiting either nuclear envelope repair or DNA damage repair pathways alone did not reduce cell viability; however, combined inhibition of both nuclear envelope and DNA repair substantially increased cell death after nuclear envelope rupture, suggesting potential new therapeutic avenues to specifically target invasive cancer cells [2].

In conclusion, the integration of our migration devices with high resolution time-lapse imaging provides a powerful new approach to study intracellular mechanics and dynamics in a variety of physiologically relevant applications, ranging from immune cell recruitment to cancer cell invasion.

References:

- [1] Patricia M. Davidson, et al., *Integr. Biol.*, 7, 1534 (2015).
- [2] Celine M. Denais, et al., *Science*, 352, 6283, 353-8 (2016).

Figure 3, right top: Time-lapse sequence depicting large nuclear deformation during migration through constriction in microfluidic device. The cell nucleus was labeled with green fluorescent protein fused to core histones. Triangulation between dense chromatin foci that served as fiducial markers was used to compute principal strain maps of nuclear deformation.

Figure 4, right below: Time-lapse sequence of a breast cancer cell exhibiting repeated nuclear envelope rupture (red arrow heads and red bars over the time stamps) during migration through $2 \times 5 \mu\text{m}^2$ constriction.

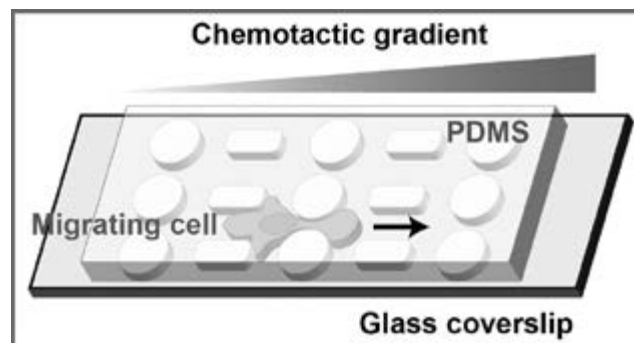


Figure 1: Schematic overview of the microfluidic migration device, including the 5 μm tall channels with 1 μm to 5 μm wide constrictions. Not depicted are the sink and source reservoirs on either end of the device to establish a chemotactic gradient across the migration channels.

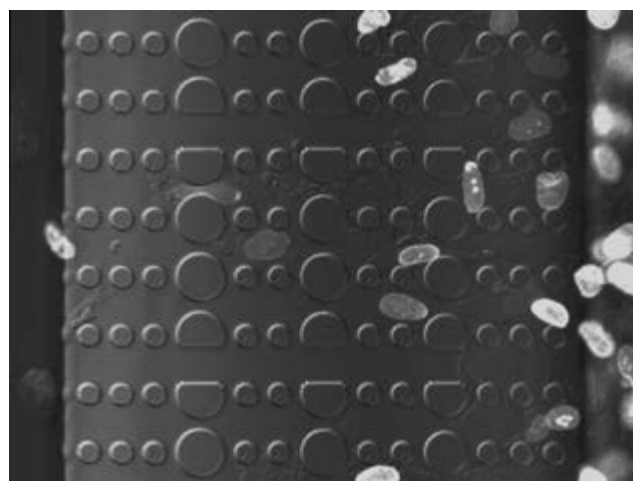
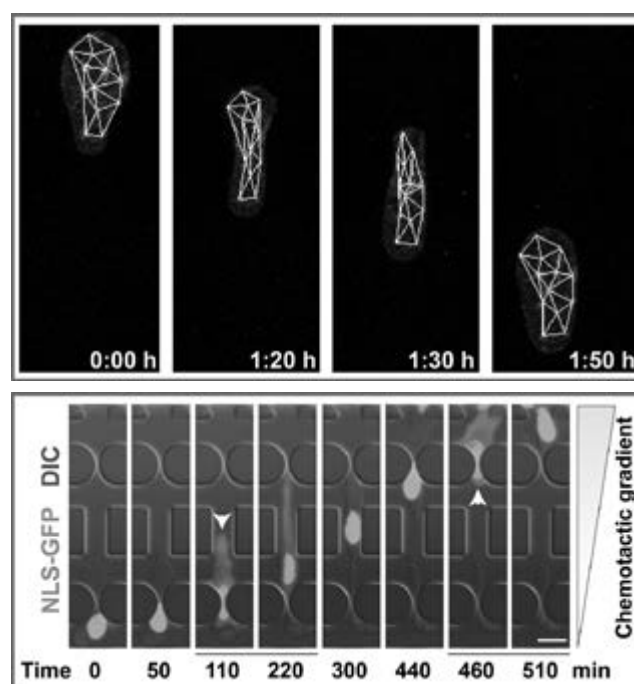


Figure 2: Micrograph of human fibroblasts with fluorescently labeled nuclei (GFP-lamin A) inside the microfluidic migration device.



Micro-Fabricated Sample Holder for Cryogenic Small Angle X-Ray Scattering (cryoSAXS) Experiments

CNF Project Number: 2157-12

Principal Investigator: Robert Thorne

User: Reet Chaudhuri

Affiliations: School of Applied and Engineering Physics, Laboratory of Atomic and Solid State Physics; Cornell University

Primary Source of Research Funding: National Science Foundation

Contact: ret6@cornell.edu, rtc77@cornell.edu

Website: <http://pages.physics.cornell.edu/~rthorne/research.html>

Abstract:

Cryogenic small angle x-ray scattering (cryoSAXS) is a tool to obtain low resolution structural images of biomolecules from a frozen solution [2]. Reproducible scattering is essential for obtaining good data, and the changes in x-ray path length or formation of cracks in the x-ray path create problems [1]. Here, we try to fabricate a low volume, fixed path length sample holder using SU-8, which is mechanically stable under cryogenic cooling, in order to overcome the limitations of the previous generation holders.

Summary of Research:

Small angle x-ray scattering (SAXS) is used to structurally image biological molecules in a solution form. This makes use of the scattered x-ray beam passed through the solution in a sample holder in order to get low resolution structural data of the molecule. Since high energy x-ray is used, radiation damage becomes a major limiting factor in the amount of solution that can be used for getting a good image. Usually about 30 μL of sample is required, which is expensive for biological samples. It has been found that cryogenically cooling the sample to 100K reduces the radiation damage by a factor of about 50 [2]. This allows us to get the same quality imaging data from a much lower volume of a sample. But in this case, the challenge is in producing reproducible frozen samples of the same x-ray path length, while keeping the sample volume down. Previous work done has achieved this by using an open top design made of etched silicon [1]. This had a major limitation of cracking of the sample on freezing. Cracks on the x-ray path length are of concern since they scatter the x-ray beam and mask the real data from the biomolecules scattering. We aim to microfabricate a sample holder which essentially overcomes these limitations.

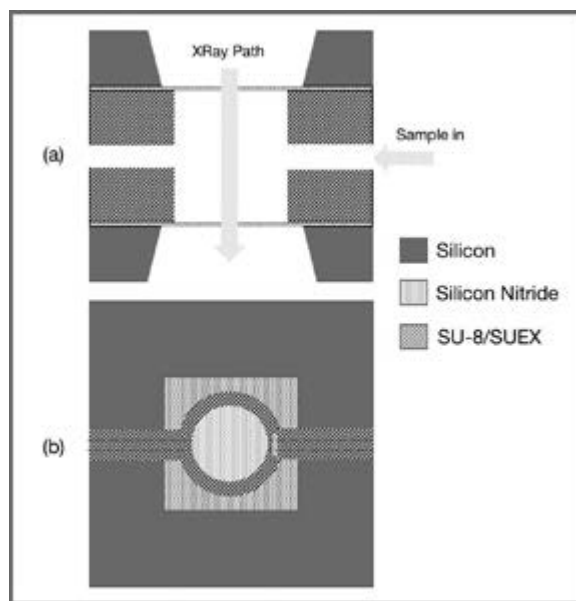


Figure 1: Prototype device being fabricated, illustrating the x-ray path and the sample filling entry. (a) Side view showing the sample holder cylinder. (b) Top view showing the silicon nitride windows.

The first step was to choose a suitable material and geometry. Since the previous sample holder was an etched parallelogram made out of silicon (Si) [1], the asymmetry of the design and the rigidity of the Si were suspected to be the major reasons for the aforementioned cracking. This was confirmed by ANSYS simulations. Hence, a more symmetric hollow cylindrical shape for the sample holder was chosen. SU-8 was chosen to be the material for making the structures. SU-8 is a commonly used epoxy-based negative photoresist, which can also be used to make stand-alone mechanical features due

to its high aspect ratio using photolithography. It proved suitable for this application due to its relative thermal conductivity (as compared to the sample) and mechanical stress properties (less rigid than Si since it's a polymer).

To test the cryogenic performance of SU-8 features over a Si substrate, 400 μm thick SU-8 100 was spun and hollow cylinders of different wall thicknesses were fabricated using contact photolithography in CNF's SÜSS MA6-BA6 contact aligner. These were then filled with different cryoprotectant samples (water, PEG, PPG) and tested by plunge cooling them in liquid nitrogen. No cracking of the frozen sample was observed, nor did the SU-8 features pop off the Si wafer due to their difference in thermal expansion coefficient. Thus, the SU-8 features held up well under low temperature conditions.

Currently, the final sample holder prototypes are being fabricated, which are SU-8 hollow cylinders

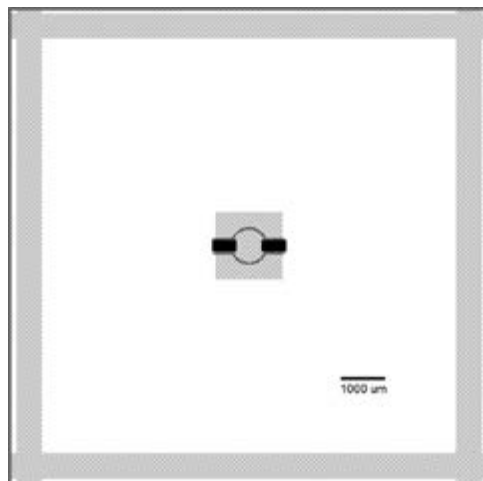


Figure 2: Mask used for photolithography. Grey: KOH etch mask for nitride windows/cleave lines. Hatched/Solid: SU-8 features.

with horizontal filling channels. 500 μm thick SUEX laminated sheets [3] are used instead of manually spinning SU-8, increasing the reliability of the feature heights. 100 nm thin furnace grown low stress nitride grown on silicon wafers is used as the x-ray windows, obtained by patterning it using the Oxford 82 Etcher.

The SU-8 sheet is then laminated and features are grown on top using the SÜSS MA6-BA6 contact aligner, after which two such wafers with 500 μm thick SU-8 features are bonded to obtain the sample holders with an x-ray path length of ~ 1 mm. Finally, the

$\langle 100 \rangle$ Si wafer is wet etched in a potassium hydroxide (KOH) bath leading to smooth nitride x-ray windows and cleave lines in the wafer.

These sample holders will next be tested for mechanical properties as well as x-ray properties in the synchrotron beamline at Cornell High Energy Synchrotron Source, and will hopefully be a step towards making cryoSAXS experiments a more accepted tool, lending its advantages over conventional SAXS.

References:

- [1] J. Hopkins, A. Katz, S. Meisburger, and A. Matthew, 227 (2015).
- [2] S.P. Meisburger, M. Warkentin, H. Chen, J.B. Hopkins, R.E. Gillilan, L. Pollack, and R.E. Thorne, Biophys. J. 104, 227 (2013).
- [3] D.W. Johnson, J. Goettert, V. Singh, D. Yemane, and B. Rouge, (n.d.).

Near-Field Optical Trapping for High-Throughput Nanoparticle Analysis

CNF Project Number: 2212-13

Principal Investigator: David Erickson

User: Perry Schein

Affiliation: Sibley School of Mechanical and Aerospace Engineering, Cornell University

Primary Source of Research Funding: US National Institutes of Health

Contact: de54@cornell.edu, pms249@cornell.edu

Abstract:

In this project we have developed a method for directly measuring the interaction potential energy and force profiles for the interactions between colloidal nanoparticles and surfaces. The measurements are made with high throughput, characterizing dozens to hundreds of nanoparticles per hour by measuring the diffusive Brownian motion of the nanoparticles normal to the surface as they are propelled along an optical waveguide by the optical scattering force. The particles are held in the evanescent field by the optical gradient force, and the motion of the particles is tracked by measuring the scattered light from the particles as they interact with this evanescent field. This is accomplished using a high frame rate camera optimized for IR light scattering. We have applied this technique to measuring metallic, dielectric, and biomolecular particles with diameters ranging from 50-1000 nm. These potential energy landscapes tell us quantitatively how “sticky” the nanoparticles are, giving insight into the colloidal stability.

Summary of Research:

Nanoparticle technologies are becoming increasingly prevalent in a wide range of applications in many industries including pharmaceuticals, cosmetics, energy, and food. These applications are enabled by the novel physical and chemical properties that arise from the high surface area to volume ratio of the nanomaterials as well as due to their physical size, which gives these materials the ability to work in confined regions. However, these unique properties come at a cost as the higher surface energy of the nanoparticles means that stability is a critical challenge when working with nanoparticle suspensions — nanoparticles must be carefully engineered to ensure that they don't clump together into aggregates or stick onto surfaces, as these behaviors will lead to failure of the nanoparticle suspension to work as intended.

Unfortunately, colloidal suspensions are incredibly complex and all existing theories fail to predict colloidal stability under practical conditions of salinity, particle volume fraction, pH, and temperature. These suspension interactions involve small forces on the pico-Newton scale and smaller, and energies on the thermal energy scale so while measuring these

interactions directly is necessary, the measurement technique used cannot be limited by thermal noise. Also, in a polydisperse sample, it is necessary to measure many particles rapidly in order to obtain a reasonable understanding of what is happening.

Existing techniques such as colloidal probe atomic force microscopy fail due to their inability to make measurements that are not limited by thermal noise, limiting the size of the particles and forces that can be studied, while total internal reflection microscopy suffers from low throughput. To fill this gap, many researchers use indirect methods like UV-Vis absorbance spectroscopy, ζ — potential measurements, or dynamic light scattering to try to infer the stability by measuring changes in the optical, electrical, or size properties of the nanoparticles but these indirect methods act only on a bulk suspension basis and fail to give a complete picture.

Here, we have developed a technique to overcome these limitations. We measure interactions on the scale of Boltzmann's constant times temperature on particles with sub-100 nm diameters. We accomplish this using a

waveguide architecture with an integrated microchannel. Initial prototypes for these devices made use of CNF tools such as the VersaLaser cutter, and the ABM contact aligner in developing the initial processes. The technique is pictured in Figure 1.

Particles in suspension interact with the evanescent field of the optical waveguide and undergo confined Brownian motion near the device. As they move up and down, they scatter light depending on their position, and over time using the Boltzmann statistics the distribution of scattered light relates to the probability of the particle being at a given position, which can then be used to map the potential energy landscape giving insight into the stability, measuring the height of the energy barrier preventing the particle from sticking.

We have performed these measurements on a wide variety of particles, achieving high throughput of several hundred particles per hour as well as reproducibility of measured energy landscapes in nominally monodisperse samples. The wide range of utility of this technique is illustrated in Figure 2 where we show measurements on gold, silver, and protein aggregate particles. Figure 3 illustrates the reproducibility of the measured potential energy wells on samples of NIST standard polystyrene spheres.

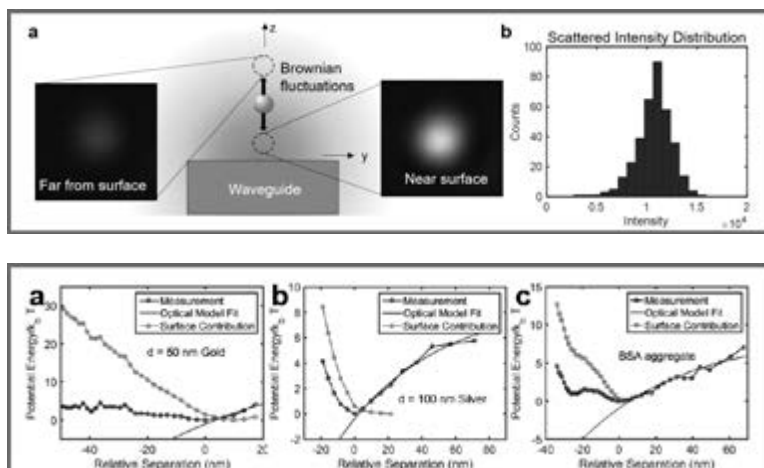


Figure 1, top: Schematic of measurement. (a) As a particle is propelled along a waveguide, it interacts with the evanescent field, scattering light. The particle undergoes confined Brownian motion in the direction normal to the surface, and more light is scattered when it is close to the surface than when it is far away. (b) Imaging the scattered light in many frames gives the distribution of scattered light intensity, which is related to particle height and the interaction energy landscape through the Boltzmann distribution.

Figure 2, bottom: Potential energy measurements for various materials including (a) 50 nm diameter gold particles, (b) 100 nm diameter silver particles, and (c) aggregates of bovine serum albumin (BSA), a model protein. The black curves illustrate the data obtained from the distribution of scattered light intensity; the blue curve represents a fit to the optical force. When this is subtracted from the black curve, the remaining contribution is due to the particle-surface interactions (red curve), indicating the energy barrier preventing the nanoparticle from sticking to the surface.

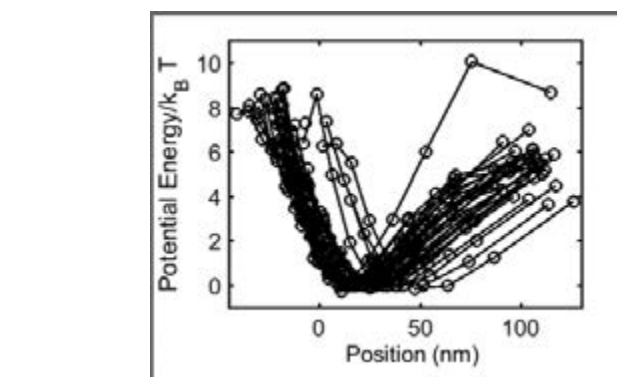


Figure 3: Population level potential energy landscapes. Each curve is an independent measurement on a different particle.

References:

- [1] Butt, H.-J., Cappella, B., and Kappl, M. "Force measurements with the atomic force microscope: Technique, interpretation and applications," Surf. Sci. Rep, 59, 1-152 (2005).
- [2] X. Gong, Z. Wang, and T. Ngai. "Direct Measurements of Particle-Surface Interactions in Aqueous Solutions with Total Internal Reflection Microscopy," Chem. Comm., 50, 6556-6570 (2014).
- [3] Schein, P., Kang, P., O'Dell, D., Erickson, D., "Nanophotonic Force Microscopy: Characterizing Particle-Surface Interactions Using Near-Field Photonics" Nano Letters 15 (2), 1414-1420 (2015).

Fabrication of DNA Stabilizing Nanofluidic Channels for High-Resolution Optical Imaging of Transcription *in vitro*

CNF Project Number: 2230-13

Principal Investigators: Barbara A. Baird¹, Warren Zipfel², John Lis³, Adam Bogdanove⁴

Users: Devin Wakefield¹, Alexander Van Slyke², Avtar Singh², Max Kushner², Dig Bijay Mahat³, Judhajeet Ray³, Fabio Cupri Rinaldi⁴

Affiliations: 1. Department of Chemistry and Chemical Biology, 2. Department of Biomedical Engineering, 3. Department of Molecular Biology and Genetics, 4. Department of Plant Pathology and Plant-Microbe Biology; Cornell University

Primary Sources of Research Funding: NIH grants DA030329 and AI018306

Contact: bab13@cornell.edu, wrz2@cornell.edu, johnlis@cornell.edu, ajb7@cornell.edu, dlw238@cornell.edu, alv54@cornell.edu, as459@cornell.edu, mgk59@cornell.edu, dbm222@cornell.edu, jr839@cornell.edu, fcr23@cornell.edu

Abstract:

In this project, we are developing a series of microfluidic devices optimized for studying DNA-protein interactions. The device design is similar to that constructed by Eric Greene at Columbia University in which thousands of DNA molecules are tethered to a lipid bilayer and placed under hydrodynamic flow to co-align DNA molecules perpendicular to nanofabricated barriers [1]. The devices will be used to quantify the binding affinities and kinetics at specific loci, using both synthetic DNA and chromatin preparations obtained from isolated nuclei.

Summary of Research:

Transcriptional activation is a primary mode of regulating gene expression. Genetic studies and genome-wide assays have provided valuable insights on transcription. However, the underlying mechanisms regulating transcription at the single-molecule level have yet to be thoroughly investigated. Much of our understanding of the complex process of transcription comes from chromatin immunoprecipitation (ChIP) methods in which a snapshot of the transcription state is taken by chemical cross-linking DNA, RNA and proteins, fragmenting the chromatin, and then pulling out protein-DNA complexes with antibodies to suspected transcription factors (TFs). Subsequent sequencing is used to identify the location of targeted TFs on the DNA at the time of cross-linking. Although this provides clear evidence of DNA-protein interactions *in vivo*, it is largely a binary approach and delivers only a crude estimate of the binding constants at play, with no information on the dynamics of the interaction.

There is a critical need for new methods capable of providing quantitative kinetic information about TF binding so that accurate models of transcription may be established. The microfluidic device designed in this project aims to provide a platform for obtaining high-resolution transcription factor binding data at the single-molecule level.

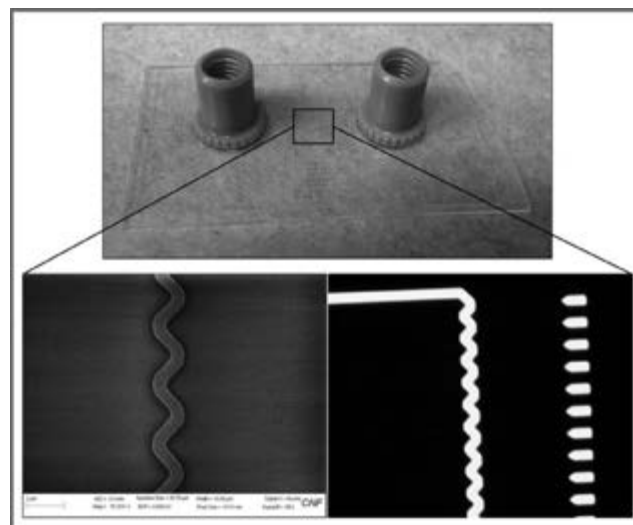


Figure 1: Microfluidic device with images of individual chrome barriers on a glass surface. The saw-tooth design is significant for trapping the DNA tethered to a lipid bilayer that is presented on either side of these chrome barriers. Left panel: SEM image of $\sim 0.5 \mu\text{m}$ wide barrier. Right panel: optical image of $1 \mu\text{m}$ wide barrier with additional anchor patterns.

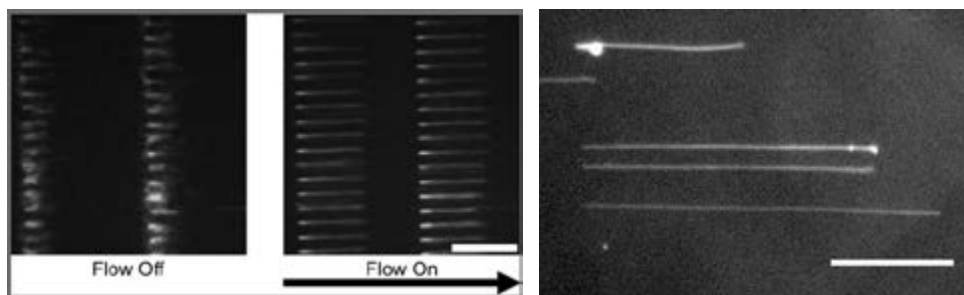


Figure 2, left: Fluorescence image of YOYO1-stained DNA curtains. The left image shows DNA molecules after pausing buffer flow while the right image shows the same DNA now extended after returning buffer flow (arrow denotes direction of flow). Scale bar 15 μm . **Figure 3, right:** Fluorescence image of chromatin curtains obtained from *Drosophila* S2 cells. Scale bar 15 μm .

To accomplish this goal, we have developed a method to prepare the required chrome-patterned surfaces using standard photolithography techniques. Clean glass wafers, coated with photoresist using the Gamma automatic coat-develop tool, are patterned using the ASML PAS 5500/300C DUV stepper. Subsequent chrome evaporation using the CVC SC4500 evaporator and a final lift-off step yields multiple arrays of ~ 20 nm tall chrome patterns. These patterns exploit a saw-tooth design (Figure 1a) to provide for effective DNA capture at regularly spaced intervals; this ensures uniform presentation of DNA for imaging. A second design incorporates an additional pattern of pentagons designed to anchor the free end of the DNA molecule (Figure 1b). Finally, the microfluidic device assembly makes use of double-sided tape to form a single channel between cut pieces of the patterned wafer and a microscope coverslip. Nanoports are attached over holes drilled into the glass surface to complete the device.

The surface surrounding the chrome barriers, inside this microfluidic device, is coated with a lipid bilayer. This lipid bilayer surface contains a biotinylated lipid that provides a binding site for streptavidin, to ultimately anchor biotinylated DNA to the surface. We are currently investigating the use of a biotinylated DNA binding protein, LacO, which binds the specific LacI site on DNA. In addition to effectively anchoring the DNA to the bilayer, this would circumvent any low efficiency in the biotinylation of DNA harvested *in vitro*. DNA bound to the bilayer surface is then able to diffuse in the direction of flow until it reaches a chrome barrier. Here, the free end of the DNA extends under the force of flow to create rows of “DNA curtains,” allowing for the observation of many co-aligned stretched DNA molecules within a single microscope field of view (Figure 2). In the second device design, the chrome pentagons act to anchor the free end of

DNA, enabling the DNA molecule to remain extended in the absence of hydrodynamic force. This allows the behavior of the DNA binding protein of interest to be investigated in the absence of outside forces.

The interaction of proteins and DNA can be visualized within these devices using prism total internal reflection fluorescence microscopy (TIRFM), a

high-resolution fluorescence microscopy technique [2]. Our goal is to adapt this research tool to study chromatin activity (Figure 3) primarily during the Heat Shock Response, and transcription activator-like effectors (TALEs) (Figure 4), at the single-molecule level [3]. These studies should greatly expand our understanding of gene regulation derived from current optical and biochemical analyses [4]. Applications for the “DNA curtains” approach extend far beyond these two specific applications, as many DNA-protein interactions are either poorly understood, or have not been previously investigated via optical methods.

References:

- [1] E.C. Greene, S. Wind, T. Fazio, J. Gorman, M.-L. Visnapuu. Chapter 14 - DNA Curtains for High-Throughput Single-Molecule Optical Imaging, in: Nils G. Walter (Ed.), *Methods in Enzymology*, Academic Press, 2010: pp. 293-315.
- [2] D. Axelrod, T.P. Burghardt, N.L. Thompson. “Total Internal Reflection Fluorescence.” *Ann. Rev. Biophys. Bioeng.* 13 (1984): 247-68.
- [3] M.J. Moscou and A.J. Bogdanove. “A Simple Cipher Governs DNA Recognition by TAL Effectors.” *Science* 326 (2009): 1501.
- [4] M.S. Buckley, H. Kwak, W.R. Zipfel, J.T. Lis. “Kinetics of promoter Pol II on Hsp70 reveal stable pausing and key insights into its regulation.” *Genes Dev.* 28 (2014): 14-19.

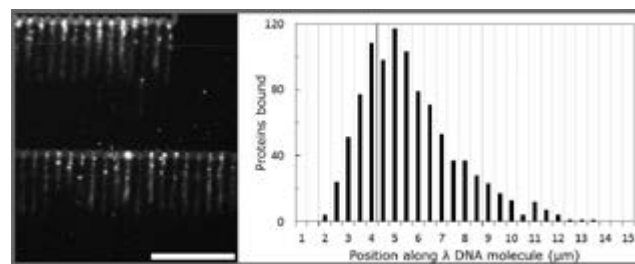


Figure 4: YOYO-1 stained DNA curtains with bound Alexa-647 labeled TAL1535. The left panel shows YOYO-1 stained DNA (green) and TAL1535-Alexa-647 (magenta) extended in the microfluidic device. The right panel shows a histogram of measured TAL protein binding positions. Red line denotes expected TAL binding location. Scale bar 15 μm .

Microfabricated Devices for Cell Organization

CNF Project Number: 2249-13

Principal Investigator: Minglin Ma

User: Wei Song

Affiliation: Department of Biological and Environmental Engineering, Cornell University

Primary Source of Research Funding: American Diabetes Association

Contact: mm826@cornell.edu, ws336@cornell.edu

Website: <http://malab.bee.cornell.edu>

Abstract:

Different types of cells dynamically self-assemble and organize themselves in a spatiotemporal and context-dependent manner [1]. In this study, we report the spatiotemporal dynamics of cell organization of a binary cellular mixture (MDA-MB-231 and MCF10A cells) seeded in microfabricated microwells. The initial seeding ratio of binary cells determined the degree of encapsulation of MCF10A cells by MDA-MB-231 cells. When cells were free to grow, the differential proliferation rate of MDA-MB-231 (low growth rate) and MCF10A cells (high growth rate) resulted in a reversed core (MDA-MB-231)-shell (MCF10A) organization at seeding ratio of 1:1 (MDA-MB-231:MCF10A) and a side-by-side aggregate structure at seeding ratio of 4:1 after long-term culture.

Summary of Research:

Fabrication of Polydimethylsiloxane Microwell.

The photomask was prepared using CNF's DWL2000 mask writer (Heidelberg Instruments). The silicon wafer was spin-coated with SU-8 2150 photoresist (MicroChem) at 500 rpm for 40 sec and then 2500 rpm for 30 sec. The wafer was covered with the photomask and exposed by a UV photolithography machine (ABM contact aligner) for 32 sec. After being developed and post-baked, the SU-8 master wafer was fabricated. The SU-8 master wafer was then used to create polydimethylsiloxane (PDMS, Sylgard 184, Dow Corning) mold. A mixture (10:1) of Sylgard 184 silicone elastomer components was casted onto the master wafer and cured at 60°C overnight to prepare a PDMS microwell. Figure 1 is a microscopic image of PDMS microwells.

Formation of Cell Aggregates in PDMS Microwells.

PDMS microwells were autoclaved, placed in a 24-well plate, and coated with 1% (w/v) Pluronic® F127 (Sigma) solution before cell seeding to prevent cell attachment on PDMS surface and facilitate formation of cell aggregates. To form cell aggregates, cell suspensions of MDA-MB-231/MCF10A mixture (MDA-MB-231:MCF10A=1:1 and 4:1, total 1.0×10^6 cells) were added to each well of 24-well plate with PDMS microwells inside. After four hours of static culture, the cells that were adhered to the interspace between microwells were removed by medium change. The cells that fell into the microwells formed

cell aggregates after overnight culture. The cell aggregates were cultured in microwells for nine days. The mixed medium (MDA-MB-231 medium:MCF10A medium=1:1 and 4:1) was changed every two days.

Figure 2 is a fluorescent image of cell segregation of MDA-MB-231 (red colour) and MCF10A (green colour) cells at 1:1 cell seeding ratio over nine days of culture. Figure 3 is a fluorescent image of cell segregation of MDA-MB-231 (red colour) and MCF10A (green colour) cells at 4:1 cell seeding ratio over nine days of culture.

Conclusions:

In summary, the initial seeding ratio and cell proliferation have significant effects on the evolution of cell organization of binary cellular mixture over long-term culture. Depending on the initial seeding ratios, the cell organization is either a core-shell (1:1) or side-by-side (4:1) aggregate by the differential proliferation rates of MDA-MB-231 and MCF10A cells.

References:

- [1] Yoshiki Sasai. Cytosystems dynamics in self-organization of tissue architecture. *Nature* 2013, 493, 318-326.

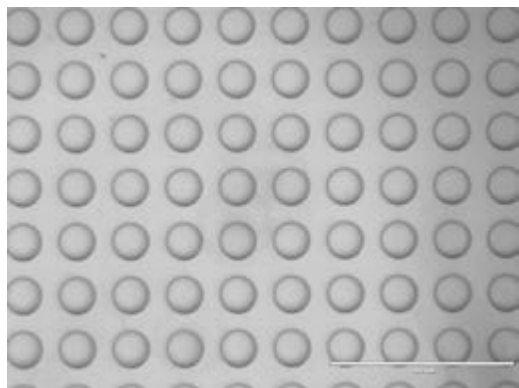


Figure 1: A microscopic image of PDMS microwells. Scale bar: 1000 μm .

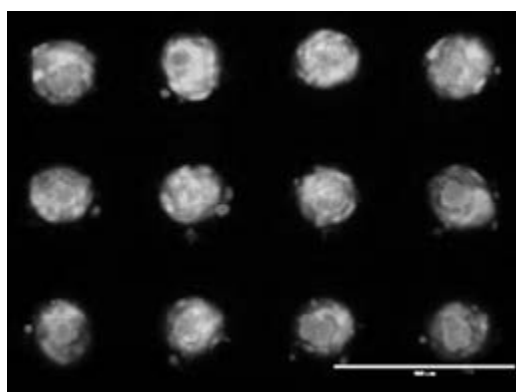


Figure 2: A fluorescent image of cell segregation of MDA-MB-231 (red colour) and MCF10A (green colour) cells at 1:1 cell seeding ratio over nine days of culture. Scale bar: 400 μm .

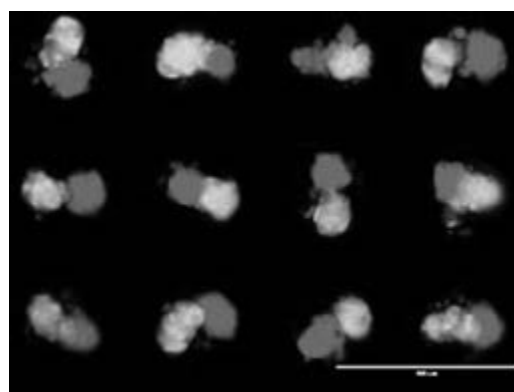


Figure 3: A fluorescent image of cell segregation of MDA-MB-231 (red colour) and MCF10A (green colour) cells at 4:1 cell seeding ratio over nine days of culture. Scale bar: 400 μm .

Temporal Correlation Between SNARE Conformational Change and Vesicle Fusion

CNF Project Number: 2260-13

Principal Investigator: Manfred Lindau

Users: Ying Zhao, Qinghua Fang, Meng Huang

Affiliations: Applied and Engineering Physics, Cornell University, Ithaca NY; Laboratory for Nanoscale Cell Biology, Max Planck Institute for Biophysical Chemistry, D-37077 Göttingen, Germany

Primary Sources of Research Funding: European Research Council Advanced Grant No. 322699 (to M.L.), National Institutes of Health Grants R21 NS088253 and MH095046 (to M.L.), and National Science Foundation Grant ECS-0335765

Contact: ML95@cornell.edu, YZ86@cornell.edu, QF24@cornell.edu, MH2236@cornell.edu

Abstract:

The temporal correlation between the conformational change of the synaptosomal-associated protein 25 (SNAP25) and individual fusion events was investigated in SNAP25 deficient embryonal mouse chromaffin cells overexpressing a modified SNARE complex reporter (mSCORE). In the mSCORE expressing cells we imaged the fluorescence resonance energy transfer (FRET) change of mSCORE localized to the plasma membrane by total internal reflection (TIR) FRET imaging and simultaneously recorded individual fusion events as amperometric spikes with a microfabricated electrochemical detector (ECD) array [1]. Our study shows that a conformational change of SNAP25 was abrupt and preceded the opening of an exocytotic fusion pore by ~ 60 ms followed by return to baseline with 900 ms time constant after a 1.1 s delay.

Summary of Research:

Individual mSCORE-overexpressing SNAP25 knockout mouse embryonal chromaffin cells were placed on an ECD array consisting of four platinum (Pt) microelectrodes patterned photolithographically on a glass coverslip (Figure 1A inset). Conformational changes in SNAP25 were monitored by FRET imaging while exocytotic catecholamine release from single vesicles was simultaneously recorded using the ECD array [2,3]. Single fusion events at the bottom of the cell were detected by the four ECD electrodes as correlated amperometric spikes. The locations of individual fusion events was determined from the fractions of molecules that were oxidized by each of the four ECD electrodes. The releasing area was defined as 2×2 pixels. In the modified probe mSCORE, the FRET donor CFP in original SCORE [5] was replaced with mCerulean3 exhibiting enhanced brightness and reduced reversible photoswitching [4]. The temporal correlation between the conformational change of SNAP25 and the individual fusion events was studied by plotting the time courses of fluorescent intensity (CFP and mCerulean3) and FRET ratio (mCerulean/Venus) at the vesicle releasing sites.

In order to improve the signal-to-noise ratio, the traces of FRET ratio as well as fluorescence were aligned at the starting point of corresponding amperometric events (the largest and earliest ECD spike) and averaged over 600 events. The averaged time courses of fluorescence at the releasing site shows an rapid increase in Venus channel and a concurrent decrease with similar amplitude in mCerulean3 channel, with a ~ 11% increase of FRET ratio, Figure 1A-C. By using the event correlation microscopy (ECOM) method, the delay of fusion pore opening after the FRET change was determined as ~ 60 ms (Figure 1D).

CNF tools used for ECD fabrication include the Heidelberg Instruments DWL 2000 to generate the ECD pattern on the photosensitive Cr mask plates, the YES image reversal oven for photoresist tone reversal, ABM's resolution mask aligner for UV exposure of the featured pattern on the photoresist-deposited wafer, the Oxford PECVD SiO₂ for deposition, and the Oxford 80 to etch the SiO₂ pattern on the wafer.

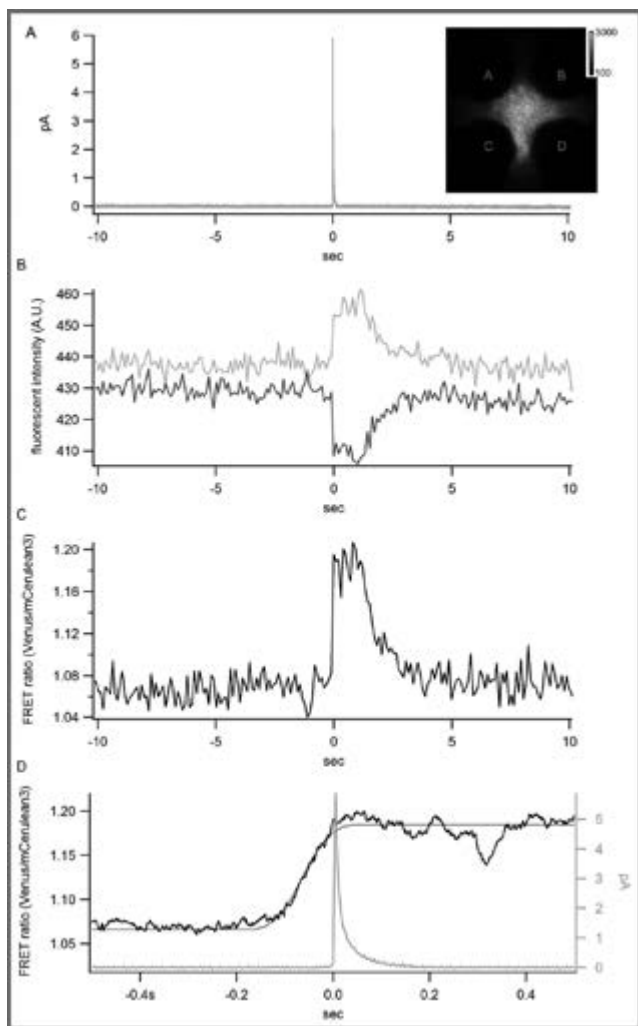


Figure 1: Conformational change of SNAP25 precedes the fusion pore opening. Inset, cell footprint on ECD array imaged in TIRF mode. A, Averaged amperometric spike obtained after temporal alignment of the spikes (sum of the four ECD spikes) at their starting time. B and C, averaged time courses of mCerulean-3 (blue in B) and Venus (yellow in B) and FRET ratio (C). D, FRET time course (black) from the data in C analyzed with ECOM method on expanded time scale, the fitting of FRET rising phase (-0.5 to +0.5 s) with the ECOM step response function (red), and ECD trace in A was also included (green).

References:

- [1] Zhao, Y., Fang, Q., Herbst, A. D., Berberian, K. N., Almers, W., and Lindau, M. (2013) Rapid structural change in synaptosomal-associated protein 25 (SNAP25) precedes the fusion of single vesicles with the plasma membrane in live chromaffin cells. *Proceedings of the National Academy of Sciences of the United States of America* 110, 14249-14254.
- [2] Hafez, I., Kisler, K., Berberian, K., Dernick, G., Valero, V., Yong, M. G., Craighead, H. G., and Lindau, M. (2005) Electrochemical imaging of fusion pore openings by electrochemical detector arrays. *Proceedings of the National Academy of Sciences of the United States of America* 102, 13879-13884.
- [3] Berberian, K., Kisler, K., Fang, Q., and Lindau, M. (2009) Improved surface-patterned platinum microelectrodes for the study of exocytotic events. *Analytical chemistry* 81, 8734-8740.
- [4] Markwardt, M. L., Kremers, G. J., Kraft, C. A., Ray, K., Cranfill, P. J., Wilson, K. A., Day, R. N., Wachter, R. M., Davidson, M. W., and Rizzo, M. A. (2011) An improved cerulean fluorescent protein with enhanced brightness and reduced reversible photoswitching. *PLoS one* 6, e17896.
- [5] An, S. J., and Almers, W. (2004) Tracking SNARE complex formation in live endocrine cells. *Science* 306, 1042-1046.

Deoxyribonucleic Acid (DNA)-Based Organic Light-Emitting Diode Device Fabrication

CNF Project Number: 2300-14

Principal Investigator: Dan Luo

User: Yue Hu

Affiliation: Department of Biological and Environmental Engineering, Cornell University

Primary Source of Research Funding: NSF Grant

Contact: DL79@cornell.edu, YH348@cornell.edu

Abstract:

We have successfully fabricated and patterned deoxyribonucleic acid (DNA) nanofibers by using a microfluidic chip with built-in pillars. DNA can be employed as an electron blocking layer to enhance electroluminescence efficiency. This work has focused on incorporating DNA nanofibers as an integral element of organic light-emitting diode (OLED) and developing the potential optical applications.

Summary of Research:

Rolling circle amplification (RCA) reaction is a robust, isothermal enzyme chemical reaction that amplifies specific DNA [1]. We have discovered that by running the RCA reaction through a microfluidic chamber pre-designed with patterned pillars (Figure 1), we can generate DNA nanofibers in that pattern (Figure 2).

DNA is a highly negative-charged biomaterial owing to a phosphate group in the side chain. Therefore, DNA can interact with cationic electron-transport materials via electrostatic interaction and further be employed as an electron blocking layer in organic light-emitting diode (OLED) devices [2].

To fabricate DNA nanofiber-based OLEDs, DNA nanofibers were formed on the top of fluorine-doped tin oxide (FTO) glass. A red-light emitting material, $\text{Ru}(\text{bpy})_3\text{Cl}_2$, was loaded into DNA nanofibers via electrostatic interaction to form a DNA- $\text{Ru}(\text{bpy})_3^{2+}$ complex film. The top aluminum electrode was finally deposited with a thickness of 100 nm using thermal evaporation.

Experiments are under way to evaluate the electroluminescence efficiency of DNA nanofiber-based OLEDs.

References:

- [1] Lee, J.B., Peng, S., Yang, D., Roh, Y.H., Funabashi, H., Park, N., Rice, E.J., Chen, L., Long, R., Wu, M., Luo, D. A mechanical metamaterial made from a DNA hydrogel. *Nature Nanotechnology*, 109, 816-820 (2012).
- [2] Nakamura, K., Ishikawa, T., Nishioka, D., Ushikubo, T., Kobayashi, N. Color-tunable multilayer organic light emitting diode composed of DNA complex and tris(8-hydroxyquinolinato) aluminum. *Applied Physics Letters*, 97, 193301 (2010).

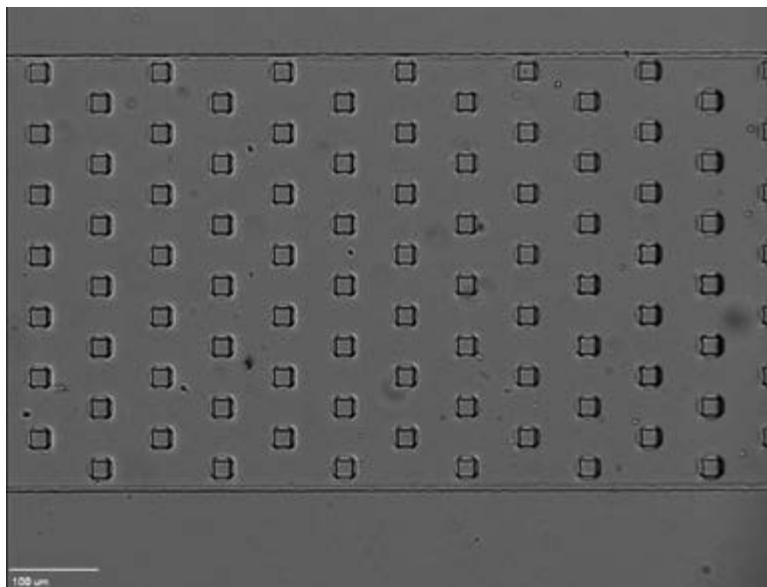


Figure 1: Microfluidic chips with staggered pillar. Micropillar =10 μm .

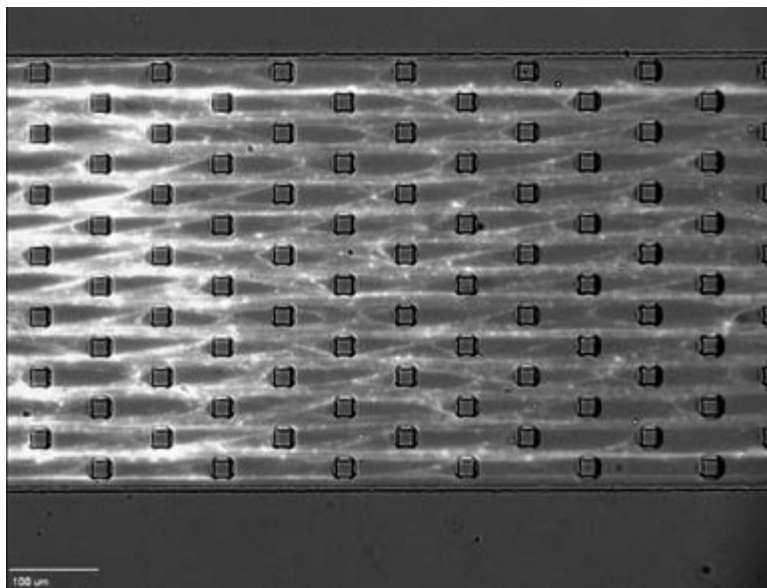


Figure 2: Patterned DNA nanofibers were produced.

Microfluidic Chip for Drop-seq Platform

CNF Project Number: 2331-15

Principal Investigator: Iwijn De Vlaminck

Users: Philip Burnham, Eamon Collins

Affiliations: Department of Physics, Meinig School of Biomedical Engineering; Cornell University

Primary Source of Research Funding: Department of Biomedical Engineering, Cornell University

Contact: idevlaminck@gmail.com, psb84@cornell.edu, epc53@cornell.edu

Website: <http://www.devlaminck.bme.cornell.edu>

Abstract:

Macosko, et al. [1], recently described Drop-seq, a platform for performing RNA-seq on thousands of single cells with high throughput and low cost (<\$0.10). The system utilizes a coflow microfluidic device to encapsulate single cells with magnetic microbeads in nanoliter droplets. We have fabricated silicon masters for replica molding of poly(dimethylsiloxane) (PDMS) devices for use in our lab's Drop-seq setup.

Summary of Research:

PDMS chips are fabricated using conventional soft lithography techniques. A chrome mask with channel design supplied by Macosko, et al., is created using the Heidelberg Mask Writer DWL2000. A silicon wafer is spin-coated with SU-8 2075 photoresist at 500 RPM for 10 seconds with acceleration of 100 RPM/s and then at 2000 RPM for 30 seconds with acceleration of 300 RPM/s. The wafer is then exposed to UV light through the chrome mask using the ABM Contact Aligner. After development of the wafer, a final hard bake is performed to anneal any SU-8 surface cracks.

Before casting with PDMS, the silicon master is coated with a single-molecule layer of FOTS (1H,1H,2H,2H-perfluorooctyl)trichlorosilane using the MVD100. This provides an antistiction coating for easier lift off of PDMS from the smaller features of the master, such as in Figure 2. Sylgard 184 PDMS prepolymer is prepared in 10:1 base to curing agent ratio and degassed in a vacuum chamber. The PDMS is then poured onto the master in a Petri© dish and cured in a 60°C oven for two hours.

After lift off from the master, ports for tubing are created using a biopsy punch. The chips are then

bonded to glass microscope slides via oxygen plasma after activation for three minutes in the Harrick Plasma Generator. The microfluidic channels are rendered hydrophobic by flowing Aquapel solution through the devices.

For Drop-seq experiments, the chip is mounted on an inverted fluorescence microscope and three syringe pumps flow oil, cell suspension, and microbeads in lysis solution through the device. Current devices produce highly uniform droplets with a diameter of approximately 100 μm , within the tolerance for Drop-seq experiments. In the future, silicon masters with taller SU-8 features may be produced to increase the size of droplets generated.

References:

- [1] Macosko EZ, Basu A, Satija R, Nemes J, Shekhar K, Goldman M, et al. Highly parallel genome-wide expression profiling of individual cells using nanoliter droplets. *Cell*. 2015;161:1202-1.

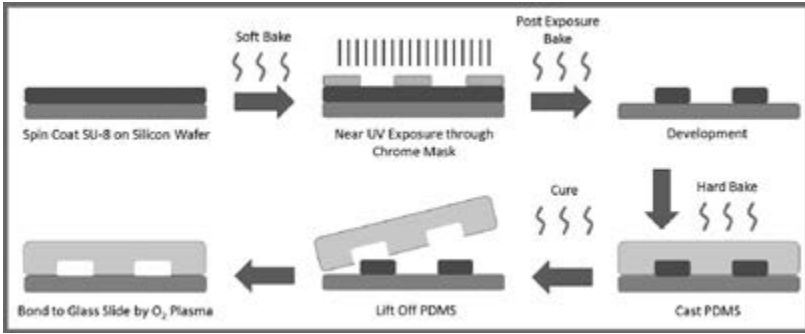


Figure 1: Flowchart describing fabrication of silicon master through to final device.

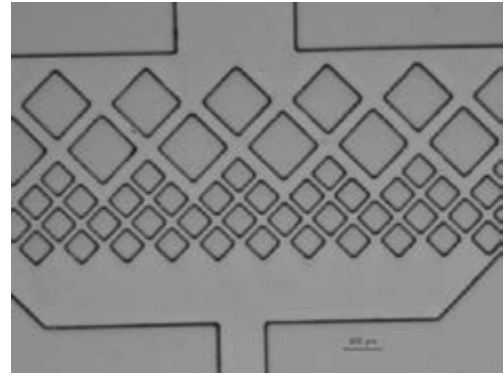


Figure 2: Filtering posts at oil inlet of device.



Figure 3: Three PDMS chips on glass microscope slide.

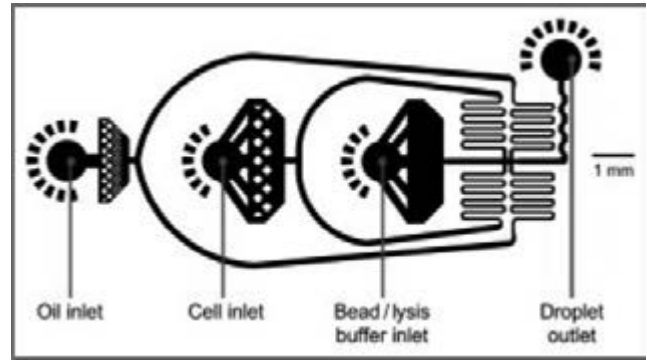


Figure 4: Design of the microfluidic channels [1].

Etching Micropatterns on Silicon Wafers towards PDMS Protein Casting on Hydrogels

CNF Project Number: 2378-15

Principal Investigator: Benjamin D. Cosgrove, Ph.D.

User: Victor Aguilar

Affiliation: Nancy E. and Peter C. Meinig School of Biomedical Engineering, Cornell University

Primary Source of Research Funding: National Institutes of Health

Contact: bdc68@cornell.edu, va233@cornell.edu

Abstract:

Protein deposition on hydrogels is a technique widely employed to functionalize microenvironments of cells; this process allows for the study of cellular development in respond to variations in the cellular niche. This project aims to generate micropatterned silicon wafers towards the creation of protein deposition wells 100 micrometers deep (a process known as stamping) in hydrogel systems. The silicon wafers were prepared for photolithography using positive photoresist (generating in wells), etched (deep silicon etching), and treated to deactivate the resist. To assess the depth of features in silicon wafer wells, average depth was assessed using CNF's P10 Profilometer.

Assessment of variations in depth based on the type of photoresist and photolithographic treatment (varying exclusively on angular speed of photoresist spreading) showed inconclusive results. Comparison between different angular speeds showed that depth variations were not significant; meanwhile, comparison between two types of positive photoresist resulted in a more significant variation in well depth. Further analysis concluded that this difference was not significant.

Optimizing the type of photoresist enables a higher degree of control on the depth of well features in the silicon wafer but is still subject to the photolithographic process. Future work will focus on establishing a protocol for tighter control on the design of features in silicon wafers.

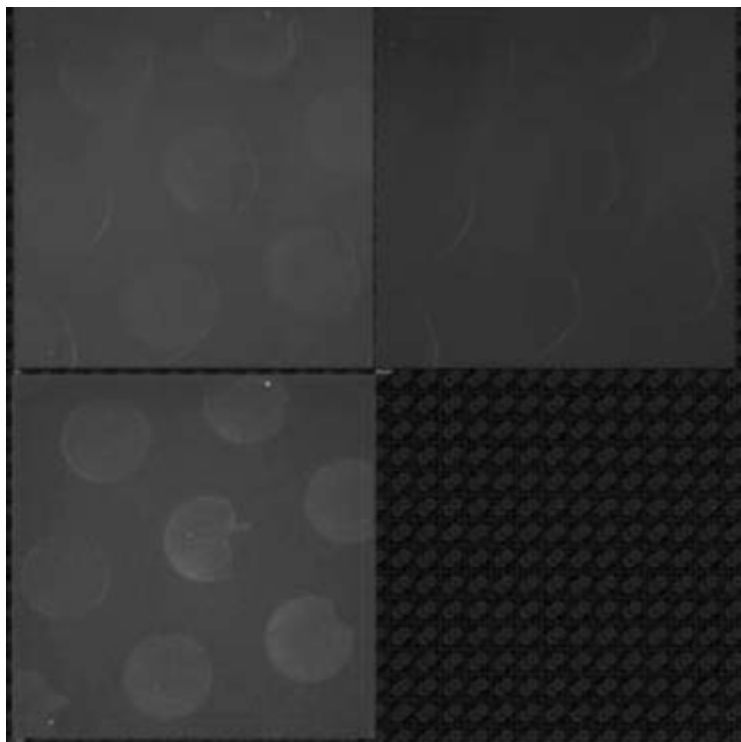


Figure 1: Identification of protein coating on hydrogel systems using fluorophore (Alexa 647) conjugation.

Introduction:

Cellular development models often take into consideration the interactions that exist between cells and between the cell and its microenvironmental niche. This niche is subject to modulation itself by the turnover of extracellular matrix (ECM) proteins and

the physical/chemical properties of the environment [1]. For the purpose of single cell tracking in a microenvironment, wells can be developed on gel systems using polydimethylsiloxane (PDMS) stamping of protein coats. Generating patterns on

the PDMS stamp itself, however, was the result of photolithographic work carried out on silicon wafers. Photolithography allows for control on the depth and type of features to be incorporated into the PDMS stamp.

Methods:

Patterning on the silicon wafer was accomplished through AutoCAD designs. These designs were employed to generate two distinct chrome masks, each possessing a distinct array of staggered dots varying in diameter (300 and 600 μm) and pitch (600 and 1200 μm). To generate depth on the silicon, wafers were prepped with positive photoresist (SPR220-3.0 or SPR220-4.5), spun at varying speeds (3000, 4500 RPM) towards controlling the overall depth of the photoresist layer. Baking and (Hamatech) development were employed for curating the resist prior to etching.

Etching protocols for deep silicon features required the use of Bosch etching (Unaxis 770), running for a total of 25-35 cycles. Etched wafers underwent resist stripping (Aura 1000) using the 45 sec/8 sec of heating setting. The last step involved a ten-minute treatment (MVD 100) for vapor deposition of C9-15 fluoroalcohol phosphate, triethoxycaprylsilane (FOTS) to ensure minimal reactivity between the photoresist and PDMS.

Results:

Crafted silicon patterns were tested for accuracy of feature size and depth. Verification of features using a P10 profilometer system revealed that variations between the actual and theoretical diameter for staggered dots on silicon wafers was negligible. Assessment of staggered dot distribution across the wafer was not performed given its lack of importance.

Depth of feature modulates heights of posts in PDMS stamps, which is a crucial feature that determines protein coat distribution in a micropatterned hydrogel

system. Aspect ratios between the height of the post and the pitch between posts is crucial to assess whether protein coating will be isolated to wells over an overall coating of the entire gel.

First to be assessed was the role of speed during photoresist spinning. It was observed that despite prior reasoning, depth of photoresist layer was not significantly altered by changes in speed, suggesting that the current range is fast enough to provide maximal resist spread on the wafer. Second to be assessed was the role of photoresist type. It was observed that modulations in photoresist type was resulting in noticeable changes in the depth of the well, with SPR220-4.5 resulting in deeper features. Later assessment showed that this difference was not significant, suggesting that depth in well was plausibly responding to the resist spreading process.

Manufactured silicon wafers were tested for the making of PDMS stamps towards the coating of hydrogel systems. Both 300 and 600 μm stamps had overall difficulties in isolating protein coats on wells, with only a fraction resulting in successful isolation of protein coats for single cell tracking studies (Figure 1). Based on these observations, it is recommended for the optimization of the aspect ratio in the PDMS posts by creating micropatterns with deeper (165 μm) wells through the use of a different photoresist, SPR220-7.0.

Acknowledgments:

We would like to acknowledge Beth Rhoades, CNF Senior Biology Associate, for aid in designing AutoCAD files and the making of chrome masks.

References:

- [1] Gilbert, P.M., et al., *Science*, 329:1078-81 (2010).

Manufacture of SU-8 Microfluidic Channel Molds for the Study of Biofilms in Bioelectrochemical Systems

CNF Project Number: 2403-15

Principal Investigator: Prof. Largus T. Angenent

User: Mr. Juan J.L. Guzman

Affiliation: Department of Biological and Environmental Engineering, Cornell University

Primary Source of Research Funding: National Science Foundation Graduate Research Fellowship, #DGE-1144153

Contact: LA249@cornell.edu, JJG276@cornell.edu

Website: <http://angenent.bee.cornell.edu/>

Abstract:

Bioelectrochemical systems have shown potential to address energy and waste treatment needs through both academic and industrial explorations. While much of this work is performed in large-scale reactors, studies in small microfluidic reactors have been very successful. The work performed in the CNF by the Angenent Lab has focused on manufacturing a new mold for microfluidic channels, manufactured with SU-8. This mold is currently being used to produce microfluidic channels for bioelectrochemical systems studying electrical current production and biofilm development over time.

Summary of Research:

Bioelectrochemical systems have shown potential to address some of our energy and waste treatment needs through both academic and industrial explorations. These systems feature electrically-active microbes donating electrons to electrodes through biofilm attachment or redox mediators. While most of the work in this field is performed in large-scale reactors, some studies have utilized microfluidic reactors, and have focused on biosensing and microbiological applications.

Previously, the Angenent Lab manufactured microfluidic electrodes and channel molds at the CNF as a biosensor to measure the electrical current response of electrically-active *Geobacter sulfurreducens* to toxic chemicals [1]. For that study, various electrode and channel dimensions were tested, and the optimal part dimensions were used for publication. While useful for that study, the masks were not ideal for future experiments requiring multiple identical parts with the optimal dimensions. This year, several experiments were planned to use the optimal parts, but only being able to use a fraction of the parts increased preparation time significantly.

Work performed in the CNF in the previous year focused on manufacturing a new arrayed mold for the microfluidic channels. Manufacturing involved printing a new mask in the Heidelberg Mask Writer DWL2000, applying SU-8 resist to the silicon wafer, and exposing the wafer and mask in the ABM Contact Aligner. Currently, the new channels have been successfully used with *Geobacter*, and results are being analyzed for publication. Future steps may involve changing dimensions further to optimize performance and manufacturing new microfluidic electrodes for different applications.

References:

- [1] Li Z., Venkataraman A., Rosenbaum M. A. and Angenent L. T. (2012). A laminar-flow microfluidic device for quantitative analysis of microbial electrochemical activity. *ChemSusChem*, Vol. 5, No. 6, pp. 1119-1123.

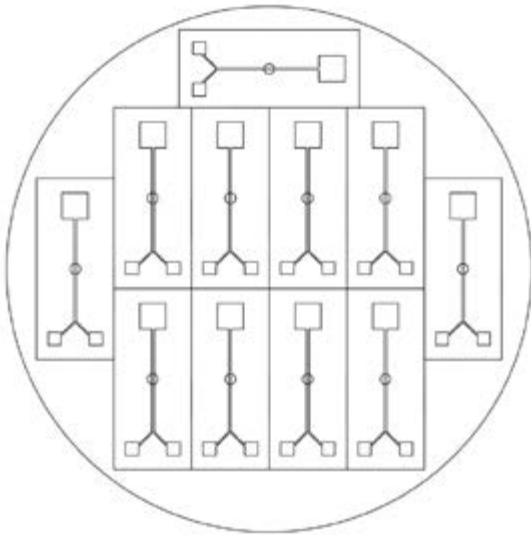


Figure 1: Computer aided design of microfluidic channel array to be printed on the mask.

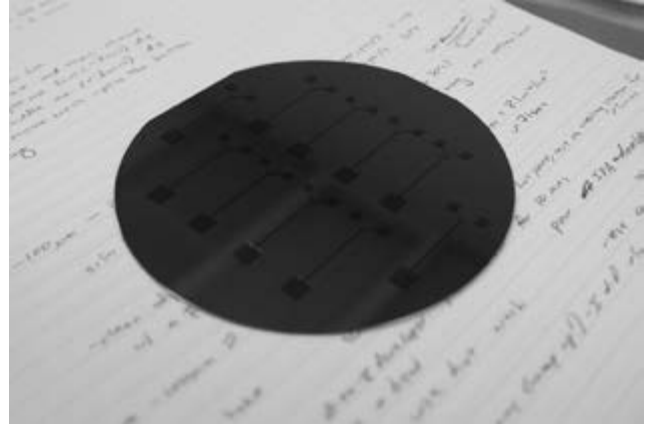


Figure 2: Microfluidic channel mold array made of SU-8 deposited on a silicon wafer.

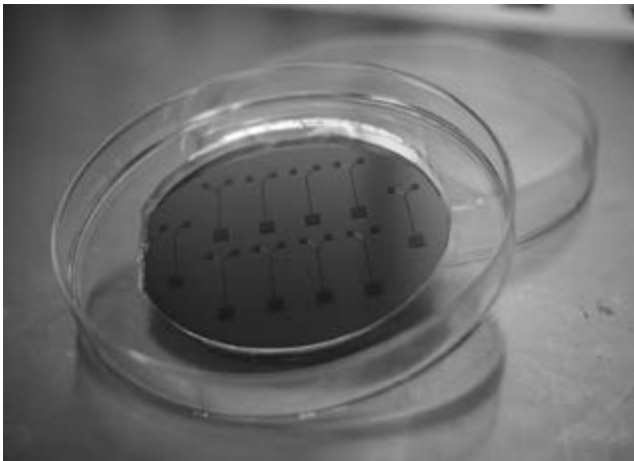


Figure 3: Microfluidic channel mold array encased in polymer after producing a batch of microfluidic channels.

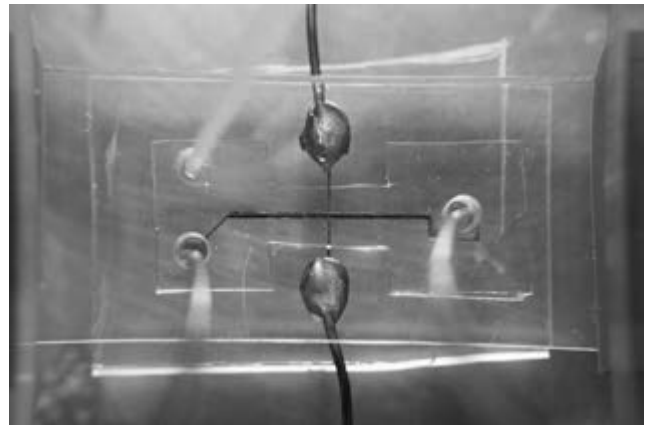


Figure 4: Hydraulic test for laminar flow using dye in the microfluidic channel.

New Approaches to Elucidate the Structure of the Tomato Fruit Cuticle

CNF Project Number: 2404-15

Principal Investigator: Jocelyn K.C. Rose

User: Francisco Romero Gascon

Affiliation: Institute of Biotechnology, Cornell University

Primary Source of Research Funding: NSF Plant Genome Research Program

Contact: jr286@cornell.edu, fr257@cornell.edu

Website: <http://labs.plantbio.cornell.edu/rose/>

Abstract:

The plant cuticle is structurally complex hydrophobic layer that covers the surface of aerial organs. It plays a critical role in the interaction between a plant and its environment and represents the primary barrier against dehydration and potentially pathogenic microbes [1]. In our lab, we are studying the structure and functions of cuticles using tomato fruit as a model system, as they have particularly thick cuticles, and so are amenable to microscopic analysis, as well as other imaging techniques.

Through our collaboration with the Cornell NanoScale Science and Technology Facility (CNF), we have been using the Zygo-profilometer to perform comparative surveys of fruit form different tomato genotypes, focusing on determining how variations in cuticle composition affect cuticle architecture and fruit traits. To our knowledge, this is the first time that this CNF facility has been used to study fruit, and as such we have developed custom methodologies to characterize our samples.

This high-resolution technique has revealed significant differences in the topography of the surfaces of fruit from a wild-type cultivar and from a tomato mutant that is impaired in the synthesis of cutin, a polyester that forms the bulk of the fruit cuticle.

Results to date suggest that cutin deficiency has an effect on the cuticle surface topography and have encouraged us to follow up these analyses by using the CNF atomic force microscope (AFM) instrument to detect differences in the biomechanical properties of these fruit genotypes. Our goal is to establish whether there is a correlation between biophysical and biomechanical attributes of the cuticles, and associated biochemical and physiological characteristics.

Summary of Research:

Plant cuticles are comprised of two main components: cutin, a polyester of mainly C16 and C18 hydroxy fatty acids or diacids, and a structurally diverse collection of aliphatic and aromatic compounds that are collectively termed waxes. We have studied the surface topography and structure of the cuticles of wild-type tomato fruit (a cultivar called M82), and a cutin-deficient mutant, named *CD1* [2]. The *CD1* mutant provides an excellent experimental system to study the role of cutin in the structure and architecture of the cuticle. In addition, to further establish whether cuticle topography changes during fruit development and ripening, we have included in our assay fruit harvested at the mature green (MG) and red ripe (RR) developmental stages.

The fruit of both genotypes have a similar appearance and size, and cells of freshly harvested fruits appear equally turgid. However, analyses of the surface profiles of MG fruit from these genotypes revealed that the cell surface of *CD1* were more far more concave than those of M82 (Figure 1). The 3D surface map model shows how the epidermal cells in *CD1*, which are delimited by the rigid cell wall, form a cavity, which may suggest disorganized cuticle architecture in the mutant. In contrast, cells of the M82 were turgid, as indicated by the red and yellow areas in Figure 1A. Similarly, a comparison of RR stage fruits revealed that the cell surface of *CD1* fruit was concave, while that of that M82 was convex. (Figure 2B and 2A, respectively).

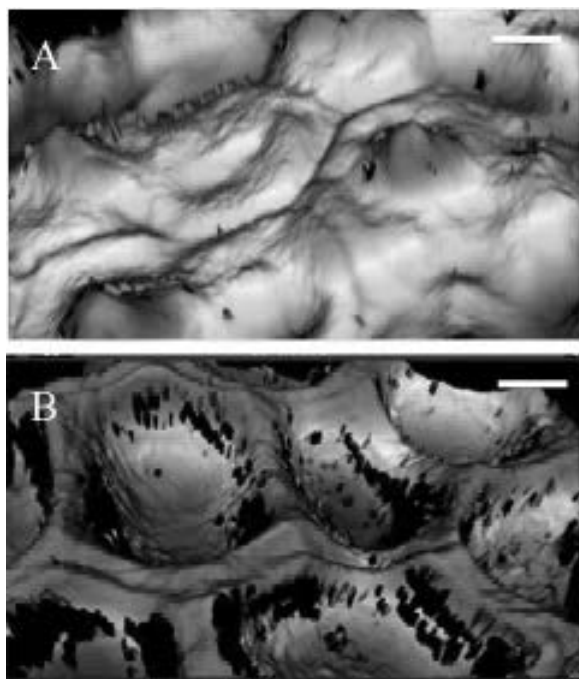


Figure 1: Surface map of M82 (A) and CD1 (B) mature green fruits. 3D model obtained with the 100× Zygo-profilometer objective. Bars scale indicates 0.01 mm.

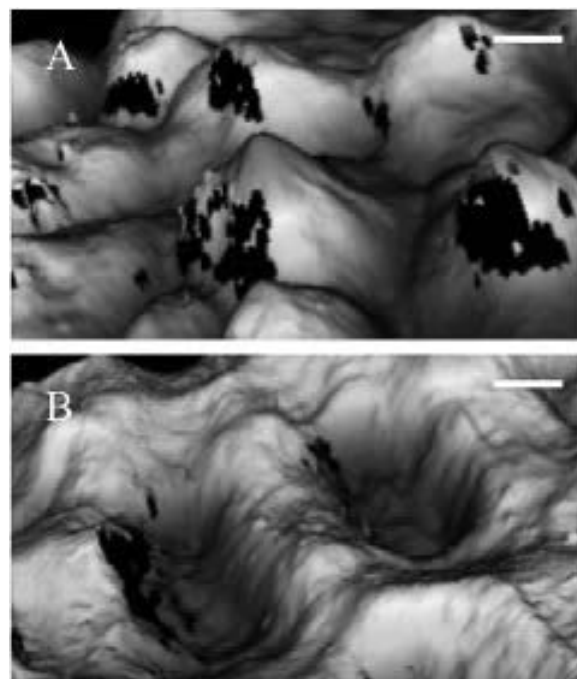


Figure 2: Surface map of M82 (A) and CD1 (B) red ripe fruits. 3D model obtained with the 100× Zygo-profilometer objective. Bars scale indicates 0.01 mm.

These results suggest no effect of the developmental stage on the cuticle topography, but significant differences between genotypes.

These differences can be correlated with specific aspects of cuticle biochemistry composition and architecture. The images shown here are representative of the data collected. In conclusion, the high-resolution images provided by the Zygo-profilometer have helped establish correlations between cuticle composition and architecture. To better understand whether biophysical and biomechanical attributes of the fruit cuticles correlate with associated biochemical and

physiological data, we will follow up these analyses using AFM.

References:

- [1] Fich, E.A., Segerson, N.A., and Rose, J.K.C. (2016). The Plant Polyester Cutin: Biosynthesis, Structure, and Biological Roles. *Annual Review of Plant Biology*, 67: 207-233.
- [2] Yeats, T.H., Huang, W., Chatterjee, S., Viart, H. M.-F., Clausen, M.H., Stark, R.E. and Rose, J.K.C. (2014). Tomato cutin deficient 1 (*CD1*) and putative orthologs comprise an ancient family of cutin synthase-like (CUS) proteins that are conserved among land plants. *The Plant Journal* 75 (5): 667-675.

Handheld Chem/Biosensor Combining Metasurfaces and Engineered Sensor Proteins to Enhance Surface Plasmon Resonance

CNF Project Number: 2430-16

Principal Investigator and User: Lori Lepak

Affiliation: Phoebus Optoelectronics, LLC

Primary Source of Research Funding: Department of Defense

Contact: llepak@phoebus-opto.com

Website: www.phoebusopto.com

Abstract:

Phoebus Optoelectronics, LLC, is a small firm focusing on custom design and advanced materials and optical device development, in the technology fields of metamaterials, photonic crystals and plasmonic crystals. Our portfolio of R&D projects covers the spectral ranges of visible light, infrared, terahertz, and microwave radiation for applications that include high resolution infrared imaging systems, wavelength and polarization filtering, tunable optical components, beam forming and steering, solar cells and renewable energy devices, and chemical and biological toxin sensors. Phoebus scientists and engineers make extensive use of the resources at the CNF for our nano/micro fabrication and testing. In the present report, we discuss recent efforts to develop a handheld surface plasmon resonance (SPR)-based biosensor.

Summary of Research:

Extraordinary optical transmission (EOT) is a phenomenon in which light is transmitted through apertures much smaller than the incident wavelength, at anomalously large intensities relative to the predictions of conventional aperture theory. EOT was first observed by T.W. Ebbesen in 1998 [1], setting off a flurry of research into metamaterials and anomalous transmission, into which Phoebus Optoelectronics was an early entrant.

For over 10 years, Phoebus has successfully incorporated metasurfaces into devices used to perform light filtering [2,3], photon sorting [4-5], polarimetric detection [6], high speed optical detection [7], and other light controlling tasks. Most recently, we have begun development of a handheld SPR-based biosensor [8], using the resources of the CNF to fabricate the optical sensor component of the device.

The underlying physics of SPR is illustrated in Figure 1. In reflection mode, a laser passes through a prism, and is incident on a gold film at angle θ , producing an evanescent wave (surface plasmon) on the opposite side of the gold film, which is in contact with the analyte solution. The angle at which SPR resonance is achieved exhibits a

significant reduction in reflectance. This resonant angle is strongly dependent on the local refractive index, within a few tens of nanometers of the gold surface, and thus is sensitive to enzyme-substrate or antibody-antigen binding events near the surface. The resonance is independent of the geometric configuration of the optical elements, such that these results also apply to devices designed to operate in transmission mode (see [8] for mathematical derivation.)

Our overall sensor device is housed within a handheld 3D printed module, shown in Figure 2. All of the optical elements are in-line for a transmission based device, and all are commercially available except for the disposable SPR biosensor chip. This disposable sensor chip consists of an engineered sensor protein, bound to a patterned gold metasurface using standard thiol-based attachment chemistry. When the designed sensor protein binds its target, the complex undergoes a large change in conformation, as illustrated schematically in Figure 3. This conformation change increases the density of the protein layer, thereby increasing the effective refractive index at the metasurface, and in turn causing a measurable change in light transmission through the metasurface.

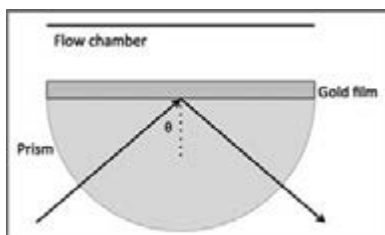


Figure 1: Surface plasmon resonance spectroscopy schematic. Reproduced from reference [8].

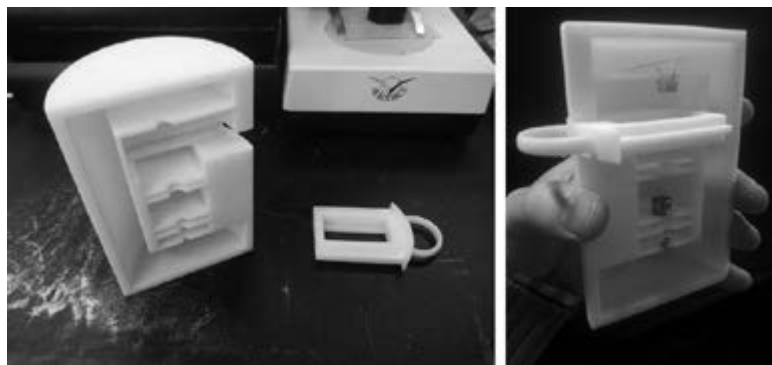


Figure 2: Completed housing for handheld SPR biosensor, including slide-in tray that holds disposable sensor chip. Left: Immediately after 3D printing. Right: Optical components (from bottom to top: laser diode, collimating lens, polarizer, and photodetector) inserted into the actual-sized housing. Reproduced from reference [8].

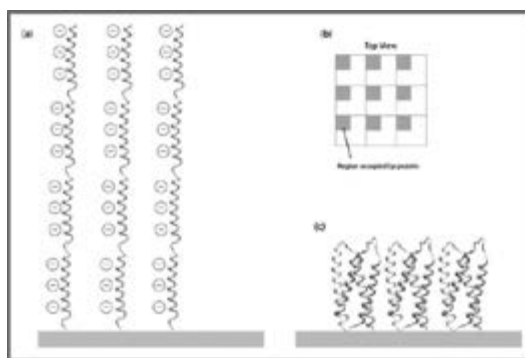


Figure 3: (a) Engineered sensor protein in extended (unbound) conformation, attached to gold metasurface. (b) Top view of sensor protein array. Shaded areas indicate surface area occupied by a single sensor protein. (c) Sensor protein in folded conformation upon binding to an analyte (not pictured). Reproduced from reference [8].

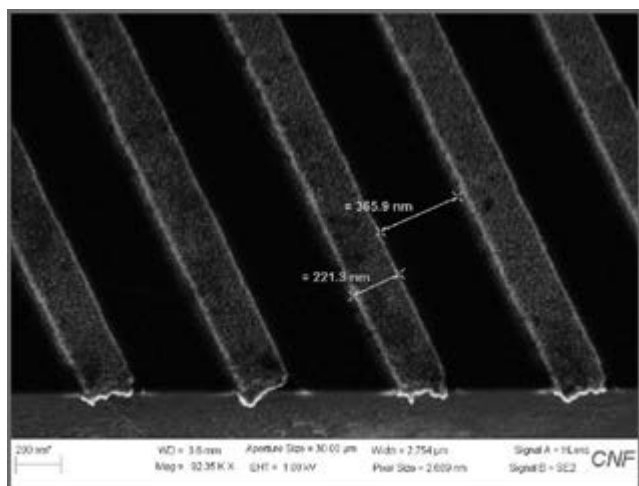


Figure 4: Cross section of a metasurface wire grid used in disposable biosensor chip. All fabrication steps for this chip (photomask design and fabrication, ASML DUV lithography, metal evaporation, and SEM imaging) were performed at the Cornell NanoScale Facility. Reproduced from reference [8].

The metasurface, shown in cross section in Figure 4, is a simple array of gold wires, which also serve as the substrate for the sensor protein. The lines were lithographically patterned using the ASML DUV stepper. We then used the molecular vapor deposition (MVD) tool to deposit a monolayer of (3-mercaptopropyl)-trimethoxysilane (MPTMS), to act as a thiol-based adhesion layer for the gold, eliminating the need for a metal adhesion layer that could negatively affect the optical properties of the device. Finally, we evaporated gold in the SC4500 evaporator, followed by liftoff, and imaging in the Zeiss SEM. As Figure 4 shows, this process is capable of consistently producing lines down to ~ 200 nm wide, with smooth enough sidewalls for an operable optical device.

References:

- [1] Ebbesen, T.W., et al., "Extraordinary optical transmission through sub-wavelength hole arrays." *Nature*, (1998). 391(6668): p. 667-669.
- [2] Crouse, D. "Numerical modeling and electromagnetic resonant modes in complex grating structures and optoelectronic device applications." *Electron Devices, IEEE Transactions on* 52.11 (2005): 2365-2373.
- [3] Crouse, D., and Keshavareddy, P. "Polarization independent enhanced optical transmission in one-dimensional gratings and device applications." *Optics Express* 15.4 (2007): 1415-1427.
- [4] Lansey, E., Crouse, D., et al. "Light localization, photon sorting, and enhanced absorption in subwavelength cavity arrays." *Optics Express* 20.22 (2012): 24226-24236.
- [5] Jung, Y.U.; Bendoy, I.; Golovin, A.B.; and Crouse, D.T. "Dual-band photon sorting plasmonic MIM metamaterial sensor." *Proc. SPIE 9070, Infrared Technology and Applications XL, 90702X* (June 24, 2014); doi:10.1117/12.2050620.
- [6] Crouse, D., and Keshavareddy, P. "A method for designing electromagnetic resonance enhanced silicon-on-insulator metal-semiconductor-metal photodetectors." *Journal of Optics A: Pure and Applied Optics* 8.2 (2006): 175.
- [7] Mandel, I.; Gollub, J.; Bendoy, I.; Crouse, D. Theory and Design of A Novel Integrated Polarimetric Sensor Utilizing a Light Sorting Metamaterial Grating. *Sensors Journal, IEEE*, (2012): Vol. PP, 99
- [8] Lepak, L., et al. "Handheld chem/biosensor using extreme conformational changes in designed binding proteins to enhance surface plasmon resonance (SPR)" *Proc. SPIE 9862, Advanced Environmental, Chemical, and Biological Sensing Technologies XIII, 9862-7* (April 17, 2016); doi:10.1117/12.2222305.

Creating an On-Chip and High Throughput Alternative to Optical Tweezers

2016 CNF REU Intern: Wagma Caravan, Chemistry, Adelphi University

CNF REU Principal Investigator: Dr. Michelle Wang, Physics, Cornell University

CNF REU Mentor: Ryan Badman, Physics, Cornell University

Primary Source of Research Funding: National Science Foundation under Grant No. ECCS-1542081

Contact: wamacaravan@mail.adelphi.edu, mdw17@cornell.edu, rpb226@cornell.edu

Abstract:

Optical trapping is one of the most common and useful measurement techniques in single molecule biological research. Current optical trapping devices typically use free space optical tweezer laser traps, which only provide low throughput, single measurements that can often take hours or days. An alternative to free space lasers is trapping in the evanescent field sharply decaying away from nanophotonic waveguide surfaces. The Nanophotonic Standing Wave Array Trap (nSWAT) created by the Wang lab is one such on-chip evanescent trap device that can provide much higher throughput measurements than free space traps, with potentially comparable trapping force. In order for the trapping force per trap in the nSWAT to match the specifications of traditional optical tweezers, higher index of refraction materials with negligible non-linear absorption effects are needed for the waveguide and the nanoparticles. Previous work utilized silicon waveguides and polystyrene beads for the nSWAT [1], but silicon had problematic non-linear absorption that limited trapping force, and polystyrene has a low refractive index. In this report we have explored both the fabrication and measurements of high refractive index waveguides and nanoparticles for higher force nSWAT trapping.

Summary of Research:

Optical tweezers are a tool commonly used to obtain “force spectroscopy” measurements through DNA stretching. Measuring DNA lengths at different forces can reveal the identities and dynamics of DNA binding proteins. The Nanophotonic Standing Wave Array Trap (nSWAT) created by the Wang lab [1], is a high throughput device that holds hundreds of optical trap centers allowing hundreds of DNA force

measurements to be performed simultaneously, see Figure 1. The nSWAT can potentially provide DNA stretching with the full force range of traditional optical tweezers. To achieve higher trapping forces, a number of parameters must be optimized, such as an increase in laser power (requiring higher power tolerance waveguide materials), an increase in the refractive index of the waveguide, and an increase in the refractive index of the trapped nanoparticle.

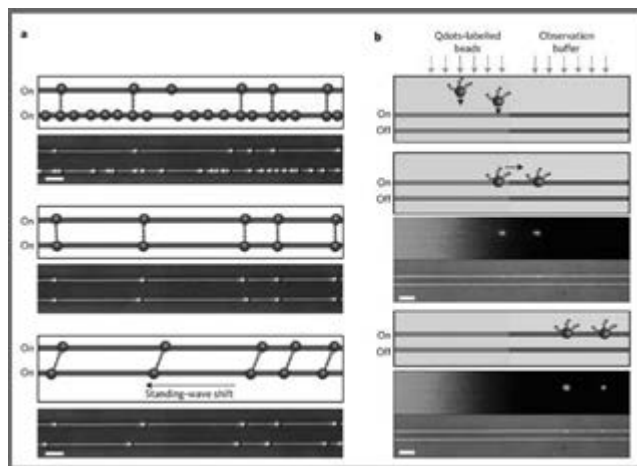


Figure 1: DNA dumbbells, formed with deoxyribonucleic acid (DNA) tethered between two polystyrene (PS) beads, being trapping and manipulated along two parallel waveguides in a nSWAT device. See Ref. [1] for more information. Reproduced with permission from Ref. [1].

Waveguides. To increase the trapping force of the nSWAT, one goal was to create low loss high index of refraction waveguides. Previously, silicon waveguides were used in the nSWAT [1], however to further increase the trapping force, tantalum pentoxide (Ta_2O_5) waveguides were fabricated this summer due to its high index of refraction (2.15 at 1064 nm), and its ability to couple 3 W or higher of 1064 nm laser power [2], relative to silicon which can only tolerate a few hundred mW of power [1].

The tantalum pentoxide films were optimized by radio frequency (RF) sputtering an oxide target in the AJA sputter deposition tool. To determine the loss of the Ta_2O_5 thin film, the Metricon prism coupler was employed. The waveguides were then etched with the Oxford 100 plasma etcher (see Figure 2) and the loss after fabrication was measured using infrared measurements.

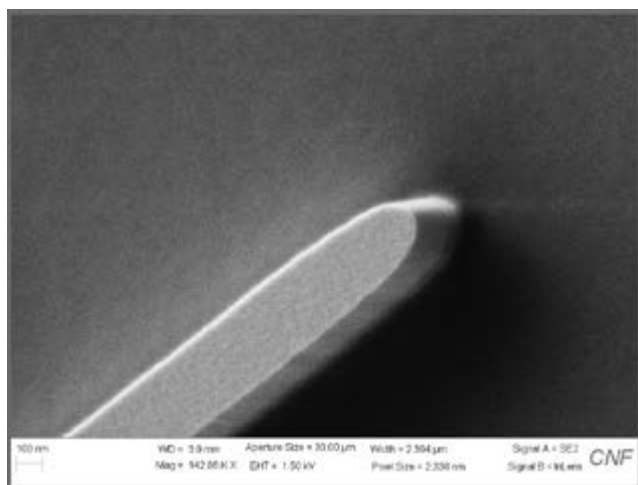


Figure 2: Scanning electron microscope (SEM) image of the tapered ends of an ultra low loss tantalum pentoxide waveguide.

The Metricon prism coupler measured an ultra-low film loss of $\ll 1$ dB/cm. Through infrared measurements the final waveguide propagation loss was found to be 0.46 ± 0.19 dB/cm, with the added loss contributions coming from the presence of bends in the waveguide pattern (higher loss than straight waveguides) and the small roughness induced from waveguide etching. We thus achieved our goal of creating a waveguide below 1 dB/cm loss at 1064 nm.

Nanoparticles. The nanoparticles tethered to DNA also need high index of refraction for an increase in trapping force. Traditionally, polystyrene beads ($n=1.55-1.59$ at 1064 nm) [1] are used for optical trapping, however the trapping force can be approximately three times higher with silicon nitride nanoparticles ($n=2.0$) or five times higher with titania nanoparticles (approximately $n=2.3$). Four types of shapes for the nanoparticles can be used on the nSWAT: spheres, disks, and long and short cylinders. All four shapes were made and tested this summer to determine which will provide the

highest force, see Figures 3 and 4 for examples of the novel non-spherical shapes.

Titania nanospheres were created through the reproduction of a previous 2004 paper [3]. The beads were then placed in phosphate buffered saline (PBS) to increase the size and stability of the nanospheres. The titania nanospheres were tethered to DNA for stretching which demonstrated that titania, although photocatalytic, does not damage DNA during typical experimental time periods. The stability and size of the beads were determined using the Zetasizer in the Nanotechnology Center (NBTC). The titania nanodisks and silicon nitride nanocylinders were fabricated through a new method and will be tested on waveguides, details will be disclosed in a future publication.

Acknowledgments:

I would like to thank members of the Wang lab for their support over the summer and Dr. Michelle Wang for hosting the project. I would also like to express gratitude to the Cornell NanoScale Science and Technology Facility (CNF) and NBTC staff and site coordinators for critical feedback on the project during presentations and support during facility use. This research was supported by the National Science Foundation under Grant No. ECCS-1542081.

References:

- [1] M. Soltani, J. Lin, R. Forties, J. Inman, S. Saraf, R. Fulbright, M. Lipson and M.D. Wang "Nanophotonic trapping for precise manipulation of biomolecular arrays," *Nature Nanotechnology* 9, 448-452 (2014).
- [2] B. S. Ahluwalia, O. G. Helleso, A. Z. Subramanian, N. M. B. Perney, N. P. Sessions, J. S. Wilkinson "Fabrication and optimization of Tantalum pentoxide waveguides for optical micro-propulsion," *Proc. SPIE 7604, Integrated Optics: Devices, Materials, and Tech. XIV, 76040W* (2010).
- [3] Eiden-Assmann, S., J. Widoniak, and G. Maret. "Synthesis and characterization of porous and nonporous monodisperse colloidal TiO_2 particles." *Chemistry of Materials* 16.1 (2004): 6-11.

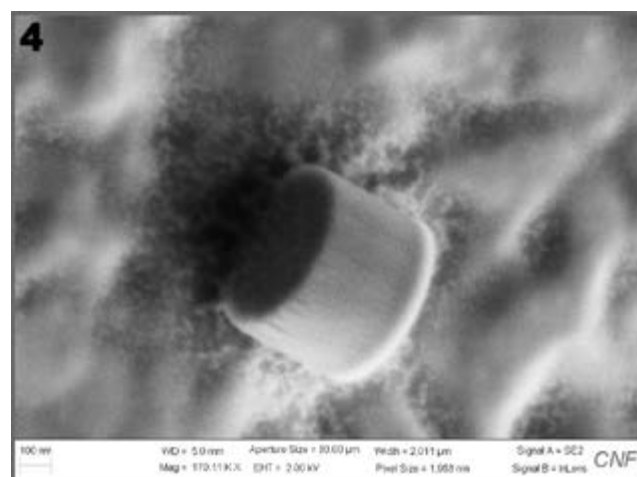
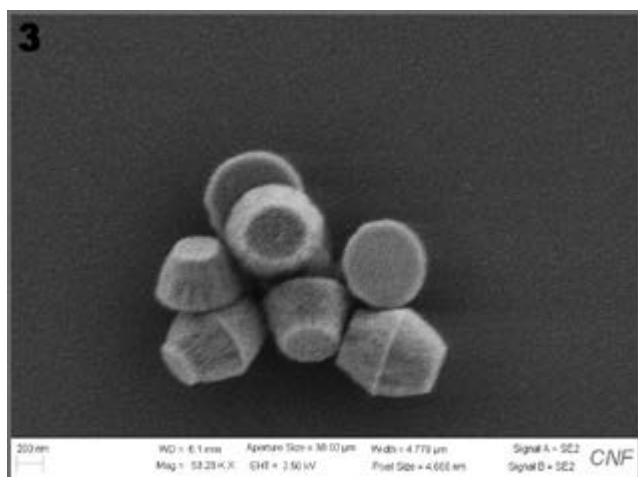


Figure 3, left: SEM of highly uniform TiO_2 trapezoidal disk nanoparticles fabricated for high force trapping on a waveguide. Figure 4, right: SEM example of straight-side-wall cylinder Si_3N_4 nanoparticle fabricated for high force trapping.

Modified Co-Planar Waveguides for Investigating Organic Semiconductors using Magnetic Resonance Force Microscopy

CNF Project Number: 863-00

Principal Investigator: John A. Marohn

User: Elizabeth Curley

Affiliation: Department of Chemistry and Chemical Biology, Cornell University

Primary Source of Research Funding: Army Research Office

Contact: jam99@cornell.edu, eac274@cornell.edu

Website: marohn.chem.cornell.edu

Abstract:

We report the modification and characterization of micrometer-scale coplanar waveguides, which simultaneously deliver oscillating radio wave and microwave magnetic fields, to include a metal top contact. These devices will be integrated into a magnetic resonance force microscope in order to investigate the charge separation mechanism of singlet fission in fully functional donor-acceptor organic electronic devices via tracking the spin relaxation of nuclear spins with 10 nm spatial and depth resolution.

Summary of Research:

The mechanism of charge generation in organic electronics is highly controversial. The model that tightly bound excitons in organics cannot split spontaneously and thus must diffuse to a junction for charge separation to occur is used by current researchers [1,2]. Additionally, polyacenes undergo a singlet fission process where a singlet exciton splits into a pair of triplet excitons. Current studies probe the optically dark triplet states using transient absorption spectroscopy or indirectly by observing a few percent changes in the photocurrent when a magnetic field is applied [1]. Femtosecond two-photon photoemission experiments by X.Y. Zhu and coworkers present evidence that triplet excitons decay to the charge transfer state through a multiexciton state faster than from the triplet exciton state. These experiments lack spatial resolution to confirm that charge separation occurs at the junction [2]. The nuclear spin-lattice relaxation time, T_1 , could be used to study the triplet excitons. The paramagnetic, spin 1, triplet states give rise to additional fluctuating magnetic fields altering the T_1 time of neighboring protons.

Magnetic resonance force microscopy (MRFM) offers sensitivity and non-invasive 3-dimensional scanning abilities and achieves 10 nm resolution by mechanically detecting resonance spins as a force or

force gradient on an attonewton sensitivity magnet on tip microcantilever [3]. Furthermore, MRFM's inherent depth resolution enables the detection of spins beneath a top contact. MRFM presents a unique opportunity to spatially map the nuclear T_1 on a fully functional device and provide corroboration into the charge separation mechanism from singlet fission in donor-acceptor devices.

Low frequency radio frequency fields (50 to 400 MHz) are required to detect nuclear spins. To achieve this, we have developed a tapered coplanar waveguide (CPW). The CPWs, fabricated at the Cornell NanoScale Science and Technology Facility (CNF), have been used to observe electron spin resonance (ESR, at 0.6 tesla), nuclear magnetic resonance (NMR, at 4 to 6 tesla fields), and the first microwave-enhanced NMR in an MRFM experiment via dynamic nuclear polarization (DNP, at 0.6 tesla) [4]. These experiments mechanically detect magnetic resonance signal from a nitroxide-doped polystyrene film, at 4.2 kelvin, and in the presence of a large magnetic field gradient from a micrometer-scale magnet tipped-cantilever. Current work is towards giving dual functionality to our existing CPW through the addition of a metal top contact that would allow a bias to be applied to the sample, thus allowing fully functioning organic electronic sandwich devices to be studied using MRFM.

Initial modified CPW were prepared by using the current tapered 50- Ω impedance CPW (5 nm Ti/200 nm Cu/30 nm Au) as a bottom contact, then 200 nm polystyrene was spun cast on top, followed by electron beam evaporation (SC4500 Odd-Hour Evaporator) of 5 nm Ti/30 nm Au (Figure 1) using a shadow mask fabricated at CNF to produce top contacts ranging from 75 $\mu\text{m} \times 2 \text{ mm}$ to 300 $\mu\text{m} \times 2 \text{ mm}$ in size, over the center region of the CPW, shown in Figure 1. The CPW are electrically connected with Al wire bonds to a commercially available PCB board equipped with SMA connectors for use with commercial signal generators for characterization. Figure 2 shows that the CPW still functions properly in the 20-1000 MHz without large changes in losses.

We are currently working on fabricating and characterizing organic solar cell devices deposited directly on the CPW. The solar cell layers, 45 nm pentacene/60 nm C_{60} Fullerene/10 nm BCP are thermally evaporated over the CPW. In solar cell sandwich devices there is an additional requirement that light needs to get to the organic layers of the device, thus cannot be entirely blocked by the top contact. Very thin thermally evaporated Al films were characterized using UV-Vis spectroscopy at pentacene max absorbance, 670 nm to find an optimal optically transparent thickness, shown in Figure 3.

Once our solar cell device performance is characterized and a protocol is developed for applying a voltage bias, future work will be to spatially map the nuclear T1 on these organic devices in order to provide corroboration of the current charge separation mechanism from singlet fission in donor-acceptor devices.

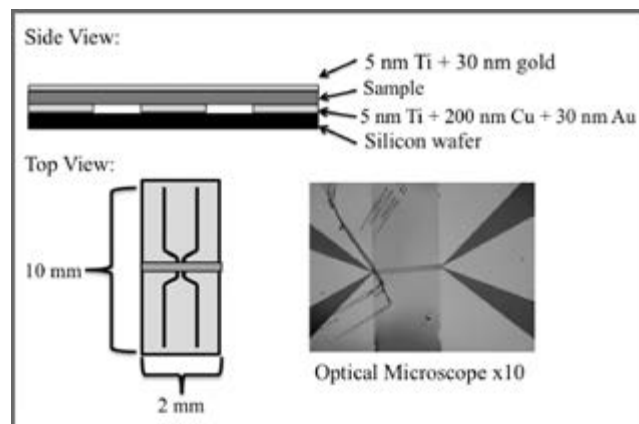


Figure 1: Top: Cartoon of side view of layers of coplanar waveguide with spun-cast sample and deposited metal contact. Bottom Left: Cartoon of top view of CPW with top contact in the center region. Bottom Right: Top view optical image of coplanar waveguide with spun-cast polystyrene and e-beam evaporated metal.

References:

- [1] Baldo, et al., Science, 2013, 340, 334.
- [2] Zhu, et al., Science, 2011, 334, 1541.
- [3] Longenecker, et al., ACS Nano, 2012, 6, 9637.
- [4] Isaac, Curley, Marohn, et al. Phys. Chem. Chem. Phys., 2016, 18, 8806.

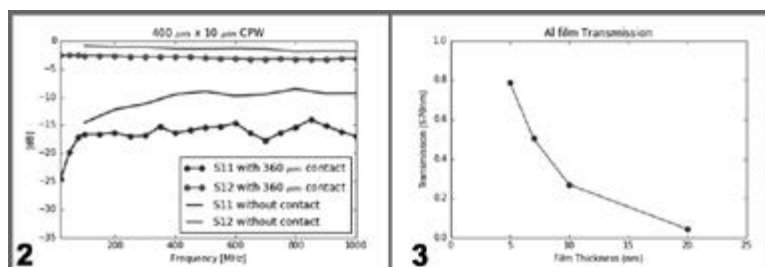


Figure 2, left: Comparing S11 and S12 parameters of a 400 $\mu\text{m} \times 10 \mu\text{m}$ center line CPW without and with 200 nm spun-cast polystyrene and e-beam evaporated 30 nm gold top contact from 100-1000 MHz.

Figure 3, right: Transmission at pentacene max absorbance (670 nm) of thermally evaporated thin Al films, 5-20 nm, taken with UV-Vis spectrometer. At 10 nm thickness, about 50% of light passes through film.

Chemical Bonding Across the Periodic Table at High and Ambient Pressures

CNF Project Number: 1371-05

Principal Investigator: Roald Hoffmann

Users: Martin Rahm, Peng Xu, Andreas Hermann

Affiliation: Department of Chemistry and Chemical Biology, Cornell University

Primary Source of Research Funding: National Science Foundation, Grant CHE-1305872

Contact: rh34@cornell.edu, martin.rahm@cornell.edu, px32@cornell.edu, a.hermann@ed.ac.uk

Website: <http://hoffmann.chem.cornell.edu/roald/>

Abstract:

We address problems of bonding, structure, and emergent properties such as superconductivity in a wide range of materials — from discrete molecules through polymers to extended solids. The behavior of matter under high pressure is of special interest, as it forms a fruitful collaboration with the group of Neil Ashcroft in Physics. The specific projects addressed in 2015-2016 include likely structures for a gold oxide, AuO; possible ternary gold hydrides, and the potential involvement of Li 1s orbitals in chemical bonding under extreme high pressure.

Summary of Research:

Computational Project. In the first of our projects for which we used CNF computational facilities we looked at AuO. When Tutankhamen's tomb was opened, the gold objects in it gleamed as on the day the tomb was sealed. Of course, the reason for this is in the electrochemical series — almost anything in the world will reduce gold ions to metallic gold. Oxides of gold thus do not appear likely candidates for stability; nevertheless Au₂O₃, with a positive heat of formation, exists, and has been studied theoretically together with Au₂O [1]. In a very nice piece of work that Andreas Hermann did, together with our Polish collaborators, we examined the potential of a 1:1 phase, AuO, at P = 1 atm, and at elevated pressure [1].

At P = 1 atm, hypothetical AuO (metastable with respect to the elements) is predicted to crystallize in a new structure type, unique amongst the late transition metal monoxides, with disproportionation of the gold ions to Au(I/III), and featuring weak Au...Au, so-called aurophilic interactions. Under pressure, familiar structure types are stabilized: to a semiconducting AgO-type structure at ~ 2.5 GPa and, with further increase of pressure up to ~ 80 GPa, to an AuSO₄-type structure containing Au₂ pairs. Finally, above 105 GPa distorted NaCl-type and CsCl-type Au(II)O structures dominate, and metallization is predicted at 329 GPa.

Lithium Project. In all of its compounds at ambient conditions on earth, the element lithium readily gives up its weakly held 2s electron, and becomes Li⁺. But could one break into the 1s shell of Li, and with proper inducements (which include extreme high pressure) make the 1s electrons of Li “chemically active”? This is the task Peng Xu, a postdoc in our group, took on.

Using a particle-swarm optimization (PSO) based structural search algorithm, as implemented in CALYPSO [2], Peng searched for the global minimum on the free-energy surface of LiF₃ over a range of elevated pressures, up to 5000 GPa. The geometry optimization and energy evaluation during structural search are performed using the plane-wave DFT code, VASP. The method has difficulties in dealing with such high pressures, high densities; at times one is led to unphysical states where atoms/ions fuse together. CNF resources are instrumental to us because we are able to start multiple runs for the same pressure, one on each node, observe the progress of each run and terminate early the ones with unphysical outcomes. In Figure 2 we show two of the lowest enthalpy structures we have found.

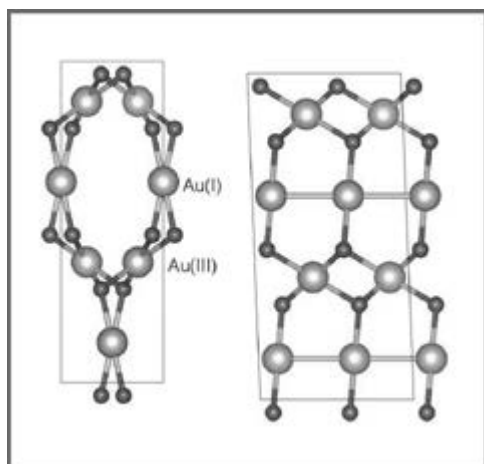


Figure 1: Two views of the most stable predicted AuO structure at $P=1$ atm.

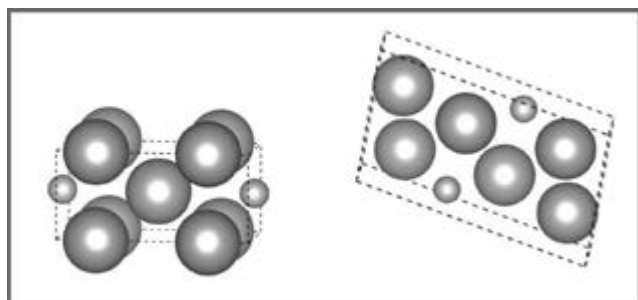


Figure 2: Two LiF_3 structures at 5000 GPa.

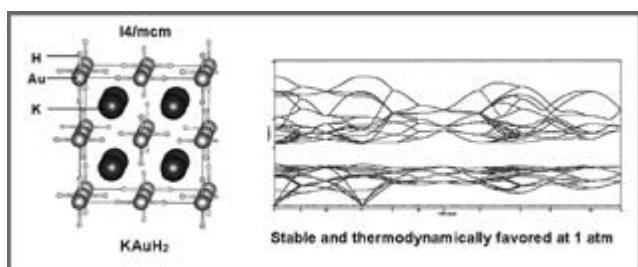


Figure 3: Predicted crystal structure of KAuH_2 , which is thermodynamically preferred and vibrationally stable at 1 atm (left). Corresponding phonon spectrum (right).

Back to Gold. Gold is one of few elements that does not have a known hydride in the condensed phase (and our theory concurs). So instead we have focused on the stabilization of gold hydride, via the introduction of a third cationic element. The mix of light hydrogen and heavier gold gives rise to both high and low frequency phonons in the lattice, which is interesting since electron-phonon coupling is a key ingredient in BCS superconductivity, which we are trying to understand. Our structure searches using CNF resources have thus far confirmed the experimentally known ground states of related A_2PdH_2 ($\text{A}=\text{alkali metal}$) ternaries [3] and predicted several ternary phases of $[\text{A}][\text{AuH}_2]$. One of these, which calculates as thermodynamically favorable with respect to the elements and other decomposition products are shown in Figure 3.

In addition to calculating the relative enthalpies of the alkali-metal hydrides, $[\text{A}]_x[\text{H}]_y$, which are well known, we are also evaluating the alkali-metal-gold binaries, $[\text{A}]_x[\text{Au}]_y$, some of which have been synthesized. We are also studying the behavior of these phases over a range of pressures, in an effort to modulate their conductivity, band gap, and relative heat of formation.

References:

- [1] "AuO: Evolving from Dis- to Comproportionation, and Back Again." A. Hermann, M. Derzsi, W. Grochala, R. Hoffmann, *Inorg. Chem.* 55, 1276-1286 (2016).
- [2] "Crystal Structure Prediction via Particle-Swarm Optimization." Wang, Y.; Lv, J.; Zhu, L.; Ma, Y. *Phys. Rev. B* 2010, 82, 94116.
- [3] Kadir, K.; Kritikos, M.; Noreus, D.; Andresen, A. F. J. *Less-Common Met.* 1991, 172-174, 36-41. Bronger, W.; Brassard, L. A. Z. *Anorg. Allg. Chem.* 1996, 622, 462-464.

Mid-Infrared Transparent Substrate for Alkylsiloxane Monolayers

CNF Project Number: 1936-10

Principal Investigator: Poul Petersen

Users: Aliyah Barrett, Stephanie Sanders

Affiliation: Department of Chemistry and Chemical Biology, Cornell University

Primary Source of Research Funding: NSF Faculty Early Career Development (NSF CAREER) Award

Contact: pbp33@cornell.edu, arb292@cornell.edu, ses422@cornell.edu

Website: <http://petersen.chem.cornell.edu/>

Abstract:

An infrared (IR) and visible transparent substrate compatible with alkylsiloxane monolayers was fabricated by coating a calcium fluoride window with SiO₂ by atomic layer deposition (ALD). Several series of mixed octadecyltrichlorosilane (OTS) and dodecyltrichlorosilane (DTS) monolayers were applied to the substrates and characterized by infrared spectroscopy and sum frequency generation (SFG). Monolayers with other chemical functionalities were also successfully adsorbed.

Summary of Research:

Self-assembled monolayers (SAMs) can be used to create highly ordered surfaces having tunable chemical functionalities. Alkylsiloxane monolayers are simple to apply, stable in a wide range of physical and chemical environments, and do not degrade appreciably even over periods of months [1]. These attributes make them ideal platforms for probing the interaction of water with various surfaces. However, the most important substrates compatible with alkylsiloxane monolayers, the silicon oxides, are not transparent through most of the infrared region. Since water also has strong absorption bands in the IR region, spectroscopy of vibrational transitions at the water-alkylsiloxane SAM interface is greatly complicated in both transmission and reflection geometries.

In this project, calcium fluoride (CaF₂, transparent 0.2-10 μm) was coated with a thin film of silicon dioxide (SiO₂) to create an IR and visible transparent substrate capable of functionalization by alkylsiloxane monolayers. Clean, optically polished CaF₂ was coated with 15 nm of SiO₂ with the Oxford ALD FlexAL at CNF. Deposition of SiO₂ on bare CaF₂ results in a substrate with SiO₂ on both sides. The substrates were then annealed at 800°C in a vacuum furnace for one hour to prevent the SiO₂ layer from delaminating. Various alkylsiloxane monolayers were then applied to the substrate by adsorption from solution.

IR spectra of the modified CaF₂ show that the thin SiO₂ layer does not absorb in the IR significantly above 1250 cm⁻¹ (Figure 1). This has made possible characterization by IR spectroscopy throughout this range, as well as SFG at the buried monolayer/water interface. Several types of monolayers have been applied to the substrates to study the effect of varying surface roughness and chemical functionality. These include mixed OTS/DTS (mixed length) as well as monomers terminated with t-butyl, bromo, thiocyno groups. They have been characterized by infrared spectroscopy (Figure 2) and SFG (Figure 3). Water structure at OTS monolayers has also been studied using SFG (Figure 4). The OD, CH, and OH stretch regions are all accessible due to the large transmission range of the substrates.

References:

- [1] Wasserman S.R., Tao Y., Whitesides G.M.; Structure and Reactivity of Alkylsiloxane Monolayers Formed by Reaction of Alkyltrichlorosilanes on Silicon Substrates. *Langmuir* 5, 1074-1087 (1989).

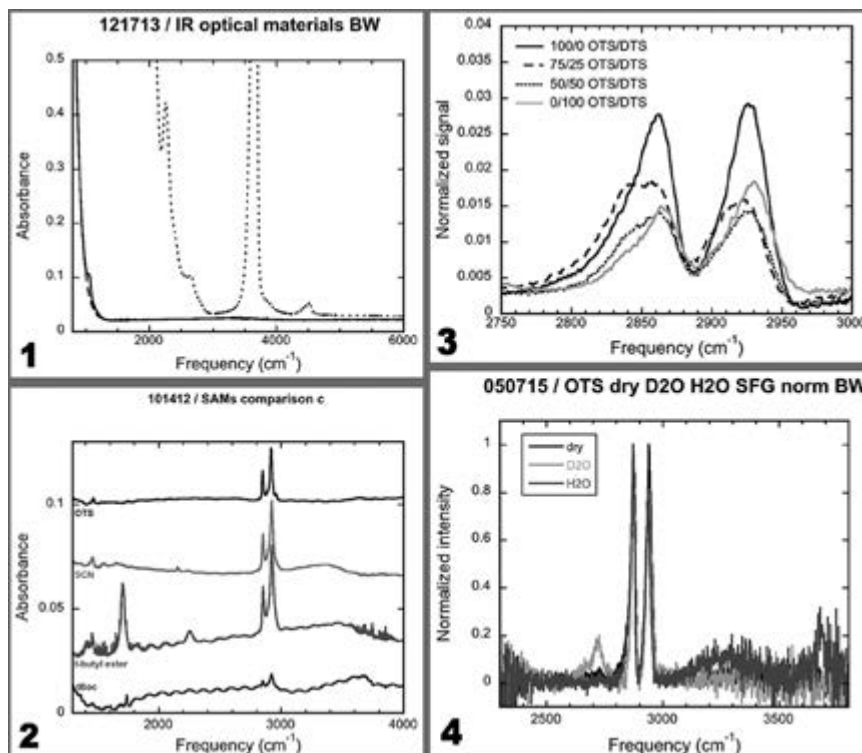


Figure 1: Absorbance of bare CaF₂ (dashed line) and SiO₂-coated CaF₂ (solid line) compared to fused silica (dotted line) in the mid IR region.

Figure 2: Transmission IR spectra of alkylsiloxane monolayers on SiO₂-coated CaF₂ showing different functional groups. The transmission range extends down well into the fingerprint region, exposing the carbonyl stretch (~1600 cm⁻¹) and CH bend (~1450 cm⁻¹).

Figure 3: Sum frequency generation spectra of mixed 18 and 12 carbon (OTS/DTS) alkane monolayers of various ratios of OTS to DTS. The methyl and methylene stretch region is shown.

Figure 4: Sum frequency generation of an OTS monolayer at the air, D₂O, and H₂O interfaces. CH stretching modes (2800-3000 cm⁻¹) are visible for all. At the D₂O interface, the non hydrogen-bonded (free) OD stretch is seen at 2725 cm⁻¹. At the H₂O interface, the hydrogen-bonded OH stretch appears as a broad peak from 3100-3500 cm⁻¹. The free OH stretch is visible at 3700 cm⁻¹.

Micrometer-Scale Coplanar Waveguides for Nanoscale Magnetic Resonance Imaging

CNF Project Number: 2125-12

Principal Investigator: John A. Marohn

Users: Corinne E. Isaac, Paméla Nasr, Elizabeth Curley

Affiliation: Department of Chemistry and Chemical Biology, Cornell University

Primary Source of Research Funding: Army Research Office

Contact: jam99@cornell.edu, cek222@cornell.edu, ptn29@cornell.edu, eac274@cornell.edu

Website: marohn.chem.cornell.edu

Abstract:

We report the design, fabrication, and characterization of micrometer-scale coplanar waveguides to simultaneously deliver oscillating radiowave and microwave magnetic fields. These devices have been integrated into a magnetic resonance force microscope (MRFM) where they have been used to observe electron spin resonance (ESR, at 0.6 tesla), nuclear magnetic resonance (NMR, at 4 to 6 tesla fields), and the first microwave-enhanced NMR in an MRFM experiment via dynamic nuclear polarization (DNP, at 0.6 tesla). These experiments mechanically detect magnetic resonance signal from a nitroxide-doped polystyrene film, at 4.2 kelvin, and in the presence of a large magnetic field gradient from a micrometer-scale magnet tipped-cantilever.

Summary of Research:

The ability to image the proton envelope of a near-native, flash-frozen, single copy of a macromolecule or macromolecular complex would be an enabling advance. Current state of the art techniques for imaging biomolecules and biomolecular complexes are limited by radiation damage, the demanding constraint of having thousands of identical copies of the molecule, or crystallized samples. Studying interesting biomolecules by nanoscale magnetic resonance imaging (nano-MRI) requires near single-spin sensitivity and a depth-of-view of 20 nm or more.

Magnetic resonance force microscopy (MRFM) offers the sensitivity and non-invasive three-dimensional scanning abilities required for nano-MRI by mechanically detecting resonant spins as a force or force-gradient on an attoneutron sensitivity microcantilever. A schematic of the MRFM experiment can be seen in Figure 1. Exciting recent advances include the < 10 nm resolution viral imaging experiment of Degen, et al. [1] and the integrated nanomagnet tipped cantilevers of Longenecker and Marohn [2] that have a demonstrated sensitivity of a few hundred proton magnetic moments. These experiments are the motivation for the work described here.

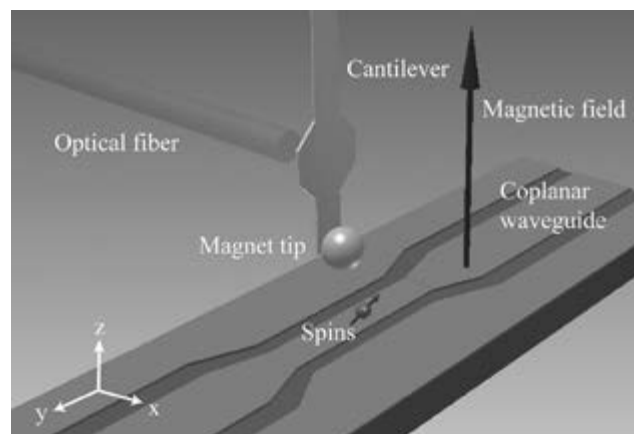


Figure 1: The MRFM experimental setup.

Previous high sensitivity MRFM experiments have used statistical fluctuations in nuclear magnetization as the signal. Detecting these random spin flips requires long signal acquisition and averaging times. To overcome this limitation we have developed a microscope capable of generating an enhanced nuclear polarization by transferring polarization from highly polarized electron spins to the lesser polarized

nuclear spins *via* dynamic nuclear polarization. This polarization transfer requires simultaneously irradiating the sample with high frequency microwave fields (up to 40 GHz) to saturate electron spins and low frequency radio frequency fields (50 to 400 MHz) to detect nuclear spins. To achieve this, we have developed a tapered coplanar waveguide (CPW). The CPWs, fabricated at the Cornell NanoScale Science and Technology Facility, were designed with a characteristic 50- Ω impedance to be electrically connected with gold wire bonds to a commercially available ceramic board equipped with SMA connectors for use with commercial signal generators.



Figure 2: SEM of a fabricated coplanar waveguide. The grid lines above and below the centerline are used to optically locate the center.

Tapered coplanar waveguides were fabricated *via* a photolithography-based protocol. Resists DSK-101-312 and UV-210 were spun-cast using the Gamma Automatic Coat-Develop Tool and exposed using the ASML 300C DUV Stepper. After developing and desmumming, a Ti/Cu/Au (5/200/30 nm) film was deposited *via* electron-beam evaporation followed by lift-off. Figure 2 shows a scanning electron microscopy image of a waveguide tapered to a 100 μm long and 5 μm wide constriction. A similar waveguide tapered to a 500 μm long and 10 μm wide wire was used to detect ESR, NMR, and hyperpolarized NMR signal from DNP [3]. The CPW was operated with just 200 mW of input power to generate an estimated oscillating field strength of 2.5 mT for frequencies below 5 GHz and a few μT for frequencies up to 20 GHz with just a few milliwatts of power dissipated across the device.

NMR signal from a 200 nm thick polystyrene film doped with 40 mM TEMPAMINE spin radicals, spun-cast on top of the CPW at 4 kelvin in an external magnetic field of 6 tesla was detected. A one-MHz wide frequency sweep centered at 256 MHz was applied to the coplanar waveguide to adiabatically invert the proton spins in the sample. The resulting change in spin polarization causes a shift in cantilever resonance

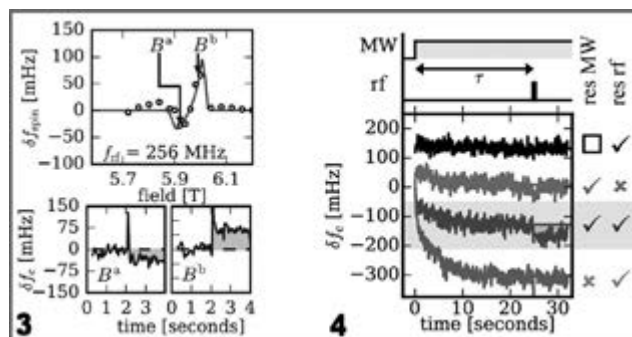


Figure 3, left: Proton NMR-MRFM signal (circles) and simulation (line) obtained using fabricated coplanar waveguides (top). Representative cantilever frequency shifts following an adiabatic inversion of spin magnetization.

Figure 4, right: Microwave-enhanced NMR-MRFM signal at an external field of 0.6 tesla. Magnetic resonance signal is observed as a frequency shift following an adiabatic rapid passage only when both the microwave frequency and radiowave frequency is in resonance — allowing for dynamic nuclear polarization.

frequency as seen in Figure 3. At fields below one tesla, the thermal ^1H spin polarization is too low to be detected following this method as seen in Figure 4. By first saturating the electron spins in the sample with on resonance microwave frequency pulses, we were able to successfully transfer polarization to the nuclear spins and detect a hyperpolarized nuclear spins signal at 0.6 tesla (Figure 4).

We are currently working to decrease the losses of our coplanar waveguide devices and simultaneously increase the maximum operating frequency from 20 GHz to 40 GHz. By decreasing the overall dimensions of these devices, we are working to couple the waveguides to millimeter scale microwave sources developed by our collaborator, Ehsan Afshari. These chip scale sources would be the first of their kind used in a physical science experiment.

References:

- [1] Degen, C. L., Poggio, M., Mamin, H. J., Rettner, C. T., and Rugar, D. "Nanoscale magnetic resonance imaging" *PNAS*, 2009, 106, 1313.
- [2] Longenecker, J. G., Mamin, H. J., Senko, A. W., Chen, L., Rettner, C. T., Rugar, D., and Marohn, J. A. "High-gradient nanomagnets on cantilevers for sensitive detection of nuclear magnetic resonance" *ACS Nano*, 2012, 6, 9637.
- [3] Isaac, C., Gleave, C., Nasr, P., Nguyen, H., Curley, E., Yoder, J., Moore, E., Chen, L. and Marohn, J. "Dynamic nuclear polarization in a magnetic resonance force microscope experiment" *Phys. Chem. Chem. Phys.* 2016, 18, 8806.

Charge Injection in Boron Nitride Nanosheets

CNF Project Number: 801-99

Principal Investigator: Dr. Michael Spencer

User: Brian Calderon

Affiliation: Electrical Engineering, Cornell University

Primary Source of Research Funding: NSF

Contact: spencer@ece.cornell.edu, brc65@cornell.edu

Abstract:

We demonstrate charge carrier injection into monolayer membranes of hexagonal boron nitride (hBN) through Ni electrodes. The nature of the charge carriers is presumed to be p-type based on the band alignment and our monolayer devices reproducibly sustain a current of up to ~ 2 μ A with an electric field of 30,000 V/cm without breaking down.

Summary of Research:

Hexagonal boron nitride (hBN) is a wide bandgap layered 2D crystal consisting of weakly interacting van der Waals bonds between layers and strongly coupled sp² hybridized bonds within layers [1]. Due to its atomic flatness and ability to only weakly scatter electrons in graphene (Gr) [2], it has primarily been used as a substrate for electronic devices based on Gr, yet its electronic properties have not been well studied [1,3]. Prior work has shown that unwrapping boron nitride nanotubes (BNNT's) into boron nitride nanosheets (BNNS) results in highly conductive layers that can sustain currents on the order of microamps [4]. In this work, we study if the same can be accomplished in large area sheets of boron nitride grown by chemical vapor deposition (CVD).

The hBN was initially grown by CVD on Cu foil and was transferred using a wet transfer approach where we spun PMMA 4% at 3000 rpm for 60s. The stack was then left to float in Cu etchant CE-100 from transene for 12 hrs. The floating PMMA/hBN layer was then transferred to DI water and left to float for another 12 hrs. After this the PMMA/hBN was scooped up in the target substrate and left to dry for 12 hrs. Finally the PMMA/hBN on the target substrate was left in a solvent solution (Microposit remover 1165 from Shipley) for 12 hrs to remove the PMMA layer. The target substrate used in this study was SiO₂ (280 nm) on p-type doped Si.

Our fabrication procedure consisted of only two layers, the first being the alignment markers and the second being the contact definition. Our contacts were Ni electrodes for this study since it has been found to serve as an ohmic contact in prior studies [3,4]. In Figure 1, we can see current-voltage (I-V) characteristics of a

typical devices at a channel lengths of 1 μ m. Figure 2 shows current as a function of voltage squared and reveals the nature of the transport in our hBN that we believe to be space charge limited [3].

As expected in the low bias regime, we can see that $I \propto V$ (see inset of Figure 1), but as the bias increases, the relation shifts to $I \propto V\lambda$ where $1.75 < \lambda < 2.5$ where the value of λ is mainly modified by charge traps and defects in the hBN film. For our devices, we find that $\lambda = 2$ is consistent with the Mott-Gurney theory of space charge conduction. The mobility was calculated using equation (1) where $\zeta = 0.7$ was used and $\epsilon_0 = 8.85e-12$ (F/m), $\epsilon_r = 3$ was taken as the average effective dielectric constant of the oxide ($\epsilon_r = 3.9$), vacuum ($\epsilon_r = 1.0$) and hBN ($\epsilon_r = 3-4$ [ref]). We estimate a value of $\mu \sim 0.6457 \text{ cm}^2 / \text{V.s}$ which is at least an order of magnitude higher than previously reported [3].

$$I = \zeta \epsilon_0 \epsilon_r \mu \frac{W}{L^2} V \quad \text{Eqtn. (1)}$$

References:

- [1] J. Yin, J. Li, Y. Hang, J. Yu, G. Tai, X. Li, Z. Zhang and W. Guo, "Boron Nitride Nanostructures: Fabrication Functionalization and Applications," *Small*, vol. doi: 10.1002/smll.201600053, pp. 1-27, 2016.
- [2] C. R. Dean, A. F. Young, I. Meric, C. Lee, L. Wang, S. Sorgenfrei, K. Watanabe, T. Taniguchi, P. Kim, K. L. Shepard and J. Hone, "Boron Nitride Substrates for high-quality graphene electronics," *Nature Communications*, vol. 5, pp. 722-726, 2010.
- [3] F. Mahvash, E. Paradis, D. Drouin, T. Szkopek and M. Siaz, "Space-Charge Limited Transport in Large-Area Monolayer Hexagonal Boron Nitride," *Nano Letters*, vol. 15, pp. 2263-2268, 2015.
- [4] H. Zeng, C. Zhi, Z. Zhang, X. Wei, W. Guo, Y. Bando and D. Goldberg, "'White Graphenes': Boron Nitride Nanoribbons via Boron Nitride Nanotube Unwrapping," *Nano Letters*, vol. 10, pp. 5049-5056, 2010.

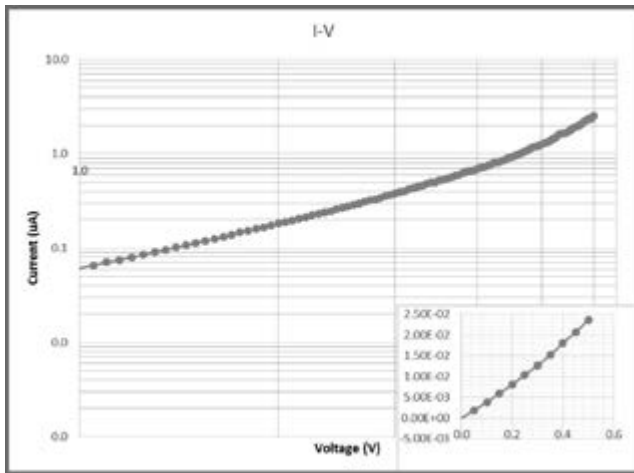


Figure 1: Typical current voltage characteristic of our two terminal devices showing the expected quadratic dependence on voltage. The measurement was taken in air on a 1 μm channel device. The inset shows the low bias regime where a linear dependence on voltage can be observed.

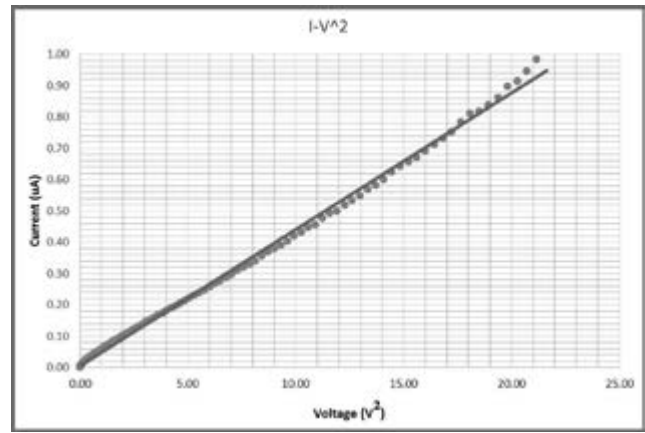


Figure 2: Current as function of voltage squared of the device depicted in Figure 2. A linear fit (red curve) was used to extract parameters needed for mobility calculations. The good correspondence of a linear fit with our data further verifies the Mott-Gurney space charge transport in our devices.

Electro Static Quadrupole Fabrication Using Silicon

CNF Project Number: 1121-03

Principal Investigator: Prof. Amit Lal

User: Vinaya Kumar Kadayra Basavarajappa

Affiliation: Electrical and Computer Engineering, Cornell University

Primary Source of Research Funding: Department of Energy (DOE)

Contact: amit.lal@cornell.edu, vk256@cornell.edu

Website: <http://sonicmems.ece.cornell.edu/>

Abstract:

In this present project, we are trying to fabricate a silicon-based electrostatic quadrupole array to focus the charged particles. Electrostatic quadrupole is basically an electrostatic lens, in which two positive and two negative electrodes are placed 90° to each other to the aperture. This arrangement will help to achieve the zero electric field at the center of these electrode arrangement. Hence, the particle at the center will experience a zero electric field. Using the CNF's Unaxis 770 Deep Si Etcher we are trying to fabricate these devices in highly doped silicon wafers.

Summary of Research:

We are interested in fabricating ElectroStatic Quadrupoles (ESQ) from silicon wafers. These ESQ wafers will be tested in vacuum with high DC and RF voltages to focus the charged particles. In Figure 1 we show the fabrication process flow for the silicon ESQ wafer. The fabrication process is started with highly doped silicon wafer (100 mm 4-inch, resistivity = 0.005-0.020 Ohm cm, thickness 490-510 μm). Later, the doped silicon wafer is oxidized and coated with silicon nitride for electrical isolation.

To supply the high voltages into the ESQ, the deposited oxide and nitride layers were patterned. And then a metal layer was deposited onto the electrode pillar regions (step 5). After forming metal contacts, the pillar structures were fabricated using deep reactive ion etching (DRIE) (step 8). Finally, to develop an ESQ unit cell, two wafers will be bonded using intermediate metal layer (step 11). These ESQ unit cells will be standing only on the oxide and nitride layers. Hence, the electrical breakdown voltage of the oxide and nitride stack layer will be an important parameter to decide on the operating voltage of the ESQ unit cell.

Figure 2 shows the fabricated device in single wafer. To form a complete ESQ unit cell we need to fabricate one more similar wafer and need to bond two wafers shown in step 11 of Figure 1.

References:

- [1] Syms, R. R. A., T. J. Tate, M. M. Ahmad, and S. Taylor. "Fabrication of a microengineered quadrupole electrostatic lens." *Electronics letters* 32, no. 22 (1996): 2094-2095.
- [2] Gear, Martin, Richard RA Syms, Steven Wright, and Andrew S. Holmes. "Monolithic MEMS quadrupole mass spectrometers by deep silicon etching." *Microelectromechanical Systems, Journal of* 14, no. 5 (2005): 1156-1166.
- [3] Tullstall, J. J., S. Taylor, R. R. A. Syms, T. Tate, and M. M. Ahmad. "Silicon micromachined mass filter for a low power, low cost quadrupole mass spectrometer." In *Micro Electro Mechanical Systems, 1998. MEMS 98. Proceedings., The Eleventh Annual International Workshop on*, pp. 438-442. IEEE, 1998.
- [4] Syms, Richard RA, Thomas J. Tate, Munir M. Ahmad, and Stephen Taylor. "Design of a microengineered electrostatic quadrupole lens." *Electron Devices, IEEE Transactions on* 45, no. 11 (1998): 2304-2311.

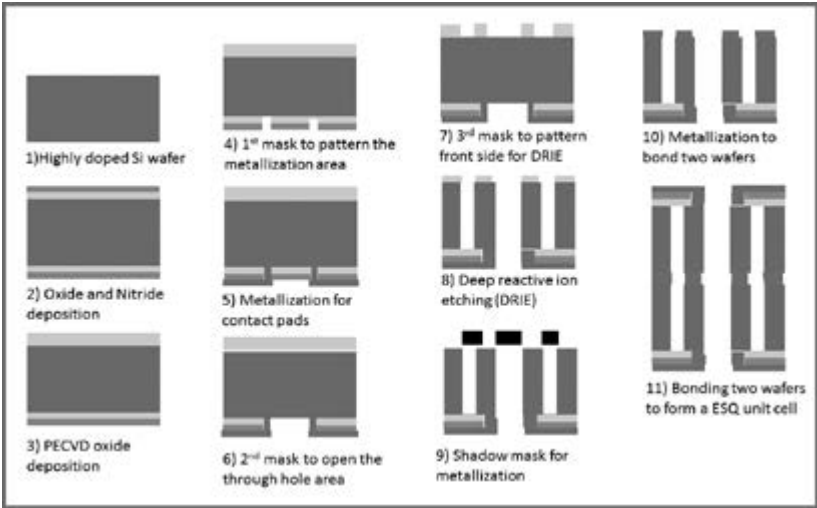


Figure 1: Cross section of the ESQ fabrication process step on a silicon wafer.

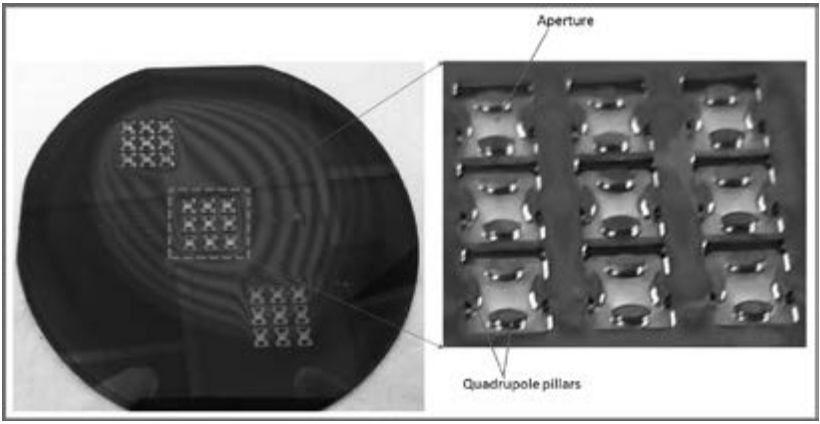


Figure 2: Silicon pillars on nitride membrane.

Silicon Dioxide and Polymer-Based Transient Electronics with Rubidium Fuel for Electrical to Thermal Energy Amplification

CNF Project Number: 1262-04

Principal Investigator: Amit Lal

Users: Ved Gund, Alexander Ruyack

Affiliation: School of Electrical and Computer Engineering, Cornell University

Primary Source of Research Funding: Defense Advanced Research Projects Agency

Contact: amit.lal@cornell.edu, vvg3@cornell.edu, arr68@cornell.edu

Website: <http://www.sonicmems.ece.cornell.edu/>

Abstract:

Sensors are pathways for gathering data, to revolutionize our understanding of both natural and man-made environments. Monolithically integrated microsystems with integrated circuits (ICs) that possess wireless transmission capabilities are pervasive to measure environmental conditions. These can be connected locally, or used with the internet-of-things (IoT) platform. Such a platform enables embedded electronics, hardware, software and sensors to interface with the physical world. This is desired for a wide range of applications including environmental sensing and monitoring and for defense applications. For microsystems with a short useful lifetime of sensors, the effort in realizing and monitoring these sensors can be prohibitive. Tracking and recovering each device individually, especially in a large-area network, is nearly impossible leading to deleterious effects of unattended electronic materials as environmental contaminants. Additionally, potential acquisition by adversaries for reverse engineering of electronics and stealing of data is undesirable. Physical elimination of sensors upon remote trigger, leaving behind little or no physical trace is one approach to solve the problem of data security and environmental contamination. With this goal, we have developed vaporizable sensor nodes with micro-packets of rubidium (Rb) as fuel to realize controlled transience of electronics.

Summary of Research:

Architecture. Figure 1 shows the unit cell of our arrayable and scalable design. The substrate is composed of a polymer blend of polypropylene carbonate (70%) and a polymer based on previous procedures [1] (30%). This ensures that the substrate is stable under ordinary conditions but vaporizes at 180°C. We achieve vaporization with nanoliter droplets of Rb, stored in one half of the transience unit cell. Rb is a high specific-power density reactive alkali metal, which we have demonstrated to be an excellent fuel for micro-combustion [2], via its oxidation that releases a large amount of energy. The Rb is protected from ambient oxygen by an impermeable ultra-thin graphene-on-nitride valve, which we have demonstrated previously as a low-power and low-energy single-use trigger [3]. Sodium bifluoride (NaHF_2) is stored in the other half of the unit cell. NaHF_2 is a salt that decomposes at 160°C to release HF, used to etch and eliminate the oxide based electronics. The heat for this is also obtained from the Rb oxidation, after the valve is triggered. The relative quantities of polymer, Rb and NaHF_2 are chosen using the energetics analysis in Figure 2 with appropriate fill factors for each material.

Fabrication. The valve, a key MEMS component of the system, is made of 360 nm of LPCVPD low-stress silicon nitride deposited in the CNF nitride furnace B4. It is 750 x 750 μm^2 . The 45 nm electrodes are made of nickel and deposited on the membrane in the CNF evaporator and patterned by lift-off. The graphene, to be transferred on

nitride, is grown on copper foil in the First Nano Carbon Nanotube and Graphene Furnace. It is then transferred onto the membrane by standard procedures using PMMA as a handle layer and rinsing in DI water, followed by PMMA etching and patterning in the Oxford 81 etcher.

Test-Structure Results. For isolated testing of polymer substrate and oxide transience, valves were filled with Rb and NaHF_2 and sealed with polymer and oxide-based backing layers respectively. The results from the testing of each are shown in Figures 3 and 4 respectively. Rb oxidation clearly shows a rise in the substrate temperature followed by etching with a highest efficiency of 9.15 %. NaHF_2 releases HF at 160°C to etch 1 μm thick thermal oxide and is also able to laterally undercut custom ICs with oxide to cause discoloration of the chips.

References:

- [1] F. M. Houlihan, et al., "Thermally Depolymerizable Polycarbonates. 2. Synthesis of Novel Linear Tertiary Copolycarbonates by Phase-Transfer Catalysis", *Macromolecules*, pp 13-19, 1986.
- [2] A Ruyack, et al., "Alkali Metal Based Micro Combustion Using Graphene Micro-valve Trigger", *IEEE PowerMEMS*, Boston, USA 2015.
- [3] V. Gund, et al. "Transient Micropackets for SiO₂ and Polymer-based Vaporizable Electronics", *IEEE MEMS*, Shanghai, China, 2016.
- [4] V. Gund et al. "Multi-modal graphene polymer interface characterization platform for vaporizable electronics", *IEEE MEMS*, Estoril, Portugal, 2015.

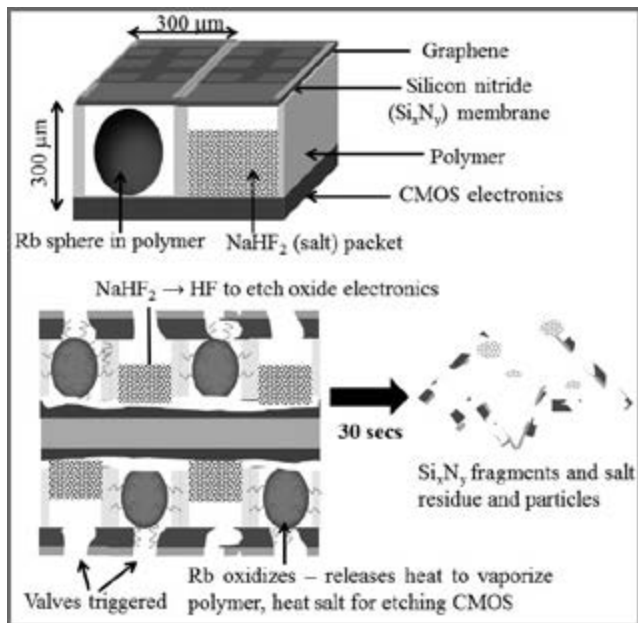


Figure 1: Unit-cell for transience: VPC substrate cavities are alternatingly filled with rubidium and sodium bifluoride (NaHF_2), sealed by graphene-on-nitride valves with CMOS electronics as the backing layer. B). Time evolution of system transience: Valves are triggered on millisecond time scales, exposing Rb to oxygen. This releases heat to decompose the VPC and the salt, which releases HF to etch the oxide. The final residue is silicon nitride and metal fragments and salt.

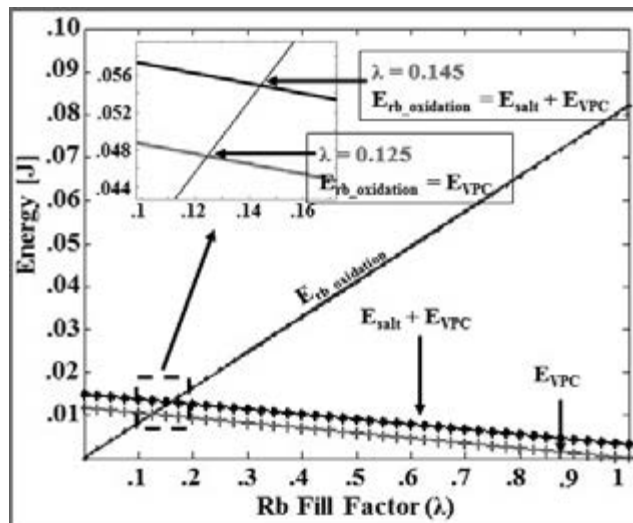


Figure 2: Analytical model for energy and stoichiometry constraints for a cubic micro-packet of side $500 \mu\text{m}$ vs. Rb fill factor in it. Heat of polymer vaporization is 110 kJ/mol and heat capacity is 1.2 kJ/(kg.K) . Rubidium energy is calculated from the enthalpy of formation of Rb_2O equal to -169.5 kJ/mol . Oxide thickness is assumed to be $10 \mu\text{m}$.

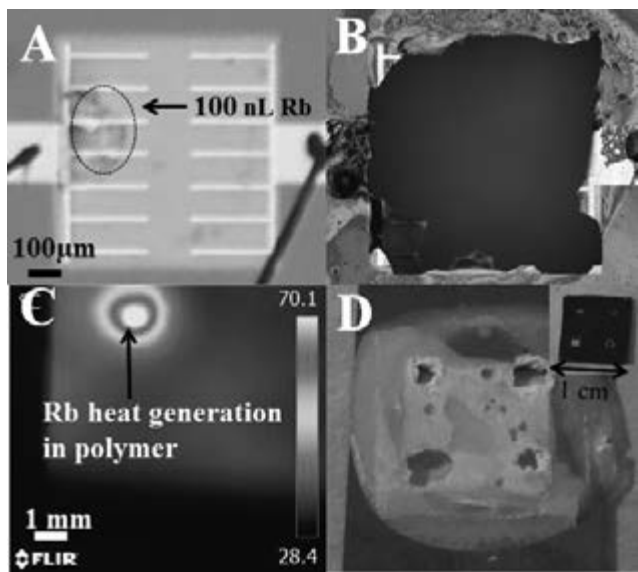


Figure 3: A). Optical micrograph of test structure; 100 nL Rb is sealed by the valve and the VPC (not seen in this picture) is used as a backing layer B). Optical micrograph of a valve post-triggering; shows $>95\%$ vaporization confirmed with image processing C). IR image of the polymer backside during Rb oxidation; the elevated VPC temperature shows energy transfer from Rb to the substrate D). Best vaporization performance of 500 nL Rb in μ -packet produces 5.2 mm^2 (determined with image-processing) etching of $125 \mu\text{m}$ thick polymer. 100% of polymer is etched below the tested valves (shown in inset).

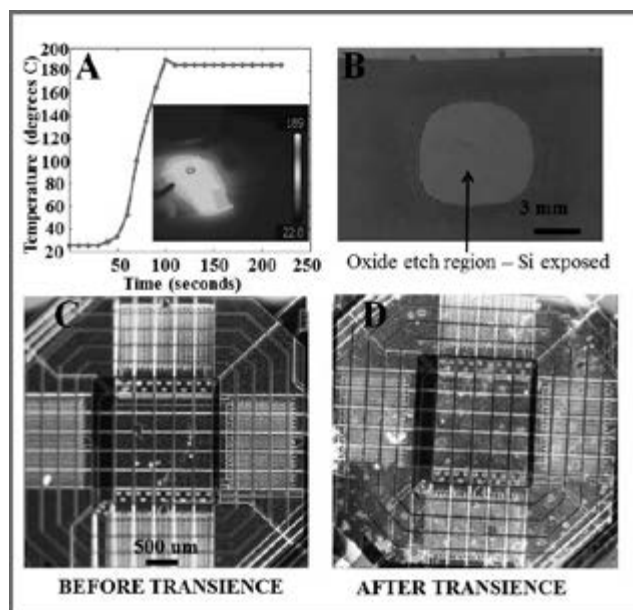


Figure 4: A). Temperature profile of membrane surface vs. time for oxide-etching test. Inset shows IR image of the chip, confirming temperature required for NaHF_2 decomposition is achieved locally B). Optical image of etched oxide substrate; $1 \mu\text{m}$ etching was confirmed with profilometry C) Optical micrographs of commercial $5 \mu\text{m}$ thinned dies C) Before and D) After etching; The discoloration shows oxide etching.

Novel Electronic and Optoelectronic Devices Using Layered Materials

CNF Project Number: 2306-14

Principal Investigator: Huili Grace Xing

User: Rusen Yan

Affiliation: School of Electrical and Computer Engineering, Cornell University

Primary Source of Research Funding: Center for Low Energy Systems Technology

Contact: grace.xing@cornell.edu, ry253@cornell.edu

Abstract:

Van der Waals (vdW) heterojunctions composed of two-dimensional (2D) layered materials are emerging as a solid-state materials family that exhibit novel physics phenomena that can power a range of electronic and photonic applications. Here we assemble the atomically thin vdW p-n junction with monolayer WSe₂ and MoS₂, and study their interlayer carrier dynamics using photocurrent spectroscopy. Through careful investigation of bias and gate dependent photocurrent at different excitation wavelengths, we resolve the intra- and inter-layer recombination process of photo-generated carriers in such a tunable p-n diode. The optoelectronic responses of vdW heterojunctions presented in this work pave the way for realizing atomically thin photodetectors, light-emitting and tunneling devices.

Summary of Research:

We construct a gate tunable vdW p-n junction composed of monolayer tungsten diselenide (WSe₂) and molybdenum disulfide (MoS₂) on a 90 silicon dioxide (SiO₂)-covered Si wafer. The vertical stacking of two crystals are realized by a home-built dry transfer stage tool with a microscope. We employ electron-beam lithography (JEOL6300) and evaporation to make Cr/Pd contacts to the exfoliated crystals. The resulting

device is annealed in forming gas for three hours under 300°C. Figure 1 shows the I-V characteristics of one representative device. In the inset of Figure 1, we respectively show the I_d-V_g for MoS₂ and WSe₂. As could be seen, WSe₂ exhibits p-type and MoS₂ n-type over the entire scanned voltage ranges.

Therefore, a p-n diode could be realized while biasing MoS₂ in moderate electron-doped and WSe₂ in hole-doped regime (V_g lies between -20 between -30 V). I_d-V_d curves measured over the heterojunctions show clear rectifying behavior is observed with I_{for}/I_{rev} > three orders of magnitude, as expected for a typical p-n junction.

We further proceed to conduct photocurrent measurements on such a vdW junction and examine its short-circuit current and open-circuit voltage responses. In Figure 2, we schematically show the optical set-up used for such measurements. A super continuum laser is used as light source to provide wide range of excitation wavelength incident on the flakes. We collect photocurrents through a Keithley 2400 source-meter unit, as a function of incident wavelength and V_{ds}.

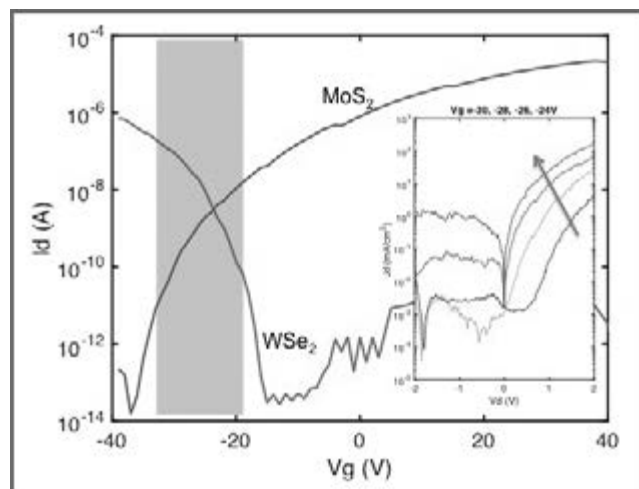


Figure 1: I_d-V_g of MoS₂ and WSe₂ crystals. The inset is I_d-V_{ds} curve measured over the junction.

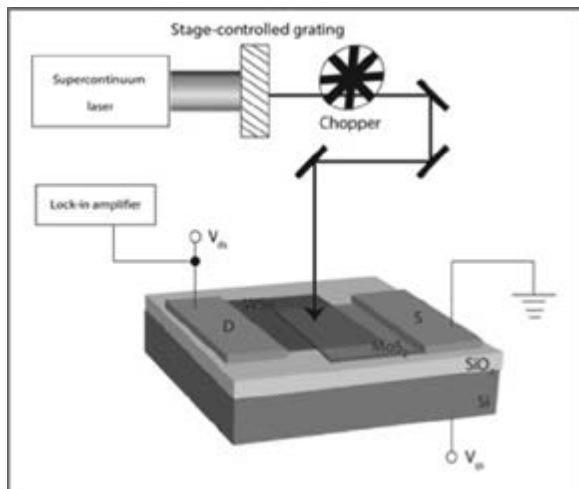


Figure 2: The schematic set-up to measure spectroscopic photocurrents.

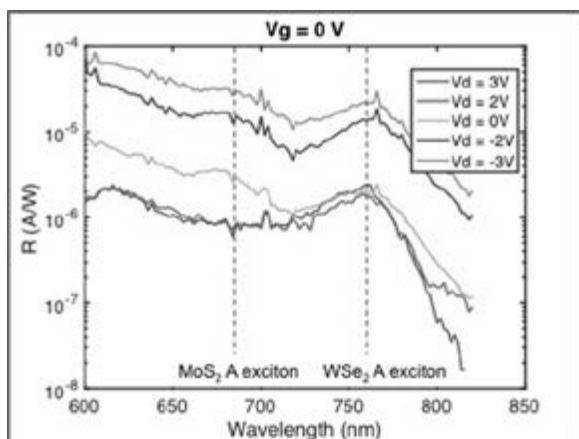


Figure 3: Measured photocurrent spectroscopy under different biases.

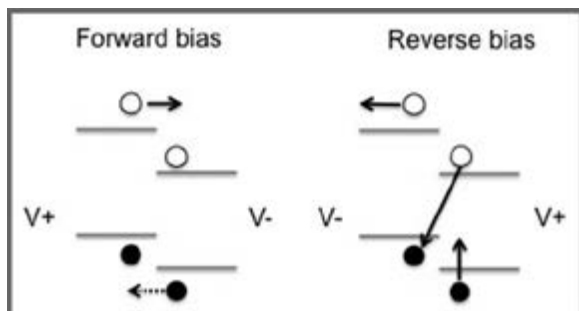


Figure 4: Band alignment and carrier separation process in vdW heterojunction.

As shown in Figure 4, the short-circuit spectroscopic photocurrents ($V_{ds} = 0$ V) are observed and exhibit a response of around 10^{-5} A/W in a wide spectrum range for only two atomically thin layers. Two prominent peaks are reliably observed that could be attributed to an exciton peak of MoS₂ (~ 680 nm) and that of WSe₂ (780 nm). The most critical advantage of using spectroscopic method to study the photoresponse of such vdW heterojunctions is that the spectroscopic features could tell the source of measured photocurrents, either from MoS₂ or WSe₂.

While $V_{ds} = 0$ V, both features of WSe₂ and MoS₂ appear, which indicates that the measured photocurrents are due to the absorption of and separation of photo-generated carriers on both monolayers. This charge transfer process could be well described by Figure 4. Under forward bias, this interlayer charge transfer process becomes more efficient with the aid of applied bias. On the contrary, while the junction is reversely biased, the measured photocurrents show only the feature of WSe₂.

The reason responsible for the disappearance of MoS₂ photoresponse is that interlayer electron-hole recombination is greatly enhanced due to the application of such external bias (as indicated with the dotted arrow in Figure 4). After the interlayer recombination of MoS₂ electrons and WSe₂ holes, electrons left in MoS₂ are quickly captured by the defect states inside the band gap, thus, photo-generated carriers in MoS₂ can not contribute to the measured photocurrents.

Overall, we have been able to construct atomically thin p-n junctions with strong photoresponse. The spectroscopic photocurrents are measured over the junction under various biases. The observed optoelectronic behavior indicates the efficient charge carrier transfer in such vdW interface and could be helpful for future design of ultrafast photodetectors and tunneling devices.

GaN-on-GaN p-n Power Diodes with $BV > 3.48$ kV and $R_{on} = 0.95$ m Ω ·cm²: A Record High Figure-of-Merit of 12.8 GW/cm²

CNF Project Number: 2307-14

Principal Investigator: Huili Grace Xing

User: Kazuki Nomoto

Affiliation: Electrical and Computer Engineering, Cornell University

Primary Source of Research Funding: ARPA-E project

Contact: grace.xing@cornell.edu, kn383@cornell.edu

Abstract:

We report GaN p-n diodes on free-standing GaN substrates: a record high Baliga's figure-of-merit (V_B^2/R_{on}) of 12.8 GW/cm² is achieved with a 32 μ m drift layer and a diode diameter of 107 μ m exhibiting a $BV > 3.4$ kV and a $R_{on} < 1$ m Ω ·cm². The leakage current density is low: 10⁻³ - 10⁻⁴ A/cm² at 3 kV. A record low ideality factor of 1.1-1.3 is signature of high GaN quality. These are among the best-reported GaN p-n diodes.

Summary of Research:

As shown in Figure 1, three device layer structures have been grown with a varying n-GaN drift layer thickness of 20, 25 and 32 μ m while keeping the rest of the layers the same. For the 20 μ m epi-design, the drift layer doping concentration was kept constant, which is confirmed by the capacitance-voltage (C-V) measurement on these power diodes; the net N_D-N_A concentration extracted from C-V measurements showed a constant value of 5×10^{15} cm⁻³ in the top 10 μ m. For the 25 and 32 μ m epi-designs, the top 6 μ m of the n-GaN drift layer was grown to have the lowest doping concentration: a net N_D-N_A concentration of $\sim 1 \times 10^{15}$ cm⁻³ was extracted from C-V measurements while a Si concentration of 2.5×10^{15} cm⁻³ was measured by secondary ion mass spectrometry (SIMS) on a similar epi-wafer. For the second n-GaN drift layer, a net N_D-N_A concentration of $2-3 \times 10^{15}$ cm⁻³ was extracted from C-V measurements in both the 25 μ m and 32 μ m power diodes.

In Figure 2 the representative cross-section of four completed diode types are shown: no field-plate (NFP) without SOG, no field-plate with SOG passivation (SOG-NFP), steep-mesa and beveled-mesa with a long field plate (LFP and beveled-LFP) that extends 20 μ m beyond the mesa bottom edge (beveled mesa with no field-plate is not shown). The diode size is defined by the bottom mesa diameter, ranging from 70 to 707 μ m.

Figure 3 shows the representative reverse bias I-V characteristics of various diode types fabricated on the 25 μ m epi-wafer. The device BV is the lowest in diodes with no field-plate ($\sim 1-1.4$ kV), as expected;

BV increases moderately in diodes with SOG passivation but no field-plate (~ 1.6 kV), improves further in diodes with long field-plate and steep mesa (~ 3.0 kV) and reaches > 3.2 kV in diodes with long field-plates and beveled mesa. It is interesting to note that employing both long field-plate and beveled mesa dramatically improves the uniformity of device performance, especially in the large area diodes (> 300 μ m); it is extraordinary that diodes with a diameter of 707 μ m (bottom mesa size) have reached a $BV > 3$ kV.

The benchmark plot is shown in Figure 4, demonstrating a record Baliga's figure-of-merit of > 12 GW/cm² obtained in the 32 μ m epi-design. Also shown is that the p-n power diode BV increases with the increasing n-GaN drift-layer thickness while R_{on} remains nearly the same ~ 1.0 m Ω ·cm². If the minority carrier lifetime is short, a p-n diode can be assumed to operate like a unipolar device, thus R_{on} is dominated by the n-GaN drift region. Assuming a carrier concentration of 5×10^{15} cm⁻³ and a mobility of 2000 cm²/Vs, the specific resistance of a 20 μ m n-GaN drift layer is calculated to be ~ 1.25 m Ω ·cm². The observed record low R_{on} might arise from other mechanisms including high level injection and photon recycling effects, which warrants further investigation.

CNF Tools Used:

Oxford PECVD, i-line stepper, PT770, EB evaporator, polyamide bake oven, and SEM.

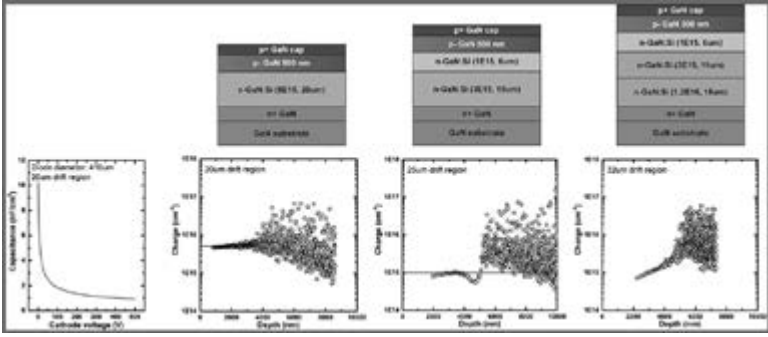


Figure 1: (upper row) MOVPE p-n junction epi-structures on free-standing GaN substrates with a varying n-GaN drift layer thickness: 20, 25 and 32 μm , while keeping all the rest of the layers the same. The carrier concentrations indicated therein are determined by C-V measurements at 100 kHz except the very bottom n-GaN layer in the 32 μm epi-design. (lower row) Measured capacitance versus cathode voltage up to 500 V for GaN-on-GaN p-n power diodes, extracted charge concentration (cm^{-3}) depth profiles in the drift layer for the corresponding epi designs.

Figure 2: Schematic cross-sections of 4 device types arising from processing variations. From left to right, with no field-plate (NFP), with SOG passivation and no field-plate (SOG-NFP), steep mesa with a long-field plate (LFP), and beveled mesa with a long-field plate (beveled-LFP). Also included are the scanning electron microscopy (SEM) cross-section images showing the steep and beveled mesa sidewalls in fabricated devices.

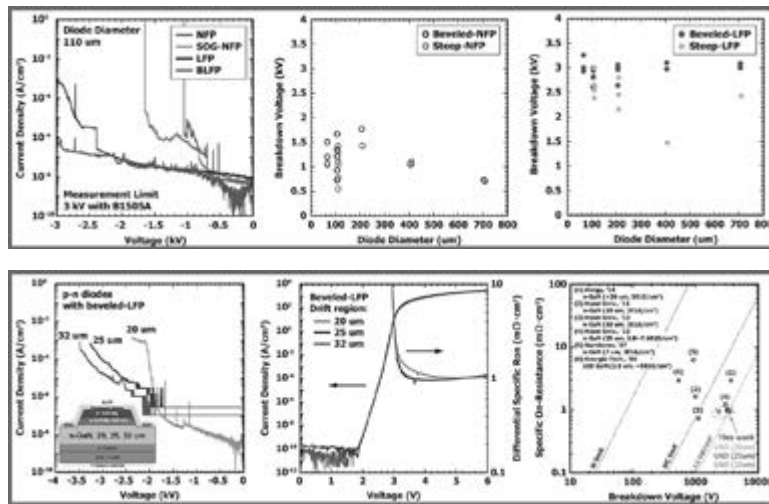
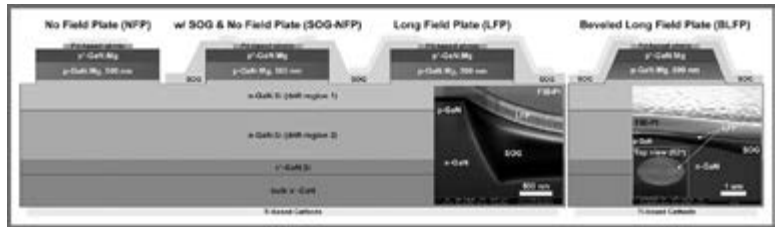


Figure 3, top: Reverse bias I-V characteristics of NFP, SOG-NFP, LFP, BLFP (beveled-LFP) GaN p-n power diodes fabricated on the 25 μm epi-wafer. With the employment of field plate, the breakdown voltage increases significantly from ~ 1 kV to ~ 3 kV for the devices with steep sidewall. Combining the field plate and the beveled mesa sidewall, the device breakdown voltage increases further to >3.2 kV. Interestingly, the breakdown voltage increases dramatically in the large area diodes employing the beveled-LFP process.

Figure 4, bottom: (left) Reverse and (middle) forward bias I-V characteristics of representative p-n diodes employing the beveled-LFP process flow. (right) Baliga's figure-of-merit benchmark plot of reported vertical GaN-on-GaN p-n diodes. The diode current and R_{on} are normalized with respect to the mesa area determined by the bottom diameter of the mesa. The specific on-resistance for all devices (this work and from the literature) is compared without considering current spreading. For the results from Hosei Univ., data have been updated since the diode area used in the original reports is the electrode size, which is smaller than the mesa size.

Vertical Ga₂O₃ Schottky Barrier Diodes on Single-Crystal β-Ga₂O₃ <-201> Substrates

CNF Project Number: 2307-14

Principal Investigator: Huili Grace Xing

User: Bo Song

Affiliation: Electrical and Computer Engineering, Cornell University

Primary Source of Research Funding: DOE ARPAE SWITCHES Project

Contact: grace.xing@cornell.edu, bs728@cornell.edu

Abstract:

We fabricated Pt/Ga₂O₃ SBDs on single-crystal β-Ga₂O₃ <-201> substrates for the first time. Ohmic contacts were obtained on the backside with a RTA process. The Pt/Ga₂O₃ SBDs on <-201> substrates show similar behavior with the devices fabricated on <010> Ga₂O₃ substrates.

Summary of Research:

Owing to the large bandgap, breakdown electric field (E_b) and high carrier mobility, wide-bandgap semiconductor (e.g., SiC and GaN)-based power devices have been extensively studied for next-generation power-switching applications [1,2]. Recently, a new wide-bandgap oxide semiconductor, gallium oxide (β-Ga₂O₃), has attracted attention for power-switching applications because it has an extremely large bandgap of 4.5~4.9 eV enabling a high breakdown voltage (V_{br}) and a high Baliga's figure-of-merit [3]. Furthermore, large-area and high-quality bulk substrates of Ga₂O₃ can be grown by low-cost methods, which remains a significant challenge for both silicon carbide (SiC) and gallium nitride (GaN). Schottky barrier diodes (SBDs), with a low turn-on voltage and a fast switching speed due to majority carrier conduction, are ideal candidates for high-power and high-speed rectifiers.

Recently, Higashiwaki, et al., has demonstrated excellent device results, which includes SBDs with V_{br} ~ 115 V on <010> Ga₂O₃ substrates (with a net doping concentration $N_D - N_A$ ~ 5×10^{16} cm⁻³) [4] and SBDs with epitaxial Si-doped n-Ga₂O₃ drift layers ($N_D - N_A$ ~ 1.4×10^{16} cm⁻³) grown by HVPE on <001> Ga₂O₃ substrates with V_{br} ~ 500 V [5]. Oishi, et al., reported Ni-based SBDs on <-201> Ga₂O₃ with a $N_D - N_A$ ~ 1×10^{17} cm⁻³ and V_{br} ~ 40 V [6].

In this work, we report Pt-based SBDs fabricated on unintentionally-doped (UID) <-201> n-type Ga₂O₃ substrates with V_{br} > 100V.

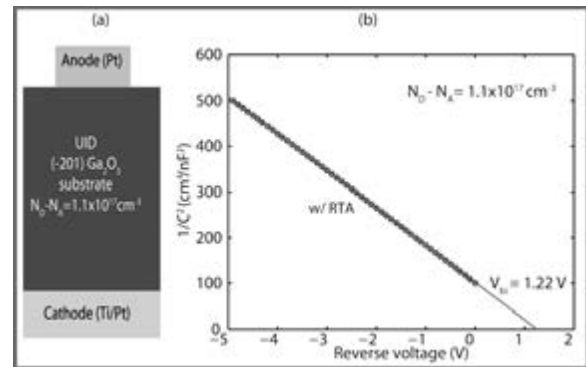


Figure 1: (a) Schematic cross section of SBDs on <-201> Ga₂O₃ substrate and (b) $1/C^2$ -V characteristics of Ga₂O₃ SBDs with RTA showing net doping concentration ~ 1.1×10^{17} cm⁻³ built-in voltage ~ 1.22 V.s.

Figure 1 shows the schematic cross section and the $1/C^2$ -V plot of the fabricated Ga₂O₃ SBDs. The net doping concentration ($N_D - N_A$) in the <-201> Ga₂O₃ substrates extracted by the $d(1/C^2)/dV$ method is ~ 1.1×10^{17} cm⁻³. The built-in potential extracted from the $1/C^2$ -vs- V plot is V_{bi} ~ 1.22 V as shown in Figure 1 (b). The substrate thickness is ~ 680 μm and the resistivity ~ 6.3 Ω/sq.

The top circular Schottky anode electrodes with diameters of 50 μm and 390 μm were fabricated on Ga₂O₃ substrates by photolithographic patterning, followed by evaporation of Pt (80 nm) as anode metal, and liftoff. The back cathode is formed by evaporation of a Ti (50 nm)/Pt (100 nm) metal stack.

A rapid thermal annealing (RTA) process at 470°C in N_2 ambient for 60 s is applied to devices labeled as w/ RTA. No additional surface passivation or field plate is employed for the devices studied in this work.

The 50 μm and 390 μm diameter diodes were used for current density-voltage (I - V) and capacitance-voltage (C - V) measurements, respectively. All measurements were performed at room temperature.

Figure 2 shows the I - V curves measured between two back-contacts separated by $\sim 160 \mu\text{m}$ on a test sample using the same substrate and metal stack with and without RTA. The contacts fabricated with the RTA process showed a reasonable ohmic behavior with high current capability. On the other hand, the as-deposited metal stack contacts show a Schottky behavior, thus allowing only very low currents. The detailed mechanism for this improvement is not yet clear and warrants further investigation.

Figures 3 (a) and (b) show the forward J - V characteristics of the SBDs in logarithmic and linear scales, respectively. The turn-on voltage is about 1 V for both cases. Near unity ideality factors of 1.02 are obtained for both SBDs with and without RTA.

The extracted $\text{Pt}/\text{Ga}_2\text{O}_3$ barrier height $q\phi_B$ is 1.53 eV and 1.35 eV for as deposited and with RTA processed, respectively. The $\text{Pt}/\langle -201 \rangle \text{Ga}_2\text{O}_3$ barrier height extracted here is close to the reported values in the range of 1.3-1.5 eV for $\text{Pt}/\langle 010 \rangle \text{Ga}_2\text{O}_3$ [4]. In Figure 3 (b), the SBD w/ RTA process shows a dramatic improvement in the forward current-carrying capability: from 34 to 400 A/cm^2 at 2 V. This is most likely a result of the improved back-contact and a reduction of $q\phi_B$. The differential on-resistance R_{on} as determined from the slope of the linear regions in Figure 3 (b) for SBD without RTA and with RTA is about 29.4 and 2.5 $\text{m}\Omega\text{-cm}^2$, respectively. Since the substrate specific resistivity along the current flowing direction is 26.5 $\text{m}\Omega\text{-cm}^2$, a R_{on} of 2.5 $\text{m}\Omega\text{-cm}^2$ is attributed to current lateral spreading from the top anode to the bottom contact.

References:

- [1] K. Nomoto, et al., EDL 37,161 (2016).
- [2] K. Nomoto, et al., IEEE IEDM (2015).
- [3] M. Higashiwaki, et al., APL 100, 013504 (2012).
- [4] K.Sasaki, et al., IEEE EDL 34, 493 (2013).
- [5] M. Higashiwaki, et al., IEEE DRC (2015).
- [6] Oishi, et al., APEX 8, 031101 (2015).

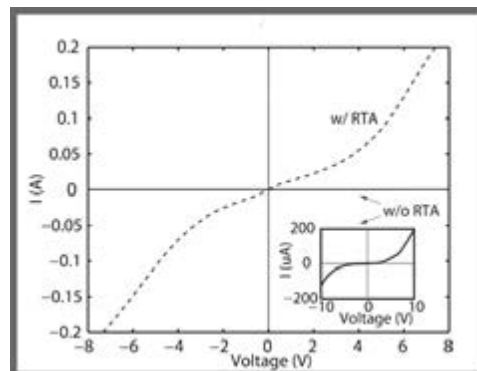


Figure 2: I - V curves measured between two contacts at the backside of an $\langle -201 \rangle \text{Ga}_2\text{O}_3$ substrate with Ti/Pt and the metal stacks at without and with RTA process conditions.

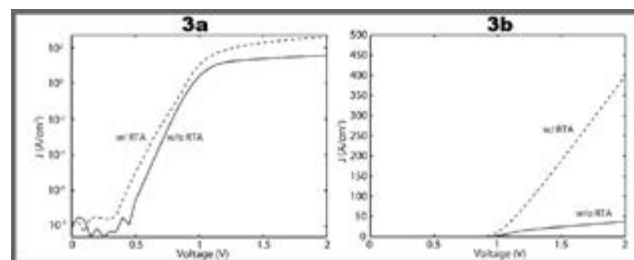


Figure 3, right: Forward J - V characteristics of Ga_2O_3 SBD without and with RTA process plotted in (a) logarithmic and (b) linear scales. With the RTA process, the back contact dramatically improves, which helps to improve the current density from ~ 34 to 400 A/cm^2 . Near unit ideality factors of 1.02 were obtained for the both SBDs and extracted barrier for SBDs without and with RTA process is 1.53 and 1.35 eV, respectively.

Fabrication of High Voltage Vertical GaN Schottky Barrier Diodes

CNF Project Number: 2307-14

Principal Investigators: Huili Grace Xing, Debdeep Jena

User: Mingda Zhu

Affiliation: School of Electrical and Computer Engineering, Cornell University

Primary Source of Research Funding: Advanced Research Project Agency

Contact: grace.xing@cornell.edu, djena@cornell.edu, mz442@cornell.edu

Abstract:

Vertical gallium nitride (GaN) devices on free-standing GaN substrates have recently attracted immense research interest [1] due to a prominence in high-voltage, high-current applications. Vertical GaN Schottky barrier diode, thanks to its low forward voltage and high switching speed, is an ideal candidate as a rectifier that is an almost universally essential component for power applications. The challenge in realizing high voltage with Schottky barrier diodes has been development of effective edge termination to prevent the premature breakdown induced by large electric fields at the edge of fabricated devices due to the electric field crowding effect [2]. In this work, slanted field plates are applied to fabricated vertical GaN Schottky barrier diodes and effectively increase the breakdown voltage from 250 V to 380 V.

Summary of Research:

The experiment is carried out on an epitaxial sample grown on free-standing gallium nitride (GaN) substrate by metalorganic chemical vapor deposition. The top epitaxial layer is silicon (Si)-doped n-GaN with a doping concentration of $\sim 1 \times 10^{16} \text{ cm}^{-3}$.

Fabrication started with SiO_2 deposition by Oxford PECVD at CNF. After the subsequent lithography process (GCA Autostep AS200), the SiO_2 in the anode area is etched away using buffered HF.

A slanted profile is created during the wet etching thanks to the photoresist hard baking process. Anode metal (Ni/Au) is then deposited after field plate layer lithography. The backside Ohmic contact is formed by depositing Ti/Au. The cross section schematic after complete process is shown in Figure 1.

The forward I - V characteristic plotted in linear scale is shown in Figure 2. The threshold voltage is extracted to be $< 0.4 \text{ V}$ with linear extrapolation method and the current density and the forward current density reaches beyond 1000 A/cm^2 at a low 2 V forward. The forward I - V characteristic of the fabricated vertical GaN Schottky barrier diode plotted in semi-logarithmic scale is shown in Figure 3, with the ideality

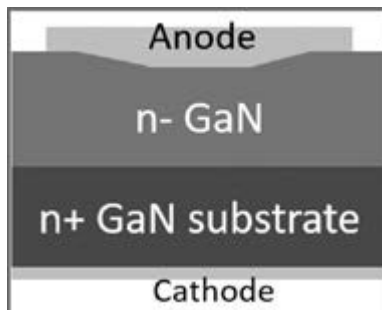


Figure 1: Cross section schematic of the fabricated vertical GaN Schottky barrier diode.

factor extracted to be 1.1. The close to 1.0 ideality factor indicated small amount of recombination involved during forward current conduction.

The reverse bias I - V characteristics of fabricated Schottky barrier diodes with and without slanted field plate is plotted in Figure 4. The fabricated Schottky barrier diode without slanted field plate shows a breakdown voltage of 250 V, while the one with slanted field plate has a breakdown voltage of 380 V. The efficacy of the slanted field

plate in improving the breakdown voltage is due to the reduced electric field at the anode edge. Further improvements can be made by carefully optimizing the field plate design.

References:

- [1] H. G. Xing, B. Song, M. Zhu, Z. Hu, M. Qi, K. Nomoto, and D. Jena, "Unique opportunity to harness polarization in GaN to override the conventional power electronics figure-of-merits," in 2015 73rd Annual Device Research Conference (DRC), 2015, vol. 4395, no. 2001, pp. 51-52.
- [2] Y. Saitoh, K. Sumiyoshi, M. Okada, T. Horii, T. Miyazaki, H. Shiomi, M. Ueno, K. Katayama, M. Kiyama, T. Nakamura, and Y. S. Å, "Extremely Low On-Resistance and High Breakdown Voltage Observed in Vertical GaN Schottky Barrier Diodes with High-Mobility Drift Layers on Low-Dislocation-Density GaN Substrates," AP Express, vol. 3, no. 8, pp. 1-3, Jul. 2010.

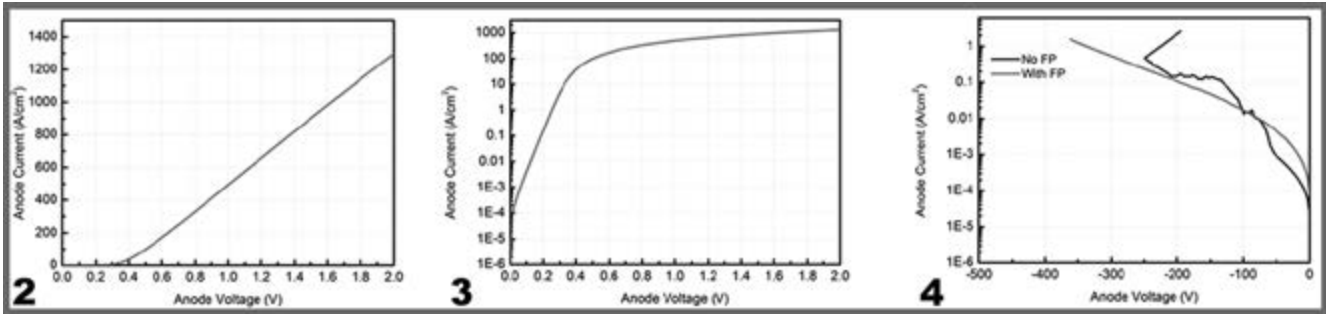


Figure 2, left: The forward I-V characteristic of the fabricated vertical GaN Schottky barrier diode plotted in linear scale.

Figure 3, middle: The forward I-V characteristic of the fabricated vertical GaN Schottky barrier diode plotted in semi-logarithmic scale.

Figure 4, right: The reverse I-V characteristic of the fabricated vertical GaN Schottky barrier diode plotted in semi-logarithmic scale.

Two-Dimensional Heterojunction Interlayer Tunneling Field Effect Transistor Process Development

CNF Project Number: 2324-15

Principal Investigator: Huili Grace Xing

User: Mingda Li

Affiliation: School of Electrical and Computer Engineering, Cornell University

Primary Source of Research Funding: Center for Low Energy Systems Technology (LEAST)

Contact: grace.xing@cornell.edu, ML888@cornell.edu

Overview:

We have used CNF facilities to develop a process for two-dimensional heterojunction interlayer tunneling field effect transistor (Thin-TFET) [1]. See Figure 1.

We have been using:

- Heidelberg Mask Writer DWL2000 for making two sets of masks; each mask set has three masks. An example mask is shown in Figure 2a.
- Yes Vapor Prime Oven to apply HDMS on the substrate to improve the adhesion between photoresist and substrate surface.
- Autostep i-line Stepper for patterning the contact metals and define oxide each mask. We can achieve $1\ \mu\text{m}$ line, and the alignment error is constantly less than $0.5\ \mu\text{m}$.
- SC4500 Odd-Hour Evaporator for evaporating metal in a lift-off process. Example of the resulting metal pattern is shown in Figure 2b.
- PT72 Etcher to descum after development, and to remove the fluoropolymer skin after buffer oxide etch process.
- Oxford ALD FlexAl to deposit ALD Al_2O_3 on thin metal, which is the gate oxide.
- Disco Dicing Saw to dice quartz substrate.
- General chemical bench and other tools.

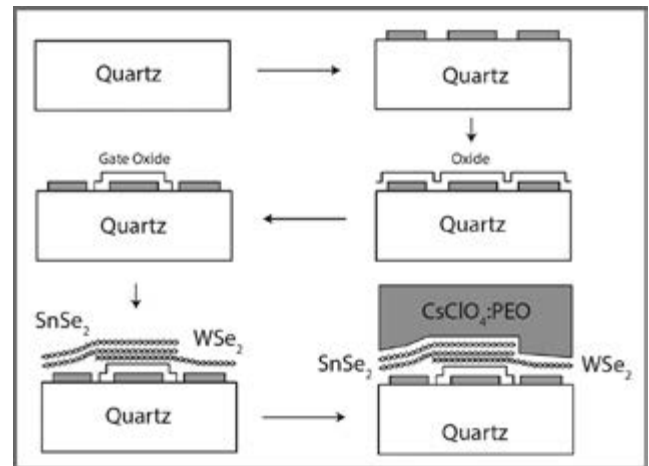


Figure 1: Process flow of two-dimensional heterojunction interlayer tunneling field effect transistor (Thin-TFET).

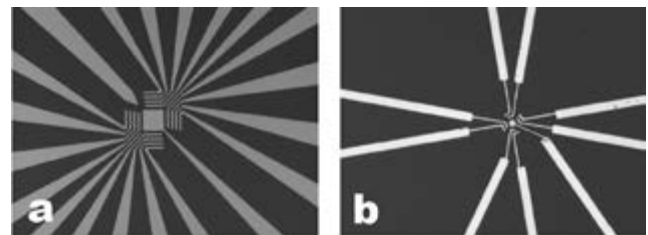


Figure 2: (a) An example mask from mask set 2 made by Heidelberg Mask Writer -DWL2000; (b) an example of finished bask contact metal patterns for mask set 1.

References:

- [1] Li, Mingda Oscar, et al. Electron Devices Society, IEEE Journal of the 3.3 (2015): 200-207.

Extreme Electron Density Devices

CNF Project Number: 2362-15

Principal Investigator: Debdeep Jena

Users: Amit Verma, Liheng Zhang

Affiliations: Electrical and Computer Engineering, Materials Science and Engineering; Cornell University

Primary Source of Research Funding: Extreme Electron Concentration Devices (EXEDE) MURI Program of the Office of Naval Research (ONR) through Grant No. N00014-12-1-0976

Contact: djena@cornell.edu, akv39@cornell.edu, lz388@cornell.edu

Abstract:

Two-dimensional electron gases (2DEGs) with extremely large electron density ($\sim 3.3 \times 10^{14} \text{ cm}^{-2}$) have been discovered recently at the heterointerface of two oxides like $\text{SrTiO}_3/\text{GdTiO}_3$, $\text{SrTiO}_3/\text{SmTiO}_3$, $\text{SrTiO}_3/\text{LaAlO}_3$ [1-3]. These high density 2DEGs are promising to realize next generation high-power devices and tunable plasmonic devices operating in mid infrared frequencies. In this project, we are optimizing processing of these materials and developing electronic devices like Schottky diodes, HEMTs and FinFETs fabricated on the thin films of these materials. Since the start of this project in June 2015, we have used CNF to optimize dry etching of SrTiO_3 , develop low contact resistance ohmic and low leakage Schottky contacts on SrTiO_3 . We have used the developed processes to realize Schottky diodes on $\text{SrTiO}_3/\text{SmTiO}_3/\text{LSAT}$ samples hosting extreme density 2DEGs and demonstrated a large 2DEG modulation of $\sim 8.5 \times 10^{13} \text{ cm}^{-2}$.

Summary of Research:

Strontium titanate (SrTiO_3) is both a gate dielectric and channel in $\text{SrTiO}_3/\text{RTiO}_3$ (R: Gd, Sm) devices. Therefore, as a first step, we studied the dry etching behavior of SrTiO_3 using inductively-coupled-plasma reactive-ion-etching (ICP-RIE) system, PT770R. BCl_3/Ar gas mixture was used to perform both chemical and physical etching. The etch rate of SrTiO_3 and its etching selectivity against Pt hard mask are measured using the Tencor P10 surface profilometer. The effects of various parameters like ICP power, chuck bias power (RIE power), chamber pressure and gas ratio on etch rate and selectivity are studied to find the best etching condition to achieve high-aspect-ratio features (ex., Fin structures to realize FinFETs).

Initially we faced the challenge of DC bias drift in ICP-RIE system due to insulating sapphire carrier wafer. After discussions with the CNF staff, we transferred the process to conducting GaAs carrier wafers and we were able to develop a repeatable SrTiO_3 dry etch process. Mesa features fabricated on $\text{SrTiO}_3/\text{SmTiO}_3/\text{LSAT}$ samples using this optimized process are shown in Figure 1. Very low mesa leakage of $\sim 10 \text{ fA/mm}$ was achieved using the developed process.

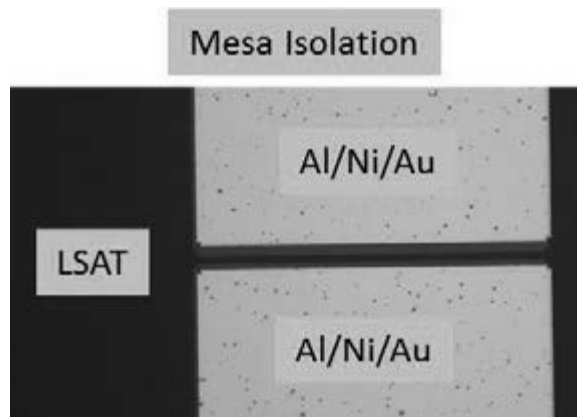


Figure 1: Optical image of the mesa-isolation test patterns fabricated on $\text{SrTiO}_3/\text{SmTiO}_3/\text{LSAT}$ samples.

Subsequently we developed Al/Ni/Au ohmic contact and Au Schottky contacts to SrTiO₃. The SrTiO₃/SmTiO₃/LSAT samples were patterned using optical lithography with the ABM contact aligner. Metals were then deposited using the e-beam evaporation system followed by liftoff. Circular Schottky diodes fabricated by this process are shown in Figure 2. Current-voltage (*I-V*) and capacitance-voltage (*C-V*) characteristics of the fabricated devices are shown in Figure 3 and Figure 4 respectively. We were able to obtain rectifying characteristics with low reverse leakage. From the *C-V* curves, we extracted the 2DEG modulation. A large 2DEG modulation of $\sim 8.5 \times 10^{13} \text{ cm}^{-2}$ was achieved.

In the future, we will be working to improve the ohmic contacts and developing three-terminal field effect transistor devices.

CNF Tools Used:

PT770R ICP-RIE etcher, ABM contact aligner, e-beam evaporator, Anatech resist strip, Tencor P-10 profilometer.

References:

- [1] A. Ohtomo and H. Y. Hwang, Nature 427, 423 (2004).
- [2] P. Moetakef, et al., Appl. Phys. Lett. 99, 232116 (2011).
- [3] J. Y. Zhang, et al., Phys. Rev. B 89, 075140 (2014).



Figure 2: Optical image of circular Au Schottky diodes fabricated on SrTiO₃/SmTiO₃/LSAT samples.

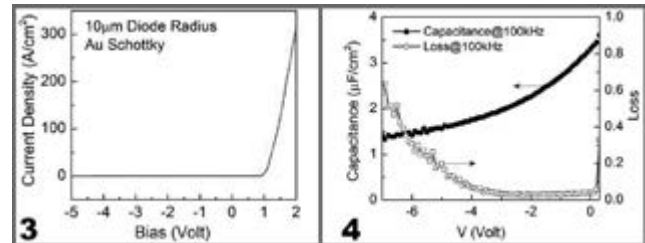


Figure 3, left: Rectifying current-voltage characteristics of the fabricated Schottky diodes. Figure 4, right: Capacitance-voltage characteristics of the Schottky diodes showing a large 2DEG modulation of $\sim 8.5 \times 10^{13} \text{ cm}^{-2}$.

Processing and Characterization of Wide-Bandgap Oxide Semiconductor Materials and Devices

CNF Project Number: 2428-16

Principal Investigator: Debdeep Jena

Users: Amit Verma, Nicholas Tanen, Liheng Zhang

Affiliations: Electrical and Computer Engineering, Materials Science and Engineering; Cornell University

Primary Source of Research Funding: NSF DMREF Program (Award Number 1534303)

Contact: djena@cornell.edu, akv39@cornell.edu, njt47@cornell.edu, lz388@cornell.edu

Abstract:

Wide bandgap semiconductors like gallium nitride (GaN) and silicon carbide (SiC) are promising to realize high-efficiency power switching devices. β -Ga₂O₃ is another wide bandgap semiconductor. It has a large energy bandgap of ~ 4.5-4.9 eV and an estimated high breakdown field of ~ 8 MV/cm [1]. These excellent material properties, suitable for high-power devices, along with recent availability of large area bulk β -Ga₂O₃ substrates grown using low cost melt-grown methods gives gallium oxide (Ga₂O₃) a competitive edge over other wide-bandgap semiconductors such as SiC and GaN [1]. In this project, we are developing the device processing technology for Ga₂O₃, along with an understanding of its heterostructures with other materials. With the developed processes and novel heterostructures, we aim to realize Ga₂O₃ high power devices. Since the start of this project in February 2016, we have used CNF to optimize dry etching of Ga₂O₃, and to develop ohmic and Schottky contacts to Ga₂O₃. We have also used the developed processes to realize Schottky diodes on Ga₂O₃ bulk substrates and AlN/Ga₂O₃ heterostructures.

Summary of Research:

To pattern materials in desired geometries and isolate devices on a chip, stable etching processes are needed. Therefore, we studied the dry etching behavior of β -Ga₂O₃ using an inductively-coupled-plasma reactive-ion-etching (ICP-RIE) system, PT770R. Using a BCl₃/Ar gas mixture, the etch rate of Ga₂O₃ and its etch selectivity against a photoresist mask are measured using the Tencor P10 surface profilometer. The effects of various parameters like ICP power, chuck bias power (RIE power), chamber pressure and gas ratio on etch rate and selectivity are studied to find the best etching condition. Etch rates exceeding ~ 50 nm/min were achieved. The etched patterns were characterized using scanning electron microscopy (SEM) and etched surface roughness was characterized using atomic force microscopy (AFM). Vertical sidewalls can be achieved using the optimized etch recipe as shown in the SEM image in Figure 1.

Subsequently we realized vertical Schottky diodes on two kinds of bulk <-201> β -Ga₂O₃ substrates, one Sn-doped ($n \sim 5 \times 10^{18} \text{ cm}^{-3}$) and another un-intentionally doped (UID) ($n \sim 10^{17} \text{ cm}^{-3}$).

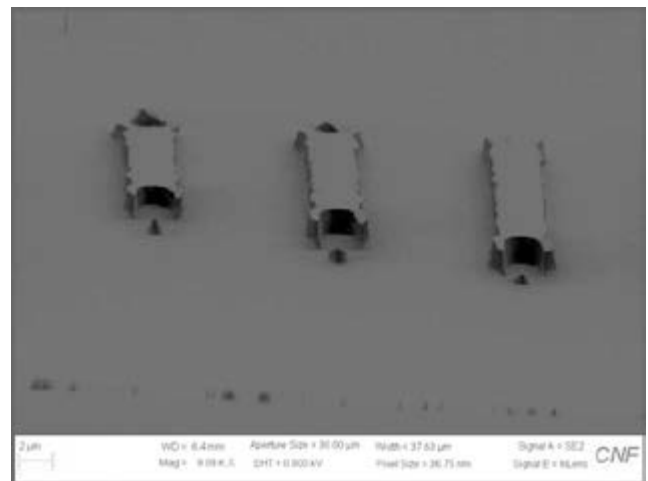


Figure 1: SEM image of etched features in β -Ga₂O₃ showing vertical sidewalls.

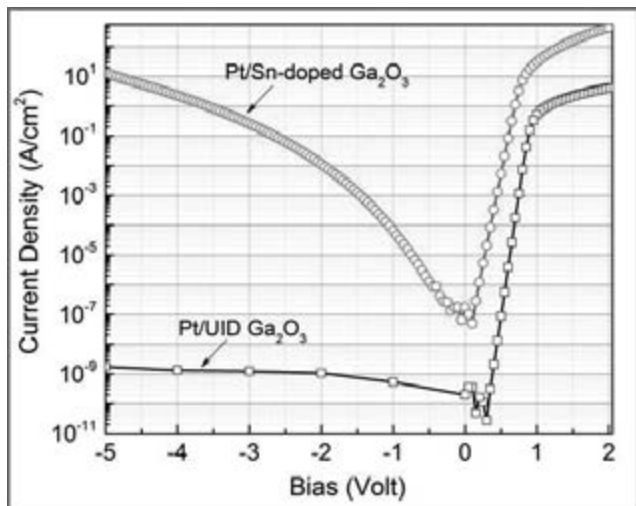


Figure 2: Current-voltage characteristics of Pt/Sn-doped Ga_2O_3 and Pt/UID- Ga_2O_3 Schottky diodes showing influence of Ga_2O_3 doping on diode forward and reverse characteristics.

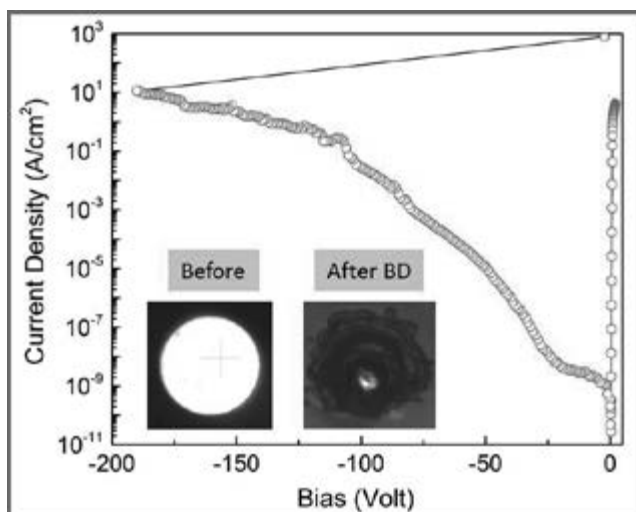
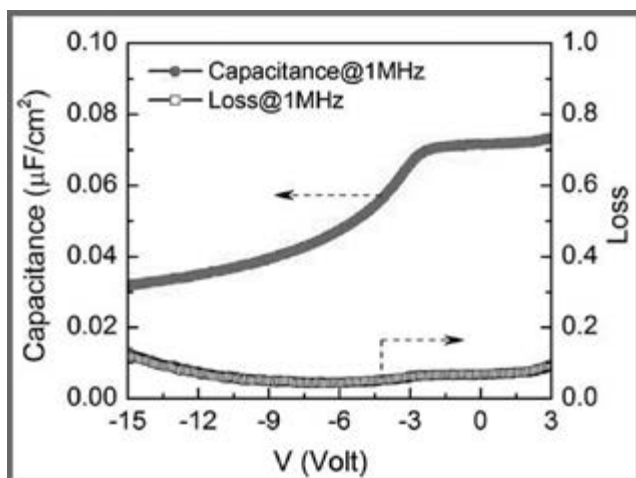


Figure 3: Reverse breakdown measurement on Pt/UID- Ga_2O_3 Schottky diode showing breakdown voltage approaching $\sim 200\text{V}$ (Inset: Optical image of the device before and after breakdown).



Diodes with four different Schottky metals (Pt, Ni, Au, Pd) were fabricated [2]. The Ga_2O_3 substrates were patterned using optical lithography with the ABM contact aligner. Metals were then deposited using the e-beam evaporation system followed by liftoff. Significant effects of doping were observed on Schottky diode current-voltage characteristics (Figure 2). In Pt Schottky diodes fabricated on UID- Ga_2O_3 substrates, we were able to obtain extremely low reverse leakage current and large reverse breakdown voltage (Figure 3).

We also studied AlN/ Ga_2O_3 heterointerfaces by fabricating vertical Schottky diodes and performing current-voltage (I - V) and capacitance-voltage (C - V) characterization [3]. Because of the polar $\langle 0001 \rangle$ orientation of AlN thin films, a two-dimensional electron gas (2DEG) is expected at the AlN/ Ga_2O_3 heterointerface. The constant value of capacitance observed in C - V of Pt/AlN/ Ga_2O_3 diodes confirms the presence of such a 2DEG [3].

Currently, we are working to improve the ohmic contacts with Ga_2O_3 and fabrication of vertical field effect transistor devices.

CNF Tools Used:

PT770R ICP-RIE etcher, Zeiss Ultra SEM, Veeco Icon AFM, ABM contact aligner, e-beam evaporator, Anatech resist strip, Tencor P-10 profilometer.

References:

- [1] M. Higashiwaki, et al., *Semicond. Sci. Technol.* 31, 034001 (2016).
- [2] A. Verma and D. Jena, "Vertical Schottky Barrier Diodes Fabricated on Un-intentionally Doped and Sn-doped $\langle -201 \rangle$ bulk β - Ga_2O_3 Substrates", *Compound Semiconductor Week (CSW 2016)*, June 2016, Toyoma, Japan (Accepted).
- [3] N. Tanen, A. Verma, S. M. Islam, L. Zhang, and D. Jena, "MBE growth and characterization of AlN thin films on bulk $\langle -201 \rangle$ β - Ga_2O_3 substrates", *North American Conference on Molecular Beam Epitaxy (NAMBE 2016)*, September 2016, Saratoga Springs, New York, USA (Submitted).

Figure 4, at left: Capacitance-voltage characteristics of the Pt/AlN/ Ga_2O_3 Schottky diodes suggesting presence of a 2DEG at AlN/ Ga_2O_3 heterointerface.

SAW Devices with Piezoresistive Graphene Pickup

2016 CNF REU Intern: Allison Smith, Electrical Engineering, Wilkes University

CNF REU Principal Investigator: Professor Amit Lal, Electrical and Computer Engineering, Cornell University

CNF REU Mentors: Benyamin Davaji, Electrical and Computer Engineering, Cornell University;

Alexander Ruyack, Electrical and Computer Engineering and Materials Science, Cornell University

Primary Source of Research Funding: National Science Foundation under Grant No. ECCS-1542081

Contact: allison.smith@wilkes.edu, amit.lal@cornell.edu, bendavaji@cornell.edu, arr68@cornell.edu

Abstract:

Surface acoustic wave (SAW) devices are used as filters in communication systems, and are also being investigated to realize Coriolis force based gyroscopes. This study presents the fabrication and measurements of SAW devices using an added graphene electrode for SAW measurement using the piezoresistive and direct electrical induction. This pickup was added to the SAW delay line interdigital transducer (IDT) structure in order to enhance the sensitivity of wave amplitude measurement. These devices were fabricated on a piezoelectric crystal substrate (lithium niobate, LiNbO_3). The devices in this study were designed for a 200 MHz center frequency, and Y-cut 128° LiNbO_3 crystals were used as the piezoelectric substrate with a $\sim 20 \mu\text{m}$ wavelength.

Background:

Hosseinadegan, et al. (engineers of the SonicMEMS Lab at Cornell University), have previously reported a high gauge factor of a piezoresistive graphene sensor for the first time [1]. The gauge factor (GF) is a measure of the piezoresistivity of a material. Based on the published work [1], the GF of graphene that was placed on top of electrodes was measured to be around 18,000, which is two orders of magnitude larger than any commercialized materials (single crystal silicon has the highest commercial GF at about 200).

Another study by Roshchupkin, et al. [2], showed that when a constant voltage is applied to electrodes with graphene over them, at some point when a SAW propagated through the graphene, the current measured zero. The SAW applies stress in the form of tension and compression to two electrodes, each of which generates a charge that is equal and opposite to the other. This difference in charges is what would allow the net current to reach zero. A change in charge carrier concentration also means there is a change in resistance that relates back to the phenomenon of the high gauge factor that was seen. Our study aims to conduct a similar experiment that will allow us to study this effect, in hopes of acquiring initial measurements of piezoresistivity using a piezoresistive graphene electrode pickup.

Summary of Research:

Both metal etching and lift-off photolithography processes were used to pattern metal electrodes on the substrates. Due to the piezoelectric and pyroelectric properties of the LiNbO_3 crystals, complications occurred during the photolithography process that caused defects in the devices. Hence, the metal etching process showed better yield. In addition, for metal etching, both wet and plasma etching techniques were used for etching the metal (Al/Ti) thin films. For our measurements, we used devices that were wet etched because that is when the best uniformity across the wafer occurred for the given feature sizes and crystal properties.

Two different types of devices were tested for this study. One was a SAW gyro-drive delay line, and the second device was one with a piezo-resistive graphene pick-up. Two types of measurements were conducted. Frequency domain measurements were performed on the gyro devices and the resulting data is plotted in Figure 1. This plot represents the ratio of power transfer for the device from the input to output over a range of frequencies. There is a peak at ~ 197.5 MHz, which is close to the designed value of 200 MHz.

Time domain measurements were performed for both the gyro device and the graphene device. Figure 2 is the resulting plot for the gyro, and we can see a clear

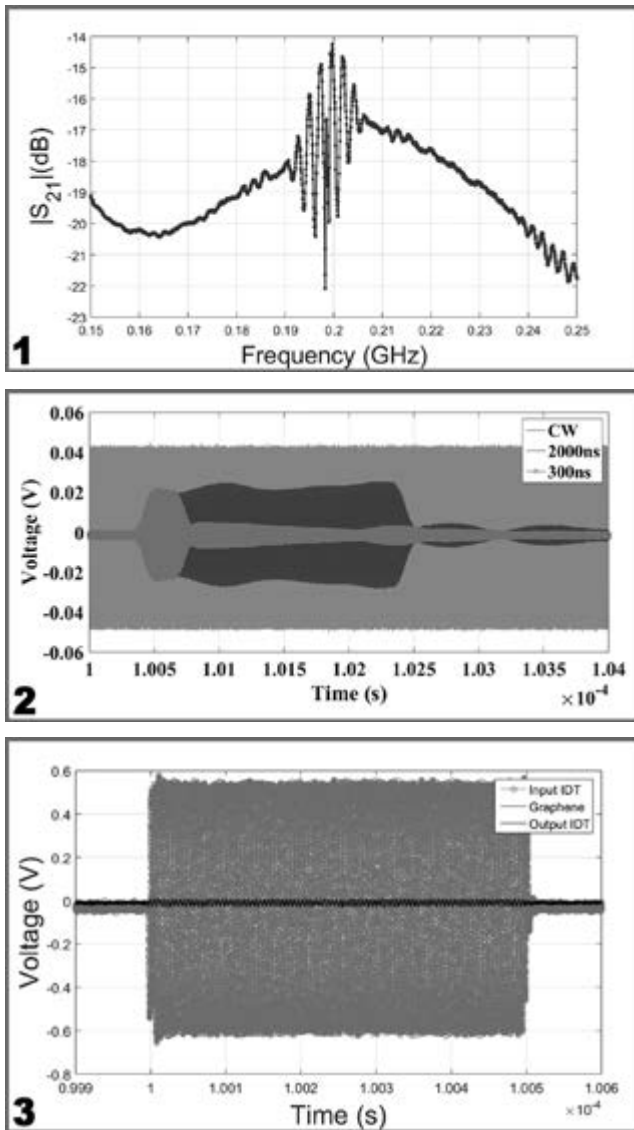


Figure 1, top: Plot of frequency domain measurements for gyro device. **Figure 2, middle:** Plot of pulsed wave input time domain measurements for gyro device. **Figure 3, bottom:** Plot of pulsed wave input time domain measurements for graphene device.

difference in voltage amplitude from the continuous wave response to the pulsed wave response, regardless of pulse width. The distorted pulsed wave output signals can be accounted for by standing waves formed by reflections of the SAW wave from the edges of the device. Figure 3 is the resulting plot for the graphene device. This plot shows the input IDT voltage, the output IDT voltage, and the graphene active probe voltage over time. It is evident from this plot that the graphene pickup shows an increased output voltage as compared to the output IDT.

Conclusions and Future Work:

The graphene probe detected a higher output voltage as compared to the output IDT, which suggests that the graphene pickup has an increased sensitivity in measuring SAW amplitudes. Further tests must be completed to confirm this and determine the mechanism of action. However, if this is confirmed, it may be possible to exploit the high gauge factor that was previously seen for further voltage amplification.

Impedance matching using the graphene pickups will significantly improve the device performance and should be considered as one of the next steps in this research. Furthermore, replacing the metal IDT electrodes with graphene electrodes could increase the SAW wave generation efficiency. These electrodes can be created using photolithography and oxygen plasma etching.

CNF Tools Used:

SUSS MicroTech MA/BA 6 contact aligner, SC4500 odd-hour evaporator, Oxford PlasmaLab 80+ RIE system, PT720-740 etcher, DISCO dicing saw, Westbond 7400A ultrasonic wire bonder.

Acknowledgements:

This material is based upon work supported by the National Science Foundation under Grant No. ECCS-1542081. This work made use of the Cornell NanoScale Science & Technology Facility, the Cornell Center for Materials Research Shared Facilities, which are supported through the NSF MRSEC program (DMR-1120296), and the SonicMEMS Lab at Cornell. I would like to thank my Principal Investigator, Professor Amit Lal, and my mentors, Alex and Ben, and all of the CNF staff and the CNF REU program coordinators for their guidance and encouragement this summer.

References:

- [1] Hosseinzadegan, H., Todd, C., Lal, A., Pandey, M., Levendorf, M., and Park, J. (2012, January). Graphene has ultra high piezoresistive gauge factor. In Micro Electro Mechanical Systems (MEMS), 2012 IEEE 25th International Conference on (pp. 611-614). IEEE.
- [2] Roshchupkin, D., Ortega, L., Zizak, I., Plotitsyna, O., Matveev, V., Kononenko, O., and Insepov, Z. (2015). Surface acoustic wave propagation in graphene film. *Journal of Applied Physics*, 118(10), 104901.

Millisecond Crystallization Kinetics of $\text{InGaO}_3(\text{ZnO})_m$

CNF Project Number: 150-82

Principal Investigator: Michael O. Thompson

Users: Kate E. Roach, David M. Lynch

Affiliation: Department of Materials Science and Engineering, Cornell University

Primary Source of Research Funding: Corning, Inc.

Contact: mot1@cornell.edu, ker79@cornell.edu, dml346@cornell.edu

Website: <http://thompson.mse.cornell.edu/>

Abstract:

$\text{InGaO}_3(\text{ZnO})_m$ alloys display natural superlattices that have previously only been grown with high temperature ($>1,000^\circ\text{C}$), long-duration anneals. In this work, we study the formation of these structures using co-sputtering of IGZO and ZnO, and laser spike annealing (LSA). Compositions from pure $\text{In}_2\text{Ga}_2\text{ZnO}_7$ to pure ZnO were explored with peak temperatures from 600°C to 1400°C and dwell times of $150\ \mu\text{s}$ to 10 ms. The kinetics of crystallization were studied using micro-wide-angle x-ray scattering with an $\sim 20\ \mu\text{m}$ FWHM beam. Using the single-scan LSA methods, structural changes as a function of the peak annealing temperature and dwell time were analyzed and the onset of crystallization was determined. Our results indicate that as-deposited Zn-rich films form nanocrystallites that are unstable and transform after annealing to equilibrium phases with lower Zn content. Activation energies for crystallization were determined to range from 1.5 to 4 eV depending on the Zn content. The increase in activation energy with higher Zn content indicates that excess Zn acts as a barrier to the growth of the equilibrium phases. We propose that the as-deposited structure of the Zn-rich films resembles a compositionally-disordered structure with locally random distributions of atoms that form cohesive layers at high temperatures.

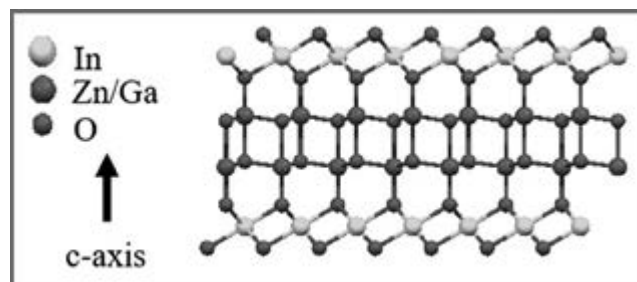


Figure 1: Ball and stick model of InGaZnO_4 ($m = 1$, phase I).

Summary of Research:

Single-crystalline $\text{InGaO}_3(\text{ZnO})_5$ has been demonstrated as an effective thin film transistor (TFT), with a field-effect mobility of $80\ \text{cm}^2/\text{Vs}$ [1]. Fabrication of this and other superlattice structures has been achieved using $>1,000^\circ\text{C}$, 9-hour furnace annealing [2,3], as well as reactive solid phase epitaxy with furnace annealing

[1,4]. In this work, we study the formation of these superlattice structures using co-sputtered IGZO and ZnO with laser spike annealing (LSA). Equilibrium phases of $m = 1, 2, 3 \dots$ will be referred to as phase I, II, III \dots . The superlattice structures are composed of InO_6 layers with $m + 1$ Zn/Ga-O_5 layers between, an example of which is shown in Figure 1.

Thin films were deposited using RF magnetron sputtering at room temperature with ZnO and $\text{In}_2\text{Ga}_2\text{ZnO}_7$ targets on SiO_2 substrates. Compositions including $m = 0.45$ ($\text{InGaO}_3(\text{ZnO})_{0.45} = \text{In}_2\text{Ga}_2\text{ZnO}_7$), $m = 0.71$, $m = 1.36$, $m = 2.63$, $m = 3.94$, $m = 5.96$ and $m = \infty$ (ZnO) were studied. To determine if film thickness impacted the superlattice formation, the substrate with film composition of $m = 3.94$ was not rotated during deposition, resulting in a thickness gradient from 40 nm to 220 nm. The thickness of the gradient film was measured using a Filmetrics F40 reflectometer. For the other homogeneous films, thickness was measured using a Tencor P10 stylus profilometer.

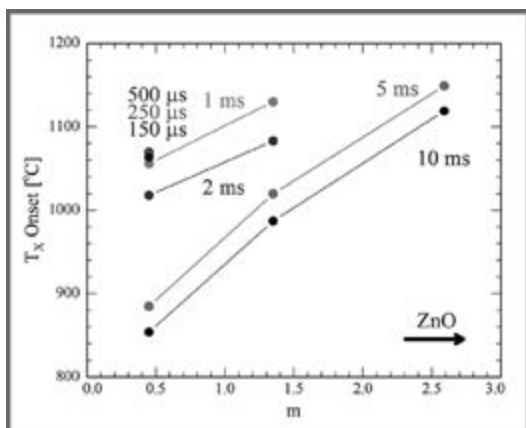


Figure 2: Crystallization temp as a function of m .

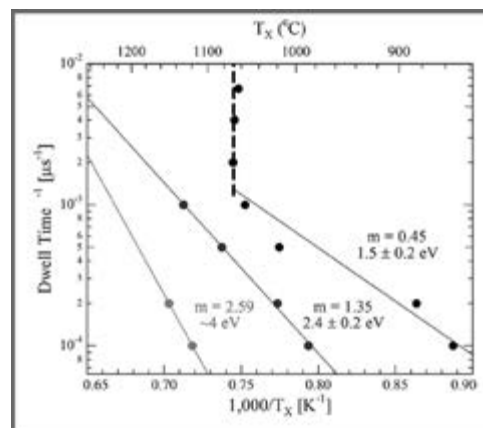


Figure 3: Inverse dwell time as a function of inverse crystallization temperature to determine activation energy.

Laser spike annealing was performed using a CO₂ laser on each film composition with peak temperatures from 600°C to 1,400°C and annealing durations from 150 μm to 10 ms. Film structure was characterized using micro-wide-angle x-ray diffraction at the Cornell High Energy Synchrotron Source with an ~ 20 μm FWHM beam width.

We found that the film compositions with $m < 2.63$ exhibited an amorphous IGZO (a-IGZO) structure as-deposited and formed phase I after LSA. Zn-rich films ($m \geq 2.63$) formed nanocrystallites as-deposited with diffraction patterns that do not match any known structures. After LSA, $m = 2.63$ formed phase I, $m = 3.94$ formed phase II, $m = 5.96$ formed phase II at lower temperatures and phase III at higher temperature, and $m = \infty$ remained as the as-deposited structure. To study the crystallization kinetics, the films that formed phase I were studied to determine the impact of zinc (Zn) on the crystallization temperature.

Figure 2 shows the onset of crystallization temperature (T_x) as a function of m . T_x is seen to increase with m , indicating that the increased Zn content inhibits the formation of phase I. Additionally, activation energies can be determined from the Arrhenius behavior of the inverse dwell time. Figure 3 shows how the activation energies for each film composition were calculated.

The increasing activation energy with Zn content again indicate that the increased Zn inhibits the formation of phase I. Near 1,070°C, the film composition of $m = 0.45$ exhibits a 'liquid-like' region of increased kinetics.

We propose that the Zn-rich films form compositionally distorted structures with atomically random arrangements as-deposited, with no superlattice structure. As the temperature increases during LSA, indium (In) atoms gain enough mobility to form cohesive layers, and the superlattice structure is formed. Indium layers are formed more easily with In-rich films, which is why the activation increases with increasing m values. For sufficiently long annealing durations, we predict the formation of an equilibrium structure with In layer spacing reflecting the overall film composition.

References:

- [1] K. Nomura, et al., Science 300(5623), 1269-1272 (2003).
- [2] D.K. Seo, et al., Acta Mater. 59(17), 6743-6750 (2011).
- [3] D.K. Seo, et al., Cryst. Growth Des. 10(10), 4638-4641 (2010).
- [4] K. Nomura, et al., J. Appl. Phys. 95(10), 5532-5539 (2004).

Recent Progress in Nanoparticle Photoresist Development for EUV Lithography

CNF Project Number: 386-90

Principal Investigator: Christopher K. Ober

User: Kazuki Kasahara

Affiliation: Department of Materials Science and Engineering, Cornell University

Primary Source of Research Funding: JSR Corporation

Contact: cko3@cornell.edu, kk855@cornell.edu

Website: <http://ober.mse.cornell.edu/>

Abstract:

Extreme ultraviolet (EUV) lithography is a promising candidate for next generation lithography. For high volume manufacturing of semiconductor devices, significant improvement of resolution and sensitivity is required for successful implementation of EUV resists. Performance requirements for such resists demand the development of entirely new resist platforms. The Ober group at Cornell University has intensely studied metal oxide nanoparticle photoresists with high sensitivity for EUV lithography applications. In this report, recent progress in metal oxide nanoparticle photoresist research will be discussed.

Summary of Research:

Currently, the industry has been relying on 193 nm immersion lithography with multi patterning to print fine features on resist materials. Extreme ultraviolet (EUV) lithography is anticipated to succeed 193 nm immersion lithography to meet the demands of the sub-10 nm node [1]. However, owing to challenges that need to be addressed such as low EUV source power and the resolution / line width roughness / sensitivity (RLS) tradeoff, EUV lithography has not yet been applied to the semiconductor industry.

To improve EUV resist performance, many groups have focused on the development of EUV resists with novel materials [2]. At Ober group in Cornell University, a hybrid nanoparticle system comprising a metal oxide core and an organic shell has been developed [3]. To date, the group has focused on largely one photoacid generator (PAG) as an additive in the vast majority of its studies. At this time, photobase generators (PBG) and new PAG applications were investigated for nanoparticle photoresist performance improvement.

From previous studies, one of the plausible patterning mechanisms of nanoparticle photoresists is a ligand exchange with the stronger binding photoacid that is generated from the photoacid generator [4]. And another plausible patterning mechanism is a condensation reaction between nanoparticles [5]. Related to the second plausible mechanism, in general,

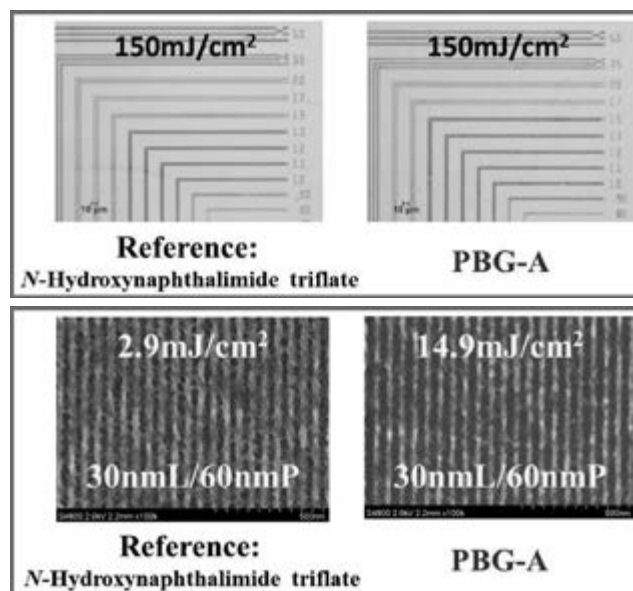


Figure 1, top: PBG evaluation result with ABM contact aligner.

Figure 2, bottom: PBG evaluation result with EUV exposure.

sol-gel condensation reaction can be catalyzed by base compounds. To explore this possibility, PBG was applied to a zirconium type nanoparticle photoresist. The resist solution contained 5% nanoparticles, 5% PAG or PBG (per nanoparticles) and PGMEA as a

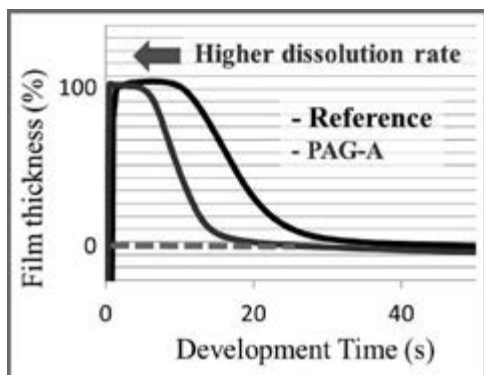


Figure 3: QCM evaluation result.

solvent. The resist was spin-coated onto a silicon wafer at 2,000 rpm for 60 sec to obtain a thin and uniform film. The film was exposed with the ABM contact aligner in CNF. Alcohol solvent was used for the developer. As demonstrated in the optical microscope pattern in Figure 1, negative tone patterns have been obtained with PBG-A. The microscale pattern quality of PBG-A is similar to that of reference PAG.

For the next step, EUV lithography was tested with the Berkeley microfield exposure tool (B-MET) at the Lawrence Berkeley National Lab (LBNL).

A 30 nmL (line) / 60 nmP (pitch) pattern was observed with the same samples described above. Using a PBG application instead of PAG worked well for EUV lithography patterning. Pattern resolution using PBG-A seemed to be better than reference PAG (N-hydroxynaphthalimide triflate). Though sensitivity with PBG-A was slightly slower than PAG, sensitivity below 20 mJ/cm² was definitely faster than traditional polymer type photoresists.

A new PAG study was also carried out — zirconium type nanoparticle photoresists with reference PAG (N-hydroxynaphthalimide triflate) and new higher dissolution rate PAG-A were tried. Higher solubility of PAG-A than reference PAG was confirmed with quartz crystal microbalance (QCM) evaluation as shown in Figure 3. Alcohol solvent was used for this test.

Electron-beam (e-beam) and EUV lithography tests were carried out with reference PAG and higher solubility PAG-A. The resist solution contained 5% nanoparticles, 5% PAG (per nanoparticles) and PGMEA as a solvent. The resist was spin-coated onto a silicon wafer. The film was exposed with the JEOL JBX9500FS e-beam lithography system in CNF and LBNL B-MET.

Figure 4 shows a 50nmL/100nmP pattern with e-beam exposure and 30nmL/60nmP with EUV exposure.

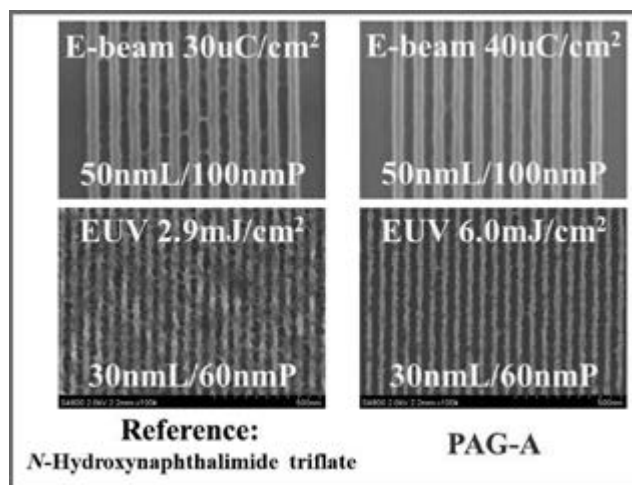


Figure 4: PAG evaluation result with e-beam and EUV exposure.

As shown in Figure 4, high dissolution rate PAG-A showed better resolution compared to reference PAG with both e-beam and EUV exposures. This result shows PAG structure and properties strongly affect lithographic performance for nanoparticle photoresists. Especially, PAG dissolution rate seems to affect nanoparticle photoresist EUV lithography performance improvement.

In this report, nanoparticle photoresist development containing new materials such as PBG and higher solubility PAG were described. From this study, we understand that nanoparticle photoresist EUV lithography performance can be improved from composition modification like PBG or higher solubility PAG use. Nanoparticle photoresists have a great deal of room for EUV lithography performance improvement.

References:

- [1] ITRS website, <http://www.itrs.net>
- [2] H. Nakagawa, T. Naruoka, T. Nagai, "Recent EUV Resists toward High Volume Manufacturing," *J. Photopolym. Sci. Technol.* 27(6), 739-746 (2014).
- [3] M. Trikeriotis, W. J. Bae, E. Schwartz, M. Krisak, N. Lafferty, P. Xie, B. Smith, P. Zimmerman, C. K. Ober, E. P. Giannelis, "Development of an inorganic photoresist for DUV, EUV, and electron beam imaging," *Proc. SPIE* 7639, 76390E1-76390E10 (2010).
- [4] M. Krysak, M. Trikeriotis, C. Ouyang, S. Chakrabarty, E. Giannelis, C. K. Ober, "Nanoparticle Photoresists: Ligand Exchange as a New and Sensitive EUV patterning Mechanism," *J. Photopolym. Sci. Technol.* 26(5), 659-664 (2013).]
- [5] L. Li, S. Chakrabarty, K. Spyrou, C. K. Ober, E. P. Giannelis, "Studying the Mechanism of Hybrid Nanoparticle Photoresists: Effect of Particle Size on Photopatterning," *Chem. Mater.* 27, 5027-5031 (2015).

Oxide Nanoparticle EUV (ONE) Photoresist Studies

CNF Project Number: 386-90

Principal Investigator: Christopher K. Ober

User: Hong Xu

Affiliation: Department of Materials Science and Engineering, Cornell University

Primary Source of Research Funding: JSR Corporation

Contact: cko3@cornell.edu, hx49@cornell.edu

Website: <http://ober.mse.cornell.edu/>

Abstract:

With the rapid development of semiconductors, today's optical lithography is reaching its physical limits, and thus alternative patterning technology is urgently desired to push chip manufacturing forward. Extreme ultraviolet (EUV) lithography, using a wavelength of 13.5 nm, is considered to be one of the most prominent candidates for next generation lithography. Prior work on metal oxide nanoparticles have shown outstanding performance using EUV exposure. However, the design of novel EUV photoresists with the properties of low line edge roughness (LER), high resolution and sensitivity conforming to industrial requirements remains a challenge. Here, we demonstrate a novel zinc oxide based nanoparticle photoresist, which possesses excellent performance under both deep ultraviolet (DUV) and electron-beam (e-beam) exposure, and serves as a promising candidate for EUV lithography.

Summary of Research:

Utilizing either zirconium or hafnium oxide (ZrO_2 or HfO_2), the Ober group has developed a series of hybrid nanoparticles composed of an inorganic core with ZrO_2 or HfO_2 and various organic ligands. These hybrid nanoparticles demonstrated excellent patterning capacity under EUV exposure [1,2]. To further improve the resolution limit and EUV sensitivity, this work is focused on synthesizing and testing new nanoparticles based on zinc oxide (ZnO).

Zinc has shown higher EUV photo-absorption over both zirconium and hafnium, thus having a higher potential to achieve the high-sensitivity desired for EUV lithography. With similar approaches we used for ZrO_2 and HfO_2 , two carboxylic acid ligands, benzoic acid (BA) and *m*-toluic acid (*m*TA) were utilized to stabilize the ZnO core. The resulting zinc oxide-benzoic acid (ZnO-BA) and zinc oxide-*m*-toluic acid (ZnO-*m*TA) nanoparticles demonstrate very good solubility in propylene glycol monomethyl ether acetate (PGMEA) and other common organic solvents, such as ethanol, acetone, and ethyl acetate. Furthermore,

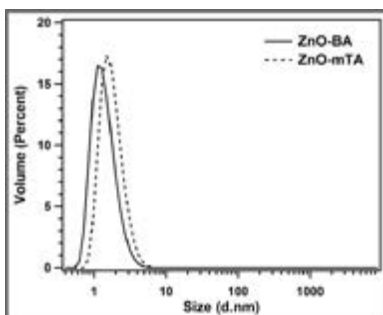


Figure 1: DLS spectra of ZnO-BA and ZnO-*m*TA nanoparticles.

dynamic light scattering (DLS) measurements (Figure 1) showed that both ZnO-BA and ZnO-*m*TA are monodisperse, with a particle size of 1.2 nm and 1.5 nm, which were smaller than our previously reported ZrO_2 and HfO_2 based nanoparticles (3-4 nm) [3]. The small particle size (1-2 nm) gives these nanoparticles the possibility to achieve high resolution and low LER in lithography.

Deep Ultraviolet (DUV) Lithography.

After physical characterization of the nanoparticles, preliminary lithographic evaluations were carried out using the CNF ASML stepper (248 nm KrF laser). The resist test formulation contains 5 wt% nanoparticles, 0.25 wt% of N-hydroxynaphthalimide triflate as photo-acid generator (PAG), and PGMEA as solvent. The resist was spin-coated onto a silicon wafer at 2000 rpm for 1 min and then soft baked on the hot plate at 110°C for 1 min. The film was then exposed with 248 nm DUV at 150 mJ/cm². Development was conducted immediately after exposure using decahydronaphthalene as developer.

Well-defined negative tone patterns were obtained for both ZnO-BA and ZnO-*m*TA nanoparticles, as indicated from scanning electron microscope (SEM) images (Figure 2), taken using the CNF Zeiss Ultra SEM. Developed by decahydronaphthalene for 15 sec, the ZnO-BA based photoresist showed 1:1 line-and-space patterns with the feature size from 500 nm (Figure 2A) to 250 nm (Figure 2B), which corresponded well to their target pattern features. Similar patterns (Figure 2C and 2D) were obtained by ZnO-*m*TA nanoparticles developed by decahydronaphthalene. No bridging problems or residue were observed on the unexposed areas (space area), meanwhile pattern loss was also shown to be negligible. Thus ZnO-BA and ZnO-*m*TA based photoresists possess very good DUV lithographic performance with low line edge roughness, and high resolution, almost reaching the limit of the mask (250 nm).

Electron-Beam Lithography. In order to explore the lithographic potential under higher resolution, ZnO-BA and ZnO-*m*TA nanoparticles were further characterized with electron-beam (e-beam) lithography, utilizing the CNF JEOL JBX9500FS electron beam lithography system. The resist test formulation contains 5 wt% nanoparticles, 0.5 wt% of N-hydroxynaphthalimide triflate as PAG, and PGMEA as the solvent. The resist was spin-coated onto a silicon wafer at 2000 rpm for 1 min and then soft baked on the hot plate at 110 °C for 1 min. The ZnO-BA film was exposed with e-beam at 100 $\mu\text{C}/\text{cm}^2$, and then developed by decahydronaphthalene for 15 sec. SEMs (Figure 3) showed 1:1 line-and-space patterns (in the middle area of each image) with the feature size from 50 nm, 45 nm, 40 nm to 35 nm, which corresponded well to their target pattern features. Residues can be found in the unexposed areas in Figures 3A-D, meanwhile a bridging problem occurred in the 40 nm and 35 nm dense patterns. Remarkably, if the organic ligand shells were slightly changed, from benzoic acid to methyl-substituted *m*-toluic acid, the lithographic performance was significantly improved: the developing time was decreased from 15 sec to 4 sec, meanwhile on the unexposed area the residue issues were completely resolved. As illustrated in Figure 4, the SEM images demonstrate good 1:1 dense patterns with the feature size from 50 nm to 35 nm, without any bridging problems.

The zinc oxide based nanoparticles possess good patterning performance under DUV and e-beam exposures, which are comparable or better than previously reported zirconium/hafnium oxide based nanoparticles [2]. Meanwhile, considering its higher EUV photo-absorption nature, this preliminary work indicates such zinc-based nanoparticles are promising candidates for EUV lithography.

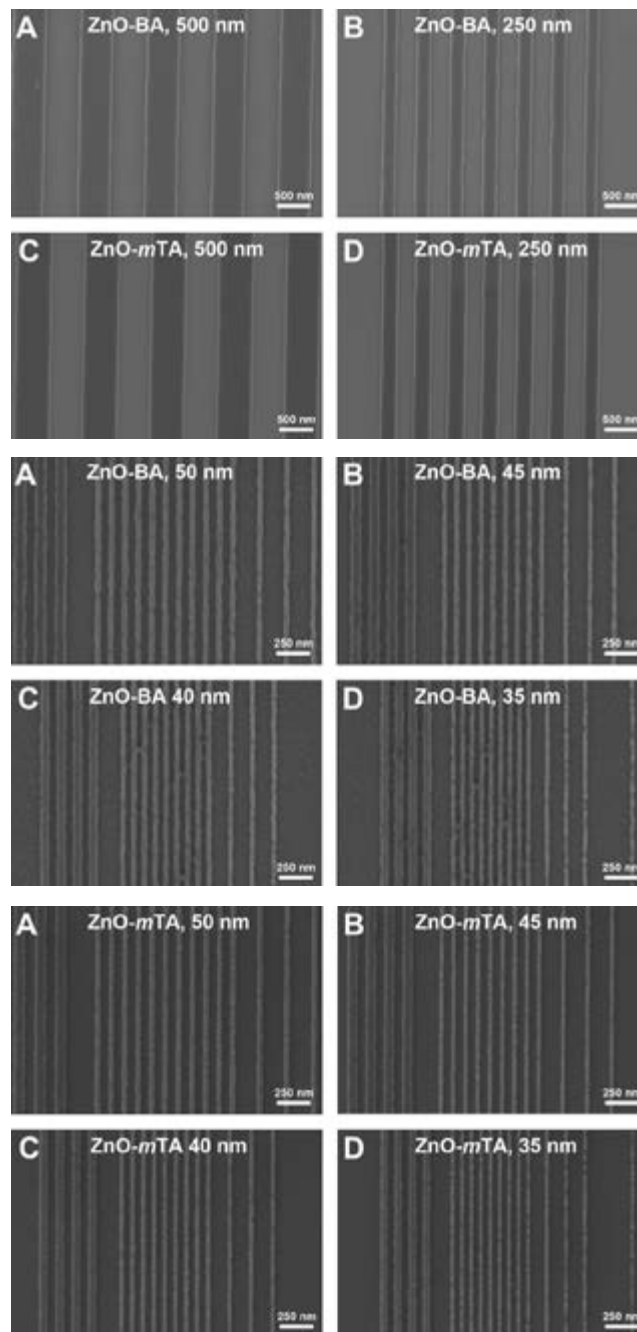


Figure 2: SEMs of DUV patterns of ZnO-based nanoparticles.

Figure 3: SEMs of e-beam patterns of ZnO-BA nanoparticles.

Figure 4: SEMs of e-beam patterns of ZnO-*m*TA nanoparticles.

References:

- [1] Trikeriotis, M.; Krysaki, M.; Chung, Y. S.; Ouyang, C.; Cardineau, B.; Brainard, R.; Ober, C. K.; Giannelis, E. P.; Cho, K., J. Photopolym. Sci. Technol. 2012, 25, 583-586.
- [2] Ouyang, C. Y.; Chung, Y. S.; Li, L.; Neisser, M.; Cho, K.; Giannelis, E. P.; Ober, C. K., Proc. SPIE 2013, 8682, 86820R.
- [3] Li, L.; Chakrabarty, S.; Spyrou, K.; Ober, C. K.; Giannelis, E. P., Chem. Mater. 2015, 27, 5027-5031.

Electrical Annealing of Thin Films Using Nanocalorimetry

CNF Project Number: 522-94

Principal Investigator: Leslie H. Allen

User: Zichao Ye

Affiliation: Materials Science and Engineering, University of Illinois at Urbana-Champaign

Primary Source of Research Funding: National Science Foundation Division of Materials Research (#1409953, #1006385 and #0735286); University of Illinois Research Board (#13187)

Contact: l-allen9@illinois.edu, zye3@illinois.edu

Website: <http://allen.matse.illinois.edu>

Abstract:

A new functionality of electrical annealing is coupled with the original nanocalorimetry system for thin film annealing. Unlike the conventional calorimetric scanning, electrical annealing performed by nanocalorimetry demands a maximum temperature (T_{max}) that is smaller than the melting point (T_m) of the sample. As compared with the conventional furnace annealing, electrical annealing can achieve similar quality of annealed films, but is faster as well as more accurate in temperature control. Electrical annealing is potentially an alternative to furnace annealing in the application of thin film growth.

Summary of Research:

Nanocalorimetry, developed in our group, is a unique chip-based technique due to its ultra-fast heating rate (5k-20k K/s) as well as high sensitivity (0.1 nJ/K). This enables a measurement of thermodynamic properties of very small amount of nanoscale materials (< 100 pmol).

Nanocalorimetry sensor (Figure 1a) is fabricated on a silicon wafer (500 μm) with a platinum metal patterned (50 nm) silicon nitride membrane (100 nm) on top, constituting the low thermal mass calorimetric cell. The metal strip serves both as a heater when current pulses are applied, and as a thermometer whose temperature coefficient of resistance (TCR) are calibrated before any experiment. Samples are deposited on the opposite side of metal thin film. Temperature scans are achieved by joule heating of sensors via a 4-point setup (Figure 1b).

A new functionality of electrical annealing is developed for thin film growth. Electrical annealing is achieved by heating nanocalorimetry samples using the same hardware as is used for regular calorimetric scanning. Electrical annealing is controlled by a series of current pulses whose magnitude and pulse duration are well-adjusted so that the maximum temperature

achieved is lower than sample T_m . In this way, the sample will be annealed, rather than melted. For a material with a certain T_m , Figure 1c and 1d compare the temperature profiles of a regular calorimetric scan and multiple electrical annealing scans. The cooling traces of the curves are estimated using Newton's Law of cooling. Thin film growth is induced by repeating

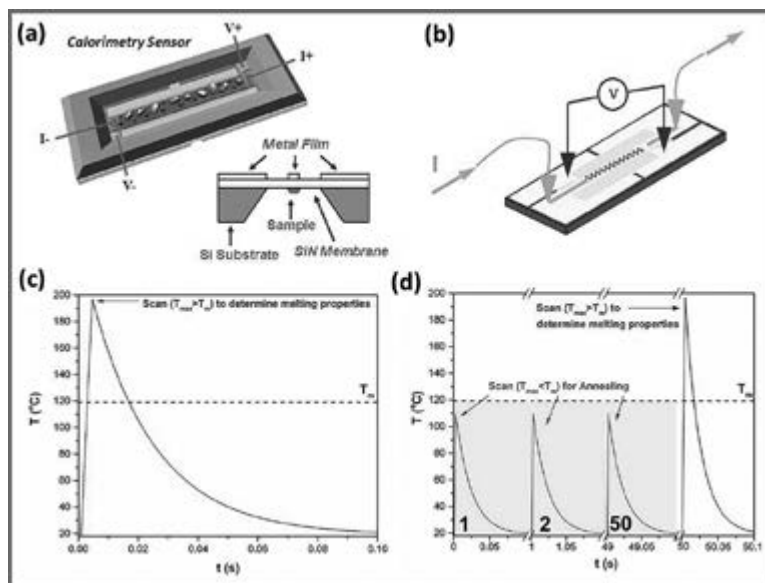


Figure 1: (a) Schematics of nanocalorimetry sensor; (b) 4-point setup for nanocalorimetry measurement; (c) and (d) show the temperature profiles of a calorimetric scan and electrical annealing scans, respectively.

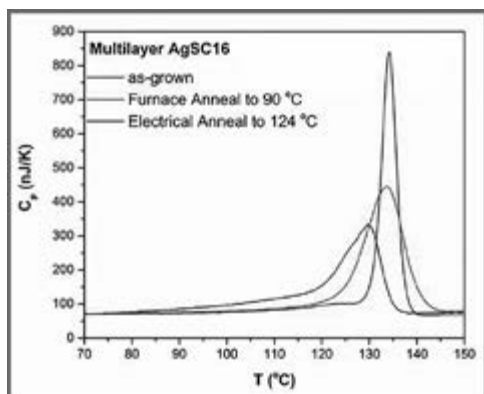


Figure 2: Melting curves for as-grown, furnace annealed and electrically annealed AgSC_{16} lamellae.

such electrical annealing pulses. Unlike electrical annealing, conventional furnace annealing of thin film is performed by transferring into a vacuum oven where sample heating occurs with extremely slow heating rates of less than 1 K/min. Due to the large thermal mass of the furnace, thermal lag between measured temperature and sample temperature is inevitable. Temperature control in furnace is not as accurate as the electrical annealing with extremely low thermal mass.

Figure 2 compares the effects of electrical annealing and furnace annealing on the crystal growth of silver hexadecanethiolate ($\text{AgSC}_{16}\text{H}_{33}$ or AgSC_{16}) lamellae. The black curve shows the melting behavior of as-grown AgSC_{16} crystals before annealing ($T_m = 129.8^\circ\text{C}$). The red and blue curves represent the first calorimetric scans on annealed AgSC_{16} films after electrical annealing to 124°C or furnace annealing to 90°C , respectively. Both annealing temperatures are lower than sample T_m , so that only layer crystallization and film growth is occurring during annealing, and no material melts. Based on the size-effect melting, the increase of T_m after annealing infers the pile up of as-grown AgSC_{16} lamellae, forming multilayer crystals.

The similarity of T_m and H_m between furnace annealed and electrically annealed samples indicates their equivalence. The major difference of the two annealed crystals is the FWHM of melting peaks. Electrical annealing significantly narrows the FWHM to 3.6°C , which approaches the limit of instrumentation broadening; whereas furnace annealed crystals with a larger FWHM value imply various dispersions of layer thicknesses, indicating only a rough control of layer stacking during furnace annealing. Therefore, electrical annealing is potentially more accurate in crystal-layer-control and is a possible alternative to furnace annealing in the use of thin film growth.

References:

- [1] Olson, E.A., et al., The design and operation of a MEMS differential scanning nanocalorimeter for high-speed heat capacity measurements of ultrathin films. *Journal of Microelectromechanical Systems*, 2003. 12(3): p. 355-64.
- [2] Efremov, M.Y., et al., Thin-Film MEMS Differential Scanning Nanocalorimetry: Heat Capacity Analysis. *Thermochimica Acta*, 2004. 412(1-2): p. 13-23.
- [3] Efremov, M.Y., et al., Ultrasensitive, fast, thin-film differential scanning calorimeter. *Review of Scientific Instruments*, 2004. 75(1): p. 179.
- [4] Hu, L., et al., Self-Assembly and Ripening of Polymeric Silver-Alkanethiolate Crystals on Inert Surfaces. *Langmuir*, 2009. 25(16): p. 9585-9595.
- [5] Hu, L., et al., Synthesis and Characterization of Single-Layer Silver Decanethiolate Lamellar Crystals. *Journal of the American Chemical Society*, 2011. 133(12): p. 4367-4376.
- [6] de la Rama, L.P., et al., Size Effect and Odd-Even Alternation in the Melting of Single and Stacked AgSC_n Layers: Synthesis and Nanocalorimetry Measurements. *Journal of the American Chemical Society*, 2013. 135(38): p. 14286-14298.
- [7] Ye, Z., et al., Nanocalorimetry study of the evolution of melting characteristics of single layer silver alkanethiolate lamella: Fast heating/cooling and electrical annealing. *Thermochimica Acta*, 2015. 603: p. 69-78.
- [8] Ye, Z., et al., Application of *in situ* Resistance and Nanocalorimetry Measurements for Nanoelectronic Thin Film Materials, Characterization and Metrology for Nanoelectronics and Nanostructures, Pan Stanford Publishing, in press, 2016.

Confinement & Template Assisted Assembly of Functional Colloids

CNF Project Number: 1208-40

Principal Investigator: Chekesha M. Liddell Watson

User: Angela C. Stelson

Affiliation: Materials Science and Engineering, Cornell University

Primary Source of Research Funding: National Science Foundation Department of Materials Research-1508592

Contact: CML66@cornell.edu, acs348@cornell.edu

Website: <https://cliddellwatson.mse.cornell.edu/>

Abstract:

Photonic bandgap materials consisting of periodic dielectrics are promising for optical applications such as light localization, spontaneous emission enhancement or suppression, and slow light. Self-assembly offers an attractive means to generate complex structural symmetry with diverse materials at submicron length-scales to promote photonic properties in the visible-infrared frequency range. Self-assembled colloidal crystals can be utilized as cost-effective and scalable templates for high dielectric materials to produce photonic crystals. The colloid structure can be controlled with forces including electric and magnetic fields, as well as entropic effects such as confinement and packing fraction. In this work, we explore the phase behavior of C60 microcrystal platelets assembled under confinement and electric fields. These anisotropic particles display a rich phase behavior as a function of the strength and frequency of the applied field, as well as confinement height and system density.

Summary of Research:

C60 Microcrystals can be synthesized in a variety of morphologies with high monodispersity including faceted rods, flower-shapes, and platelets, among others [1,2]. Assembly of such anisotropic particles under confinement incommensurate with an integer layer number of particles dramatically expands the array of phases available [2]. Electric fields produce a variety of frequency dependent effects in colloidal solutions, including dipolar interactions between the particles and osmotic currents in the fluid [3]. Combining multiple assembly forces yields greater control over inter-particle interactions, further expanding the library of structures available.

Substrates for electric field-directed assembly under confinement were fabricated in the CNF cleanroom. Borosilicate wafer substrates were patterned with Cr/Au electrodes with 300 μm spacing using the CHA Industries evaporation system. Lithographically patterned spacers (SU-8 2050) were patterned to attain a wedge-type confinement cell. Each wafer yielded two substrates, and wafers were partitioned with a Versalaser VSL3.50 Engraver. Confinement cells were assembled and filled with microcrystals in solution. Electric fields were applied to the confinement cells, and assembly was observed in real-time under a microscope.

C60 platelets were assembled under in-plane and out-of-plane confinement and exposed to fields of strength

2.6-8.0 kV/cm and frequencies ranging from 100 Hz to 3 MHz. For lower frequencies, string-fluid behavior is observed for in-plane and out-of-plane confinements at low particle density. For higher volume fractions in-plane confinement results in hexagonal packing, while out of plane confinement results in coexistent regions of in-plane hexagonal packing with out-of-plane chains. At high frequencies (above 1.7 MHz), the inter-particle interactions change, resulting in coexistent square and hexagonal packings for in-plane confinement and disordered columnar packings. This complex phase behavior demonstrates the promise of pairing confinement assembly with electric-field induced interactions to produce complex new structural symmetries for templated photonic crystals.

References:

- [1] Penterman, Sonny J., et al. "Anisometric Colloidal Fullerene Rod and Platelet Solvates with Enhanced Photoluminescence." *Advanced Optical Materials* 2.11 (2014): 1024-1030.
- [2] Penterman, Sonny J., and Chekesha M. Liddell Watson. "Anisometric C 60 fullerene colloids assisted by structure-directing agent." *CrystEngComm* 18.10 (2016): 1775-1781.
- [3] Muangnapoh, Kullachate, et al. "Degenerate crystals from colloidal dimers under confinement." *Soft matter* 10.48 (2014): 9729-9738.
- [4] Demiro?rs, Ahmet Faik, et al. "Directed self-assembly of colloidal dumbbells with an electric field." *Langmuir* 26.18 (2010): 14466-14471.

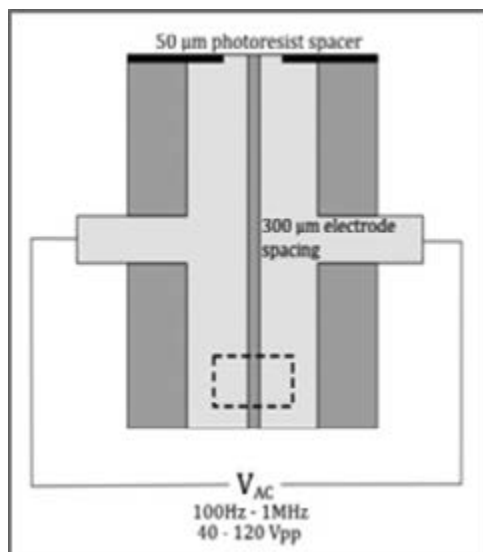


Figure 1: A) Schematic of microfabricated electric field-confinement cell with a top-down view. The region of monolayer-confined assembly is outlined by a dotted line. Electrodes are attached to an AC voltage source. B) Schematic of electric field confinement cell with a side view. Particles (not to scale) are shown within the region of assembly between the electrodes confined to the plane via a coverslip.

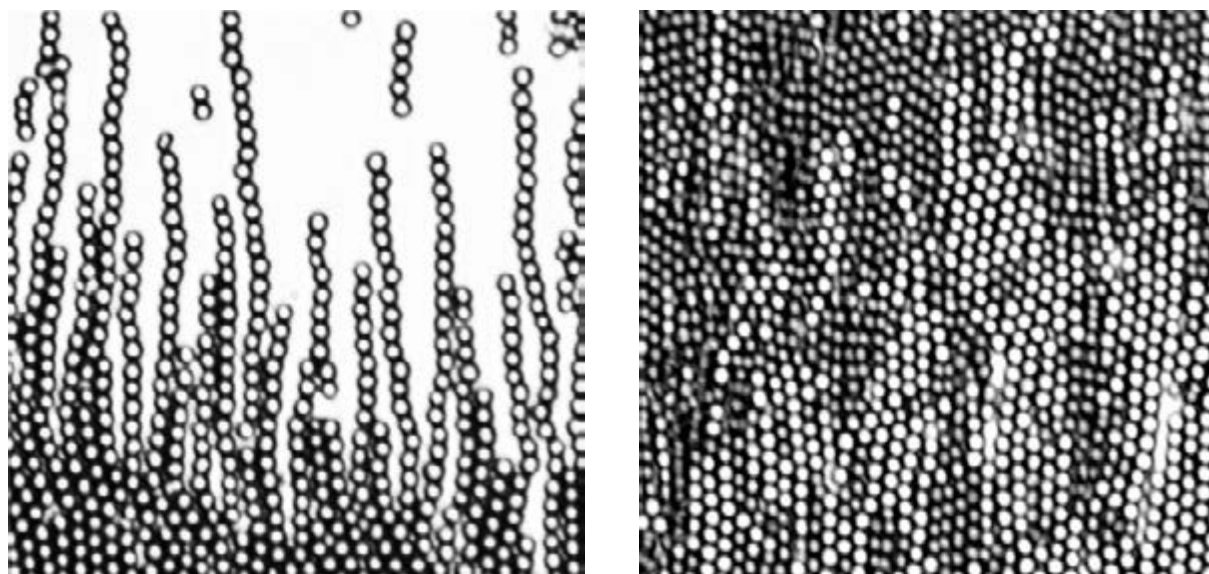


Figure 2, left: Assembly of C60 platelets under electric field and in-plane monolayer confinement. Assembly is shown at field strength = 2.6 kV/cm and frequency = 10 kHz. Images are taken at 100x magnification.

Figure 3, right: Assembly of C60 platelets under electric field and out-of-plane monolayer confinement. Assembly is shown at field strength = 8.0 kV/cm and frequency = 100 Hz. Images are taken at 100x magnification.

Mimicry of Biological Adhesion Through Fabrication of Fibrillar Surfaces

CNF Project Number: 1225-04

Principal Investigator: Anand Jagota

Users: Nichole Asermely, Zhenping He

Affiliation: Department of Chemical and Biomolecular Engineering, Lehigh University

Primary Source of Funding: Department of Energy (DE-FG02-07ER46463)

Contact: anj6@lehigh.edu, nma315@lehigh.edu, zh214@lehigh.edu

Abstract:

Shape complementarity can be used to enhance adhesion selectively between elastomeric surfaces. Complementary arrays of surface structures, such as one-dimensional ridges or fibrils arranged in a two-dimensional lattice, can inter-digitate to achieve adhesion enhancement controlled by shape recognition. It has been shown that relative misorientation is accommodated by defects that are meso-scale screw dislocations. The arrangement of such dislocations plays a critical role in determining the mechanical properties of the interface. In this project, we study the geometric properties of one-dimensional (ridge/channel) and two-dimensional (arrays of pillars) shape-complementary interfaces in the presence of relative misorientation (twist) and difference in lattice spacing. Relative misorientation without difference in lattice spacing is accommodated by arrays of screw dislocations. Difference in lattice spacing without misorientation is accommodated by arrays of edge dislocations. In general, we observe arrays of dislocations with mixed screw and edge character. The spacing and orientation of these arrays can be predicted accurately using the geometry of Moiré patterns. More broadly, we show that soft materials with shape-complementary patterns can be used to generate meso-scale dislocations of arbitrary edge and screw character at the length scale of tens of microns. Because these are easily observed optically, this system can be used to study dislocations and their interaction with each other.

Sample Fabrication:

The fabrication process is illustrated schematically in Figure 1a.

Patterned polydimethylsiloxane (PDMS, Sylgard 184) samples were prepared by molding elastomer base/curing agent mixture with a ratio of 10 parts by weight of elastomeric base to 1 part by weight of curing agent into an etched silicon wafer coated with a thin layer of silane. Samples were cured at different temperatures, with cure time based on the curing temperature. Temperatures used in this experiment include room temperature (denoted by RT; average laboratory room temperature was between 23°C and 25°C) and from 40°C to 110°C in 10°C increments. The room temperature samples were cured for at least two days to ensure solidification of the PDMS. Samples cured at 40°C were cured for four hours; all samples

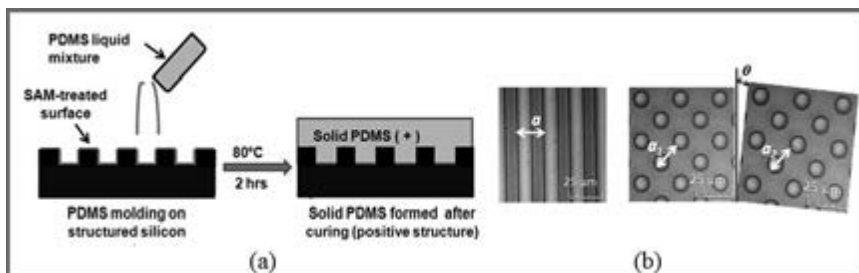


Figure 1: (a) Schematic illustration of the sample fabrication process. (b) Optical micrographs of ridge-channel and fibrillary samples.

cured above 40°C were cured for two hours. A thin razor was then used to cut the samples free from the silicon wafer and tweezers were used to carefully peel the PDMS from the wafer. Doing so maintained the structural integrity of both the wafer and sample. Figure 1(b) shows optical micrographs of the ridge-channel and fibrillary samples.

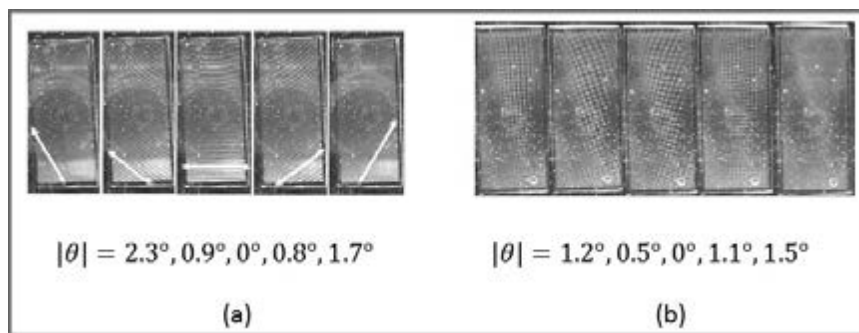


Figure 2: (a) Patterns of striations at the interface between nominally complementary ridge-channel surfaces with varying misorientation angles. (b) Patterns for a sample set with a square arrangement of fibrils, for several different misorientation angles. Both the density and orientation of the patterns changes systemically with change in misorientation angle.

Set-Up For Experiments Under Controlled Misorientation:

To control the relative misorientation or twist between the two patterned PDMS strips, we assembled a set-up including a rotational stage to provide precise control of orientation (relative twist) (Newport Motion Controller Model ESP301, Newport Rotation Stage). The set-up comprises a lower rotational stage on which we mount the lower piece of the PDMS sample pair. We fix the glass slide to a load cell to measure and control the normal force (~ 0.5 N) and the load cell is attached to the rotation stage. The top piece of glass with the gel and sample is clamped above the bottom portion of the set-up through a fixture attached to a micromanipulator capable of movement in three dimensions. The samples are viewed from above by a camera. In an experiment with a typical sample pair, one could, through the use of the micromanipulator, manually adjust the strips to be within $\pm 2^\circ$ of perfect alignment, as determined *a posteriori*. The upper sample was brought into contact with the lower one under a load of about 0.5 N. The samples were then separated by the manipulator, and the rotation stage was used to change angular orientation of the lower piece of the sample pair in steps of 0.1° . Spontaneous patterns appeared as the samples were pressed together; pictures of the sample were taken in contact and under load.

Moiré Patterns and Defects:

Figure 2(a) shows the pattern of striations observed on a sample where the two sides have slightly different periodic spacing. We observe striations that are defects and convert into dislocations with mixed screw and edge character. With increasing misorientation, not only does the distance between striations decrease, but their inclination with respect to the sample also changes systematically. Each lighter striation in this case becomes a dislocation with the same Burgers vector. Because the Burgers vector has non-zero components both along and orthogonal to the dislocation direction, the dislocations themselves have mixed edge and screw character.

Figure 2(b) shows patterns observed on a sample set where the two strips of PDMS have slightly different periodic spacing. As for the ridge-channel samples, patterns remain even when there is no misorientation. As misorientation changes, the pattern changes orientation and its density also changes systematically. As the absolute value of the misorientation angle decreases, the spacing density of the dislocation strips decreases as well. These patterns, their density and orientation, can be predicted accurately using the geometry of Moiré patterns.

Block Copolymer-Directed Gyroidal Mesoporous Superconductors

CNF Project Number: 1356-05

Principal Investigator: Ulrich Wiesner

Users: Peter Beaucage, Qi Zhang, Fumiaki Matsuoka, Shaun Alvarado

Affiliation: Department of Materials Science and Engineering, Cornell University

Primary Sources of Research Funding: National Science Foundation Single Investigator Award (DMR-1409105),
National Science Foundation Graduate Research Fellowship (to PAB)

Contact: ubw1@cornell.edu, pab275@cornell.edu, qz224@cornell.edu, fm388@cornell.edu, sja94@cornell.edu

Website: <http://wiesner.mse.cornell.edu>

Abstract:

Superconductors with mesoscale ordering and porosity are expected to have properties very different from their bulk counterparts. The exploration of these properties has been limited, however, by the lack of tunable, versatile, and robust wet-chemical synthesis methodologies to mesostructured superconductors. We report the synthesis of gyroidal niobium nitride (NbN) superconductors from gyroidal block copolymer self-assembly-derived niobium oxide. The resulting materials have a T_c of about 7.8 K, a critical current density of 440 A cm⁻² at 100 Oe and 2.5K, and a mesoscale lattice with the I4₃₂ (alternating gyroid) structure with d_{100} spacings between 27 and 36 nm. We expect that block copolymer-inorganic hybrid co-assembly will prove to be a scalable, tunable platform for exploration of the impacts of mesoscale order and porosity on superconducting properties.

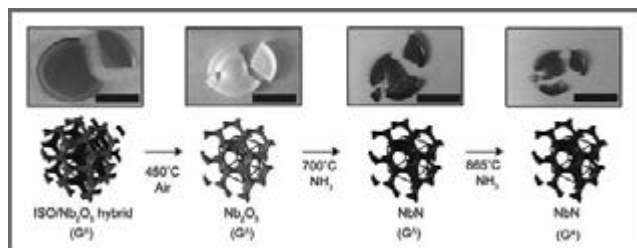


Figure 1: Schematic of synthesis and processing steps with photographs of the final materials. Block terpolymers (ISO) are combined with the Nb₂O₅ sol-gel precursors in a common solvent. Hybrid block copolymer/Nb₂O₅ alternating gyroid (GA) structures are generated by solvent evaporation-induced self-assembly. After calcination in air, the mesoporous Nb₂O₅ GAs are transformed to NbN GAs in a two-step nitriding process. Scale bars in all photographs represent 1 cm. Modified from [3].

Summary of Research:

Ordered mesoscale (10-100 nm) porosity in superconductors is expected to dramatically affect their properties, including their critical field, critical current, and flux pinning behavior. Despite ongoing interest in mesoscale science [1], little investigation has been made in this area, due primarily to the lack of a versatile synthetic approach to producing superconductors with controlled mesoscale order.

In recent decades, block copolymer self-assembly has proven to be a robust tool for directing the structure

of functional inorganic materials on the mesoscale with tunable morphologies and length scales [2]. In this work [3], we used an ABC triblock terpolymer, poly(isoprene-*b*-styrene-*b*-ethylene oxide) (ISO), to structure direct niobium oxide (Nb₂O₅) sol-gel nanoparticles. The nanoparticles segregate to only one domain of the terpolymer, producing a mesoscale-ordered oxide hybrid. This hybrid is etched using the CNF's Oxford PlasmaLab RIE system to remove capping layers that form as a byproduct of the film casting process. After etching, the films are heated in air to 450°C, which removes the polymer and produces a freestanding niobium oxide film with mesostructure derived from the polymer. This oxide film is then annealed at high temperature in flowing ammonia gas to produce NbN, while retaining the mesoscale structure of the parent oxide. A two-step nitriding process is necessary to produce a final material that both retains mesoscale order and is superconducting.

Throughout all processing steps, the material retains its mesoscale porosity, as shown by scanning electron microscopy in Figure 2 and small angle x-ray scattering in Figure 3. Because the structure of the material is derived from a block copolymer, we are able to vary the length scale of the mesoscale order by changing the polymer molar mass. Materials produced from a 64 kg mol⁻¹ ISO have a final lattice spacing of 27 nm, while those produced from an

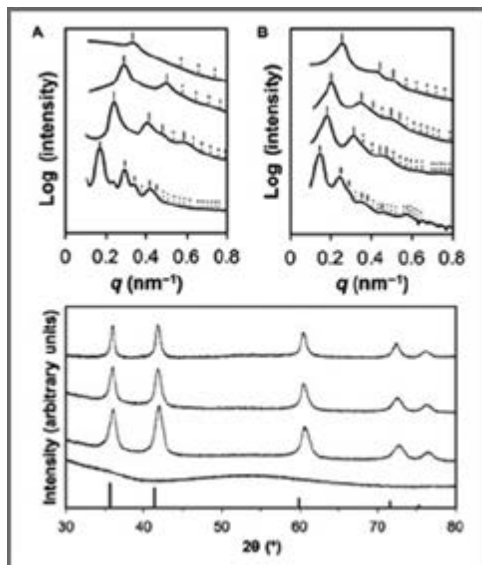


Figure 2: (A and B) SAXS patterns of samples derived from ISO-64k (A) and ISO-86k (B) at various processing stages. From bottom to top: ISO/oxide hybrids; samples calcined at 450°C in air; samples nitrified at 700°C; and sample nitrified at 850°/865°C. Observed (solid) and expected (dashed) peak positions for the GA structure are indicated by ticks above each curve. Curves for the ISO-86k-derived samples were integrated using a selected angular range as a result of the significant orientation of the mesostructure. (C) Powder XRD patterns of samples at various processing stages. From bottom to top: Sample calcined at 450°C in air; sample nitrified at 700°C; sample nitrified at 850°C; and sample nitrified at 865°C. All patterns are from samples derived from ISO-64k, except for the top trace, which is from a sample derived from ISO-86k. Bottom tick marks indicate expected peak positions and relative intensities for a cubic rock salt NbN pattern (Powder Diffraction File card 04-008-5125). Reproduced from [3].

86 kg mol⁻¹ ISO have a 36 nm lattice spacing. We demonstrate the superconducting properties of the materials in Figure 4. Vibrating sample magnetometry (VSM) measurements demonstrate an unambiguous superconducting transition at a critical temperature of 7.8 K. Four-point resistance measurements performed using devices fabricated in the CNF confirm this transition (Figure 4C). We expect that this tunability can be extended to provide a versatile platform for exploration of the novel superconducting properties introduced by the mesoscale ordering.

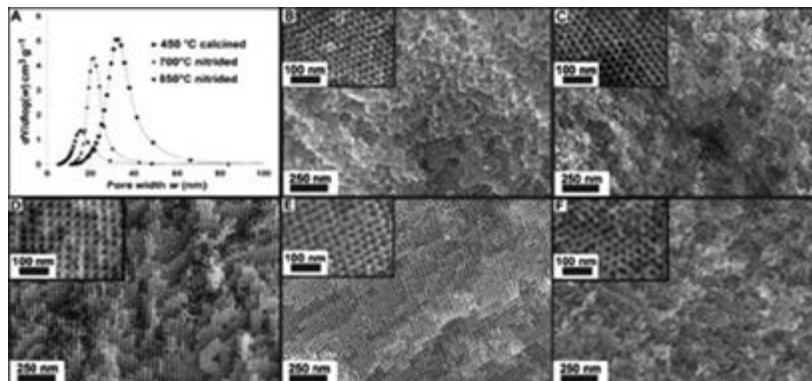


Figure 3: (A) Pore size distributions from N₂ sorption measurements for ISO-64k-derived samples at various processing stages. (B to F) SEM images of mesoporous samples at different processing stages. ISO-64k-derived gyroidal NbN (B) after nitrifying at 700°C and (C) after nitrifying at 850°C. (D) ISO-86k-derived gyroidal Nb₂O₅ after calcination at 450°C in air. ISO-86k-derived gyroidal NbN (E) after nitrifying at 700°C and (F) after nitrifying at 865°C. Reproduced from [3].

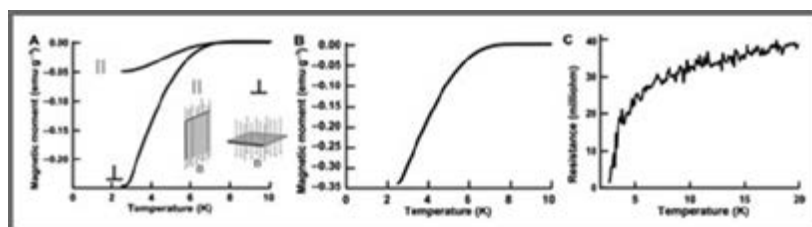


Figure 4: (A) Temperature-dependent magnetization from 2.5 to 10K for ISO-64k-derived NbN films in an applied field of 200 Oe, with their long axis oriented either parallel (top; ||) or perpendicular (bottom; ⊥) to the applied field (see insets for the different geometries tested). (B) Temperature-dependent magnetization from 2.5 to 10 K for ISO-86k-derived NbN films in an applied field of 100 Oe, with their long axis oriented perpendicular to the field. (C) Temperature-dependent four-point electrical resistance of ISO-86k-derived NbN films showing a drop beginning at approximately 7K. Reproduced from (3).

References:

- [1] U.S. Department of Energy Basic Energy Sciences, "From quanta to the continuum: Opportunities for mesoscale science" (2012); available at www.meso2012.com.
- [2] M. C. Orillall, U. Wiesner, Block copolymer based composition and morphology control in nanostructured hybrid materials for energy conversion and storage: Solar cells, batteries, and fuel cells. *Chem. Soc. Rev.* 40, 520 (2011).
- [3] S.W. Robbins, et al., Block copolymer self-assembly directed synthesis of mesoporous gyroidal superconductors. *Science Advances* 2, e1501119 (2016).

Investigation on Hydrogen Diffusivity in Palladium-Based Alloys

CNF Project Number: 1400-05

Principal Investigator: Robert B. van Dover

User: Boyu Guo

Affiliation: Department of Materials Science and Engineering, Cornell University

Primary Source of Research Funding: Cornell University

Contact: vandover@cornell.edu, bg429@cornell.edu

Abstract:

The development of a palladium (Pd) alloy that has high H_2 permeability and minimal degradation by impurities such as H_2S and CO would enable a cost effective approach to separate H_2 from syngas. We are developing a method that allows simultaneous analysis of H_2 permeability in 89 different ternary Pd-X-Y alloy compositions using sputter deposition and photolithography. The permeability can be inferred by using an indicator that changes color when exposed to H_2 in a controlled thin film geometry. Preliminary results have validated our method.

Summary of Research:

Hydrogen (H_2) is a promising source for a future energy economy due to its high energy density and lack of harmful emissions when reacted with O_2 from the atmosphere. H_2 can be generated easily from various sources [1]. Obtaining H_2 from syngas, a mixture of H_2 , H_2O , and CO_2 , and some CO, H_2S is a compelling option because of the low cost and low energy consumption if a gas separation membrane is used [2]. Pd is well known to have a high H_2 permeability, which makes it a good candidate for the H_2 separation membrane. However, the Pd surface is poisoned by carbon monoxide or sulfur-containing gasses. In recent years the research focus has shifted from pure Pd to Pd based alloys that are relatively low cost and more stable. The goal of our research is to develop a method that allows us to rapidly test the H_2 permeability of Pd based alloys with a wide range of

compositions, and to determine the susceptibility of the alloys to poisoning by H_2S and CO.

In order to determine the H_2 permeability of Pd-based membranes under any gas composition, the separation membrane needs to be exposed to ambient gas and in direct contact with hydrogen indicator. A schematic of sample geometry is illustrated in Figure 1.

Si_3N_4 has hydrogen diffusivity of 10^{-19} cm²/s under room temperature, which makes it an excellent hydrogen barrier [3]. Hydrogen gas can only enter the Pd in areas that are not covered with Si_3N_4 . Upon contact with the Pd alloy surface, H_2 dissociates into H atoms and diffuses into the Y layer underneath. Yttrium acts as a hydrogen sink because the enthalpy of hydride formation is approximately -110 kJ/(mol H) in Y whereas it is only -19 kJ/(mol H) in Pd [4]. The Y films acts as an indicator of H concentration because it changes color from silvery to blue when hydride forms. Since the H permeability of Pd is orders of magnitude higher than that of Y, lateral diffusion occurs entirely within the Pd alloy while vertical diffusion into the Y layer leads to visually obvious blue regions [4]. The color is observed through the transparent glass substrate, and can be used to quantitatively determine the hydrogen permeability of the corresponding Pd alloy above.

The three components are deposited onto a transparent 3-inch glass substrate using sputter deposition. In order to check the validity of our method, pure Pd was sputtered instead of Pd alloy, and Y and Si_3N_4

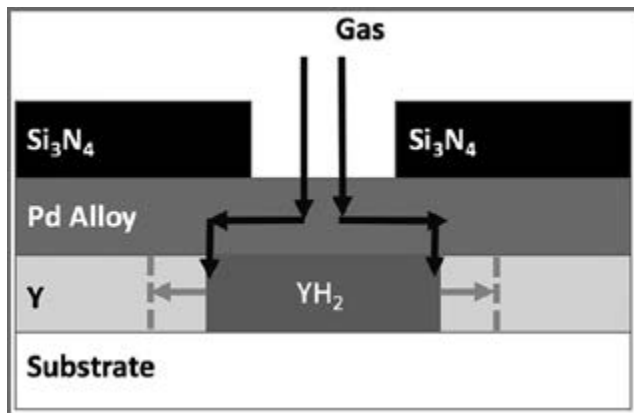


Figure 1: Side view of sample geometry for an individual device.

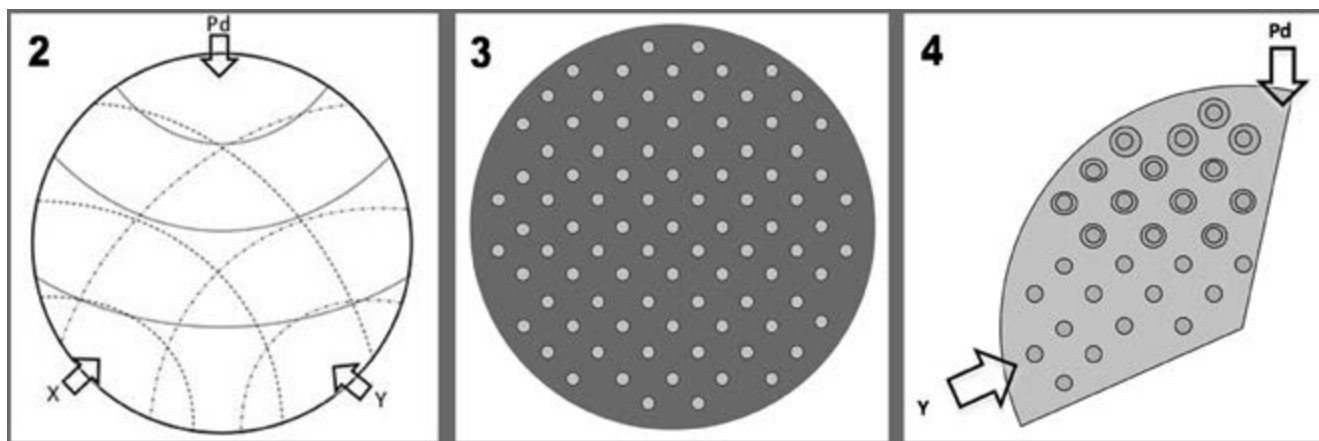


Figure 2, left: Schematic showing the sputtering direction and concentration gradients for Pd cosputtered with two other elements, 'X' and 'Y'. Figure 3, center: Depiction of sample surface after photolithography. The dark grey area corresponds to regions protected by the Si_3N_4 diffusion barrier, while the light grey dots represent exposed Pd. Figure 4, right: Schematic showing the substrate after exposure. Blue dots represent YH_2 formed after exposure while black circles represent holes in the Si_3N_4 diffusion barrier.

were sputtered using the 'X' and 'Y' guns. The center thicknesses of Y, Pd, and Si_3N_4 are 25 nm, 40 nm and 75 nm respectively. This geometry allows us to systematically determine the effect of the thickness each layer.

Photolithography is used to pattern the Si_3N_4 layer on sample surface to expose Pd layer. As shown in Figure 3 a total of 89 2 mm diameter holes are created to allow parallel examination of 89 combinations of Pd, Y and Si_3N_4 thickness. After the sample is primed with hexamethyldisilazane, Shipley 1813 is spun onto the substrate to achieve a thickness of approximately 1.3 μm . The photoresist is then baked at 115°C for 60 seconds. The resist is exposed using the SÜSSMA6-BA6 contact aligner and developed using the Hamatech-Steag wafer processor with AZ 300 MIF developer. The sample then is dry etched with CF_4 for 90 seconds to remove Si_3N_4 under exposed area, followed by 30 seconds of O_2 etch to remove any organic residue. The photoresist is removed using acetone and the sample surface is cleaned with isopropanol.

The sample is then exposed to 1:19 $\text{H}_2:\text{N}_2$ gas mixture in a custom-built tube furnace for 16 hours before being removed for analysis. A schematic of the sample after exposure is shown in Figure 4. Only the dots corresponding to the thickest Y region gave observable

blue coloration giving us good information on the Y thickness to target. Furthermore, dots in the region with greatest Pd thickness are clearly larger than those in the region where the Pd is thinner. The result meets our expectation that thicker Pd must have a higher H permeance, qualitatively confirming the validity of the method and process. The next steps will be to deploy this method to Pd based alloys with uniform Y indicator thickness, and to develop a quantitative mathematic model from which we can infer H permeability in the Pd alloy from the YH_2 dot size.

References:

- [1] B.N. Lukyanov, et al., Catalytic reactors with hydrogen permeation membrane separation, Chem. Eng. J. 154 (2009) 258-266.
- [2] S.N. Paglieri and J.D. Way, Innovations in Palladium Membrane Research, Separation and Purification Methods, 31 (2002) 1-169.
- [3] George C. Yu and S.K. Yen, Hydrogen diffusion coefficient of silicon nitride thin films, Applied Surface Science 201 (2002) 204-207.
- [4] de Man, et al., Combinatorial method for direct measurements of the intrinsic hydrogen permeability of separation membrane materials, J. Membrane Sci. 444 (2013) 70-76.

Charge Transport and Localization in Atomically Coherent Quantum Dot Solids

CNF Project Number: 1645-08

Principal Investigator: Tobias Hanrath¹

User: Kevin Whitham²

Affiliations: 1. Chemical and Biomolecular Engineering, 2. Materials Science and Engineering; Cornell University

Primary Source of Research Funding: Department of Energy through Grant DE-SC0006647

'Charge Transfer Across the Boundary of Photon-Harvesting Nanocrystals'

Contact: th358@cornell.edu, kw242@cornell.edu

Website: <http://hanrath-group.cbe.cornell.edu>

Abstract:

Epitaxial attachment of quantum dots into ordered superlattices enables the synthesis of quasi-two-dimensional materials that theoretically exhibit features such as Dirac cones and topological states and have major potential for unprecedented optoelectronic devices. Here we fabricated superlattices with the quantum dots registered to within a single atomic bond length (limited by the polydispersity of the quantum-dot building blocks), but missing a fraction (20%) of the epitaxial connections.

Summary of Research:

Recent experimental efforts to improve the electronic properties of quantum dot solids have focused on increasing inter-dot coupling by replacing organic ligands with inorganic ligands or by ligand removal. Oriented-attachment is a simple route to simultaneously increase inter-dot coupling and enforce translational order, as demonstrated in several recent reports [1].

Oriented attachment of lead selenide nanocrystals (PbSe NCs) can be controlled by ligand desorption from selected facets [1]. A colloidal dispersion of 6.5 nm diameter PbSe NCs in hexane was dispersed on ethylene glycol. Subsequently ethylene diamine was injected into the ethylene glycol sub-phase. We propose that ethylene diamine, an L-type ligand, binds selectively to Pb atoms on {100} facets, desorbing as L-Pb(O₂CR)₂. After deprotection, NCs undergo oriented attachment to fuse with {100} facets of proximate NCs.

The nature of the epitaxial connections between NCs is revealed by aberration-corrected scanning transmission electron microscopy (STEM) of monolayer areas, shown in Figure 1. Atomic resolution images show that oriented attachment

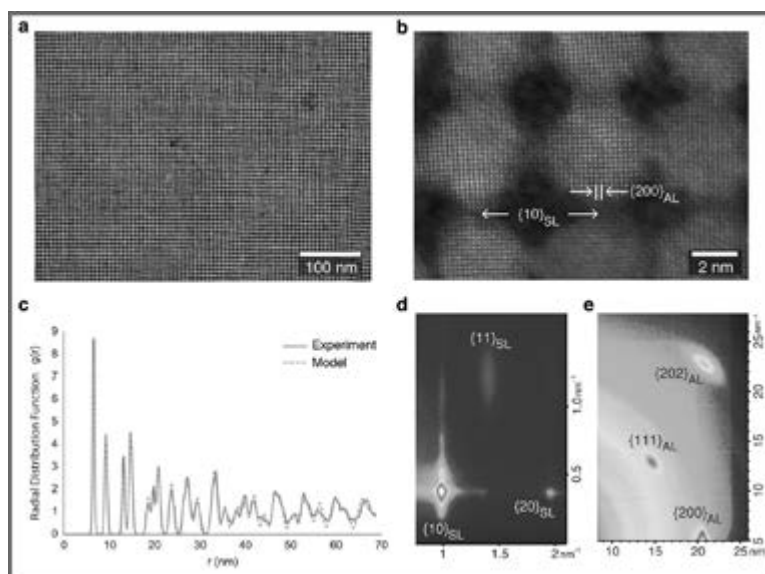


Figure 1: **a-b**, Annular dark field scanning transmission electron microscopy shows **a**, superlattice structure and **b**, atomic structure. **c**, Measured radial distribution function and calculated radial distribution function of a paracrystalline square lattice with 3.4% translational disorder. **d**, Grazing incidence small angle x-ray scattering (GISAXS) image shows reflections of a square superlattice (SL). **e**, Grazing incidence wide angle x-ray scattering (GIWAXS) image shows alignment of the atomic lattices (AL) of the nanocrystals.

occurs in the $\langle 100 \rangle$ crystallographic directions. To quantify translational order in the superlattice structure, we calculated the radial distribution function (RDF) based on NC locations directly extracted from STEM images. Using a paracrystalline model, we fit the measured RDF with only one free parameter and find the standard deviation of the nearest neighbor distance to be 0.22 nm or approximately one Pb-Se bond length (0.306 nm).

Highly doped Si wafers (< 0.02 ohm-cm) with 200 nm of dry thermal oxide annealed in forming gas were purchased from Addison Engineering. Oxide was removed from the backside in 6:1 (vol.) buffered oxide etch before thermal evaporation of 10 nm Al then 70 nm Au for the gate contact using a CHA Industries evaporator. On the front side, a layer of LOR5A lift-off resist (MicroChem) was deposited by spin-coating at 3,000 RPM for 45 seconds followed by a soft-bake at 180°C for 4 minutes. Shipley 1805 was deposited by spin-coating at 5,000 RPM for 30 seconds then baked at 90°C for 60 seconds before pattern transfer using an MA6 mask aligner (Karl-Suss) and developed with AZ-726 (MIF). Electrodes were deposited by thermal evaporation of 3 nm chrome and 30 nm gold followed by lift-off in n-methyl-2-pyrrolidone.

Transfer curves (current vs. gate voltage) in Figure 2b show ambipolar transport. We find that electron and hole transport are thermally activated (hopping) with conductance decreasing exponentially with decreasing temperature, a clear sign of carrier localization. We find that charge carriers are localized to just a few NCs at a gate bias of ± 40 V. We note that Coulomb blockade should not be an important factor in the measured temperature range (see Supplementary Information).

We measure mobilities of $0.54 \text{ cm}^2/\text{Vs}$ for holes and $0.2 \text{ cm}^2/\text{Vs}$ for electrons at 245 K. Despite relatively good mobilities compared to ligand exchanged quantum dot, the localization length reveals that transport is still far from band-like.

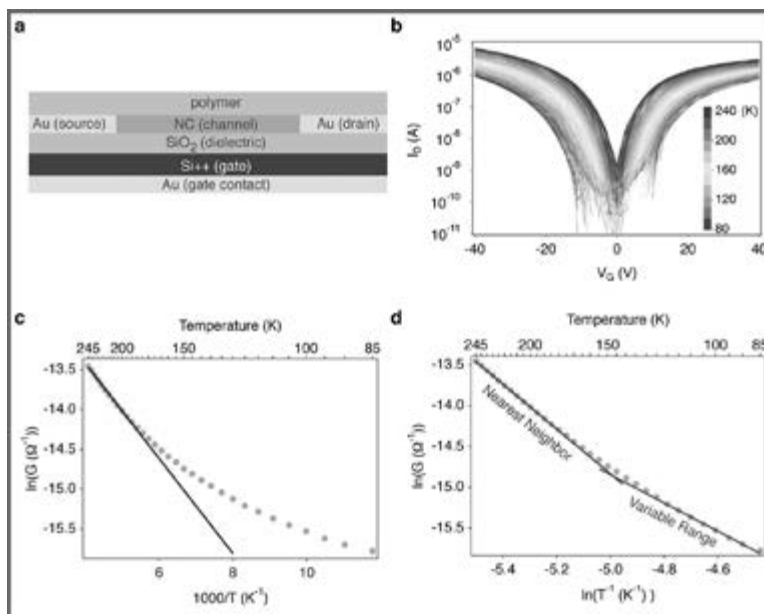


Figure 2: **a**, Cross-sectional schematic of the field-effect transistor. The gate is formed by highly doped silicon (Si++) with a 200 nm dielectric layer of SiO₂. The source and drain electrodes were patterned on the SiO₂ to form a channel 100 nm \times 3 nm. A layer of photo-cured polymer served as a barrier between the NC layer and ambient water and oxygen. **b**, Transfer curves show ambipolar transport with electron current at positive gate voltage (V_G) and hole current at negative gate voltage. The source-drain bias was 1 V. The conductance was measured every 5 K from 85 K to 245 K. **c**, An Arrhenius plot of electron conductance at a gate bias of 22 V with a source-drain bias of 1 V. The solid line is a linear fit to the higher temperature data. **d**, A log-log plot of the data in panel c. Straight lines illustrate that the data is not a single power law over this temperature range.

References:

- [1] William J Baumgardner, Kevin Whitham, and Tobias Hanrath. Confined-but-connected quantum solids via controlled ligand displacement. *Nano letters*, 13(7):3225-3231, 2013.

Nanostructured Polymer Brush

CNF Project Number: 1757-09

Principal Investigators: Christopher K. Ober², Jürgen Rühle³, Oswald Prucker³

Users: Wei-Liang Chen¹, Matthias Menzel³

Affiliations: 1. School of Chemical and Biomolecular Engineering, Cornell University.

2. Materials Science and Engineering; Cornell University. 3. IMTEK, University of Freiburg

Primary Source of Research Funding: National Science Foundation, Deutsche Forschungsgemeinschaft

Contact: ck03@cornell.edu, wc497@cornell.edu

Website: <http://cober.mse.cornell.edu/index.html>

Abstract:

The nano-scale morphologies of patterned polymer brushes derived from photolithography processing were investigated. Polymer brush structures created by top-down and bottom-up processes were evaluated using poly(tert-butyl methacrylate) (PtBMA) as the polymer. Under selected conditions, unique reversible structures between lens-like and box-like were formed and detailed structural characterization was done. This modification on the polymer brushes makes them potential candidates for stimuli-responsive materials.

Summary of Research:

Polymers can achieve various morphologies due to their “soft” properties, unlike hard materials such as metals and ceramics. By proper control the structures and morphologies of polymers can be tuned using light [1], heat [2] and solvent immersion [3]. In photolithography, a polymeric photoresist (PR) utilizes light to induce a solubility change in defined areas and then subsequent solvent development is used to remove the soluble region. As a result the insoluble part remains and can act as a mask for further processing steps such as an etch mask or sacrificial layer for lift-off.

Generally, a PR can be categorized into one of two classes; either positive or negative tone. After exposure through a mask, a solvent developer is used to remove either the unexposed (negative tone) or exposed (positive tone) regions of the PR. Nanoscale patterns can be easily achieved through the photolithography process, but the profile is limited to right angle structures. In this study we show that using surface tethered PtBMA polymer brushes, we can make nanoscale reversible morphologies that could switch between box and lens shape based on different solvent immersion. PtBMA brushes were synthesized by surface-initiated free radical polymerization on a silicon wafer following a previously published process [4]. A modified top-down process based on the work of Henning, et al. [5], was used to pattern the polymer brushes and a fluorinated polymer (CYTOP, Asahi Glass). By applying the same process we also

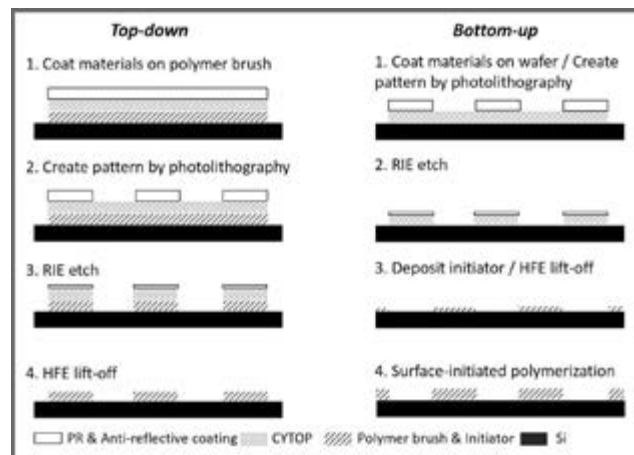


Figure 1: Bottom-up and top-down process for pattern fabrication.

patterned CYTOP as template for creating polymer brushes through a bottom-up process. Figure 1 shows the procedure used to create top-down and bottom-up patterned PtBMA polymer brushes.

Figures 2a, and b show how the polymer brush morphology can be changed based on the solvent chosen for two different pattern sizes. Top-down PtBMA brushes were firstly soaked in toluene and dried to investigate the relaxation of the patterned brush. The relaxed polymer brush topography can form either a “plain” between the pattern edges or a

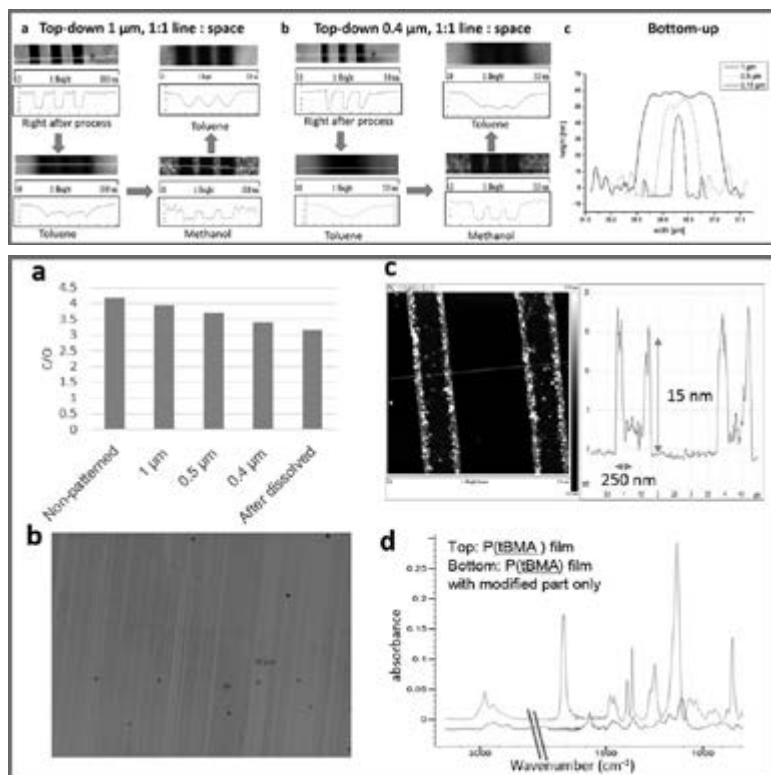


Figure 2, top: AFM scan images for patterned PtBMA brush: a) top-down 1 μm , b) top-down 0.4 μm , c) bottom-up brush, after process.

Figure 3, bottom: Detailed characterization of sidewall residual. a. Carbon/oxygen atomic ratio on bulk and patterned (1:2 line:space) PtBMA film derived from XPS scan. b. Optical microscope image. c. AFM scan image. d. ATR-FTIR on residuals of sidewall after solvent immersion.

lens-like shape depending on solvent exposure. To see if the solvent choice changes the brush morphology, the relaxed polymer brushes were soaked in methanol, which is a non-solvent for PtBMA. Surprisingly, the brushes returned to their right-angle profile and this structural change was later proven to be a reversible process by soaking the brushes again in toluene.

To do comparisons and further investigation, bottom-up processed PtBMA brushes were made. The brush showed a lens-like shape as shown in Figure 2c. It did not change its shape even after it had been soaked with fluorinated solvent during processing. No structural change in the brushes created from bottom-up processing indicates that the changes seen in the top-down created brushes is due to the processing of the polymer. It is known that organic materials can form additional covalent bonds during reactive ion etching (RIE) processes that result in a crosslinked material.

To characterize sidewall structures, a spin-coated film of PtBMA was patterned by the sample top-down process and then investigated. In Figure 3a, a decrease

in the C/O ratio was observed with XPS as the pattern size became smaller. This could be due to an increase of the relative sidewall content in the structure since the atomic ratio of sidewall has a smaller C/O ratio. Furthermore, the same PtBMA patterned film was immersed in 50 OC THF to dissolve the region of the film that was not affected by RIE. Residual material could be seen by optical microscope (Figure 3b) and was characterized by AFM and XPS studies (labeled as “dissolved” in Figure 3a). In Figure 3c we see the thickness of the sidewall is ~ 250 nm wide and 15 nm thick. The area affected by RIE should remain after the effect of solvent immersion, therefore, the AFM measurement must be from aggregation of the sidewall polymer, which was 300 nm thick. Under this assumption the plasma penetration depth should be around 13 nm.

ATR-FTIR spectra of the residual and the PtBMA film is shown in Figure 3d. Formation of the ketone, ester, and C-C bonds could be observed together with disappearance of tert-butyl and original carbonyl group. Formation of new oxygen containing groups must be more than the loss of the old one based on a decrease of the C/O ratio derived from XPS study. Crosslinking could be formed by C-C or C-O-C altogether in the RIE process. Different morphologies formed by patterning of PtBMA polymer brushes created by both top-down and bottom-up approaches were investigated. A stimuli-responsive structure in top-down created brushes was observed. After processing, the PtBMA film showed crosslinking only at the edges of the patterned structure. This could be used to tune structures and create designed morphologies. Further applications include, but are not limited to, anti-fouling and stimuli-responsive materials.

References:

- [1] Kopyshv, A., Galvin, C. J., Genzer, J., Lomadze, N. and Santer, S. *Langmuir* 29, 13967-13974 (2013).
- [2] He, Q., Küller, A., Grunze, M. and Li, J. *Langmuir* 23, 3981-3987 (2007).
- [3] de Groot, G. W. et al. *ACS Appl. Mater. Interfaces* 5, 1400-1407 (2013).
- [4] Prucker, O. and Rühle, J. *Macromolecules* 31, 592-601 (1998).
- [5] Chang, J.-F., Gwinner, M. C., Caironi, M., Sakanoue, T. and Sirringhaus, H. *Adv. Funct. Mater.* 20, 2825-2832 (2010).

Genetically Designed Photonic Crystal Nanocavities

CNF Project Number: 1889-10

Principal Investigator: Antonio Badolato

User: Yiming Lai

Affiliation: Department of Physics and Astronomy, University of Rochester

Primary Source of Research Funding: NSF

Contact: antonio.badolato@gmail.com, lmign@pas.rochester.edu

Abstract:

We report on the experimental realization of genetically designed two-dimensional photonic crystal nanocavities (PCNs) made in membranes with low index contrast. Our PCNs are made in silicon membrane monolithically embedded in SiO_2 . They show quality (Q)-values above 10^5 while maintaining a mode volume close to the diffraction limit and a very small footprint. Being truly compatible with the current complementary metal-oxide semiconductor (CMOS) technology, our PCNs represent new building blocks in ultra-dense integrated photonics.

Summary of Research:

Membrane PCNs represent a powerful and versatile tool for fundamental studies and applications in nanophotonics because of the presence of modes with ultra-small modal volume (V) and high Q -values. The L3 PCN is the most popular and widespread design, due to its compactness, and small mode volume. Here, we used a genetic algorithm combined to guided-mode expansion (GME) method [1,2] and finite-difference time-domain FDTD to find a global maximum of the Q -values of these designs, by varying the positions of few neighboring holes. Such an optimal design shows a computed Q up to $Q_{\text{ideal}} = 2 \times 10^7$, at the resonant wavelength $\lambda = 1555$ nm, and FDTD method computed mode volume $V = 0.96(\lambda/n)^3$. To validate our design, we fabricated many L3 PCNs in commercially available SOI wafers. The SOI wafer consisted of a 220 nm top silicon layer and a 3 μm buried oxide (BOX) layer on a silicon substrate. The PCN pattern was defined by electron beam

lithography (EBL) (JEOL 9500) using positive e-beam resist. The pattern was transferred from the resist to the silicon top-layer by fluorine based inductively coupled plasma dry etching and the BOX layer was removed by dilute HF wet etching. Figure 1(a) shows the SEM top view image of the PCN region.

The fundamental cavity mode resonance was measured by cross-polarization resonant scattering (RS) spectroscopy [3]. Figure 1(b) shows the RS spectrum of our super-L3 PCN fundamental mode measured on the cavity displaying the highest Q [4]. Fitting of the cavity resonance with a Fano-lineshape demonstrates $Q_{\text{exp}} = 1.96 \times 10^6$.

This corresponds to an experimentally observed $Q_{\text{exp}}/V > 2 \times 10^6 (\lambda/n)^{-3}$, which ranks our cavity among the highest Q_{exp}/V ever reported in 2D PCNs. We notice that the other nominally identical PCNs all displayed a clear resonance with Q -factors lying systematically in the one million range, one order of magnitude higher than previous designs.

While membrane PCNs feature superb optical properties, such as the ultra-high Q/V , some limitations have hampered their applications. For example, because PCN membranes are surrounded by air they are necessarily exposed to the environment. The surface of the membrane tends to get contaminated or oxidized more easily, and the performance of the devices may degrade over time. Furthermore, the mechanical instability, low thermal conductivity of the PCN membrane and the requirement for removing the BOX layer of the SOI wafer also make it difficult

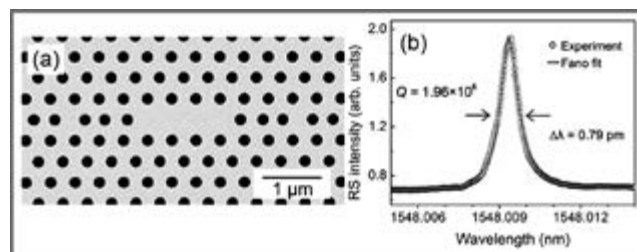


Figure 1: (a) SEM top view image of the PCN. (b) Resonant scattering spectrum of the super-L3 PCN (open dots). Best-fitted Fano lineshape (red line) gives a linewidth of 0.79 pm, i.e., $Q = 1.96 \times 10^6$.

to integrate the PhC membrane with other optical devices on the same chip. We uniquely designed a PCN in the SOI platform that doesn't need the removal of the BOX layer and still preserve an ultra-high Q/V .

The designed SOI-PCN is clad with SiO_2 and features FDTD-computed $Q_{\text{ideal}} = 4.4 \times 10^5$ at $\lambda = 1567$ nm. To validate the design, several SOI-PCNs were fabricated following the same fabrication process as described above except in the final step, we covered the PCNs with $1.5 \mu\text{m}$ thick low pressure chemical vapor deposition (LPCVD) high temperature oxide instead of undercutting the BOX layer as shown in the inset of Figure 2. The fabricated devices showed $Q_{\text{exp}} = 3.94 \times 10^5$ (Figure 2).

To date, this is the highest Q/V value ever reported in photonic crystal nanocavities with low index contrast [5].

References:

- [1] L. C. Andreani and D. Gerace, Phys. Rev. B 73, 235114 (2006).
- [2] M. Minkov and V. Savona, Scientific Reports 4, 5124 (2014).
- [3] M. Galli, et al., Appl. Phys. Lett. 94, 71101 (2009).
- [4] Y. Lai, et al., Appl. Phys. Lett. 104, 241101 (2014).
- [5] Y. Lai, et al., to be submitted.

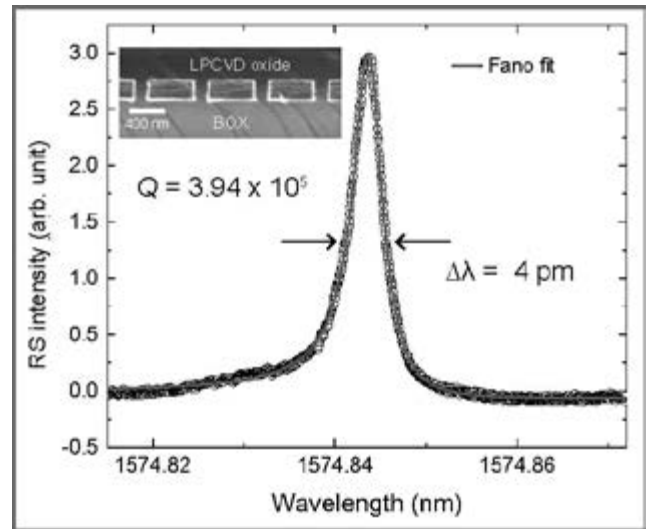


Figure 2: Resonant scattering spectrum of the SOI-PCN (open dots). Best-fitted Fano lineshape (red line) gives a linewidth of 4 pm , i.e., $Q = 3.94 \times 10^5$. Inset: SEM cross section image of the SOI-PCN after covered by the LPCVD high temperature oxide.

Immobilization of Cubic Boron Nitride (c-BN) Particles on Silicon and Quartz Substrates

CNF Project Number: 2063-11

Principal Investigator: Dr. Michael G. Spencer

User: Athith Krishna

Affiliation: School of Electrical and Computer Engineering, Cornell University

Primary Sources of Research Funding: Boeing; Engineering Learning Initiatives

Contact: spencer@ece.cornell.edu, ak857@cornell.edu

Abstract:

The research seeks to address the conductivity measurements of doped cubic-boron nitride (c-BN) particles. This report proposes a systematic method to immobilize cubic-boron nitride particles on silicon and quartz substrates. The process utilizes photoresist as an adhesive to achieve the objective.

Summary of Research:

Studies show that the synthetically formed cubic boron nitride (c-BN) is the second hardest material after natural diamond [1]. Since its first documented synthesis in 1957 [2], this material has been of interest to researchers and industrialists alike for its novel electrical, mechanical, thermal and optical properties. Because of its wide band gap and good thermal conductivity [3], c-BN has the potential to be used in high temperature and high power electronics with the added advantage of being doped by both p- and n-type substances.

c-BN particles have a tendency to move away from their position when put under electrical characterization probes in an effort to obtain their IV (current-voltage)-curves. As observed in our previous experiments, the particles move due to mechanical pressure on one side when the probes touch the

particles. To carry out a successful process using two probes — and to extend that process to more probes for even better measurements — it was suggested the particles be immobilized on the surface of the substrate so they cannot not move due to the probes. This being the main motivation for this experiment, we use photoresist (PR) as the adhesive medium to immobilize the c-BN particles.

A general procedure was used for both Si and quartz substrates. The choice of photoresist used, graphitization temperature and time were varied on samples to get the desired results. Adhesion was verified using tape testing. The following general process was used to graphitize the PR on the substrate [4]:

- a) SPR-220-3. photoresist was spun on the substrate at 3000 rpm for 60s to form a capping layer,

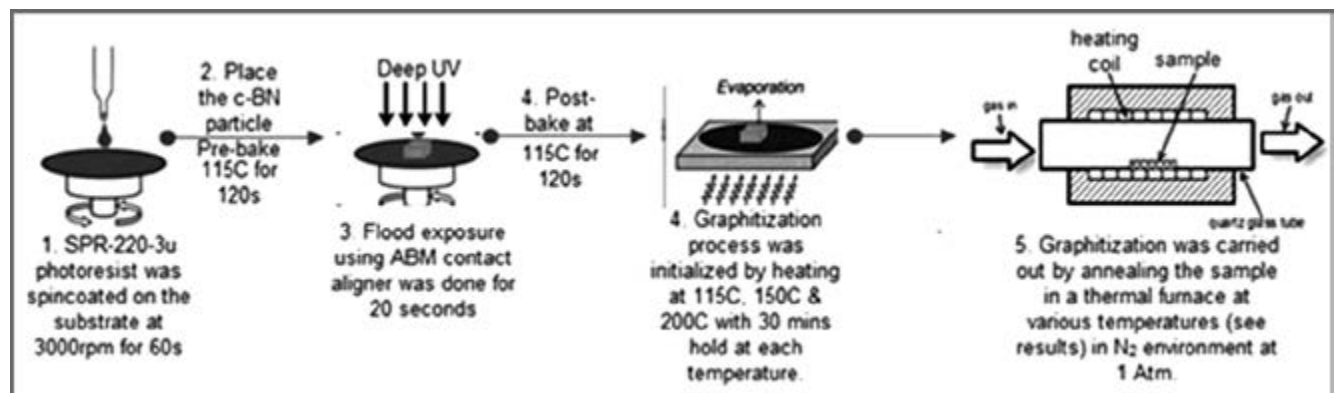


Figure 1: Process outline used for immobilization of c-BN particles.

- b) A single c-BN particle was placed by hand on the substrate. The substrate was then pre-baked at 115°C for two minutes and a blank exposure of the whole surface was done for 20s on ABM contact aligner. Post-exposure bake was carried out at 115°C for two minutes,
- c) A three step hard-baking process was carried out at 115°C, 150°C and 200°C with 30 minutes hold at each temperature,
- d) Graphitization of the photoresist layer was carried out at different temperatures — 300°C, 500°C, and 850°C — for silicon and quartz substrates under 1 atm pressure for 40 minutes, with various samples to test its effectiveness. Figure 1 shows the schematic of the procedure used.

Taking the samples up to 850°C leads to flaking for thicker 7 μm photoresist, and particles do not adhere for the thinner 3 μm photoresist when used on silicon. Using quartz as the substrate is better than silicon. This might be due to the higher stability of quartz compared to silicon. From the results we can see that taking the samples up to 850°C leads to undesirable results. But, for cases where experiments are to be carried out immediately after the immobilization, usage of thick photoresist with 850°C can be used. But when thin photoresist is used, it better to not go up to 850°C.

The best set of conditions seem to be 300°C on the thin photoresist. But a hypothesis could be made that we could find a temperature between 300°C and 500°C where we could expect a maximum particle immobilization on the substrate. This is because, even at 500°C, we obtain similar results as 300°C.

Thus, optimal conditions for graphitization and immobilization are: Quartz substrate, 3 μm photoresist, and furnace annealing at 300°C and 500°C with 40 min hold at each temperature.

Scope for the future of this work includes the following:

- (i) Surface transfer doping of c-BN particles. This is a novel method to obtain n-type c-BN using F4-TCNQ (tetracyanoquinodimethane), a polymer,
- (ii) Ion implantation doping of c-BN using beryllium (p-type) and silicon (n-type),
- (iii) Once we have four contacts on the particle, we can perform four-probe Hall effect conductivity measurements,
- (iv) Ellipsometry measurements on the immobilized samples.

References:

- [1] Vel, L., G. Demazeau, and J. Etourneau. "Cubic Boron Nitride: Synthesis, Physicochemical Properties and Applications." *Materials Science and Engineering: B*: 149-64. Print.
- [2] Mirkarimi, P. B., K. F. McCarty, and D. L. Medlin. "Review of Advances in Cubic Boron Nitride Film Synthesis." *Materials Science and Engineering: R: Reports*: 47-100. Print.
- [3] G. E. Spriggs (2002) P. Beiss, R. Ruthardt, H. Warlimont (ed.) Springer Materials.
- [4] K. Vassilevski, N. Wright, I. Nikitina, A. Horsfall, A. O'Neill, M. Uren, K. Hilton, A. Masterton, A. Hydes and C. Johnson, 'Protection of selectively implanted and patterned silicon carbide surfaces with graphite capping layer during post-implantation annealing', *Semiconductor Science and Technology*, vol. 20, no. 3, pp. 271-278, 2005.

Silicon-Based Anti-Reflection Coating for Terahertz Optics

CNF Project Number: 2196-13

Principal Investigator: Michael Niemack

Users: Patricio Gallardo, Brian Koopman, Brenna Mockler

Affiliation: Department of Physics, Cornell University

Primary Source of Research Funding: Cornell University

Contact: niemack@cornell.edu, pag227@cornell.edu, bjk98@cornell.edu, bem73@cornell.edu

Abstract:

The increasing size of detector arrays for sub-millimeter and millimeter wavelength astronomy drives the need for large aperture, high index of refraction, low loss, cryogenic refracting optics [1]. Silicon (Si) is an excellent material for these applications, given its index of refraction ($n = 3.4$), low loss and relatively high thermal conductivity. However, Si requires anti-reflection coatings in order to be used in a variety of projects, and specifically — the Atacama Cosmology Telescope (ACT) and the Cerro Chajnantor Atacama Telescope (CCAT). These coatings need to be thermally matched to be suitable for cryogenic applications. Currently ACT uses anti-reflection coatings that are machined using a dicing saw in order to create sub-wavelength patterns in Si; these patterns are designed to modify the refractive index of Si to minimize reflections. Limitations on the feature size achievable with a dicing saw drive the need to use deep reactive ion etch to achieve $40\ \mu\text{m}$ and smaller feature sizes. At the Cornell NanoScale Facility, we built a double-sided coated Si sample having features with a pitch of $50\ \mu\text{m}$ and approximately a $48\ \mu\text{m}$ depth. This sample is composed of two optical quality wafers that were bonded using high temperature direct Si bonding. Optical testing of this sample yielded a high transmission in the 900 GHz band.

Summary of Research:

Introduction. Recent developments of cryogenically cooled, large superconducting detector arrays for (sub) millimeter astronomy have increased the need for optical systems with high throughput and diffraction limited performance. Silicon (Si) is an excellent material at these wavelengths given its index of refraction ($n_{\text{Si}} = 3.4$), low loss and relatively high thermal conductivity. To achieve the desired optical throughput for astronomical applications it is essential to mitigate the 30% reflection that arises when light passes from free space to Si [1].

In this work, we investigate the implementation of a metamaterial made out of deep reactive ion etched (DRIE) lithographically defined silicon structures at the $\sim 50\ \mu\text{m}$ scale that will later be slumped and bonded to a silicon lens. Results from this project will be used in the optical design of the Short Wavelength Camera (SWCam), the first-light instrument for the Cerro Chajnantor Atacama Telescope (CCAT), a 25-meter diameter (sub)millimeter telescope to be located in northern Chile.

Anti-Reflection Coatings and Metamaterials. To avoid the natural reflection loss that arises when light passes from a low refractive index material (free space, for example) to a high refractive index (n) material (silicon in this case), it is possible to cover the surface of the refractive element with a quarter wavelength, $\lambda/4$, layer of a material with an index of refraction of \sqrt{n} . The silicon index, n_{Si} , and the wavelength requirement ($350\ \mu\text{m}$) of SWCam sets a target thickness of $50\ \mu\text{m}$ for our $\lambda/4$ anti-reflection (AR) coating.

It has been shown [1] for longer wavelengths that a dicing-saw-patterned quarter-wavelength layer of silicon can achieve a transmission better than 99%. Shorter wavelengths, however impose tight constraints on the available fabrication methods due to the need for smaller features. The dicing saw method becomes impracticable for $50\ \mu\text{m}$ and smaller feature sizes. These fabrication constraints motivate our exploration of lithographically defined patterns.

Current Status. We designed, simulated and built a thin layer of silicon made out of $40\ \mu\text{m}$ wide square holes with a pitch of $50\ \mu\text{m}$ in a 4-inch diameter, 1 mm thick wafer. This layer was lithographically defined and then etched using the Unaxis DRIE equipment available at the CNF. Etching depth was measured and controlled using a Zygo optical profiler also available at the CNF. Figure 1 shows a 3D representation of the patterns that were etched in the substrate. Optical characterization was done using a Fourier Transform Spectrograph and presented in Reference [2].

We are able to produce two single sided optical quality coated wafers and use direct bonding (at 1100°C) to bond them together. To bond the two wafers, we used a high temperature furnace and the MOS clean setup at CNF. Characterization of the bonded wafer pair was done on the Schott IR inspector also available at the CNF. Figure 2 shows an infrared transmission image showing our latest bond of two single-sided AR coated silicon wafers. Only one bubble can be seen. We believe that we can still fine tune our bonding procedure to minimize the occurrence of bubbles. The sample shown is a 4-inch wafer.

We optically tested our samples in the NASA Goddard Fourier Transform Spectrometer. At cryogenic temperatures (4 Kelvin) our sample shows excellent transmission, better than 99% at 900 GHz, which fulfills our transmission requirement.

Conclusion and Future Work:

DRIE is a promising technique to fabricate metamaterial sub wavelength thin film anti reflective coatings. We have made and optically characterized one sided samples [2]. Currently we are able to produce $50\ \mu\text{m}$ scale features on a full 4-inch wafer surface and used high temperature direct bonding to bond two silicon pieces together. Multiple samples can be obtained from 4-inch bonded wafers. Optical characterization with a Fourier Transform Spectrometer has shown that our samples achieved excellent transmission, better than 99% at 900 GHz. Our next steps include the development of a double layer coating to extend the operation bandwidth and exploring a technique to bend a thin wafer into a curved surface to allow bonding to a silicon lens.

References:

- [1] R. Datta, et al, Large-aperture wide-bandwidth anti-reflection-coated silicon lenses for millimeter wavelengths, Applied Optics, Vol. 52, Issue 36, pp. 8747-8758 (2013).
- [2] Wheeler, et al. Antireflection coatings for submillimeter silicon lenses. SPIE Proc. 9153, 91532Z (2014).

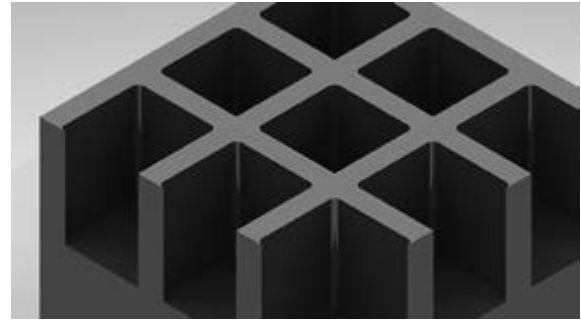


Figure 1: Three dimensional representation of the metamaterial structure. The pitch for this design is $\sim 50\ \mu\text{m}$, square holes are $\sim 40\ \mu\text{m}$ in size. Depth is $\sim 48\ \mu\text{m}$.



Figure 2: Infra-red transmission image of the two bonded wafers. There is only one bubble of size $\sim 4\ \text{cm}^2$. Multiple $1\ \text{cm}^2$ samples can be cut from this for further characterization in a Fourier Transform Spectrometer.

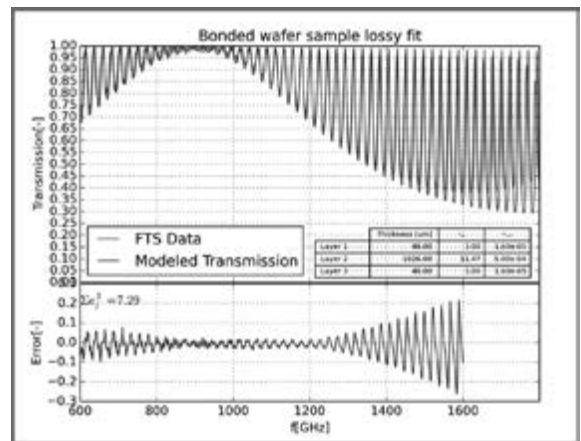


Figure 3: Cryogenic transmission of the tested sample. Excellent transmission ($> 99\%$) was achieved in the 900 GHz band.

Thermal Effects in One- and Two- Dimensional Micro-Electro-Mechanical Resonators

CNF Project Number: 762-99

Principal Investigators: Jeevak M. Parpia, Harold G. Craighead

Users: Roberto De Alba, Abhilash T. Sebastian

Affiliation: Department of Physics, Cornell University

Primary Source of Research Funding: National Science Foundation

Contact: jmp9@cornell.edu, hgc1@cornell.edu, rd366@cornell.edu, at654@cornell.edu

Website: parpia.lassp.cornell.edu, hgc.cornell.edu

Abstract:

Micro-electro-mechanical systems (MEMs) resonators with reduced dimensionality make novel and extremely sensitive systems with which to measure ultra-weak forces, detect gases, or construct oscillators for personal electronics. We have fabricated two very different classes of resonators with the goals of understanding their material properties and probing new physics. Firstly, we have made two-dimensional tensioned drums of suspended graphene and tracked their resonant frequencies in real-time as they are annealed at high-temperatures. Such experiments bring to light the effects of surface contaminants, membrane wrinkles, and other non-idealities that will ultimately limit graphene's usefulness as MEMs elements. Secondly, we have made composite nanowires of high-stress silicon nitride coated with a film of superconducting niobium. These one-dimensional wires have a cross-section (50 nm square) that is less than the coherence length of superfluid helium-3, and will be used at ultra-low temperatures to study superfluid behavior as disorder is generated by the vibrating wire. We have characterized these wires at room temperature, and observed thermally induced self-oscillation caused by impinging laser light.

Summary of Research:

Graphene's atomic thinness, large surface area, and electrical integrability make it an extremely promising MEMs material for commercial and scientific applications. Its low mass and high tension are pre-requisites for atomic-scale mass sensors [1], and its tunable frequency has already been used to make electrical filters, frequency mixers [2], and voltage-controlled oscillators [3]. One of the issues that graphene devices currently face, however, is surface contamination. Polymers used during fabrication (e.g., for transfer of graphene from its growth substrate to the device substrate) invariably leave residue that add unnecessary mass and degrade electrical performance.

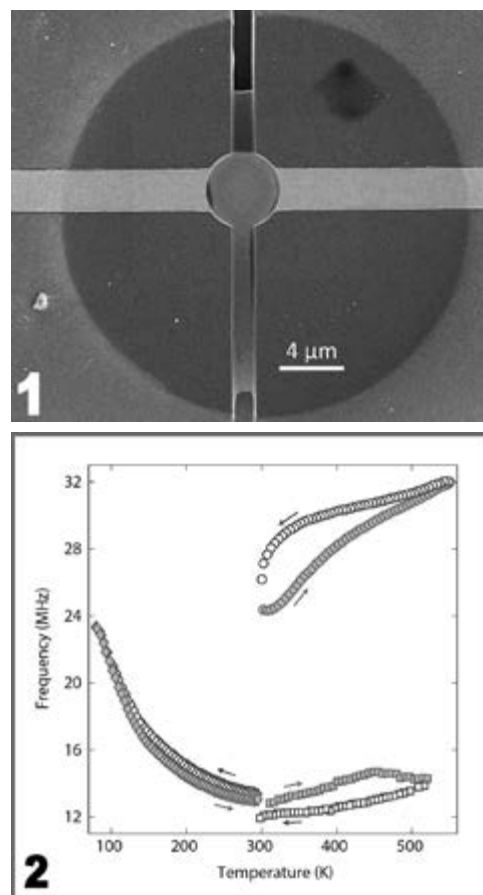


Figure 1, top: Electron micrograph of a circular graphene MEMs resonator. The central membrane is suspended above a 1.3 μm trench and driven capacitively via a platinum back-gate (deposited using SC4500 evaporator). Platinum Source and Drain leads (left to right) contact the graphene from underneath.

Figure 2, bottom: Resonant frequency of graphene membranes during thermal cycling. Diamonds: Low-temperature behavior of an as-fabricated graphene membrane. Squares: The same membrane during its first annealing cycle. Changes in the resonant frequency are irreversible and indicative of graphene slippage. Circles: Behavior of a second device after many annealing cycles. The hysteresis loop is reproducible and suggests slow internal cooling of the graphene sample.

After fabrication, annealing is typically performed in a hydrogen-argon environment at 250°C to remove the majority of this polymer mass, but a thin film of residue always remains [4]. The presence of this residue can cause stark deviations from the theoretically expected mechanical properties of graphene (negative thermal expansion, high elastic modulus, etc.) — a result that is common within the published experimental reports.

Topographical defects such as membrane ripples can also strongly influence graphene mechanics. These can either be present during fabrication, or generated during high-temperature annealing by thermally induced strain [5]. To study the impact of these various thermal effects on graphene resonators, we have designed an experimental test chamber in which we can track the resonant frequency (i.e., membrane tension) of a graphene device continuously as it is heated from room temperature to 250°C. Simultaneously tracking the resonator's quality factor (Q) reveals how device performance is affected by polymer removal, ripple formation, and membrane-substrate slippage caused by graphene thermal contraction. These results are complemented by similar measurements in the -200°C to 20°C range to examine the behavior of the graphene-polymer composite system more broadly.

MEMs nanowire experiments are also underway, with the joint goals of providing a new and powerful probe of superfluid Helium³, and studying the unique nonlinear mechanics of the wires themselves. The wires have extremely high aspect ratios, with lengths of 40 μm and square cross-sections of 50 nm. Their frequencies and quality factors have been characterized at room temperature (prior to and after metallization with 15 nm niobium), revealing a factor of ~ 10 drop in Q. Interestingly, the metallized wires undergo spontaneous self-driven oscillations if they are illuminated with laser light of the appropriate wavelength and intensity. This result is caused by optical absorption (and resulting thermal expansion) of niobium as the wire moves within the optical field, and has been reported in a similar system previously [6,7]. Unlike other systems, however, these nanowires demonstrate hybrid limit-cycle-Duffing behavior when a strong external drive signal is applied in conjunction with the intense laser light. Understanding these nonlinear opto-mechanical effects could help overcome viscous damping of these nanowires in air or liquid helium, and pave a path towards more compact MEMs oscillators for telecommunications applications.

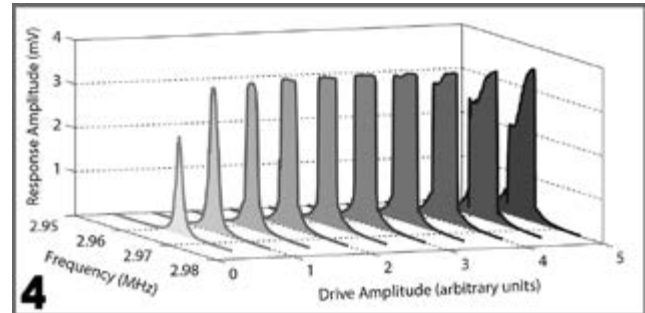
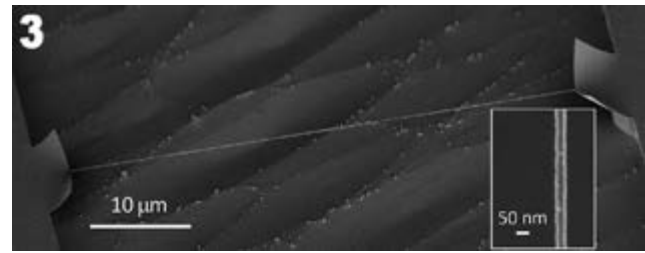


Figure 3, top: Angled electron micrograph of a high-stress silicon nitride nanowire coated with 15 nm of sputtered niobium (MRL nitride furnace and AJA sputter tool). The wire length is 50 μm and cross-section width is 50 nm. It is suspended above an 8 μm trench. Inset: close-up image of the nanowire.

Figure 4, bottom: Vibrational response of a nanowire once it is undergoing laser-induced self-oscillation. The wire motion can be entrained using a weak external drive signal near the resonance frequency (flat-top traces), but gives way to a Duffing-type response at high drive amplitudes (right-most traces).

References:

- [1] Chaste, J., et al. A nanomechanical mass sensor with yoctogram resolution. *Nat. Nanotechnol.* 7, 301-4 (2012).
- [2] De Alba, R., et al. Tunable phonon-cavity coupling in graphene membranes. *Nat. Nanotechnol.* (accepted, 2016).
- [3] Chen, C., et al. Graphene mechanical oscillators with tunable frequency. *Nat. Nanotechnol.* 8, 923-7 (2013).
- [4] Lin, Y.-C., et al. Graphene Annealing.: How Clean Can It Be? *Nano Letters* 12, 414-29 (2012).
- [5] Bao, W., et al. Controlled ripple texturing of suspended graphene and ultrathin graphite membranes. *Nat. Nanotechnol.* 4, 562-6 (2009).
- [6] Aubin, K., et al. Limit Cycle Oscillations in CW Laser Driven NEMS. *J. Microelectromech. Syst.* 13, 1018-26 (2004).
- [7] Blocher, D., et al. Multiple limit cycles in laser interference transduced resonators. *Int. J. Nonlinear Mech.* 52, 119-26 (2013).

Self-Folding with Graphene Bimorphs

CNF Project Number: 900-00

Principal Investigators: Paul McEuen, Itai Cohen

Users: Marc Miskin, Kyle Dorsey, Baris Bircan

Affiliations: Laboratory of Atomic and Solid State Physics, School of Applied and Engineering Physics, Kavli Institute for Nanoscale Science, Cornell; Cornell University

Primary Source of Research Funding: National Science Foundation (DMREF DMR-1435999), Air Force Office of Scientific Research (MURI FA 9550-16-1-0031)

Contact: PLM23@cornell.edu, itai.cohen@cornell.edu, mm2325@cornell.edu, kjd96@cornell.edu

Website: <http://www.mceuengroup.lassp.cornell.edu/>

Abstract:

Two dimensional materials provide a platform for design of microscale structures and machinery. We report a graphene-SiO₂ bimorph actuator fabricated using atomic layer deposition. We demonstrate mechanical response of the actuator in response to diverse stimuli such as temperature, pH, and ion concentration.

Summary of Research:

At the macroscale, it is clear that cutting and folding are two powerful techniques that can be used to transform simple sheets of material into complex three dimensional structures. Yet, it is unclear if the same ideas can be scaled and work with equal efficiency when the sheet of material is one atom thick. We have developed a new technique that let us program two layer stacks, or bimorphs, made of graphene and ultrathin films to self-fold via differential stress (presented schematically in Figure 1). Our approach works in the extreme regime of bimorph folding: we construct bimorphs that optimize folding efficiency when one layer is atomically thin. In other words, our current research embodies the world record for the thinnest bimorph actuators.

By applying this technique in concert with lithographic patterning, we have produced a powerful platform to build three dimensional structures at the nanoscale. Figure 2 shows graphene glass bimorphs patterned by our method. These devices are made by first growing a 2 nm-thick film of silicon dioxide onto a substrate with atomic layer deposition (ALD), to which graphene is transferred. Photolithography and plasma etching are used to pattern the graphene-glass stack into a desired geometry, in this case arrays of cantilever beams (see Figure 2). By etching the substrate beneath the deposited silicon-dioxide, the device can be removed from the surface, allowing it to fold in free space in fluid. A bimorph attached to a micromanipulator probe is shown in Figure 3.

The key engineering parameter for these systems is the curvature, which increases in proportion to the strain mismatch between the bimorph layers. For bimorphs built around atomically thin membranes, strains on the order of 10^{-3} produce radii of curvature on the order of $1 \mu\text{m}$; a scale roughly 10 to 100 times smaller than achieved with bimorphs that do not use atomic membranes. In Figure 3, folding is being driven in response to heating. Specifically, a 1064 nm laser is heating the probe holding the device to produce a strain difference between the layers. However, strain can be generated by a wide range of other driving fields: our preliminary research has found glass-graphene bimorphs can be made sensitive to pH, salt concentrations, and applied voltages.

Bimorphs built by combining atomic membranes with ALD presents a broad range of sensing and actuation mechanisms. By changing the ALD layer from silicon dioxide to zinc-oxide, we should be able to make bimorphs driven by piezoelectric effects. By surface functionalizing the graphene layer, it should be possible to make bimorphs that respond to specific, targeted biomolecules. Moreover, by moving to multilayer stacks, we should be able to achieve bi-directional folding and articulation. Finally, we intend to make bimorphs entirely from the growing family of two dimensional materials, such as hexagonal boron nitride and molybdenum disulfide. Altogether this work shows that atomic membrane bimorphs are a general platform for the construction of customizable parts that sense and respond to environmental stimuli at the nanoscale.

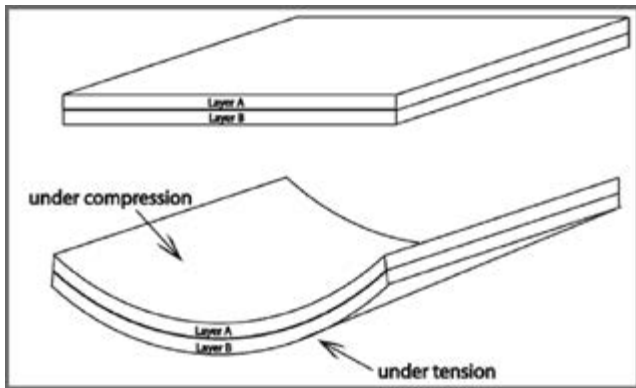


Figure 1: Schematic illustration of bimorph bending mechanism.



Figure 2: Arrays of graphene bimorph cantilever beams imaged in a transmission optical microscope.

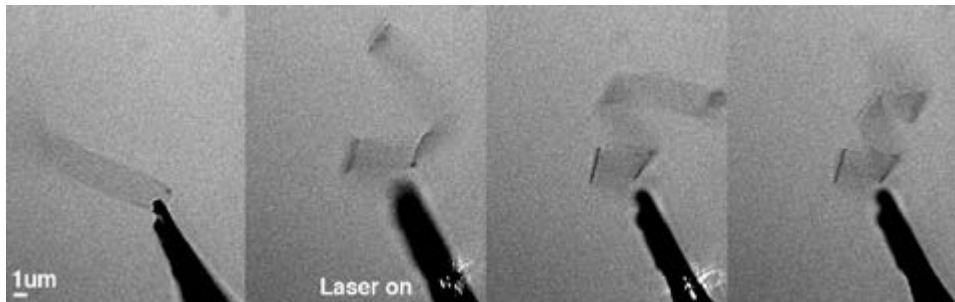


Figure 3: Graphene bimorph bending in response to temperature. As the bimorph is heated with the laser, the bimorph curls with a tight radius of curvature.

Near Zero Power Electrostatic Switches

CNF Project Number: 1121-03

Principal Investigators: Amit Lal, Alyosha Molnar

Users: Leanna Pancoast, Benjamin Davaji, Visarute Pinrod, Sunwoo Lee

Affiliation: Department of Electrical and Computer Engineering, Cornell University

Primary Source of Research Funding: Defense Advanced Research Projects Agency

*Contact: amit.lal@cornell.edu, am699@cornell.edu, lap258@cornell.edu,
bendavaji@cornell.edu, vp239@cornell.edu, sl933@cornell.edu*

Abstract:

There is always a push to increase the battery life of current electronics. Rather than getting more efficient batteries, we can instead increase the efficiency of the devices we make and use. Transistors are prevalent in modern electronics, but traditional MOSFETs have considerable leakage current when they are supposed to be off. Mechanical switches remove that off-state leakage current to allow little to no power consumed when the switch is deactivated. A one mask process is used to fabricate laterally actuated electrostatic switches.

Summary of Research:

Electrostatic actuated devices rely on an applied voltage to move structures. We made several designs, but will focus on a cantilevered switch, as shown in Figure 1. A free moving beam is connected to ground while a voltage is applied to a bias point. The voltage difference means the beam is attracted to the bias and will start to move. With an appropriately placed or drain, the beam will make contact.

We use a one mask process in order to fabricate nanometer scale electrostatic mechanical switches, check out the process flow in Figure 2. We start off with purchased silicon-on-oxide (SOI) wafers. We degenerately P-dope the substrate using the boron in the furnaces available in the CNF, which improves conductivity of the silicon and reduces some of the built-in stress of the SOI wafers. Further annealing in a furnace reduces the bowing of the wafers caused by stress. We use the CVC sputter deposition system to deposit a 100 nm film of MoSi_2 to further increase the conductivity of our switches. The ASML DUV stepper is used to pattern sub-300 nm sized features onto the wafer. The Oxford 82 etcher is used to etch through the MoSi_2 and deep reactive ion etching (DRIE) is used to go through the silicon device layer. We dice the wafer and use vapor HF to release our devices before testing.

Figure 1 shows a fabricated device with a modified process due to some unavoidable issues in fabrication. The device is then covered with Ti and Au and tested in a vacuum. A voltage sweep is applied to a bias point of the device while reading the current at the drain. Figure 3 shows the results: a turn on voltage of 70 V is found and turn off voltage of 30 V.

The issues we ran into with our first process have been resolved and we will be able to bring the turn on voltage down considerably with a proper process flow.

References:

- [1] Amponsah, K., N. Yoshimizu, S. Ardanuc, and A. Lal. "Near-kT Switching-Energy Lateral NEMS Switch." In 2010 5th IEEE International Conference on Nano/Micro Engineered and Molecular Systems (NEMS), 985-88, 2010. doi:10.1109/NEMS.2010.5592599.

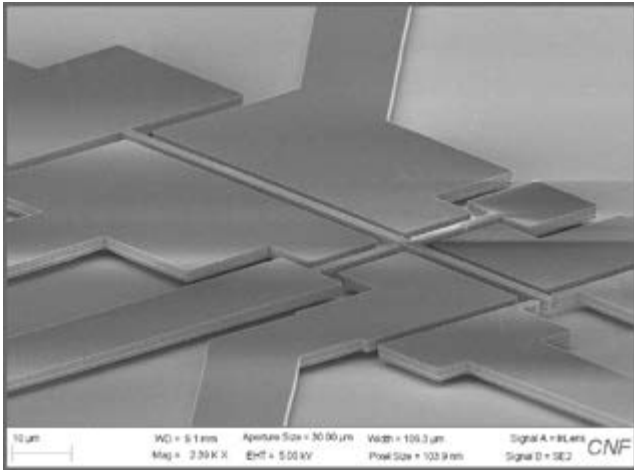


Figure 1: A fabricated switch viewed with a 70 degree chuck in the Zeiss Ultra Scanning Electron Microscope. This has no MoSi₂ and skipped steps b) and c) shown in Figure 2.

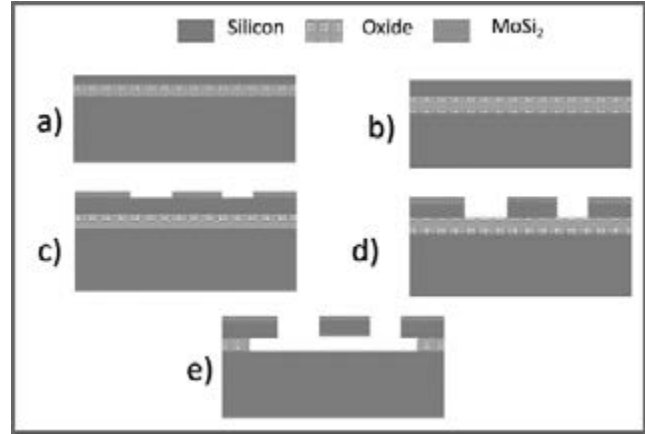


Figure 2: Fabrication Process. a) Silicon on Insulator wafer, dope and anneal the wafer. b) Deposit MoSi₂ onto the wafer. c) pattern and etch MoSi₂. d) Deep Reactive Ion Etch through Si. e) Vapor HF release.

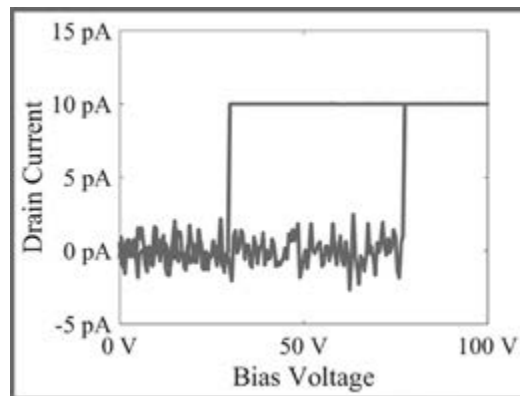


Figure 3: The switch shown in Figure 1 is covered in Au after fabrication due to DRIE roughness causing some problems and then tested under vacuum. Using a different DRIE tool will remove this problem in the future. The beam is set at 0V and the drain electrode is set at 200mV with a 10 pA compliance. The bias voltage is swept from 0 V to 100 V while reading the current through the drain.

Micro Components for Self-Calibrating Inertial Sensors

CNF Project Number: 1122-03

Principal Investigator: Prof. Amit Lal

Users: Visarute Pinrod, Sachin Nadig

Affiliation: School of Electrical and Computer Engineering, Cornell University

Primary Sources of Research Funding: Defense Advanced Research Projects Agency (DARPA),
Primary and Secondary Calibration on Active Layer (PASCAL) Program

Contact: amit.lal@cornell.edu, vp239@cornell.edu, spn36@cornell.edu

Website: <http://sonicmems.ece.cornell.edu/>

Abstract:

We present self-calibrating inertial sensors with atomically stable optical feedback. The system consists of an integrated microelectromechanical systems (MEMS) inertial measurement unit (IMU) mounted on a $25.4 \times 25.4 \times 0.5$ mm multi-axis piezoelectric mechanical stimuli stage with a platform disk of diameter 7.5 mm capable of *in situ* calibration. The stage can inject rotation dither rates and accelerations as high as $100^\circ/\text{sec}$ and 90 m/s^2 , respectively. The stage position feedback is provided by using an atomically stable laser shining through a grating mounted on the stage. High speed optical image sensors pick up a diffraction pattern that provides stage position. A microcontroller controls the stage excitation, read an output from IMU, calculate stage position from diffraction patterns, and provide a calibrated acceleration and rotation speed. We measure the gyroscope cross-axis sensitivities of 2.4%, which is within the IMU specifications.

Summary of Research:

An electronic MEMS IMU on a single package brings together a 3-axis gyroscope, a 3-axis accelerometer, and other sensors leading to applications such as IMU-assisted GPS navigation, and rate-based motion tracking. Because of scale factor drift and bias fluctuation, these small, low cost, and low power IMUs cannot be used for navigation for a long time. Adding an *in situ* and long term stable calibration layer allows higher accuracy navigation in different environmental conditions for longer time.

The active calibration layer consists of a piezoelectric mechanical stage, an atomically stable laser source, a grating, and an image sensor as optical feedback as shown in Figure 1. A $25.4 \times 25.4 \times 0.5$ mm lead zirconium titanate (PZT) plate is spin-coated with photoresist to protect the surface, and laser cut to define electrodes and stage shape [1]. The stage is designed to give pure excitation [2,3]. A PZT gyroscope can be monolithically integrated to center the stage [4]. Alternatively, a commercial IMU can be mounted upside down and wire bonded to the electronics by Westbond 7400A Ultrasonic Wire Bonder as shown in Figure 2a [5-7].

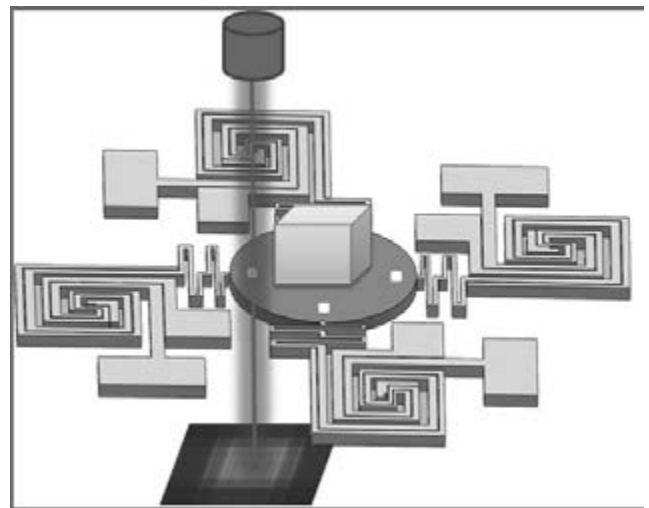


Figure 1: 3D illustration of PZT dither stage with eight electrodes for mechanical stimulate IMU in three modes with integrated grating for optical feedback.

A block diagram in Figure 2b shows that a microcontroller controls stage excitation, and reads data out from the IMU. A picture of a control board is shown in Figure 2c. An output from IMU excited by an open loop dither stage and a commercial shaker

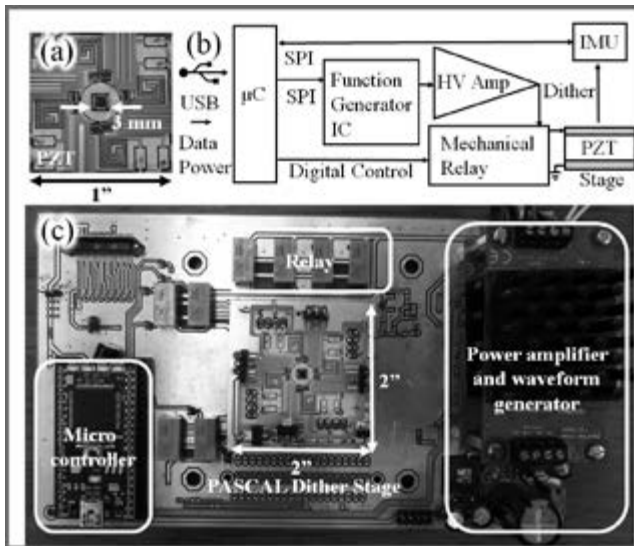


Figure 2: (a) 6-DOF IMU (MAX21105) mounted on PZT dither stage (b) Block diagram and (c) Picture of the control board used to calibrated the IMU

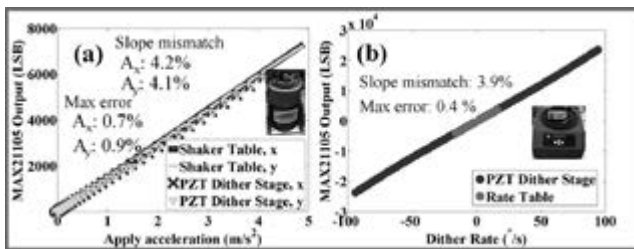


Figure 3: (a) Measured x-and y-axis acceleration output using PZT dither stage, and Vibration research VR2500 vibration controller (b) Measured z-axis angular speed scale factor using PZT dither stage and Ideal Aerosmith 12700VS rate table.

table and a rate table is shown in Figure 3a, and 3b. Optical feedback with atomically stable laser adds long term stability [8]. Optical feedback consists of shining a laser through a nickel grating on silicon nitride membrane, of which a photograph is shown in Figure 4a. A microscope photograph of a grating surface is shown in Figure 4b.

The grating is fabricated by depositing silicon nitride by low-pressure chemical vapor deposition (LPCVD) nitride furnace on double polished silicon wafer. Back side nitride opening is etched by Oxford PlasmaLab 80+ reactive ion etching (RIE) System, nickel grating was deposited by an SC4500 evaporator, and lift off to define pattern. The silicon nitride membrane is released in potassium hydroxide (KOH) etch bath. The grating die is cut out from the wafer by laser cutting. The stability of the optical feedback system with the grating is under 10 ppm as shown in Figure 4c.

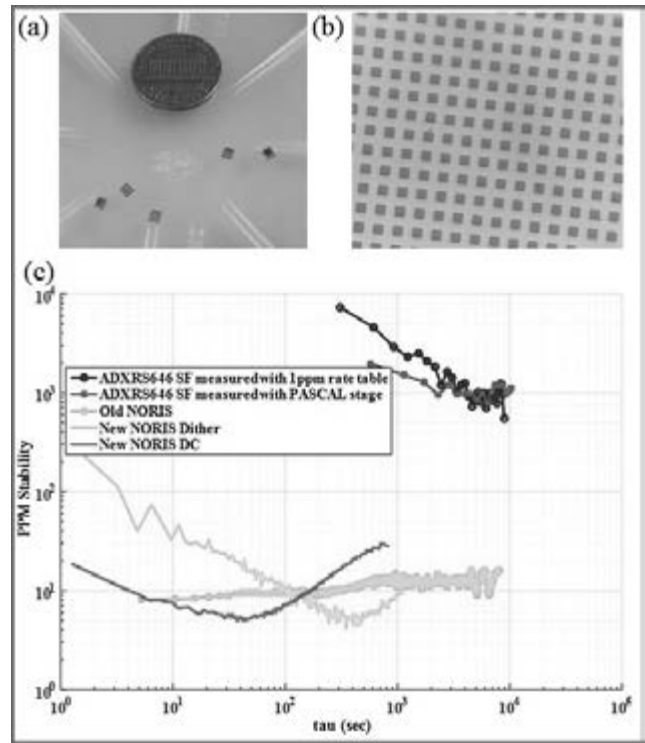


Figure 4: (a) Photograph of a grating dies (b) Microscope photograph of the grating surface (c) PPM stability of an optical feedback system.

References:

- [1] Nadig, Sachin, Serhan Ardanuc, and Amit Lal. "Planar laser-micro machined bulk PZT bimorph for in-plane actuation." Applications of Ferroelectric and Workshop on the Piezoresponse Force Microscopy (ISAF/ PFM), 2013 IEEE International Symposium on the. IEEE, 2013.
- [2] Nadig, Sachin, Serhan Ardanuc, and Amit Lal. "Monolithic piezoelectric in-plane motion stage with low cross-axis-coupling." Micro Electro Mechanical Systems (MEMS), 2014 IEEE 27th International Conference on. IEEE, 2014.
- [3] Lal, Amit, Sachin Nadig, and Serhan Mehmet Ardanuc. "Monolithic PZT Actuator, Stage, and Method for Making." U.S. Patent No. 20,160,072,041. 10 Mar. 2016.
- [4] Nadig, Sachin, Serhan Ardanuc, and Amit Lal. "Self-calibration compatible Z-axis bulk PZT vibratory gyroscope." Solid-State Sensors, Actuators and Microsystems (TRANSDUCERS), 2015 Transducers-2015 18th International Conference on. IEEE, 2015.
- [5] Nadig, Sachin, et al. "Multi-modal mechanical stimuli stage for in-situ calibration of MEMS gyroscopes." Inertial Sensors and Systems (ISISS), 2015 IEEE International Symposium on. IEEE, 2015.
- [6] Nadig, Sachin, et al. "In-run scale factor and drift calibration of MEMS gyroscopes with rejection of acceleration sensitivities." 2016 IEEE International Symposium on Inertial Sensors and Systems. IEEE, 2016.
- [7] Pinrod, Visarute, et al. "Piezoelectric micro dither stage calibration of 6-axis IMU." 2016 IEEE 29th International Conference on Micro Electro Mechanical Systems (MEMS). IEEE, 2016.
- [8] Nadig, Sachin, et al. "DOME-DISC: Diffractive optics metrology enabled dithering inertial sensor calibration." Micro Electro Mechanical Systems (MEMS), 2014 IEEE 27th International Conference on. IEEE, 2014.

Particle Fabrication for Rheology Measurement of Structured Suspensions

CNF Project Number: 1177-03

Principal Investigator: Abraham D. Stroock

User: Neeraj Nitin Sinai Borker

Affiliation: The Sibley School of Mechanical and Aerospace Engineering, Cornell University

Primary Source of Research Funding: National Science Foundation

Contact: abe.stroock@cornell.edu, ns762.cornell.edu

Abstract:

The ability to control dynamics of individual particles in a suspension allows precise control over the macroscopic properties of materials, in particular developing anisotropic materials from processing flow. Recently it has been theoretically established that a class of rigid particles exhibit non-tumbling behavior in a simple shear flow without the application of external forces [1]. These particles have a topology of a high-aspect ratio ring with a well-defined cross-sectional geometry, that allows control over how the particle rotates and translates in shearing flows. The major challenges in fabricating these ring shaped particles are that they have overhanging components and they have a tendency to buckle due to its high aspect ratios. Our work focuses on the fabrication of these particles of size of about a few 1000 μm with feature sizes of around 5 μm using photolithography tools with the objective of measuring rheology of a suspension of such particles.

Summary of Research:

Over the past few months, we have developed a process to fabricate high aspect ratio ring shaped particles on a 10 mm Si-wafer using multi-step photolithography. Photolithography is chosen as means of fabricating the particles of interest shown in Figure 1. This is not only due to the simplicity of the process, but also due to its ability to produce particles in bulk with reproducible results. The particles are fabricated using multi-step photolithography using an epoxy based negative photoresist SU-8 that contains acid-labile groups and a photoacid generator.

Irradiation produces a low concentration of a strong acid that acts as a catalyst for the cross-linking process on application of heat. SU-8 is used for its mechanical

reliability and chemical resistance to electrolytes. For lifting the particles off the wafer a thin sacrificial layer of Omnicoat is applied, which can be selectively dissolved over SU-8 at the last step to get a suspension of particles. Alignment marks are etched in a 100 mm wafer, 1 μm in depth. A sacrificial layer of Omnicoat of 300 nm is deposited on the wafer that will be used to lift the particles off the wafer. In the current process two layers of 5 μm and 12 μm respectively are spun on a 100 mm Si-wafer that has alignment marks etched in it. Figure 2 briefly describes the two major exposure steps in the process that will produce ring shaped particles with a "L-shaped" cross section seen in Figure 1A. The film thicknesses measured using the profilometer is shown in Figure 3.

The objective is to test the dynamics of particles with the theoretical findings about the rheology of the suspension. The particles will be collected by dissolving the sacrificial layer and transferring it to a buffer solution with a stabilizing surfactant NP40. Particles with an overhanging structures, as shown in Figure 1B, will be fabricated in the coming months.

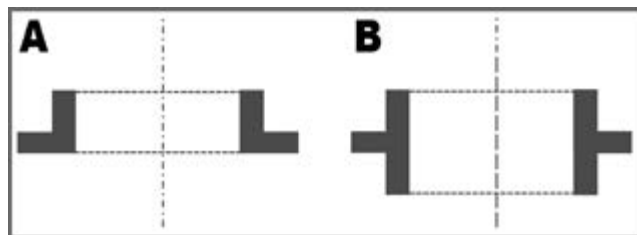


Figure 1: (a) Cross-section of a ring-shaped particles with a cross-section that resembles an "L-shape" cross-section, that are currently being fabricated. (b) Cross-section of a ring shaped particle with an overhang.

References:

- [1] Singh, Vikram, Donald L. Koch, and Abraham D. Stroock. "Rigid ring-shaped particles that align in simple shear flow." *Journal of Fluid Mechanics* 722 (2013): 121-158.

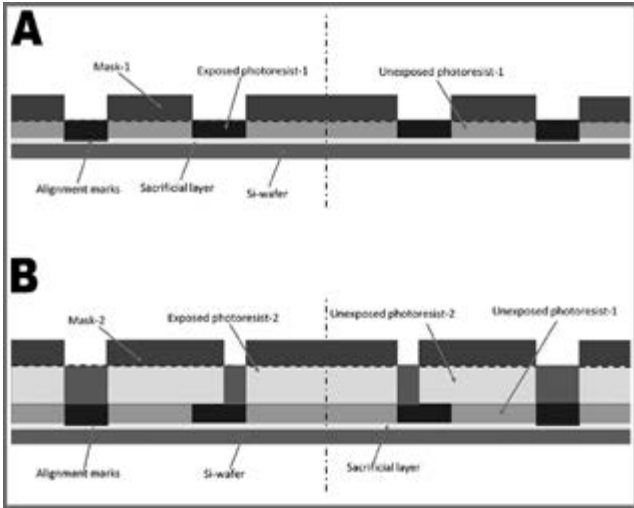


Figure 2: Sketch of the intermediate steps in a multilayer photolithography using negative photoresist SU-8 2000 series. (a) The exposure step using the first layer mask (b) exposure step using the second layer mask.

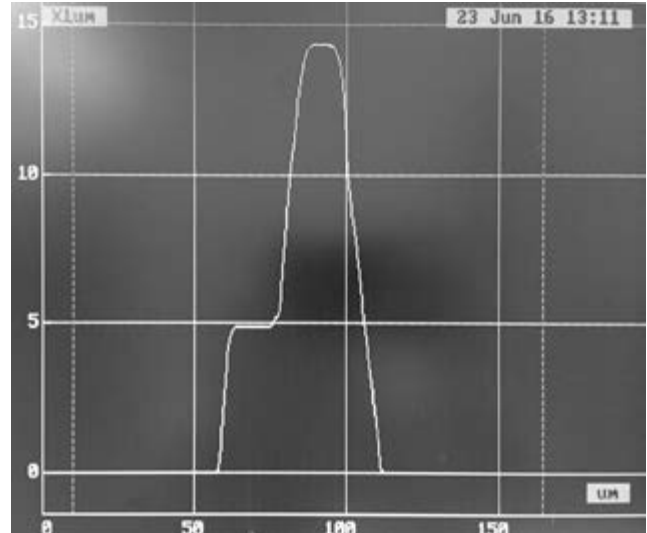


Figure 3: Profilometer measurement of the height profiles of an "L-shape" cross-section.

HBAR as a High Frequency High Stress Generator

CNF Project Number: 1380-05

Principal Investigator: Sunil A. Bhave¹

User: Tanay A. Gosavi²

Affiliations: 1. Electrical and Computer Engineering, Purdue University;
2. Electrical and Computer Engineering, Cornell University

Primary Source of Research Funding: SRC

Contact: bhave@purdue.edu, tag75@cornell.edu

Abstract:

In this paper we report on a high-overtone bulk acoustic resonator (HBAR) as a high stress generator by measuring f - Q product of various tones and overtones from room temperature to 80 Kelvin. HBARS provide excellent acoustic isolation from anchor losses as the modes are confined within the high finesse acoustic cavity made from single crystal diamond or silicon carbide (SiC) substrates. Their high Q and linearity makes them robust transducers for generating up to 20 MPa AC stress with small drive voltages at gigahertz frequencies, which is instrumental in manipulating spin-defect qubits in these materials.

Summary of Research:

MacQuarrie, et al. [1,2], have demonstrated acoustically mediated spin-state control of nitrogen-vacancy centers in diamond. They further demonstrated complete coherent control by driving Rabi oscillations between $|+1\rangle$ and $|.1\rangle$ spin states. Similar di-vacancy based spin-defects have also been observed in SiC [3]. With ease of wafer scale integration of SiC on Si these quantum technologies have capabilities for developing solid-state wafer-scale hybrid quantum systems. Interrogating and controlling the di-vacancy spins in SiC with a mechanical resonator can be achieved through the use of an HBAR. This is similar to the system that was implemented in experiments by MacQuarrie, et al. [1,2].

For understanding the limits of HBAR as a stress generator in SiC and diamond and compare it to silicon we fabricated HBARS on SiC, diamond and silicon substrates. We then measured quality factor as a function of temperature from 80K to room temperature at multiple resonant frequencies for each sample. The quality factors measured were then used to estimate the maximum stress generated at an anti-node inside the wafer using a 1D analytical model of an HBAR.

We discovered that the maximum stress generated in the HBAR doesn't increase linearly with the quality factor and were able to verify this saturation of stress with Comsol simulations.

From our measurements and analysis, we note that HBARS on SiC have tremendous potential for generating stress at GHz frequencies and hence they play an active role in the new generation of hybrid quantum sensors and systems.

References:

- [1] E. R. MacQuarrie, T. A. Gosavi, N. R. Jungwirth, S. A. Bhave, and G. D. Fuchs, "Mechanical spin control of nitrogen-vacancy centers in diamond," *Phys. Rev. Lett.*, vol. 111, no. 22, p. 227602, 2013.
- [2] E. R. MacQuarrie, T. A. Gosavi, A. M. Moehle, N. R. Jungwirth, S. A. Bhave, and G. D. Fuchs, "Coherent control of a nitrogen-vacancy center spin ensemble with a diamond mechanical resonator." *Optica*, vol. 2, no. 3, pp. 233-238, Mar. 2015.
- [3] A. L. Falk, P. V. Klimov, B. B. Buckley, V. Ivády, I. A. Abrikosov, G. Calusine, W. F. Koehl, Á. Gali, and D. D. Awschalom, "Electrically and mechanically tunable electron spins in silicon carbide color centers," *Phys. Rev. Lett.*, vol. 112, no. 18, p. 187601, 2014.

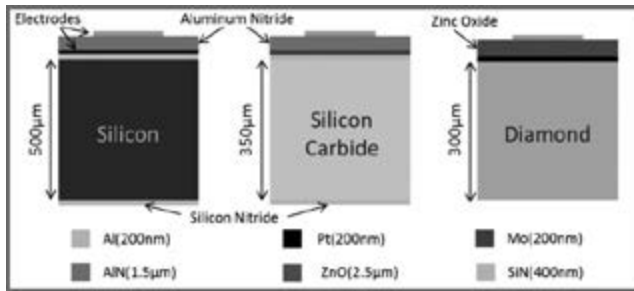


Figure 1: Device geometries and material stacks for HBARs fabricated on silicon, SiC and diamond substrates.

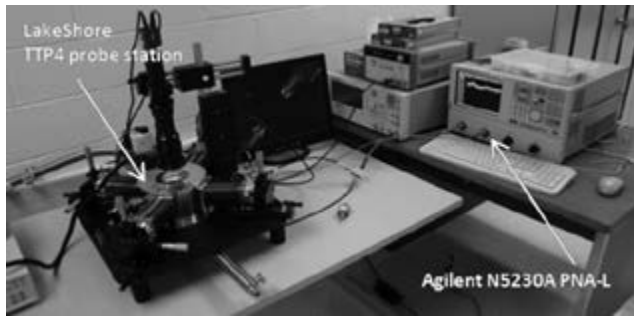


Figure 2: Device characterization setup comprising of LakeShore probe station and Agilent network analyzer.

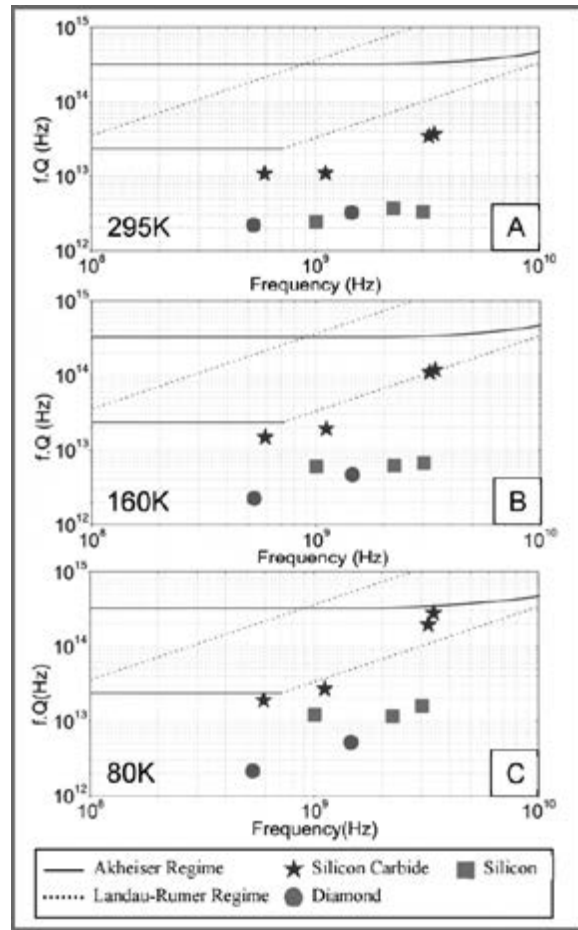


Figure 3: Frequency-Quality factor product vs. Frequency graphs of HBAR resonances measured at temperatures 295K (plot A), 160K (plot B) and 80K (plot C). Data points on the plots represent measured resonances of silicon (red), diamond (green) and silicon carbide (blue) HBARs. The lines on the graph represent the two different phonon-phonon dissipation limited fQ values calculated for these materials at room temperature. In case of diamond we only see Landau-Rumer regime of damping as it has high thermal conductivity.

HBAR Materials	Stress @ 295K	Stress @ 80K
Silicon -3.02GHz	2.20 MPa	2.90 MPa
Diamond -1.45GHz	1.43 MPa	1.51 MPa
Silicon Carbide -3.40GHz	4.05 MPa	6.15 MPa

Figure 4: Stress generated by HBAR for 1V drive.

The Nanoaquarium; A Device for *in situ* Electron Microscopy of Processes in Liquids

CNF Project Number: 1542-07

Principal Investigator: Haim H. Bau

User: Joseph M. Grogan

Affiliation: Mechanical Engineering and Applied Mechanics, the University of Pennsylvania, Philadelphia, PA, USA

Primary Source of Research Funding: National Science Foundation-CBET 1066573 and NSF CMMI 1129722

Contact: bau@seas.upenn.edu, jgrogan@seas.upenn.edu

Website: <http://bau.seas.upenn.edu>

Abstract:

The nanoaquarium is a nanofluidic platform for *in situ* electron microscopy of processes in liquid media. The nanoaquarium consists of a hermetically sealed, thin (~100 nm tall) liquid cell sandwiched between two electron-transparent silicon nitride membranes. The nanoaquarium is equipped with micro patterned electrodes. The device has been used to image electrochemical deposition and etching, growth and dissolution of nanoparticles, diffusion limited aggregation, crystallization, nucleation and bubble growth, nanobubble migration, interfacial phenomena, to assess the interactions between electron radiation and fluids, and to pattern nanostructures without a need for a mask.

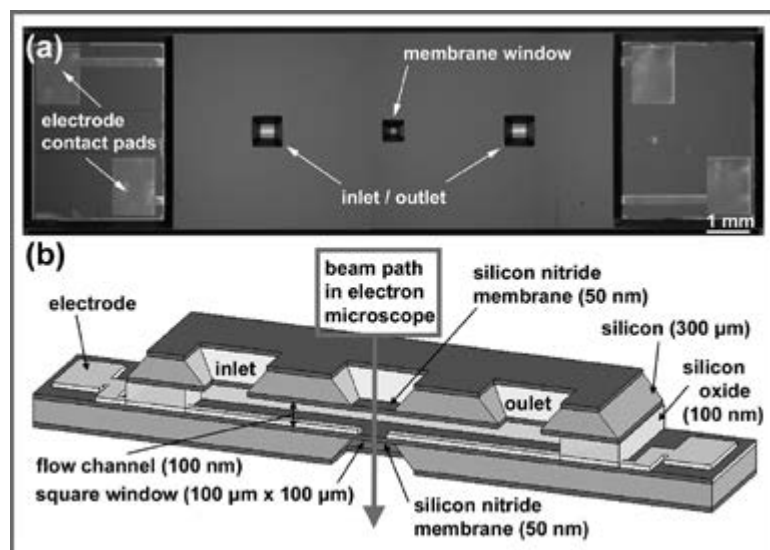


Figure 1: A photograph of the nanoaquarium (top) and a schematic of the nanoaquarium's cross-section (bottom).

Summary of Research:

The nanoaquarium is a custom-designed, microfabricated, nanofluidic device for *in situ* electron microscopy of processes taking place in liquids and of objects submerged in liquids (Figure 1). Two thin (< 50 nm), electron-transparent silicon nitride

membranes sandwich a thin liquid layer, ranging in thickness from tens of nanometers to a few microns. The cell is hermetically sealed from the vacuum environment of the electron microscope. Due to its small thickness, the liquid layer does not significantly scatter electrons, allowing nanoscale resolution imaging of objects suspended in the confined liquid. The nanoaquarium contains electrodes patterned on the silicon nitride membrane for electrochemical experiments.

The fabrication of the device was accomplished with direct bonding of silicon wafers coated with silicon nitride. One of the wafers contains a thin film of patterned silicon oxide that defines the shape and height of the imaging chamber and the liquid conduits. The use of direct wafer bonding eliminates risk from potential contamination from glue, epoxy, and other sealing materials and assures a hermetic seal. Use of a dielectric material as the spacer allows electrodes to be directly incorporated into the device. A schematic of the nanoaquarium is depicted in Figure 1.

The fabrication process has been previously described [1]. Our lab, in collaboration with others, has used

nanoaquariums to study nanoparticle aggregation and colloidal crystal growth dynamics [2-4]; interactions of nanoparticles with moving interfaces [5]; electron beam-induced radiolysis [12-14]; bubble nucleation, growth and detachment [6,10,12]; crystallization [8,16]; and electroplating [9,11,17]. We have also demonstrated the use of the electron beam as a “pen” to pattern nanowires without a need for a mask [12]. The device was patented [18].

Since *in situ* electron microscopy produces large quantities of data, we have recently developed automated image processing algorithms to extract useful quantitative measures of the observed phenomena [17]. As examples, we examined metal electro-deposition at electrode surfaces; beam-induced nanocrystal formation and dissolution; and bubble nucleation, growth and migration. These three experiments were used to demonstrate a fully automated workflow for the extraction of, among other things, interface position, RMS roughness, lateral wavelength, local normal velocity, and the projected area of the evolving phase as functions of time (Figure 2). The relevant algorithms have been implemented in Mathematica and posted on the web [19].

Acknowledgments:

Electron microscopy was performed at the Penn Regional Nanotechnology Facility at the University of Pennsylvania and at the IBM TJ Watson Research Center.

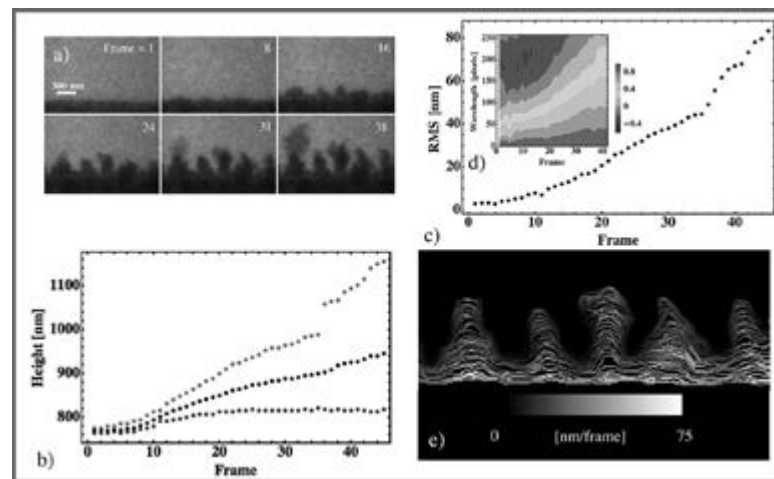


Figure 2 [17,19]: a) Selected frames from a video of an evolving electrodeposited copper film imaged with TEM. b) Maximum (red), minimum (blue), and average (black) growth height as functions of frame number. c) RMS roughness of the growth height as a function of time. d) Contours of the autocorrelation function of the surface roughness as a function of spatial shift and frame number. e) A heat map of the normal growth speed.

References:

- [1] Grogan, J. M. and Bau, H. H., 2010, The Nanoaquarium: A Platform for *in situ* Transmission Electron Microscopy in Liquid Media. *Journal of Microelectromechanical Systems* 19, 885-894.
- [2] Grogan, J. M., Rotkina, L., and Bau, H. H., 2011, *In situ* liquid-cell electron microscopy of colloid aggregation and growth dynamics. *Phys. Rev. E* 83, 061405.
- [3] Grogan, J., Schneider N., Ross, F., and Bau, H. H., 2012, The Nanoaquarium: A New Paradigm in Electron Microscopy, *Journal of the Indian Institute of Science* 92:2.
- [4] Grogan, J., and Bau, A. H. H., 2010, Nanoaquarium for *in situ* Electron Microscopy in Liquid Media <http://arxiv.org/abs/1010.3286>,
- [5] Grogan, J. M., and Bau, H. H., 2011, Real Time Electron Microscope Imaging of Nanoparticle Motion Induced by a Moving Contact Line. <http://arxiv.org/abs/1110.3273>.
- [6] Grogan, J. M., Ross, F. M., Bau, H. H., 2012, Electron Beam Artifacts in Liquid-Cell Electron Microscopy, <http://arxiv.org/abs/1210.3380>.
- [7] Grogan, J.M., and Bau, H.H., 2011.: *In situ* Liquid Cell TEM/STEM with the Nanoaquarium, *Microscopy and Microanalysis* 17, Supplement S2, 532-533.
- [8] Park, J. H., Grogan, J. M., Bau, H.H., Kodambaka, S., and Ross, F.M., 2012, *In situ* Liquid Cell Transmission Electron Microscopic Observation of Electron Beam Induced Au Crystal Growth in a Solution, *Microscopy and Microanalysis* 18, Supplement S2, 1098-1099.
- [9] Grogan, J.M., Park, J.H., Ross, F.M. and Bau, H.H., 2012, Liquid Cell *in situ* Electron Microscopy: Interfacial Phenomena and Electrochemical Deposition, *Microscopy and Microanalysis* 18, Supplement S2, 1160-1161.
- [10] Grogan, J., Ross, F., and Bau, H. H., 2013, Beam-Sample Interactions during Liquid Cell Electron Microscopy, *Microscopy and Microanalysis*, 19 (Suppl. 2), 408-409.
- [11] Schneider, N., M., Park, J-H, Grogan, J., Kodambaka, S., Steingart, D., A., Ross, F. M., and Bau, H.H., 2013, *In situ* Electrochemical Measurements in the Nanoaquarium, *Microscopy and Microanalysis*, 19 (Suppl. 2), 422-423.
- [12] Grogan, J.; Schneider, N.; Ross, F.; Bau, H., 2014, Bubble and pattern formation in liquid induced by an electron beam, *Nano Letters* 14 (1), 359-364.
- [13] Schneider N., Norton, M., Mendel, B., Grogan, J., M., Ross, F., and Bau, H. H., 2014, Electron-Water Interactions and Implications for Liquid Cell Electron Microscopy, *Journal Physical Chemistry Part C*, 118, 22373-22382.
- [14] Schneider, N.M., Norton, M.M., Mendel, B.J., Grogan, J.M., Ross, F.M. and Bau, H.H., 2014, “Radiolysis during Liquid Cell Electron Microscopy,” *Microscopy and Microanalysis* 20, Supplement S3, pp 1516-1517.
- [15] Schneider, N.M., Park, J.H., Grogan, J.M., Kodambaka, S., Steingart, D.A., Ross, F. M. and Bau, H. H., 2014, Visualization of Active and Passive Control of Morphology during Electrodeposition, *Microscopy and Microanalysis* 20, Supplement 3, pp 1530-1531.
- [16] Park, J.H.; Schneider, N.; Grogan, J.; Reuter, M.; Bau, H.; Kodambaka, S.; and Ross, F., 2015, Control of Electron Beam-Induced Au Nanocrystal Formation Kinetics through Solution Chemistry, *Nano Letters* 15 (8) 5314-20. DOI: 10.1021/acs.nanolett.5b01677.
- [17] Schneider, N.M.; J.H. Park; M.M. Norton; F.M. Ross; H.H. Bau, 2016, Automated Analysis of Evolving Interfaces during *in situ* Electron Microscopy. *Advanced Structural and Chemical Imaging* 2:2. DOI: 10.1186/s40679-016-0016-z.
- [18] Grogan, J., and Bau, H.H., “Flow Cells For Electron Microscope Imaging With Multiple Flow Streams,” United States Patent 9,196,457. Awarded 11/24/2015.
- [19] Schneider, N.M., Quantitative-Image-Analysis. In: [github.com. https://github.com/NMSchneider/Quantitative-Image-Analysis](https://github.com/NMSchneider/Quantitative-Image-Analysis). Accessed 13 Feb 2015.

Fabrication of Holey Silicon Nitride Membranes

CNF Project Number: 2343-15, 2344-15, 2345-15

Principal Investigators: James Hone, Jeffrey Kysar

User: Christopher DiMarco

Affiliation: Mechanical Engineering, Columbia University

Primary Source of Research Funding: National Science Foundation

Contact: jh2228@columbia.edu, jk2079@columbia.edu, csd2117@columbia.edu

Abstract:

Graphene has proven to have incredible mechanical properties. Mechanically exfoliated graphene has demonstrated to be the strongest material ever characterized. These properties were probed through the nanoindentation of free-standing graphene membranes [1]. To fully utilize its strength, it is desirable to span larger length scales while maintaining these properties. Chemical vapor deposition (CVD) has proved to be a viable method of growing large sheets of graphene [2,3]. Although CVD grown graphene is polycrystalline, the nanoindentation of suspended membranes has proven that the film still achieves a significant portion of its fracture [4]. The next logical step is to find a way to integrate graphene into a three dimensional structure. One way of doing this is by layering graphene into a laminar composite. As these composites are layered, it is desirable to not only repeat the nanoindentation experiments, but to attempt suspension over larger areas with the test. To achieve this, the fabrication of holey silicon nitride membranes with a range of hole diameters is required. Cornell NanoScale Facility was used for the wafer scale processing of these membrane devices.

Summary of Research:

The Cornell NanoScale Facility (CNF) was used for the fabrication of a large number of square silicon/silicon nitride grids with a holey suspended silicon nitride membrane. The goal was to fabricate six different membrane types, each with a different set of alternating through-hole diameters: (1) 100 and 50 μm , (2) 50 and 25 μm , (3) 25 and 10 μm , (4) 10 and 5 μm , (5) 5 and 2 μm , and (6) 2 and 1 μm . Each membrane window was designed to be 500 μm and the grid itself to be 3 mm on the diagonal.

Using CNF's available computer lab with available design software, L'Edit was used to design two five-inch masks to be used with the contact mask aligner. The top-side mask design featured a repeated array of the six different membrane designs to cover a majority of a four-inch silicon wafer and the bottom-side mask design were windows to allow for the suspension of the membrane and break-lines to separate the grids. The five-inch masks were purchased from CNF's cleanroom store and their Heidelberg DSL mask writer was used to write the patterns on each mask. After the masks were written, the photoresist was developed and the underlying chrome etched using the Hamatech HMR 900 Chemical Processes tool to

set the intended pattern. The photoresist was removed and the masks were cleaned using their Hot Strip Bath setup.

A 220 nm thick low-stress nitride layer was grown on bare four-inch diameter silicon wafers (purchased from the CNF store) using the LPCVD furnace after the wafers were MOS cleaned. Next, the wafers were processed one side at a time. In CNF's photolithography area, the top-side was spin-coated and cured with a layer photoresist and then the SÜSS MA6-BA6 contact aligner was used to expose the wafer with the top-side mask (i.e., the membrane holes). The photoresist was developed effectively using a Hamatech HMR 900 Chemical Processes tool. The Oxford Plasma 81 was used to etch the exposed nitride until the underlying Si was revealed using one of the standard recipes available by CNF. Once the holes were confidently etched through the nitride with verification of the P-10 profilometer, the photoresist mask was removed and the wafer was cleaned using the Hot Strip Bath. This process was then repeated for the back-side of the wafer with the bottom-side mask (i.e., the membrane window and the grid break-lines).

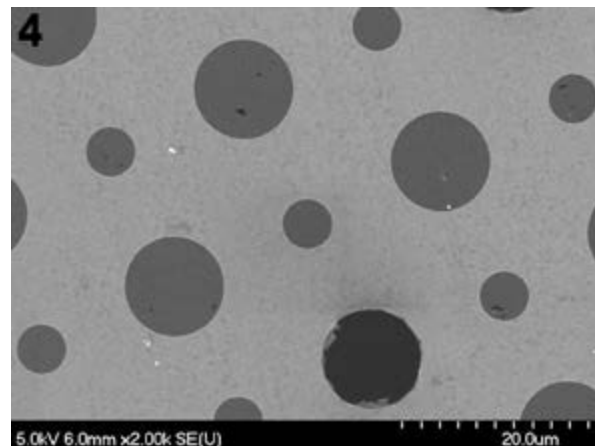
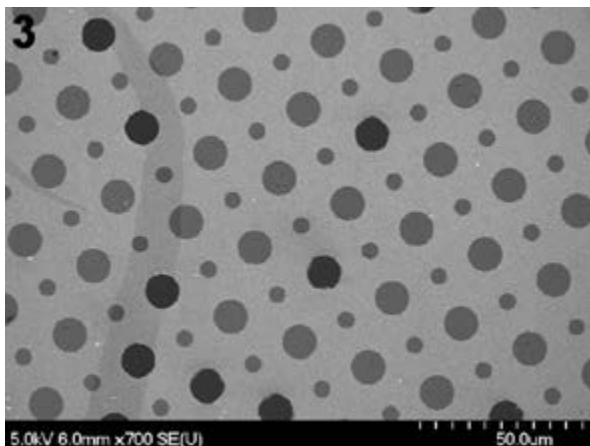
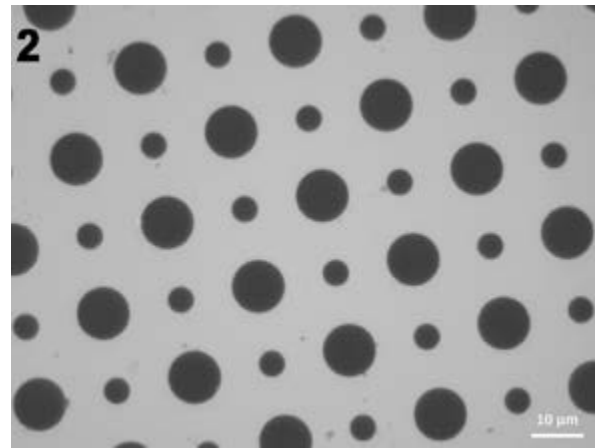
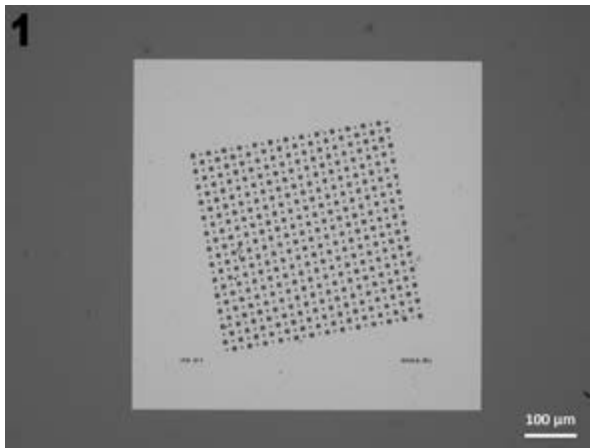


Figure 1: Optical image at 10X magnification of a fabricated suspended nitride membrane with 10 and 5 μm holes. Figure 2: Optical image at 100X magnification of a fabricated suspended nitride membrane with 10 and 5 μm holes. Figure 3: SEM image at 700X magnification of a fabricated suspended nitride membrane with 10 and 5 μm holes with suspended monolayer CVD graphene. Figure 4: SEM image at 2kX magnification of a fabricated suspended nitride membrane with 10 and 5 μm holes with suspended monolayer CVD graphene.

Once the patterning was completed, the patterned nitride was used as a mask to etch the silicon in order to suspend the nitride membranes and break-lines. This was accomplished using CNF's heated KOH Etch setup and their chemical resistant wafer holder. The wafer holder was especially important to selectively etch the back-side. This allowed for the topside surface to be protected and for the membranes to remain intact during the aggressive etching process.

The membranes were successfully manufactured after much iteration and troubleshooting. Currently, we have begun to suspend our own CVD graphene over the holes using standard transfer techniques. We hope to begin creating layered composites and performing mechanical testing soon.

References:

- [1] C. Lee, X. Wei, J. W. Kysar, and J. Hone, "Measurement of the Elastic Properties and Intrinsic Strength of Monolayer Graphene," *Science*, vol. 321, pp. 385-388, 2008.
- [2] X. Li, W. Cai, J. An, S. Kim, J. Nah, D. Yang, et al., "Large area synthesis of high quality and uniform graphene films on copper foils," *Science*, vol. 324, pp. 1312-1314, 2009.
- [3] K. S. Kim, Y. Zhao, H. Jang, S. Y. Lee, J. M. Kim, J.-H. Ahn, et al., "Large-scale pattern growth of graphene films for stretchable transparent electrodes," *Nature*, vol. 457, pp. 706-710, 2009.
- [4] G.-H. Lee, R. C. Cooper, S. J. An, S. Lee, A. van der Zande, N. Petrone, et al., "High-Strength Chemical-Vapor-Deposited Graphene and Grain Boundaries," *Science*, vol. 340, pp. 1073-1076, 2013.

High Temperature Near-Field Thermal Rectifier

CNF Project Number: 2357-15

Principal Investigator: Prof. Sidy Ndao

User: Mahmoud Elzouka

Affiliation: Mechanical and Materials Engineering, University of Nebraska-Lincoln

Primary Source of Research Funding: 2015-2016 Layman Seed Award from the University of Nebraska-Lincoln Office of Research and Economic Development, awarded to Ndao

Contact: sndao2@unl.edu, melzouka2@unl.edu

Website: <http://nmrl.unl.edu/>

Abstract:

The ambitions to explore harsh environments (deep in the earth, or far at Venus) require alternative technologies other than electronics that fail at high temperature and ionizing radiation. Meanwhile, the abundance of waste heat gives rise to the trend of waste heat recovery, which yet hasn't been applied to logic devices. Consequently, scientists' attention has been directed to developing thermal memory and logic devices that use heat instead of electricity to perform computations. However, most of the proposed technologies operate at room or cryogenic temperatures, due to their dependence on material's temperature-dependent properties. Here in this research, we show experimentally—for the first time—the use of near-field thermal radiation (NFTR) to achieve thermal rectification at high temperatures, which can be used to build high temperature thermal diodes for performing logic operations at harsh environments. We achieved rectification between two heat terminals through the coupling between NFTR and the size of a micro/nano gap separating the terminals, engineered to be a function of heat flow direction.

Summary of Research:

NFTR is a mode of transferring heat via thermal radiation between two surfaces, which occurs when the vacuum gap separating them becomes very small (i.e., comparable to the radiation wavelength) [1]. NFTR's intensity has been shown to increase exponentially with decreasing separation gap [2], resulted from the tunneling of the evanescent surface waves between the two surfaces as they are brought close enough to each other. In comparison to far-field thermal radiation, NFTR is therefore more suitable for heat transfer tailoring applications [3] since its intensity can be controlled by carefully manipulating the separation gap. Here in this research, we achieve thermal rectification between two temperature terminals by coupling their separation vacuum gap to their respective temperatures. This coupling allows for the radiative heat transfer rate between the two terminals (which depends on the gap size) to be a function of heat flow direction.

The NanoThermoMechanical rectifier is conceptually composed of a fixed terminal (the upper part), a moving terminal (the lower part), and a thermally-expandable structure connected to the moving terminal, as shown in Figure 1. The principle of operation is illustrated in

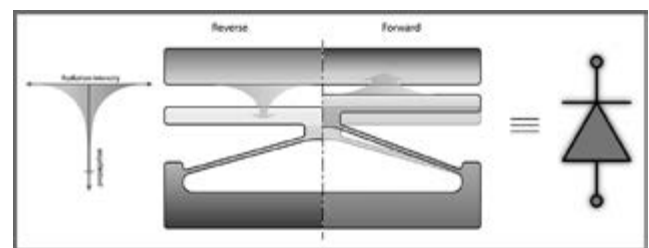


Figure 1: Near-field NanoThermoMechanical rectification concept.

Figure 1: when the fixed terminal's temperature is set high and the moving terminal's temperature is set low (left half of Figure 1), then the expansion mechanism (the v-shaped bent-beam actuator) is not activated and the separation gap between the two terminals is unchanged (i.e., large).

Since the NFTR decreases exponentially with the increase in the separation gap, the larger gap corresponds to lower heat transfer rate. This case is referred to as reverse bias. Once the temperatures are switched, the moving terminal, which is now set to

a higher temperature (right half of Figure 1), moves towards the fixed one. Consequently, the separation gap is decreased, which in turn increases the heat transfer rate by NFTR. This case is referred to as forward bias.

The fabrication of a diode sketched in Figure 1, can be achieved using conventional microfabrication techniques. However, measuring the heat transfer between the two terminals can pose a formidable challenge due to the relatively low thermal radiation heat transfer rates in comparison to conduction heat transfer through the terminals' supports, increasing the uncertainties in measurements.

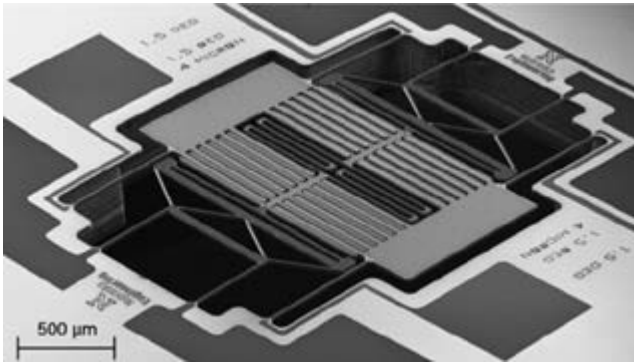


Figure 2: False-color scanning electron micrograph of a quarter of the proof-of-concept microdevice.

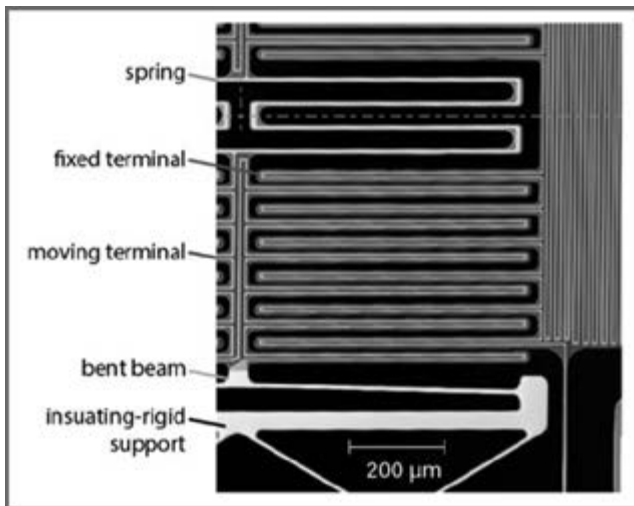


Figure 3: Scanning electron micrograph showing the isometric view of the proof-of-concept microdevice.

To increase the accuracy of heat transfer measurements, we have designed and fabricated a proof-of-concept microdevice that employs 24 pairs of moving and fixed terminals sharing the same slim-isolating-supporting structure as shown in Figure 2 and 3. The microdevice was made out of a 20- μm -thick silicon substrate using standard microfabrication techniques. The microdevice's main components are shown in Figure 2.

In addition to the basic components of the NanoThermoMechanical rectifier, we have included two thin-film platinum microheaters to manipulate and measure the temperatures of the two terminals independently, and to measure the heat transfer between them. The platinum heaters were deposited over a thermally grown oxide using electron beam evaporation (CVC SC4500). Afterwards, the device's structure was realized by reactive ion etching (RIE) the oxide layer using Oxford PlasmaLab 80, and deep reactive ion etching (DRIE) the silicon device layer using Unaxis 770 Deep Si Etcher. The device was released to realize the suspended structure using similar etching techniques to the front side etching. The precision in dimensions were realized thanks to projection photolithography (ASML PAS 5500/300C DUV Stepper) that was used for all lithography steps, with a reduction of 4:1 and a deep ultraviolet light source ($\lambda=248\text{ nm}$).

We have measured a maximum thermal rectification of 10.9% at terminals' temperatures of 375 K and 530 K. The maximum operating temperature of the microdevice is as high as about 600 K, demonstrating this technology's suitability to operate at high temperatures.

References:

- [1] Song B, Fiorino A, Meyhofer E, Reddy P. Near-field radiative thermal transport: From theory to experiment. *AIP Adv* 2015; 5: 053503.
- [2] St-Gelais R, Zhu L, Fan S, Lipson M. Near-field radiative heat transfer between parallel structures in the deep subwavelength regime. *Nat Nanotechnol* 2016. doi:10.1038/nnano.2016.20.
- [3] Park K, Zhang Z. Fundamentals and Applications of Near-Field Radiative Energy Transfer. *Front Heat Mass Transf* 2013; 4. http://_wildcard_thermalfluidscentral.org/journals/index.php/Heat_Mass_Transfer/article/view/304 (accessed 1 Dec2015).

Nano-Optomechanical Devices and Applications

CNF Project Number: 1997-11

Principal Investigator: Qiang Lin

User: Rui Luo

Affiliations: Electrical and Computer Engineering, The Institute of Optics; University of Rochester

Primary Source of Research Funding: National Science Foundation (Grant Number: ECCS-1351697)

Contact: qiang.lin@rochester.edu, ruiluo@rochester.edu

Abstract:

In the past year, we have been working at Cornell NanoScale Facility (CNF) mainly for a project involving patterning lithium niobate (LN) thin films. Though we have not published any results involving fabrication at CNF, in this report, we would like to summarize the fabrication steps we have done.

Summary of Research:

E-Beam. We used the CNF e-beam tool, JEOL 9500, to pattern ZEP on our LN thin film. The LN thin film is on silicon oxide buffer layer, which is on top of silicon or LN substrates. The patterns are mainly microdisk photonic resonators. Figure 1 shows the SEM of one typical microdisk pattern on the LN thin film with ZEP developed.

Etching. We use the CNF AJA ion-milling tool to do LN thin film etching. We have tried to put chips with as-developed ZEP patterns and chips with ZEP reflow into the etching machine. Without reflow, the sidewall of etched LN film is pretty vertical, but on the ZEP sidewall there is redeposited LN from the physical etching process. With reflow, the ZEP sidewall will be a slope instead of being vertical, and the LN sidewall will also be a slope transferred from the ZEP profile. Figure 2 shows the SEM pictures of ion-milling etching profiles with (left) and without (right) reflow. Note that the sidewalls are not as smooth as what we want, so in the future the etching recipe remains to be optimized for sidewall roughness.

Future Work:

In the future, our work will focus on optimizing etching recipes, and undercutting silicon dioxide, to make testable devices.

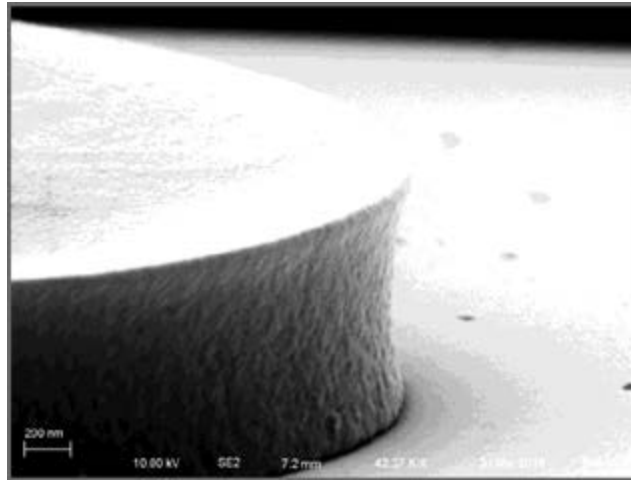


Figure 1: SEM of developed ZEP profile after e-beam exposure.

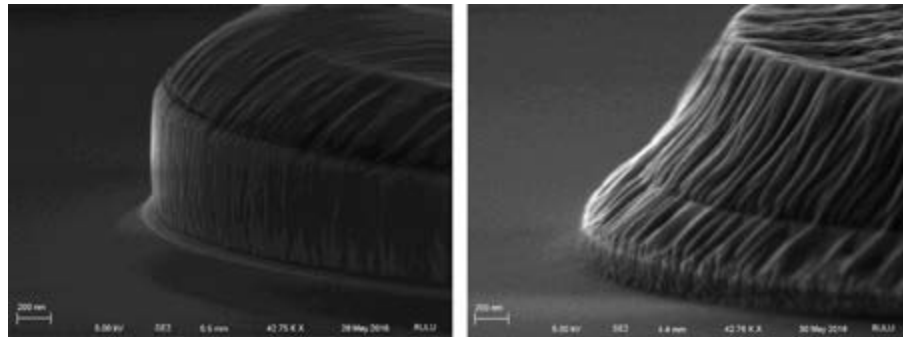


Figure 2: SEMs of ZEP on LN film after ion-milling (left: without reflow, right: with reflow).

High Visibility Time-Energy Entangled Photon Pairs from a Silicon Microdisk Resonator

CNF Project Number: 1997-11

Principal Investigator: Qiang Lin

User: Steven Rogers

Affiliation: Department of Physics and Astronomy, University of Rochester

Primary Source of Research Funding: National Science Foundation (Grant Number: ECCS-1351697)

Contact: qiang.lin@rochester.edu, steven.rogers@rochester.edu

Abstract:

The micro-electronics revolution has enabled numerous and far reaching breakthroughs that have changed the landscape of modern civilization. These impacts could not have occurred if the leap from former bulky electronic components to integrated devices was not taken. A similar paradigm shift is occurring for quantum optics. The envisioned integrated chips will incorporate all the necessary functionality to serve as standalone quantum processing devices. This work pertains to the development of ultra-pure photons sources for such integrated quantum device platforms. Here, we demonstrate a high-quality (Q) silicon microdisk source capable of generating telecom band biphotons that exhibit nearly perfect quantum interference.

Summary of Research:

Integrated quantum devices are poised to enable breakthroughs in many areas, including quantum communication [1], quantum simulation [2], quantum computing [3,4], and quantum metrology [5]. Classical photonics has delivered a global fiber optic infrastructure, which is positioned to assume an additional role as the communication network for quantum photonic states. Time-energy entangled photon pairs are promising candidates to serve as the information carriers in such a network [1]. When considering this envisioned network of quantum processing devices, fidelity is of paramount importance. The realization of increased complexity and successful scaling requires ultra-pure sources [3,4]. A very promising source of ultra-pure time-energy entangled photon pairs is seen in Fig. 1.

The scanning electron microscope (SEM) image shows a high-Q silicon microdisk fabricated from a standard silicon-on-insulator wafer. The device has a radius of $4.5 \mu\text{m}$ and thickness of 260 nm . A $\text{C}_4\text{F}_8/\text{SF}_6$ chemistry was utilized in an inductively coupled plasma-reactive ion etching (ICP-RIE) process on the UNAXIS 770 deep silicon etcher. The recipe was optimized for smooth device sidewalls (see Figure 1),

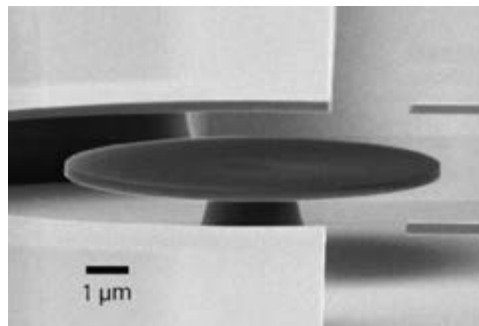


Figure 1: An SEM of the silicon microdisk sitting on a silica pedestal.

which reduces scattering losses and improves the optical quality (Q) of the device. Additionally, a hydrofluoric acid (HF) undercut was employed to suspend the silicon microdisk above the oxide layer.

Pump laser light was evanescently coupled into and out of the device through a tapered optical fiber that excites the

whispering gallery modes (WGMs), as seen by the cavity transmission trace in Figure 2.

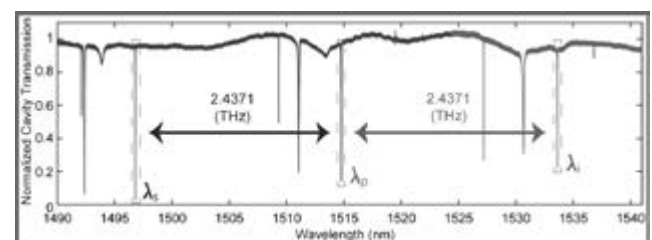


Figure 2: A cavity transmission trace demonstrating the mode structure of the device.

The cavity resonances used for time-energy entangled photon generation are indicated by dashed boxes and exhibit optical Q s of ~ 0.5 million (intrinsic). By employing a suspended structure, light is strongly confined within the single-crystalline silicon, which prohibits the generation of broadband Raman noise photons.

Time-energy entanglement is an intrinsic property of biphotons created through spontaneous four-wave mixing (SFWM), due to energy conservation [6]. After proper dispersion engineering, we were able to achieve highly efficient cavity-enhanced SFWM within the microdisk. By pumping the central resonance at 1515.7 nm, highly correlated signal (1496.8 nm) and idler (1534.3 nm) photon pairs were created. The biphotons were then prepared in path entangled states via an unbalanced Mach-Zehnder interferometer (UMZI) and detected using time-correlated single photon counting as proposed by Franson [7].

High resolution measurements were enabled through use of a novel phase locking system that stabilized and controlled the phase of the interferometer. The combination of the ultra-pure microdisk source and active phase stabilization technique allowed for the observation of high visibility two-photon interference, as seen in Figure 3.

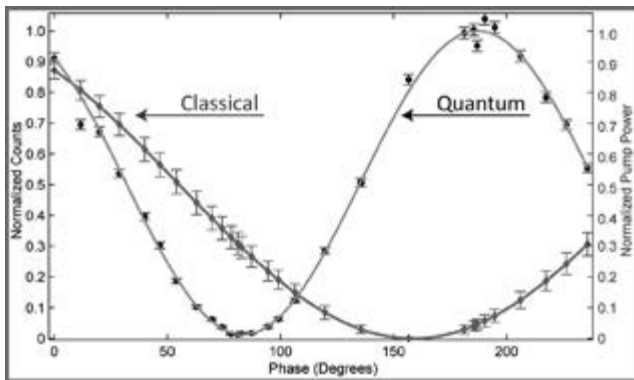


Figure 3: An observation of nearly perfect time-energy entanglement and comparison between classical and quantum interference.

Coincidence counts, without background subtraction, are plotted along with a sinusoidal fit corresponding to the curve labeled “Quantum.” The classical pump power through the UMZI is plotted along with a sinusoidal fit corresponding to the curve labeled “Classical.” A two-photon interference visibility exceeding 50% requires a non-classical description and from the quantum sinusoidal fit in Figure 3, it was revealed that the biphotons exhibited an interference visibility of $(96.6 \pm 1.1)\%$, which confirmed the presence of time-energy entangled states. This remarkably high

quantum interference visibility was achieved at a large pair generation rate of $(4.40 \pm 0.07) \times 10^5$ pairs/s at an ultra-low pump power dropped into the cavity of $22 \mu\text{W}$. To the best of our knowledge, this is the highest raw quantum interference visibility for time-energy entangled photons from a micro/nanoscale source, to date [8-13].

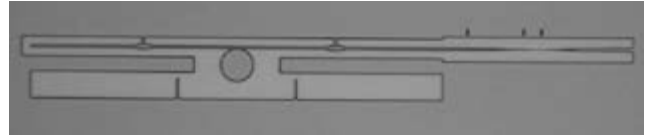


Figure 4: A next generation device incorporating a suspended silicon waveguide and adiabatic power coupling region.

The device shown in Figure 4 was created as a continuation of the research described above. It serves as an upgrade to our previous coupling scheme, which relied on evanescent coupling between a tapered optical fiber and the microdisk. In that system, the large phase mismatch between the silica optical fiber and silicon microdisk precluded accessing the fundamental mode of the device. Additionally, the former coupling scheme was not conducive to a fully integrated architecture. These issues may be remedied with the device depicted in Figure 4, which incorporates a suspended silicon waveguide to couple into the resonator. The waveguide was tapered down to a width of 150 nm to allow for highly efficient adiabatic power coupling between the tapered waveguide and tapered optical fiber. Preliminary results have been promising and indicate that we are now able to access the fundamental mode family of the device.

References:

- [1] Gisin, N. and Thew, R. Nat. Photonics 1, 165 (2007).
- [2] Aspuru-Guzik, A. and Walther, P. Nature Phys. 8, 285 (2012).
- [3] Knill, E., et al. Nature 409, 4652 (2001).
- [4] O'Brien, J. L., et al. Nat. Photonics 3, 687-695 (2009).
- [5] Lee, H., et al. J. Mod. Opt. 49, 23252338 (2002).
- [6] Kwiat, P.G., et al. Phys. Rev. A 47, R2472 (1993).
- [7] Franson, J. D. Phys. Rev. Lett. 62, 2205-2208 (1989).
- [8] Silverstone, J. W., et al. Nat. Photonics 8, 104 (2013).
- [9] Wakabayashi, R., et al. Opt. Express 23, 1103-1113 (2015).
- [10] Preble, S. F., et al. Phys. Rev. Applied 4, 021001 (2015).
- [11] Grassani, D., et al. Optica 2, 88-94 (2015).
- [12] Xiong, C., et al. Optica 2, 724-727 (2015).
- [13] Ramelow, S., et al. arXiv:1508.04358v1 (2015).

Label-Free Characterization of Protein Aggregates and Nanoparticles Using Near-Field Light Scattering Microscopy

CNF Project Number: 2156-12

Principal Investigator: David Erickson

User: Dakota O'Dell

Affiliation: Department of Applied and Engineering Physics, Cornell University

Primary Source of Research Funding: National Institutes of Health

Contact: de54@cornell.edu, dlo46@cornell.edu

Website: <http://www.ericksonlab.org/>

Abstract:

The behavior of a nanoparticle in solution depends strongly on the particle's size. For this reason, accurately characterizing the size of individual nanoparticles is a key quality control issue in a wide range of fields and applications. In this work, we present a statistical analysis technique for determining the radius of single particles as they travel along a one-dimensional (1D) nanophotonic waveguide under an optical microscope. By accounting for the optical forces within the evanescent field of the waveguide, we can distinguish both dielectric and metallic particles by size with less than one second of video for each particle.

Summary of Research:

To understand the behaviors of colloidal particles and biomolecules in solution, it is important to have precise knowledge of the size and structure of individual particles. Developing a robust, high-throughput nanoparticle sizing technique is therefore of great interest for a wide range of industrial applications. Several current methods for measuring particle size use optical light, such as nanoparticle tracking analysis (NTA) [1] and dynamic light scattering (DLS) [2]. Unfortunately, NTA is limited in throughput due to long observation times, and DLS is unreliable for polydisperse samples due to ensemble averaging. Here, we have developed a novel photonic light scattering technique that performs rapid analysis of the size of individual particles at high-throughput by employing localized optical forces.

For this technique, we apply near-field optical forces to achieve stable trapping of single nanoparticles over a silicon nitride nanophotonic waveguide. We fabricated our prototype waveguides in the CNF using the JEOL 9300 and standard electron beam lithography processing. We then place the fabricated chip (with 40 1D waveguides) into a microfluidic channel that can be used to deliver nanoparticles to the waveguide surface. The waveguide is then end fire coupled to an 1064 nm diode laser to generate the evanescent field.

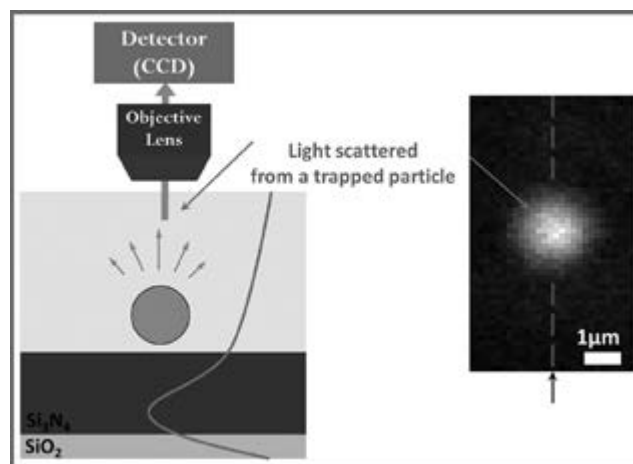


Figure 1: Schematic of the experimental setup. The nanoparticle is held stably within the evanescent field of the optical waveguide. The particle then scatters the infrared light, which can be collected through a microscope objective and focused onto a CCD camera.

After fabricating and assembling the chips, we optically trap individual nanoparticles above the waveguide surface. When a particle is close to the surface, it will scatter the 1064 nm light, which can be focused through a microscope objective and collected

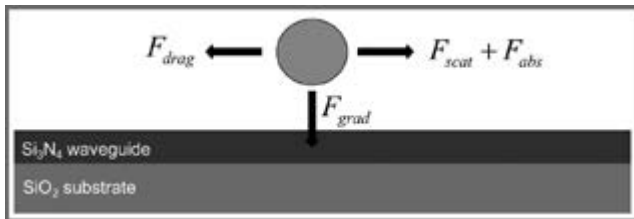


Figure 2: Relevant forces for the waveguide geometry. In addition to the optical gradient force that holds the particle within the evanescent field, there is also a forward scattering force along the direction of optical propagation. The scattering force will propel the particle down the waveguide, but is also balanced by a hydrodynamic drag force. As a result, the particle rapidly reaches a high terminal velocity that can be measured by tracking the particle motion.

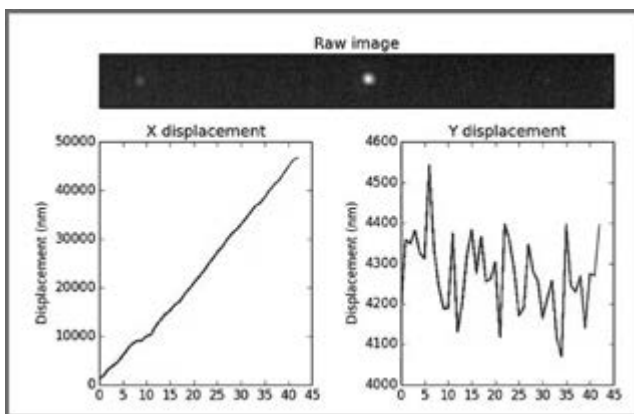


Figure 3: Example data from trapped polystyrene sphere. As the particle interacts with the waveguide, it will be propelled by a size-dependent forward scattering force. The magnitude of this force is found by tracking the motion of the particle centroid over time in two dimensions.

onto a CCD detector. This scattering pattern can then be localized with subpixel precision to determine the position of the particle. With a high frame rate camera, this allows us to observe the dynamics of the particle as it moves within the evanescent field to probe its properties. A schematic of the setup is shown in Figure 1.

Within the evanescent field, the nanoparticle experiences a number of optical and hydrodynamic forces, as shown in Figure 2. Although the particle will be held stably in two dimensions by the gradient force, it will also be propelled along the propagation axis of the waveguide by a size-dependent forward scattering force. This force is counterbalanced by drag, resulting in a terminal velocity that depends strongly on the

radius (R^5). By tracking the motion and determining the velocity, therefore, particles can be separated by even small differences in size.

Figure 3 shows one frame of an example data set for a polystyrene nanoparticle. In each frame, the nanoparticle position is determined through subpixel localization. The motion can then be tracked over time. Along the x direction (or the direction of optical propagation), we see a linear trend of displacement versus time, corresponding to a terminal velocity as predicted. Along y, we see random fluctuations from confined Brownian motion.

By comparing the velocity obtained through this method for various particles, it is possible to segregate particles with only modest differences in size. Figure 4 shows the results of 3 sets of experiments trapping $R = 150$ nm gold nanospheres, $R = 100$ nm silver nanospheres, and aggregates of bovine serum albumin (BSA). Although the gold nanoparticles are only 50% larger in radius than the silver, there is more than 500% difference in the measured velocity.

This result suggests that nanophotonic light scattering could be developed further into a highly sensitive sizing technique.

References:

- [1] Filipe V., Hawe, A., Jiskoot, W. "Critical Evaluation of Nanoparticle Tracking Analysis (NTA) by NanoSight for the Measurement of Nanoparticles and Protein Aggregates." *Pharmaceutical Research*. 2010; 27(5):796-810.
- [2] Hoo, C.M., et al. "A comparison of atomic force microscopy (AFM) and dynamic light scattering (DLS) methods to characterize nanoparticle size distributions." *Journal of Nanoparticle Research* 10.1 (2008): 89-96.

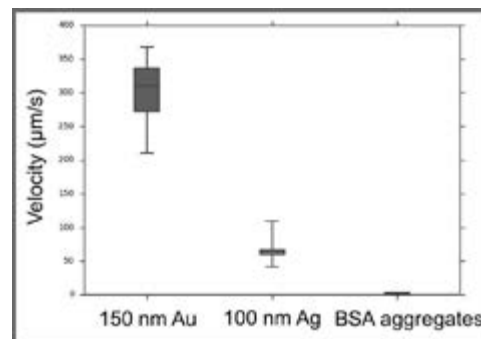


Figure 4: Comparison of measured velocities for particles of different sizes. Due to the strong (R^5) dependence on the size, $R = 150$ nm and $R = 100$ nm can be clearly differentiated.

Fabrication of Silicon Single-Photon Avalanche Diodes (SPADs)

CNF Project Number: 2232-13

Principal Investigator: Massimo Ghioni

User: Angelo Gulinatti

Affiliation: Dipartimento di Elettronica, Informazione e Bioingegneria, Politecnico di Milano

Primary Source of Research Funding: National Institutes of Health, Grant 5R01-GM095904

Contact: massimo.ghioni@polimi.it, angelo.gulinatti@polimi.it

Website: www.everyphotoncounts.com

Abstract:

Single photon avalanche diodes (SPADs) are devices capable of signaling the arrival of a photon by means of a synchronous electrical pulse. They are enabling technologies for many applications in fields ranging from quantum physics to life science. Our aim is to develop new generations of SPAD detectors to meet the requirements of most demanding applications in terms of single pixel performance and multi-pixel integration.

Summary of Research:

Many applications in fields ranging from biology to material science, from quantum physics to astronomy, from biochemistry to quantum cryptography require the detection of single photons in the visible and near-infrared region of the spectrum. Although single-photon detection has been achieved for many years by using photo-multiplier tubes (PMTs), in the last years single photon avalanche diodes (SPADs) emerged as a valid alternative to PMTs and, thanks to their remarkable performance, in the last decade they started replacing PMTs in the most demanding applications like single molecule analysis, quantum cryptography, laser ranging, etc.

A SPAD is a p-n junction reverse biased above the breakdown voltage in a metastable state in which no current flows. When a photon is absorbed into the device active area, a self-sustained avalanche is

triggered by the photo-generated electron-hole pair. The macroscopic current that results from this process allows for a simple detection of the photon itself [1]. During years 2014-2015, we fabricated devices with the structure represented in Figure 1. Compared to thin SPADs [1], these detectors provide higher photon detection efficiency (PDE) in the red/near-infrared region of the spectrum thanks to an increased thickness of the absorption layer (about 12 μm vs. 5 μm) [2]. However, they require the introduction of deep trenches for attaining electrical isolation between multiple devices on monolithic arrays [3] and may also require guard rings (not shown in Figure 1) to be operated at high bias voltages without suffering of edge breakdown.

The experimental characterization of the red-enhanced SPADs manufactured during years 2014-2015 highlighted a few technological problems related to the last steps of the fabrication process (backend technology). These resulted in: a) a reduced thickness of the antireflective coating, b) guard-rings shorted with the cathode, and c) interconnection metals broken in some regions of each wafer. The aforementioned issues limited the performance and/or the functionality of the fabricated devices. In particular, issue a) resulted in a reduction of the PDE of about 30%. Similarly, issue b) did not compromise the functionality of the detectors, but prevented the use of the guard-rings to avoid a premature edge breakdown. This means that, among all manufacturing splits, only those designed to have a low breakdown voltage (around 30-35V) can be actually tested.

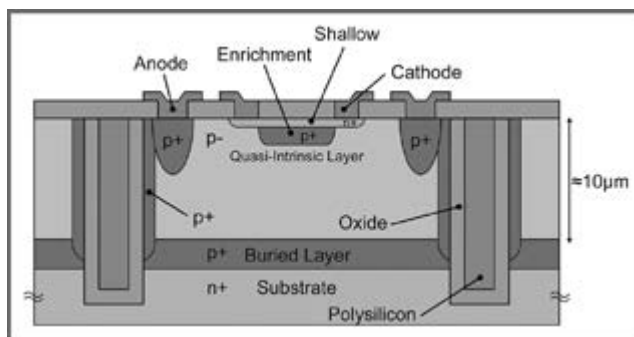


Figure 1: Cross-section of a Red-Enhanced SPAD with deep trenches.

On the contrary, issue c) made completely useless the devices affected by this problem. Unfortunately, these included all the 48-pixel SPAD arrays to be used in the high-throughput SMA setup to be developed in collaboration with Prof. Weiss and Dr. Michalet group at University of California Los Angeles (UCLA) [4]. A thorough investigation allowed us to identify the causes of the problems. In particular, issues a) and b) are due to the high etching rate of the chemistry used before the aluminum deposition. They can be solved by resorting to a more diluted chemistry. Issue c) is due to a photoresist adhesion problem during the wet etching of the aluminum. It can be addressed by using a reactive ion etching (RIE) process instead of the wet etching.

Since all the issues are related to the last steps of the fabrication, we investigated the possibility of reworking the wafers processed during years 2014-2015 by stripping the last layers and re-depositing them. In particular, we began by stripping the aluminum interconnection layer and the antireflective coating. Then we re-deposited a thick oxide layer by means of GSI plasma-enhanced chemical vapor deposition (PECVD). After patterning and plasma-etching the contact openings respectively with GCA Autostep 200 and Oxford 82, we re-deposited a layer of aluminum by using the CVC magnetron sputter system. Interconnects have been patterned again with Autostep 200 and plasma-etched by using PlasmaTherm740 RIE system. Finally, the thick PECVD oxide has been stripped from the detector active area and replaced with a thin oxide layer to serve as an antireflective coating.

Inspection and preliminary experimental characterization [3] showed that the reworking process effectively solved the aforementioned issues. In particular, Figure 2 shows a comparison of interconnects integrity before (top) and after (bottom) reworking. Figure 3 reports the reverse current-voltage characteristic at the active junction of three SPADs implanted with different enrichment doses; the corresponding breakdown values range from 25V to 65V and demonstrate the effectiveness of guard-rings in preventing edge breakdown [3].

Finally, Figure 4 reports an example of the PDE as a function of the wavelength, measured on a reworked SPAD, biased at an overvoltage $V_{ov} = 15V$.

References:

- [1] M. Ghioni, et al., "Progress in Silicon Single-Photon Avalanche Diodes," IEEE J. Select. Topics Quantum Electron., vol. 13, pp. 852-862, 2007.
- [2] A. Gulinatti, et al., "New silicon SPAD technology for enhanced red-sensitivity, high-resolution timing and system integration," J. Modern Optics, vol. 59, pp. 1489-1499, 2012.
- [3] A. Gulinatti, et al., "Silicon technologies for arrays of Single Photon Avalanche Diodes," presented at the SPIE Commercial + Scientific Sensing and Imaging, 2016, vol. 9858, p. 98580A.
- [4] X. Michalet, et al., "Silicon Photon-Counting Avalanche Diodes for Single-Molecule Fluorescence Spectroscopy," IEEE J. Sel. Top. Quantum Electron. vol. 20, 3804420, 2014.

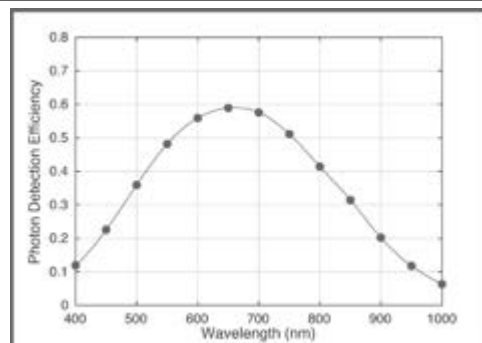
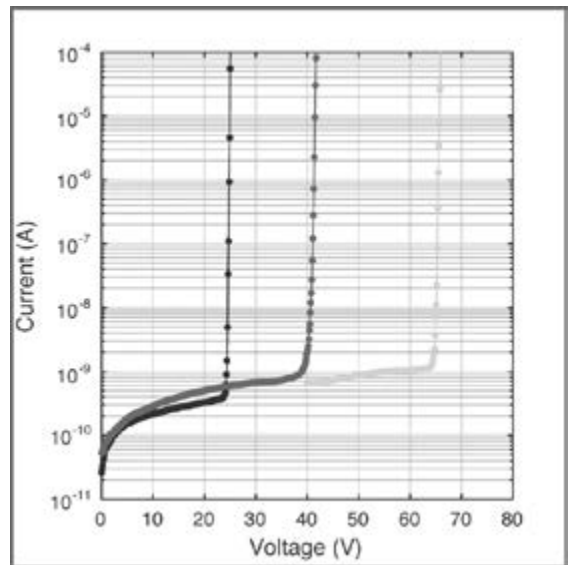
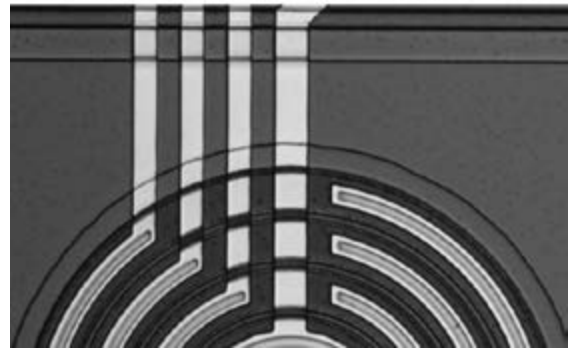
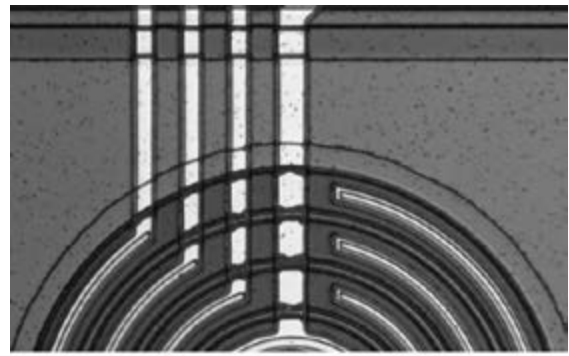


Figure 2, top: Microphotograph of some interconnects before (top) and after (bottom) reworking.

Figure 3, middle: Reverse current-voltage characteristic of three SPADs with different enrichment doses.

Figure 4, bottom: PDE measured on a SPAD biased at an overvoltage of 15V.

Titanium Dioxide Enables Visible Integrated-Evanescent Raman Sensors

CNF Project Number: 2255-13

Principal Investigator: Jin Suntivich^{1,2}

Users: Christopher C. Evans^{2,3}, Chengyu Liu^{2,4}, Anoosha Murella⁵

Affiliations: 1. Materials Science and Engineering Department, Cornell University; 2. Kavli Institute at Cornell for Nanoscale Science, Cornell University; 3. Laboratory for Atomic and Solid State Physics, Cornell University; 4. School of Applied and Engineering Physics, Cornell University; 5. 2015 CNF REU Intern, Materials Science and Engineering, Arizona State University

Primary Sources of Research Funding: 1-4. Cornell Center for Materials Research, Kavli Institute at Cornell Fellowship and Cornell Start-Up; 5. 2015 NNIN REU Program at Cornell (NSF Grant No. ECCS-0335765)

Contact: jsuntivich@cornell.edu, cce34@cornell.edu, CL986@cornell.edu

Website: suntivich.mse.cornell.edu

Abstract:

We explore titanium dioxide (TiO₂) for visible evanescent Raman sensing. Using straight waveguides with visible wavelengths, we observe signal 100x greater than previous reports in silicon nitride using a 785 nm pump. Furthermore, we demonstrate TiO₂ micro-ring resonators to enhance both pumping efficiency and Stokes emission to reduce the device's footprint.

Summary of Research:

Fully-integrated on-chip Raman sensors are a critically needed technology for drug discovery, medical diagnostics, threat detection, and environmental-quality monitoring. We utilize a waveguide design using the evanescent field outside of a dielectric to pump and collect Raman scattering to realize this technology [1,2] (Figure 1a).

This approach enables a length-dependent increase in Raman signal. To operate at visible (as opposed to near-infrared) wavelengths to take advantages of increased Raman cross sections (scaling as λ^{-4}) and reduced-mode volumes (scaling as λ/n) [1], we need a material that can operate at visible wavelengths with

minimal losses and background fluorescence [3]. TiO₂ is an excellent candidate for this application [2] due to its high refractive index (> 2.4) and wide indirect bandgap that limits fluorescence. We take advantage of a lift-off fabrication approach [4] (Figure 1b) to reduce losses, enable visible operation, and maintain a highly surface-localized mode (Figure 1c). Furthermore, this planar approach allows us to engineer photonic cavities to use resonances to increase pumping efficiency and enhance Stokes emission [5].

We explore several common solvents as model analytes. In Figure 2a, we show typical Raman signal from toluene using a 532 nm TM pump.

We observe a low and slowly varying background signal that allows us to retrieve the Raman signal using standard baseline-subtraction methods (Figure 2a). To demonstrate the wavelength flexibility of TiO₂-based systems, we measure identical toluene signal to a commercial Raman microscope within the "fingerprinting window" (700-1300 cm⁻¹) at several pump wavelengths (Figure 2b).

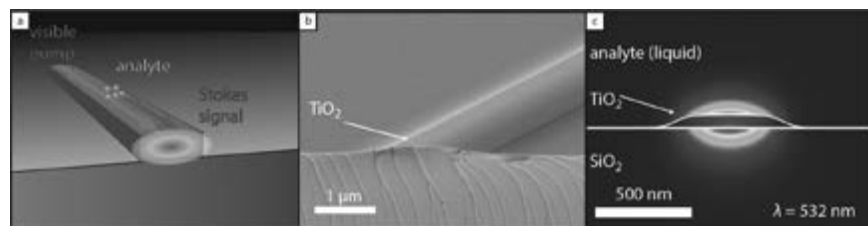


Figure 1: a) A waveguide-based evanescent Raman scattering device, showing the waveguide, analyte, and the guided pump and Stokes beams. b) Scanning-electron micrograph (SEM) of a typical TiO₂ waveguide fabricated using our dielectric lift-off technique. c) The transverse-magnetic mode profile of our waveguide using a pump wavelength of 532 nm, showing the highly surface-localized evanescent field.

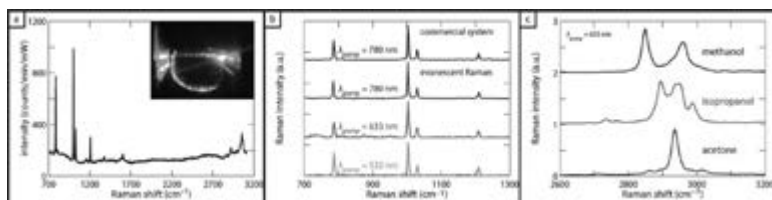


Figure 2: Demonstrations of evanescent Raman scattering using TiO_2 waveguide devices. a) Collected Raman signal from toluene using a 532 nm pump wavelength showing strong Raman scattering and weak background signal (inset: guided green light in a typical 1 cm wide TiO_2 chip with liquid on top). b) Comparison of Raman signal of toluene taken using a commercial Raman microscope and our evanescent Raman system at several wavelengths. c) We compare different solvents and observe differences in the Raman spectra of the C-H bonds.

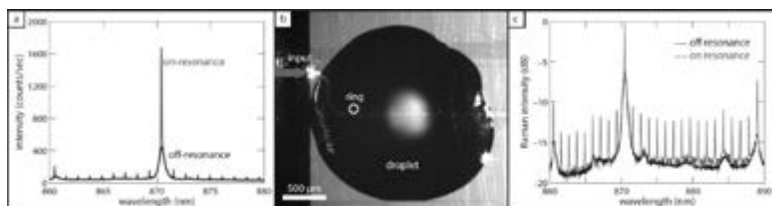


Figure 3: a) Resonantly-enhanced Raman scattering of 3-nitrotoluene around 870 nm (1350.2 cm^{-1}) using a ring resonator with a radius of $50 \mu\text{m}$, showing the signal when a 780 nm laser is tuned off and on the ring's resonance. Each peak corresponds to a resonant mode of the cavity. b) Microscope image of the 3-nitrotoluene experimental setup. The droplet partially covers the bus waveguide, thus, the off-resonance background is mostly due to this bus-waveguide signal. We note the ring location with a dotted line. c) Plotting an extended spectrum on a log-scale, we measure uniform on-resonance enhancement above the baseline of approximately 6 dB.

In addition, we measure changes in the C-H band using different solvents at a fixed wavelength (Figure 2c).

To compare our experimental efficiency to previous reports [1,2], we measure isopropanol using a 7 mm long waveguide with a 1.3 mW of pump power around 532 nm and record typical counting rates of 1600 counts/sec/mW within the 819 cm^{-1} Raman peak above baseline. Accounting for all sources of loss, this rate corresponds to a single-direction conversion efficiency, $\zeta(L)/L$, of $4 (\pm 2) \times 10^{-9}/\text{cm}$, consistent with the theoretical bi-directional conversion efficiency of $5.9 \times 10^{-9}/\text{cm}$ for this geometry [1,2]. Remarkably, our experimental efficiency is two orders of magnitude larger than previous experimental values in silicon nitride ($\sim 10^{-11}/\text{cm}$) for similar geometries using 785 nm [1]. Thus, by exploiting visible wavelengths with

high-index, low-loss TiO_2 waveguides, we can significantly increase the evanescent Raman conversion efficiency.

To further increase Raman scattering, we take advantage of the pump and Purcell enhancement by forming high quality-factor ring-resonators using standard fabrication methods. We utilize CNF's ASML deep-ultraviolet stepper and Oxford 100 etcher in the process. For general-purpose Raman enhancement, we fabricate a device with a $150 \mu\text{m}$ radius with a narrow free-spectral range (Figure 3a). We see peaks indicative of Purcell enhancement when we tune the pump wavelength (780 nm) on resonance. Reducing the size of the resonator to $50 \mu\text{m}$ (Figure 3b) allows us to selectively enhance specific peaks (Figure 3c) to form compact, species-specific sensors.

We use TiO_2 nanophotonics to enable highly efficient evanescent Raman scattering at visible wavelengths and demonstrate waveguide ring-resonators for cavity-enhanced evanescent Raman scattering to enable highly compact and efficient devices. Our work shows the importance of exploring new materials to overcome challenges in functional photonics such as label-free, low-cost, high performance sensing devices.

References:

- [1] A. Dhakal, et al. "Evanescent excitation and collection of spontaneous Raman spectra using silicon nitride nanophotonic waveguides," *Opt. Lett.* 39, 4025-8 (2014).
- [2] A. Dhakal, et al. "Efficiency of evanescent excitation and collection of spontaneous Raman scattering near high index contrast channel waveguides," *Opt. Express* 23, 27391-404 (2015).
- [3] J. S. Kanger, et al. "Stimulated Raman Gain Spectroscopy of Thin Layers Using Dielectric Waveguides," *J. Phys. Chem.* 100, 16293-16297 (1996).
- [4] C. C. Evans, et al. "Low-loss titanium dioxide waveguides and resonators using a dielectric lift-off fabrication process," *Opt. Express* 23, 11160-11169 (2015).
- [5] A. Badolato, et al. "Deterministic coupling of single quantum dots to single nanocavity modes," *Science* 308, 1158-61 (2005).

Fabrication of Custom Diffractive Fourier Optics Devices for Functional Neuronal Imaging Using Extended Volume MFM

CNF Project Number: 2292-14

Principal Investigator: Cornelia I. Bargmann

Users: Sara Abrahamsson, Philip Kidd

Affiliation: Lulu and Anthony Wang Laboratory for Neural Circuits and Behavior,
The Rockefeller University, New York City, NY

Primary Source of Research Funding: Leon Levy Foundation

Contact: cori@rockefeller.edu, sabrahamss@rockefeller.edu, pbk3@cornell.edu

Abstract:

We have designed and produced various multifocus gratings (MFGs) – diffractive optical devices for multifocus microscopy (MFM). The MFGs are placed in the Fourier plane of a wide-field optical imaging system, such as a microscope, to produce an instant three-dimensional (3D) image of the object imaged. This enables fast and simultaneous imaging of an extended 3D sample volume at the full resolution of the imaging system used. The fabrication process involved direct laser writing, deep UV-lithography, wet etching and multilevel reactive ion etching. Devices were fabricated and applied in a microscopy project at the Rockefeller University, NY for functional neuronal imaging using genetically expressed calcium dyes.

Summary of Research:

Multifocus microscopy (MFM) is an optical microscopy technique for instant 3D imaging of extended sample volumes [1]. Prototype parts for our initial MFM system were made commercially, however we also desired to fabricate more complex devices for improved performance. We were not able to find a commercial vendor for producing these parts.

At CNF, we obtained training and tool access for developing the more complex designs. Tools used at the CNF were mainly the Heidelberg mask writer DWL 2000, the Hamatech-Steag mask processors, the ASML 300C DUV stepper, the dicing saw, and the Oxford 82 etcher.

Improved light efficiency for imaging sensitive biological specimens and single molecule imaging is a crucial parameter for any live imaging system. An optical device with a multi-phase grating function (Figure 1) can improve light-transmission to the desired imaging orders to 89%, whereas a binary design is limited to 67% efficiency. We fabricated devices using a combination of direct laser writing, deep UV lithography and reactive ion etching. Parts performed as expected and are currently used in the laboratory of Cori Bargmann at the Rockefeller University for functional imaging of neural activity,

using the calcium indicator GCaMP, in living specimens of *Caenorhabditis elegans* (*C. elegans*) under olfactory stimulation in a microfluidic chip.

References:

- [1] Fast multicolor 3D imaging using aberration-corrected multifocus microscopy, S. Abrahamsson, J. Chen, B. Hajj, S. Stallinga, J. Wisniewski, G. Mizuguchi, P. Soule, F. Mueller, C. Darzacq, X. Darzacq, C. Wu, C.I. Bargmann, D.A. Agard, M. Dahan, and M.G.L. Gustafsson, *Nat Methods*, 10:60-3 (2013).
- [2] *MultiFocus Polarization Microscope (MF-PolScope) for 3D polarization imaging of up to 25 focal planes simultaneously, S. Abrahamsson, S.B. Mehta, A. Verma, M. McQuilken, C.I. Bargmann, A.S. Gladfelter and R. Oldenbourg, *Opt. Express* 23: 7734-7754 (2015).
- [3] *Multifocus microscopy with precise color multi-phase diffractive optics applied in functional neuronal imaging, S. Abrahamsson, R. Ilic, J. Wisniewski, B. Mehl, L. Yu, L. Chen, M. Davanco, L. Oudjedi, J.B. Fiche, B. Hajj, X. Jin, J. Pulupa, C. Cho, M. Mir, M. ELBeheiry, X. Darzacq, M. Nollmann, M. Dahan, C. Wu, T. Lionett, J. A. Liddle and C.I. Bargmann, *Biomed. Opt. Express* (2016).

*Performed with devices fabricated at CNF.

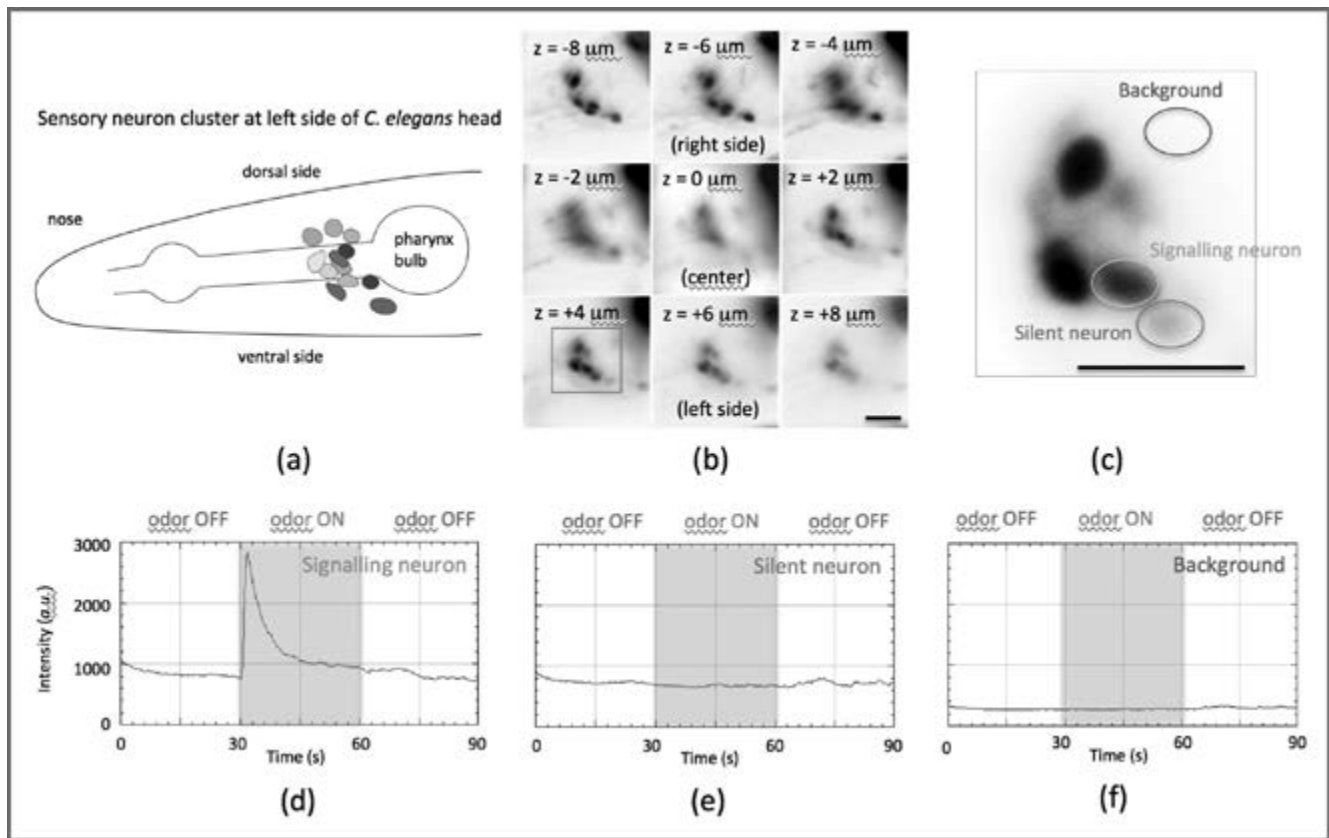


Figure 1: Illustration of functional neuronal imaging in *C. elegans* using MFM components fabricated at CNF, from our most recent publication [3]. Neuronal signaling in response to odor in *C. elegans* visualized using the calcium indicator GCaMP6s expressed in sensory neurons.

(a) Cartoon of the sensory neuron cluster on the left side of the animal's head. The right side of the head has a mirror-symmetrical cluster of neurons.

(b) MFM image from a movie recorded using the multi-phase MFG, showing the two clusters of sensory neuron pairs on each side of the head. Successive focal planes in the MFM image are separated by $2\ \mu\text{m}$ steps covering a total depth of $18\ \mu\text{m}$. The lateral field of view in each focal plane image tile is $\approx 40 \times 40\ \mu\text{m}^2$. The living animal is immobilized in a microfluidic chamber and imaged during olfactory stimulation with benzaldehyde odor (almond smell). Several neurons can be seen responding to odor stimulation in the movie **Visualization 1**. Images **b** and **c** have been time-averaged since all neurons are not active in a single time-point. Data has been contrast adjusted, background-subtracted and is displayed using an inverse lookup table.

(c) View of the cluster of neurons in the focal plane $z = +4$ indicated by the blue square in **b**.

(d) Intensity profile plot of the GCaMP6s signal of the neuron indicated by the green oval in **c** shows an on response to the addition of benzaldehyde odor.

(e) Intensity profile plot of the GCaMP6s signal of the neuron indicated by the pink oval in **c** does not show response to the odor stimulation but has a constant baseline fluorescence level.

(f) Intensity profile plot of the background in the region indicated by the blue oval in **c**, where there are no labeled neurons present. The three intensity plots in **d-f** are made from equal image areas and displayed in the same scale of arbitrary units (camera pixel counts). Scale bars in **b** and **c** represent $10\ \mu\text{m}$.

Pixelated Polarizer for IR Focal Plane Array

CNF Project Number: 2359-15

Principal Investigator and User: Lori Lepak

Affiliation: Phoebus Optoelectronics, LLC

Primary Source of Research Funding: Department of Defense

Contact: llepak@phoebus-opto.com

Website: www.phoebusopto.com

Abstract:

Phoebus Optoelectronics, LLC, is a small firm focusing on custom design and advanced materials and optical device development, in the technology fields of metamaterials, photonic crystals and plasmonic crystals. Our portfolio of R&D projects covers the spectral ranges of visible light, infrared, terahertz, and microwave radiation for applications that include high resolution infrared imaging systems, wavelength and polarization filtering, tunable optical components, beam forming and steering, solar cells and renewable energy devices, and chemical and biological toxin sensors. Phoebus scientists and engineers make extensive use of the resources at the CNF for our nano/micro fabrication and testing. In this report, we discuss the development of a metamaterial-based pixelated focusing polarizing device.

Summary of Research:

Extraordinary optical transmission (EOT) is a phenomenon in which light is transmitted through apertures much smaller than the incident wavelength, at anomalously large intensities relative to the predictions of conventional aperture theory. EOT was first observed by T.W. Ebbesen in 1998 [1], setting off a flurry of research into metamaterials and anomalous transmission, into which Phoebus Optoelectronics was an early entrant. For over 10 years, Phoebus has successfully incorporated metasurfaces into devices used to perform light filtering [2,3], photon sorting [4,5], polarimetric detection [6], high speed optical detection [7], optical sensing of biological and chemical toxins [8], and other light controlling tasks. In the present report, we present recent developments toward the development of a pixelated focusing polarizer.

The current industry standard for pixelated polarizers is a wire grid geometry. However, this decades-old technology has been developed to its full potential, in that the further optimization of wire grid pixels is limited by optical physics itself. Each wire grid diffracts light very strongly, so that as the transmission of individual pixels increases, the cross talk between neighboring pixels increases as well, which decreases resolution.

We have developed an on-chip pixelated polarimeter device which sidesteps this fundamental tradeoff between cross talk and transmission, by using metasurfaces

in place of wire grids, to simultaneously minimize diffraction and better collimate the transmitted light. In our first-generation IR polarimeter, which is currently commercially available, each pixel has the structure shown in Figure 1, with four arrays of wires oriented at 0° , 45° , 90° , and 135° to each other. Each array is capable of acting as a graded index lens to focus and collimate transmitted light. At the same time, the phase delay produced by the four arrays together allow the pixel as a whole to behave as a polarizer to control the phase of the light.

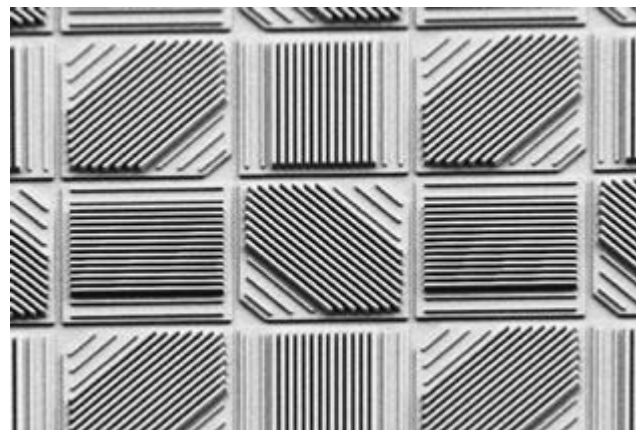


Figure 1: SEM image of metasurface-based IR polarimeter, currently commercially available from Phoebus, and initially developed at CNF.

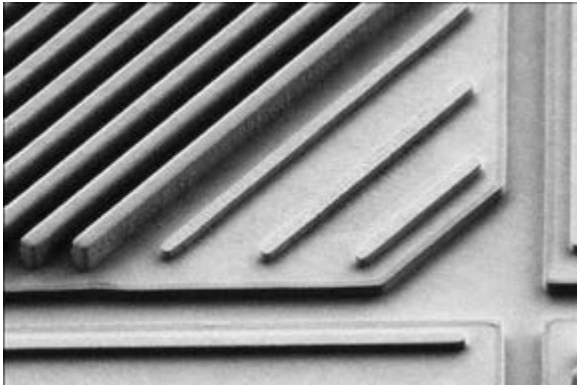


Figure 2: A single sub-pixel at higher magnification. These high aspect ratio features with smooth sidewalls were fabricated at CNF using the ASML DUV stepper and dry etch tools.

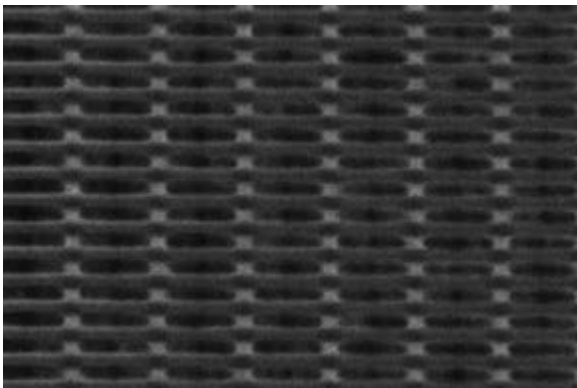


Figure 3: Another candidate metasurface structure for a second-generation focusing polarimeter device currently in development, fabricated at CNF using the JEOL 9500 e-beam lithography system.

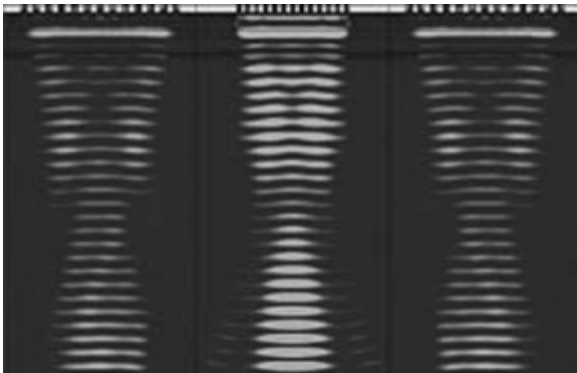


Figure 4: Numerical simulation of three adjacent pixels of our IR polarimeter device, indicating minimal crosstalk between pixels.

A higher magnification image of a typical array (Figure 2) illustrates the high aspect ratios and smooth sidewalls that are essential for the high-quality performance of our metasurface structures. We are currently developing additional metasurface designs, such as the one shown in Figure 3, which are tailored to operate in other spectral ranges. All of these structures are made possible by the CNF instrumentation, particularly the ASML DUV stepper, the JEOL 9500 e-beam, and several of the plasma etch tools.

Preliminary computer simulations, shown in Figure 4, demonstrate the ability of our metasurface structures to simultaneously deliver higher transmittance and lower cross talk between pixels than the current generation of wire-grid-based pixelated polarimeters. Our metastructures combine the advantages of extremely high extinction ratios (>10000:1), high transmission, and lower cross talk between pixels than the current state-of-the-art wire grid technology.

References:

- [1] Ebbesen, T.W., et al., "Extraordinary optical transmission through sub-wavelength hole arrays." *Nature*, (1998). 391(6668): p. 667-669.
- [2] Crouse, D. "Numerical modeling and electromagnetic resonant modes in complex grating structures and optoelectronic device applications." *Electron Devices, IEEE Transactions on* 52.11 (2005): 2365-2373.
- [3] Crouse, D., and Keshavareddy, P. "Polarization independent enhanced optical transmission in one-dimensional gratings and device applications." *Optics Express* 15.4 (2007): 1415-1427.
- [4] Lansey, E., Crouse, D., et al. "Light localization, photon sorting, and enhanced absorption in subwavelength cavity arrays." *Optics Express* 20.22 (2012): 24226-24236.
- [5] Jung, Y.U; Bendoyim, I; Golovin, A.B.; and Crouse, D.T. "Dual-band photon sorting plasmonic MIM metamaterial sensor." *Proc. SPIE 9070, Infrared Technology and Applications XL, 90702X* (June 24, 2014); doi:10.1117/12.2050620.
- [6] Crouse, D., and Keshavareddy, P. "A method for designing electromagnetic resonance enhanced silicon-on-insulator metal-semiconductor-metal photodetectors." *Journal of Optics A: Pure and Applied Optics* 8.2 (2006): 175.
- [7] Mandel, I.; Gollub, J.; Bendoyim, I; Crouse, D. Theory and Design of A Novel Integrated Polarimetric Sensor Utilizing a Light Sorting Metamaterial Grating. *Sensors Journal, IEEE*, (2012): Vol. PP, 99.
- [8] Lepak, L., et al. "Handheld chem/biosensor using extreme conformational changes in designed binding proteins to enhance surface plasmon resonance (SPR)" *Proc. SPIE 9862, Advanced Environmental, Chemical, and Biological Sensing Technologies XIII*, 9862-7 (April 17, 2016); doi:10.1117/12.2222305.

Making Silicon Grating Test Samples for Scatterometry System

CNF Project Number: 2449-16

Principal Investigator: Thomas Brown

User: Steve Head

Affiliation: The Institute of Optics, University of Rochester

Primary Source of Research Funding: National Science Foundation Grant PHY-150727

Contact: tbrown2@ur.rochester.edu, stephenhead2@gmail.com

Abstract:

Three small (< 1-inch) samples made of up 1-D silicon gratings were made using electron-beam lithography (JEOL9500) and Bosch process etching (Unaxis 770), in order to test the capabilities of an experimental scatterometry system.

Summary of Research:

For the purpose of testing the scatterometry system that we built at University of Rochester [1], three test samples were created at CNF. The starting point was a few pieces of a silicon wafer with two polished sides, one of which had been previously (inadequately) coated with Al_2O_3 as an antireflection coating for 1064 nm. CNF staff member Amrita Banerjee used the FilMetric F50-EXR to measure the Al_2O_3 coating, which was found to be ~ 14 nm thinner than desired. CNF staff member Vince Genova then used the atomic layer deposition machine Gemstar-6 to deposit the remaining 14 nm.

The electron-beam lithography resist spinners were used to coat the remaining bare silicon side of the wafer pieces with gL2000 (also known as ZEP520A) 1:1 in anisole at 1500 rpm for one minute, followed by a pre-bake on a hot plate at 170°C for approximately five minutes. The samples were then exposed in the JEOL 9500, developed in hexyl acetate for two minutes, and rinsed for 45 seconds in isopropyl alcohol (IPA). The Unaxis 770 etcher was used with the photonics recipe to etch the samples, one of them going through a 40 second main etch step and two of them going through a 50 second etch step.

The resist was rinsed off using acetone and IPA, and CNF staff member Aaron Windsor removed the leftover fluoropolymer from the Unaxis770 using the PlasmaTherm72, set to 150 watts and 30 standard cubic centimeters per minute of oxygen for 20 seconds.

The pattern is shown after being etched onto a sample in Figure 1. The samples were milled into using the focused ion beam capabilities of the University of

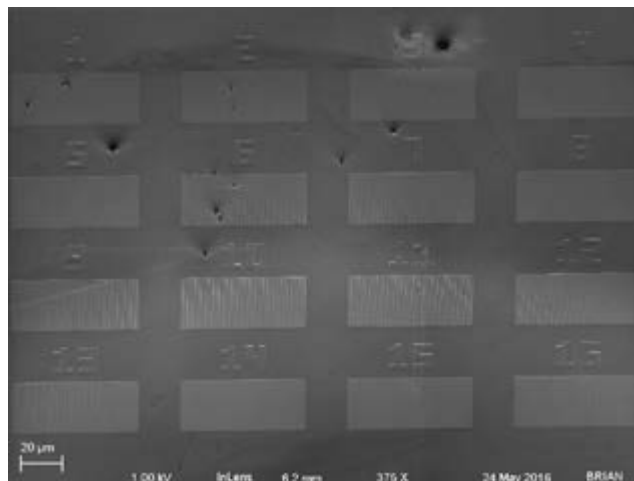


Figure 1: Full exposed region of sample 3 tilted 38 degrees vertically in SEM.

Rochester URnano facility's Auriga scattering electron microscope (SEM), and cross sectional SEM images at a 54 degree incident angle are shown in Figures 2-4. Sample 1 was ~ 92 nm deep, samples 2 and 3 were ~ 117 nm deep, and all three samples have critical dimensions ranging from ~ 200 nm - ~245 nm over gratings 1 through 16.

References:

- [1] T. Brown, M. Alonso, A. Vella, M. Theisen, S. Head, S. Gillmer, and J. Ellis "Focused beam scatterometry for deep subwavelength metrology," Proc. SPIE 8949 (2014).

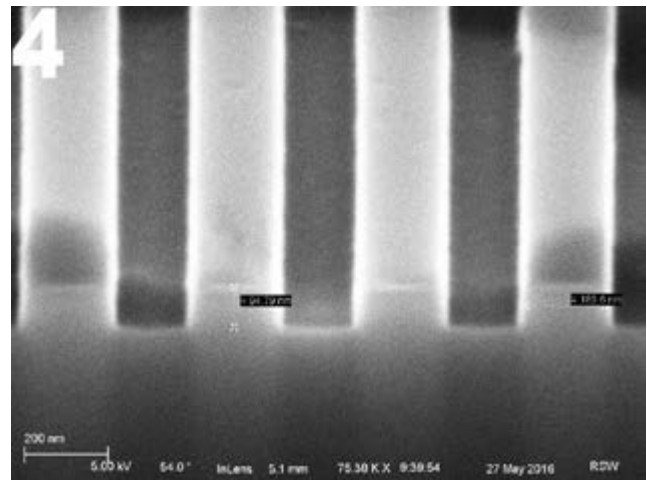
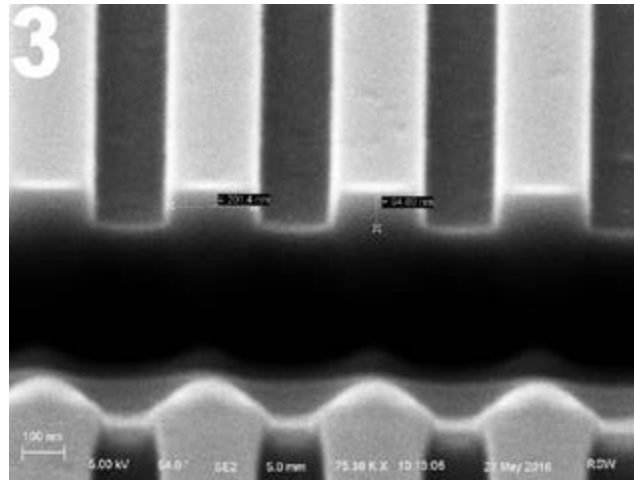
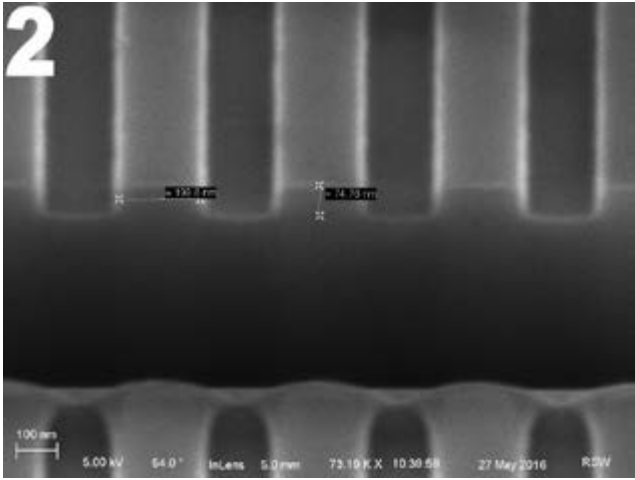


Figure 2-4: Cross sections of samples 1, 2, and 3, respectively, after focused ion beam cut.

Fabricating Self-Rolling Microtubes for Tuning Semiconductor Bandgaps

2016 CNF REU Intern: Maya Martirosyan, Physics, Harvey Mudd College

CNF REU Principal Investigator: Prof. Grace Xing, Materials Science & Engineering and Electrical & Computer Engineering, Cornell University

CNF REU Mentor: Rusen Yan, Electrical & Computer Engineering, Cornell University

Primary Source of Research Funding: National Science Foundation under Grant No. ECCS-1542081

Contact: mmartirosyan@g.hmc.edu, grace.xing@cornell.edu, ry253@cornell.edu

Abstract:

The coupling between the mechanical and the optoelectronic properties of a semiconductor suggest the possibility of tuning a semiconductor's bandgap by applying mechanical strain. Transparent insulator materials can be used to roll two-dimensional (2D) semiconductors to apply mechanical strain and observe the resulting optical properties. Using silicon nitride (SiN_x) layers of differential strain, we fabricated self-rolling microtubes, the smallest of which have dimensions of $10 \times 20 \mu\text{m}$. The diameter of the microtubes can be controlled by tuning the stress and the thickness of our SiN_x bilayer.

Introduction:

A semiconductor's bandgap determines its optical and electrical properties. However, these properties are coupled with the mechanical properties of the semiconductor. It has been shown that an applied uniaxial strain can alter the bandgap of 2D molybdenum disulfide (MoS_2) semiconductors, which gives rise to powerful applications such as tunable photodetectors, LEDs, and electro-optical modulators, as well as nanoscale stress sensors [1].

Our goal is apply strain to a 2D semiconductor by making it curl. We will roll the 2D semiconductor by attaching it onto a self-rolling microtube of a transparent insulator material, in our case silicon nitride (SiN_x). Bilayer SiN_x will roll due to differential stresses between the layers [2,3]. The aim of my project was to create these self-rolling microtubes. Once rolled, we can test the optical properties of the semiconductor in order to determine the changes in its bandgap.

Summary of Research:

We used bilayer SiN_x with a bottom compressive film and a top tensile film in order to create self-rolling structures. The Oxford plasma-enhanced chemical vapor deposition (PECVD) tool was used to deposit our

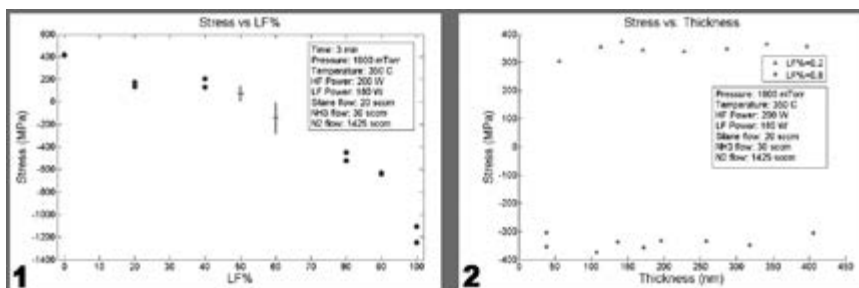


Figure 1, left: Stress vs. LF% for depositing SiN_x on the Oxford PECVD, which tells us how to control the stress of each SiN_x layer by changing the percentage of time that low frequency signal is used to ionize the plasma. Figure 2, right: Stress vs. Thickness for depositing SiN_x on the Oxford PECVD, which means we can tune the thickness of a film without affecting its stress.

SiN_x layers. The diameter of our rolled-up microtubes is primarily influenced by both the thickness and the stress of the layers. Thinner SiN_x layers result in tubes of smaller diameters [2]. As seen in Figure 1, the stress of the layer can be tuned by changing the ratio between the amount of low frequency signal (LF) and high frequency signal (HF) used to excite the plasma during deposition (this parameter is called LF%). The thickness of a film can be tuned by changing the deposition time without affecting the stress of the film, as shown in Figure 2.

For our SiN_x bilayers, we chose to have the highest possible compressive and tensile stresses for each layer to best match the literature, which meant using $\text{LF}\% = 100$ for compressive films, and $\text{LF}\% = 0$ for tensile films [2].

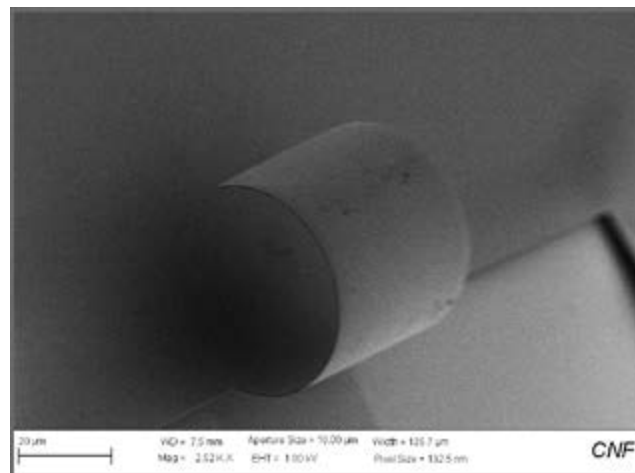
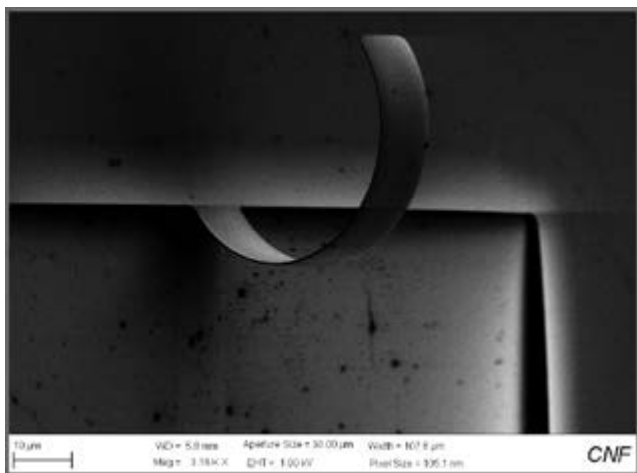


Figure 3, left: Curled cantilever with dimensions 10 x 70 microns. Image taken using SEM tool at a 45 degree angle. **Figure 4, right:** Curled cantilever with dimensions 40 x 200 microns. Image taken using SEM tool at a 45 degree angle.

We chose to try two designs in our fabrication process. Both designs included a rectangular pattern that would curl upward off the surface of the substrate and form microtubes. The rectangular patterns ranged from aspect ratios of 1:2 to 1:7, and from widths of 10-160 μm .

Design I required making a 20 nm thick Ge rectangular mesa using e-beam evaporation, and depositing and patterning bilayer SiN_x on top using optical lithography and RIE etching [2]. Then, the Ge mesa was isotropically wet etched with 30% wt. H_2O_2 at 70°C from one side of our rectangular features, releasing the rectangular structures. We were not able to successfully release our structures with this design, but it is the most similar to the procedure used in the literature, and is still a viable design.

Design II required making a 20 nm thick Ge layer using e-beam evaporation, depositing bilayer SiN_x on top and patterning a cantilever structure using optical lithography and RIE etching. Then, three sides of the cantilever were undercut and released by isotropically wet etching the Ge with 30% wt. H_2O_2 at 70°C and drying with IPA. We were successful in getting microtubes to roll along their longitudinal axis, as desired.

Results and Conclusions:

Using SEM imaging, we were able to obtain pictures of our self-rolling microtubes that were made using Design II. Both images in Figure 3 and Figure 4 were from a wafer where the stress of SiN_x compressive layer was -1150 MPa, the thickness of compressive layer was 109 nm, the stress of SiN_x tensile layer was 415 MPa, and the thickness of tensile layer was 134 nm. The feature in Figure 4 was released after a longer wet etch time than the feature in Figure 3, since the feature in Figure 4 is significantly larger and thus needs more time for the wet etch to undercut the entire feature.

Future Work:

With our fabrication procedure working, we can next make tubes of different diameters by changing the thickness of the SiN_x bilayer. Additionally, it will be important to characterize the diameter of the tubes as a function of SiN_x film thickness. These tubes can then be used to strain 2D MoS_2 semiconductors and measure their optical properties. Characterization of the Oxford PECVD, Oxford 80 Etcher, and ABM contact aligner can be refined as well. Lastly, other alternatives may be explored to create microtubes, such as polyimide, a stressed polymer, or LPCVD silicon nitride, but the strain control in these films needs to be understood first.

CNF Tools Used:

Oxford PECVD, SC4500 odd-hour evaporator, Oxford 82 etcher, ABM contact aligner, Flexus film stress measurement, P10 profilometer, Heidelberg Mask Writer-DWL2000, Zeiss Ultra/Supra SEM.

Acknowledgements:

I would like to thank my PI, Prof. Grace Xing, and my mentor, Rusen Yan, for instructing and helping me throughout my project. I would also like to thank the CNF REU Program Coordinators and the CNF Staff. This research was supported by the National Science Foundation under Grant. No. ECCS-1542081.

References:

- [1] H.J. Conley, B. Wang, J.I. Ziegler, R.F. Haglund, Jr., S.T. Pantelides, and K.I. Bolotin. "Bandgap Engineering of Strained Monolayer and Bilayer MoS_2 ." *Nano Letters* 2013 13 (8), 3626-3630.
- [2] W. Huang, S. Koric, X. Yu, K. J. Hsia, and X. Li. "Precision Structural Engineering of Self-Rolled-up 3D Nanomembranes Guided by Transient Quasi-Static FEM Modeling." *Nano Letters* 2014 14 (11), 6293-6297.
- [3] P. Froeter, X. Yu, W. Huang, F. Du, M. Li, I. Chun, S.H. Kim, K. Hsia, J. Rogers, and X. Li. "3D hierarchical architectures based on self-rolled-up silicon nitride membranes." *Nanotechnology* 24, 475301 (2013).

Nanosecond-Timescale Low Error Switching of In-Plane Magnetic Tunnel Junctions Through Dynamic Oersted-Field Assisted Spin-Hall Effect

CNF Project Number: 111-80

Principal Investigators: Prof. Daniel C. Ralph, Prof. Robert A. Buhrman

User: Sriharsha V. Aradhya

Affiliations: Physics, Kavli Institute at Cornell, School of Applied and Engineering Physics; Cornell University

Primary Source of Research Funding: IARPA

Contact: dcr14@cornell.edu, buhrman@cornell.edu, sva24@cornell.edu

Website: <http://arxiv.org/abs/1605.02104>

Abstract:

The spin-Hall effect enables the conversion of a charge current flowing in a heavy metal into a pure spin current orthogonal to both the direction of the current flow and the spin polarization. This effect has recently been rigorously quantified as being strong enough in the metals platinum, tantalum and tungsten to efficiently switch the magnetic orientation in thin-film nanomagnets. A key development in terms of applications of this effect is through the fabrication of three-terminal nanostructures in which the spin-Hall effect can be elegantly utilized to electrically write information into a nanomagnet. We demonstrate fast-pulse switching of in-plane-magnetized magnetic tunnel junctions (MTJs) within 3-terminal devices in which spin-transfer torque is applied to the MTJ by the giant spin-Hall effect in platinum. We measure reliable switching, with write error rates down to 10^{-5} , using current pulses as short as just 2 ns in duration. This represents the fastest reliable switching reported to date for any spin-torque-driven magnetic memory geometry, and corresponds to a characteristic time scale that is significantly shorter than predicted possible within a macrospin model for in-plane MTJs subject to thermal fluctuations at room temperature. This report summarizes our latest successes in fast switching of these devices fabricated at the Cornell NanoScale Science and Technology Facility.

Summary of Research:

The spin-Hall effect is a consequence of large spin-orbit coupling in heavy metals [1,2] due to which a pure spin current can be obtained by sending current through nanometer-thick metallic channels (typically ~5 nm of Pt, Ta or W). This spin current results in the accumulation of excess spins [3] on the surface of the channel that can exert a torque on an adjacent nanomagnet [4,5]. The magnetic orientation of this switchable nanomagnet ('free layer'; typically ~1-2 nm of $\text{Fe}_{60}\text{Co}_{20}\text{B}_{20}$) is detected by using a second nanomagnet ('reference layer'; typically ~4 nm of FeCoB) separated by a tunnel barrier (typically 1-2 nm of MgO). Figure 1 shows the schematic representation of such a device where the tunneling magnetoresistance (TMR) of the magnetic tunnel junction (MTJ) provides the read-out of the magnetic state of the free layer.

The fabrication starts with the deposition of the materials stack on a 4-inch Si/SiO₂ wafer using DC and RF magnetron sputtering.

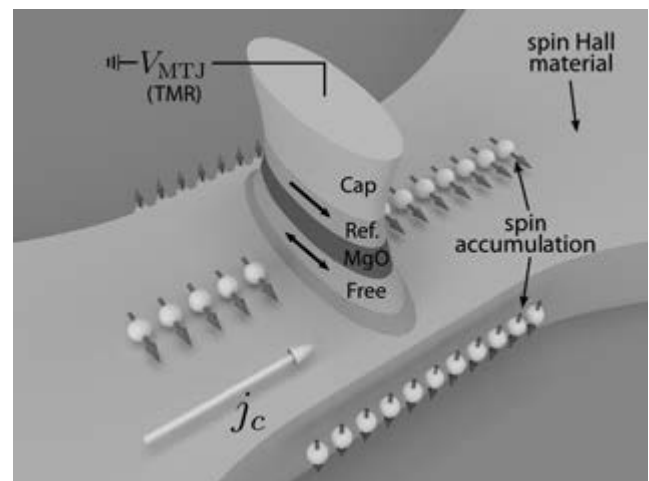


Figure 1: Schematic of a three terminal device consisting of a magnetic tunnel junction patterned on top of a spin-Hall channel.

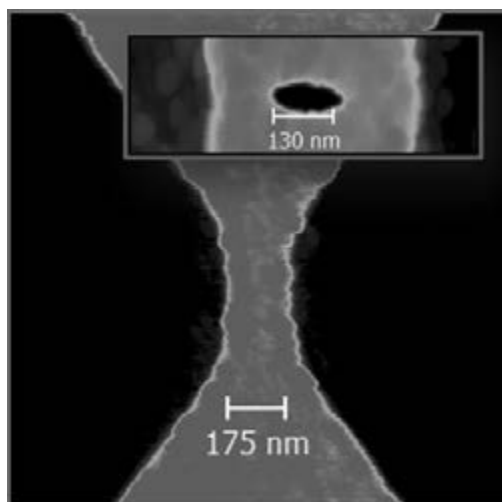


Figure 2: Atomic force microscopy images obtained with Veeco Dimension Icon shows channels with width ~ 175 nm. Inset: AFM image after SiO_2 lift-off showing access to the top of the nanopillar.

Briefly, the fabrication recipe is as follows: (1) photolithography followed by Ti/Pt deposition of alignment marks, (2) photolithography followed by ion-mill etching to isolate the devices and define the channels, (3) e-beam lithography followed by ion-mill etching to define nanopillars, (4) deposition followed by lift-off of SiO_2 , and finally (5) photolithography followed by Ti/Pt deposition to make top and bottom contacts to the nanopillar. Of particular importance to this process is the usage of the ASML deep-UV photolithography tool, which routinely yields ~ 175 nm features critical for defining narrow spin-Hall channels (Figure 2). The JEOL 6300 e-beam tool is equally important in being able to define nanopillars down to $\sim 50 \times 130$ nm ellipses that make up the MTJ itself (Figure 2, inset).

For switching measurements have focused on spin-Hall channels consisting of Ta/Pt/Hf: a combination of materials that results in a higher effective spin torque than has been achievable with a bare Pt base layer [6]. We deposited a Ta(1)|Pt(5)|Hf(0.7)|FeCoB(1.6)|MgO| (synthetic antiferromagnet)|IrMn|Ru(4) multilayer and followed the fabrication flow outlined above to pattern elliptical MTJs with lateral dimensions of $190 \text{ nm} \times 45, 75$ or 110 nm on top of 300 nm wide channels. These high, medium and low aspect ratio devices, respectively are tested for differences in high speed switching behavior.

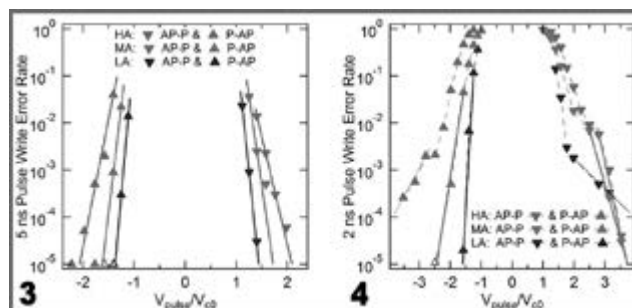


Figure 3, left: Write error rates for 5 ns pulses.

Figure 4, right: Write error rates for 2 ns pulses.

In order to gauge the fast switching response of these devices, rectangular pulses of durations $t = 0.25$ - 10 ns and 65 ps rise time are delivered to the channel by a Picosecond Pulse Labs 10,070A pulse generator. The tunnel junction state is read out after each switching attempt by a lock-in amplifier using a $10 \text{ M}\Omega$ reference resistor. Figure 3 and 4 show the write error rate (WER) of the three aspect ratio devices as a function of applied voltage for 5 and 2 ns pulse widths, respectively.

We clearly see that the WERs can be driven down below 10^{-5} , which indicates high reliability. In addition, the dependence of the WER on the aspect ratio indicates that the Oersted field from the current in the channel has a significant effect on the switching behavior. We therefore address this new advantageous switching mechanism as dynamic Oersted field assisted spin-Hall switching (DOFA-SHE).

References:

- [1] M. I. Dyakonov, Phys. Lett. 35A, 459-460 (1971).
- [2] J. Hirsch, Phys. Rev. Lett. 83, 1834-1837 (1999).
- [3] Y. K. Kato, R. C. Myers, A. C. Gossard, D. D. Awschalom, Science. 306, 1910-3 (2004).
- [4] L. Liu, T. Moriyama, D. C. Ralph, R. A. Buhrman, Phys. Rev. Lett. 106, 036601 (2011).
- [5] L. Liu, et al., Science. 336, 555-8 (2012).
- [6] M. H. Nguyen, et al., Appl. Phys. Lett., 106, 222402, (2015).

Strong Spin-Hall Effect in the Antiferromagnet PtMn

CNF Project Number: 111-80

Principal Investigator: Robert A. Buhrman

Users: Shengjie Shi, Yongxi Ou

Affiliation: Applied and Engineering Physics, Cornell University

Primary Source of Research Funding: Office of Naval Research

Contact: buhrman@cornell.edu, ss2882@cornell.edu, yo84@cornell.edu

Abstract:

Manipulating magnetism in ferromagnetic nanostructures with an in-plane current has become feasible due to the “giant” spin-Hall effect (SHE) that occurs in certain heavy metal (HM)/ferromagnet (FM) systems, as characterized by the spin-Hall ratio (angle) [1]. Recently a new class of heavy metal (HM) alloys, the non-collinear antiferromagnet (AF), Mn_3Ir and Cu-Au-I type AF, $X_{50}Mn_{50}$ ($X = Fe, Pd, Ir, \text{ and } Pt$) have been reported to exhibit SHE as spin current sources, opening up a new area in the rapidly advancing field of “antiferromagnet spintronics” [2]. By using interface engineering to reduce the spin memory loss (SML) in the best instances we obtain a spin torque efficiency of about 0.24. This is more than twice the previously reported spin torque efficiency. We also find that the apparent spin diffusion length in platinum manganese (PtMn) is surprisingly long, about 2.3 nm. We achieve current-induced switching in perpendicularly magnetized samples, which shows great potential for future spin torque memory development.

Summary of Research:

We deposited our samples using magnetron sputtering system and patterned the samples and electric contacts using $5\times$ g-line stepper at CNF.

We performed a systematic study of the SHE in several PtMn/FM systems employing spin-torque ferromagnetic resonance on in-plane magnetized FM layers (see Figure 1) and the harmonic response Hall-effect measurements on FM layers with perpendicular magnetic anisotropy (PMA). Based on spin torque efficiencies we got for different thicknesses of PtMn, we determined that the spin diffusion length in PtMn is relatively long, about 2.3 nm (Figure 2). We find damping-like spin torque efficiency to vary significantly with both the deposition order for a given PtMn/FM system and between the different FM systems, but to be relatively consistent between IPM and PMA samples with the same constituents.

To date research on the SHE from AFs has utilized the implicit assumption that there is no interfacial spin flip scattering or “spin memory loss” (SML) when the spin current traverses the interface to apply a torque to the FM. However the existence of a large SML at some Pt/FM interfaces, together with the negative enthalpy of formation of Mn with both Fe and Ni that can promote interface intermixing, raises the question whether there may also be a significant SML

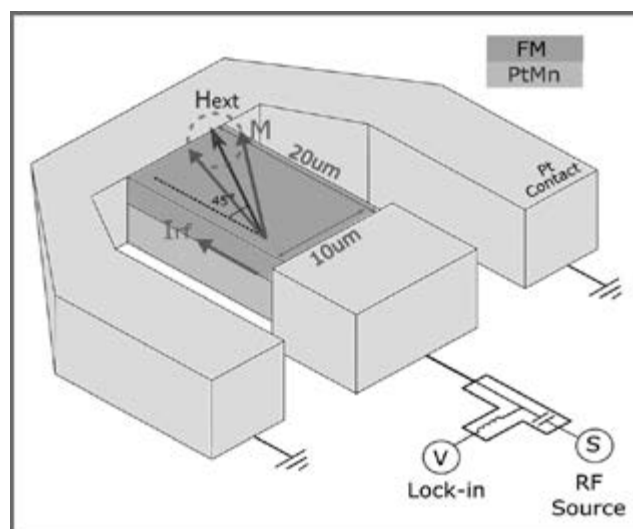
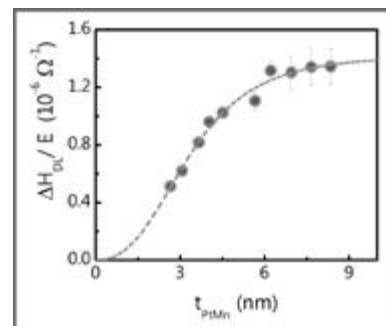


Figure 1, top: Schematic of ST-FMR measurement. The Pt contact is 150nm thick.

Figure 2, right: Damping-like effective field per unit applied electric field for samples Ta(1)/PtMn(t_{PtMn})/Hf(0.8)/FeCoB(0.7)/MgO as a function of PtMn thickness, t_{PtMn} .



at PtMn/FM interfaces, which would mean that the internal spin Hall angle within PtMn could actually be much higher than previously reported. Working with several different PtMn/FM systems here we establish that this is indeed the case. We studied samples where a thin (0.25 nm - 0.8 nm) Hf layer is inserted between the PtMn and the FM to suppress strong SML at the interface. We obtain a spin torque efficiency of about 0.24 in Ta/PtMn(8)/Hf(0.25)/FeCoB(0.8)/MgO/Ta sample.

We also fabricated hall bar structures on the PMA samples. Schematic of the sample structure and measurement method is depicted in Figure 3. We obtained strong PMA in several material systems where a square and abrupt change of Hall resistance is observed when we sweep the external field in perpendicular direction relative to the sample plane. We obtained robust current-induced switching in these PMA samples (Figure 4) under an external field in the direction of switching current. This demonstrates the potential for utilizing PtMn in perpendicular magnetic tunneling junction (p-MTJ) and three-terminal device applications.

References:

- [1] L. Liu, O. J. Lee, T. J. Gudmundsen, D. C. Ralph, and R. A. Buhrman, Phys. Rev. Lett. 109, 096602 (2012).
- [2] W. Zhang, M. B. Jungfleisch, F. Freimuth, W. Jiang, J. Sklenar, J. E. Pearson, J. B. Ketterson, Y. Mokrousov, and A. Hoffmann, Phys. Rev. B 92, 144405 (2015).

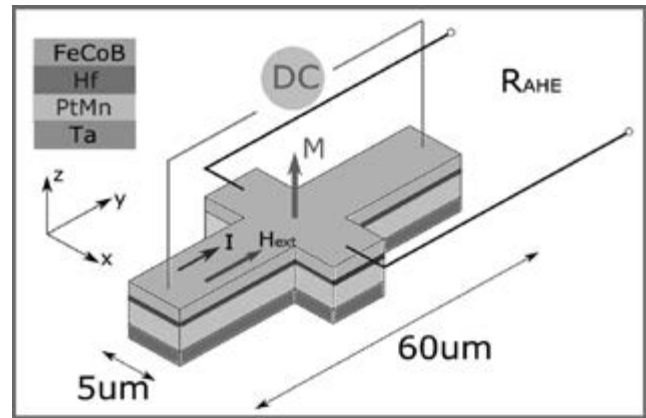


Figure 3: Schematic of the Hall-bar samples used to study field- and current-induced switching.

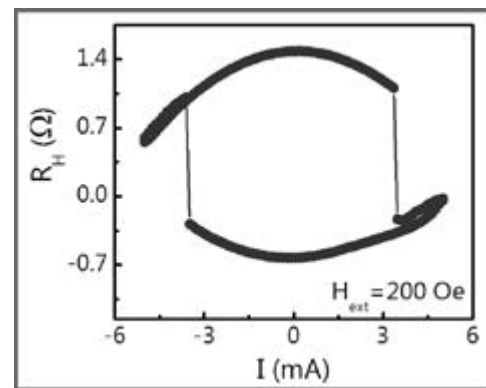


Figure 4: Current-induced switching of the same sample with an external magnetic field (200 Oe) applied in-plane along the current direction.

Generating Controllable Polarization Spin Currents through the Anomalous Hall Effect in FeGd

CNF Project Number: 598-96

Principal Investigator: Daniel C. Ralph

User: Jonathan D. Gibbons

Affiliation: Physics, Cornell University

Primary Source of Research Funding: NSF

Contact: dcr14@cornell.edu, jg833@cornell.edu

Abstract:

We have probed spin currents generated through the anomalous Hall effect in an exchange-biased iron gadolinium (FeGd) alloy. We have used the in-plane second-harmonic technique to detect magnetic dynamics excited in a cobalt iron boron (CoFeB) sensor layer by the applied currents, observing the dependence on the angle of the magnetization of the FeGd layer. We find results that may be indicative of the presence of spin currents with controllable spin polarization.

Background:

Spin currents can be used to apply spin transfer torques, allowing us to manipulate or switch the magnetization of ferromagnetic layers. The spin-Hall effect has generated a lot of interest as a generating source for such spin currents. However, in non-magnetic materials, the spin-Hall effect generates spin currents with a spin polarization determined by geometry. This restriction limits what spin torques can be generated.

The underlying physics that gives rise to the spin-Hall effect in normal metals causes the anomalous Hall effect in ferromagnetic materials, generating a transverse Hall current. However, the effect still generates a spin current, as well. Taniguchi, et al. [1], have predicted that the spin current generated by the anomalous Hall effect will have a spin polarization parallel to the magnetization of the generating layer. By controlling the magnetization of the generating layer, it is then possible to control the spin polarization of the spin current. A magnetic sensor layer can be used to detect the effects of this spin current and extract the spin polarization of the spin current. Such a situation is shown in Figure 1.

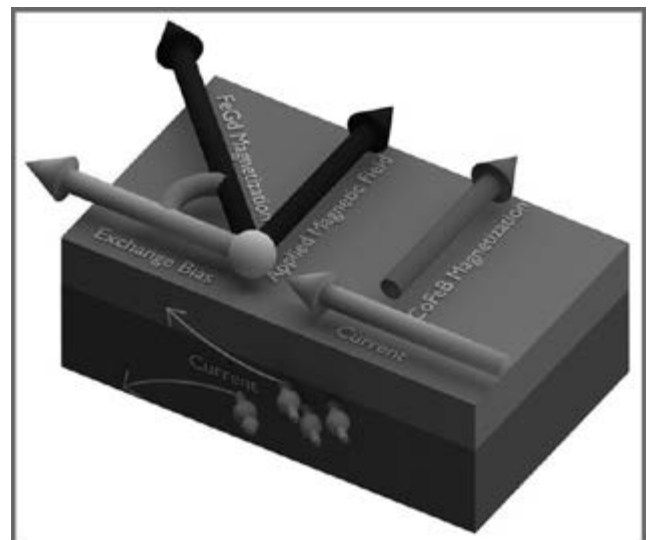


Figure 1: A diagram of the anomalous Hall effect. Spin carriers aligned parallel to the anomalous Hall layer are deflected in opposite directions based on their spin.

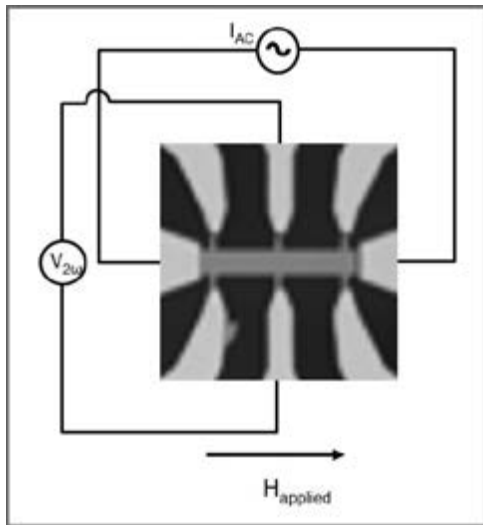


Figure 2: An image of a Hall bar with a diagram of our experimental setup. We apply a slowly varying current and detect the Hall voltage on the second harmonic.

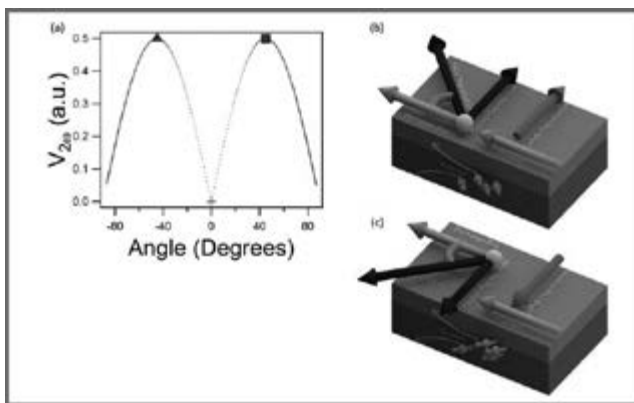


Figure 3: The predicted second harmonic due to a spin current generated with controllable spin polarization for our geometry. (a) The predicted signal. (b and c) The orientations of the relevant magnetic layers at the points corresponding to the triangle (b) and square (c) shown in (a).

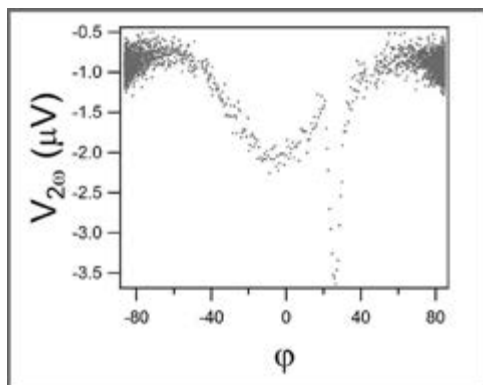


Figure 4: Measured second harmonic signal as a function of angle. Measurements taken at room temperature.

Fabrication:

We create IrMn (10 nm)/FeGd (4 nm)/Hf (2 nm)/CoFeB (2 nm)/Hf (3 nm) multilayers in a CCMR/Ralph group sputter system. The iridium manganese (IrMn) layer exchange biases the FeGd, and the internal hafnium (Hf) layer isolates the two ferromagnetic layers. The FeGd layer is the spin current generating layer, and the CoFeB is the sensor layer. The top Hf layer is a capping layer.

We use the optical lithography tools at CNF to make masks and pattern our devices into $80 \mu\text{m}$ by $20 \mu\text{m}$ Hall bars. We define the bars using a Buhrman group ion mill. We then use a lift-off process to deposit electrical contacts. For this process, we use the CNF optical lithography tools to pattern the sample and the CNF AJA sputter system to deposit Ti-Pt leads. We then anneal the samples to above the Néel temperature of the IrMn layer, and cool in field to define a direction for the exchange bias. Finally, we characterize the sample using the CNF AFM and a CCMR VSM.

Experiment:

We apply a slowly-varying DC current to Hall bars. This current generates a spin current, which applies a torque and moves a magnetic layer. This movement is detected through the second harmonic Hall voltage. A diagram of our experimental setup, including a picture of our device, is shown in Figure 2. We model the expected behavior of the pinned ferromagnetic layer based on VSM characterization, and use this to predict the field-dependence of the second harmonic signal. The predicted behavior is shown in Figure 3.

Results:

We electrically detect the state of the magnetic layers. We find interesting dependence of the second harmonic signal across different temperature regimes. The raw data at room temperature is shown in Figure 4. We have yet to separate parasitic signals from our desired signal. The data is consistent with our predictions, but may also derive from other sources. Additional work is needed.

References:

- [1] T. Taniguchi, J. Grollier, and M. D. Stiles, Phys. Rev. Appl. 3, 044001 (2015).

Creating Skyrmions Using Spin Transfer Torque

CNF Project Number: 598-96

Principal Investigator: Daniel C. Ralph

Users: Jennifer Grab, Alison Rugar

Affiliation: Department of Physics, Cornell University

Primary Source of Research Funding: National Science Foundation

Contact: dcr14@cornell.edu, jlg373@cornell.edu, aer245@cornell.edu

Abstract:

Skyrmions are topologically protected quasiparticles in the form of stable spin textures in a magnetic material. Because skyrmions can be smaller than the domain size in a ferromagnet, they are promising candidates for high density information storage. Finding an efficient way to create and annihilate individual skyrmions under ambient conditions is an important first step toward realizing skyrmion-based technologies. In this project, we attempt to create skyrmions using a spin-valve-like device. If this work is successful, it will offer a relatively simple method for creating isolated magnetic skyrmions for further study and manipulation.

Summary of Research:

Skyrmions are encountered in a number of different material systems. Of particular interest experimentally are systems with a strong Dzyaloshinskii-Moriya Interaction (DMI), which favors helical spin textures. Skyrmion lattices have been observed in materials with bulk DMI, for example manganese silicide [1] and iron germanium [2], at cryogenic temperatures. More recently, isolated skyrmions have been created and observed in heavy metal / ultrathin ferromagnet systems with perpendicular magnetic anisotropy (PMA) and strong interfacial DMI [3,4].

Our devices consist of a cobalt (Co) / platinum (Pt) multilayer and copper spacer patterned into a nanopillar on top of a bulk Co/Pt bilayer with strong DMI (Figure 1). The purpose of the nanopillar is to generate a spin polarized current, which is expected to reverse the magnetization of the film underneath the pillar via spin transfer torque. Micromagnetic simulations predict that we should be able to excite a skyrmion breathing mode, which will have a large

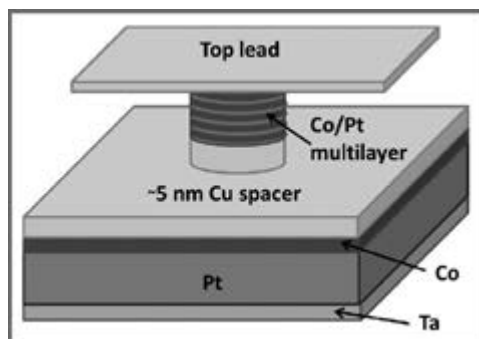


Figure 1: Device geometry.

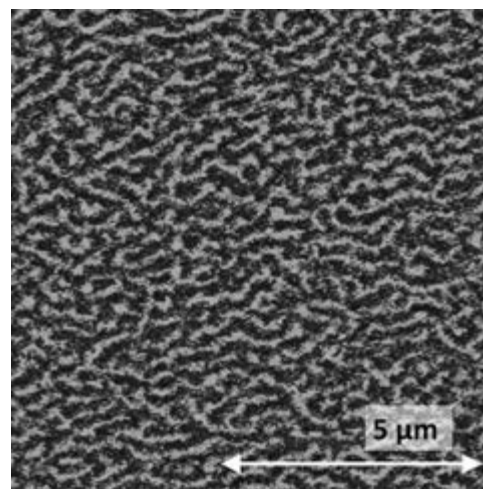


Figure 2: Magnetic force microscopy image showing helical stripe domains in one of our Co/Pt bilayer films.

resistance signal distinguishable from the switching of the entire bottom layer. Both the multilayer and bilayer have PMA as confirmed by vibrating sample magnetometry and Hall measurements. Imaging of our bilayer films using magnetic force microscopy in the Veeco Icon shows that they have a helical domain structure (Figure 2), which is favorable for the formation of skyrmions.

Fabrication Process:

First, the entire material stack is grown using magnetron sputtering in our group's Kurt J. Lesker sputter system. Then, photolithography and ion milling are used to etch all the way to the substrate and define the bottom leads. Nanopillars are fabricated using a negative resist recipe in the CNF's JEOL 6300 electron beam lithography system, and then endpoint detection in the ion mill is used to etch down to the copper spacer. Immediately after etching, the sample is quickly transferred to the Even Hour Evaporator, and about 80 nanometers (nm) of silicon dioxide is deposited to protect the sides of the pillar from oxidizing. The silicon dioxide is removed from the top of the pillar via liftoff. Next, we deposit an additional 70 nm layer of silicon dioxide around the pillar to prevent the top and bottom leads from shorting together. The silicon dioxide is removed from the bottom leads using the Oxford 81 plasma etcher. Lastly, we deposit top and bottom contacts using the AJA sputter system and liftoff.

Results and Conclusion:

Four point magnetoresistance measurements of completed devices show switching of the free and fixed layers, as expected (Figure 3). When we apply a DC current through the nanopillar at a constant magnetic field, we observe current dependent switching (Figure 4). Switching events that are symmetric with respect to current sign are thermal, whereas events that are dependent on current sign are likely due to spin transfer torque. We observe current-induced switching of both the bilayer, at lower fields, and the nanopillar, at higher fields. We are currently working on additional measurements to determine whether any of the bilayer switching events correspond to the creation of a domain beneath the nanopillar.

Once we have working devices in which we can demonstrate the formation of a skyrmion, further measurements can be done to determine characteristics, such as stability, of the skyrmions. It should also be possible to excite skyrmion dynamics in our devices using an AC current. Lastly, if this project is successful, then this will open the door for many interesting future experiments. For example, we can try to manipulate the skyrmion with an in-plane spin Hall torque and possibly read it out with another nanopillar.

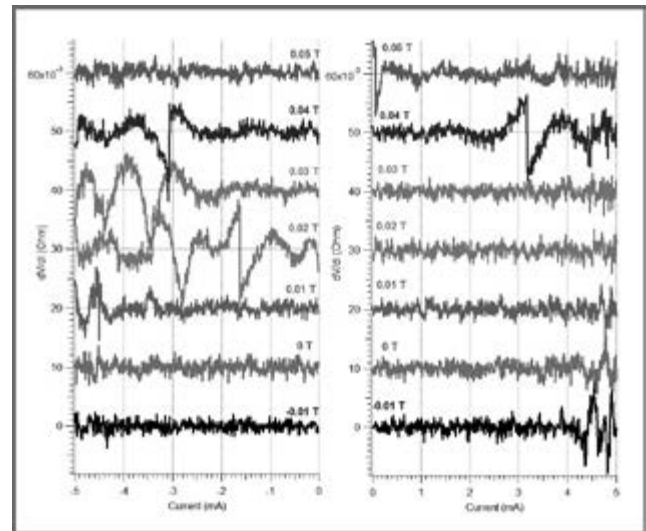
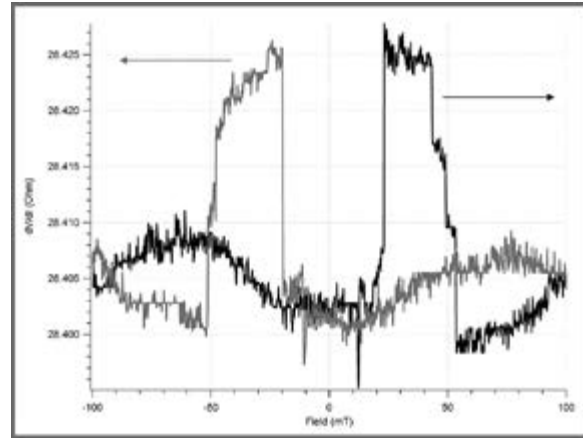


Figure 3, top: Example four point magnetoresistance data demonstrating switching of the free and fixed layers in a device. The lower resistance state corresponds to the fixed and free layers aligned parallel to each other, while the higher resistance state corresponds to antiparallel alignment.

Figure 4, bottom: Current-induced switching in one of our devices under various applied magnetic fields at both positive and negative current.

References:

- [1] X. Z. Yu, et al., Nano Lett., 13 (8), 3755 (2013).
- [2] X. Z. Yu, et al., Nature Materials 10, 106-109 (2011).
- [3] S. Woo, et al., Nature Materials 15, 501-506 (2016).
- [4] W. Jiang, et al., Science 349 (6245), 283-286 (2015).

Measuring the Spin-Hall Effect in Rare Earth Thin Films

CNF Project Number: 598-96

Principal Investigators: Daniel C. Ralph, Darrell Schlom, David Muller

Users: Neal Reynolds, Jonathan Gibbons, Robin Collette*, John Heron, Kayla Nguyen

*Affiliations: Physics, Materials Science and Engineering, Cornell University; * 2015 NNIN REU Program at CNF Intern*

Primary Sources of Research Funding: Qualcomm, Defense Advanced Research Projects Agency,

** 2015 NNIN REU Program at Cornell (NSF Grant No. ECCS-0335765)*

Contact: dcr14@cornell.edu, schlom@cornell.edu, dm24@cornell.edu,
ndr37@cornell.edu, jg833@cornell.edu, rc3007@ship.edu

Abstract:

The spin-Hall effect occurs in non-magnetic metals and results in the flow of a spin current transverse to the flow of charge. Aside from the potential utility of this phenomenon for spin-based electronics, this effect is also interesting from a fundamental physics perspective as it depends strongly on the material's spin-orbit coupling and band structure. Based on this we expect the lanthanide series of elements with 4f levels near the Fermi level to have a potentially large spin-Hall effect. In this report we discuss measurements of the spin-Hall effect of the lanthanide metals Gd, Dy, Ho, and Lu.

Summary of Research:

The spin-Hall effect is generally believed to be due to the sum of intrinsic contributions from a given material's band structure and extrinsic contributions due to asymmetric scattering from impurities. Recent theoretical and experimental work has suggested that the lanthanide series elements with 4f levels near the Fermi level might have a large intrinsic spin-Hall effect due to the large orbital angular momentum associated with the 4f states [1,2]. We report on the spin-Hall effect in the nominally 4f⁷, 4f⁹, 4f¹⁰, and 4f¹⁴ lanthanide metals gadolinium, dysprosium, holmium, and lutetium, respectively.

Bilayers of Fe and Lu were grown on <0001> sapphire substrates using molecular beam epitaxy (MBE) in collaboration with the Schlom group. The films were confirmed to be smooth by atomic force microscopy and low-incidence angle x-ray reflectivity (XRR) measurements. Multilayers of Gd, Dy, Ho with Hf and Py were grown using DC magnetron sputtering. Micron-scale devices were then fabricated out of the thin film by using a four-layer photolithography process at the Cornell NanoScale Facility (CNF).

First polycrystalline platinum alignment marks and contact pads were deposited onto the thin film using sputter deposition and lift-off. Devices were then defined by using photolithography and Ar ion milling. An insulating layer of SiO_x was deposited over the entire chip using sputter deposition. The buried contacts pads were then uncovered using Ar+CHF₃ plasma etching and top leads of polycrystalline

platinum putdown by using sputter deposition and lift off. CNF's 5× g-line stepper was used for all photolithography. An optical image of a finished device is shown in Figure 1.

Measurements of the spin-Hall angle of the RE samples were done using two complementary techniques where possible: spin-torque ferromagnetic resonance (ST-FMR) and dc-biased ST-FMR [3,4]. Both techniques use the application a radio frequency signal to excite resonant dynamics in the ferromagnetic Fe or Py layer to then allow us to measure a voltage signal that depends on the amplitude and phase response of the resonance. The strength of the spin-Hall effect can be determined either from the amplitude of the resonance or the dependence of the resonance linewidth on direct current. We find that the two types of measurement are in good agreement.

The resulting (preliminary) values for the effective spin-Hall effect efficiencies for each rare earth metal are Gd = 2.7%, Dy = 3.5%, Ho = 9%, and Lu = 1.4%, summarized in Figure 2.

References:

- [1] T. Tanaka and H. Kontani, Phys. Rev. B 81, 224401 (2010).
- [2] K. Ueda, C.F. Pai, A. J. Tan, M. Mann, and G. S. D. Beach, Appl. Phys. Lett. 108, 232405 (2016).
- [3] L. Liu, T. Moriyama, D. C. Ralph, and R. A. Buhrman, PRL 106, 036601, (2011).
- [4] L. Liu, C. F. Pai, Y. Li, H. W. Tseng, D. C. Ralph, and R. A. Buhrman, Science 366, 555 (2012).

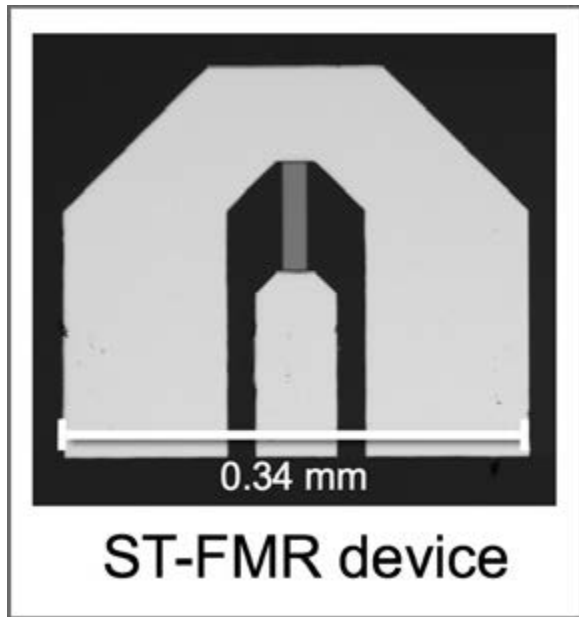


Figure 1: Optical images of completed devices from the same die for second harmonic measurements (Hall bar), spin-torque ferromagnetic resonance measurements (ST-FMR), and spin pumping/inverse spin-Hall effect measurements (Coplanar waveguide).

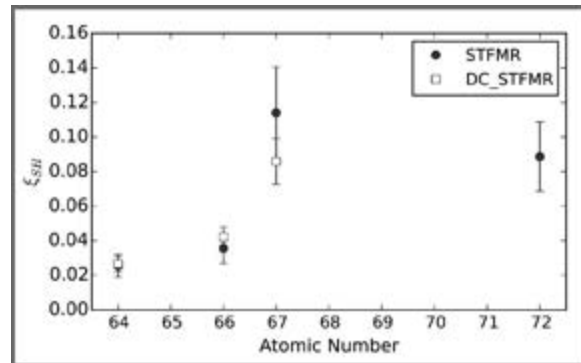


Figure 2: Graph of measured spin-Hall ratio from ST-FMR and DC-biased ST-FMR vs. atomic number and thus f electron filling.

Current-Generated Spin-Orbit Torques in MoS₂ / Ferromagnet Bilayers

CNF Project Number: 598-96

Principal Investigators: Robert Buhrman, Jiwoong Park, Daniel Ralph

Users: Gregory Stiehl, David MacNeill, Hui Gao, Marcos Guimaraes

Affiliations: Applied and Engineering Physics, Chemistry and Chemical Biology, Physics; Cornell University

Primary Source of Research Funding: National Science Foundation (DMR-1406333);

Army Research Office (W911NF-15-1-0447)

Contact: buhrman@cornell.edu, jp275@cornell.edu, dcr14@cornell.edu, gms263@cornell.edu,

djm398@cornell.edu, hg369@cornell.edu, mg787@cornell.edu

Website: <http://ralphgroup.lassp.cornell.edu/>

Abstract:

We discuss fabrication techniques for transition metal dichalcogenide (TMD) / ferromagnet bilayer microwave waveguides and present measurements of current-generated torques in these bilayers for the semi-conducting TMD MoS₂. TMDs present a unique opportunity to study interfacial spin-orbit torques at the two dimensional limit due to a wide range in material properties and large spin-orbit coupling. Thin TMD films are grown by chemical vapor deposition are incorporated into ferromagnet / TMD bilayers by off-axis sputtering of the ferromagnet to avoid damage to the TMD surface. Measurements of the current-generated torque are made by spin-torque ferromagnetic resonance.

Summary of Research:

Current-generated spin-orbit torques are a promising route for efficient switching of new magnetic memory technologies. Recent work on transition metal dichalcogenide (TMD) / ferromagnet bilayers has demonstrated that TMDs are interesting sources of spin-orbit torques [1,2]. Here, we discuss methods of ferromagnet deposition to minimize damage to the monolayer TMD film, wafer-scale fabrication techniques for TMD/ferromagnetic bilayers, as well as present measurements demonstrating the presence of spin-orbit torques in bilayers consisting of the semi-conducting TMD MoS₂ and the ferromagnet permalloy (Py = Ni₈₁Fe₁₉).

Continuous monolayer thick MoS₂ is grown by metal-organic chemical vapor deposition (MOCVD) [3] onto a thermally oxidized high resistivity silicon wafer. The films are transferred to the Cornell Center for Materials Research (CCMR) Lesker sputtering system where an off-axis (grazing angle) DC magnetron sputtering gun is used to deposit 6 nm of Py at a background Ar pressure of 4 mtorr. The high angle of incidence (> 85°) minimizes the impinging kinetic energy of the deposited material and thereby reduces damage to the monolayer thick MoS₂ film. The MoS₂ / Py bilayers are passivated by a subsequent deposition of a 2 nm thick aluminum film. Alternatively, Py films

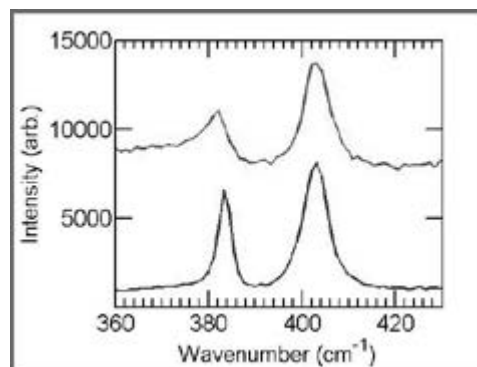


Figure 1: Raman spectra of MoS₂ before (blue, bottom) and after (green, top) off-axis sputter deposition of Py.

may be deposited by evaporation (CNF odd-hour evaporator), but this requires the presence of a thin (1 nm) titanium sticking layer and generally produces poorer quality magnetic films.

To ensure that the sputtering process does not damage the MoS₂ film, Raman measurements are performed before and after the ferromagnet deposition (Figure 1). No significant shifts in the MoS₂ Raman peak locations

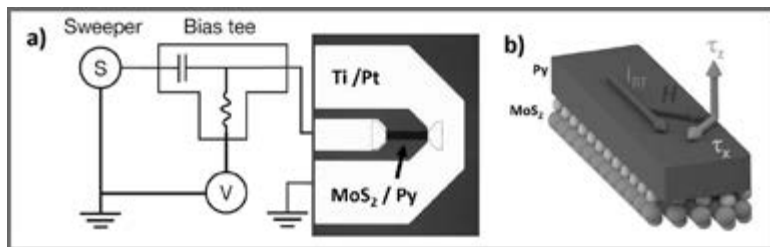


Figure 2: a) Schematic of ST-FMR circuit and picture of finished device, bar is $16 \times 80 \mu\text{m}$. b) Layout of device geometry, applied current, field and observed torques.

are observed for the sputtered bilayer films. The slight broadening of the peaks may be due to coupling of the MoS_2 phonon modes to the Py or mild damage to the MoS_2 . However, the observed broadening is less than expected due to damage from standard on-axis sputtering [4].

Water sensitivity and ease of delamination in MOCVD MoS_2 films present some minor challenges for fabrication: the films cannot be subjected to water developer or wet solvent without a passivated clamping layer to protect it, and in addition cannot be subjected to ultra-sonic vibration. To pattern the MoS_2 / Py bilayers into microwave waveguides with dimensions ranging from $2 \times 10 \mu\text{m}$ to $20 \times 80 \mu\text{m}$, we first deposit 60 nm of SiO_2 by sputtering (CNF AJA Sputter tool) to act as a clamping layer. Bars are defined using photolithography (5 \times g-line stepper) and a CHF_3 / Ar RIE (Oxford 81) to transfer the pattern into the SiO_2 , where the AlO_x cap and Py layer are used as etch stops. A subsequent O_2 plasma clean is used to remove the photoresist.

The MoS_2 / Py bilayers are etched into bars by Ar ion milling using the patterned SiO_2 cap as a hard mask. The devices are then re-capped with 20 nm of SiO_2 (CNF AJA Sputter tool) and a second round of photolithography is performed (5 \times g-line stepper) to define electrical contact pads. A CHF_3 / Ar RIE (Oxford 81) is used to etch away the SiO_2 in the region of the MoS_2 / Py bar where contact to the electrical leads are made, followed by a deposition of Ti(5nm) / Pt(100nm) (CNF AJA Sputter tool) and an over-night liftoff in acetone. An image of a finished device is shown in Figure 2a.

Measurements of the current-generated spin-orbit torque in the MoS_2 / Py bilayer are made by spin-torque ferromagnetic resonance (ST-FMR) [4]. A GHz frequency current is applied to the bar (Figure 2a) and an in-plane magnetic field is swept from 2500 Oe to 0 Oe at 45° from the current direction (Figure 2b), driving the ferromagnet through its resonance condition. A DC mixing voltage is measured, and the observed

resonance feature (Figure 3) is fit as a function of symmetric and antisymmetric lorentzians to determine the torques present in the bilayer. As described by L. Liu, et al. [5], the presence of a symmetric component to the fit implies that spin-orbit torques are present in the bilayer system.

The presence of current-generated spin-orbit torques in TMD / ferromagnet bilayers for TMDs studied thus far (MoS_2 [1] and WTe_2 [2]), motivates a wider study of the many possible TMDs with their broad range of spin-orbit couplings, conductivities and crystal structures, as potential sources of spin-torque. Further, utilization of wafer-scale growths of TMDs provides a more direct route to potential applications in efficient switching of new magnetic memories.

References:

- [1] W. Zhang, et al. Research Update: Spin transfer torques in Permalloy on monolayer MoS_2 . APL Mater. 4, 032302 (2016).
- [2] D. MacNeil, G. M. Stiehl, M. H. D. Guimaraes, R. A. Buhrman, J. Park, and D. C. Ralph. Control of spin-orbit torques through crystal symmetry in WTe_2 /ferromagnetic bilayers. arXiv1605.02712 (2016).
- [3] K. Kang, et al. High-mobility three-atom-thick semiconducting films with wafer-scale homogeneity. Nature 520, 656-660 (2015).
- [4] C.-T. Chen, E. A. Casu, M. Gajek, and S. Raoux. Low-damage high-throughput grazing-angle sputter deposition on graphene. Appl. Phys. Lett. 103, 033109 (2013).
- [5] L. Liu, T. Moriyama, D. C. Ralph, and R. A. Buhrman. Spin-torque ferromagnetic resonance induced by the spin Hall effect. Phys. Rev. Lett. 106, 036601 (2011).

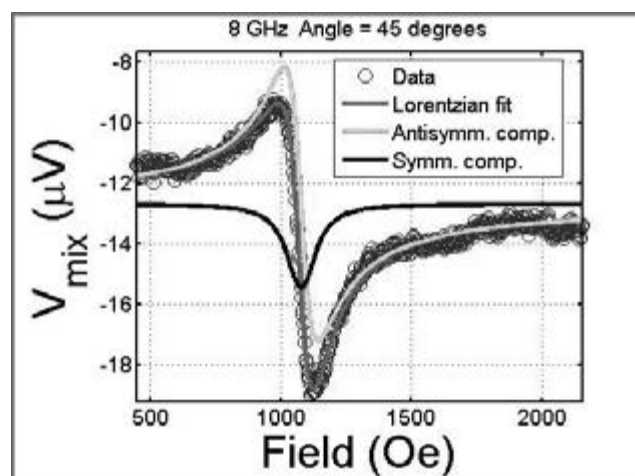


Figure 3: ST-FMR mixing voltage as a function of applied magnetic field with an 8 GHz current excitation.

Electronic Transport of Topological One-Dimensional Channels in Two-Dimensional Materials

CNF Project Number: 900-00

Principal Investigator: Paul McEuen

User: Lei Wang

Affiliation: Physics, Cornell University

Primary Source of Research Funding: Multidisciplinary University Research Initiative

Contact: PLM23@cornell.edu, LW578@cornell.edu

Abstract:

The tunability of charge transport by electric field effect plays the most important role in modern electronics. Along with charges, electrons in a crystal also carry more degrees of freedom, such as spin and valley. The manipulation of spin transport has been experimentally pursued in the last two decades, such as giant magnetoresistance devices and magnetic tunneling transistors – which is believed to be faster and uses less power. The control of valley degree of freedom has recently been theoretically predicted in graphene and transition metal dichalcogenide. In bilayer graphene, there exists a structural spontaneity where one of the graphene layers shifts by an atomic spacing with respect to the other, resulting in AB and BA stacking domains with soliton-like structural boundaries between them. Carriers on this chiral edge states have their valleys linked to their propagation direction (valley-momentum locked). Based on this property, here, we try to experimentally demonstrate a valley switching device.

Summary of Research:

Our previous work has experimentally identified a type of one-dimensional (1D) channel in bilayer graphene not on the disordered edge but inside the bulk [1]. It is due to a structural spontaneous symmetry breaking in CVD bilayer graphene, where one of the graphene layers shifts by an atomic spacing with respect to the other, resulting in AB and BA stacking domains with soliton-like structural boundaries between them [1]. These AB and BA phases can be directly imaged using transmission electron microscopy. Each soliton consists of an atomic-scale registry shift between the two graphene layers occurring over 6-11 nm [1].

Recently, this AB-BA domain boundaries on exfoliated bilayer graphene flake on SiO₂ substrate can be identified using near-field infra scanning technique [2]. Dual-gated devices on SiO₂ were made on regions with and without the domain boundary. Devices with the domain boundary behaved differently from the insulating characteristic of the single-domain ones. The domain boundary exhibits electron transport characteristics on a 1D channel, with mean free path measured to be around 400 nm at 4 K [2].

To study the electronic transport property along these 1D domain walls, we have made high quality devices

by identifying bilayer graphene flakes with domain walls using the near-field scanning method [2] and sandwiching them with hexagonal boron nitride flakes using the van der Waals transfer technique [3] (Figure 2). Using the electron beam lithography tool (JEOL 6300) in CNF, we have fabricated several dual-gated devices (Figure 3).

As the bandgap of the bilayer graphene being opened by applying a perpendicular displacement field, the bulk part of bilayer graphene becomes insulating and electron transport is confined to the domain wall.

The measured resistance values quantized to about 0.5 (h/e^2) over a 500 nm long channel are observed (Figure 4).

References:

- [1] Alden, J. S., et al. Strain solitons and topological defects in bilayer graphene. *Proc. Natl Acad. Sci. USA* 110, 11256-11260 (2013).
- [2] Ju, L., et al. Topological valley transport at bilayer graphene domain walls. *Nature*, 520, 650-655 (2015).
- [3] Wang, L., et al. One-dimensional electrical contact to a two-dimensional material. *Science* 342, 614-617 (2013).

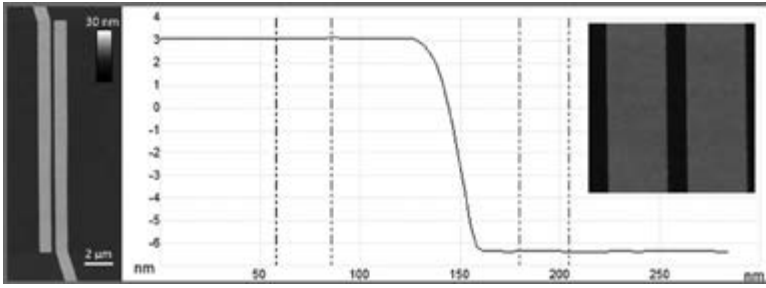


Figure 1: Split metal bottom gate. AFM topography image of split metal gate fabricate on SiO_2 substrate, the total thickness of the metal layers Cr/Au is measured to be 9 nm. The roughness of the metal surface is shown to be within ± 0.3 nm, and the separation between the two gates is 180 nm.

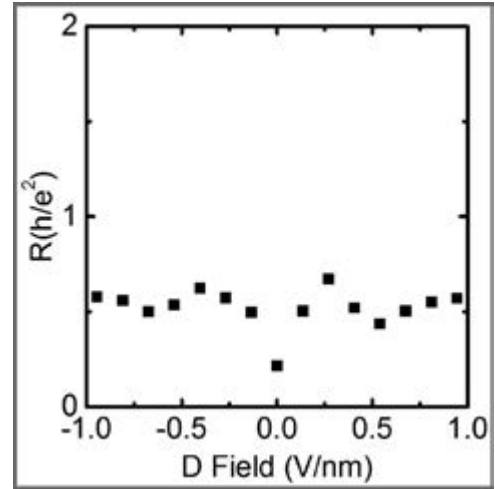


Figure 4: Resistance vs. displacement field induced by the top and bottom gates. The resistance values quickly saturated to $\frac{1}{2} (h/e^2)$ as the bandgap opened by the out-of-place displacement field.

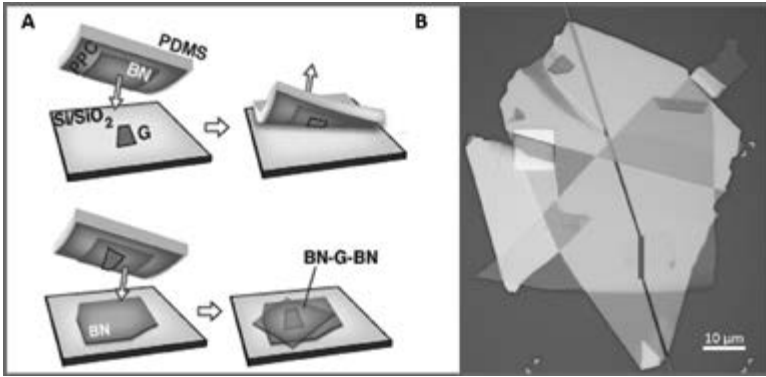


Figure 2: Transfer BN/graphene/BN stack on to split metal back gate. A. Procedures to prepare BN/Graphene/BN by our van der Waals transfer method [3]. B. Optical image showing the BN/Graphene/BN stack on the metal split gate.

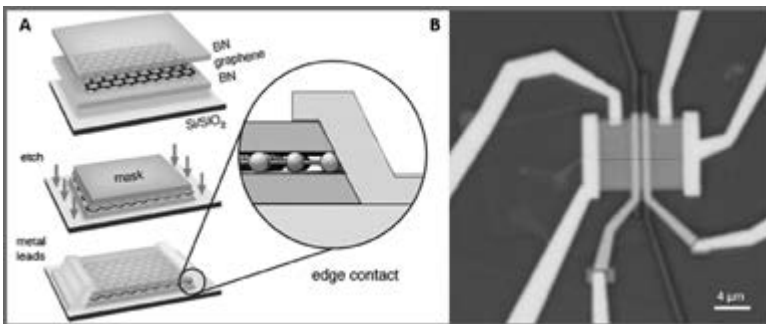


Figure 3: Device fabrication process. A. Electrical contacts are made on the edge of the graphene layer by etch the BN/graphene/BN stack [3]. B. Optical image of the device image with split top gate being aligned to the split bottom gate.

Vortex Dynamics in Nanofabricated Superconducting Devices

CNF Project Number: 1314-05

Principal Investigator: Britton L.T. Plourde

Users: Kenneth Dodge, JJ Nelson, Ibrahim Nsanzineza

Affiliation: Department of Physics, Syracuse University

Primary Sources of Research Funding: National Science Foundation (NSF-DMR-1105197); Army Research Office

Contact: bpourde@syr.edu, krdodgej@syr.edu, jjnelson@syr.edu, insanzin@syr.edu

Website: <http://plourdelab.syr.edu>

Abstract:

We fabricate superconducting microwave devices for studying the dynamics of vortices and quasiparticles at low temperatures. Vortices are quantized bundles of magnetic flux that thread many different superconductors over a particular range of applied magnetic field. Our experiments are aimed at investigating loss mechanisms that can limit the performance of superconducting circuits for quantum information processing. In addition to probing the loss in these circuits that arises from trapped magnetic flux, we are also studying the effects of non-equilibrium quasiparticles that result when superconducting digital control circuitry is operated in close proximity to quantum devices.

Summary of Research:

Superconducting microwave circuits play an important role in quantum information processing. Circuits composed of Josephson junctions and capacitors with superconducting electrodes can serve as qubits, the fundamental element of a quantum computing architecture. Various loss mechanisms limit the ultimate performance of these devices, including trapped magnetic flux vortices and quasiparticles. Vortices can be trapped in the superconducting electrodes when background magnetic fields are present and contribute dissipation when driven with microwave currents [1]. Quasiparticles are excitations above the superconducting ground state and also result in microwave losses in superconducting electrodes. Various mechanisms can lead to the generation of excess quasiparticles, including the operation of superconducting digital control circuitry in close proximity to qubits [2]. Thus, techniques for controlling the trapping of vortices and the mitigation of quasiparticles are critical to the development of large-scale quantum information processors with superconducting circuits.

We are fabricating a system of superconducting, thin-film microwave resonators for studying the loss contributed by trapped flux over the frequency

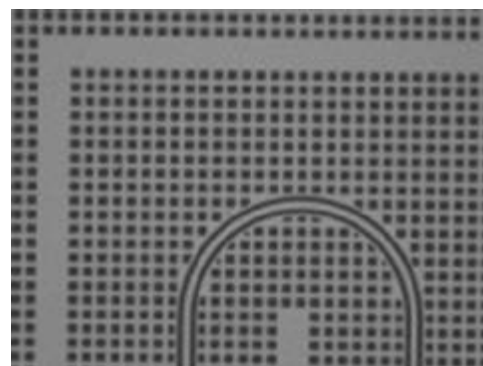


Figure 1: Optical micrograph of portion of superconducting aluminum microwave resonator for studying effects of magnetic flux vortices and quasiparticles on microwave loss. Large continuous regions of superconducting ground-plane allow for trapping of vortices for relatively small magnetic fields.

range from 2-11 GHz [1]. By cooling the resonators in different magnetic fields, we are able to probe the loss from vortices as a function of field at the resonance frequencies contained in our design. With the addition of surface trenches patterned with electron-beam lithography and reactive ion etching, we are able to control the dissipative contribution from trapped vortices [3].

We have also developed resonator layouts optimized for trapping and detecting one vortex at a time for probing the interactions between a single vortex and a single microwave photon. This is allowing us to explore fundamental properties of a single vortex in a superconductor at low temperatures. We have applied this technique to study the interaction between vortices and dissipative quasiparticles in a superconductor, where the vortex core can trap quasiparticles, thus reducing the overall dissipation in the superconducting circuit [4]. We have also

extended this technique to devices containing Al-AlO_x-Cu tunnel junctions, which allow us to inject quasiparticles controllably. This permits us to measure directly the effects of quasiparticles on the resonator quality factors as well as the interactions of vortices with the quasiparticles [5].

In addition, we are working on fabricating and testing devices containing superconducting quantum circuits as well as digital control circuitry with various techniques for controlling the trapping of magnetic flux and the mitigation of stray quasiparticles.

We fabricate our microwave resonators from various superconducting films, including aluminum, deposited onto silicon wafers in our electron-beam evaporator at Syracuse University. We define the patterns on the CNF's ASML stepper and transfer them into the films with a combination of reactive ion etching and wet-etch processing. We define the electrodes for our Josephson tunnel junctions with electron-beam lithography on the JEOL9500. We measure these circuits at temperatures down to 50 mK in our lab at Syracuse University.

References:

- [1] Song, C., Heitmann, T.W., DeFeo, M.P., Yu, K., McDermott, R., Neeley, M., Martinis, John M., Plourde, B.L.T.; "Microwave response of vortices in superconducting thin films of Re and Al"; *Physical Review B* 79, 174512 (2009).
- [2] McDermott, R., Vavilov, M.G.; "Accurate Qubit Control with Single Flux Quantum Pulses"; *Physical Review Applied* 2, 014007 (2014).
- [3] Song, C., DeFeo, M.P., Yu, K., Plourde, B.L.T.; "Reducing microwave loss in superconducting resonators due to trapped vortices"; *Applied Physics Letters* 95, 232501 (2009).
- [4] Nsanzineza, I., Plourde, B.L.T.; "Trapping a single vortex and reducing quasiparticles in a superconducting resonator"; *Physical Review Letters* 113, 117002 (2014).
- [5] Nsanzineza, I., Patel, Umesh, Dodge, K.R., McDermott, R., Plourde, B.L.T.; "Superconducting resonators with trapped vortices under direct injection of quasiparticles"; *Bull. Am. Phys. Soc.* 2016, <http://meetings.aps.org/Meeting/MAR16/Session/R48.3>.

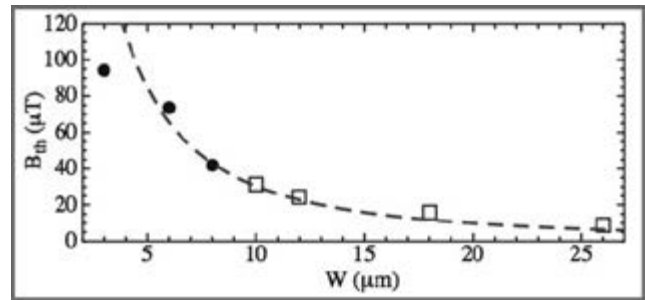


Figure 2: Measurement of threshold magnetic field for trapping magnetic flux vortices in multiple superconducting aluminum microwave resonators with different center conductor linewidths.

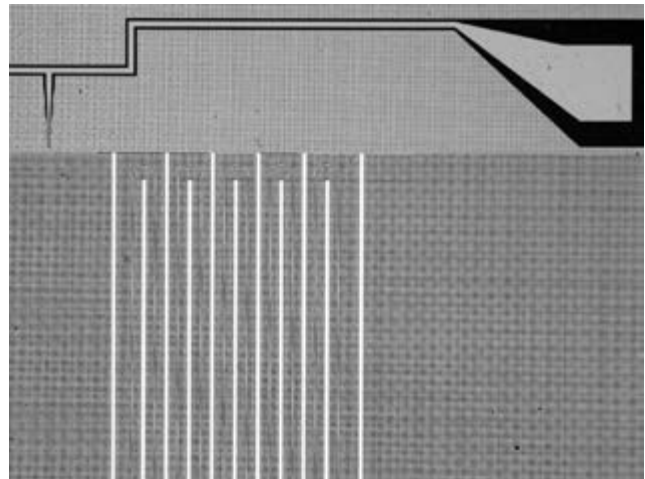


Figure 3: Optical micrograph of superconducting Al microwave resonator with Cu trace and Al-AlO_x-Cu tunnel junction for quasiparticle injection measurements. Fabricated in collaboration with McDermott Research Group at University of Wisconsin, Madison.

Large Scale van der Waals Electronics with Atomic Level Controllability

CNF Project Number: 1486-06

Principal Investigator: Jiwoong Park^{1,2}

Users: Kan-Heng Lee³, Kibum Kang¹

Affiliations: 1. Department of Chemistry and Chemical Biology, 2. Kavli Institute at Cornell for Nanoscale Science, 3. School of Applied and Engineering Physics; Cornell University

Primary Sources of Research Funding: Air Force Office of Scientific Research, Cornell Center for Material Research, Cornell NanoScale Science and Technology Facility (CNF), National Science Foundation, National Research Foundation of Korea

Contact: jpark@cornell.edu, kl692@cornell.edu, kk545@cornell.edu

Website: park.chem.cornell.edu

Abstract:

In the report, we demonstrate van der Waals (vdW) tunnel devices with atomic level programmability uniform in large scale with our metal-organic chemical vapor deposition (MOCVD) growth [1] and newly-developed stacking process [2]. The device array fabricated by standard photolithography over $5 \times 5 \text{ mm}^2$ area shows deviation corresponding to less than 0.15 layers variations. Heterostructure vdW tunnel device is also demonstrated and shows new physical properties that cannot be achieved with single element system. The new technique presented will help to bring vdW materials into industrial relevant technology and scale for next generation electronics.

Summary of Research:

vdW materials such as graphene and transition metal dichalcogenides (TMDs) are under intensive study in recent year due to their unique properties. One of the important properties is the layered structure formed by vdW interactions between its atomically thin layers, which allows layer-by-layer stacking from monolayer and accordingly provides programmability of the material at atomic level. Nevertheless, existing method to assemble the vdW films, such as direct multilayer growth or stacking with exfoliated vdW materials, show poor controllability and/or scalability that impedes the applications of the materials. Recently, our group has developed MOCVD to grow TMDs (MoS_2 , MoSe_2 , WS_2 , WSe_2) as uniform monolayer in wafer scale [1]. In this report, we combine MOCVD-grown TMDs with our newly-developed large-scale stacking method [2] to perform fabrication of vdW tunnel devices with atomic level programmability uniform in large scale. Device array are shown as Figure 1.

Based on our stacking method, we do fabrication with standard photolithography (PL) over an area of $5 \times 5 \text{ mm}^2$ on chip. The process includes: i) bottom gold electrode is e-beam evaporated (CNF tool: SC4500 Odd/Even) on fused silica and defined by PL (ABM Contact Aligner) followed by wet etching; ii) programmed vdW film is transferred;

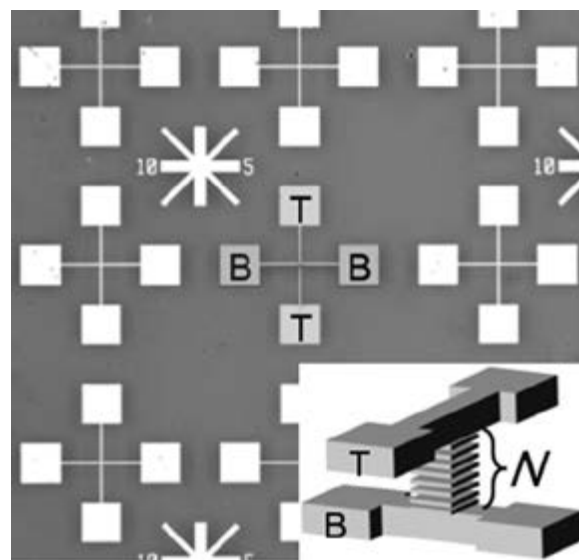


Figure 1: Device array fabricated by standard photolithography. Inset: devices structure includes a top (T) and a bottom (B) gold electrode and a programmable vdW films sandwiched at the crossing. The crossing is $5 \times 5 \mu\text{m}^2$.

iii) top gold electrode is made in exactly the same way as the bottom; and iv) the excessive vdW films outside the crossing is etched away by plasma (Glen 1000 Resist Strip). The electrical characterization is measured with probe station (IV Probe Station).

We first demonstrate the layer-by-layer control in number of layer (N) with the gold/MoS₂/gold tunnel device. We measure the I-V curves with 3-, 6-, 9-layer MoS₂ in Figure 2(a). It is observed that all devices show the signature I-V curve of tunneling. Moreover, the current level decreases exponentially when N is increased, showing that carriers are tunneling through the whole MoS₂ film as shown by the inset schematics.

Quantitatively, in Figure 2(b), it shows that the N -dependence of zero-bias resistance (R_0A) in our experiment follow the theoretical tunneling equation (dash line) with barrier height $\phi_B = 0.5$ eV. In addition, the inset histogram of R_0A shows that for the device array of $N = 7$, the uncertainty of the devices over the 5×5 mm² area is only 35% of the average, equivalent to as small as 0.15 layer variation. This shows our large area uniform control of N in the vdW films.

Finally, we also program the vdW film with heterostructure. Figure 3 shows the I-V characteristic of a 3-layer MoS₂/3-layer WS₂ vdW film, noted as Mo/W, in comparison to a 6-layer MoS₂ device. It clearly shows that only Mo/W device has the diode behavior. The new property in the heterostructure points out that our composition programmability also provide a method to design new functions that cannot be achieved with single element systems.

In conclusion, we perform vdW electronics with the number of layer and composition being controlled at atomic level. This demonstration of the large scale material engineering will pave the way toward future electronics such as atomically-thin integrated circuitry.

References:

- [1] "High-mobility three-atom-thick semiconducting films with wafer scale homogeneity," K. Kang*, S. Xie*, L. Huang, Y. Han, P. Y. Huang, K. F. Mak, C.-J. Kim, D. A. Muller, and J. Park (* equal contribution), Nature 520, 656 (2015).
- [2] "Wafer Scale van der Waals Films with Programmable Composition and Ultraclean Interface," K. Kang*, K. Lee*, Y. Han, G. Hui, S. Xie, D. A. Muller, and J. Park (* equal contribution), in preparation.

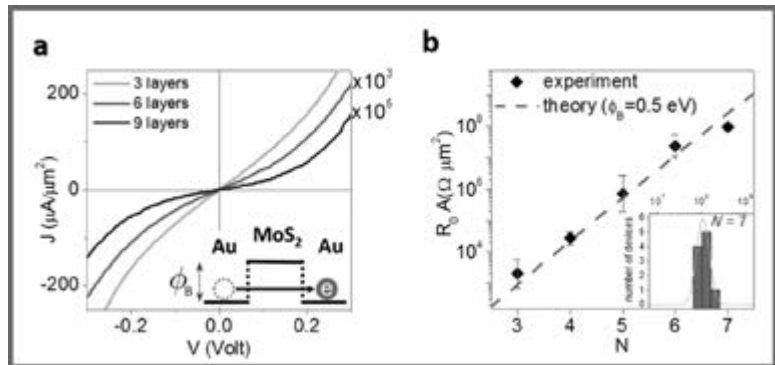


Figure 2: Characteristic of the as-fabricated gold/MoS₂/gold devices. (a) The I-V characteristic of representative devices with 3-, 6-, 9-layer of MoS₂. Inset: theoretical band structure for the occurring tunneling. (b) Zero-bias tunnel resistance of the devices from $N = 3$ to $N = 7$ and the theoretical tunnel equation (dash line, $\phi_B = 0.5$ eV). Inset: histogram for the device array of $N = 7$.

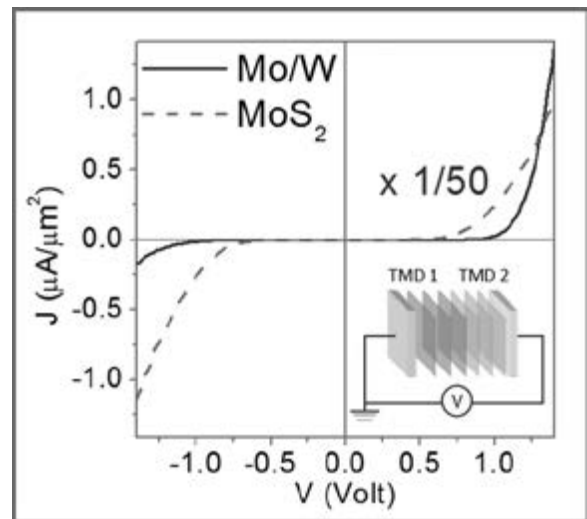


Figure 3: Comparison of the gold/6-layer MoS₂/gold and gold/Mo/W/gold device. Only Mo/W shows diode behavior. Inset: Schematics of the Mo/W device and measurement configuration.

Fabrication of Nanofluidic Cavities for Superfluid ^3He Studies

CNF Project Number: 1520-07

Principal Investigator: Jeevak M. Parpia

User: Abhilash Thanniyil Sebastian

Affiliation: Department of Physics, Cornell University

Primary Source of Research Funding: National Science Foundation

Contact: jmp9@cornell.edu, at654@cornell.edu

Website: <http://parpia.lassp.cornell.edu>

Abstract:

We demonstrate fabrication of nanofluidic cavities for superfluid helium-3 (^3He) studies. Superfluid ^3He is confined to nano-slab geometries inside nano-fluidic cavities. Cavities are etched in silicon (Si) and bonded to glass or Si by anodic or fusion bonding techniques. The details of cavity fabrication, characterization are discussed. Experiments using nuclear magnetic resonance and torsion pendulum are employed to study the ^3He in the chambers.

Summary of Research:

Superfluid ^3He is a p-wave superfluid and has proved to be a model system for studying exotic fermion pairing in unconventional superconductors. Multiple superfluid phases are realized in ^3He and the superfluid phases differ from each other on the basis of the spatial distribution of the energy gap [1]. Properties of superfluid ^3He are also highly tunable and one can use pressure to change the stability of the different superfluid phases and tune the superfluid transition temperature by approximately a factor of 2.5, from 0.9 mK at 0 bar to 2.44 mK at 34 bar.

Confinement of ^3He in a nano-cavity is one way we can tune the properties of the superfluid. Here in this work we use nanofabricated cavity for confining ^3He in a thin slab. Cavities of depths 50, 100, 200, 300, 600, 1100 nm are fabricated. By confining, we study the surface properties of the superfluid, and the superfluidity of thin films [2,3]. To make the cell in which we confine the fluid, we bond Si or glass to a patterned piece of Si in which the cavity is defined and etched. It is important to have very smooth surfaces, on the nanometer scale, in order that the surface roughness does not contribute significantly to the helium properties being measured.

The fabrication process for the nanocavity has three major steps. First, create the step in the silicon surface

for the cavity. Second, etch through the fill line hole and the backside concentric circles to ease the epoxy keying in. Third, clean and prepare the surfaces, and then bond the Si to silicon or glass to complete the cell. A schematic of the fabrication process is shown in Figure 1. Figure 2 shows the mask diagram of the cell pattern. The grey color portion shows the cavity region. AFM measurements on the surface roughness of the etched Si and glass surface is found to be nearly smooth with a surface roughness less than 1 nm for both glass and Si. After the cavity fabrication the cells are bonded using anodic and fusion bonding techniques. Infrared and optical microscope images of the bonded cells are shown in Figure 3.

References:

- [1] A. J. Leggett, Rev. Mod. Phys. 47, 331-414 (1975).
- [2] Levitin, et al., Science 340, 841, 2013.
- [3] N. Zhelev, et al., [article under preparation for Physical Review Letters].

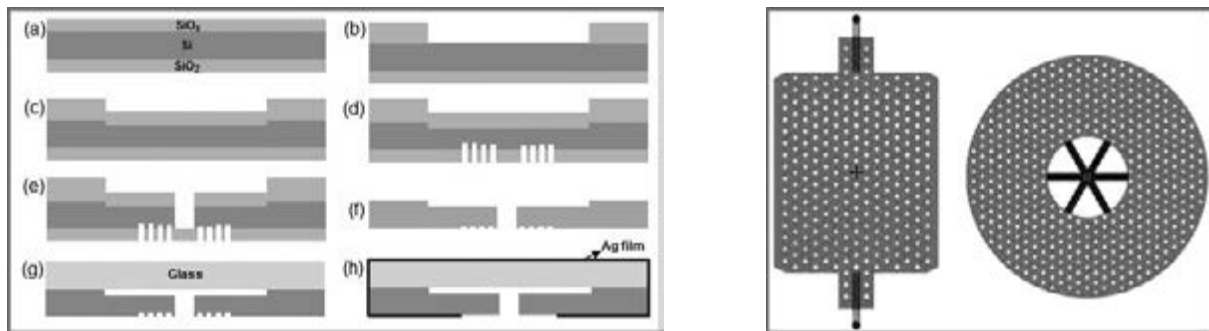


Figure 1, left: Steps used in the fabrication cavities in Si. (a) Grow thick thermal oxide. (b) Etch the oxide in the cavity region (Dry + Wet). (c) Thermally oxidize the wafer (define cavity depth). (d) Using DRIE, etch a series of concentric circles around the fill line. (e) Etch through the wafer to define the fill line hole. (f) Remove all oxide using HF. (g) Bond Si to glass or Si piece (h) Sputter deposit silver film on the outside surfaces.

Figure 2, right: Design of the cavity pattern with posts. Grey layer is the layer of the cavities space where helium will reside.

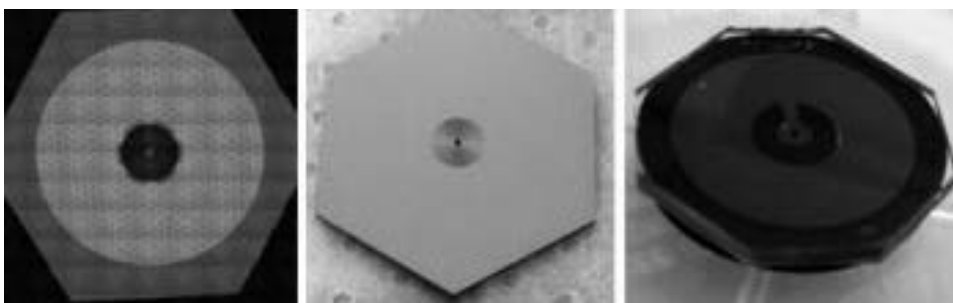


Figure 3: Infra-red microscope image the Si-Si fusion bonded cells and photograph of an 1100 nm cavity cell bonded by anodic bonding. These cells are designed for torsion pendulum experiments.

Fabrication of Nanoscale Josephson Junctions for Quantum Coherent Superconducting Circuits

CNF Project Number: 1735-08

Principal Investigator: Britton L.T. Plourde

Users: Caleb Howington, Matthew Hutchings, Indrajeet, JJ Nelson, Haozhi Wang

Affiliation: Department of Physics, Syracuse University

Primary Source of Research Funding: Army Research Office

Contact: bplourde@syr.edu, howingtonc@gmail.com, mdhutc01@syr.edu, indraje@syr.edu, jjnelson@syr.edu, hwang42@syr.edu

Website: <http://plourdelab.syr.edu>

Abstract:

We fabricate nanoscale superconductor tunnel junctions and other structures for experiments involving quantum coherent circuits. Such circuits have shown great promise in recent years for explorations of quantum mechanics at the scale of circuits on a chip and for forming qubits, the foundational elements of a quantum computer. The quantum state of these superconducting qubits can be manipulated with microwave radiation at low temperatures. In addition, we are developing other superconducting metamaterial structures with novel microwave mode spectra for coupling to superconducting qubits.

Summary of Research:

The unique properties of nanoscale Josephson junctions enable a wide range of novel superconducting circuits for investigations in many diverse areas. In recent years, circuits composed of such junctions have emerged as promising candidates for the element of a quantum computer, due to the low intrinsic dissipation from the superconducting electrodes and the possibility of scaling to many such qubits on a chip [1]. The quantum coherent properties of the circuits are measured at temperatures below 50 mK with manipulation of the qubit state through microwave excitation.

We are currently working on a variety of experiments involving these nanoscale Josephson junctions and other superconducting structures that will allow us to probe novel quantum effects in our microwave circuits. With particular combinations of superconducting lumped-circuit elements, it is possible to engineer metamaterial transmission lines that exhibit novel mode structures characteristic of left-handed materials [2]. We are fabricating such metamaterial transmission lines from Al and Nb films on Si and characterizing these at low temperatures [3,4]. We are working on experiments to couple these left-handed lines to superconducting qubits for experiments involving the exchange of microwave photons. In addition, we are fabricating other superconducting circuits for forming

low-temperature detectors of single microwave photons and for implementing a new scheme for the efficient readout of the quantum state of superconducting qubits [5-6]. We are also studying the transient nonlinear dynamics of Josephson junction-based circuits at low temperatures [7].

We pattern these circuits at the CNF with nanoscale structures defined with electron-beam lithography integrated with photolithographically defined large-scale features. The junctions are fabricated using the standard double-angle shadow evaporation technique, in which a resist bilayer of copolymer and PMMA is used to produce a narrow PMMA airbridge suspended above the substrate. Evaporation of aluminum from two different angles with an oxidation step in between forms a small Al-AlO_x-Al tunnel junction from the deposition shadow of the airbridge. We have developed a process for defining these junctions with electron-beam lithography and we perform the aluminum evaporations in a dedicated chamber at Syracuse. We pattern large-scale features using the ASML stepper, with electron-beam evaporation of Al, sputter-deposition of Nb, and PECVD deposition of SiO₂. Measurements of these circuits are performed in cryogenic systems at Syracuse University, including a custom dilution refrigerator for achieving temperatures of 30 mK.



Figure 1: Optical micrograph of aluminum superconducting metamaterial transmission line resonator, patterned photolithographically on ASML stepper.



Figure 2: Zoomed-in optical micrograph of superconducting aluminum metamaterial transmission line showing multiple unit cells of interdigitated capacitors and meander-line inductors.

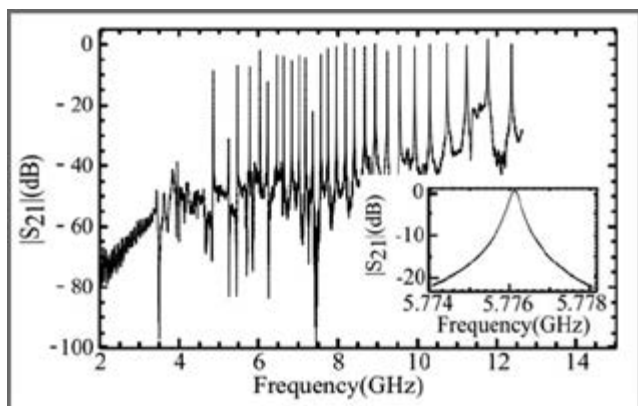


Figure 3: Measurement of microwave transmission through metamaterial resonator as a function of microwave frequency at 50 mK.

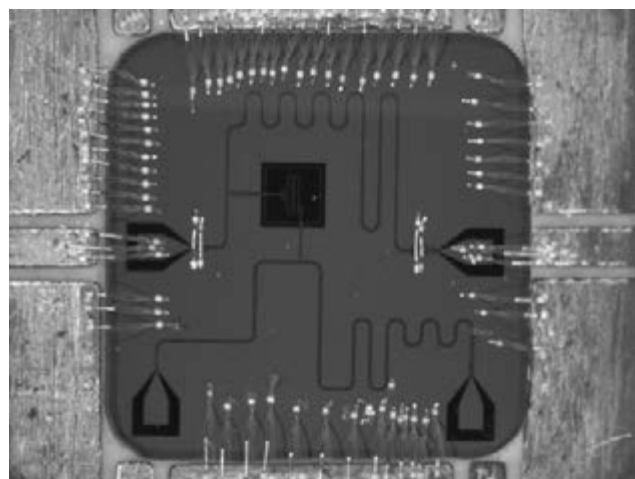


Figure 4: Optical micrograph of wire-bonded chip with superconducting qubit and two readout resonators for coupling to microwave photomultiplier.

References:

- [1] Clarke, J. and Wilhelm, F.K.; "Superconducting quantum bits"; Nature, 453, 1031 (2008).
- [2] Egger, D.J. and Wilhelm, F.K.; "Multimode Circuit Quantum Electrodynamics with Hybrid Metamaterial Transmission Lines"; Physical Review Letters 111, 163601 (2013).
- [3] Plourde, B.L.T., Wang, Haozhi, Rouxinol, Francisco, LaHaye, M.D.; "Superconducting metamaterials and qubits"; Proceedings of the SPIE 9500, Quantum Information and Computation XIII, 95000M (2015).
- [4] Wang, H., Hutchings, M. Indrajeet, Sager, Rouxinol, F., LaHaye, M., Plourde, B.L.T., Taketani, B.G., Wilhelm, F.K.; "Coupling a Transmon Qubit to a Superconducting Metamaterial Resonator"; Bull. Am. Phys. Soc. 2016, <http://meetings.aps.org/Meeting/MAR16/Session/K48.9>.
- [5] Govia, L.C.G., Pritchett, Emily J., Xu, Canran, Plourde, B. L. T., Vavilov, Maxim G., Wilhelm, Frank K., McDermott, R.; "High-fidelity qubit measurement with a microwave-photon counter"; Physical Review A 90, 062307 (2014).
- [6] Howington, Caleb, Hutchings, M., Ribeill, Guilhem, Pechenezhskiy, Ivan, Vavilov, Maxim G., Wilhelm, Frank K., McDermott, R., Plourde, B.L.T.; "Multi-qubit measurements with a Josephson Photomultiplier"; Bull. Am. Phys. Soc. 2016, <http://meetings.aps.org/Meeting/MAR16/Session/S48.15>.
- [7] Bhupathi, P., Groszkowski, Peter, DeFeo, M. P., Ware, Matthew, Wilhelm, Frank K., Plourde, B. L. T.; "Transient dynamics of a superconducting nonlinear oscillator"; Physical Review Applied 5, 024002 (2016).

Development of Superconductor Circuits for Readout of Quantum Nanomechanical Resonators

CNF Project Number: 1851-09

Principal Investigator: Prof. Matthew LaHaye

Users: Yu Hao, Dr. Francisco Rouxinol

Affiliation: Department of Physics, Syracuse University

Primary Sources of Research Funding: National Science Foundation Faculty (NSF) Early Career Development Program (CAREER) Grant, number 1056423; NSF Materials World Network Grant 1312421

Contact: mlahaye@syr.edu, yuhao@syr.edu, rouxinol@gmail.com

Website: <http://lahayelab.syr.edu/>

Abstract:

The LaHaye lab (Syracuse University) has been actively utilizing the nanofabrication facilities at Cornell NanoScale Science and Technology Facility (CNF) to develop a new hybrid quantum system that involves the integration of nanomechanical systems with state-of-the-art technology from the field of superconducting quantum computing. The LaHaye group is now studying the complex behavior of this quantum electromechanical system and optimizing it for experiments to generate non-classical states of motion of the nanomechanical device [1]. With further development, this system could have applications for quantum information processing, quantum thermodynamics, and the study of fundamental topics that are of central interest to emerging quantum-enabled technologies.

Summary of Research:

Hybrid quantum systems — systems consisting of multiple elements with distinct functionality that each behave quantum mechanically — are being developed for a range of quantum-enabled applications, including quantum information processing and quantum-limited sensing [2,3]. They also offer prospects for studying fundamental topics of direct relevance to these applications, such as quantum decoherence [4-6] and quantum fluctuation theorems [7,8].

The LaHaye group is developing a particular hybrid quantum system that could serve as a versatile platform for pursuing many of these directions (Figures 1 and 2). The system is composed of three devices: a superconducting quantum bit (qubit) [9], superconducting microwave resonator (SMR) [10], and flexural nanomechanical resonator (nanoresonator) [1]. These components are integrated on a silicon wafer and can be coupled together and probed via the application of DC and microwave signals.

In the first series of experiments being pursued by the LaHaye group, the qubit serves as an element for manipulating and measuring the nanoresonator; similarly, the SMR functions to control and probe the state of the qubit. This architecture is analogous to that of systems used in cavity and circuit quantum electrodynamics, where atoms and artificial atoms — such as superconducting quantum bits — are used for studying the quantum properties of light [10]. It

is thus expected that this electromechanical analog should enable exploration of quantum behavior of the nanoresonator [5,6,11]. For instance, it should allow for the creation and measurement of nanoresonator superposition states, which would enable experiments to probe decoherence with the nanoresonator [5,6] and also be an important step toward utilizing the nanoresonator as quantum coherent circuit element (such as quantum switch [12], transducer [13], or memory device [14]).

Over the past year, the LaHaye group has begun to probe the interactions between the components of this tripartite system at milli-Kelvin temperatures where each element resides in its quantum ground state [1]. Measurements thus far have been performed in the weak coupling limit between the nanoresonator and qubit, where the strength of their mutual interaction is weaker than the relaxation rate of the nanoresonator, which is dominated by elastic energy loss through the nanoresonator's structural supports to the substrate. In this limit, the nanoresonator acts like a thermal bath absorbing and imparting energy to the qubit. Experiments are under development to probe the inherent asymmetry of the nanoresonator's quantum noise in this regime. New samples incorporating membrane-style nanoresonators (Figures 3 and 4) are also being designed to improve the interaction strength between the qubit and nanoresonator, and to decrease the clamping loss that dominates the

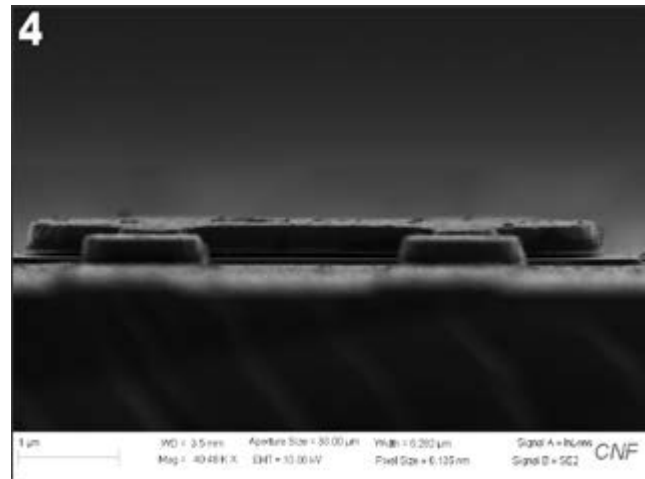
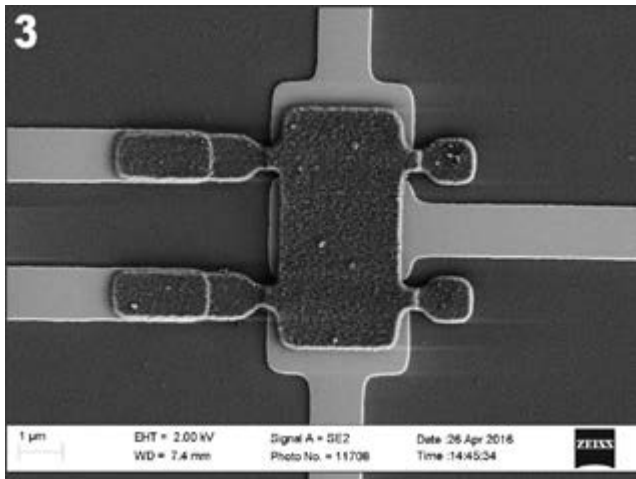
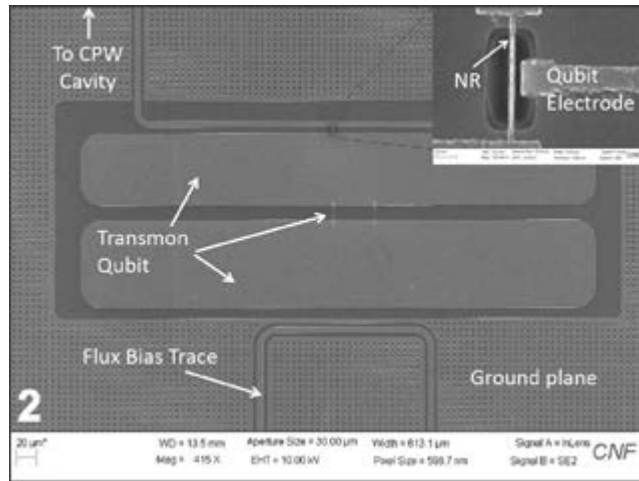
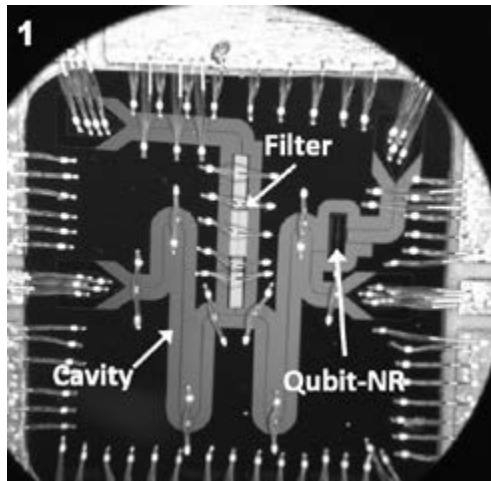


Figure 1: An optical image displaying a birds-eye-view of the hybrid quantum system fabricated at CNF and Syracuse by the LaHaye group. The system is composed of a superconducting coplanar waveguide microwave cavity (SMR in the text), a superconducting transmon qubit and a flexural nanoresonator. **Figure 2:** A scanning electron micrograph illustrating a closer view of the transmon qubit and nanostructure (inset). The transmon is composed of two aluminum/aluminum oxide Josephson junctions (center) and a niobium shunt capacitor, which is formed by the two large pads visible in the image. The suspended nanostructure is fabricated from aluminum; the third in-plane mode of this beam serves as the nanoresonator in this work. **Figure 3:** A scanning electron micrograph of the new generation of nanoresonators being developed by the LaHaye group. Here the nanoresonator is formed from a suspended aluminum plate. **Figure 4:** A side view scanning electron micrograph of the device shown in Figure 3.

nanoresonator's dissipation in current experiments. Such modifications should enable access to the strong-coupling regime, which will then make this hybrid quantum electromechanical system a viable candidate for the many research directions outlined above.

Our devices are patterned on 4-inch, <100>-oriented silicon wafers (> 10 kΩ-cm resistivity). We pattern large-scale features, including the SMR (Figure 1), using CNF's ASML 300C Stepper. The qubit and first generation nanoresonators are fabricated using electron-beam lithography (Figure 2). This has been accomplished using CNF's electron beam writer JEOL 9500, followed by a double-angle evaporation of aluminum at SU; the nanoresonator are released by a reactive ion etch process using CNF's Oxford 82. Fabrication of the second generation of nanoresonators (Figures 3 and 4) is accomplished in a multi-step

process utilizing the ASML, the PT740 etcher, and Oxford 81 or 82.

References:

- [1] F. Rouxinol, et al. arXiv: 1605.01454 (2016).
- [2] G. Kurizki, et al. Proc. Natl. Acad. Sci. USA 112, 3866 (2015).
- [3] Z. Xiang, et al. Phys. Rev. Lett. 85, 623 (2013).
- [4] M. Aspelmeyer, et al. Phys. Today 65 (7), 29 (2012).
- [5] A. Armour and M.P. Blencowe, New J. Phys. 10, 095005 (2008).
- [6] D.W. Utami and A.A. Clerk, Phys. Rev. A 78, 042323 (2008).
- [7] M. Campisi, P. Hanggi, and P. Talkner, Rev. Mod. Phys. 83, 771 (2011).
- [8] F. Brito, et al. New J. Phys. 17, 075002 (2015).
- [9] J. Clarke and F.K. Wilhelm, Nature 453, 1031 (2008).
- [10] M.H. Devoret and R.J. Schoelkopf, Science 339, 1169 (2013).
- [11] E.K. Irish and K.C. Schwab, Phys. Rev. B 68, 155311 (2003).
- [12] M. Mariani, et al. Phys. Rev. B 78, 104508 (2008).
- [13] J. Bochmann, et al. Nat. Phys 9, 712 (2013).
- [14] T.A. Palomaki, et al. Nature 495, 210 (2013).

Fabrication of Superconducting Devices for Quantum Information Science

CNF Project Number: 1873-10

Principal Investigator: Britton L.T. Plourde

Users: Daniela Bogorin, Matthew Hutchings, Yebin Liu

Affiliation: Department of Physics, Syracuse University

Primary Source of Research Funding: Intelligence Advanced Research Projects Agency

Contact: bpourde@syr.edu, dfbogori@syr.edu, mdhutc01@syr.edu, yliu166@syr.edu

Website: <http://plourdelab.syr.edu>

Abstract:

We are fabricating nanoscale superconductor tunnel junctions and microwave resonators for investigations in quantum information science. Such circuits have shown great promise in recent years for forming qubits, the elements of a quantum computer. We are developing architectures involving multiple superconducting qubits and microwave resonators. This involves a combination of photolithographic processing of large-scale features and electron-beam lithography for the tunnel junctions.

Summary of Research:

In recent years, circuits composed of nanoscale Josephson junctions have emerged as promising candidates for the foundational element of a quantum computer, due to the low intrinsic dissipation from the superconducting electrodes and the possibility of scaling to many such qubits on a chip [1]. The quantum coherent properties of the circuits are measured at temperatures below 50 mK with manipulation of the qubit state through microwave excitation.

We are working to develop architectures involving multiple superconducting qubits coupled to multiple low-loss microwave resonators — composed of both planar structures [2-4] and three-dimensional waveguides [5]. We probe the coupling between each qubit and resonator by measuring the dispersive shift of the resonator frequency with the qubit detuned from the resonator. Some of our experiments are aimed at developing schemes for the rapid exchange of excitations between a qubit and a resonator [2].

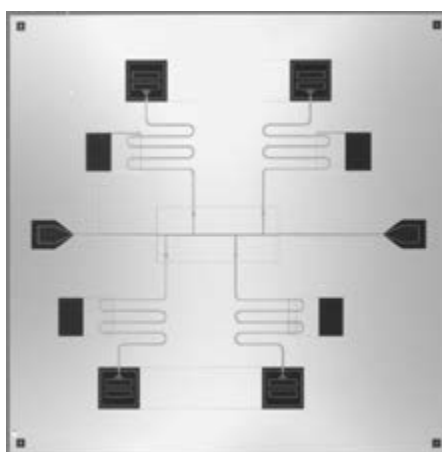


Figure 1: Optical micrograph of chip containing four superconducting qubits, each of which is coupled to a coplanar waveguide readout resonator for microwave measurements.

We are also investigating two-qubit gates for generating entanglement between circuits [3] as well as qubits with reduced sensitivity to magnetic flux [4].

We pattern these circuits at the CNF with nanoscale structures defined with electron-beam lithography integrated with photolithographically defined large-scale features on Si and sapphire substrates. The junctions are fabricated using the standard double-angle shadow evaporation technique, in which a resist bilayer of copolymer and PMMA is used to produce a narrow PMMA airbridge suspended above the substrate. Evaporation

of aluminum from two different angles with an oxidation step in between forms a small Al-AlO_x-Al tunnel junction from the deposition shadow of the airbridge. We have developed a process for defining these junctions with electron-beam lithography on the JEOL 9500 and we perform the aluminum evaporations in a dedicated vacuum chamber at

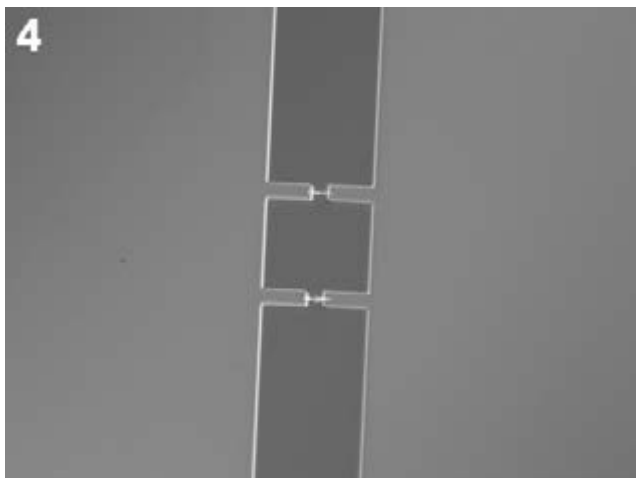
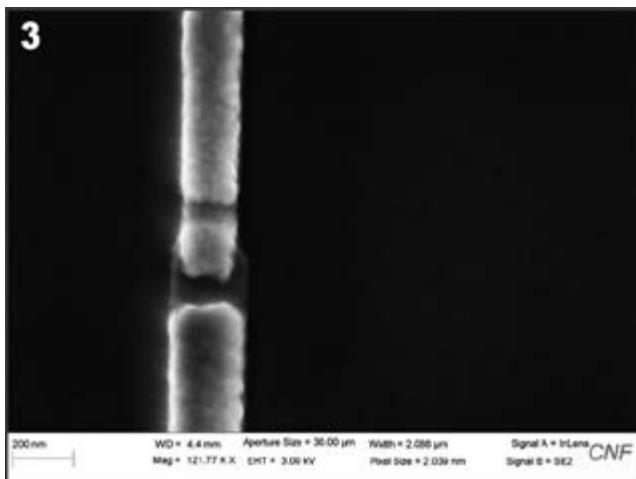
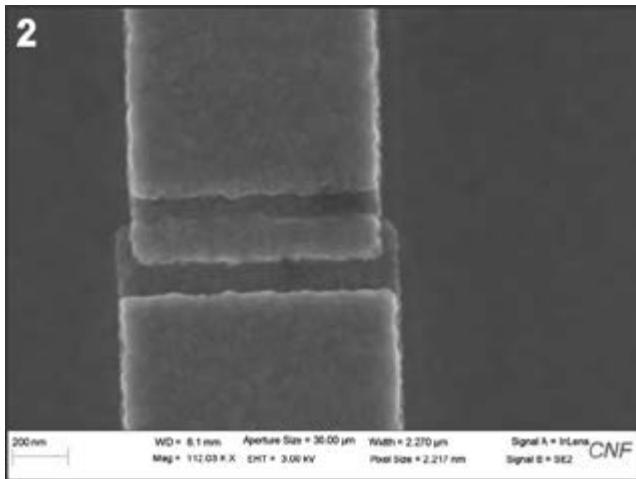


Figure 2: Scanning electron micrograph of large Al-AlO_x-Al tunnel junction at center of superconducting qubit; electron-beam lithography performed on JEOL 9500.

Figure 3: Scanning electron micrograph of small Al-AlO_x-Al tunnel junction at center of superconducting qubit; electron-beam lithography performed on JEOL 9500.

Figure 4: Optical micrograph of flux-tunable superconducting qubit showing Nb capacitor pads and Al traces with Al-AlO_x-Al tunnel junctions.

Syracuse. We pattern large-scale features using the ASML, with sputter deposition of superconducting Nb films in a dedicated vacuum system at Syracuse University. Microwave measurements of these circuits are performed in cryogenic systems at Syracuse University, including a custom dilution refrigerator for achieving temperatures of 30 mK.

References:

- [1] Clarke, J. and Wilhelm, F.K.; "Superconducting quantum bits"; *Nature*, 453, 1031 (2008).
- [2] Strand, J.D., Ware, Matthew, Beaudoin, Felix, Ohki, T. A., Johnson, B.R., Blais, Alexandre, Plourde, B.L.T.; "First-order sideband transitions with flux-driven asymmetric transmon qubits"; *Physical Review B* 87, 220505(R) (2013).
- [3] Corcoles, A. D., Gambetta, Jay M., Chow, Jerry M., Smolin, John A., Ware, Matthew, Strand, J. D., Plourde, B.L.T., Steffen, M.; "Process verification of two-qubit quantum gates by randomized benchmarking"; *Physical Review A* 87, 030301(R) (2013).
- [4] Hutchings, M., Ware, Matthew, Liu, Y., Hertzberg, Jared B., Chow, Jerry M., Plourde, B.L.T.; "Dephasing of superconducting asymmetric transmon qubits"; *Bull. Am. Phys. Soc.* 2016, <http://meetings.aps.org/Meeting/MAR16/Session/Y48.5>.
- [5] "Copper Waveguide Cavities with Reduced Surface Loss for Coupling to Superconducting Qubits"; D.F. Bogorin, D.T. McClure, M. Ware, B.L.T. Plourde; *IEEE Transactions on Applied Superconductivity* 24(4), 1700207 (2014).

Teepee-like Photonic Crystal with High Absorption and Very Low Reflection

CNF Project Number: 1880-10

Principal Investigator: Shawn-Yu Lin

Users: Ping Kuang, Anthony Post, Brian Frey

Affiliation: Future Chips Constellation, Rensselaer Polytechnic Institute, Troy, NY 12180

Primary Source of Research Funding: Department of Energy

Contact: sylin@rpi.edu, kuangp2@rpi.edu, posta@rpi.edu, freyb2@rpi.edu

Abstract:

Using a novel process, we have created a photonic crystal (PC) that exhibits very low reflection and high absorption over the visible wavelength range, even at off-normal angles as high as 60° . The pattern consists of periodic inverted cones, called "Teepee-like." The Teepee-like PC has a Gaussian-type gradient-index profile, causing it to act as an antireflection coating (ARC) [1], and it exhibits parallel-to-interface refraction (PIR), giving it high absorption [2]. It has been demonstrated elsewhere [3] that the average absorption of our Teepee-like PC on $500\ \mu\text{m}$ silicon (Si) film is $\sim 98.5\%$ for $\lambda = [400, 1000\ \text{nm}]$. Even with a Si film thickness as thin as $10\ \mu\text{m}$, the absorption remains high, $\sim 94.7\%$ for $\lambda = [400, 1000\ \text{nm}]$. Therefore, this PC has promising applications in solar cell technology as current solar cells utilize thick films. Our goal is to devise an optimized and repeatable recipe that can be followed to mass produce this structure with the highest absorption and lowest reflection possible.

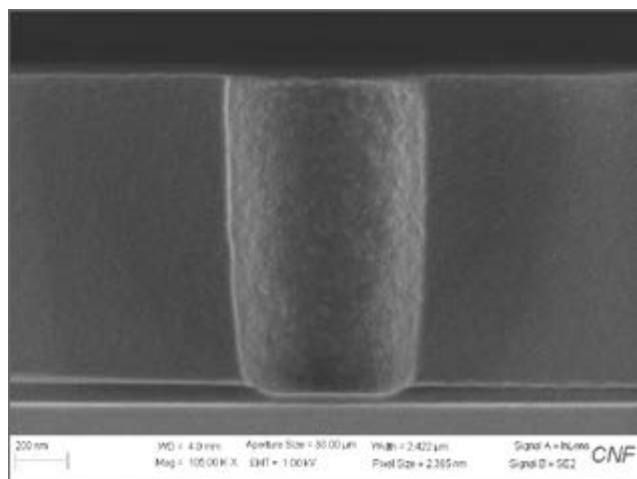


Figure 1: Side view of the wafer after exposure but before any etching. From top to bottom the layers are UV1400, DUV42, and Si wafer. The exposure is a cylinder.

Summary of Research:

The Teepee-like PC is created by first spin-coating a bare Si wafer with an $\sim 60\ \text{nm}$ DUV42 resist layer, followed by an $\sim 1200\ \text{nm}$ UV1400 resist layer using the Gamma Automatic Coat-Develop Tool. With the ASML 300C DUV Stepper, deep ultraviolet (DUV)

photolithography is performed with a square lattice mask pattern of circles. The exposed wafer is post-exposure baked at 110°C and then immersed in 726-MIF developer. The exposure creates cylinders in the UV1400 resist (Figure 1). After the exposure, the DUV42 resist at the bottom of the cylinders is etched away, revealing the Si wafer below. A reactive ion etch (RIE) consisting of sulfur hexafluoride (SF_6), trifluoromethane (CHF_3), and oxygen (O_2), is used to etch the Teepee-like PC into the Si (Figure 2). Subsequently, the remaining resists are etched away. A passivation layer of silicon dioxide (SiO_2) is conformally grown on the surface by wet oxidation and then annealing, both at 900°C . The SiO_2 layer acts as an ARC. The optical data is collected with an integrating sphere setup.

The parameters to adjust are: lattice constant of Teepee-like PC, diameter of circles on mask pattern, DUV exposure energy, Si etch forward power, and Si etch time, in that order. Narrowing down the optimal parameters involves varying all these and analyzing the resultant shape of the PC. The important features of the Teepee-like PC to note after etching are: undercut (horizontal etch), etch depth, etch smoothness, and valley shape (shape at the bottom of etch). By adjusting the previously mentioned parameters, these features vary.

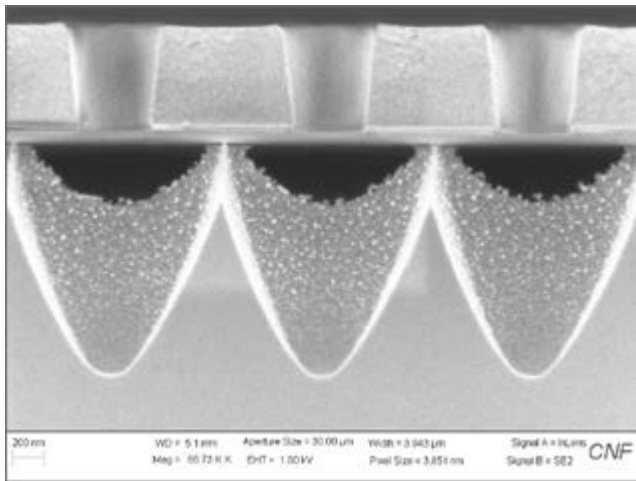


Figure 2: Side view of the wafer after Si etching. Displays the Teepee-like PC. The resist and ARC layers are still present in this figure, but were later removed.

Increasing Parameter	Feature
Diameter of Circle	Increases Undercut Rounder Valleys
Exposure Energy	Increases Undercut Rounder Valleys
Etch Power	Increases Undercut Rounder Valleys Increases Etch Depth Rougher Etch
Etch Time	Increases Undercut Increases Etch Depth

Figure 3: Table summarizing the effects of increasing a certain parameter in the creation of the Teepee-like PC. 'Rougher Etch' means the sidewalls of the Teepee-like PC have more surface irregularities. Lower etch powers yield smoother sidewalls.

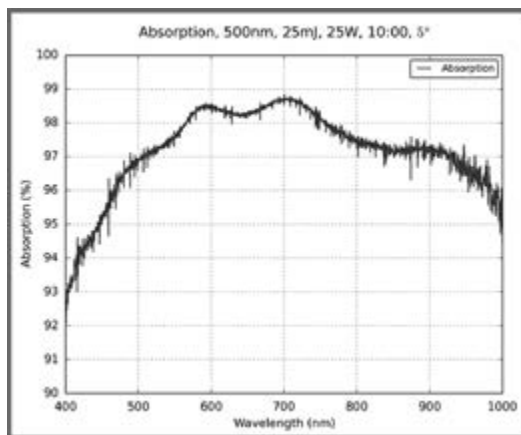


Figure 4: Absorption data measured from integrating sphere for the Teepee-like PC sample shown in Figure 2, after the resist and ARC are removed and SiO₂ layer is grown. For $\lambda = 400$ to 1000 nm, the minimum absorption is $\sim 92\%$. A maximum of $\sim 98.6\%$ is attained at $\lambda = 700$ nm. Data was taken at 5° off-normal incidence to prevent reflected light from escaping the integrating sphere.

Increasing the diameter of the mask circles and the exposure energy both increase the undercut and cause rounder valleys because they increase the area revealed to the etch. Increasing the etch power also increases the undercut and causes rounder valleys, but additionally increases the etch depth and makes the etch rougher. After these parameters have been set, the etch time is adjusted to optimize the structure. Increasing the etch time increases the undercut and the etch depth. Changing the lattice constant of the PC does not affect the features, but it will affect the absorption of the PC [4]. These results are summarized in Figure 3.

To exhibit high absorption and antireflection, there needs to be sufficient undercut of the Si wafer so that the Teepee-like feature overlaps, as shown in Figure 2. Overlap causes the PC to have a Gaussian-type gradient-index profile, giving it high antireflection [1]. Sharper valleys causes light to be trapped better within the PC, increasing the absorption. Increasing the depth of the feature adds to the optical path length of incident light, increasing the absorption.

Knowing the effects of changing the process parameters, the Teepee-like PC can be created with specific features. Moving forward, we will analyze the absorption and reflection of more samples to see the effect of changing the features, with the goal of selecting the features that yield the best performance. Figure 4 shows the absorption data over the visible wavelength range of one the Teepee-like PC in Figure 2, which is one of the better performing samples. The absorption over the visible range is high with a maximum of almost 99%. Not shown here is the transmission data, which is negligible over the same range. This means whatever light is not absorbed is mostly reflected.

The Teepee-like PC we have developed exhibits high absorption and very low reflection even on thin $10 \mu\text{m}$ Si films. As we continue to refine the process, we look to maximize the PC's optical properties. Doing so allows films thinner than current standards to be used, which will decrease the cost of solar cell technology.

References:

- [1] M. Chen, et al. Applied Optics, 46, 26 (2007).
- [2] A. Chutinan and S. John. Physical Review A. 78, 023825 (2008).
- [3] P. Kuang, et al. ACS Nano. Preprint.
- [4] S. Eyderman, et al. J. Applied Phys. 118, 023103 (2015).

Chiral Atomically Thin Films

CNF Project Number: 2061-11

Principal Investigator: Jiwoong Park

User: ChulJoo Kim

Affiliation: Department of Chemistry and Chemical Biology, Cornell University

Primary Sources of Research Funding: Cornell Center for Materials Research, Air Force Office of Scientific Research, Samsung Global Research Outreach, National Research Foundation of Korea

Contact: jp275@cornell.edu, ck389@cornell.edu

Website: <http://park.chem.cornell.edu/index.html>

Abstract:

We report giant circular dichroism (CD) in ultrathin chiral films, only two atoms thick. Our films are based on bilayer graphene with interlayer rotation of opposite polarities and display remarkably strong CD with a maximum ellipticity of $6.5 \text{ deg}/\mu\text{m}$, one of the highest intrinsic values ever reported. Their CD spectra are highly programmable, as the peak energy and sign are tuned by precisely controlling the interlayer rotation angle (θ) and polarity. Its origin is the large in-plane magnetic moment associated with the interlayer optical transition, consistent with our first-principles calculations. Our approach, which is directly applicable to other layered materials, can provide a powerful platform for generating ultrathin chiral metamaterials and structurally programming their interactions with other chiral degrees of freedom associated with photons, molecules, and spin polarized electrons.

Summary of Research:

Chiral materials possess left- and right-handed counterparts linked by mirror symmetry. These materials are useful for advanced applications in polarization optics [1,2], stereochemistry [3,4] and spintronics [5]. In particular, the realization of spatially uniform chiral films with atomic-scale control of their handedness could provide a powerful means for developing nanodevices with novel chiral properties. However, previous approaches based on natural or grown films [1,2], or arrays of fabricated building blocks [6-8], could not offer a direct means to program intrinsic chiral properties of the film on the atomic scale. Here, we report a chiral stacking approach, where two-dimensional materials are positioned layer-by-layer with precise control of the interlayer rotation (θ) and polarity, resulting in tunable chiral properties of the final stack [9].

Figure 1a describes our approach for generating the chiral twisted bilayer graphene (tBLG) with precisely controlled interlayer structures (θ and rotational polarity). It relies on two key steps: first, a single layer graphene film is grown with a uniform crystalline orientation over the entire film, and second, this

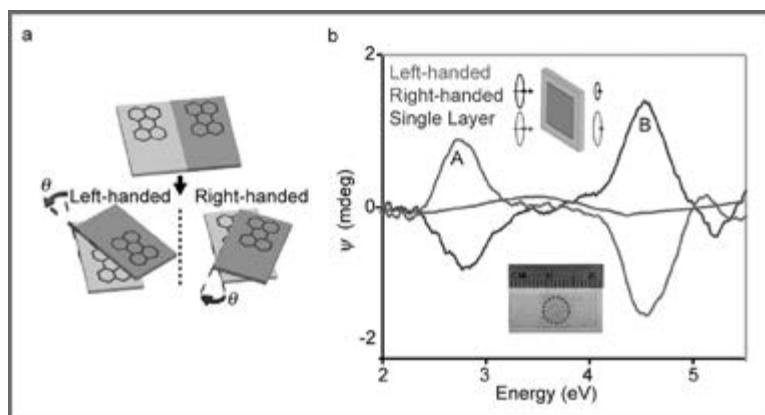


Figure 1: (a) Schematic of chiral stacking process for generating left- and right-handed tBLG films. (b) CD spectra measured from a pair of chiral tBLG films.

film is cut into multiple pieces and is stacked layer-by-layer with a controlled θ_{stack} based on the known crystalline orientation, while rotating counter-clockwise or clockwise to form left- or right-handed films connected by a mirror plane (vertical dashed line), respectively. Using our method, we generate chiral tBLG films, where their θ and handedness are controlled uniformly over several millimetres with a high yield of interlayer coupling.

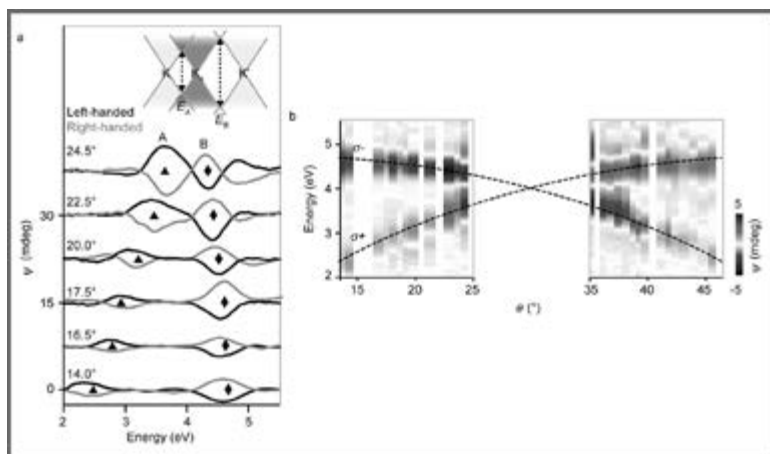


Figure 2: (a) CD spectra in chiral tBLG pairs with different θ . (black: left-handed, grey: right-handed). (b) 3D CD plot as a function of θ (x axis) and energy of incident light (y axis), taken from 29 tBLG samples in total.

Our chiral tBLG films show strong CD and absorb left and right circularly polarized light by different amounts, as shown in Figure 1b. It plots the ellipticity (Ψ) spectra, referred to also as CD spectra in this letter, measured from the left-handed (red) and right-handed (blue) tBLG samples with $\theta_{\text{stack}} = 16.5^\circ$, and single layer graphene (grey), shown for comparison. Here, Ψ characterizes the polarization change of the light transmitting perpendicularly through the films (upper schematic, Figure 1b), and is proportional to the absorption difference between the two circularly polarized light (I_L and I_R) according to the relationship, $\Psi = (I_L - I_R)/2(I_L + I_R)$. Unlike the CD spectra of single layer graphene that show negligible values over the entire measurement photon energy range, the CD spectra of left- and right-handed tBLG each show two strong peaks, one with a positive sign and the other with a negative sign, regardless of the in-plane sample orientation.

The magnitude of the CD peak (as large as 4.3 mdeg in Figure 2a) we observe is extraordinarily large given the two atoms thickness of our twisted bilayer graphene films ($t_{\text{BL}} = 0.66$ nm). In comparison, a much thicker film would be needed to generate a CD peak of similar magnitude in other natural chiral molecules. (e.g., 50 nm for D-glucose, 100 μm for camphorsulfonic acid) [7]. Indeed, the ellipticity normalized to the film thickness, a material-specific parameter, is as large as 6.5 deg/ μm in our chiral twisted bilayer graphene ($\theta = 24.5^\circ$, Figure 2a), one of the highest intrinsic values ever reported.

The giant CD effect is universally observed from all our tBLG films with their CD peak energy and sign directly tunable using θ and rotational polarity. Figure 2a presents data from six chiral pairs of tBLG (black: left-handed, grey: right-handed) with different θ , all of which show giant CD with the main spectral features discussed above.

Figure 2b further shows a 3D colour plot of Ψ (red: positive, blue: negative) from 29 tBLG samples. The most striking feature in Figure 2b is the two lines (denoted $\sigma+$ and $\sigma-$), along which all CD peaks are found. Along the $\sigma+$ line, we find strongly positive Ψ , corresponding to **Peak A** of left-handed film or **Peak B** of right-handed film. Significantly, the peak energy- θ relation closely follows that of the interlayer optical transition (dotted lines) previously studied by both experiments and theory based on a tight binding model. We show that these chiral properties originate from the large in-plane magnetic moment associated with the interlayer optical transition.

Our approach, which is generally applicable to other layered materials, can provide a powerful platform for generating and integrating ultrathin devices based on chiral metamaterials with programmed interactions with other chiral objects, including photons, molecules, and spin polarized electrons.

References:

- [1] Phys. Rev. Lett. 104, 163901 (2010).
- [2] Molecular Light Scattering and Optical Activity (Cambridge Univ. Press, 2009).
- [3] March's Advanced Organic Chemistry: Reactions, Mechanisms and Structure (Wiley, 2007).
- [4] Chiral Photochemistry (Marcel Dekker, 2004).
- [5] Science 331, 894-897 (2011).
- [6] Phys. Rev. Lett. 95, 227401 (2005).
- [7] Appl. Phys. Lett. 103, 213101 (2013).
- [8] Nature 468, 422-425 (2010).
- [9] Nano Lett. 14, 5706-5711 (2014).
- [10] Nano Lett. 14, 3353-3357 (2014).

Phase Sensitive Imaging of Magnetization Dynamics in Spin Hall Multilayers

CNF Project Number: 2091-11

Principal Investigator: Gregory D. Fuchs

Users: Feng Guo, Jason M. Bartell, Isaiah Gray

Affiliation: School of Applied and Engineering Physics, Cornell University

Primary Source of Research Funding: AFOSR

Contact: gdf9@cornell.edu, fg228@cornell.edu, jb864@cornell.edu, ig246@cornell.edu

Website: <http://fuchs.research.engineering.cornell.edu>

Abstract:

We develop a phase-sensitive imaging technique for studying magnetization dynamics in patterned magnetic structures. With the time resolved anomalous Nernst effect (TRANE) and extensions, we apply picosecond laser heating to image the magnetic precession phase of spin Hall multilayer samples. Our ferromagnetic resonance (FMR) measurements quantify the phase and amplitude for both the magnetic precession and the electric current, which allows us to establish the total driving field orientation and the strength of spin Hall effect. In a channel of uniform width, we observe a large spatial variation of the FMR phase laterally across the channel. We interpret our findings in the context of electrical measurement using the spin-transfer torque ferromagnetic resonance technique and show that observed phase variation introduces a systematic correction into the spin Hall efficiency if spatial phase and amplitude variations are not taken into account.

Summary of Research:

A good magnetic microscope allows us to visualize the dynamics of tiny magnets. This capability is particularly important to the field of spintronics, where researchers are working to harness the spin of electrons to efficiently manipulate magnetic orientation. It is a challenge, however, to find a microscope that operates with enough speed and sensitivity to capture the gigahertz motion of magnetic dynamics. An even

bigger challenge is to find a microscope that “sees” both the motion of the magnetization and the current of electrons used to manipulate it. In this work we demonstrate an approach to simultaneously image magnetic orientation and electric current. Furthermore, with phase sensitive imaging, we quantify the spin Hall efficiency in micron-size devices — a critical figure of merit for engineering future magnetic memories.

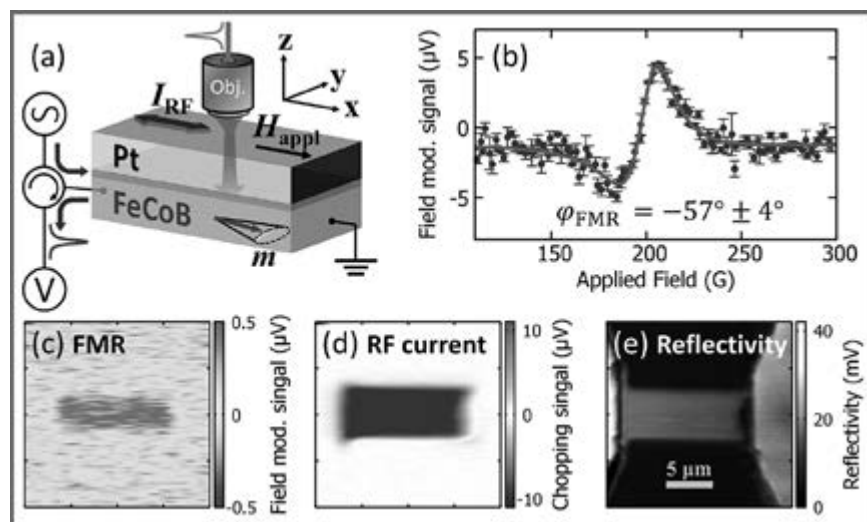


Figure 1: (a) Schematics of the measurement principle for the time-resolved anomalous Nernst effect (TRANE) microscopy. (b) Example of a ferromagnetic resonance (FMR) spectrum using field modulation. Images measured at a fixed field of 208 G: (c) field modulated FMR signal, (d) RF current signal and (e) laser reflectivity.

The measurement principle of TRANE microscopy [1-3] is depicted in Figure 1(a). We focus 3 ps laser pulses from a Ti:Sapphire laser on the sample. The vertical transient thermal gradient is induced by local laser heating, which generates a voltage pulse corresponding to the magnetization projection in the y direction, through the anomalous Nernst effect (ANE) [4,5]. Additionally, the increase in the local resistivity due to transient heating produces a voltage corresponding to the stroboscopic time-slice of RF driving current, enabling us to image the local driving current amplitude and phase. Therefore, the stroboscopic detection implemented in TRANE microscopy provides access to both amplitude and phase information of ferromagnetic resonance (FMR) and RF current, as shown in Figures 1(c) and (d) respectively.

To demonstrate an approach to image the FMR phase, we combine multiple FMR images to calculate the phase variation. In the example shown in Figure 2, we fix the RF current phase and then combine six FMR images at various applied fields (from 185 G to 215 G), to reconstruct both phase and amplitude images, shown in Figure 2 (a) and (b) respectively. The main feature of the phase image is that the phase is quasi-uniform near the center, and it increases near the edges. The phase variation is more prominent along the y -direction than that in the x -direction. In contrast, the FMR amplitude is large near the center and decreases towards either edge, as expected.

Finally we introduce a method to evaluate the systematic correction in the conventional electrical technique due to a spatially varying precession mode. The commonly adopted technique, spin-torque ferromagnetic resonance (ST-FMR), requires the assumption of uniform precession. Thus the phase nonuniformity introduces a sizeable phase correction resulting from, as shown in Figure 3. We conclude that the ST-FMR technique does not necessarily reflect the phase value (and thus spin Hall efficiency) in the middle of the sample, rather it provides a spatially averaged phase.

In conclusion, our measurement technique provides new capability for studying magnetization dynamics, in particular, the local magnetic response to the driving

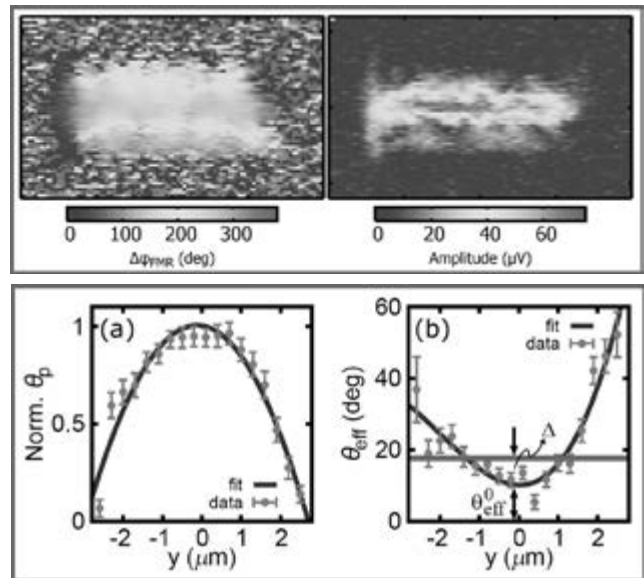


Figure 2, top: By fixing the FMR phase at -24° and using six FMR images at various applied fields, we can decompose (a) the relative FMR phase variation and (b) the FMR amplitude.

Figure 3, bottom: Spatial distributions of (a) the normalized precession amplitude and (b) effective driving field angle. The blue curves in (a) and (b) are the polynomial fits of the data (gray points). The red line in (b) is the resultant driving field angle that would be obtained from ST-FMR. (Δ is the phase correction.)

current. It can be used to study current induced torques in magnetic devices. For our $5 \mu\text{m}$ wide channels it is essential to include a correction for spatial variations of both precession phase and amplitude to correctly quantify the spin Hall efficiency from electrical measurements.

References:

- [1] Bartell, et al, Nature Communications 6, 8460 (2015).
- [2] Guo, et al, Physical Review Applied 4, 044004 (2015).
- [3] Guo, et al, Physical Review B 93, 144415 (2016).
- [4] Slachter, et al, Physical Review B 84, 020412 (2011).
- [5] Weiler, et al, Physical Review Letters 108, 106602 (2012).

Continuous Dynamical Decoupling of a Single Nitrogen-Vacancy Center in Diamond

CNF Project Number: 2126-12

Principal Investigator: Professor Gregory D. Fuchs

User: Evan R. MacQuarrie

Affiliation: School of Applied and Engineering Physics, Cornell University

Primary Sources of Research Funding: The Office of Naval Research (N000141410812), the Cornell Center for Materials Research with funding from the NSF MRSEC Program (No. DMR-1120296), and the Department of Energy Office of Science Graduate Fellowship Program (DOE SCGF), made possible in part by the American Recovery and Reinvestment Act of 2009, administered by ORISE-ORAU under Contract No. DE-AC05-06OR23100

Contact: gdf9@cornell.edu, erm223@cornell.edu

Website: <http://fuchs.research.engineering.cornell.edu/>

Abstract:

The spin state of the nitrogen-vacancy (NV) center in diamond is a promising platform for sensing and quantum information technologies, but magnetic field noise can dephase NV center qubits, limiting their performance. By continuously driving spin transitions with the lattice strain generated by a mechanical resonator, we engineer eigenstates that are less sensitive to magnetic noise. Using this protocol, we extend the inhomogeneous dephasing time of an individual NV center from $T_2^* = 2.7 \pm 0.1 \mu\text{s}$ to $15 \pm 1 \mu\text{s}$ and model the dependence of this enhancement on the amplitude of the mechanical driving field.

Summary of Research:

A qubit's inhomogeneous dephasing time T_2^* provides a useful benchmark of the qubit's utility. For sensing qubits, a longer T_2^* increases sensitivity to quasi-static fields. For quantum information applications, a longer T_2^* provides more time for the execution of gate operations. A qubit accumulates phase at the energy difference between its constituent states ($\hbar = 1$). Environmental noise that affects these energy levels thus introduces random phase fluctuations into the qubit's evolution, dephasing the qubit and limiting T_2^* .

Magnetic field fluctuations from paramagnetic impurities often limit T_2^* in solid state spin qubits such as the nitrogen-vacancy (NV) center in diamond. Dephasing from these field fluctuations can be refocused with pulsed dynamical decoupling (PDD) protocols based on the principle of spin echoes. Although PDD can extend T_2^* of a single NV center to the homogeneous dephasing time T_2 or longer [1], these pulsed techniques often limit the bandwidth of sensing qubits and rarely commute with gate operations applied to information qubits. As an alternative to PDD, continuous dynamical decoupling (CDD) protocols recast the qubit into a "dressed" basis where the new eigenstates are less sensitive to environmental noise [2,3].

In this work, we perform CDD by driving the magnetically-forbidden $|m_s=+1\rangle \leftrightarrow |-1\rangle$ spin transition with lattice strain generated by a mechanical resonator [4-7]. The dressed basis generated by such a driving field has eigenstates $\{|0, m, p\rangle$ where $|m\rangle$ and $|p\rangle$ are equal superpositions of $|+1\rangle$ and $|-1\rangle$. Figure 1 shows how these energy levels respond to magnetic field fluctuations. By mechanically dressing the NV center spin, we open up an avoided level crossing between $|+1\rangle$ and $|-1\rangle$ such that a qubit composed of $|m\rangle$ and $|p\rangle$ will be less sensitive to magnetic field fluctuations.

To generate the mechanical driving fields used to dress the NV center, we fabricate a high-overtone bulk acoustic resonator (HBAR) from a single-crystal diamond substrate. Our resonator consists of a $3 \mu\text{m}$ thick zinc oxide (ZnO) piezoelectric film sandwiched between a titanium/platinum ground plane and an aluminum top contact that was lithographically patterned using the GCA $5\times$ g-line stepper in the Cornell NanoScale Science and Technology Facility. Applying a gigahertz-frequency voltage across the ZnO film launches acoustic waves into the diamond, which then acts as a Fabry-Pérot cavity to generate a frequency comb of standing wave resonances.

The resonator used in this work was driven at a $\omega_{\text{mech}}/2\pi = 586$ MHz resonance that had a quality factor of $Q = 2700$. On the diamond face opposite the ZnO transducer, we use the GCA 5× stepper to fabricate antenna for magnetic spin control. The final device is pictured in Figure 2.

To quantify the protection offered by mechanical CDD, we perform Ramsey style measurements of T_2^* in the dressed and undressed bases. To execute such a measurement in the undressed basis, we first initialize the NV center into $|0\rangle$ via optical pumping.

We then apply a magnetic $\pi/2$ -pulse resonant with the $|0\rangle \leftrightarrow |-1\rangle$ transition to create an equal superposition of $| -1\rangle$ and $|0\rangle$. After a free evolution time τ , a second $\pi/2$ -pulse returns the spin to $|0\rangle$ where a fluorescence read-out quantifies the qubit's coherence. Repeating this sequence as a function of τ measures the dephasing and yields $T_2^* = 5.4 \pm 0.2 \mu\text{s}$ for the $\{0, -1\}$ qubit. Because both states in the $\{+1, -1\}$ qubit are sensitive to magnetic noise, T_2^* for the $\{+1, -1\}$ qubit will be half this value.

A Ramsey measurement in the dressed basis follows a modified version of the previous sequence. A continuous mechanical driving field Ω is applied to dress the NV center, and the $\pi/2$ -pulses are replaced by double-quantum π -pulses [8] that generate equal superpositions of $|m\rangle$ and $|p\rangle$. Figure 3 shows the results of such a dressed Ramsey measurement, with T_2^* of the $\{+1, -1\}$ qubit indicated by the shaded region. Dressing the NV center spin with $\Omega = 581 \pm 2$ kHz extends T_2^* from $2.7 \pm 0.1 \mu\text{s}$ to $15 \pm 1 \mu\text{s}$.

As shown in Figure 4, the protection offered by CDD scales linearly with Ω . Scatter in the data is attributed to non-zero detunings of Ω . By calculating the root mean square (rms) phase fluctuation from magnetic noise, we see that the qubit loses its first order sensitivity to magnetic field fluctuations as Ω begins to dominate the magnetic field noise. The power handling capabilities of our device prohibited probing the ultimate limits of mechanical CDD, but the protection is expected to continue increasing until noise in Ω becomes the dominant source of dephasing.

By continuously driving the $|+1\rangle \leftrightarrow |-1\rangle$ spin transition with resonant lattice strain, we have performed mechanical CDD to extend T_2^* of a single NV center. The protection demonstrated here provides a promising route towards enhanced T_2^* in NV center technologies.

References:

- [1] L. Childress, et al., Science 314, 281-285 (2006).
- [2] N. Timoney, et al., Nature 476, 185-188 (2011).
- [3] X. Xu, et al., PRL 109, 070502 (2012).
- [4] E. R. MacQuarrie, et al., Optica 2, 233-238 (2015).
- [5] E. R. MacQuarrie, et al., PRL 111, 227602 (2013).
- [6] E. R. MacQuarrie, et al., PRB 92, 224419 (2015).
- [7] A. Barfuss, et al., Nature Phys. 11, 820-824 (2015).
- [8] H. J. Mamin, et al., PRL 113, 030803 (2014).

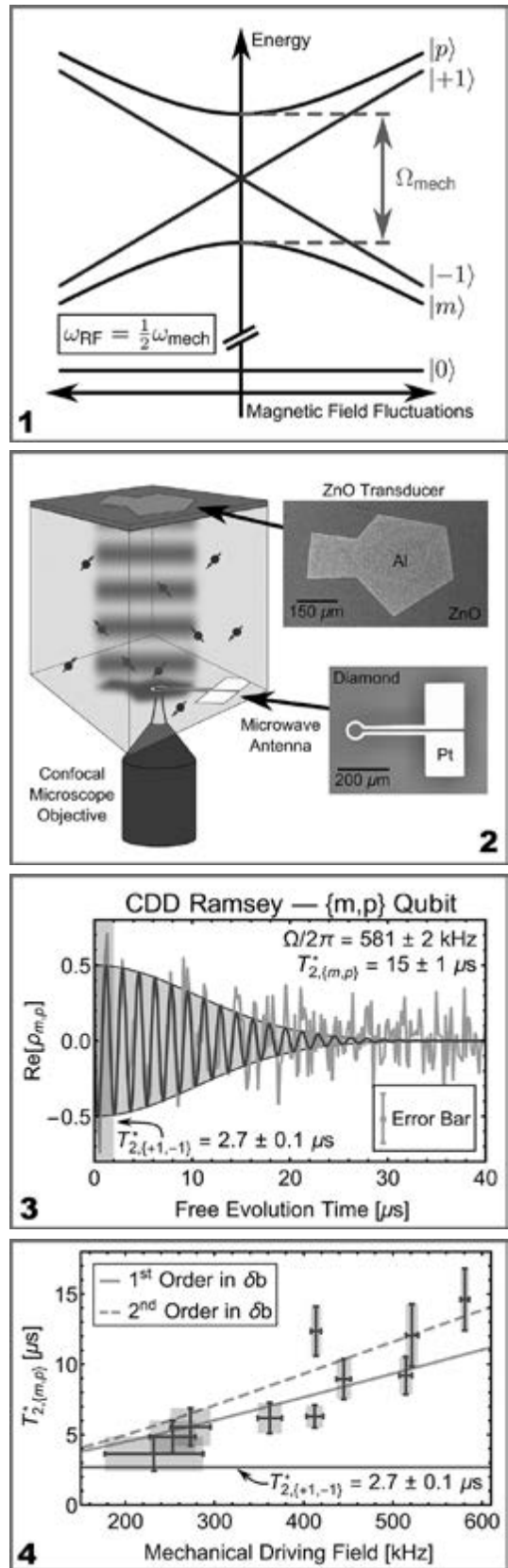


Figure 1: Energy levels of the dressed and undressed NV center spin states plotted in the reference frame rotating at half the mechanical carrier frequency. **Figure 2:** Device schematic. **Figure 3:** Ramsey measurement of T_2^* in the dressed basis. The shaded region signifies the undressed T_2^* . **Figure 4:** The dressed T_2^* , plotted as a function of Ω .

Fabrication of Aligned Substrates

CNF Project Number: 2343-15, 2344-15, 2345-15

Principal Investigator: James Hone

User: Cheng Tan

Affiliation: Department of Mechanical Engineering, Columbia University

Primary Source of Research Funding: MRSEC, INDEX, AFOSR-2D

Contact: jh2228@columbia.edu, cheng.tan@columbia.edu

Website: <http://hone.me.columbia.edu/>

Summary of Research:

To support our efforts at Columbia University, we have ongoing projects at Cornell NanoScale Facility (CNF) to fabricate alignment marks on SiO₂/Si wafers. To fabricate these wafers, the Gamma Automatic Coat-Develop Tool (Gamma) is used to coat the wafers with photoresist, as well as to develop the photoresist post-exposure. To pattern the wafers, the ASML 300C Deep Ultraviolet Stepper was used to expose the photoresist. Post development, the wafers were descummed using the Anatech Plasma Etcher. The alignment metals were then evaporated using Nanobiotechnology Center's (NBTC) batch evaporation system. Post evaporation, the wafers underwent lift off followed by a resist strip in both the bath and the Anatech Plasma Etcher.

The purpose of these alignment marks is to facilitate the electron beam lithography processes here at Columbia, where we prepare and transfer samples to the prepared wafers, and align them using the marks. By using the wafer scale processing at CNF, we are able to produce large numbers of wafers in relative short amounts of time, speeding up our processes as a whole.

Chromium to Optimize Spin-Orbit Torques on Magnetic Devices

2016 CNF REU Intern: Ana Sofia (Sofie) de Olazarra, Physics, Pomona College

CNF REU Principal Investigator: Dr. Daniel Ralph, Physics, Cornell University

CNF REU Mentors: Jonathan Gibbons and Neal Reynolds, Physics, Cornell University

Primary Source of Research Funding: National Science Foundation under Grant No. ECCS-1542081

Contact: asd02014@mymail.pomona.edu, dcr14@cornell.edu, jgg833@cornell.edu, neal.d.reynolds@gmail.com

Abstract:

Magnetoresistive random access memory (MRAM) relies on storing information in the magnetization states of nanomagnets. This presents a need for an effective and localized technique for manipulating the magnetic orientation of nanomagnets. One possible method of doing so is to employ spin-transfer torques, which can be generated through the spin Hall effect (SHE). SHE is observed when a charge current is applied to a metal with strong spin-orbit coupling, causing electrons to be deflected according to their spin orientations. These spins accumulate along the boundaries of the metal, giving rise to a transverse spin current that can subsequently exert a spin-transfer torque on an adjacent ferromagnetic layer. Samples with a Cr layer and a $\text{Co}_6\text{Fe}_2\text{B}_2$ or Py ferromagnetic layer were fabricated. Spin-torque ferromagnetic resonance (ST-FMR) and vibrating sample magnetometer (VSM) measurements were performed on the devices. The findings suggest that the spin Hall angle of Cr is at least 1.8 percent.

Introduction:

Magnetoresistive random access memory (MRAM) is a strong contender in the quest to identify a source of high-density, non-volatile memory storage. Precisely reorienting a nanomagnet's magnetization continually challenges researchers. Current-induced spin-transfer torques in heavy metals can be used to locally manipulate the magnetic orientation of magnetic devices extremely efficiently [1]. Current-induced spin-transfer torques are a product of spin currents, which can be induced by the spin Hall effect (SHE). The ratio of the induced spin current to the applied charge current, otherwise known as the spin Hall angle, is a common figure of merit for how effectively a material can generate spin-transfer torques given some applied charge current. Previous research has suggested that chromium may have a large spin Hall angle, making it a particularly interesting material to study [2].

Experimental Procedure:

We began our device fabrication process by sputter depositing a 7 nm or 8 nm chromium (Cr) layer and a 2 to 10 nm ferromagnetic layer onto approximately 1 cm by 1 cm sapphire wafer pieces. Permalloy (Py) or cobalt iron boron ($\text{Co}_6\text{Fe}_2\text{B}_2$) was used for the ferromagnetic layer. A 2 nm aluminum capping layer was deposited in order to prevent the lower layers from oxidizing. We proceeded to pattern Cr/ $\text{Co}_6\text{Fe}_2\text{B}_2$ and Cr/Py ST-FMR devices onto our samples through

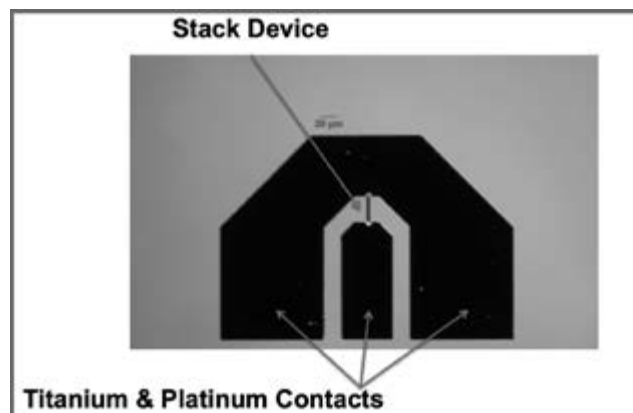


Figure 1: Device geometry used for ST-FMR measurements.

optical lithography and ion etching techniques. Finally, titanium (Ti) and platinum (Pt) contacts were deposited onto the devices via sputter deposition, followed by a lift off process to remove the excess Ti/Pt and leave behind only the contacts.

We faced a variety of challenges during the fabrication and measurement processes, including: adhesion issues of the Ti/Pt contacts, resonant frequency peaks that were presented at amplitudes far smaller than expected, and highly resistive devices. These issues, combined with observations that photoresist may have been stuck under the contact pads causing

adhesion issues, lead us to believe that our devices are somewhat compromised.

Measurements on our devices comprised mainly spin-torque ferromagnetic resonance (ST-FMR). We began our ST-FMR measurements by lowering an RF probe to the Ti/Pt electrical contacts on our devices. We then applied a charge current of controllable radio frequency, and swept an in-plane magnetic field between -0.20 T and 0.20 T. Subsequently, we observed a resonant frequency peak due to the interaction between the current-induced torques and the precession frequency of the ferromagnetic layer. This precession in the ferromagnetic layer's magnetization yielded an oscillating anisotropic magnetoresistance (AMR). The combination of the RF resistance oscillation with the RF frequency created a DC mixing voltage, which we measured over a variety of controllable frequencies.

In addition to the ST-FMR measurements, we also spent time characterizing the AMR of the devices and determining the saturation magnetization of $\text{Co}_6\text{Fe}_2\text{B}_2$ and Py. AMR occurs when the electrical resistance is dependent upon the angle between the direction of the current and the direction of the magnetization. Because applied spin torques rotate the magnetization during ST-FMR, it was necessary to characterize the AMR of the devices. Additionally, it was necessary to obtain the saturation magnetization for $\text{Co}_6\text{Fe}_2\text{B}_2$ and Py using a vibrating sample micrometer (VSM) — because as saturation magnetization increased, the ease with which we reoriented the magnet decreased.

Results and Conclusions:

The results of our analysis on our Cr 8 nm/Py 5 nm device can be seen in Figure 2. These results suggest that the spin Hall angle of chromium is at least approximately 1.8 percent. Because we observed very strange resistance values in our measurements for the

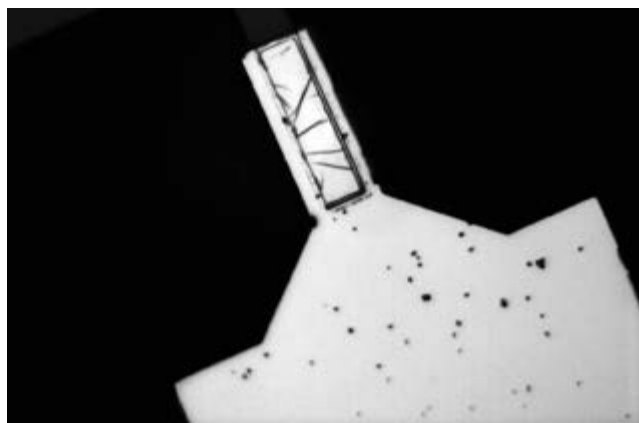


Figure 2: Roughness/wrinkles beneath contact pads on ST-FMR device for Cr 7nm/ $\text{Co}_6\text{Fe}_2\text{B}_2$ 10 nm sample suggest that photoresist may be stuck under contact pads.

Cr 7 nm sample and the Cr with Py sample, it is likely that our initial calculation for the spin Hall angle may have been somewhat inflated. Thus, we made a more conservative guess for the shunting factor, giving us a value of about 1.8 percent for the angle. These resistance issues, coupled with the fabrication issues we faced, suggest that there is quite a bit of room for improvement for creating more successful devices.

Future Work:

More devices should be fabricated using a more gentle process in order to ensure more accurate results. Additional ST-FMR measurements should be done on more reliable Cr/ $\text{Co}_6\text{Fe}_2\text{B}_2$ and Cr/Py samples in order to more accurately determine the spin Hall angle of Cr.

CNF Tools Used:

Class 1 resist spinners, Class 2 resist spinners, 5X stepper, AJA sputterer, Oxford 81/82.

Acknowledgments:

I would like to acknowledge my principal investigator, Dr. Daniel Ralph, and my mentors, Jonathan Gibbons and Neal Reynolds. I would also like to thank CNF REU Program Coordinator Melanie-Claire Mallison and the entire CNF staff. Finally, I would like to thank the National Science Foundation for their support under Grant No. ECCS-1542081.

References:

- [1] Liu, L. (2014). Manipulation of Magnetic Moment Using The Spin Current From Magnetic and Non-Magnetic Materials. (Doctoral Dissertation). Cornell University, Ithaca, NY.
- [2] Qu, D., Huang, et al. Inverse spin Hall effect in Cr: Independence of antiferromagnetic ordering. *Phys.Rev. Lett.* 92, 020418 (2015).
- [3] Mellnik, A. R., et al. Spin-transfer torque generated by a topological insulator. *Nature* 511, 449-451 (2014).

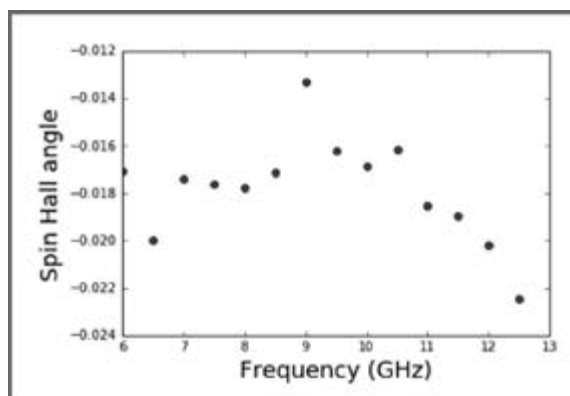


Figure 3: Spin Hall angle data Cr/Py device.

Improving Dopant Activation in III-V Materials using Laser Spike Annealing

CNF Project Number: 150-82

Principal Investigators: Michael Thompson, Paulette Clancy

Users: Victoria Sorg, Megan Hill

Affiliations: Materials Science and Engineering, Chemical and Biomolecular Engineering; Cornell University

Primary Source of Research Funding: Semiconductor Research Corporation (SRC)

Contact: mot1@cornell.edu, pc@icse.cornell.edu, vcs26@cornell.edu, moh9@cornell.edu

Abstract:

The high temperatures and short annealing times (sub-ms to ms) of laser spike annealing (LSA) have the potential to increase activation of ion-implanted compound semiconductors to levels necessary for use in future generations of CMOS technology. These conditions enable access to both metastable activation levels after ion implantation, and extended process temperatures without deactivation from *in situ* doped metastable films. Single stripe LSA scans were conducted to probe carrier activation in both ion implanted and *in situ* doped $\text{In}_{0.53}\text{Ga}_{0.47}\text{As}$ as a function of peak annealing temperature and heating dwell. Temperatures under LSA were directly measured up damage using platinum resistors and calibrated to the known decomposition behavior of a polymer and gold melt. Carrier concentration across a single laser stripe were optically measured using micro Raman spectroscopy calibrated to the plasmon coupled modes, providing a full map of the activation behavior as a function of temperature. The onset of activation occurred for a 5 ms dwell at 800°C with the onset of damage at 1060°C. These measurements are crucial to establish conditions for future studies of dopant activation by LSA.

Summary of Research:

As silicon transistor technology enters the sub 10 nm regime, major scaling challenges remain. Ultimately, a shift towards a new device architectures and geometries are needed, but a possible solution to continue scaling over the next few decades is to replace the silicon channel and source drain contacts with higher mobility materials [1]. Compound semiconductors, such as $\text{In}_{0.53}\text{Ga}_{0.47}\text{As}$ (InGaAs), are strong candidates for low power n-type materials due to their high electron mobility. However, challenges arise when attempting to maximize dopant activation during thermal processing due to thermal budget limitations. With long timescale annealing of InGaAs, active Si doping concentrations in ion-implanted and samples with grown-in active dopants converge toward a fixed net donor solubility limit of $1.4 \times 10^{19} \text{ cm}^{-3}$ [2].

In this project, sub-millisecond LSA was investigated as a method to improve the activation of ion-implanted dopants and to limit deactivation of grown-in dopants in InGaAs. LSA uses a continuous-wave, line focused laser scanned over a sample to rapidly heat and quench samples (rates of 10^6 K/s and 10^5 K/s , respectively). Using spatially resolved measurements perpendicular to the single laser annealing scan,

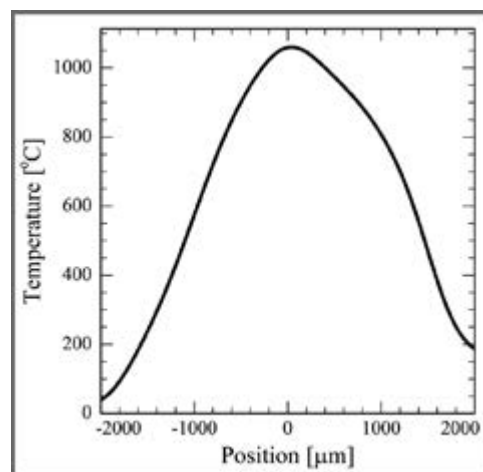
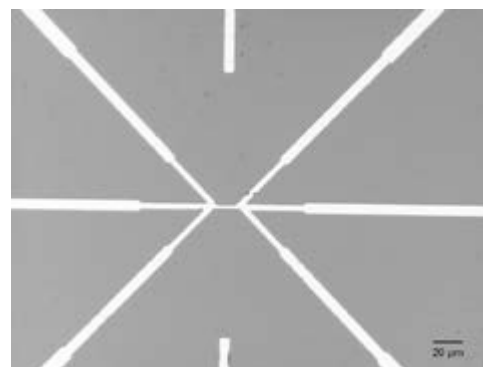


Figure 1, top: Image of fabricated platinum thermistor used to measure time and position resolved measurements of laser annealing temperature. Figure 2, bottom: Laser annealing spatial temperature profile perpendicular to the laser scan direction for a 5 ms, 137 W anneal.

a continuous range of annealing temperatures can be tested from room temperature to the highest annealing temperature reached.

Two types of samples were used to study dopant behavior with LSA; ion-implanted and molecular beam epitaxy (MBE) grown samples. First, 300 nm $\text{In}_{0.53}\text{Ga}_{0.47}\text{As}$ films on semi-insulating InP substrates were heavily doped by ion implantation to a dose of $5 \times 10^{14} \text{ cm}^{-2} \text{ Si}^+$ at 10 keV. Separately, samples with active Si dopant concentrations of $3 \times 10^{19} \text{ cm}^{-3}$ were grown using MBE on semi-insulating InP substrates. Both sample types were capped to prevent arsenic loss at high temperatures with 15 nm of atomic layer deposited Al_2O_3 . Samples were laser annealed using a 5 ms dwell with 980 nm light from a diode laser. As the direct bandgap of InGaAs absorbs the laser light, annealing is extremely efficient.

Direct measurements of the annealing temperatures were made using 20 μm platinum resistors (“thermistors”) on the InGaAs (Figure 1). Thermistors were electrically insulated by 50 nm SiO_2 grown by plasma enhanced chemical vapor deposition (PECVD) with the Oxford 100. Liftoff masks for the platinum thermistor and metal contacts were patterned using optical lithography with metal films deposited using the CVC SC4500 combination thermal/e-gun evaporation system. These thermistors were scanned under the LSA while we measured resistance (directly proportional to temperature) as a function of time and position. Measurements over a range of laser power and annealing dwells were used to calibrate the temporal and spatial characteristics of the annealing beam.

The dwell dependent decomposition behavior of a polymer (poly(styrene-block-methyl methacrylate), 70 wt.% polystyrene) was studied on well-characterized silicon substrates to establish absolute temperature references. On InGaAs samples, 60 nm films of the polymer were spun and the decomposition was characterized after LSA by measuring the thickness changes using the P-10 Profilometer. As a second calibration point, gold dots were deposited with the CVC SC4500 thermal evaporation system. Absence of gold melt under LSA established an upper bound to the damage threshold on InGaAs.

Using thermistors, polymer decomposition, and gold dots, we were able to probe the annealing temperature of InGaAs on InP during LSA. Using 137 W, 5 ms anneal, the peak temperature reached was approximately 1060°C (Figure 2). At these conditions, approximately 50% of samples crack due to thermal stress. We used these annealing conditions in subsequent studies to characterize the dopant activation and deactivation behavior of InGaAs.

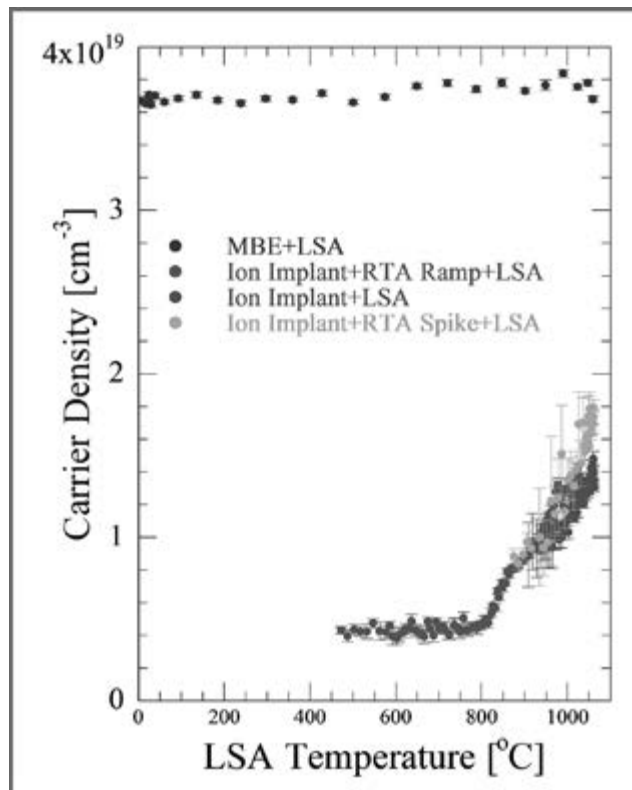


Figure 3: Activation behavior as a function of temperature for silicon doped InGaAs samples.

Using Raman spectroscopy to measure carrier concentrations [3] as a function of annealing temperature, we were able to characterize the dopant activation behavior of InGaAs (Figure 3). We found that LSA-induced activation began at 800°C and increased until damage at 1060°C. LSA was able to activate Si dopants after ion implantation to concentrations in excess of the solubility limits identified in longer timescale annealing methods. However, LSA was most effective at activating dopants that had been annealed on longer timescale previously to repair implantation damage. In contrast with lower temperature and longer timescale annealing, samples with high metastable carrier concentrations were stable with no evidence of deactivation under the short timescales of LSA. Overall, the high annealing temperatures and short timescales of LSA was found to be effective at activating ion-implanted dopants and maintaining high carrier concentrations for grown in dopants.

References:

- [1] H. Riel, et al., MRS Bull. 39, 668 (2014).
- [2] A.G. Lind, et al., J. Vac. Sci. Technol. B, Nanotechnol. Microelectron. Mater. Process. Meas. Phenom. 33, 021206 (2015).
- [3] R. Cuscó, et al., Phys. Rev. B 65, 035210 (2001).

Charge Trapping and Degradation in Organic and Quantum Dot Transistors Studied using Kelvin Probe Force Microscopy

CNF Project Number: 863-00

Principal Investigator: Prof. John Marohn

Users: Louisa Smieska, Ryan Dwyer, Syed Ali Moeed Tirmzi

Affiliation: Department of Chemistry and Chemical Biology, Cornell University

Primary Source of Research Funding: National Science Foundation, Division of Materials Research (NSF-DMR 1006633)

Contact: jam99@cornell.edu, lmb327@cornell.edu, rpd78@cornell.edu, st759@cornell.edu

Website: marohn.chem.cornell.edu

Abstract:

We fabricated bottom-gate, bottom-contact transistors, which were used in a Kelvin probe trap-clearing spectroscopy experiment to characterize charge detrapping mechanisms in *n*-channel organic semiconductors for the first time. We have also fabricated lead sulfide quantum dot transistors with a perylene encapsulation layer that allows stable transistor operation in ambient conditions for days.

Summary of Research:

Organic semiconductor materials are appealing for low-cost, high area electronic applications, but better electron transport materials are needed to realize complementary logic circuits and enable organic electronics with high operating speeds and low power consumption. Perylene diimide (PDI) derivatives have relatively high electron mobility, but PDI transistors can suffer performance instabilities in the form of threshold voltage shifts and lowered mobilities due to charge trapping. New PDIs with lowest unoccupied molecular orbitals (LUMOs) below 0.4 eV relative to vacuum have been proposed and synthesized in order to reduce these instabilities [1].

We used time- and wavelength-resolved frequency-modulated Kelvin probe force microscopy (FM-KPFM) to examine the spatial distribution of traps and trapping / trap clearing mechanisms in high LUMO PDI transistors, as shown in Figure 1 [2]. Figure 2 shows that electron traps in four high-LUMO PDI derivatives exhibited a wide range of responses to visible light that did not track with the LUMO level.

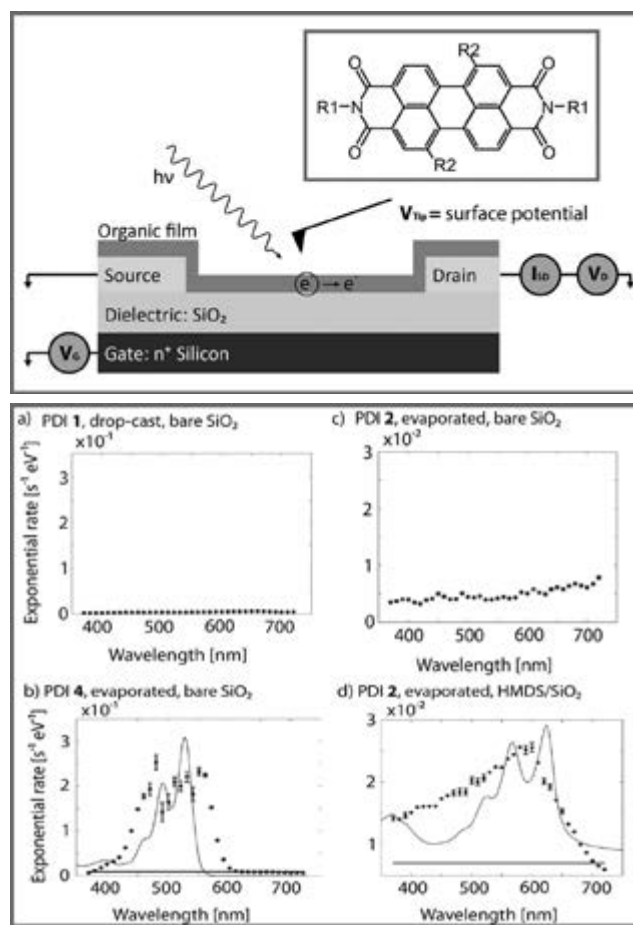


Figure 1: Sketch of trap-clearing spectroscopy experiment used to investigate electron traps in PDI thin-film transistors (Smieska, Marohn, et al., Ref 2). Figure 2: Light-induced trap-clearing spectra in PDIs, reported as single exponential time constant (Smieska, Marohn, et al., adapted from Ref 2).

This shows that thermodynamic stability alone does not predict the behavior of electron traps in PDI thin-film transistors. The dramatically different spectra observed for the same PDI evaporated on untreated silicon dioxide (c) versus hexamethyldisiloxane-treated silicon dioxide (d) indicate that the surface treatment changes the dominant trapping mechanism in these PDI thin-film transistors.

Surface passivation of colloidal quantum dots with halide ligands is a promising way to enhance the stability and performance of quantum dot devices. The best performing quantum dot solar cells (10 percent efficient) use lead sulfide (PbS) quantum dots with tetrabutylammonium iodide (TBAI) as a ligand [3], but the films are still very air sensitive. Even for nominally air-stable films, transport measurements must be taken in an inert atmosphere to prevent degradation.

Field effect transistor measurements of nanocrystal films combined with KPFM are a powerful tool to study transport dynamics [4]. We fabricated 5 μm channel bottom-gate bottom-contact transistor substrates with interdigitated electrode and prepared PbS TBAI field effect transistors. PbS quantum dots were spin cast on the substrate followed by ligand exchange. These devices showed ambipolar behavior when measured in inert environment — when electrical measurements were performed in air, the transistor characteristics of as prepared devices degraded completely within minutes. To make device characterization under ambient conditions possible, a thin layer (100 to 200 nm) of parylene C was deposited on the quantum dot films (PDS 2010 LABCOTER). This thin encapsulation layer allows electrical measurements in ambient conditions for at least two days without any obvious change in transport properties.

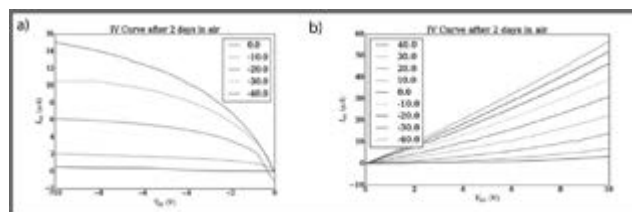


Figure 3: Encapsulated lead sulfide quantum dot source drain current versus source drain voltage, for different gate voltages (shown in legend).

Our room temperature, thin encapsulation layer strategy produces results comparable to specially designed atomic layer deposition chambers for quantum dot FET encapsulation [5]. The increased stability afforded by the encapsulation layer will allow us to perform a full array of KPFM measurements to elucidate charge transport and trapping dynamics in quantum dot transistors.

References:

- [1] Zhan, X., et al. Rylene and related diimides for organic electronics. *Advanced Materials* 23, 268-284 (2010).
- [2] Smieska, L. M., Li, Z., Ley, D., Braunschweig, A. B., and Marohn, J. A. Trap-clearing spectroscopy in perylene diimide derivatives. *Chem. Mater.* 28, 813-820 (2016).
- [3] Lan, X., et al. Passivation using molecular halides increases quantum dot solar cell performance. *Advanced Materials* 28, 299-304 (2015).
- [4] Zhang, Y., Chen, Q., Alivisatos, A. P., and Salmeron, M. Dynamic charge carrier trapping in quantum dot field effect transistors. *Nano Lett.* 15, 4657-4663 (2015).
- [5] Liu, Y., et al. PbSe quantum dot field-effect transistors with air-stable electron mobilities above $7 \text{ cm}^2 \text{V}^{-1} \text{ s}^{-1}$. *Nano Lett.* 13, 1578-1587 (2013).

Physically-Based Spatial Varying Anisotropic BRDF for Metal-Finishing Surface

CNF Project Number: 2056-11

Principal Investigator: Bruce Walter

User: Zhao Dong

Affiliation: Computer Science, Cornell University

Primary Source of Research Funding: Autodesk

Contact: bjw@graphics.cornell.edu, zd@graphics.cornell.edu

Website: <http://www.cs.cornell.edu/Projects/metalappearance/>

Abstract:

The way a surface reflects light is represented by its bidirectional reflectance distribution function (BRDF). In this project we investigated ways to predict the visual appearance of metal surfaces based solely on knowledge of their surface microgeometry. This approach has several advantages over conventional radiometric appearance capture methods, especially in being able to simultaneously achieve both high spatial and angular resolution.

Summary of Research:

We tested prediction methods based on both geometric and wave optics, compared the results to reference measurements from a gonireflectometer and using the CNF's Zygo optical profilometer, and found good agreement. We also explored ways to represent and synthesize the visual spatial texture that is characteristic of brushed metals surfaces.

Our methods can be used to improve the visual fidelity of metal rendering in computer generated imagery.

References:

- [1] Zhao Dong, Bruce Walter, Steve Marschner, and Donald P. Greenberg, "Predicting Appearance from Measured Microgeometry of Metal Surfaces", ACM Transactions on Graphics, December 2015. <http://dl.acm.org/citation.cfm?id=2815618>

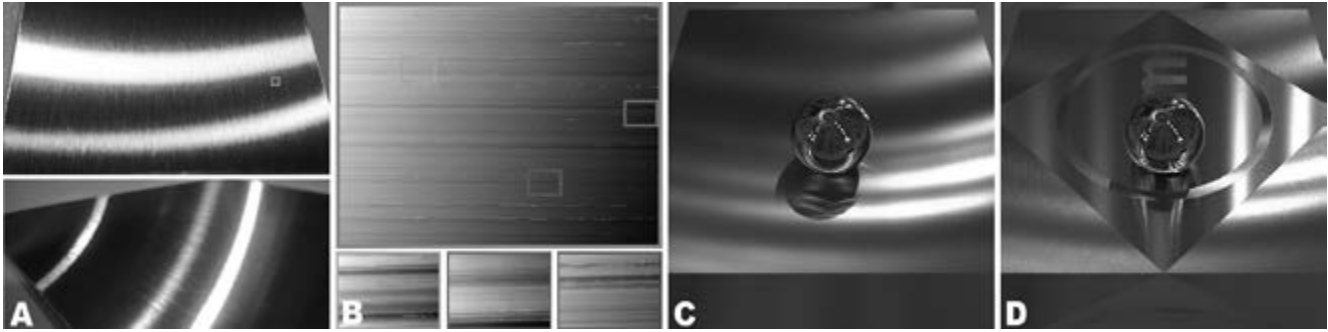


Figure 1: We present a method to predict the appearance of complex surfaces, such as this stainless steel #4 sample, from its micro-scale geometry. Commercial profilometers can rapidly measure surfaces with sub-wavelength resolution, and we develop and validate methods to predict BRDFs from the surface data. The method can predict both average BRDFs and characteristic textures, or spatial variations, that are visually important for our example materials. (A) Brushed stainless photographs. (B) Measured surface microgeometry. (C) Predicted anisotropic BRDF. (D) Spatially variant BRDF.

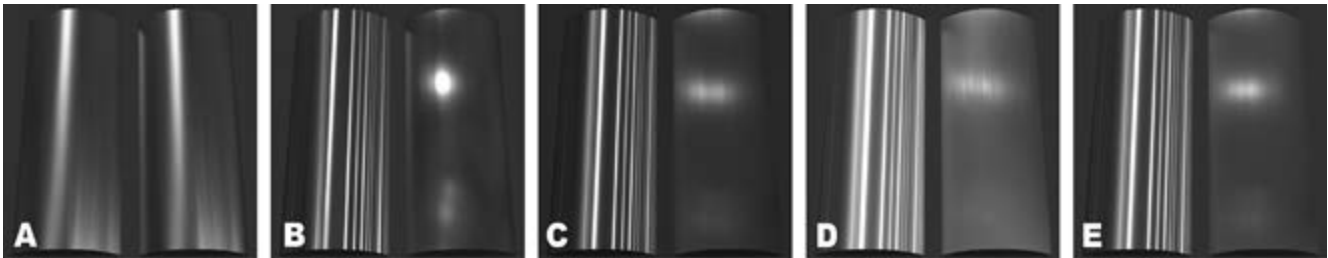


Figure 2: Images rendered using our profilometer-derived geometric NDFs. Each image shows sections of two cylinders, where the BRDF has been rotated 90 degrees on the second cylinder. For the anisotropic samples, the brushing direction is horizontal on the left cylinder and vertical on the right. The cylinders use spatially uniform BRDFs with any apparent texturing caused by angular variations within the BRDFs. Copper's color is due to its Fresnel term. (A) QPanel. (B) Stainless#4. (C) Stainless#3. (D) Aluminum#4. (E) Copper#4. (See reference [1].)

Nanoscale Periodic Features with DUV and 5x Stepper Lithography

CNF Project Number: 2217-13

Principal Investigator: Ioannis Kymissis

User: Tanya Garza

Affiliation: Department of Electrical Engineering, Columbia University, New York, NY

Primary Source of Research Funding: National Science Foundation

Contact: johnkym@ee.columbia.edu, tcg2112@columbia.edu

Website: <http://kymissis.columbia.edu>

Abstract:

Lithography with the ASML 300C DUV stepper has been used in previous years to produce pillar features with diameters as small as 232 nm. This past year work with the ASML 300C DUV stepper was expanded to include process optimization of hole features with diameters of 306 nm, 408 nm, and 446 nm. Initial investigation was also done to produce hole features with diameters of 408 nm and 446 nm with the GCA 5x stepper tool.

Summary of Research:

In previous years, a process for patterning nanophotonic pillar structures was developed at CNF that used the ASML 300C DUV stepper to pattern 4-inch borosilicate float glass wafers ("borofloat"), 4-inch fused silica wafers, and 4-inch silicon wafers. Pillar features like those shown in Figure 1 were fabricated with diameters of 232 nm, 270 nm, 306 nm, 408 nm, 612 nm and 816 nm. The features were patterned using UV210-0.3 resist with AR3 and DUV42P antireflective coating, were exposed with the ASML 300C DUV lithography system, and then etched with the Oxford plasma etchers. Optimal depth of focus (DOF), exposure dose, and etch time were determined for nanophotonic patterns in fused silica by varying these parameters incrementally and examining the resultant features. Photonic crystal geometry was examined in the SEM and photonic crystal performance was assessed optically via extraction of waveguided light.

Results during pillar feature optimization showed that distorted pillar patterns, which looked more like holes than pillars, gave higher extraction of waveguided light. In the past year, work began to pattern periodic hole features instead of pillars. Initial tests were done using the same exposure conditions that were used for the pillar features for a nominal hole size of 306 nm. It was found that a much higher exposure dose was required to clear the hole area. Figure 2 shows uncleared hole features produced

using the pillar exposure conditions. Higher exposure doses led to more uniformly cleared holes, but they were significantly smaller than the commercial mask features.

A new commercial mask was made with intentionally oversized hole patterns to account for the reduction of the hole size during exposure with the ASML DUV stepper. Two enlargement methods were done to account for the reduction observed in the SEM. The first method was to increase the hole feature diameter on the mask by the percentage (in this case 36%), which would have made the observed holes the correct size. The second method was to increase the hole feature diameter by a fixed amount (in this case 81 nm), which would make the holes the correct size. This method was done with data from the 306 nm hole design with optimized exposure conditions and applied to hole features with design diameters of 306 nm, 408 nm, and 446 nm. It was found that using a fixed 81 nm increase in the mask feature size resulted in features sizes closest to that designed. Figure 3 shows 306 nm holes produced from mask features with an 81 nm diameter increase.

Initial work was also done to adapt the ASML process to the GCA 5x stepper for minimum feature sizes of 408 nm and 446 nm. The motivation for this change was to take advantage of the wider availability of similar tools among foundries for these larger feature sizes.

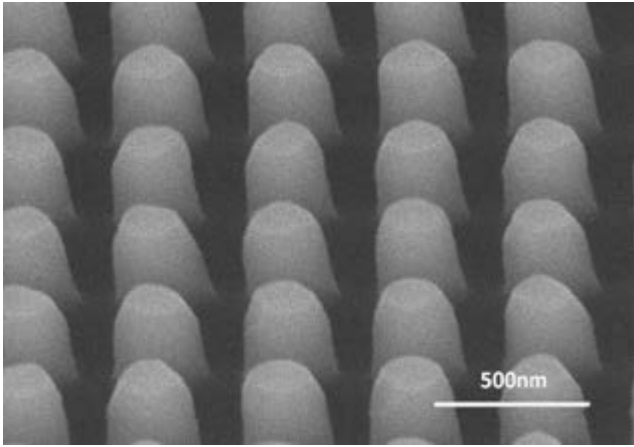


Figure 1: SEM image of photonic crystal pattern, nominally with 270 nm pillar features, fabricated in fused silica with a process developed with the ASML 300C DUV stepper.

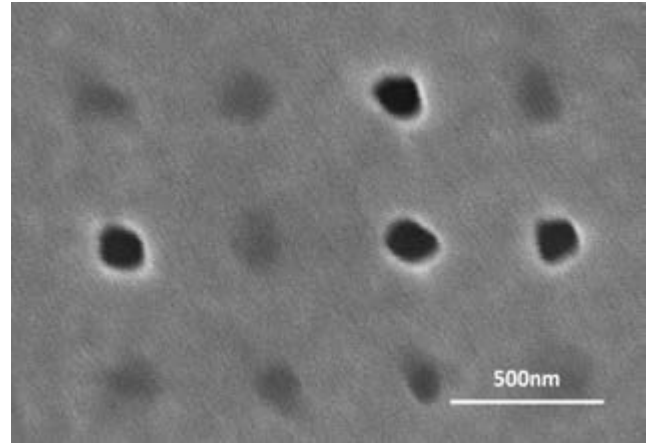


Figure 2: SEM image of photonic crystal pattern, nominally with 306 nm hole features, fabricated in fused silica with process parameters developed with ASML 300C DUV stepper for pillar features.

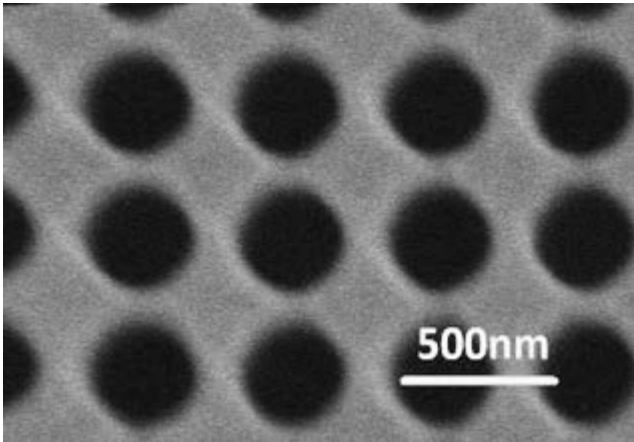


Figure 3: SEM image of photonic crystal pattern, nominally with 306 nm hole features, fabricated in fused silica with a process developed with ASML 300C DUV stepper and commercial mask with an additional 81 nm of diameter to account for lensing effects in the tool.

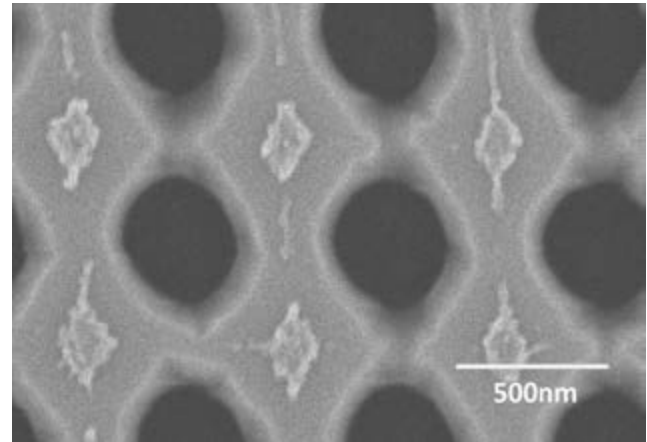


Figure 4: SEM image of photonic crystal pattern, nominally with 446 nm hole features, fabricated in fused silica with a process developed with GCA 5x stepper.

A mask with hole patterns with diameters of 408 nm and 446 nm was made with the Heidelberg DWL2000 mask writer at CNF. A coarse DOF and exposure dose variation study was done with these features on the GCA 5x stepper to narrow exposure conditions to produce the best crystal pattern performance and geometry. Photonic crystal geometry was examined in the SEM and photonic crystal performance was assessed optically via extraction of waveguided light.

Based on the results of this analysis, narrower DOF and exposure dose windows were determined that will be used in future work. Figure 4 shows an SEM of the best features produced in this coarse exposure condition study. This figure shows anisotropic deformation that is larger in one axis than the other. This is reminiscent of 232 nm diameter features produced with the ASML

DUV stepper. As the GCA 5x stepper specifications are for feature resolution below 900 nm, this minimal asymmetrical deformation for 408 nm and 446 nm diameters holes is quite reasonable.

In summary, the DUV process described previously for periodic pillar features has been expanded to include an optimized process for periodic hole features. This DUV hole patterning process requires a mask with an additional 81 nm increase in hole diameters to produce design diameters of 306 nm, 408 nm, and 446 nm etched into fused silica. Initial work to determine exposure conditions to produce periodic hole features with diameters of 408 nm and 446 nm using the GCA 5x stepper has had promising results showing a small but acceptable amount of asymmetrical feature deformation.

GaN Vertical Power p-n Diodes on Ammonothermal GaN Substrates; A Process Development at CNF

CNF Project Number: 2350-15

Principal Investigators: Huili Grace Xing, Debdeep Jena

User: Zongyang Hu

Affiliation: Electrical and Computer Engineering, Cornell University

Primary Source of Research Funding: ARPAe-Sixpoint

Contact: grace.xing@cornell.edu, zh249@cornell.edu

Abstract:

Vertical GaN power p-n diode processes have been developed using CNF. The project includes device fabrication, imaging and electrical test of GaN homoepitaxial p-n junction structures on ammonothermal GaN substrates. High performance GaN-on-GaN vertical p-n diodes have been demonstrated. Large forward currents (forward turn-on voltage of 3.3V, forward current of 300A/cm² at 3.5V and 1000A/cm² at 4V), 300V reverse breakdown voltage (estimated 4MV/cm electric field at breakdown, highest reported in literatures so far) and at least 12 orders of magnitude current on/off ratio have been measured in these devices.

Summary of Research:

Gallium nitride (GaN) has been widely considered as one of the most promising wide band gap semiconductors for development of next generation power semiconductor devices. The theoretical power performance of GaN predicted by the Baliga's figure-of-merit is 1000x higher than that of Si and nearly 2x higher than SiC. Though record-high power diode performance has been demonstrated in GaN compared to all other semiconductor materials [1], the lack of low-cost, low-dislocation-density bulk substrate limits the feasibility of application for GaN based devices.

The goal of ARPA-E Sixpoint project is to develop high quality, inexpensive GaN substrates using ammonothermal method, and demonstrate high performance and repeatability of vertical GaN power devices. The development of fabrication processes for GaN based power devices is also a critical component in this project.

Device fabrication includes metal deposition (e-beam evaporation of Ti, Pd, Au), dry etching (Cl-based plasma etching), photolithography (Autostep i-line stepper), dielectric deposition (PECVDSiO₂). Device sizes are 50um~700um. Optical microscope, profilometer and AFM are used frequently to observe sample surfaces during processes.

The device processes and main CNF tools used are described briefly as the following:

1. Beveled p GaN mesa etching
 - SiO₂ mask deposition (Oxford PECVD)
 - Litho and wet etching of SiO₂ (Autostep i-line Stepper)
 - Dry etching of p GaN (PT770 etcher)
2. Top ohmic contact deposition
 - Litho and Pd/Au ohmic contacts (SC4500 evaporator)
3. Passivation
 - Dielectric passivation (Spinner)
 - Lithography
 - Wet etch to open contact holes
4. Field plate
 - Litho and field plate deposition, liftoff
5. Bottom contact deposition
 - Photoresist coating and cleaning
 - Ti/Au back ohmic contacts, liftoff

The schematic device structure is depicted in Figure 1. The epitaxial structure is grown by metal organic chemical vapor deposition (MOCVD) on bulk GaN substrates. The thick (8 μm) n-GaN region is the most critical part for the electrical characteristics of the GaN p-n diodes. Highest GaN crystal quality with

lightly doped Si is desired for higher voltage blocking under reverse biases. All other impurities need to be controlled at minimal concentrations. The p-type GaN growth and p-type ohmic contact processes have been optimized for low on resistance under forward biases. Spin-on-glass has been used for dielectric passivation and support of the field plate, so that a very low profile slope can be created. The beveled mesa and field plates are designed to mitigate electrical field crowding at the edge of the p-n junction and the corners of the mesa [2]. An optical image of the GaN device chip after fabrication is shown in Figure 2. The devices have sizes ranging from 50 μm to 700 μm (not shown in figure). The forward current-voltage curve of a typical GaN p-n diode is plotted in Figure 3. The forward current at $V < 2.4\text{V}$ is lower than the lower limit of the measurement system. The diode turns on at $\sim 3.3\text{V}$ (in linear scale not shown), and the current reaches 300 A/cm^2 at 3.5V and 1000 A/cm^2 at 4V, which meets our project goal for the forward current density. Devices have good uniformity at different positions on the 10 \times 10 mm^2 chip. Devices with and without field plates do not show significant difference under forward biases. The reverse current-voltage characteristics of a group of GaN p-n diodes with 110 μm diameter are plotted in Figure 4. The breakdown voltages are all $\sim 300\text{V}$, which shows good uniformity of the material quality and processes across the chip. The larger diodes with up to 700 μm diameter have similar breakdown voltages. Capacitance-voltage measurement has been performed on these diodes, and charge distribution inside the n-GaN has been analyzed (results not shown due to limited space). The charge concentration ranges from $3 \times 10^{16} \text{ cm}^{-3}$ to $3 \times 10^{17} \text{ cm}^{-3}$ at different positions in the n-GaN.

According to one-dimensional Poisson simulation, the maximum electric field inside the p-n junction can reach 4MV/cm under 300V breakdown voltage. This is the highest critical electric field ever reported [3], which shows the high crystal quality of the epitaxy and substrate. Future work will focus on reducing the charge concentration, improving the breakdown voltage and run-to-run repeatability of the device performance.

References:

- [1] Z. Hu, K. Nomoto, B. Song, M. Zhu, M. Qi, M. Pan, X. Gao, V. Protasenko, D. Jena and H.G. Xing, Appl. Phys. Lett. 107, 243501 (2015).
- [2] K. Nomoto, Z. Hu, B. Song, M. Zhu, M. Qi, R. Yan, V. Protasenko, E. Imhoff, J. Kuo, N. Kaneda, T. Mishima, T. Nakamura, D. Jena and H. Xing, IEEE International Electron Devices Meeting (IEDM), 9.7.1 (2015).
- [3] I. C. Kizilyalli, A. P. Edwards, H. Nie, D. Disney and D. Bour, IEEE Trans. Electron Devices, 60, 3067 (2013).

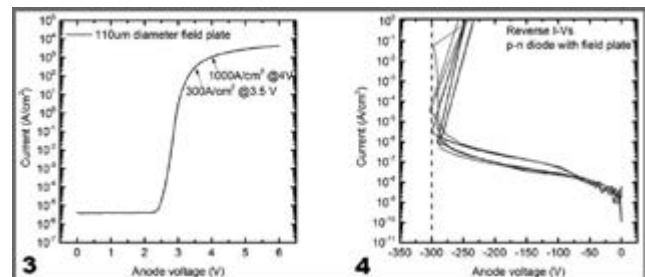
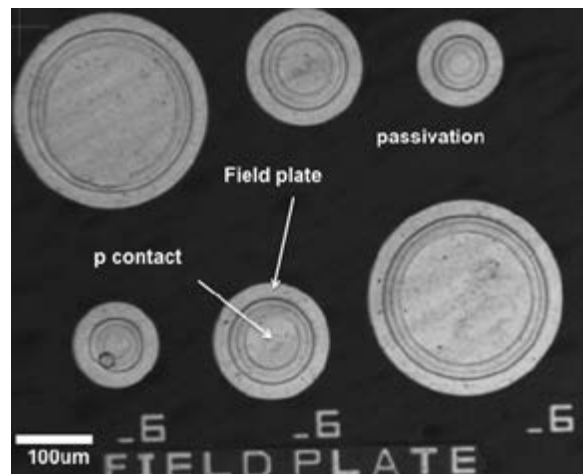
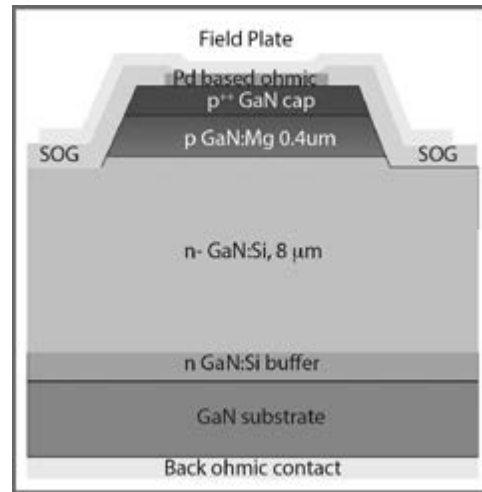


Figure 1, top: Schematic cross section of a vertical GaN power p-n diode with field plate edge termination.

Figure 2, middle: Part of a GaN power p-n diode chip imaged under the optical microscope.

Figure 3, bottom left: Forward current-voltage characteristics of a typical vertical GaN power p-n diode fabricated at CNF.

Figure 4, bottom right: Reverse current-voltage characteristics of a group of vertical GaN power p-n diodes on one chip.

Growing Silicon Oxide using Dry Deposition Process to Support R&D Work at University of Pennsylvania

CNF Project Number: 2352-15

Principal Investigator: Noah Clay

Users: Meredith Metzler, Christopher Martin

Affiliation: Quattrone Nanofabrication Facility, University of Pennsylvania

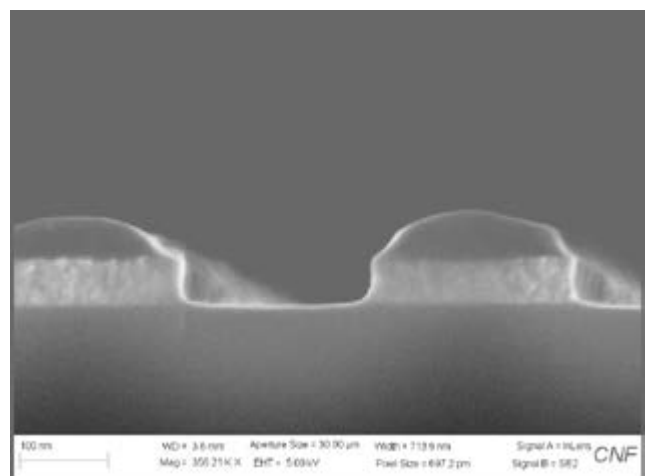
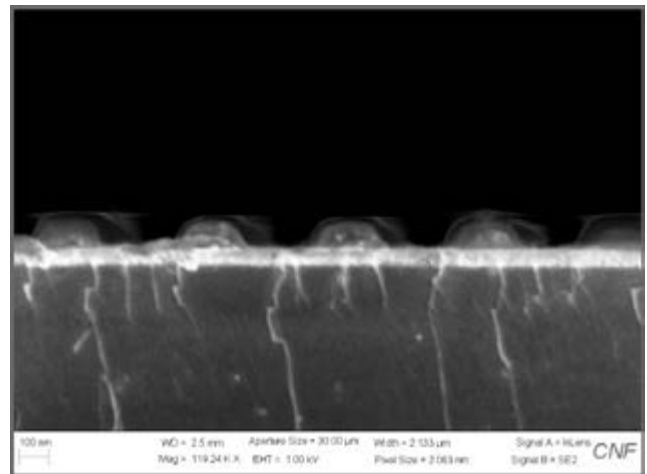
Primary Source of Research Funding: University of Pennsylvania

Contact: nclay@seas.upenn.edu, metzlerm@seas.upenn.edu, chris.martin@tornado-spectral.com

Summary of Research:

The Quattrone Nanofabrication Facility at The University of Pennsylvania is grateful to have access to the Cornell NanoScale Facility in support of our user's research efforts. This project includes use of the furnaces for thermal oxidation of silicon, use of the MVD100 for depositing FOTS on silicon masters for SCIL template fabrication, use of the etch capabilities and the SEMs. Most of this work is supported through the remote program.

Images taken on the Zeiss Ultra SEM: Figures 1 and 2 show, respectively, results from nanoimprint lithography residual layer etch development efforts and etch development of a subsequent tantalum pentoxide etch using the NIL pattern and residual layer etch process from Figure 1.



Growth and Characterization of Ultra-Strong Multi-Layer Graphene

CNF Project Number: 2386-15

Principal Investigator: Sol M. Gruner

User: Gabrielle Illava

*Affiliations: Macromolecular Diffraction Facility at Cornell High Energy Synchrotron Source (MacCHESS),
Cornell Biophysics/Physics Department; Cornell University*

*Primary Sources of Research Funding: IT,U558387,6635; MacCHESS is funded by the National Institutes of Health,
under grant GM-103485 from the National Institute of General Medical Sciences*

Contact: smg26@cornell.edu, GL1432@cornell.edu

Website: <http://bigbro.biophys.cornell.edu/>

Abstract:

Graphene is a single atom thick hexagonal carbon lattice with incredible electronic and mechanical properties. Since its discovery in 2004, graphene has been proven to be the strongest material known to humankind [1]. It is because of this strength that we are attempting to use it for atomically thin, x-ray transparent and vacuum tight windows as well as a material in which we hermetically wrap wet protein crystals for x-ray diffraction. At the Macromolecular Diffraction Facility at Cornell High Energy Synchrotron Source (MacCHESS), we are interested in advancing microcrystallography technologies. Reducing the amount of material between the x-ray source, sample, and detector is crucial to being able to extract the highest quality data from diffraction experiments. Most graphene devices utilize polymethylmethacrylate (PMMA) as a support layer. However, PMMA degrades upon exposure to an x-ray beam [2], and graphene is significantly weakened by contamination [1]. Therefore any amount of polymer on the graphene window would be problematic. The solution we have found to this problem is to grow large grain multi-layer graphene (LGMLG) that is strong enough to stand alone with no polymer backing. By adapting a chemical vapor deposition (CVD) process using the First Nano Carbon Nanotube and Graphene (CNT/Graphene) Furnace with the help of Phil Infante, we have combined several graphene recipes to optimize the characteristics of LGMLG.

Summary of Research:

Monolayer graphene is normally grown using CVD on copper foil under vacuum [3]. The initial MLG recipe was able to produce greater than tetra-layer graphene on copper by increasing the pressure within the growth chamber during the growth step [4]. This was cleverly accomplished by increasing the hydrogen gas flow to the maximum rate while also reducing the power of the vacuum pump. Initial analysis with Raman spectroscopy, done through Cornell Center for Materials Research whose facilities are supported through the NSF MRSEC program (DMR-1120296), showed that growths done at 240 mTorr produced non-uniform layers that were sometimes bilayer and often greater than four layers of graphene. These results were confirmed through scanning electron microscopy (SEM), using the Zeiss Ultra High Resolution Field Emission SEM at CNF, see Figures 1 and 2; as well as dark-field transmission electron microscopy (TEM), using CCMR's FEI T12 Spirit TEM STEM.

The strength of the multilayer growth was such that we were able to work with it without a polymer backing as hoped; however it was still very delicate and an alternate approach to increase tensile strength was considered. Graphene is weakest at the grain boundaries, and introducing an oxidation step before the growth step has been shown to increase grain size and thus reduce the occurrence of boundaries over large mono-layer growths [5]. In order to achieve the correct oxygen/argon ratio, a measurement was taken of the pressure change with oxygen at its lowest flow rate, and then the argon flow was adjusted so that the proper ratio was reached. When comparing Figure 2 (MLG) to Figure 3 (LGMLG), it is apparent that the irregularities in grain size are reduced and that overall grain size has increased.

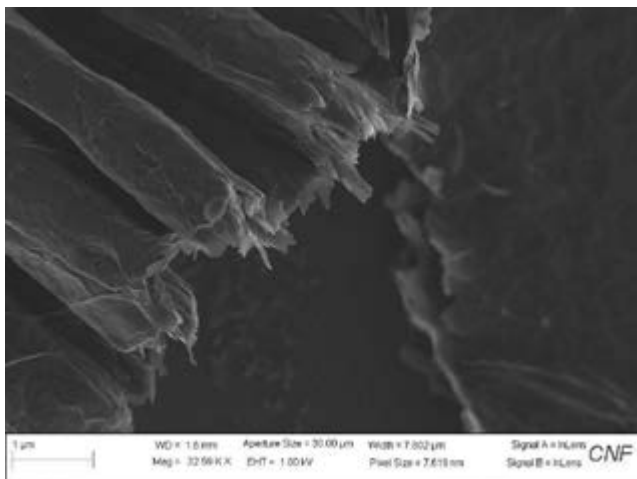


Figure 1: Fold of MLG graphene after transfer to silicon nitride TEM grid that allows for side view of multiple layers.

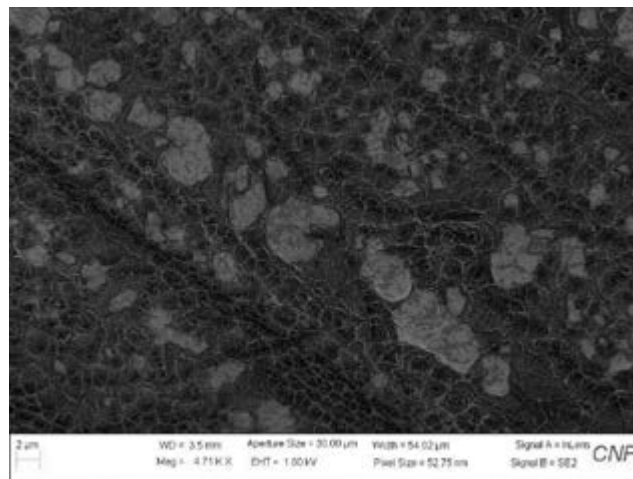


Figure 2: No oxidation step, 15m growth. Light regions: mono/bi layer; dark regions: MLG. Grain size spanning from $< 1 \mu\text{m}$ to $3 \mu\text{m}$.

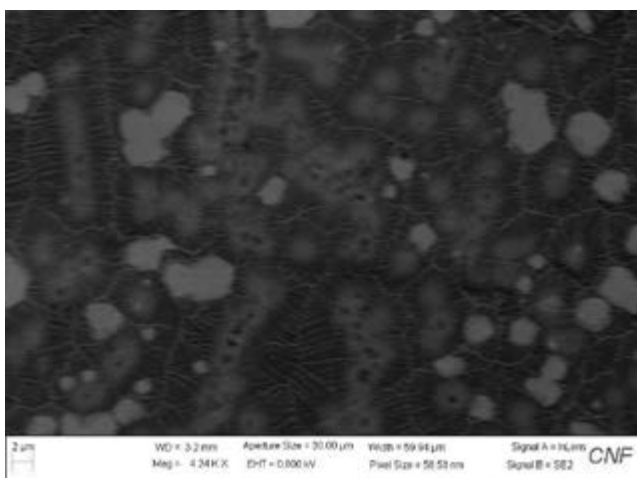


Figure 3: Extended 90m growth after five minute oxidation step with average grain size of $\sim 12 \mu\text{m}$.

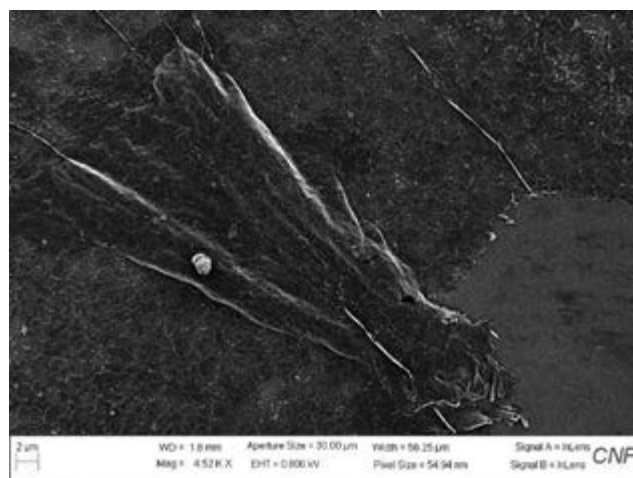


Figure 4: The graphene dragon, an interesting fold of MLG after transfer to silicon nitride TEM grid.

This graphene is currently being used at MacCHESS for diffraction studies of known proteins so that other features of experimental design may be tested. Additionally, LGMLG will continue to be used for vacuum testing of x-ray transparent windows that are $100 \mu\text{m}$ in diameter and characterized further with atomic force microscopy (AFM). Also, included in Figure 4 is an incredibly lucky image of what appears to be a graphene dragon (see cover!).

References:

- [1] Lee, C. (2008). "Measurement of the Elastic Properties and Intrinsic Strength of Monolayer Graphene". *Science* 321 (385), 385-388.
- [2] Yates, B. W. and Shinozaki, D. M. (1993). "Radiation degradation of poly(methyl methacrylate) in the soft x-ray region". *J. Polym. Sci. B Polym. Phys.*, (31) 1779-1784.
- [3] Li, X., et al. (2009). "Large-area synthesis of high-quality and uniform graphene films on copper foils". *Science* (324), 1312-1314.
- [4] Sun, Z., et al. (2012). "Large-Area Bernal-Stacked Bi-, Tri-, and Tetralayer Graphene" *ACS Nano* (11), 9790-9796
- [5] Lee, G.-H., et al. (2013). "High-Strength Chemical-Vapor-Deposited Graphene and Grain Boundaries," *Science*, (340), 6136, 1073-1076.

Experimental Study of the Resolution Limits — and PDMS and Electroplating Applications — of ADEX/SUEX Dry Photolithographic Film

CNF Project Number: 2398-15

Principal Investigator: Don Johnson¹

User: Bruce McKee²

Affiliations: 1. DJ DevCorp, 2. CNF Nanofabrication Consultant

Primary Source of Research Funding: DJ DevCorp

Contact: don@djdevcorp.com, bruce.mckee7@gmail.com

Website: DJ DevCorp (www.djdevcorp.com), Bruce McKee (www.brucecmckee.org)

Abstract:

ADEX and SUEX are newly-developed photolithographic dry-film sheets pre-cut to wafer or substrate dimensions. The sheets — in thicknesses from 5 μm to 500 μm — are laminated to flexible or rigid surfaces with an inexpensive office laminator, and are ready to use in minutes. These dry sheets are ideal for high aspect ratio lithography, and eliminate the bubbles, edge bead, thickness non-uniformity, and hotplate leveling problems associated with thick wet photoepoxy resists.

Given this potential for accelerating research requiring thick films, our CNF project seeks to:

1. Experimentally determine the thickness and resolutions limits of ADEX and SUEX dry film sheets on silicon wafers, glass substrates, and copper-coated PCB materials.
2. Develop ADEX and SUEX-based processes for creating PDMS and electroplating molds.
3. From the work on goals #1 and #2, document the “best research practices” for handling, processing, and applying ADEX and SUEX in an academic cleanroom environment.

Summary of Research:

Our initial research has focused on developing a repeatable, CNF-compatible substrate lamination process for silicon wafers.

This work started with draft processes developed by DJ DevCorp and its initial customers [1,2]. CNF staff scientist Dr. Beth Rhoades worked closely with us to modify these draft processes so that they were compatible with CNF tooling and the new SKY laminator in the CNF Class-2 resist processing room.

This collaboration helped identify and document the critical processing steps necessary to laminate films without damaging either the film or the substrate. Dr. Rhoades incorporated this information into new process recipes for laminating and processing 100, 200, and 500 μm thick films on 4-inch silicon wafers.

Our future work will use these new recipes as a building block to determine ADEX/SUEX resolution limits with standard UV exposure tools, as well as develop and document “best practices” for applying ADEX/SUEX to PDMS molding and electroplating.

References:

- [1] ADEX Epoxy Thin Film Rolls/Sheets Preliminary Data Sheet Product.
- [2] SUEX Epoxy Thick Film Sheets (TDFS) Preliminary Data Sheet.

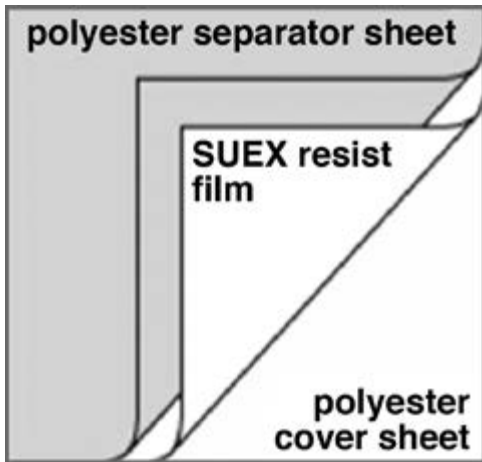


Figure 1: ADEX and SUEX dry films are protected with plastic cover sheets.

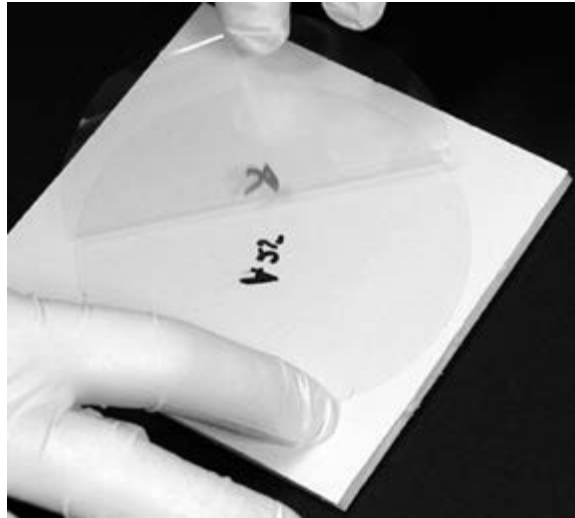


Figure 2: Removing dry film protective plastic sheet prior to lamination.



Figure 3: Dry film lamination using an inexpensive office pouch laminator.

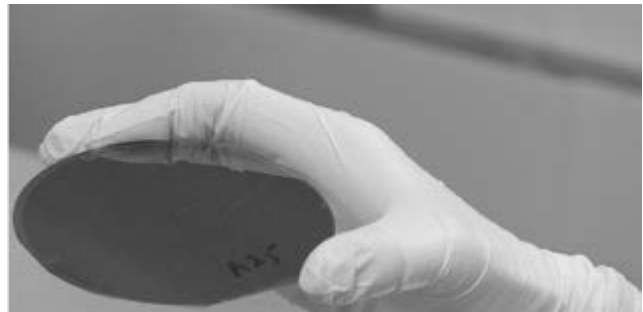


Figure 4: Dry film on a 4-inch silicon wafer.

Two-Step Photolithography for Fabrication of High Aspect Ratio SU-8 Rings

2016 CNF REU Intern: Ryan James Branch,
Chemical Engineering, University of Michigan – Ann Arbor

CNF REU Principal Investigator: Dr. Abraham Duncan Stroock,
Robert Frederick Smith School of Chemical and Biomolecular Engineering, Cornell University
CNF REU Mentor: Neeraj Nitin Sinai Borker, Sibley School of Mechanical and Aerospace Engineering, Cornell University
Primary Sources of Research Funding: National Science Foundation under Grants No. ECCS-1542081 and No. 1435013
Contact: rjbrjb@umich.edu, abe.stroock@cornell.edu, ns762@cornell.edu

Abstract:

When suspended in a linear, low Reynolds number flow, most axisymmetric particles will rotate in periodic orbits. However, there exist certain shapes that are predicted in theory to resist this tumbling motion, and instead reach an equilibrium orientation, coming to a halt. If these theoretical predictions can be confirmed, particles of such shapes would be very valuable in applications where suspensions with a high degree of anisotropy are desired, such as fiber reinforced composites. We investigated the fabrication of one such shape, a ring with an “L”-shaped cross section, depicted in the top of Figure 1. Photolithographic techniques offer the benefit of simultaneous production of different sized particles, in large enough quantities for rheological experiments. We characterized and optimized a process to fabricate these shapes out of the negative photoresist SU-8, due to its ability to form strong, well defined, and chemically resilient structures. With aspect ratios ranging from 12 to 100, the rings created through this process were of the appropriate dimensions and surface regularity, possessing both rigidity and structural stability when released into solution.

Summary of Research:

The goal was to create ring particles with an “L”-shaped cross section (shown in the top of Figure 1) having a base height of $5\ \mu\text{m}$, and a total height of $17\ \mu\text{m}$. By varying the diameter of the particles, we provided a basis for experimental confirmation of the predicted fluid mechanical properties of these rings; their tumbling behavior can be calculated based on their aspect ratio. Masks were created to facilitate the

fabrication of rings with outer diameters between 200 and $1700\ \mu\text{m}$.

We developed a procedure to reliably fabricate rings of this shape out of SU-8, an epoxy based negative photoresist, which has been previously used to create well-defined nonspherical particles [1]. An outline of the photolithographic steps is shown in Figure 2.

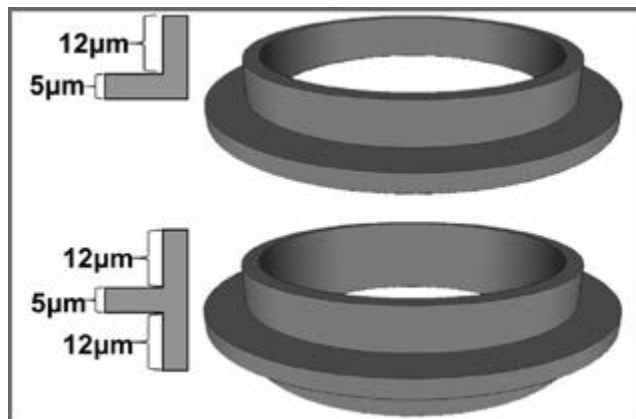
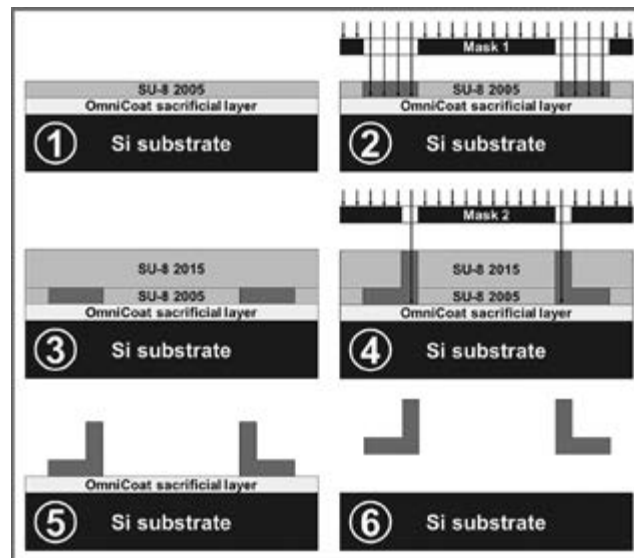
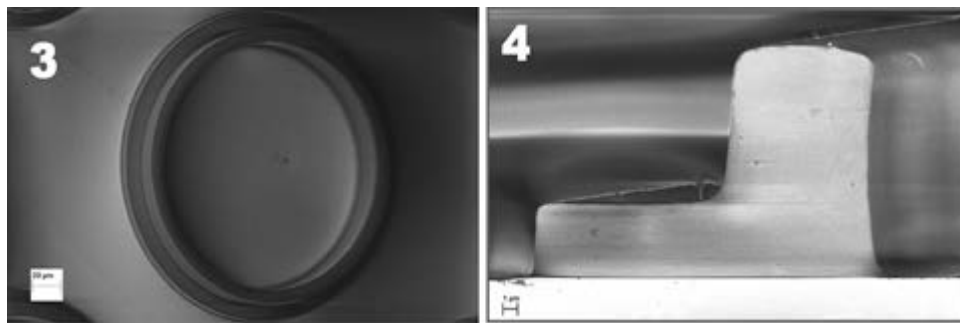


Figure 1, above: Comparison of cross section and overall shape for “L”-shaped ring vs. ring with fore-aft symmetry. Figure 2, right: Outline of photolithography process used to fabricate ring particles with “L”-shaped cross sections.



The process can be summarized as follows: First, on the surface of a 4-inch silicon wafer, a sacrificial layer of OmniCoat™ (which is later dissolved to facilitate particle release) was spin-coated. Then, a 5 μm thick layer of SU-8 2005 was spun and exposed, using the ABM contact aligner, to form the base layer of the ring. A post-exposure bake step was carried



*Figure 3, left: SEM of completed SU-8 ring particle, viewed with a tilt of 35 degrees.
Figure 4, right: SEM of cross section of ring, achieved by scoring and breaking wafer.*

out in order to preserve the cross linked structure in this first layer, which would otherwise be destroyed through diffusion of solvent from the following layer [2]. Next, a 12 μm thick layer of SU-8 2015 was spun and exposed to form the upper portion of the ring. The wafer was then cut into 14.25 mm squares using a dicing saw, such that each piece contained rings of a given aspect ratio. These pieces were developed using SU-8 developer, then hard baked in order to anneal any cracks in the rings, and strengthen the SU-8 epoxy material. From there, Remover PG was used to dissolve the OmniCoat layer, in combination with a sonicator to release the particles into solution.

Preceding the release step, the dimensions of the rings were characterized with the P10 profilometer. To understand other characteristics of the shape, such as surface defects and sidewall profile, scanning electron microscopy (SEM) was employed, as shown in Figures 3 and 4. By scoring and breaking a piece of a wafer which contained rings on the surface, we could view the cross sectional profile to further confirm that the shape produced fit our desired parameters.

Beyond the “L”-shaped rings, we explored various methods for fabricating a modified ring shape that possesses fore-aft symmetry. Figure 1 shows the differences in cross section and overall ring shape. While more difficult to fabricate due to the overhanging portion of the structure, such a shape would resist the tumbling motion at a much lower aspect ratio, and resist drifting transverse to the direction of flow. Our most promising results in this regard came from the creation of ring shaped “trenches” out of a positive photoresist, which were then filled with SU-8. However, difficulty filling trenches past a depth of 5 to 9 μm, as well as solvent diffusion at areas of contact with different resist, prevented us from successfully creating this more complicated particle. Down the line, the incorporation of a metal layer to stop diffusion or even act as an in-line mask could potentially address these issues.

Results and Conclusions:

A process was defined such that particles of the appropriate height dimensions can reliably be manufactured on a large enough scale for fluidic experiments to be carried out. For the entire range of diameters produced, the particles were observed to remain rigid and structurally stable when released into solution. Work on fore-aft symmetric particles provides information for future attempts to create ring shapes with overhang features.

Future Work:

The fabricated particles can be suspended in a viscous solution and flow visualization experiments performed in order to confirm the theoretical properties such shapes are predicted to exhibit. Using insights from our preliminary explorations, more could be done to achieve the fore-aft symmetric SU-8 ring particles.

CNF Tools Used:

ABM contact aligner, DISCO dicing saw; P10 profilometer; Zeiss Supra SEM.

Acknowledgments:

Dr. Abraham D. Stroock, Neeraj Nitin Sinai Borker, Dr. Donald L. Koch, CNF REU Program Coordinators and CNF Staff. This work was performed in part at the Cornell NanoScale Facility, a member of the NNCI, which is supported by the NSF (Grant ECCS-1542081). This project is supported by NSF Award No. 1435013.

References:

- [1] Badaire, Stéphane, et al. “Experimental investigation of selective colloidal interactions controlled by shape, surface roughness, and steric layers.” *Langmuir* 24.20 (2008): 11451-11463.
- [2] Bohl, Benjamin, et al. “Multi-layer SU-8 lift-off technology for microfluidic devices.” *Journal of Micromechanics and Microengineering* 15.6 (2005): 1125.

INDEX OF REPORTS BY CNF PROJECT NUMBER

111-80	148, 150	1542-07	124	2249-13	38
150-82	86, 186	1645-08	102	2255-13	138
386-90	88, 90	1726-08	18	2260-13	40
522-94	92	1735-08	168	2292-14	140
598-96	152, 154, 156, 158	1738-08	20	2300-14	42
657-97	2	1757-09	22, 104	2306-14	70
731-98	4	1851-09	170	2307-14	72, 74, 76
762-99	6, 8, 112	1858-10	24	2324-15	78
801-99	64	1859-10	26	2331-15	44
848-00	10	1873-10	172	2343-15	126, 182
863-00	56, 188	1880-10	174	2344-15	126, 182
900-00	114, 160	1889-10	106	2345-15	126, 182
996-01	18	1936-10	60	2350-15	194
1119-03	12	1940-10	28	2352-15	196
1121-03	66, 116	1997-11	130, 132	2357-15	128
1122-03	118	2056-11	190	2359-15	142
1177-03	120	2061-11	176	2362-15	80
1208-40	94	2063-11	108	2378-15	46
1225-04	96	2065-11	30	2386-15	198
1255-04	14	2091-11	178	2398-15	200
1262-04	68	2125-12	62	2403-15	48
1314-05	162	2126-12	180	2404-15	50
1356-05	98	2156-12	134	2428-16	82
1371-05	58	2157-12	32	2430-16	52
1380-05	122	2196-13	110	2449-16	144
1400-05	100	2212-13	34		
1486-06	164	2217-13	192		
1520-07	166	2230-13	36	2016 CNF REU Program	
1540-07	16	2232-13	136	54, 84, 146, 184, 202

INDEX OF REPORTS BY CNF USERS & PRINCIPAL INVESTIGATORS

A

Abrahamsson, Sara	140
Aguilar, Victor	46
Allen, Leslie H.	92
Alvarado, Shaun	98
Angenent, Largus T.	48
Aradhya, Sriharsha V.	148
Asermely, Nichole	96

B

Badman, Ryan	20, 54
Badolato, Antonio	106
Baird, Barbara A.	18, 36
Bargmann, Cornelia I.	140
Barrett, Aliyah	60
Bartell, Jason M.	178
Basavarajappa, Vinaya Kumar Kadayra	66
Bau, Haim H.	124
Beaucage, Peter	98
Bhave, Sunil A.	122
Bircan, Baris	114
Black, II, Winston L.	12
Bogdanove, Adam	36
Bogorin, Daniela	172
Borker, Neeraj Nitin Sinai	120, 202
Branch, Ryan (2016 CNF REU)	202
Brown, Thomas	144
Buhrman, Robert A.	148, 150, 158
Burnham, Philip	44

C

Calderon, Brian	64
Caravan, Wagma (2016 CNF REU)	54
Chaudhuri, Reet	32
Chen, Wei-Liang	104
Clancy, Paulette	186
Clay, Noah	196
Cohen, Itai	114
Collette, Robin	156
Collins, Eamon	44
Cordero, Roselynn	22
Cosgrove, Benjamin D.	46
Craighead, Harold G.	6, 8, 112
Curley, Elizabeth	56, 62

D

Davaji, Benyamin	84, 116
Davidson, Patricia	30
De Alba, Roberto	112
de Olazarra, Ana Sofia (2016 CNF REU)	184
De Vlaminck, Iwijn	44
DelNero, Peter	16
DiMarco, Christopher	126
Dodge, Kenneth	162
Dong, Zhao	190
Dorsey, Kyle	114
Dwyer, Ryan	188

E

Elzouka, Mahmoud	128
Erickson, David	24, 34, 134
Evans, Christopher C.	138

F

Fang, Qinghua	40
Fedorchak, Gregory	30
Fischbach-Teschl, Claudia	16
Frey, Brian	174
Fuchs, Gregory D.	178, 180

G

Gallardo, Patricio	110
Gao, Hui	158
Garza, Tanya	192
Gascon, Francisco Romero	50
Ghioni, Massimo	136
Gibbons, Jonathan D.	152, 156, 184
Gillilan, Richard E.	28
Gingerich, Marcus	2
Gosavi, Tanay A.	122
Grab, Jennifer	154
Gray, Isaiah	178
Grogan, Joseph M.	124
Gruner, Sol M.	198
Guimaraes, Marcos	158
Gulinatti, Angelo	136
Gund, Ved	68
Guo, Boyu	100
Guo, Feng	178
Guzman, Juan J.L.	48

H

Hanrath, Tobias	102
Hao, Yu	170
He, Zhenping	96
Head, Steve	144
Hermann, Andreas	58
Heron, John	156
Herzog, Walter	14
Hill, Megan	186
Hoffmann, Roald	58
Hone, James	126, 182
Hopkins, Jesse	28
Howington, Caleb	168

Hu, Yue	42
Hu, Zongyang	194
Huang, Manjie	28
Huang, Meng	10, 40
Hutchings, Matthew	168, 172

I

Illava, Gabrielle	28, 198
Indrajeet	168
Isaac, Corinne E.	62

J

Jagota, Anand	96
Jena, Debdeep	76, 80, 82, 194
Johnson, Don	200

K

Kang, Kibum	164
Kasahara, Kazuki	88
Kidd, Philip	140
Kim, ChulJoo	176
Koopman, Brian	110
Krishna, Athith	108
Kuang, Ping	174
Kushner, Max	36
Kymissis, Ioannis	192
Kysar, Jeffrey	126

L

LaHaye, Matthew	170
Lai, Yiming	106
Lal, Amit	66, 68, 84, 116, 118
Lammerding, Jan	30
Lee, Kan-Heng	164
Lee, Sunwoo	116
Leonard, Timothy	14
Lepak, Lori	52, 142
Li, Mingda	78

Liddell Watson, Chekesha M.	94
Lin, Qiang	130, 132
Lin, Shawn-Yu	174
Lindau, Manfred	10, 40
Ling, Lu	16
Lis, John	36
Liu, Chengyu	138
Liu, Yebin	172
Lu, Jie	4
Luo, Dan	42
Luo, Rui	130
Lynch, David M.	86

M

Ma, Minglin	38
MacMullan, Melanie	28
MacNeill, David	158
MacQuarrie, Evan R.	180
Mahat, Dig Bijay	36
Marohn, John A.	56, 62, 188
Martin, Christopher	196
Martirosyan, Maya (2016 CNF REU)	146
Matsuoka, Fumiaki	98
McEuen, Paul	114, 160
McKee, Bruce	200
Menzel, Matthias	104
Metzler, Meredith	196
Miller, Paula	4
Miskin, Marc	114
Mockler, Brenna	110
Molnar, Alyosha	116
Morgan, John	16
Muller, David	156
Murella, Anoosha	138

N

Nadig, Sachin	118
Nasr, Paméla	62
Ndao, Sidy	128

Nelson, JJ	162, 168
Nguyen, Kayla	156
Niemack, Michael	110
Nomoto, Kazuki	72
Nsanzineza, Ibrahim	162
Nurmukhanov, Aibar	22

O

O'Dell, Dakota	134
Ober, Christopher K.	22, 88, 90, 104
Ou, Yongxi	150

P

Pancoast, Leanna	116
Park, Jiwoong	158, 164, 176
Parpia, Jeevak M.	112, 166
Petersen, Poul	60
Pinrod, Visarute	116, 118
Plourde, Britton L.T.	162, 168, 172
Post, Anthony	174
Prucker, Oswald	104

R

Rahm, Martin	58
Ralph, Daniel C.	148, 152, 154, 156, 158, 184
Ramezani, Meraj	18
Ray, Judhajeet	36
Reinhart-King, Cynthia A.	26
Reinholt, Sarah J.	6
Reynolds, Neal	156, 184
Rinaldi, Fabio Cupri	36
Roach, Kate E.	86
Rogers, Steven	132
Rose, Jocelyn K.C.	50
Rouxinol, Francisco	170
Rugar, Alison	154
Rühe, Jürgen	104
Ruyack, Alexander	68, 84

S

Sanders, Stephanie	60
Santiago-Pinero, Michael	12
Sawatsky, Andrew	14
Schein, Perry	34
Schlom, Darrell	156
Schutter, Brian	146
Sebastian, Abhilash T.	112, 166
Shi, Shengjie	150
Shire, Douglas	2
Shuler, Michael L.	4
Singh, Avtar	36
Smieska, Louisa	188
Smith, Allison (2016 CNF REU)	84
Snodgrass, Ryan	24
Song, Bo	74
Song, Wei	38
Sorg, Victoria	186
Spencer, Michael G.	64, 108
Stelson, Angela C.	94
Stiehl, Gregory	158
Stroock, Abraham D.	12, 16, 120, 202
Suntivich, Jin	138
Swei, Anisa	30

T

Tan, Cheng	182
Tanen, Nicholas	82
Thompson, Michael O.	86, 186
Thorne, Robert	32
Tian, Harvey C.	8
Tirmzi, Syed Ali Moeed	188

V

van Dover, Robert B.	100
Van Slyke, Alexander	36
VanderBurgh, Jacob	26
Verma, Amit	80, 82
Vincent, Olivier	12

W

Wakefield, Devin	18, 36
Walter, Bruce	190
Wang, Haozhi	168
Wang, Lei	160
Wang, Michelle	20, 54
Wang, Ying	4
Whitham, Kevin	102
Wiesner, Ulrich	98

X

Xing, Huili Grace	70, 72, 74, 76, 78, 146, 194
Xu, Hong	90
Xu, Peng	58

Y

Yan, Rusen	70, 146
Ye, Fan	20
Ye, Zichao	92

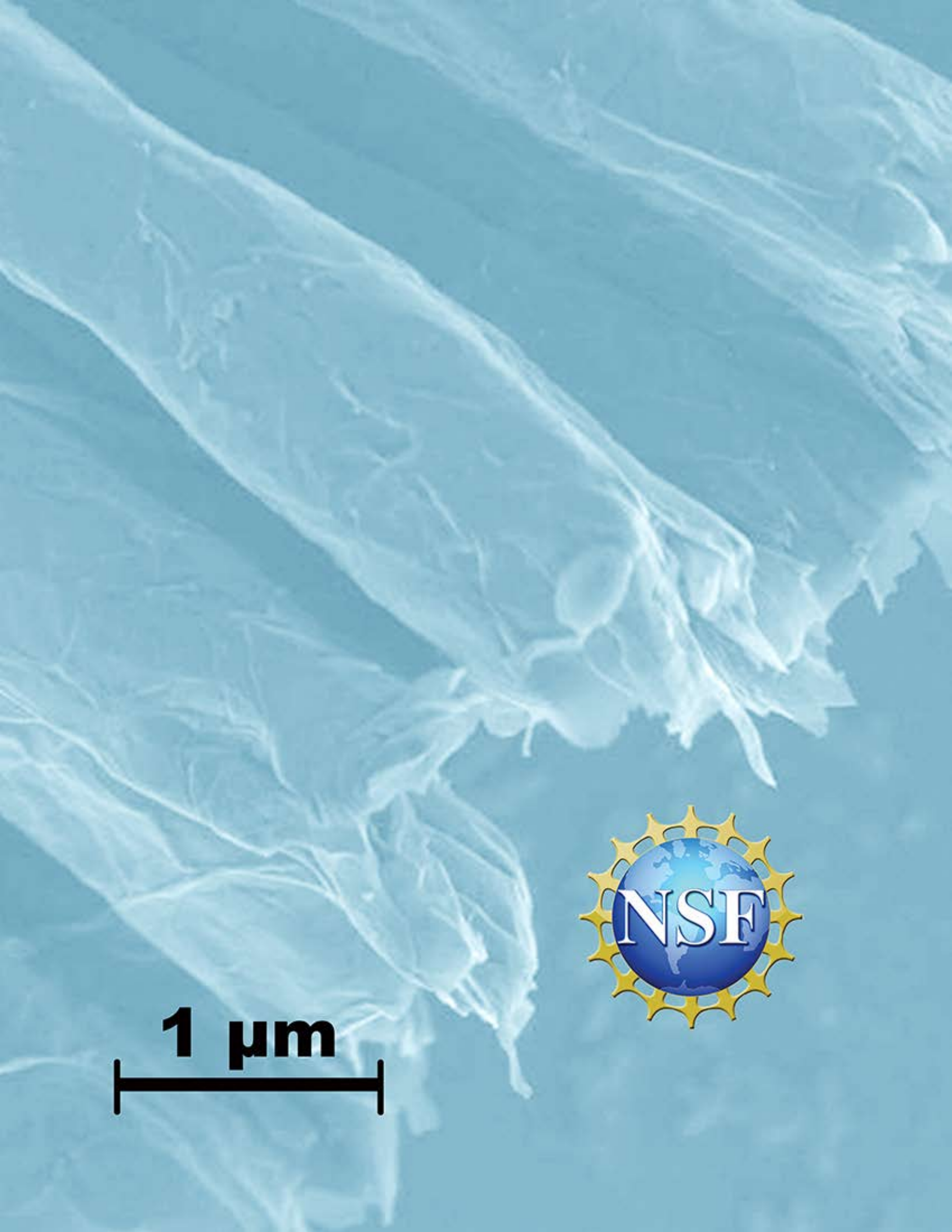
Z

Zhang, Liheng	80, 82
Zhang, Qi	98
Zhao, Ying	40
Zhu, Mingda	76
Zhu, Siyu	12
Zipfel, Warren	36

The CNF 2015-2016 Research Accomplishments were formatted by

:: Ms. Melanie-Claire Mallison ::

She welcomes your comments at mallison@cnf.cornell.edu



1 μm

A black horizontal scale bar with vertical end caps, indicating a length of 1 micrometer.